UNIVERSIDAD COMPLUTENSE DE MADRID

Facultad de Ciencias Físicas
Departamento de Física Aplicada I
(Termología)

TESIS DOCTORAL

Development of polymer nono-fiber, micro-fiber and hollow-fiber membranes for desalination by membrane distillation.

Desarrollo de membranas polméricas de nano-fibras, micro-fibras y fibra hueca para la desalación por destilación en membrana

MEMORIA PARA OPTAR AL GRADO DE DOCTOR
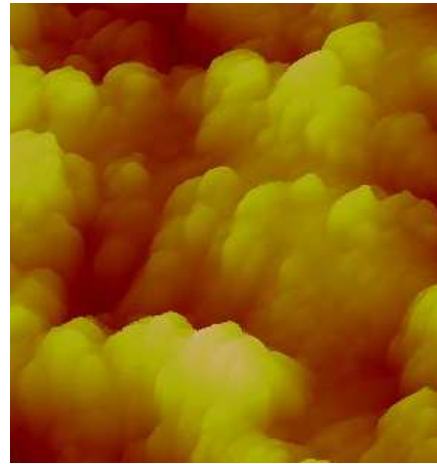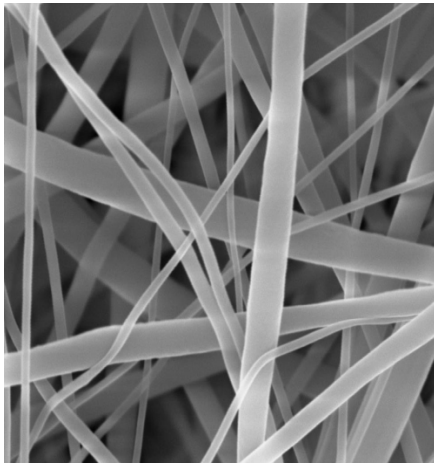
PRESENTADA POR

Mohamed Essalhi

Director

Mohamed Khayet Souhaimi

Madrid, 2014

UNIVERSIDAD COMPLUTENSE DE MADRID

Development of polymer nano-fiber, micro-fiber and hollow-fiber membranes for desalination by membrane distillation

Desarrollo de membranas poliméricas de nano-fibras, micro-fibras y fibra hueca para la desalación por destilación en membrana

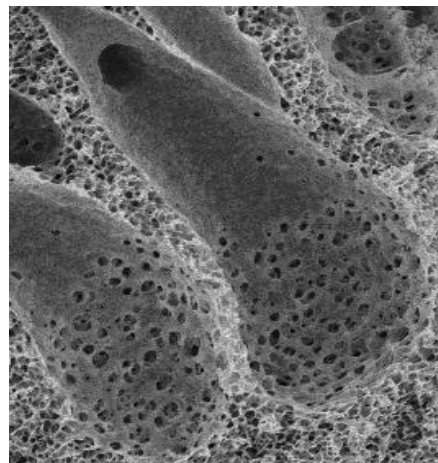**MOHAMED ESSALHI**
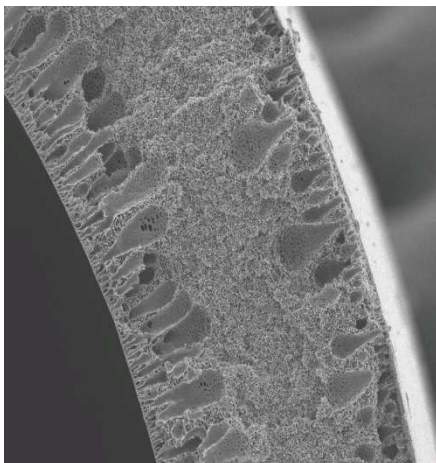
Doctoral Thesis

Madrid 2014

UNIVERSIDAD COMPLUTENSE DE MADRID

Development of polymer nano-fiber, micro-fiber and hollow-fiber membranes for desalination by membrane distillation

MOHAMED ESSALHI

Doctoral Thesis

Madrid 2014

UNIVERSIDAD COMPLUTENSE DE MADRID

DEPARTMENT OF APPLIED PHYSICS I

FACULTY OF PHYSICS

Development of polymer nano-fiber, micro-fiber and hollow-fiber membranes for desalination by membrane distillation

MOHAMED ESSALHI

Doctoral Thesis 2014

Supervised by:

Dr. MOHAMED KHAYET SOUHAIMI

Department of Applied Physics I
Faculty of Physics
University Complutense of Madrid (UCM)
Avda. Complutense s/n, 28040
Madrid (Spain)

Madrid, May 2014

Madrid, 22nd May 2014

To whom it may concern:

Dr. **Mohamed Khayet Souhaimi**, Professor at the Department of Applied Physics I, Faculty of Physics, University Complutense of Madrid,

DECLARES:

That the present research study, entitled *"Development of polymer nano-fiber, micro-fiber and hollow-fiber membranes for desalination by membrane distillation"* and presented by Mr. Mohamed Essalhi for the award of the degree of Doctor in Sciences Physics, has been developed under my supervision at the Department of Applied Physics I, Faculty of Physics, University Complutense of Madrid.

The Thesis is fully adequate in scope and quality as a dissertation for the Degree of Doctor of Philosophy in Sciences Physics with the International Mention. The Thesis has been approved, 24th April 2014, by the Council of the Department of Applied Physics I, Faculty of Physics, of the University Complutense of Madrid.

In witness thereof and for all pertinent purposes, this document is issued and signed in Madrid, on 22nd May 2014.

Singed:

Dr. Mohamed Khayet Souhaimi

Department of Applied Physics I
Faculty of Physics
University Complutense of Madrid
Avda. Complutense s/n, 28040, Madrid (Spain)
Tel. +34-91-394-5185; Fax. +34-91-394-5191; E-mail: khayetm@fis.ucm.es

Acknowledgements

LIST OF PUBLICATIONS AND CONTRIBUTION IN CONGRESSES AND CONFERENCES

- Publications derived from the PhD. Thesis:

1. "*Application of a Porous Composite Hydrophobic/Hydrophilic Membrane in Desalination by Air Gap and Liquid Gap Membrane Distillation: A Compartative Study*".
Autors (b.o signature): **M. Essalhi**, M. Khayet.
Journal: Separation and Purification Technology
Submitted, SEPPUR-D-14-00906   Date: 2014

2. "*Self-sustained webs of polyvinylidene fluoride electrospun nano-fibers: Effects of polymer concentration and desalination by direct contact membrane distillation*".
Authors: **M. Essalhi**, M. Khayet
Journal: Journal of Membrane Science
Volume: 454   Pages: 133-143   Date: 2014

3. "*Self-sustained webs of polyvinylidene fluoride electrospun nanofibers at different electrospinning times: 2. Theoretical analysis, polarization effects and thermal efficiency*".
Authors (b.o signature): **M. Essalhi**, M. Khayet
Journal: Journal of Membrane Science
      Volume: 433   Pages: 180-191   Date: 2013

4. "*Self-sustained webs of polyvinylidene fluoride electrospun nanofibers at different electrospinning times: 1. Desalination by direct contact membrane distillation*".
Autors (b.o signature): **M. Essalhi**, M. Khayet
Journal: Journal of Membrane Science
      Volume: 433   Pages: 167-179   Date: 2013

5. "*Response surface modelling and optimization of electrospinning nanofiber membrane*".
Autors (b.o signature): **M. Essalhi**, M. Khayet, C. Cojocaru, M. C Garcia Payo, P. Arribas.
Journal: The open Nanoscience Journal.
      Volume: 7   Pages: 7-17   Date: 2013

6. "*Surface segregation of fluorinated modifying macromolecule for hydrophobic/hydrophilic membrane preparation and application in air gap and direct contact membrane distillation*".
Autors (b.o signature): **M. Essalhi**, M. Khayet
Journal: Journal of Membrane Science
      Volume: 417-418   Pages: 163-173   Date: 2012

7. "*Hollow fiber spinning experimental design and analysis of defects for fabrication of optimized membranes for membrane distillation*".
Autors (b.o signature): M. Khayet, C. Cojocaru, **M. Essalhi**, M.C. García-Payo, P. Arribas, L. García-Fernández
Journal: *Desalination*

     Volume: 287   Pages: 146-158   Date: 2012

8. "*Water desalination by membrane distillation using PVDF-HFP hollow fiber membrane*".
Autors (b.o signature): M. C. Garcia-Payo, **M. Essalhi**, M. Khayet, L. García Fernández, K. Charif and H. Arafat.
Journal: Membrane Water Treatment

     Volume: 1   Pages: 215-230   Date: 2010

9. "*Effects of PVDF-HFP concentration on membrane distillation performance and structural morphology of hollow fiber membranes*".
Autors (b.o signature): M.C. García-Payo, **M. Essalhi**, M. Khayet.
Journal: Journal of Membrane Science

     Volume: 347   Pages: 209–219   Date: 2010

10. "*Preparation and characterization of PVDF-HFP copolymer hollow fiber membranes for membrane distillation*".
Autors (b.o signature): M.C. García-Payo, **M. Essalhi**, M. Khayet.
Journal: Desalination

     Volume: 245   Pages: 469–473   Date: 2009

- Chapter books:

11. "*Fundamentals of membrane distillation*".
Autors (b.o signature): **M. Essalhi**, M. Khayet.
Book title: Pervaporation, vapour permeation and membrane distillation: Principles and applications
Editors: Angelo Basile, Alberto Figoli, Mohamed Khayet
Editorial: Woodhead Publishing
Chapter 10.   Date: 2014

12. "*Membrane distillation (MD): General description*".
Autors (b.o signature): **M. Essalhi**, M. Khayet.
Book title: Solid-Liquid Separation
Editor: Mathias Stolarski
Editorial: Elsevier   Date: 2014

- Other publications:

13. "*Artificial neural network modelling and response surface methodology of desalination by reverse osmosis*".
Autors (b.o signature): M. Khayet, C. Cojocaru, **M. Essalhi**
Journal: Journal of Membrane Science
    Volume: 368   Pages: 202-214   Date: 2011

14. "*Thermal conductivity of carbon nanotubes and graphene in epoxy nanofluids and nanocomposites*".
Autors (b.o signature): Mario Martin-Gallego, Raquel Verdejo, Mohamed Khayet, Jose Maria Ortiz de Zarate, **Mohamed Essalhi**, Miguel Lopez-Manchado
Journal: Jornal of Nanoscale Research Letters
    Volume: 6(1)   Pages: 1-7   Date: 2011

15. "*Optimization of solar powered reverse osmosis desalination pilot plant by response surface methodology*".
Autors (b.o signature): M. Khayet, **M. Essalhi**, C. Armenta Deu, C. Cojocaru, N. Hilal.
Journal: Desalination
    Volume: 261   Pages: 284–292   Date: 2010

- Contribution in congresses and conferences:

1. "*Estudio de la eficiencia energética en la destilación en membranas con cámara de aire utilizando membranas poliméricas de fibra hueca*".
Autors (b.o signature): L. García-Fernández, **M. Essalhi**, M.C. García-Payo, M. Khayet
Congress: XXXIV Reunión Bienal de la Real Sociedad Española de Física
Place: Valencia (Spain)   Type of presentation: Oral   Date: 15-19 Julio 2013

2. "*Double layered membranes for desalination by air gap membrane distillation and direct contact membrane distillation*".
Autors (b.o signature): **M. Essalhi**, M. Khayet
Congress: 1st International Conference on Desalination Using Membrane Technology
Place: Sitges (Spain)   Type of presentation: Póster   Date: 7-10 April 2013

3. "*Theoretical and experimental studies on desalination through self-sustained electro-spun nano-fibrous membranes*".
Autors (b.o signature): **M. Essalhi**, M. Khayet
Congress: 1st International Conference on Desalination Using Membrane Technology
Place: Sitges (Spain)   Type of presentation: Oral   Date: 7-10 April 2013

4. "*Fabrication and Characterization of Electro-Spun Nano-Fibrous Membranes for Desalination by Membrane Distillation*".
Autors (b.o signature): **M. Essalhi**, M. Khayet
Journal: Procedia Engineering
             Volume: 44   Pages: 235-237   Date: 2012

5. "*Spinning an Optimized Hollow Fiber Membrane for Desalination by Membrane Distillation using Experimental Statistical Designs*".
Autors (b.o signature): **M. Essalhi**; L. Fernández, P. Arribas, M.C. García-Payo, M. Khayet
Journal: Procedia Engineering
        Volume: 44   Pages: 1786-1787   Date: 2012

6. "*Spinning an optimized hollow fiber membrane for desalination by membrane distillation using experimental statistical designs*".
Autors (b.o signature): **M. Essalhi**, L.Fernández, P. Arribas, M.C. García-Payo, M. Khayet
Congress: EUROMEMBRANE Queen Elizabeth II Conference Centre
Place: London (UK)   Type of presentation: Póster   Date: 23-27 Sep 2012

7. "*Fabrication and characterization of electro-spun nano-fibrous membranes for desalination by membrane distillation*".
Autors (b.o signature): **M. Essalhi**, M. Khayet
Congress: EUROMEMBRANE Queen Elizabeth II Conference Centre
Place: London (UK)   Type of presentation: Oral   Date: 23-27 Sep 2012

8. "*Transporte No-Isotermo de Vapor de Agua a Través de Redes Nano-Fobrosas Fabricadas por Electrohilatura*".
Autors (b.o signature): **M. Essalhi**, M. Khayet
Congress: XIII Encuentro Inter-Bienal del Grupo Especializado de Termodinámica (GET)
Place: Orense (España)   Type of presentation: Oral   Date: 03-05 Sep 2012

9. "*Aplicación de la metodología de superficie de respuesta para modelar y optimizar el proceso de Electrohilatura "Electrospinning"*".
Autors (b.o signature): **M. Essalhi**, M. Khayet, C. Cojocaru, M. C. García-Payo, P. Arribas
Congress: XXXIII Reunión Bienal de la RSEF, 21º Encuentro Ibérico de Enseñanza de la Física.
Place: Santander (España) Type of presentation: Oral   Date: 19-23 Sep 2011

10. "*Modelling and optimization of swiping gas membrane distillation of sucrose aqueous solution*".
Autors (b.o signature): M. Khayet, A. Baroudi, C. Cojocaru, **M. Essalhi**
Congress: International Workshop on Membrane Distillation and Related technologies
Place: Ravello (SA) Italia Type of presentation: Póster   Date: 09-12 Oct 2011

11. "*Epoxy Nanocomposites of Carbon Nanotubes and Graphene: Cure Behaviour, DMTA Study and Thermal Conductivity*".
Autors (b.o signature): Mario Martin-Gallego, Raquel Verdejo, Mohamed Khayet, Jose Maria Ortiz de Zarate, **Mohamed Essalhi**, Miguel Angel Lopez-Manchado
Congress: IX Congreso Nacional de Materiales Compuestos
Place: Girona (España)   Type of presentation: Oral   Date: 05-08 Jul 2011

12. "*Modelling and Optimization of solar powered BWRO plants*".
Autors (b.o signature): M. Khayet, **M. Essalhi**, C. Cojocaru, C. Armenta-Deu, N. Hilal
Congress: the 2nd International Chemical Engineering Conference
Place: Amman (Jordan)   Type of presentation: Póster   Date: 11-13 Oct 2010

13. "*Response surface methodology and optimisation of solar powered reverse osmosis plant for brackish water desalination*".
Autors (b.o signature): M. Khayet, **M. Essalhi**, C. Armenta-Deu, C. Cojocaru, and N. Hilal
Congress: The fifth International Conference on Thermal Engineering: Theory and Application
Place: Marrakech Type of presentation: Póster   Date: 10-14 May 2010

14. "*Olive mill wastewater treatment and concentration by membrane distillation using Polytetrafluoethelyne membrane*".
Autors (b.o signature): A. El-Abbassi, A. Hafidi, M. Khayet, **M. Essalhi**, M.C García-Payo
Congress: The fifth International Conference on Thermal Engineering: Theory and Application
Place: Marrakech   Type of presentation: Póster   Date:10-14 May 2010

15. "*Aplicación de la metodología de superficie de respuesta para optimizar el proceso de separación osmosis inversa*".
Autors (b.o signature): **M. Essalhi**, M. Khayet, C. Cojocaru
Congress: XXXII Reunión Bienal de la RSEF, 19º Encuentro Ibérico de Enseñanza de la Física.
Place: Ciudad Real (España) Type of presentation: Oral   Date: 07-11 Sep 2009

16. "*Desalación mediante destilación en membranas con contacto directo utilizando membranas de fibra hueca copolímericas*".
Autors (b.o signature): M.C. García Payo, **M. Essalhi**, K. Charfi, M. Khayet,
Congress: XXXII Reunión Bienal de la RSEF, 19º Encuentro Ibérico de Enseñanza de la Física.
Place: Ciudad Real (España)   Type of presentation: Oral   Date: 07-11 Sep 2009

17. "*Porous copolymer hollow fiber membrane separation and characterization: Direct Contact Membrane Distillation*".
Autors (b.o signature): M. Khayet, M.C. García Payo, **M. Essalhi**
Congress: Seventeenth Symposium on Thermophysical Properties, Third conference on Thermophysical Properties and Transfer Processes of Refrigerants.
Place: Colorado (USA)   Type of presentation: Póster   Date: 21-26 Jun 2009

International scientific short stays:

1- University Paul Sabatier (Toulouse, France): Laboratory of Chemical Engineering.
   December 05th 2011 to March 06th 2012 (3 months)
   Supervisor: Professor Pierre Aïmar

   Subject: Preparation of PVDF porous hollow fiber membranes and their mechanical, functional and chemical characterization for membrane distilaltion. Correlation between the viscosity of the polymer solution and the final structure of the membranes.

2- University Cadi Ayyad (Marrakech, Morocco): Laboratory of Food Sciences in the Faculty of Sciences Semlalia
   April 01st 2009 to 30th June 2009 (3 months)
   Supervisor: Professor Abdellatif Hafidi

   Subject: Treatment of olive mill industrial wastewater with different membrane processes (Ultrafiltration and Membrane Distillation).

Development of polymer nano-fiber, micro-fiber and hollow-fiber membranes for desalination by membrane distillation

ABSTRACT

During last sixty years, membrane science and technology have been incessantly improving trying to find solutions to various environmental issues related with water and energy. This observed improvement is mainly due to the impressive developments of advanced materials used for the fabrication of synthetic membranes and modules as well as the evolution of different related systems, pilot plants and new generation equipments. Because of the worldwide increasing demand of drinkable water, various membrane processes have been proposed for the treatment of seawater, brackish water and different types of industrial wastewaters including brines. These can be divided in two groups:

i)- Isothermal membrane processes such as the hydrostatic pressure-driven membrane processes (i.e. microfiltration, MF; ultrafiltration, UF; nanofiltration, NF and reverse osmosis, RO), the osmotically-driven process forward osmosis (FO), the electric potential-driven process electrodialysis (ED), etc.

ii)- Non-isothermal membrane processes such as thermo-osmosis (TO) and membrane distillation (MD) that can use waste heat and renewable energy sources such as solar energy.

In general, non-isothermal transport phenomena through membranes have received much less attention than the corresponding isothermal counterparts. However, during last 13 years interest on membrane distillation (MD) technology has increased significantly in different experimental and theoretical aspects. This is attributed to its outstanding advantages especially in desalination field producing not only distilled water but also ultra-pure water. In fact, MD is known 50 years ago but only recently it has made its way towards industrial applications. It is still need to be improved further in various key aspects. The main drawback is the lack of membranes designed specifically for MD. The used membranes in MD purposes are fabricated for other membrane processes, MF and UF. In other words, still there is no company in the market offering MD membranes. Therefore the technology is still not fully used

commercially. The offered membrane modules and pilot plants are expensive and mostly are restricted to only some research groups for their further evaluations and experimental improvements at laboratory scale not for their industrial applications.

It is worth quoting that a significant interest on the design and development of membranes for MD technology is increasing during last decade. About 23% of the total published studies on MD during last 10 years (up to 31st December 2013) are focused on membrane fabrication and membrane modification for MD purposes. Therefore, the main objective of this PhD. Thesis is to develop novel and advanced membranes of different shapes and structures for desalination by MD. It consists on the following chapters:

The first chapter covers a comprehensive historical perspective of MD, the possible MD configurations, the important key characteristics of MD, the membranes used so far in MD, the modules proposed for MD, the required characteristics of an adequate MD membrane and a suitable module, the different transport mechanisms through MD membranes and theoretical models, the fields of applications of MD and future trends related to interesting and promising research fields in MD. All this broad MD reference base was reported in two chapter books [1,2].

The second chapter is dedicated to a novel porous composite hydrophobic/hydrophilic membrane proposed for desalination by different MD configurations. This type of membrane was prepared by the simple phase inversion method, in a single casting step, using a blend polymer solution containing a fluorinated surface modifying macromolecule (SMM) and a hydrophilic polymer, polyetherimide (PEI). During membrane formation, SMM migrates to the top membrane surface increasing its hydrophobicity and decreasing its pore size, nodule size and roughness parameters. The membrane was characterized by different techniques. It was found that the thickness of the porous hydrophobic top layer was around 4 μm. The MD experiments were performed for different sodium chloride aqueous solutions and various operating conditions using direct contact membrane distillation (DCMD), air gap membrane distillation (AGMD) and liquid gap membrane distillation (LGMD). Comparative studies have been made between these MD configurations. Compared to AGMD and LGMD, the water production rate was found to be higher for DCMD because of the low resistance to mass transport

achieved by the diminution of the water vapor transport path length through the hydrophobic thin top-layer of the membrane. This bi-layered hydrophobic/hydrophilic membrane proved to be attractive for desalination by DCMD technology instead of AGMD. The obtained results were published in [3]. Interesting results were derived from the performed comparative study of LGMD and AGMD. These results were compiled for publication [4].

Nowadays, the hollow fiber membrane configuration is the most favored membrane geometry in most industrial membrane separation applications. Hollow fiber membrane modules exhibit large surface area per unit volume. Furthermore, hollow fiber membranes are mechanically self-supporting, have good flexibility and are easy to assemble in modules. The third chapter deals with different types of hollow fiber membranes prepared by the dry/wet spinning method using different solutions of poly(vinylidene fluoride-hexafluoropropylene), PVDF-HFP and the additive polyethylene glycol (PEG). The effects of various spinning parameters (concentration of the copolymer, concentration of the additive, air gap length, temperature, internal coagulant flow rate, take-up speed and pressure) on the morphological characteristics of the prepared fibers have been investigated. Various characterization techniques were employed to determine the necessary MD characteristics of the hollow fiber membranes. First attempts were made applying a fractional factorial design and the steepest ascent method for possible fabrication of hollow fibers. The developed approach permits localization of the region of experimentation, defect-free spinning conditions, to produce hollow fibers. An optimal hollow fiber membrane exhibiting the highest performance index and the greatest global desirability (i.e. high permeate flux and salt rejection factor) was fabricated using the determined optimum spinning conditions. The prepared PVDF-HFP hollow fiber membranes were used for desalination by direct contact membrane distillation (DCMD). An increase in the PVDF-HFP concentration of the spinning solution resulted in a decrease in the precipitation rate and a transition of the cross-section structure from a *finger-type* structure to a *sponge-type* structure; whereas the increase of the PEG content in the spinning solution resulted in a faster coagulation of the PVDF-HFP copolymer and a transition of the cross-section internal layer structure from a *sponge-type* structure to a *finger-type* structure. In addition, water entry pressure values were decreased, whereas both the void volume fraction and the DCMD permeate flux increased with decreasing

the copolymer concentration. These results were published in the following three papers [5,6,7,8].

In order to reduce the heat transfer by conduction through the MD membrane and increase the thermal efficiency of the MD process, micro- and nano-fibrous membranes with a high void volume fraction were proposed. The fourth chapter is about micro- and nano-fibrous membranes prepared by electrospinning for desalination by MD. Different self-sustained electrospun membranes (ENMs) were prepared using the polymer polyvinylidene fluoride (PVDF) and different electrospinning parameters. The statistical experimental design and response surface methodology (RSM) have been used to develop predictive models for simulation and optimization of ENMs. The optimum operating conditions guarantying a small PVDF fiber diameter with a narrow distribution were determined. The obtained permeate fluxes in this study are higher than those reported so far for ENMs. The results were published in [9].

The effects of the PVDF concentration on the characteristics of ENMs and their DCMD performance were investigated for the first time. The viscosity, electrical conductivity and surface tension of the used PVDF solutions were measured, and the effects of the PVDF concentration on the fiber diameter, thickness, water contact angle, inter-fiber space, void volume fraction, liquid entry pressure, mechanical and thermal properties of the ENMs were studied. Among the prepared ENMs, the optimized membrane exhibiting the highest DCMD performance was prepared with 25 wt% PVDF concentration. The results were reported in [10].

A systematic experimental study on the effects of membrane thickness on the DCMD performance was also carried out for the first time in chapter 4. It was observed an enhancement of the thickness and the liquid entry pressure of water with the increase of electrospinning time, a decrease of the mean size of the inter-fiber space; whereas no significant changes were observed for the diameter of the electrospun fibers, the void volume fraction and the water contact angle. The effects of the ENMs thickness on the DCMD performance was studied for different feed temperatures and sodium chloride feed aqueous solutions with concentrations up to 60 g/L, which is about two times greater than a typical seawater concentration. The permeate flux of the ENMs is lower for longer electrospinning time and the obtained permeate fluxes in this study are higher than those reported so far for PVDF ENMs. These results were published in [11].

A novel theoretical model that considers the gas transport mechanisms through the inter-fiber space of ENMs was also developed for DCMD in chapter 4. The theoretical model involves the structural characteristics of the ENMs, the heat transfer mechanisms and the nature of mass transport through self-sustained webs of ENMs. In contrast to what it is reported in other theoretical MD studies considering Bosanquet equation with equal mass transport contributions for Knudsen diffusion and ordinary molecular diffusion, in this PhD. Thesis, the contribution of each mass transport mechanism was considered variable and it was evaluated. It was found that the Knudsen contribution increases with the increase of the ratio of the mean electrospun fiber diameter to the inter-fiber space. The predicted permeate fluxes were compared with the experimental ones and reasonably good agreements between them were found. It was observed an enhancement of the thermal efficiency with the increase of the feed temperature, being in all cases for all studied ENMs greater than 78.8%, and the heat transfer by conduction was less than 20% of the total heat transferred through the ENMs. These values are better than those observed for other membranes used in MD demonstrating that ENMs are advanced membranes and more adequate for water production with high energy efficiency. These results were published in **[12]**.

Finally, some general and interesting conclusions from the present PhD. Thesis together with future research studies are summarized in the last chapter.

Keywords:

Membrane Distillation; Nano-fiber; Micro-fiber; Hollow fiber; Novel membranes; Advanced membranes; Polymeric membranes; Flat-sheet membrane; Hollow fiber membrane; Nano-fibrous membrane; Micro-fibrous membrane; Porous membrane; Hydrophobic membrane; Phase inversion; Dry/jet wet spinning; Electrospinning; Membrane characterization; Desalination; Water production; Water treatment; Heat and mass transport; Theoretical analysis; Statistical experimental design; Optimization; Response surface methodology; Surface modifying macromolecule; Membrane modification; Composite hydrophobic/hydrophilic membrane; polyvinylidene fluoride; poly(vinylidene fluoride-hexafluoropropylene); Polyetherimide; Scanning electron microscopy; Atomic force microscopy; Porometry; Gas permeation test; Liquid entry pressure; Pore size distribution; Porosity; Contact angle; Differential scanning calorimetry; Mechanical tests, etc.

Desarrollo de membranas poliméricas de nano-fibra, micro-fibra y fibra hueca para la desalación por destilación en membrana

RESUMEN

Durante los últimos sesenta años, la ciencia y tecnología de membranas han estado en continuo desarrollo tratando de encontrar soluciones a diversos problemas medioambientales relacionados con el agua y la energía. Esta observada mejoría se debe principalmente a los avances tan impresionantes de materiales avanzados para la fabricación de membranas y módulos así como de la evolución de distintos sistemas, plantas piloto y equipos de última generación. Debido a la creciente demanda de agua potable a nivel mundial, se han propuesto diversos procesos de membrana para el tratamiento de agua de mar, agua salobre y de diferentes tipos de aguas residuales industriales, incluyendo salmueras. Estos procesos se dividen en dos grupos:

i)- Procesos isotérmicos como los procesos de membrana impulsados por presión hidrostática (i.e. microfiltración, MF; ultrafiltración, UF; nanofiltración; NF y ósmosis inversa, OI); el proceso de membrana impulsado por presión osmótica, la ósmosis directa (OD); el proceso de membrana impulsado por potencial eléctrico, la electrodiálisis (ED), etc.

ii)- Procesos no-isotérmicos como la termo-ósmosis (TO) y la destilación en membrana (DM) que pueden utilizar calor residual y fuentes de energía renovable como la energía solar.

En general, los fenómenos no-isotérmicos de transporte a través de membranas han recibido mucha menos atención que los isotérmicos. Sin embargo, durante los últimos 13 años el interés en la tecnología de destilación en membrana (DM) ha aumentado considerablemente en diferentes aspectos tanto teóricos como experimentales, debido a sus notables ventajas especialmente en el campo de la desalación permitiendo la producción no solamente de agua destilada pero también de agua ultra-pura. De hecho, la DM se conoce hace 50 años, pero sólo recientemente ha abierto camino hacia sus aplicaciones industriales. Todavía se tiene que seguir mejorando en varios aspectos clave. El principal inconveniente es la falta de membranas diseñadas específicamente para la DM. Las membranas utilizadas hasta la fecha en la DM se fabrican para otros

propósitos y procesos de membrana, MF y UF. En otras palabras, todavía no hay aparecido en el mercado ninguna empresa que ofrezca membranas DM. Por consiguiente la tecnología DM no se encuentra totalmente implementada a nivel comercial. Los módulos de membrana disponibles y las plantas piloto DM son caros. Además, en la mayoría de las veces sus usos son limitados por el fabricante a algunos grupos de investigación para sus evaluaciones y mejoras experimentales a escala de laboratorio no para sus aplicaciones industriales.

Se ha visto durante la última década un interés creciente en el diseño y desarrollo de membranas para la tecnología DM. Alrededor del 23% de los estudios publicados sobre la DM durante los últimos 10 años (hasta el 31 de Diciembre de 2013) se centraron en la fabricación de membranas y modificación de las mismas para la DM. Por lo tanto, el principal objetivo de esta Tesis Doctoral es desarrollar nuevas membranas de diferentes formas y estructuras para la desalación por DM.

En el primer capítulo se presenta una reseña histórica de la DM, sus posibles configuraciones, sus características clave más importantes, las membranas utilizadas hasta el momento en la DM, los módulos propuestos para la DM, las características que debe cumplir una membrana DM y un módulo adecuado para la aplicación DM, los diferentes mecanismos de transporte a través de una membrana DM y los modelos teóricos relacionados, los campos de aplicación de la DM y finalmente las tendencias futuras de la DM relacionadas con los campos de investigación más interesantes y prometedores. Toda esta amplia información ha sido recogida en dos capítulos de libros **[1,2]**.

El segundo capítulo trata sobre la fabricación y caracterización de un nuevo tipo de membranas porosas compuestas hidrófoba/hidrofílicas para la desalación empleando diferentes configuraciones DM. Esta membrana fue preparada por el simple método de inversión de fase, en una sola etapa, empleando una disolución polimérica que contiene una macromolécula modificadora de superficie fluorada (SMM) y un polímero hidrofílico polieterimida (PEI). Durante la formación de la membrana, la SMM migra a su superficie superior aumentando su hidrofobicidad y reduciendo su tamaño de poro, nódulo y rugosidad. La membrana fue caracterizada por medio de diferentes técnicas. Se consiguió preparar membranas con una capa superior hidrófoba y porosa muy delgada con un espesor de alrededor de 4 μm. Los experimentos de DM se realizaron

con disoluciones acuosas de cloruro sódico de diferentes concentraciones y varias condiciones de operación utilizando destilación en membrana con contacto directo (DMCD), destilación en membrana con cámara de aire (DMCA) y destilación en membrana con cámara de líquido (DMCL). Se llevaron a cabo estudios comparativos entre estas configuraciones DM. Se observó una alta tasa de producción de agua en la configuración DMCD debido a la baja resistencia al transporte de masa, conseguida por la simple disminución de la distancia que recorren las moléculas de vapor de agua a través de la capa hidrófoba delgada de la membrana. Se confirmó que la membrana de doble capa hidrófoba/hidrofílica es más atractiva para la tecnología de desalación por DMCD en vez de la DMCA. Los resultados de los estudios de este tipo de membrana en las configuraciones DMCD y DMCA fueron publicados en [3]. Los resultados más interesantes derivados de la comparación entre la DMCL y la DMCA fueron recogidos en [4].

Hoy en día la membrana de fibra hueca es la geometría más demandada en la mayoría de las aplicaciones de separación industriales. Los módulos de membranas de fibra hueca exhiben una gran área superficial por unidad de volumen. Además, las membranas de fibra hueca son mecánicamente auto-sostenidas, son más flexibles y fáciles de montar en módulos. El tercer capítulo es sobre diferentes membranas de fibra hueca preparadas por el método de hilatura por inversión de fase seco/mojado "dry/wet spinning" empleando diferentes disoluciones del co-polímero poli(fluoruro de vinilideno-hexafluoropropileno), PVDF-HFP y del aditivo polietilenglicol (PEG). Se investigaron los efectos de varios parámetros de fabricación (concentración del co-polímero, concentración del aditivo, longitud del hueco de aire, temperatura, flujo del coagulante interno, velocidad de desalojo de las fibras durante su formación y presión sobre la disolución co-polimérica) en las características morfológicas y estructurales de las fibras huecas preparadas. Se emplearon varias técnicas de caracterización para determinar los parámetros necesarios en una membrana DM de fibra hueca. Los primeros intentos se realizaron aplicando el diseño factorial fraccionado y el método de ascenso de máxima pendiente "steepest ascent method" para determinar la región de experimentación y posible fabricación de fibras huecas sin defectos. Se determinaron las condiciones de hilatura óptimos y se logró fabricar una membrana de fibra hueca óptima exhibiendo altos flujos de permeado y factores de rechazo de sales. Las membranas de fibra hueca PVDF-HFP preparadas se utilizaron en el proceso de desalación por

destilación en membrana con contacto directo (DMCD). El aumento de la concentración de PVDF-HFP en la disolución co-polimérica resultó en una disminución de la velocidad de coagulación del PVDF-HFP y una transición de la estructura interna de la membrana de una estructura *tipo dedo "finger-type structure"* a una estructura *esponjosa*; mientras que el incremento de la cantidad del aditivo PEG en la disolución co-polimérica aumentó la velocidad de coagulación del PVDF-HFP provocando una transición de la estructura interna de la membrana del tipo *esponjoso* a un estructura *tipo dedo*. Además, con la disminución de la concentración de PVDF-HFP, la presión de entrada de líquido dentro de los poros de la membrana se redujo; mientras que tanto la fracción de volumen vacío como el flujo de permeado por DMCD ambos aumentaron. Los resultados fueron publicados en **[5,6,7,8]**.

Con el fin de reducir la transferencia de calor por conducción a través de la membrana DM y aumentar la eficiencia térmica del proceso DM, se propusieron membranas micro- y nano-fibrosas con alta fracción de volumen vacío. El cuarto capítulo trata sobre membranas avanzadas micro- y nano-fibrosas (ENMs) preparadas por electro-hilatura "electro-spinning" para la desalación por DM. Diferentes membranas ENMs fueron preparadas usando el polímero fluoruro de polivinilideno (PVDF) y diferentes parámetros de electro-hilatura. En un principio, se utilizó el diseño experimental estadístico y la metodología de superficie de respuesta (RSM) para desarrollar modelos predictivos de simulación y optimización de las membranas ENMS. Se determinaron las condiciones óptimas de fabricación con el fin de preparar fibras de PVDF de pequeños diámetros con una distribución estrecha. Los flujos de permeado obtenidos en este estudio fueron superiores a los publicados hasta el momento para las membranas ENMs. Los resultados relacionados fueron publicados en **[9]**.

Por primera vez se investigó el efecto de la concentración del polímero PVDF en las características de las membranas ENMs y en su rendimiento en la desalación por DMCD. La viscosidad, la conductividad eléctrica y la tensión superficial de las disoluciones de PVDF fueron medidas y se investigaron los efectos de la concentración de PVDF en el diámetro de la fibra, espesor de la membrana, ángulo de contacto que forma el agua encima de la membrana, espacio entre fibras, fracción de volumen vacío, presión de entrada de líquido dentro del espacio entre fibras, propiedades mecánicas y térmicas de las membranas, etc. Entre todas las membranas ENMs preparadas, la membrana óptima que exhibe el más alto rendimiento de DMCD fue fabricada con una

concentración de PVDF en la disolución de 25 % en peso. Estos resultados fueron recogidos en el artículo **[10]**.

Se llevó a cabo por primera vez un estudio experimental sistemático sobre los efectos del espesor de la membrana en el rendimiento de la DMCD. Con el aumento del tiempo de electro-hilatura, se observó un aumento del espesor de las membranas ENMs y de su presión de entrada de líquido en el espacio entre sus fibras; así como una disminución del espacio medio entre fibras. No se detectaron cambios significativos del diámetro de las fibras, de la fracción de volumen vacío de las membranas ENMs y de su hidrofobocidad. El efecto del espesor de las membranas ENMs en el rendimiento de la DMCD se estudió para diferentes temperaturas de alimentación y disoluciones salinas de cloruro sódico con concentraciones hasta 60 g/L que es una concentración dos veces mayor que la concentración típica de agua de mar. El flujo de permeado es menor para las membranas preparadas con mayor tiempo de electro-hilatura y los flujos de permeado obtenidos en este estudio son superiores a los publicados hasta el momento para membranas ENMs preparadas con el polímero PVDF. Estos resultados fueron publicados en **[11]**.

Se desarrolló un nuevo modelo teórico que considera los mecanismos de transporte de gases a través del espacio entre fibras de las membranas ENMs utilizadas en la DMCD. El modelo teórico tiene en consideración las características estructurales de las membranas ENMs, los mecanismos de transferencia de calor y la naturaleza del transporte de masa a través de la red de fibras. A diferencia de lo publicado hasta la fecha en varios estudios teóricos de DM que consideran la ecuación de Bosanquet con igual contribución de transporte de masa para la difusión tipo Knudsen y la difusión molecular, por primera vez en esta Tesis Doctoral la contribución de cada mecanismo de transporte de masa fue considerada variable y evaluada. Se observó un amento en la contribución tipo Knudsen con el incremento de la razón entre el diámetro de la fibra y el espacio entre fibras. Los flujos de permeado calculados por medio del modelo teórico fueron comparados con los flujos de permeado experimentales encontrándose buenos acuerdos entre ambos. Se observó un incremento en la eficiencia térmica con el aumento de la temperatura de la disolución alimento, siendo en todos los casos para todas las membranas ENMs estudiadas mayor de 78.8%, y el calor transferido por conducción a través de las membranas ENMs inferior al 20% del calor total transferido. Estos valores son mejores que los obtenidos para otras membranas utilizadas en la DM

demostrando que las membranas ENMs son adecuadas para la producción de agua con una alta eficiencia energética. Estos resultados fueron publicados en **[12]**.

Por último, algunas conclusiones generales más interesantes derivadas de la presente Tesis Doctoral junto con futuros estudios de investigación se resumen en el último capítulo.

Palabras clave:

Destilación en Membrana; Nano-fibra; Micro-fibra; Fibra hueca; Nuevas membranas; Membranas avanzadas; Membranas poliméricas; Membrana plana; Membrana de fibra hueca; Membrana nano-fibrosa; Membrana micro-fibrosa; Membrana porosa; Membrana hidrófoba; Inversión de fases; Hilatura seco/mojado; Electro-hilatura; Caracterización de membranas; Desalación; Producción de agua; Tratamiento de agua; Transporte de calor y masa; Análisis teórico; Diseño experimental estadístico; Optimización; Metodología de superficie de respuesta; Macromolécula modificadora de superficie; Modificación de membranas; Membrana compuesta hidrófoba/hidrofílica; Fluoruro de polivinilideno; Poli (fluoruro de vinilideno-co-hexafluoropropileno); Polieterimida; Microscopía electrónica de barrido; Microscopía de fuerza atómica; Porometría; Permeación de gas; Presión de entrada de líquido; Distribución de tamaño de poro; Porosidad; Ángulo de contacto; Calorimetría diferencial de barrido; Ensayos mecánicos, etc.

References:

[1] M. Essalhi, M. Khayet, Fundamentals of membrane distillation, Chapter in Book: Pervaporation, vapour permeation and membrane distillation: Principles and applications, Editors: Angelo Basile, Alberto Figoli, Mohamed Khayet, Editorial: Woodhead Publishing (2014).

[2] M. Essalhi, M. Khayet, Membrane distillation (MD): General description, Chapter in Book: Solid-Liquid Separation, Editor: Mathias Stolarski, Editorial: Elsevier (2014).

[3] M. Essalhi, M. Khayet, Surface segregation of fluorinated modifying macromolecule for hydrophobic/hydrophilic membrane preparation and application in air gap and direct contact membrane distillation, Journal of Membrane Science, 417-418 (2012) 163-173.

[4] M. Essalhi, M. Khayet, Application of a porous composite hydrophobic/hydrophilic membrane in desalination by air gap and liquid gap membrane distillation: A compartative study, Separation and Purification Technology, Submitted, Ref. SUPPUR-D-14-00906, (2014).

[5] M.C. García-Payo, M. Essalhi, M. Khayet, Effects of PVDF-HFP concentration on membrane distillation performance and structural morphology of hollow fiber membranes, Journal of Membrane Science, 347 (2010) 209–219.

[6] M.C. García-Payo, M. Essalhi, M. Khayet, Preparation and characterization of PVDF-HFP copolymer hollow fiber membranes for membrane distillation, Desalination, 245 (2009) 469–473.

[7] M. Khayet, C. Cojocaru, M. Essalhi, M.C. García-Payo, P. Arribas, L. García-Fernández, Hollow fiber spinning experimental design and analysis of defects for fabrication of optimized membranes for membrane distillation, Desalination, 287 (2012) 146-158.

[8] M.C. Garcia-Payo, M. Essalhi, M. Khayet, L. García Fernández, K. Charif, H. Arafat, Water desalination by membrane distillation using PVDF-HFP hollow fiber membrane, Membrane Water Treatment, 1 (2010) 215-230.

[9] M. Essalhi, M. Khayet, C. Cojocaru, M. C Garcia Payo, P. Arribas, Response surface modelling and optimization of electrospinning nanofiber membrane, The open Nanoscience Journal, 7 (2013) 7-17.

[10] M. Essalhi, M. Khayet, Self-sustained webs of polyvinylidene fluoride electrospun nano-fibers: Effects of polymer concentration and desalination by direct contact membrane distillation, Journal of Membrane Science, 454 (2014) 133-143.

[11] M. Essalhi, M. Khayet, Self-sustained webs of polyvinylidene fluoride electrospun nanofibers at different electrospinning times: 1. Desalination by direct contact membrane distillation, Journal of Membrane Science, 433 (2013) 167-179.

[12] M. Essalhi, M. Khayet, Self-sustained webs of polyvinylidene fluoride electrospun nanofibers at different electrospinning times: 2. Theoretical analysis, polarization effects and thermal efficiency, Journal of Membrane Science, 433 (2013) 180-191.

INDEX

CHAPTER 1

MEMBRANE DISTILLATION (MD):
GENERAL DESCRIPTION AND FUNDAMENTALS

1.1. Membrane Distillation (MD): General Description

Contents:

1.1.1. Membrane Distillation Separation Technology and its Variants

1.1.2. Membrane Distillation Modules and Fluid Flow

1.1.3. Membrane Distillation Applications: Filtration and Separation

1.1.4. Tips, Remarks and Future Directions in MD

References

Abstract:

During last 13 years interests on membrane distillation (MD) technology has increased significantly in different experimental and theoretical aspects. In this chapter, MD is described in general including terminology, history, possible MD configurations, membranes, modules and applications in different fields. Membranes together with their required characteristics as well as recent commercial modules offered by some companies are provided. An overview of different MD applications is also reported. Tips on MD improvements, related interesting research fields, advised membranes and modules including fluid flow dynamics are indicated.

1.1.1. Membrane Distillation Separation Technology and its Variants

Membrane distillation (MD) is a separation process that involves both non-wetting porous membrane and phase change generally applied for the treatment of solutions in which water is the major component for:

- Separation of water from dissolved solutes and production of distilled/potable water including ultra-pure water,
- Concentration of non-volatile dissolved solutes in aqueous solutions and recycling of valuable materials,
- Removal of volatile solutes from aqueous solution and their concentration in the permeate including separation of azeotropic mixtures, etc.

In this process, separation is carried out based mainly on the two phase changes, evaporation and condensation. Evaporation occurs at the liquid/vapour interfaces formed at one side of non-wetted pores of a hydrophobic membrane, inside the membrane module, whereas condensation step can be taken place inside or outside the membrane module, depending on the MD variant. These involved two phase change phenomena are the origin of the term MD, similar to conventional distillation. Other terms such as thermo-pervaporation, pervaporation, membrane evaporation, capillary distillation and transmembrane distillation were used before 1986 [1,2]. However, MD is known since June 1963, when Bodell filed the first patent on MD [3]. However, the first MD publication was done in form of paper four years later in 1967 [4]. Since then interest in MD process has been faded quickly because the obtained water production rate was low compared to other processes such as reverse osmosis (RO). In the early of the 1980s MD has recovered much interest when novel membranes with better characteristics and modules became available [5-15].

The membrane required for MD applications must be porous and at least one of its layers must be hydrophobic and must not be wetted by the liquid phase. Only vapor is transported through this hydrophobic layer being the driving force the transmembrane partial pressure gradient. In addition, the membrane must not alter the vapor/liquid equilibrium of the involved compounds and condensation must not occur inside its pores. The hydrophobic nature of the membrane prevents liquid aqueous solutions from entering its pores due to the surface tension forces resulting in the formation of liquid/vapor interfaces at the extremes of each pore. In most cases, to establish the transmembrane driving force and the necessary latent heat for evaporation, the feed

aqueous solution is heated to temperatures between 30ºC and 90ºC (i.e. below the boiling point of the aqueous liquid feed solution). Therefore, simultaneous heat and mass transfer occur in this process.

To establish the necessary driving force, different MD variants can be considered. The differences between them are made only in the permeate side (Fig. 1.1.1):

i)- *Direct contact membrane distillation* (DCMD): An aqueous solution colder than the feed solution is circulated tangentially to the permeate side of the membrane. The transmembrane temperature difference induces the necessary vapor pressure difference. In this case the volatile molecules of the feed aqueous solution (water or volatile organic compounds, VOCs) evaporate at the hot feed liquid/vapor interface, cross the membrane pores in vapor phase and condense at the cold liquid/vapor interface inside the membrane module. Care must be taken in this case in order to prevent wetting of the pores from the permeate side of the membrane when using VOCs having low surface tension. During the treatment of aqueous solutions containing VOCs, the concentration of the volatile solute in the permeate aqueous solution will increase and will be high compared to the feed aqueous solution. Therefore the risk of membrane pore wetting from the membrane permeate side will be high. En general, DCMD is used for production of distilled/potable water using feed aqueous solutions containing non-volatile solutes, e.g. desalination.

ii)- *Sweeping gas membrane distillation* (SGMD): A gas, such as air or nitrogen, sweeps the permeate side of the membrane carrying the evaporated molecules outside the membrane module for condensation. In this MD variant the gas temperature and its hydrostatic pressure are kept below those of the feed aqueous solution. SGMD is used mostly for distilled/potable water production, concentration of solutes in the feed membrane side as well as the removal and concentration of VOCs in aqueous solutions. This variant is sometimes called membrane gas stripping or membrane air stripping (MAS) [16-18]. When a dense and selective membrane is used in the membrane module instead of a porous and hydrophobic membrane, the process is termed sweeping gas pervaporation [19,20].

iii)- *Air gap membrane distillation* (AGMD): In this case a cold condensing surface is placed inside the membrane module and a stagnant air gap is interposed between the membrane and the condensation surface to solve the problem of heat loss by conduction through the membrane, which leads to relatively low thermal efficiency of MD. The evaporated volatile molecules cross first the membrane pores and the air gap thickness to finally condense over the cold surface inside the membrane module. The permeate water exits from the bottom part of the membrane module taking advantage of the gravity. Because condensation is carried out over a cold surface rather than directly on the membrane surface, AGMD variant can be applied in fields where the DCMD is limited such as the removal of VOCs from aqueous solutions. In addition, AGMD is also applied for potable/distilled water production and concentration of non-volatile solutes in the feed aqueous solutions. Because the permeate flux has to overcome the air barrier between the membrane and the condensing surface it is reduced depending on the effective air gap width.

iv)- *Liquid gap membrane distillation* (LGMD): This is another variant of MD combining both DCMD and AGMD configurations. In this case the air gap between the membrane and the cold surface is kept to be filled by a stagnant cold liquid solution, frequently the produced distilled water. AGMD module is used but the air gap space between the membrane and the condensing surface is filled with the produced water. The permeate water exits from the top part of the membrane module. This configuration also received the name permeate gap membrane distillation (PGMD). Like DCMD, LGMD is also applied generally for water production and concentration of non-volatile solutes in the feed side of the membrane module. If the air gap between the membrane and the cold surface is filled with any solid material such as a porous support, sand or sponge material, the process is called material gap membrane distillation (MGMD) although this claimed new configuration is either AGMD or LGMD [21].

v)- *Thermostatic sweeping gas membrane distillation* (TSGMD): This MD variant combines both SGMD and AGMD in order to minimize the temperature of the sweeping gas, which increases considerably along the membrane module length because of the heat transferred from the feed side through the membrane to the permeate side. In SGMD, the gas temperature, the heat transfer rate and the mass transport through the membrane change during the gas progression along the membrane module. The

presence of the cold wall in the permeate side reduces the increase of the sweeping gas temperature resulting in an enhancement of the driving force and the water production rate as a consequence. TSGMD can also be applied for distilled/potable water production, concentration of the non-volatile solutes in the feed aqueous solution and concentration of VOCs in aqueous solutions.

vi)- *Vacuum Membrane Distillation* (VMD): In this case vacuum or a low pressure is applied in the permeate side of the membrane module by means of a vacuum pump. The downstream pressure is maintained below the saturation pressure of volatile molecules to be separated from the feed aqueous solution. External condensers are needed to collect the permeate. At laboratory scale, nitrogen liquid cold traps are often used when a very low downstream pressure is applied. VMD is generally used for separation of VOCs from water. Membranes having smaller pore size (i.e. less than 0.45 μm) than in the other MD variants are used providing that in VMD the risk of pore wetting is high. When a dense and selective membrane is used in the membrane module instead of a porous and hydrophobic membrane this process is termed pervaporation [22].
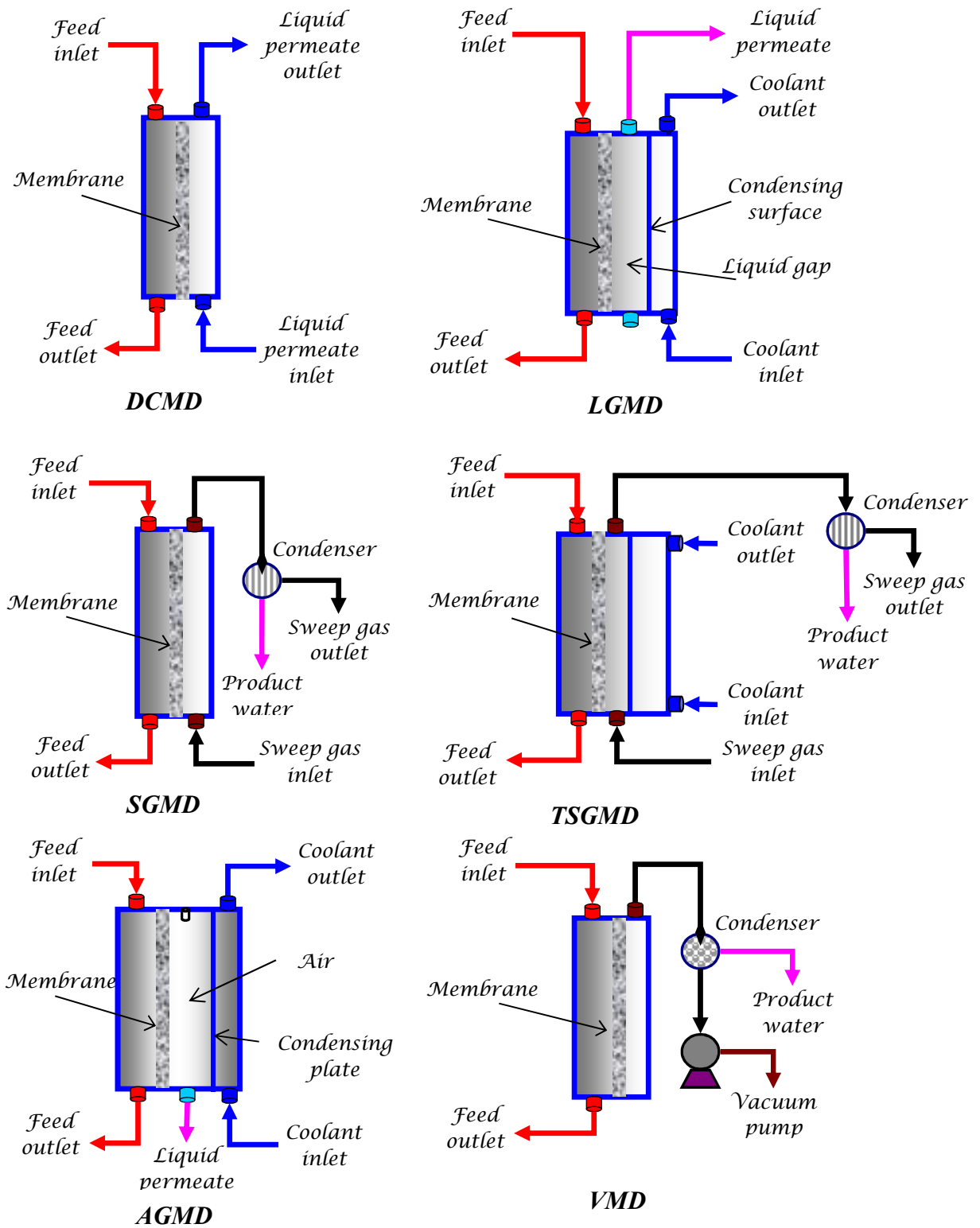
Figure 1.1.1. MD process variants: DCMD, SGMD; AGMD; LGMD; TSGMD and VMD.

For a given application, an adequate MD configuration is selected among the above cited MD variants taking into consideration the type of the feed solution, their benefits and drawbacks. Currently, MD technology is gaining an increasing importance in membrane processes (Fig. 1.1.2) and becomes more attractive than other popular separation processes because MD:

- exhibits high rejection factors (near 100%) of non-volatile solutes present in water such as ions, macromolecules, colloids, cells, etc.

- can be operated at lower temperatures than conventional distillation so that waste heat and/or alternative energy sources, such as solar and geothermal can be used.

- can be operated at lower operating hydrostatic pressures than conventional pressure-driven membrane processes used in filtration and liquid separation (i.e. reverse osmosis, RO; nanofiltration, NF; ultrafiltration, UF; microfiltration, MF).

- can be combined with other processes in integrated systems (i.e. pressure-driven membrane processes; forward osmosis, FO, etc.).

- uses membranes with less demanding membrane mechanical properties and reduced chemical interactions with process solution.

- it needs smaller spaces compared to conventional distillation processes.

- can be used in applications where other processes cannot be applied or their applications are very expensive (e.g. treatment of aqueous solutions with high osmotic pressures or with a solute concentration near saturated solution).

- requires less pre-treatment steps compared to other membrane processes.

- exhibits less fouling propensity compared to other pressure-driven membrane processes.

In spite all these cited advantages, the main limitation of MD is the drawback of membrane pore wetting. This can be avoided by using membranes with high liquid entry pressure (*LEP*) of feed solution inside the membrane pores (i.e. high hydrophobicity membranes, high water contact angles) and small maximum pore size, and the feed aqueous solution when containing solutes with low surface tension must be sufficiently dilute. This limits MD for certain applications such as the separation of organic/organic solutions and the treatment of highly concentrated aqueous solutions with surfactants, alcohols and VOCs in general. The present MD technology is still need

to be improved for its adequate industrial implementation in different separation applications. Multi-staged MD systems, development of adequate membranes and membrane modules for MD, improvement of economical and energy efficiency of MD systems are actual proposed research areas.

As it can be seen in Fig. 1.1.2, interest on MD has increased significantly. Among the published papers in International Journals up to 31st December 2013, the most used MD variant is DCMD with 58.6 % of the MD published studies because in this configuration condensation phenomenon is carried out inside the membrane module leading in this way to a simple operation mode. However, compared to the other MD variants the air entrapped within the pores of a membrane used in DCMD results in a high mass transfer inefficiency, while the heat loss by conduction through the membrane, which is considered heat loss in MD is high. In contrast, SGMD is the least studied MD variant with only 4.5 % of the MD published studies because this MD variant requires external condensers to collect the permeate and a source for gas circulation. However, SGMD combines a relatively low conductive heat loss through the membrane with a reduced mass transfer resistance. As occurred in AGMD variant, in SGMD there is a gas barrier that reduces the heat loss by conduction through the membrane. Nevertheless, compared to AGMD variant the gas in SGMD sweeps the membrane resulting in higher mass transfer coefficients and therefore higher permeate fluxes. It is worth noting that the calculated percentages of the two MD variants TSGMD and LGMD are negligible. In practically all the published MD studies, commercial microporous hydrophobic membranes available in capillary or flat sheet forms, have been used although these membranes were prepared initially for other purposes, for example microfiltration (MF). Some commercial membranes commonly used in MD are presented in Table 1.1.1.

Table 1.1.1. Some commercial membranes used in MD (membrane thickness, δ, mean pore size, d_p; porosity, ε; liquid entry pressure of water in the membrane pores, LEP_w) (Reprinted from [23] Khayet 2011, copyright (2011), with permission from Elsevier).

Membrane type	Membrane name	Manufacturer	Material	δ (μm)	d_p (μm)	ε (%)	LEP_w (kPa)
Flat sheet membranes	TF200	Gelman	PTFE/PP [a]	178	0.20	80	282
	TF450				0.45		138
	TF1000				1.00		48
	GVHP	Millipore	PVDF [b]	110	0.22	75	204
	HVHP			140	0.45		105
	Gore		PTFE	64	0.2	90	368
				77	0.45	89	288
			PTFE/PP [a]	184	0.2	44	463
	Enka		PP	100	0.1	75	--
	3MA	3M Corporation		91	0.29 [c]	66	--
	3MB			81	0.40 [c]	76	
Capillary membranes	Accurel ® S6/2 MD020CP2N [d]	AkzoNobel Microdyn		450	0.2	70	140
	MD020TP2N	Enka Microdyn		1550	0.2	75	--
	Accurel ® BFMF 06-30-33 [e]	Enka A.G. Euro-Sep		200	0.2	70	

[a] Flat sheet polytetrafluoroethylene, PTFE, membranes supported by polypropylene, PP, or polyethylene, PE.
[b] Flat sheet polyvinylidene fluoride, PVDF, membranes.
[c] Maximum pore size.
[d] Shell-and-tube capillary membrane module: Filtration area: 0.1 m^2, inner capillary diameter: 1.8 mm; length of capillaries: 470 mm.
[e] Shell-and-tube capillary membrane module: Filtration area : 0.3 m^2, inner capillary diameter: 0.33 mm, length of capillaries: 200 mm.

A membrane for MD application has to meet the following requirements simultaneously [24]:

- good thermal stability for temperatures ranging from ambient temperature up to the boiling temperature of water,

- high chemical resistance to a wide range of aqueous solutions,

- high permeability membranes taking into account that there is an increase of the permeate flux with the increase of the membrane pore size and porosity, and with a decrease of the membrane thickness and pore tortuosity;

- high liquid entry pressure (*LEP*), which is the minimum transmembrane hydrostatic pressure that is applied on the membrane before liquid solution penetrates into the pores. The *LEP* is characteristic of each membrane. It is high for membranes prepared with a high hydrophobicity material (i.e. large water contact angle) and a small maximum pore size. However, when using a membrane with a small maximum pore size, the *LEP* is high but the permeability of the membrane is low.

- narrow pore size distribution,

- low thermal conductivity because the heat transferred by conduction through the membrane from the feed to the permeate side is heat loss in MD. This conductive heat loss is greater for thinner membranes. However, using thicker membranes contradicts the achievement of high permeability. Therefore, a compromise exists between a membrane having a high permeability and a low heat transfer by conduction.

It is worth noting that only 16.8 % of the MD published studies are focused on membrane engineering for MD, i.e. design and fabrication of membranes specifically for MD (Fig. 1.1.2). Very few authors have considered the possibility of manufacturing novel membranes and membrane module designs specifically for MD applications [23-25]. Hydrophobic porous membranes can be prepared by different techniques depending on the properties of the used materials that should be selected according to criteria including compatibility with the feed aqueous solutions, cost, ease of fabrication and assembly, useful operating temperatures and thermal conductivity, which must be as low as possible. Microporous membranes can be made by sintering, stretching, phase inversion or thermally-induced phase separation (TIPS) [24,26,27]. The MD membrane

can be a single hydrophobic layer (i.e. conventional and most used membrane type), a composite porous bi-layered hydrophobic / hydrophilic membrane or composite tri-layered hydrophilic/hydrophobic/hydrophilic or hydrophobic / hydrophilic / hydrophobic porous membranes. Both supported and unsupported membranes with different structures are used in MD and their pore sizes ranges between 10 nm to 1 μm. Recently nanostructured, hybrid and exotic membranes are designed for MD applications [23,24,28]. As can be seen in Fig. 1.1.2 there is a growing interest on membrane engineering for MD and therefore the future of MD is promising as a consequence.
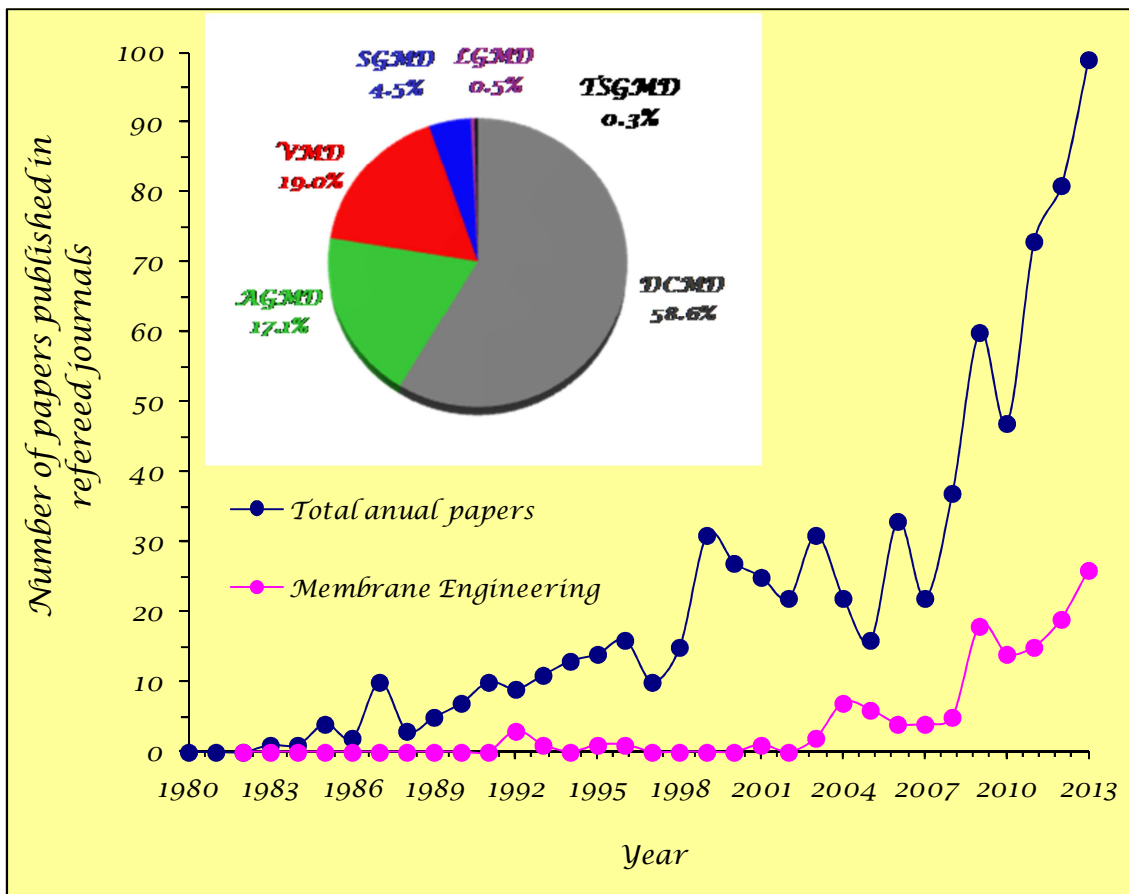

Figure 1.1.2. Growth of MD activity up to 31st December 2013 represented as a plot of number of papers published in refereed journals per year, annual published studies on membrane design and fabrication for MD applications and percentages of the studied MD variants.
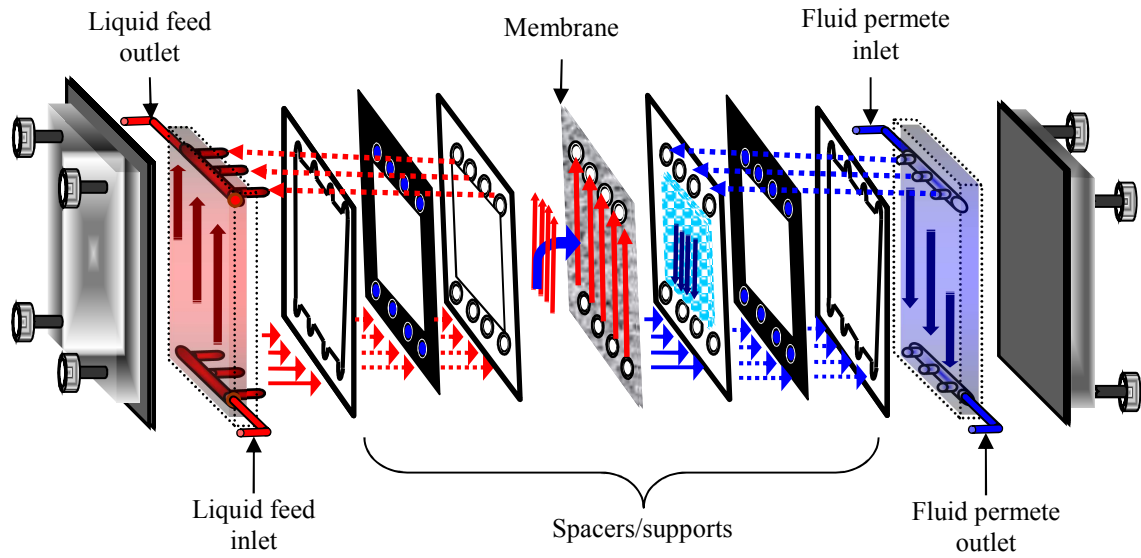
15

1.1.2. Membrane Distillation Modules and Fluid Flow

Various types of membrane modules were designed for each MD variant and tested in different systems and applications. There are three major MD module configurations, which are plate-and-frame module, shell-and-tube or tubular module and spiral wound membrane module. Figure 1.1.3 shows schematic diagrams of these modules. Different types of membranes were packed in a large variety of module configurations and tested in MD systems.

The magnitude of the permeate flux obtained in the MD process is also affected significantly by the module design, the MD configuration and its operating conditions not only the membrane itself. In addition to the previously mentioned membrane requirement, a good module to be used in MD must:

- exhibit a high packing density (i.e. high membrane surface area) with an optimized size and a high membrane module performance (i.e. high permeability and high separation factor),
- use housing with high resistance to chemicals, pressures and temperatures (i.e. high thermal stability),
- pack properly the membrane in potting resins, free of cracks and with a good adhesion,
- permit its drying in case of membrane wetting problem as well as easy inspection and defects reparation,
- allow high feed and permeate flow rates tangentially to the membrane or in cross-flow mode including baffles, spacers and/or turbulent promoters in order to increase the heat and mass transfer coefficients, reduce the effects of the both the temperature polarization (i.e. thickness of the thermal boundary layer) and concentration polarization (i.e. thickness of the concentration boundary layer) and increase the thermal efficiency,
- provide high mass and heat transfer rates between the bulk solutions and the membrane surface,
- satisfy low pressure drop along the membrane module length to prevent excessively high transmembrane hydrostatic pressures that may cause wetting of membrane pores,

- guarantee uniform flows throughout the whole membrane module avoiding dead corners and channel formation,

- guarantee low heat loss to the environment and if possible a good heat recovery system,

- avoid erosion problems by using for example plastic materials,

- contain a membrane support if necessary, that must be chosen to be strong enough to prevent deflection or rupture of the membrane,

- be properly designed allowing an easy cleaning and membrane replacement, with low scaling, low fouling, etc.

(a)

(b)

Figure 1.1.3. MD modules: (a) plate-and-frame; (b) shell-and-tube or tubular and (c) spiral wound membrane module for AGMD or LGMD variants (Reprinted from [29] Winter et al., 2011, copyright (2011), with permission from Elsevier; Reprinted from [30] Winter et al., 2012, copyright (2012), with permission from Elsevier). (To be continued).

18

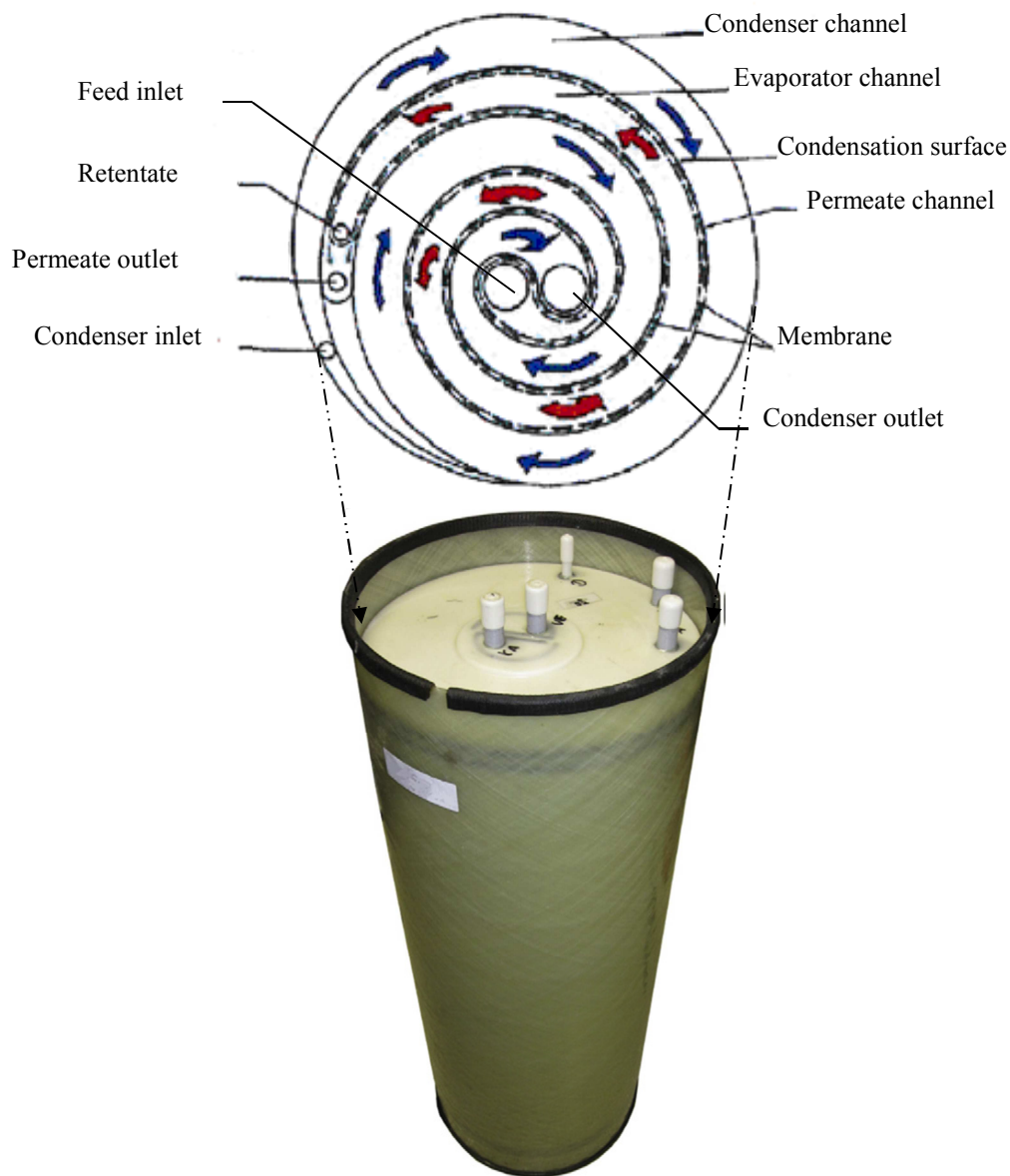**Figure 1.1.3**. MD modules: (a) plate-and-frame; (b) shell-and-tube or tubular and (c) spiral wound membrane module for AGMD or LGMD variants (Reprinted from [29] Winter et al., 2011, copyright (2011), with permission from Elsevier; Reprinted from [30] Winter et al., 2012, copyright (2012), with permission from Elsevier). (Continuation).

It is to be noted that the choice of a membrane module for each *MD* configuration is usually determined by both economic and operative conditions. Most of laboratory scale membrane modules are plate-and-frame modules designed for use with flat sheet membranes due to their versatility and simplicity in fabrication, as compared to the spiral wound or shell-and-tube membrane modules. In fact, flat sheet membranes can easily be removed from a plate-and-frame module for their examination, cleaning or replacement and the same module can be used to test different membranes. However, tubular or shell-and-tube membrane modules fabricated using capillary or hollow fiber membranes are more attractive than plate-and-frame modules fabricated with flat sheet membranes because much higher membrane surface area to module volume ratio can be packed. The packing density of plate-and-frame membrane modules can vary between 100 and 400 m^2/m^3 depending on the number of membrane sheets [24]. On the other hand, a large number of membrane capillaries or hollow fibers can be packed in the modules with packing densities of about 600 - 1200 m^2/m^3 [24]. In the case of hollow fiber membranes the inner diameters are even smaller, 50 - 100 μm, and thousands of hollow fibers can be packed in shell and tube membrane modules with very high packing densities, which may reach 3000 m^2/m^3. Capillary or hollow fiber membranes do not require any support and are an integrated part of the module. The main inconvenient is the membranes in these last modules can not be replaced easily in case the membrane pores are wetted by liquid solutions. Capillary membranes were also assembled in plate-and-frame membrane modules in cross-flow mode to reduce the temperature polarization effect by increasing the heat transfer coefficients [31]. Considerably enhanced water production rate in both DCMD and VMD configurations were achieved. Flat sheet membranes were also arranged in spiral wound modules as shown in Fig. 1.1.3 and the membrane packing density normally ranges between 300 and 1000 m^2/m^3, depending on the channel height. Spiral wound modules for MD has been first proposed in 1982 by Gore & Associated Co. [7] and then by Hanbury and Hodgkiess three years later [32]. Later, commercial spiral wound membrane modules were used in DCMD [33], AGMD or LGMD variants with an integrated heat recovery for the design of solar-powered desalination system [34].

The majority of the designed membrane modules for MD were more academically orientated than industrially. Several attempts of commercialization have failed due to difficulties in engineering aspects. Reliability of the membrane module is still a serious issue in MD and each configuration imposes certain fluid dynamic conditions on both

feed and permeate sides. Actually, the availability of industrial MD modules is one of the limitations for MD process industrial implementation. A historical survey together with different designs of membrane modules for MD was described in details in [24]. Nowadays, the most relevant companies and research institutions in the world developing MD membrane modules and applying MD on a commercial scale are:

- **Scarab Development AB and XZero AB (Sweden)**: Scarab Development AB was founded in 1973 in order to exploit low temperature distillation technologies. Plate-and-frame AGMD module design was patented by Scarab in 1981 (Fig. 1.1.4a). The Swedish company XZero acquired the license to use Scarab´s technology in semiconductor industry for producing ultrapure water systems with zero liquid discharge [35]. The AGMD modules have been tested by different institutions in Sandia National Laboratory in the US [36], by the University of Texas at El Paso sponsored by the US Bureau of Reclamation [37,38], using solar thermal collectors in Spain and Mexico under the frame of MEDESOL project [39] and in the Royal Institute of Technology (Department of Energy Technology) in Stockholm (Sweden) for water purification in cogeneration plants [40].

- **Fraunhofer Institute for Solar Energy System and SolarSpring GmbH (Germany)**: In 2003 Fraunhofer ISE began developing spiral wound AGMD modules with different sizes and with an integrated heat recovery for different solar-powered desalination systems installed in the Island of Gran Canaria in Spain, Jordan, Egypt, Mexico, Pantelleria in Italy and Amarika in Namibia (Fig. 1.1.3c, Fig. 1.1.4b) [34,41-47]. These modules were also considered for LGMD. SolarSpring GmbH, based in Freiburg, Germany, was founded in 2009 as a spin-off of Fraunhofer ISE. Its overall objective is the design and installations of decentralized autonomous systems for remote areas.

- **Memstill, TNO (Netherlands Organisation for Applied Scientific Research), Keppel Seghers (Belgium) and Aquastill (The Netherlands)**: Memstill technology initiated its technology development in 1999 and emerged during 2006. It was developed by a consortium including TNO (Netherlands Organisation for Applied Scientific Research) and Keppel Seghers Belgium N.V. (formerly known as Seghers Keppel Technology N.V.). The design consists of an AGMD module, in which the cold

saline water flows through a condenser with non-permeable walls, increasing its temperature due to the condensing permeate, and then passes through a heat exchanger where additional heat is added before entering in direct contact with the membrane (Fig. 1.1.4-c, first pilot modules with 300 m^2 of membrane) [48]. The technology was patented by TNO in 1999 and 2005 and licensed to Aquastill (founded in 2008) and Keppel Seghers. Memstill pilot plants have been operating since 2006 in Singapoore, in Belgium (BASF Antwerp) and in the Netherlands [49]. In Singapore (Jurong Island), the plans of Memstill were to operate at 100 m^3 per day on a petroleum refinery. It was claimed a thermal energy consumption as low as 56 to 100 kWh/m^3 with a *GOR* as high as 11.2 calculated for feed temperatures of 80 – 90 ºC with an electrical energy of 0.75 kWh/m^3 [34]. In 2008 and 2009, there was a large investment to reduce the cost of this type of MD modules [49]. It was observed that since 2012 Aquastill offers AGMD, DCMD and LGMD installations.

- **Memsys (Germany, Singapoore) and Aquaver (The Netherlands)**: The Memsys system is based on vacuum enhanced multi effect AGMD variant incorporating heat recovery and recycling in a plat-and-frame membrane module (Fig. 1.1.4d). The Stages are composed of alternative hydrophobic membrane and foil (Polypropylene, PP) frames. Each stage recovers the heat of condensation providing a multiple-effect design while the distillate is produced in each evaporation/condensation stage and in the condenser. The module components are made of PP, which eliminates corrosion and scaling and allows large-scale cost efficient production. The company´module production started in 2010 and their pilot plants have been installed in Singapore, Australia and India among others [49,50]. In Singapoore, Memsys Clearwater Pte Ltd and Nanyang Technological University (NTU) are collaborating on the treatment of water contaminated with oil. In November 2011, Memsys and Aquaver (part of Ecover Group) agree on exclusive license agreement to cooperate worldwide on small scale units for potable water supply and process water applications. In 2012, Memsys awarded EWI grant to build a 50 m^3/day MD test system at Senoko Power Plant, the largest power supplier in Singapore. General Electric Co. (GE) and Memsys Clearwater Pte Ltd (Germany and Singapore) have entered into an agreement to develop Memsys´s MD technology for the unconventional resource applications including shale gas, coal seam gas and other fuels recovered by hydraulic fracturing (high saline produced water). With Concord Enviro Systems Pvt Ltd of Mumbai (India), Germany´s Memsys

have signed a global license agreement for co-operation on treating molasses waste-water from sugar industries [51].
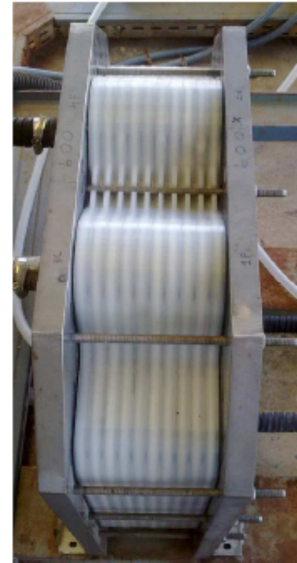
(a)

(b)

Figure 1.1.4. Commercial modules: (a) Scarab AB and XZero AB [35,36,40,52], (b) Fraunhofer ISE (Reprinted from [29] Winter et al., 2011, copyright (2011), with permission from Elsevier), (c) Memstill (Reprinted from [50] Jansen et al., 2013, copyright (2013), with permission from Elsevier; Reprinted from [53] Hanemaaijer et al., 2006, copyright (2006), with permission from Elsevier), (d) Memsys (Reprinted from [54] Zhao et al, 2013, copyright (2013), with permission from Elsevier; Reprinted from [55] Ong et al., 2012, copyright (2012), with permission from Elsevier). (To be continued)

(c)

Figure 1.1.4. Commercial modules: (a) Scarab AB and XZero AB [35,36,40,52], (b) Fraunhofer ISE (Reprinted from [29] Winter et al., 2011, copyright (2011), with permission from Elsevier), (c) Memstill (Reprinted from [50] Jansen et al., 2013, copyright (2013), with permission from Elsevier; Reprinted from [53] Hanemaaijer et al., 2006, copyright (2006), with permission from Elsevier), (d) Memsys (Reprinted from [54] Zhao et al, 2013, copyright (2013), with permission from Elsevier; Reprinted from [55] Ong et al., 2012, copyright (2012), with permission from Elsevier). (To be continued)

24

| Frame | Single stage with welded frames + covering plates | Multiple stages |

1 - Electrical preheater
2 - MEMD control unit
3 - Power delivery unit
4 - Vacuum pump
5 - Siphons

6 - Modules (6)
7 - Steam raiser unit (SRU)
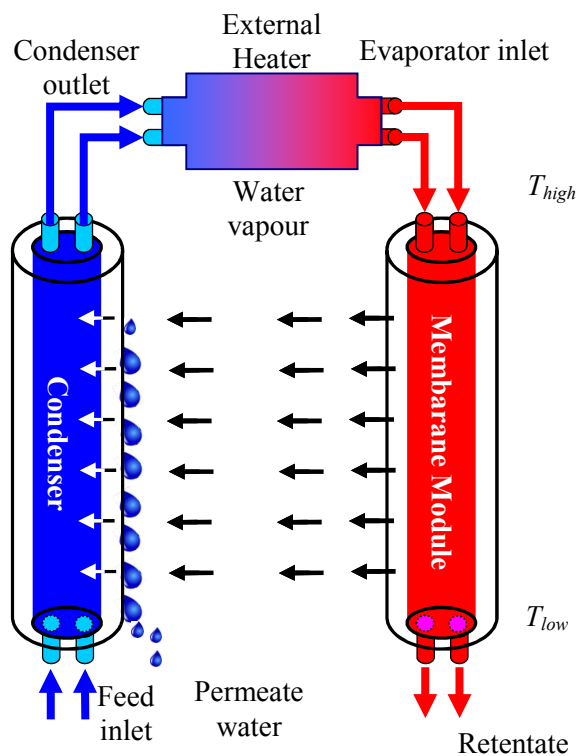8 - Condenser
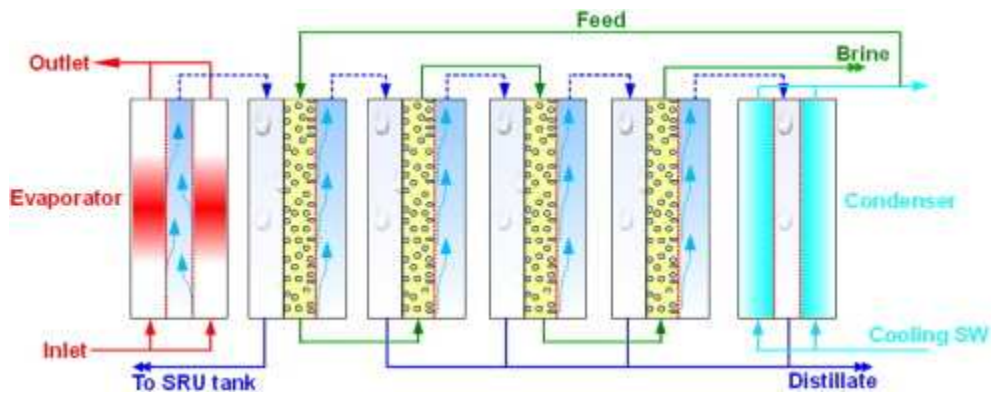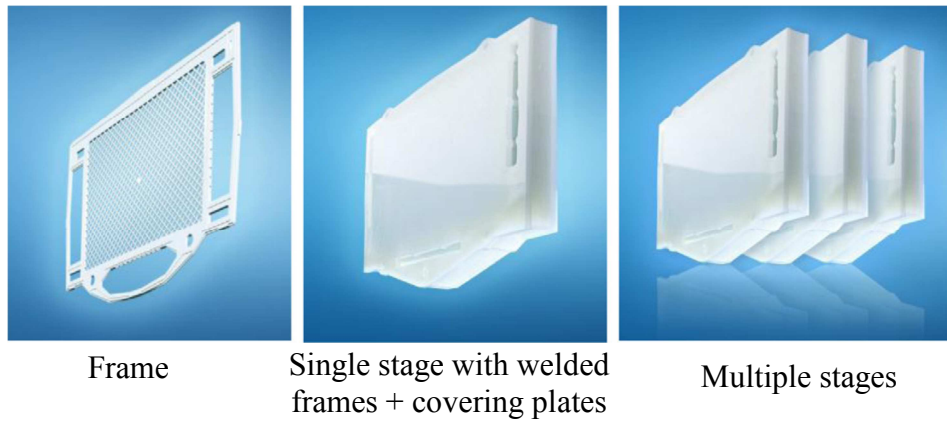9 - Distillate tank
10 - SRU distillate tank

(d)

Figure 1.1.4. Commercial modules: (a) Scarab AB and XZero AB [35,36,40,52], (b) Fraunhofer ISE (Reprinted from [29] Winter et al., 2011, copyright (2011), with permission from Elsevier), (c) Memstill (Reprinted from [50] Jansen et al., 2013, copyright (2013), with permission from Elsevier; Reprinted from [53] Hanemaaijer et al., 2006, copyright (2006), with permission from Elsevier), (d) Memsys (Reprinted from [54] Zhao et al, 2013, copyright (2013), with permission from Elsevier; Reprinted from [55] Ong et al., 2012, copyright (2012), with permission from Elsevier). (Continuation)
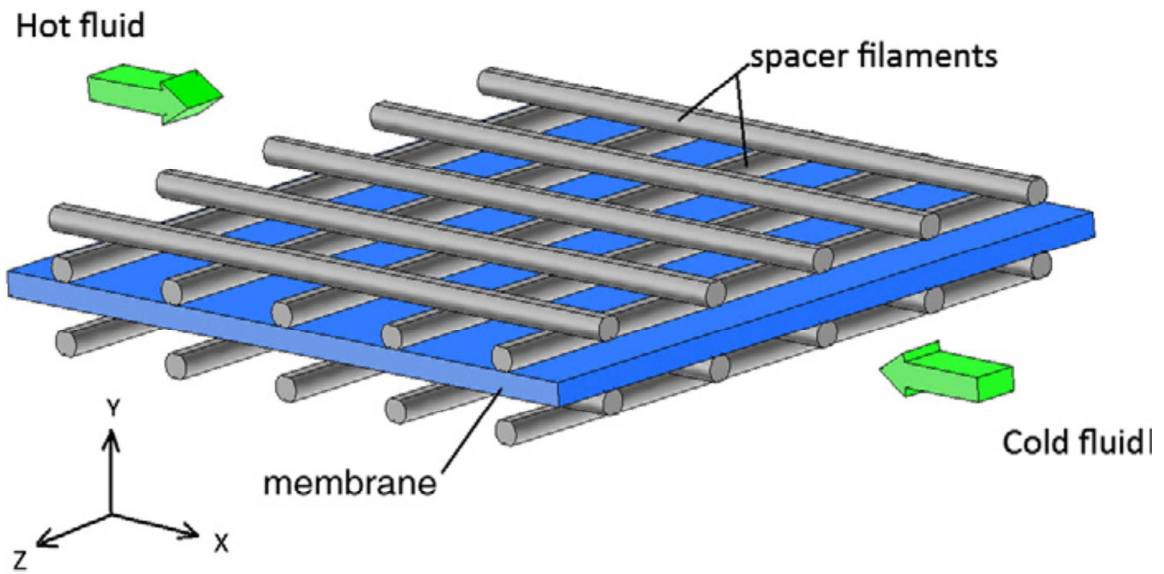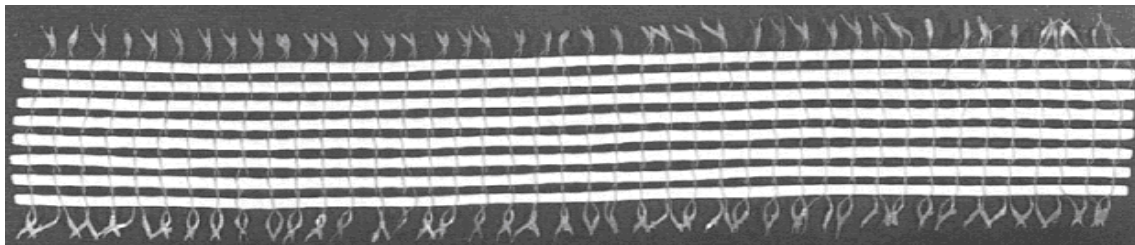
Other compact modules including solar MD modules were presented by different research institutions [24,56-60]. In addition to the development of novel MD membranes, researchers have investigated strategies to improve the MD process such as optimizing MD operating parameters (i.e. flow rates and temperatures) and designing novel modules to reduce temperature polarization, concentration polarization, fouling, scaling, pressure drop and therefore enhance permeate flux [31,61-67].

The permeate flux in MD increases with the increase of the feed flow rate or permeate flow rate in the MD module channels when these are operated under laminar or transitional flow hydrodynamic regimes, whereas it tends to an asymptotic value when the flow regime is turbulent. As the flow rate increases the thickness of the thermal and/or the concentration boundary layers in the membrane module channels become thin and results in low effects of temperature polarization and concentration polarization. For example, in SGMD variant the sweeping gas flow rate is together with the feed temperature are the important parameters controlling the permeate flux of MD [68]. The main temperature polarization in SGMD is located in the air phase and permeate flux in the SGMD process is mostly controlled by the heat transfer through the air boundary layer.

Computational fluid dynamics (CFD) techniques was applied for optimum design of different MD membrane modules [69-73]. Thermo-fluid dynamics of a MD module showed that spacers can significantly affect temperature gradients within its channel, permitting to design an optimal spacer (Fig. 1.1.5) [63,71,73,74]. It was also suggested that by adding baffles to the modules the fluid dynamics may reduce the temperature polarization effect responsible for low permeate fluxes in MD modules (Fig. 1.1.5). Inserting baffles in membrane modules creates fluid instabilities in the liquid flow and the formed vortices improve the mixing between the boundary layer (i.e. temperature and concentration layers) of the membrane. Furthermore, if the fibers are twisted or braided (Fig. 1.1.5) instead of been arranged straight or in a fabric, more turbulent and uniform flow outside the fibers can be produced leading to an enhancement of both heat and mass transfer coefficients in the shell side of the membrane [63,75]. Bundles with twisted or braided fibers act as static mixers around the fibers. However, special care must be taken because the used spacers or baffles filled channels have an electrical energy penalty because of the increase of the backpressure [73,76,77].

(a)

(b)
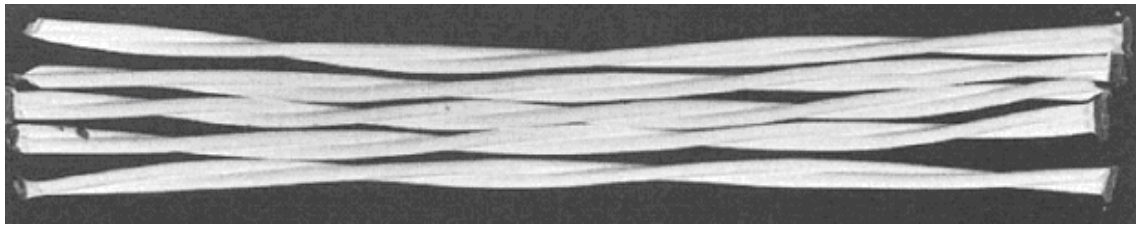
(c)
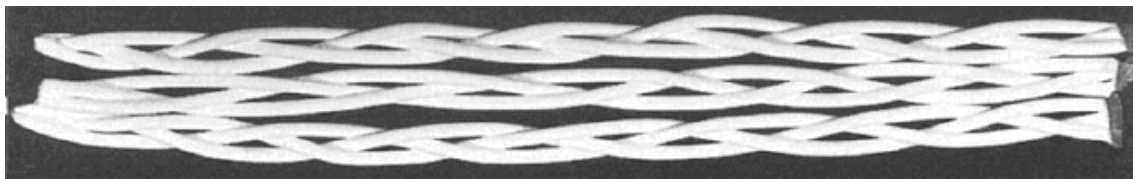
(d)

Figure 1.1.5. Spacer-filled MD channel (a) (Reprinted from [71] Shakaib et al., 2012, copyright (2012), with permission from Elsevier); membrane fibers arranged in fabric (b), twisted (c) and braided (d) configurations (Reprinted from [75] Schneider et al., 1988, copyright (1988), with permission from Elsevier); different module design and hollow fiber configurations (e) (Reprinted from [63] Teoh et al., 2008, copyright (2008), with permission from Elsevier); and Images of possible baffles for capillaries or hollow fiber membrane modules (f) (Reprinted from [74] Ahmad & Mariadas, 2004, copyright (2004), with permission from Elsevier). (To be continued)
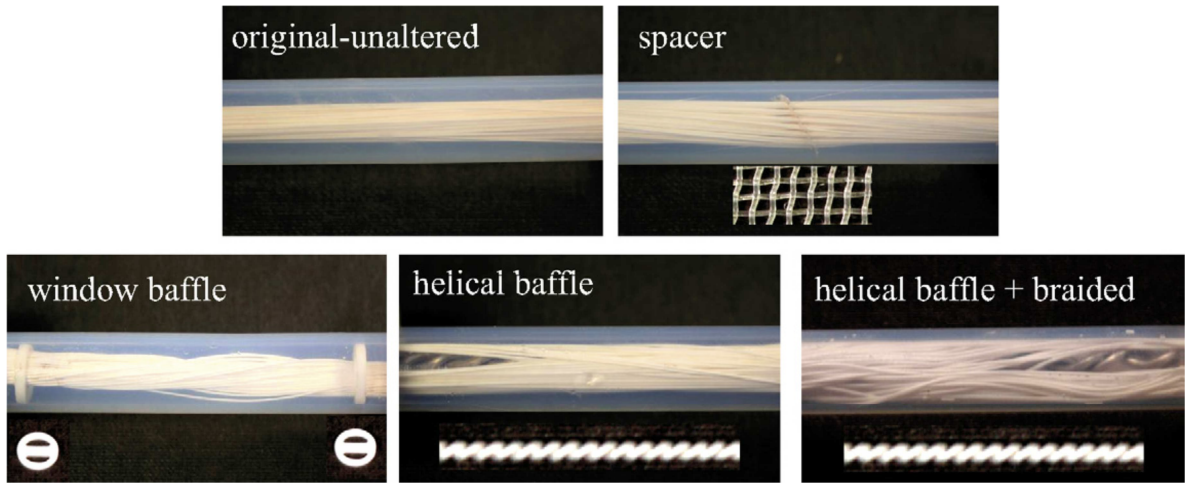
(e)

(f)

Figure 1.1.5. Spacer-filled MD channel (a) (Reprinted from [71] Shakaib et al., 2012, copyright (2012), with permission from Elsevier); membrane fibers arranged in fabric (b), twisted (c) and braided (d) configurations (Reprinted from [75] Schneider et al., 1988, copyright (1988), with permission from Elsevier); different module design and hollow fiber configurations (e) (Reprinted from [63] Teoh et al., 2008, copyright (2008), with permission from Elsevier); and Images of possible baffles for capillaries or hollow fiber membrane modules (f) (Reprinted from [74] Ahmad & Mariadas, 2004, copyright (2004), with permission from Elsevier). (Continuation)

1.1.3. Membrane Distillation Applications: Filtration and Separation

MD technology is gaining an increasing importance in separation processes and it is currently applied for environmental, chemical, petrochemical, metallurgical, food, pharmaceutical and biotechnology industries. In general, the MD typical applications are summarized in Fig. 1.1.6.

- Brackish water and seawater desalination: This is the most considered MD application for water production because the obtained salt rejection factor is very close to 100% (i.e. practically a total rejection of salts). In the case of a feed aqueous solution containing non-volatile components, either electrolytes (sodium chloride, NaCl; potassium chloride, KCl; lithium bromide, LiBr; etc.) or no-elyctrolytes (glucose, sucrose, fructose, etc.) only water molecules flow through the membrane pores in vapour phase. It must be pointed out that 20% of the world´s population has inadequate access to drinking water although over two-thirds of the planet is covered with water (99.3% of the total water is either too salty as seawater or inaccessible as ice caps). Moreover, water is potable only when it contains less than 500 ppm of salt. Table 1.1.2 presents as an example the permeate fluxes of some membranes commonly used for desalination by different MD variants.

It was observed that the temperature of the feed solution is the most significant MD operating parameter controlling the MD permeate flux. Generally, it is admitted that there is an exponential increase of the MD permeate flux with the feed temperature because the partial vapour pressure increases exponentially with the temperature following an Arrhenius type of dependence ($J \propto e^{-A/T}$ where J is the permeate flux, T is the absolute temperature and A is a constant) [78]. Remember that the transmembrane vapour pressure is the driving force for mass transfer in MD. A linear increase of the MD permeate flux with the vapour pressure difference between the feed and permeate was obtained [79-81]. The MD flux is lower for higher permeate temperature and higher non-volatile solute concentration of the feed solution [23,24,82,83]. Moreover, the permeate flux was found to be greater for membranes having larger pore sizes. In AGMD variant it was observed a decrease of the permeate flux with the increase of the air gap thickness between the membrane and the condensing surface because of the increase of the resistance to mass transfer in the air gap of the membrane module [79,81,84,85].
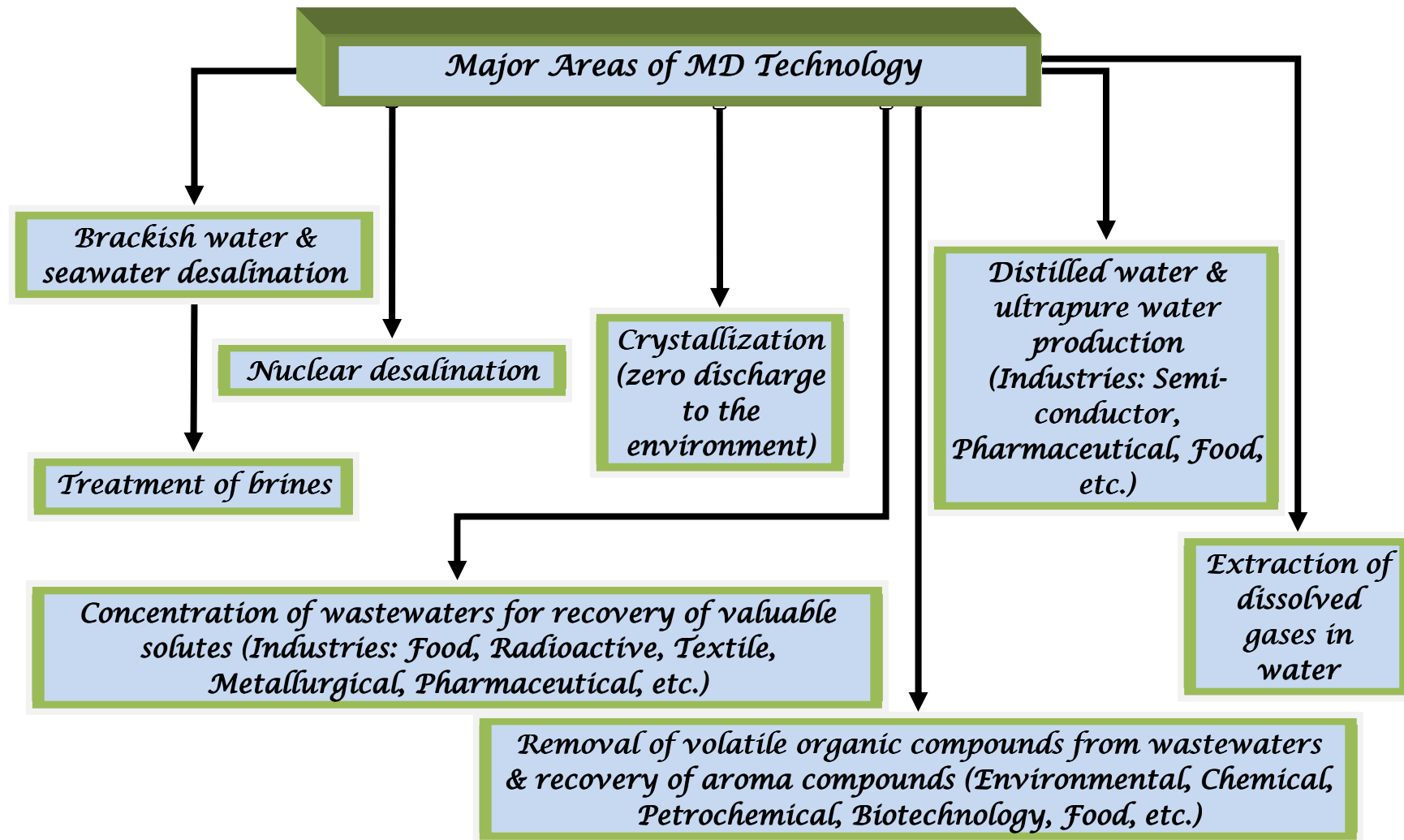
Figure 1.1.6. Typical fields applications of MD technology.

Table 1.1.2. Reported permeate fluxes (J_w) and salt rejection factors (α) of different membranes used for desalination by different MD variants. Feed temperature (T_f), permeate temperature in DCMD (T_p), temperature difference between feed and permeate in DCMD (ΔT), cooling temperature in AGMD (T_c), liquid flow rate (Q_f), liquid circulation velocity (v_f), air gap width in AGMD (a), electrical conductivity of the permeate (ψ_p), electrical conductivity of the feed (ψ_f).

Membrane	J_w (10^{-3} kg/m².s)	Observation	Ref.
GVHP	13.52	DCMD: Distilled water as feed; T_f=90.7ºC; T_p=19.7ºC.	[86]
	9.00	DCMD: Distilled water as feed; T_f=70ºC; T_p=20ºC.	[87]
	0.89	DCMD: 3 g/L NaCl; ΔT=10ºC; T_f=51.9ºC.	[88]
	0.83	DCMD: 64.5 g/L NaCl; ΔT=10ºC; T_f=52.7ºC.	[88]
	2.28	AGMD: T_f=50ºC, T_c=20ºC, Q_f=70 L/h, a=1.8 mm, distilled water.	[89]
HVHP	18.61 16.39 11.11	Deareation *DCMD*; T_f=80ºC; T_p=21ºC Distilled water NaCl (14 g/L) NaCl (25 g/L).	[90]
	10.80	DCMD: Distilled water as feed; T_f=70ºC; T_p=20ºC.	[87]
	7.31 1.94 1.67	AGMD: a=0.8 m, T_c=7ºC T_f=82ºC, tape water (ψ_f=297μS/cm). T_f=52ºC, tape water, (ψ_f=297μS/cm, 99% salt rejection). T_f=52ºC, seawater model solution, (ψ_f=37.6 mS/cm, ψ_p=1100 μS/cm).	[89]
TF200	18.69	DCMD: Distilled water as feed; T_f=80.1ºC; T_p=20.1ºC.	[86]
	2.90	DCMD: 1.9 g/L NaCl; ΔT=10ºC; T_f=52.2ºC.	[88]
	2.23	DCMD: 64.5 g/L NaCl; ΔT=10ºC; T_f=52.7ºC.	[88]
	1.31	AGMD: T_f=70ºC, T_c=30ºC, distilled water as feed.	[91]
TF450	14.19	AGMD: T_f=71ºC, T_c=13.9ºC, 30 g/L NaCl, a=3 mm, Q_f=205 L/h, α = 99.92%.	[92]
	13.11	AGMD: T_f=71ºC, T_c=13.9ºC, 30 g/L NaCl, a=5.6 mm, Q_f=183 L/h, α = 99.98%.	[93]
	8.67	AGMD: T_f=59ºC, T_c=13.9ºC, 30 g/L NaCl, a=5.6 mm, Q_f=205 L/h, α = 99.98%.	[93]
3MA	25.2 22.5 19.8	DCMD: T_f=74ºC; T_p=20ºC; distilled water as feed 19.5 g/L; 42.2 g/L.	[94]
3MB	21.6	DCMD: Distilled water as feed; T_f=70ºC; T_p=20ºC.	[94]

- Treatment of concentrated brines: MD is proposed to solve the problem of brine disposal although the MD permeate flux declines as the concentration of salt in water is increased due to the decrease of the partial vapor pressure of the salt feed solution

[24,95-97]. It was demonstrated that MD can be applied for processing high salinity aqueous solutions and concentrated brines derived from other separation processes such as RO and NF instead of their discharge to the environment. It must be pointed out that pressure-driven membrane processes are not able to treat concentrated brines (i.e. > 75 g/L of salt) because of their high osmotic pressures. Therefore, various hybrid processes integrating MD as a final stage with other separation pressures such as pressure-driven membrane processes and crystallization were proposed looking at zero salty water discharge [98-102]. Pure water is recovered by MD while the resulting saturated salt aqueous solutions are used in crystallization process from which precipitated solids can be produced and enabling the formation of high quality crystals. This technology is also termed membrane distillation crystallization (MDC). Recently some researches starts on the development of membranes for MD-crystallization [101].

- Concentration of wastewaters containing valuable compounds: MD technology has been applied successfully for the treatment of wastewaters derived from different origins for recovery of valuable compounds and production of water less hazardous to the environment. The types of treated wastewaters are pharmaceutical wastewater containing taurine, concentration of biological solutions (bovine plasma, bovine blood, protein), metallurgical wastewater, textile wastewater contaminated with dyes, wastewater reclamation in space, olive oil mill wastewater for polyphenols recovery, waters contaminated with boron, arsenic, heavy metals, ammonia (NH_3), coolant liquid (i.e. glycols), humic acid, acid solutions rich in specific compounds for example the concentration of hydrogen iodide (HI) and sulphuric acid aqueous solutions of interests in hydrogen energy production from water, radioactive wastewater solutions (i.e. nuclear desalination), brine and other undrinkable water sources, etc. [24,33,103,104-116].

One of the advantages of using MD technology is the possibility to operate at low temperatures of feed aqueous solutions. Therefore, MD was proved to be successfully applicable in fields where high temperatures result in degradation of the valuable compounds present in food wastewaters (i.e. concentration of milk, concentration of must, which is the juice obtained from grape pressing containing sugars and various aroma compounds and for the concentration of many other types of juices including orange juice, mandarin juice, apple juice, sugarcane juice, etc.) [85,117-122].

- Removal of trace volatile organic compounds (VOCs) and dissolved gases from wastewaters: Various dilute mixtures containing VOCs at different concentrations were tested by different MD variants for VOCs extraction from water. These are alcohols (i.e. methanol, ethanol, isopropanol and n-butanol), halogenated VOCs (i.e. chloroform, trichloroethylene and tetrachloroethylene), benzene, acetone, acetonitrile, ethylacetate, methylacetate, methylterbutyl ether etc. [19,22,24,78,91,123-134]. Such applications are appropriate for environmental, chemical, petrochemical and biotechnology industries. Successful applications were also observed in food processing for recovery of volatile aroma compounds from juices [135], for ethanol recovery from fermentation broth [91,136,137] and for breaking azeotropic mixtures (e.g. hydrochloric acid/water, propionic acid/water and formic acid/water azeotrope mixtures [78,136,138,139]. In MD, both water and VOCs are transported through the pores of the membrane and therefore the vapour pressure in the permeate side must be adequately chosen to reach good selectivities. MD was also proposed as an alternative separation technology for extraction of dissolved gases in water such as oxygen and ammonia, but only very few studies were reported in this field [78,127,140,141].

- Distilled and ultrapure water production: MD is based on membrane evaporation and condensation phenomena. Therefore, when using adequate membranes for MD with narrow pore size distribution (see section 1.1.1), the produced water exhibits a high quality providing that a high rejection factor of non-volatile solutes, very close to 100%, are achieved. A high quality water with an electrical conductivity as low as 0.8 μS/cm with 0.6 ppm TDS (total dissolved solids) was produced by MD [142]. Because the produced water is very pure it is suitable for use in medical, pharmaceutical and semi-conductor industrial sectors [24,36,143] .

Most of the above cited MD applications are reviewed in the recent published book by Khayet and Matsuura [24]. Furthermore, different propositions to improve product quantity and quality and reduce energy consumption were reported including integrated MD technology to other conventional processes such as distillation systems (i.e. multi-effect distillers), to pressure-driven membrane processes (RO, UF, NF, forward osmosis, FO), to alternative energy sources such as solar and geothermal energy, and also to nuclear installations where waste heat can be recovered [28,31,34,37,39,41-51,54-60,98,118,144-160]. Solar ponds and solar collectors can be used to provide heat

(solar thermal) or electrical energy (solar photovoltaic panels) requirements to operate a MD plant. Figure 1.1.7 shows as an example a solar powered MD plant.

It is worth quoting that since the first publication in the field of solar assisted MD by Hogan et al. [58] in 1990 using flat plate solar collectors, various research studies were reported in the MD literature incorporating different solar devices to MD modules and tested in different countries around the world [34,37,38-40,42-47,56,58-60,153-158]. However, up to now few studies are published on MD economics, energy analysis and costs evaluations [161]. Wide dispersed and confusing water production costs (WP_{Cost}) and specific energy consumption (E_C) analysis are reported. The E_C varies from about 1 to 9000 kWh/m^3 while the WP_{Cost} varies from \$0.3/m^3 to \$130/m^3. These scattered values are due to the different type and size of the MD systems, type of feed processed water, energy source, energy recovery systems, cost of energy, economic analysis procedure, etc. Some commercial MD applications are still under evaluation due to the high energy consumption, high costs of membrane modules, difficulties with long time operation and membrane wettability among others.

Recently, a value of 27.6 kJ/kg (7.67 kWh/m^3) was reported as the theoretical minimum energy consumption of single-pass MD associated with a heat recovery system (i.e. heat exchanger) proposed for seawater desalination at 60ºC. For RO with a typical recovery of 50% this value is much lower, around 3.18 kJ/kg (0.88 kWh/m^3), although RO uses high cost electric energy [162,163]. Nevertheless, MD is claimed to be an attractive low cost process for clean water production when low grade thermal energy is available.

(a)

Figure 1.1.7. Schema (a), images (b) and heat flows and losses in a typical sunny day (c) of a solar AGMD plant installed in Amarika (Namibia) in 2010 (by Fraunhofer ISE) (4 m³/day at alternating temperatures 65-80ºC, 12 modules 168 m² membrane, raw water, drilling well 28000 ppm, solar thermal flat plate collectors single glazed 232 m², 12 m³ integrated heat storage, brine cooling tower) (Reprinted from [47] Schwantes et al, 2013, copyright (2013), with permission from Elsevier). (To be continued)

(b)

Figure 1.1.7. Schema (a), images (b) and heat flows and losses in a typical sunny day (c) of a solar AGMD plant installed in Amarika (Namibia) in 2010 (by Fraunhofer ISE) (4 m^3/day at alternating temperatures 65-80ºC, 12 modules 168 m^2 membrane, raw water, drilling well 28000 ppm, solar thermal flat plate collectors single glazed 232 m^2, 12 m^3 integrated heat storage, brine cooling tower) (Reprinted from [47] Schwantes et al, 2013, copyright (2013), with permission from Elsevier). (To be continued)

(c)

Figure 1.1.7. Schema (a), images (b) and heat flows and losses in a typical sunny day (c) of a solar AGMD plant installed in Amarika (Namibia) in 2010 (by Fraunhofer ISE) (4 m³/day at alternating temperatures 65-80ºC, 12 modules 168 m² membrane, raw water, drilling well 28000 ppm, solar thermal flat plate collectors single glazed 232 m², 12 m³ integrated heat storage, brine cooling tower) (Reprinted from [47] Schwantes et al, 2013, copyright (2013), with permission from Elsevier). (Continuation)

1.1.4. Tips, Remarks and Future Directions in MD

After more than forty five years of hard and continuous researches, recently MD technology begins to acquire industrial interests boosted by some companies such as Memsys, Memstill, Scarab Development AB, Keppel Seghers and Fraunhofer ISE among others. Still MD researchers are looking for identification of new applications of MD process including integrated MD systems to other separation processes. In addition, few research studies are reported on long term MD performance and membrane fouling (i.e. deposition of particles, colloids, emulsions, suspensions, macromolecules, etc.) and microorganism growth on membrane surface (i.e. membrane biofouling) although fouling phenomena in MD are significantly lower than those faced in other pressure-driven membrane separation processes [15,31,75,79,81,85,113,114,118,142,151,164-172]. Membrane fouling and scaling in MD can lead to wetting of the membrane pores and reduce the effective membrane area. As consequence the MD water production rate together with the water quality and the separation or rejection factors are reduced. MD researchers are now discussing various issues such as the energy consumption especially that of the recent proposed commercial MD plants, the water production cost, the difficulties faced with long term operation, the simultaneous risk of membrane wetting, scaling and fouling. Among the areas that are roughly studied are membrane engineering for preparation of improved and novel membranes, membrane modules designed specifically for MD applications and optimized coupling of renewable energy systems to MD plants.

REFERENCES

[1] A.C.M. Franken, S. Ripperger, Terminology for membrane distillation, European Society of Membrane Science and Technology, Issued January (1988).

[2] K. Smolders, A.C.M. Franken, Terminology for membrane distillation, Desalination, 72 (1989) 249-262.

[3] B.R. Bodell, Silicone rubber vapor diffusion in saline water distillation, United States Patent Serial No. 285,032, 1963.

[4] M.E. Findley, Vaporization through porous membranes, Ind. Eng. Chem. Process Des. Dev., 6 (1967) 226-230.

[5] K. Esato, B. Eiseman, Experimental evaluation of Gore-Tex membrane oxygenator, Journal of Thoracic and Cardiovascular Surgery, 69 (1975) 690-697.

[6] D.Y. Cheng, Method and apparatus for distillation, United States Patent Serial No. 4,265,713, 1981.

[7] D.W. Gore, Gore-Tex membrane distillation, Proc. of the 10th Ann. Convention of the Water Supply Improvement Assoc. Honolulu, USA, July 25-29 (1982).

[8] D.Y. Cheng, S.J. Wiersma, Composite membrane for a membrane distillation system, United States Patent Serial No. 4,316,772, 1982.

[9] D.Y. Cheng, S.J. Wiersma, Apparatus and method for thermal membrane distillation, United States Patent Serial No. 4,419,187, 1983.

[10] D.Y. Cheng, S.J. Wiersma, Composite membrane for a membrane distillation system, United States Patent Serial No. 4,419,242, 1983.

[11] L. Carlsson, The new generation in sea water desalination: SU membrane distillation system, Desalination, 45 (1983) 221-222.

[12] Catalogue of Enka AG presented at Europe-Japan Joint Congress on Membranes and Membrane Processes, Stresa, Italy, June (1984).

[13] K. Schneider, T.J. van Gassel, Membrandestillation, Chem. Ing. Tech., 56 (1984) 514-521.

[14] S.I. Andersson, N. Kjellander, B. Rodesjo, Design and field tests of a new membrane distillation desalination process, Desalination, 56 (1985) 345-354.

[15] T.J. Van Gassel, K. Schneider, An energy-efficient membrane distillation process, in E. Drioli and M. Nagaki (Eds.), Membranes and Membrane Processes, Plenum Press. New York. 343-348, 1986.

[16] H. Mahmud, A. Kumar, R.M. Narbaitz, T. Matsuura, Membrane air stripping: A process for removal of organics from aqueous solutions, Sep. Sci. Tech., 33 (1998) 2241-2255.

[17] R.S. Juang, S.H. Lin, M.C. Yang, Mass transfer analysis on air stripping of VOCs from water in microporous hollow fibers, J. Membr. Sci., 255 (2005) 79-87.

[18] F. Gascons Viladomat, I. Souchon, V. Athès, M. Marin, Membrane air-stripping for aroma compounds, J. Membr. Sci., 277 (2006) 129-136.

[19] R.L. Calibo, M. Matsumura, J. Takahashi, H. Kataoka, Ethanol stripping by pervaporation using porous PTFE membrane, J. Ferment. Technol., 65 (1987) 665-674.

[20] E. Korngold, E. Korin, Air sweep water pervaporation with hollow fiber membranes, Desalination, 91 (1993) 187-197.

[21] L. Francis, N. Ghaffour, A.A. Alsaadi, G.L. Amy, Material gap membrane distillation: A new design for water vapor flux enhancement, J. Membr. Sci., 448 (2013) 240-247.

[22] M. Khayet, T. Matsuura, Pervaporation and vacuum membrane distillation processes: Modeling and experiments, AIChE J., 50 (2004) 1697-1712.

[23] M. Khayet, Membranes and theoretical modeling of membrane distillation: a review, Adv. Colloid Interface. Sci., 164 (2011) 56-88.

[24] M. Khayet, T. Matsuura, Membrane Distillation: Principles and Applications, Elsevier, The Netherlands 2011.

[25] M. Khayet, T. Matsuura, J.I. Mengual, M. Qtaishat, Design of novel direct contact membrane distillation membranes, Desalination, 192 (2006) 105-111.

[26] M. Mulder, Basic principles of membrane technology. Kluwer Academic Publishers, Dordrecht, The Netherlands 1996.

[27] D.R. Lloyd, Microporous membrane formation via thermally-induced phase separation, Part 1, Solid-liquid phase separation, J. Membr. Sci., 52 (1990) 239-261.

[28] M. Essalhi, M. Khayet, Self-sustained webs of polyvinylidene fluoride electrospun nanofibers at different electrospinning times: 1. Desalination by direct contact membrane distillation, J. Membr. Sci., 433 (2013) 167-179.

[29] D. Winter, J. Koschikowski, M. Wieghaus, Desalination using membrane distillation: Experimental studies on full scale spiral wound modules, J. Membr. Sci., 375 (2011) 104-112.

[30] D. Winter, J. Koschikowski, S. Ripperger, Desalination using membrane distillation: Flux enhancement by feed water deaeration on spiral-wound modules, J. Membr. Sci., 423-424 (2012) 215-224.

[31] B. Li, K.K. Sirkar, Novel membrane and device for direct contact membrane distillation-based desalination process, Ind. Eng. Chem. Res., 43 (2004) 5300-5309.

[32] W.T. Hanbury, T. Hodgkiess, Membrane distillation: An assessment, Desalination, 56 (1985) 287-297.

[33] G. Zakrewska-Trznadel, M. Harasimowicz, A.G. Chmielewski, Concentration of radioactive components in liquid low-level radioactive waste by membrane distillation, J. Membr. Sci. 163 (1999) 257-264.

[34] K. Tarnacki, M. Meneses, T. Melin, J. van Medevoort, A. Jansen, Environmental assessment of desalination processes: Reverse osmosis and memstill®, Desalination, 296 (2012) 69-80.

[35] www.Xzero.se

[36] C. Liu, Polygeneration of electricity, heat and ultrapure water for the semiconductor industry, Heat & Power Technology, Department of Energy Technology, Royal Institute of Technology, Stockholm, Sweden, Master of Science Thesis. 2004.

[37] J. Walton, H. Lu, C. Turner, C. Solis, H. Hein, Solar and Waste Heat Desalination by Membrane Distillation, Desalination and Water Purification Research and Development Program Report No. 81. U.S. Department of the Interior. Bureau of Reclamation. April (2004).

[38] H. Lu, J.C. Walton, A.H.P. Swift, Desalination coupled with salinity-gradient solar ponds, Desalination, 136 (2001) 13-23.

[39] J.B. Gálvez, L. García-Rodríguez, I. Martín-Mateos, Seawater desalination by an innovative solar-powered membrane distillation system: The MEDESOL project, Desalination, 246 (2009) 567-576.

[40] A. Kullab, A. Martin, Membrane distillation and applications for water purification in thermal cogeneration plants, Sep. Purif. Technol., 76 (2011) 231-237.

[41] J. Koschikowski, M. Rommel M. Wieghaus, Solar thermal membrane distillation for small-scale desalination plants, ISES World Congress, Orlando. 6-12 August (2005).

[42] F. Banat, N. Jwaied, M. Rommel, J. Koschikowski, M. Wieghaus, Desalination by a "compact SMADES" autonomous solar-powered membrane distillation unit, Desalination, 217 (2007) 29-37.

[43] F. Banat, N. Jwaied, M. Rommel, J. Koschikowski, M. Wieghaus, Performance evaluation of the "large SMADES" autonomous desalination solar-driven membrane distillation plant in Aqaba, Jordan, Desalination, 217 (2007) 17-28.

[44] H.E.S. Fath, S.M. Elsherbiny, A.A. Hassan, M. Wieghaus, J. Koschikowski, M. Vatansever, PV and thermally driven small-scale, stand-alone solar desalination systems with very low maintenance needs, Desalination, 225 (2008) 58-69.

[45] J. Koschikowski, M. Wieghaus, M. Rommel, V.S. Ortin, B.P. Suarez, J.R.B. Rodríguez, Experimental investigations on solar driven stand-alone membrane distillation systems for remote areas, Desalination, 248 (2009) 125-131.

[46] R.G. Raluy, R. Schwantes, V.J. Subiela, B. Peñate, G. Melián, J.R. Betancort, Operational experience of a solar membrane distillation demonstration plant in Pozo Izquierdo-Gran Canaria Island (Spain), Desalination, 290 (2012) 1-13.

[47] R. Schwantes, A. Cipollina, F. Gross, J. Koschikowski, D. Pfeifle, M. Rolletschek, V. Subiela, Membrane distillation: Solar and waste heat driven demonstration plants for desalination, Desalination, 323 (2013) 93-106.

[48] C. Dotremont, B. Kregersman, S. Puttemans, P. Ho, J. Hanemaaijer. Memstill: A near-future technology for sea water desalination, ICOM 2008, Honolulu, Hawaii, 12-18 July (2008).

[49] A. Jansen, J.H. Hanemaaijer, J.W. Assink, E. van Sansbeek, Ch. Dotremont, J. van Medevoort, Pilot plants prove feasibility of a new desalination technique, Asian Water. 26 (2010) 22-26.

[50] A.E. Jansen, J.W. Assink, J.H. Hanemaaijer, J. van Medevoort, E. van Sonsbeek, Development and pilot testing of full-scale membrane distillation modules for deployment of waste heat, Desalination, 323 (2013) 55-65.

[51] Concord Enviro Systems uses Memsys´technolog to treat molasses wastewater, Membrane Technology. 11 (2012) 1-16.

[52] www.scarab.se, Scarab Development AB, Stockholm, Sweden.

[53] J.H. Hanemaaijer, J.V. Medevoort, A.E. Jansen, C. Dotremont, E.V. Sonsbeek, T. Yuan, L.D. Ryck, Memstill membrane distillation – a future desalination technology, Desalination, 199 (2006) 175–176.

[54] K. Zhao, W. Heinzl, M. Wenzel, S. Büttner, F. Bollen, G. Lange, S. Heinzl, N. Sarda, Experimental study of the memsys vacuum-multi-effect-membrane-distillation (V-MEMD) module, Desalination, 323 (2013) 150-160.

[55] C.L. Ong, W. Escher, S. Paredes, A.S.G. Khalil, B. Michel, A novel concept of energy reuse from high concentration photovoltaic thermal (HCPVT) system for desalination, Desalination, 295 (2012) 70-81.

[56] A. Cipollina, M.G. Di Sparti, A. Tamburini, G. Micale, Development of a membrane distillation module for solar energy seawater desalination, Chem. Eng. Res. Des., 90 (2012) 2101-2121.

[57] A. Hausmann, P. Sanciolo, T. Vasiljevic, M. Weeks, M. Duke, Integration of membrane distillation into heat paths of industrial processes, Chem. Eng. J., 211-212 (2012) 378-387.

[58] P.A. Hogan, Sudjito. A.G. Fane, G.L. Morrison. Desalination by solar heated membrane distillation, Desalination, 81 (1990) 81-90.

[59] T.C. Chen, C.D. Ho, Immediate assisted solar direct contact membrane distillation in saline water desalination, J. Membr. Sci., 358 (2010) 122-130.

[60] Y.D. Kim, K. Thu, N. Ghaffour, K.C. Ng, Performance investigation of a solar-assisted contact membrane distillation system, J. Membr. Sci., 427 (2013) 345-364.

[61] T.Y. Cath, V.D. Adams, A.E. Childress, Experimental study of desalination using direct contact membrane distillation: a new approach to flux enhancement, J. Membr. Sci., 228 (2004) 5-16.

[62] L. Martínez, J.M. Rodríguez-Maroto, Effects of membrane and module design improvements on flux in direct contact membrane distillation, Desalination, 205 (2007) 97-103.

[63] M.M. Teoh, S. Bonyadi, T.S. Chung, Investigation of different hollow fiber module designs for flux enhancement in the membrane distillation process, J. Membr. Sci., 311 (2008) 371-379.

[64] X. Yang, R. Wang, L. Shi, A.G. Fane, M. Debowski, Performance improvement of PVDF hollow fiber-based membrane distillation process, J. Membr. Sci., 369 (2011) 437-447.

[65] K. He, H.J. Hwang, M.W. Woo, I.S. Moon, Production of drinking water from saline water by direct contact membrane distillation (DCMD), J. Ind. Eng. Chem., 17 (2011) 41-48.

[66] L. Martínez-Díez, M.L. Vázquez-González, A method to evaluate coefficients affecting flux in membrane distillation, J. Membr. Sci., 173 (2000) 225-234.

[67] M. Qtaishat, T. Matsuura, B. Kruczek, M. Khayet, Heat and mass transfer analysis in direct contact membrane distillation, Desalination, 219 (2008) 272-292.

[68] M. Khayet, M.P. Godino, J.I. Mengual, Thermal boundary layers in sweeping gas membrane distillation processes, AIChE J., 48 (2002) 1488-1497.

[69] A. Cipollina, A.D. Miceli, J. Koschikowski, G. Micale, L. Rizzuti, CFD simulation of a membrane distillation module channel, Desalination and Water Treatment, 6 (2009) 177-183.

[70] H. Yu, X. Yang, R. Wang, A.G. Fane, Analysis of heat and mass transfer by CFD for performance enhancement in direct contact membrane distillation, J. Membr. Sci., 405-406 (2012) 38-47.

[71] M. Shakaib, S.M.F. Hasani, I. Ahmed, R.M. Yunus, A CFD study on the effect of spacer orientation on temperature polarization in membrane distillation modules, Desalination, 284 (2012) 332-340.

[72] Z. Xu, Y. Pan, Y. Yu, CFD simulation on membrane distillation of NaCl solution, Front. Chem. Eng. Chin., 3 (2009) 293-297.

[73] X. Yang, H. Yu, R. Wang, A.G. Fane, Analysis of the effect of turbulence promoters in hollow fiber membrane distillation modules by computational fluid dynamic (CFD) simulations, J. Membr. Sci., 415-416 (2012) 758-769.

[74] A.L Ahmad, A. Mariadas, Baffled microfiltration membrane and its fouling control for feed water of desalination, Desalination, 168 (2004) 223-230.

[75] K. Schneider, W. Hölz, R. Wollbeck, Membranes and modules for transmembrane distillation, J. Membr. Sci., 39 (1988) 25-42.

[76] S. Al-Sharif, M. Albeirutty, A. Cipollina, G. Micale, Modelling flow and heat transfer in spacer-filled membrane distillation channels using open source CFD code, Desalination, 311 (2013) 103-112.

[77] K.L. Wang, E.L. Cussler, Baffled membrane modules made with hollow fiber fabric, J. Membr. Sci., 85 (1993) 265 -278.

[78] M.C. García-Payo, M.A. Izquierdo-Gil, C. Fernández-Pineda, Air gap membrane distillation of aqueous alcohol solutions, J. Membr. Sci., 169 (2000) 61-80.

[79] F.A. Banat, J. Simandl, Theoretical and experimental study in membrane distillation, Desalination, 95 (1994) 39-52.

[80] H. Kurokawa, K. Ebara, O. Kuroda, S. Takahashi, Vapor permeate characteristics of membrane distillation, Sep. Sci. Technol., 25 (1990) 1349-1359.

[81] F.A. Banat, J. Simandl, Desalination by membrane distillation: A parametric study, Sep. Sci. & Tech., 33 (1998) 201-226.

[82] K.W. Lawson, D.R. Lloyd, Review: membrane distillation, J. Membr. Sci., 124 (1997) 1-25.

[83] M.S. El-Bourawi, Z. Ding, R. Ma, M. Khayet, A framework for better understanding membrane distillation separation process: Review, J. Membr. Sci., 285 (2006) 4-29.

[84] A.S. Jonsson, R.Wimmerstedt, A.C. Harrysson, Membrane distillation: A theoretical study of evaporation through microporous membranes, Desalination, 56 (1985) 237-249.

[85] S. Kimura, S. Nakao, S. Shimantani, Transport phenomena in membrane distillation, J. Membr. Sci., 33 (1987) 285-298.

[86] M. Khayet, A.O. Imdakm, T. Matsuura, Monte Carlo simulation and experimental heat and mass transfer in direct contact membrane distillation, Int. J. Heat Mass Transfer., 53 (2010) 1249-1259.

[87] J. Phattaranawik, R. Jiraratananon, A.G. Fane, Effect of pore size distribution and air flux on mass transport in direct contact membrane distillation, J. Membr. Sci., 215 (2003) 75-85.

[88] M. Khayet, C. Cojocaru, M.C. García-Payo, Application of response surface methodology and experimental design in direct contact membrane distillation, Ind. Eng. Chem. Res., 46 (2007) 5673-5685.

[89] M.A. Izquierdo-Gil, M.C. García-Payo, C. Fernández-Pineda, Air gap membrane distillation of sucrose aqueous solutions, J. Membr. Sci., 155 (1999) 291-307.

[90] R.W. Schofield, A.G. Fane, C.J.D. Fell, R. Macoun, Factors affecting flux in membrane distillation, Desalination, 77 (1990) 279-294.

[91] C. Gostoli, G.C. Sarti, Separation of liquid mixtures by membrane distillation, J. Membr. Sci., 41 (1989) 211-224.

[92] M. Khayet, C. Cojocaru, Air gap membrane distillation: desalination, modelling and optimization, Desalination, 287 (2012) 138-145.

[93] M. Khayet, C. Cojocaru, Artificial neural network modelling and optimization of desalination by air gap membrane distillation, Sep. Purif. Tech., 86 (2012) 171-182.

[94] K.W. Lawson, D.R. Lloyd, Membrane distillation: II. Direct contact MD, J. Membr. Sci., 120 (1996) 123-133.

[95] A. Alkhudhiri, N. Darwish, N. Hilal, Treatment of high salinity solutions: Application of air gap membrane distillation, Desalination, 287 (2012) 55-60.

[96] Y. Wu, E. Drioli, The behaviour of membrane distillation of concentrated aqueous solution, Water Treat., 4 (1989) 399-415.

[97] L. Mariah, CA. Buckley, C.J. Brouckaert, E. Curcio, E. Drioli, D. Jaganyi, D. Ramjugernath, Membrane distillation of concentrated brines-Role of water activities in the evaluation of driving force, J. Membr. Sci., 280 (2006) 937-947.

[98] S. Bouguecha, M. Dhahbi, Fluidized bed crystalliser and air gap membrane distillation as a solution to geothermal water desalination, Desalination, 152 (2003) 237-244.

[99] X. Ji, E. Curcio, S. Al Obaidani, G. Di Profio, E. Fortanova, E. Drioli, Membrane distillation-crystallization of seawater reverse osmosis brines, Sep. Purf. Tech., 71 (2010) 76-82.

[100] J.P. Mericq, S. Laborie, C. Cabassud, Vacuum membrane distillation of seawater reverse osmosis brines, Water Research, 44 (2010) 5260-5273.

[101] F. Edwie, T.S. Chung, Development of hollow fiber membranes for water and salt recovery from highly concentrated brine via direct contact membrane distillation and crystallization, J. Membr. Sci., 412-422 (2012) 111-123.

[102] G. Chen, Y. Lu, W.B. Krantz, R. Wang, A.G. Fane, Optimization of operating conditions for a continuous membrane distillation crystallization process with zero salty water discharge, J. Membr. Sci., 450 (2014) 1-11.

[103] Y. Wu, Y. Kong, J. Liu, J. Zhang, J. Xu, An experimental study on membrane distillation-crystallization for treating waste water in taurine production, Desalination, 80 (1991) 235-242.

[104] D. Hou, J. Wang, X. Sun, Z. Luan, Ch. Zhao, X. Ren, Boron removal from aqueous solution by direct contact membrane distillation, J. Hazardous Materials, 177 (2010) 613-619.

[105] V. Calabró, E. Drioli, F. Matera, Membrane distillation in the textile wastewater treatment, Desalination, 83 (1991) 209-224.

[106] T.Y. Cath, D. Adams, A.E. Childress, Membrane contactor processes for wastewater reclamation in space, II. Combined direct osmosis, osmotic distillation, and membrane distillation for treatment of metabolic wastewater, J. Membr. Sci., 257 (2005) 111-119.

[107] A. El-Abbassi, H. Kiai, A. Hafidi, M.C. García-Payo, M. Khayet, Treatment of olive mill wastewater by membrane distillation using polytetrafluoroethylene membranes, Sep. & Purif. Tech., 98 (2012) 55-61.

[108] A. El-Abbassi, A. Hafidi, M. Khayet, M.C. García-Payo, Integrated direct contact membrane distillation for olive mil wastewater treatment, Desalination, 323 (2013) 31-38.

[109] M. Gryta, K Karakulski, The application of membrane distillation for the concentration of oil-water emulsions, Desalination, 121 (1999) 23-29.

[110] M. Khayet, J.I. Mengual, G. Zakrzewska-Trznadel, Direct contact membrane distillation for nuclear desalination. Part. II. Experiments with radioactive solutions, Int. J. Nuclear Desalination, 2 (2006) 56-73.

[111] C. Rincón, J.M. Ortiz de Zárate, J.I. Mengual, Separation of water and glycols by direct contact membrane distillation, J. Membr. Sci., 158 (1999) 155-165.

[112] P.P. Zolotarev, V.V. Urgozov, I.B. Volkina, V.N. Nikulin, Treatment of waste water for removing heavy metals by membrane distillation, J. Hazardous Mater., 37(1994) 77-82.

[113] M. Khayet, J.I. Mengual, Effect of salt concentration during the treatment of humic acid solutions by membrane distillation, Desalination, 168 (2004) 373-381.

[114] M. Khayet, A. Velázquez, J.I. Mengual, Direct contact membrane distillation of humic acid solutions, J. Membr. Sci., 240 (2004) 123-128.

[115] G. Caputo, C. Felici, P. Tarquini, A. Giaconia, S. Sau, Membrane distillation of HI/H_2O and H_2SO_4/H_2O mixtures for the sulphur-iodine thermochemical process, Int. J. of Hydrogen Energy, 32 (2007) 4736-4743.

[116] D. Qu, J. Wang, D. Hou, Z. Luan, B. Fan, C. Zhao, Experimental study of arsenic removal by direct contact membrane distillation, J. Hazardous Materials, 163 874-879.

[117] E. Drioli, B.L. Jiao, V. Calabró, The preliminary study on the concentration of orange juice by membrane distillation, Proc. Int. Soc. Citriculture, 3 (1992) 1140-1144.

[118] V. Calabró, B.L. Jiao, E. Drioli, Theoretical and experimental study on membrane distillation in the concentration of orange juice, Ind. Eng. Chem. Res., 33 (1994) 1803-1808.

[119] S. Bandini, G.C. Sarti, Concentration of must through vacuum membrane distillation, Desalination, 149 (2002) 253-259.

[120] S. Gunko, S. Verbych, M. Bryk, N. Hilal, Concentration of apple juice using direct contact membrane distillation, Desalination, 190 (2006) 117-124.

[121] O.S. Lukanin, S.M. Gunko, M.T. Bryk, R.R. Nigmatullin, The effect of content of apple juice biopolymers on the concentration by membrane distillation, J. Food Engineering, 60 (2003) 275-280.

[122] S. Nene, S. Kaur, K. Sumod, B. Joshi, K.S.M.S. Raghavarao, Membrane distillation for the concentration of raw-cane sugar syrup and membrane clarified sugarcane juice, Desalination, 147 (2002) 157-160.

[123] M. Khayet, T. Matsuura, Preparation and characterization of polyvinylidene fluoride membranes for membrane distillation, Ind. & Eng. Chem. Res., 40 (2001) 5710-5718.

[124] E. Hoffman, D.M. Pfenning, E. Philippsen, P. Schwahn, M. Seiber, R. When, D. Woerman, Evaporation of alcohol/water mixtures through hydrophobic porous membranes, J. Membr. Sci., 34 (1987) 199-206.

[125] Y. Fujii, S. Kigoshi, H. Iwatani, M. Aoyama, Selectivity and characteristics of direct contact membrane distillation type experiment: I. Permeability and selectivity through dried hydrophobic fine porous membranes, J. Membrane Sci., 72 (1992) 53-72.

[126] Y. Fujii, S. Kigoshi, H. Iwatani, M. Aoyama, Y. Fusaoka, Selectivity and characteristics of direct contact membrane distillation type experiment: II. Membrane treatment and selectivity increase, J. Membr. Sci., 72 (1992b) 73-89.

[127] S. Bandini, C. Gostoli, G.C. Sarti, Separation efficiency in vacuum membrane distillation, J. Membr. Sci., 73 (1992) 217-229.

[128] G.C. Sarti, C. Gostoli, S. Bandini, Extraction of organic components from aqueous streams by vacuum membrane distillation, J. Membr. Sci., 80 (1993) 21-33.

[129] F.A. Banat, J. Simandl, Removal of benzene traces from contaminated water by vacuum membrane distillation, Chem. Eng. Sci., 51 (1996) 1257-1265.

[130] S. Bandini, A. Saavedra, G.C. Sarti, Vacuum membrane distillation: experiments and modeling, AIChE J., 43 (1997) 398-408.

[131] N. Couffin, C. Cabassud, V. Lahoussine-Turcaud, A new process to remove halogenated VOCs for drinking water production: vacuum membrane distillation, Desalination, 117 (1998) 233-245.

[132] S. Bandini, G.C. Sarti, Heat and mass transport resistances in vacuum membrane distillation per drop, AIChE J., 45 (1999) 1422-1433.

[133] M.A. Izquierdo-Gil, G. Jonsson, Factors affecting flux and ethanol separation performance in vacuum membrane distillation (VMD), J. Membr. Sci., 214 (2003) 113-130.

[134] A.M. Urtiaga, G. Ruiz, I. Ortiz, Kinetic analysis of the vacuum membrane distillation of chloroform form aqueous solutions, J. Membr. Sci., 165 (2000) 99-110.

[135] R. Bagger-Jorgensen, A.S. Meyer, C. Varming, G. Jonsson, Recovery of volatile aroma compounds from black currant juice by vacuum membrane distillation, J. Food Eng., 64 (2004) 23-31.

[136] H. Udriot, A. Araque, U. von Stockar, Azeotropic mixtures may be broken by membrane distillation, Chem. Eng. J., 54 (1994) 87-93.

[137] F.A. Banat, J. Simandl, Membrane distillation for dilute methanol: Separation from aqueous streams, J. Membr. Sci., 163 (1999) 333-348.

[138] M.C. García-Payo, C.A.. Rivier, I.W. Marison, U. von Stockar, Separation of binary mixtures by thermostatic sweeping gas membrane distillation: II. Experimental results with aqueous formic acid solutions, J. Membr. Sci., 198 (2002) 197-210.

[139] TM. omaszewska, M. Gryta, A.W. Morawski, Study on the concentration of acids by membrane distillation, J. Membr. Sci., 102 (1995) 113-122.

[140] Z. Ding, L. Liu, Z. Li, R. Ma, Z. Yang, Experimental study of ammonia removal from water by membrane distillation (MD): the comparison of three configurations, J. Membr. Sci., 286 (2006) 93-103.

[141] M.S. El-Bourawi, M. Khayet, R. Ma, Z. Ding, Z. Li, X. Zhang, Application of vacuum membrane distillation for ammonia removal, J. Membr. Sci., 301 (2007) 200-209.

[142] K. Karakulski, M. Gryta, A. Morawski, Membrane processes used for potable water quality improvement, Desalination, 145 (2002) 315-319.

[143] P.K. Weyl, Recovery of demineralized water from saline waters, United States Patent US3340186A 1967.

[144] W. Heinzl, S. Büttner, G. Lange, Industrialized modules for MED desalination with polymer surfaces, Desalination and Water Treatment, 42 (2012) 177-180.

[145] Memsys-NTU partnership aims to enhance water desalination technology, Membrane Technology, 2 (2011) 1-16.

[146] G. Zakrewska-Trznadel, M. Harasimowicz, A.G. Chmielewski, Membrane processes in nuclear technology-application for liquid radioactive waste treatment, Sep. Pur. Tech., 22-23 (2001) 617-625.

[147] M.C. De Andrés, J. Doria, M. Khayet, L. Peña, J.I. Mengual, Coupling of a membrane distillation module to a multieffect distiller for pure water production, Desalination, 115 (1998) 71-81.

[148] V. Calabró, G. Pantano, M. Kang, R. Molinari, E. Drioli, Experimental study on integrated membrane processes in the treatment of solutions simulating textile effluents. Energy and exergy analysis, Desalination, 78 (1990) 257-277.

[149] E. Drioli, F. Laganá, A. Criscuoli, G. Barbieri, Integrated membrane operations in desalination processes, Desalination. 122 (1999) 141-145.

[150] A. Criscuoli, E. Drioli, Energetic and exegetic analysis of an integrated membrane desalination system, Desalination, 124 (1999) 243-249.

[151] M. Gryta, K. Karakulski, A.W. Morawski, Purification of oily wastewater by hybrid UF/MD, Water Res., 35 (2001) 3665-3669.

[152] A. Criscuoli, E. Drioli, A. Capuano, B. Memoli, V.E. Andreucci, Human plasma ultrafiltrate purification by membrane distillation: process optimisation and evaluation of its possible application on-line, Desalination. 147 (2002) 147-148.

[153] M. Rommel, M. Wieghaus, J. Koschikowski, Solar powered desalination: an autonomous water supply, Desalination, 3 (2008) 22-24.

[154] F. Banat, N. Jwaied, Autonomous membrane distillation pilot plant unit driven by solar energy: experiences and lessons learned, Int. J. Sustainable Water & Environmental Syst., 1 (2010) 21-24.

[155] X. Wang, L. Zhang, H. Yang, H. Chen, Feasibility research of potable water production via solar-heated hollow fiber membrane distillation system, Desalination, 247 (2009) 403-411.

[156] F. Suareza, S. Tyler, A. Childress, A theoretical study of a direct contact membrane distillation system coupled to a salt-gradient solar pond for terminal lakes reclamation, Water Res., 44 (2010) 4601-4615.

[157] J. Mericq, S. Laborie, C. Cabassud, Evaluation of systems coupling vacuum membrane distillation and solar energy for seawater desalination, Chem. Eng. J., 166 (2011) 596-606.

[158] Z. Ding, L. Liu, M.S. El-Bourawi, R. Ma, Analysis of a solar-powered membrane distillation system, Desalination, 172 (2005) 27-40.

[159] K.Y. Wang, M.M. Teoh, A. Nugroho, T.S. Chung, Integrated forward osmosis-membrane distillation (FO-MD) hybrid system for the concentration of protein, Chem. Eng. Sci., 66 (2011) 2421-2430.

[160] C.R. Martinetti, A.E. hildress, T.Y. Cath, High recovery of concentrated RO brines using forward osmosis and membrane distillation, J. Membr. Sci., 331 (2009) 31-39.

[161] M. Khayet, Solar desalination by membrane distillation: Dispersion in energy consumption analysis and water production costs (a review), Desalination, 308 (2013) 89-101.

[162] S. Lin, N.Y. Yip, M. Elimelech, Direct contact membrane distillation with heat recovery: Thermodynamic insights from module scale modelling, J. Membr. Sci., 453 (2014) 498-515.

[163] M. Elimelech, W.A. Phillip, The future of seawater desalination: energy, technology, and the environment, Science, 333 (2011) 712-717.

[164] K. Sakai, T. Muroi, K. Ozawa, S. Takesawa, M. Tamura, T. Makane, Extraction of solute-free water from blood by MD, Am. Soc. Artif. Intern. Organs, 32 (1986) 397-400.

[165] K. Sakai, T. Koyano, T. Muroi, M. Tamura, Effects of temperature and concentration polarization on water vapour permeability for blood in membrane distillation, The Chemical Eng. J., 38 (1988) B33-B39.

[166] J.M. Ortiz de Zárate, C. Rincón, J.I. Mengual, Concentration of bovine serum albumin aqueous solutions by membrane distillation, Sep. Sci. & Tech., 33 (1998) 283-296.

[167] M. Gryta, M. Tomaszewska, J. Grzechulska, A.W. Morawski, Membrane distillation of NaCl solution containing natural organic matter, J. Membr. Sci., 181 (2001) 279-287.

[168] E. Drioli, Y. Wu, Membrane distillation: An experimental study, Desalination, 53 (1985) 339-346.

[169] M. Gryta, Concentration of saline wastewater from the production of heparin, Desalination, 129 (2000) 35-45.

[170] M. Gryta, The assessment of microorganism growth in the membrane distillation system, Desalination. 142 (2002) 79-88.

[171] M. Gryta, Long-term performance of membrane distillation process, J. Membr. Sci., 265 (2005) 153-159.

[172] S. Srisurichan, R. Jiraratananon, A.G. Fane, Humic acid fouling in the membrane distillation process, Desalination, 174 (2005) 63-72.

1.2. Fundamentals of Membrane Distillation

Contents:

1.2.1. Introduction: Non-isothermal membrane processes

1.2.2. Key characteristics of membrane distillation

1.2.3. Types of membranes and membrane module configurations for membrane distillation

1.2.4. Membrane distillation theory

> **1.2.4.1.** Models of mass transfer through the MD membrane
>
>> **1.2.4.1.1.** Knudsen model
>>
>> **1.2.4.1.2.** Molecular diffusion model
>>
>> **1.2.4.1.3.** Viscous or poiseuille flow model
>>
>> **1.2.4.1.4.** Combined flow models
>>
>> **1.2.4.1.5.** Dusty gas model
>>
>> **1.2.4.1.6.** Recent models
>
> **1.2.4.2.** Models of heat transfer in MD process
>
> **1.2.4.3.** Temperature, concentration and vapor pressure polarization phenomena: heat and mass transfer boundary layers
>
>> **1.2.4.3.1.** Temperature polarization
>>
>> **1.2.4.3.2.** Concentration polarization
>>
>> **1.2.4.3.3.** Vapor pressure polarization

1.2.5. Typical application of membrane distillation technology

1.2.6. Conclusions

References

Abstract:

The study of non-isothermal flux of air through porous media dates back to 1873, while the existence of a non-isothermal liquid transport through membranes was first described in 1907. This phenomenon termed Thermo-osmosis (TO) did not involve any liquid/vapor phase transition and was carried out through both dense and porous hydrophilic membranes. About 50 years later, when porous hydrophobic membranes were used and the non-isothermal vapor transport was studied through dry pores, the phenomenon was known as Membrane Distillation (MD). This non-isothermal membrane separation process is applied mostly in desalination and for the treatment of different types of wastewaters including brines for water production. It is known 50 years ago but only recently it has made its way toward industrial applications. It is still need to be improved further in various key aspects. Compared to TO, much more interest is being devoted to MD. Up to 31st December 2013, the total number of published papers on MD is more than 7 times greater than that of TO.

Moreover, a significant increasing interest on MD technology has been observed during last 13 years in both its experimental and theoretical aspects including MD membrane engineering. More than 58% of the research studies were performed using the direct contact membrane distillation (DCMD) configuration. An abrupt increase of investigations on fabrication and modification of membranes for MD is seen during last 10 years. However, this consists only in 16.8% of the total published studies on MD. On the other hand, near 40% of the MD studies dealt with theoretical models. This chapter book covers a comprehensive historical perspectives of TO and MD, important key characteristics of MD, membranes used in MD and possible MD technological configurations, different transport mechanisms through MD membranes and developed theoretical models, different fields of applications of MD, future trends related to interesting and promising research fields in MD, sources of further information and some valuable advises.

1.2.1. Introduction: Non-isothermal membrane processes

During recent years, membrane separation processes and transport phenomena through different types of membranes have gained considerable importance going at high speed both at academic and industrial levels. This is due to their wide field of applications, high separation efficiency and the continuous development of novel and advanced synthetic membranes, new generation modules and emerging membrane processes.

The thermodynamic disequilibrium through any type of membrane either porous or dense is the responsible for the transport phenomena of matter and/or energy through the membrane. This imbalance can be induced by a pressure difference, a temperature difference, a concentration difference, an electrical potential difference, or in general, by a difference of the chemical potential of species between the feed and permeate phases of the membrane. Depending on the driving force and the type of the synthetic membrane, different separation processes can be distinguished as summarized in Fig. 1.2.1.

Membrane processes are usually considered from the point of view of the Thermodynamics of Irreversible Processes, which as it is well known, does not provide any description of the phenomenon at the molecular level. For example, when a temperature difference is applied between both sides of a membrane a conjugate heat flux is produced in the direction from high to low temperature based on Fourier´s law together with a coupled or cross-flow of mass whose mechanism is generally dependent on the membrane type (dense, porous, electrically charged or activated, hydrophobic, etc.). Depending on the mechanism responsible for this mass flow Thermo-osmosis (TO) or Membrane Distillation (MD) are distinguished (Fig. 1.2.1).
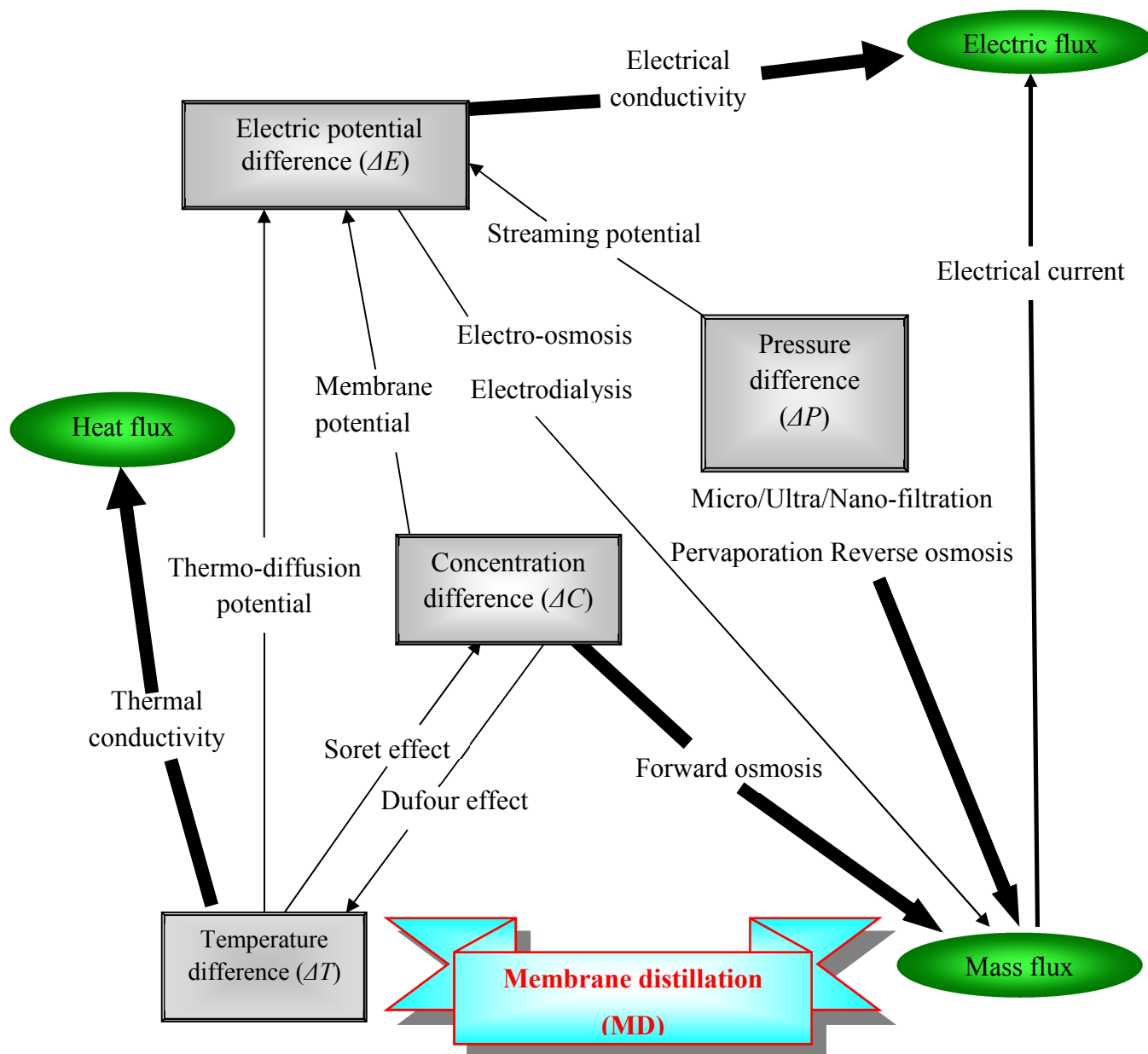
Fig. 1.2.1. Membrane separation processes: Fluxes and driving forces through synthetic membranes.

In general, non-isothermal transport phenomena through membranes have received much less attention than the corresponding isothermal counterparts (e.g. the pressure-driven membrane processes Reverse Osmosis (RO), Nanofiltration (NF), Ultrafiltration (UF) and Microfiltration (MF). Today RO is, undoubtedly, the membrane process more industrially implemented for desalination of water to produce potable water with an actual cost lower than 0.5 US$/m^3. This is due to the continuous development of appropriate synthetic membranes since 1957 when Reid and Breton [1] found that

cellulose acetate (CA) was a suitable material for membrane fabrication. The pioneering studies of Loeb and Sourirajan in 1963 were also key factors improving the selectivity and water production of such membranes by introducing various additives in the polymer CA solutions [2].

The study of non-isothermal flux of matter dates back to 1873 when some qualitative results were published by Feddersen [3] observing air flow through different porous media (platinum sponge, gypsum, etc.) caused solely by temperature difference while the pressure was uniform. It was observed that the detected gas flow always took place in the direction from lower to higher temperature. Feddersen called this phenomenon "Thermal Diffusion". Today, this nomenclature is used for another effect referring to the movement of particles inside any continuous mixture (i.e. multi-component system) under gradients of temperature, at constant pressure and concentration, and in absence of membranes.

The existence of non-isothermal liquid transport through membranes was first described by Lippman in 1907 [4] and five years later it was investigated in more detail by Aubert [5]. This phenomenon known as Thermo-osmosis (TO) or Thermal Osmosis (TO) did not involve any liquid/vapor phase transition and can be carried out through both electrically charged or uncharged, dense or porous, hydrophilic membranes. At present, there is a relative lack of publications on TO due to several reasons. The most significant one is the lack of interest from the industrial point of view. Additionally, since the TO permeate flux is very small, the experiments are complicated, very long and laborious. It is therefore not surprising that there were discrepancies, both qualitative and quantitative, between the results obtained by different authors, even when similar systems were employed.

In 1952, the understanding of the Thermodynamics of Irreversible Processes had progresses to the point that Denbigh and Raumann [6] could formulate a viable theory of TO and interpreted in the framework of the theory their obtained quantitative data.

It were the studies of Haase´research group [7-9], which demonstrated the existence of TO through uncharged membranes using non-electrolyte solutions. Later, in the first volumes of the prestigious Journal of Membrane Science, Vink and Chisthi in 1976 [10] and Mengual et al. in 1978 [11], corroborated this finding with pure water and cellulose acetate (CA) membranes. In addition, until the 1960s researchers believed that non-isothermal transport could only exist through dense membranes [12,13]. On the contrary, subsequent contributions [14-17] claimed that when liquid solutions are used,

the membrane pore filled with liquid behaved, under a temperature gradient, as a microscopic Soret cell. This phenomenon was termed Thermo-Dialysis (TD).

Parallel to the TO developments, it was suggested that if appropriate hydrophobic membranes were developed, the pores could stay dry, forming liquid/vapor interfaces at their sides as can be seen in Fig. 1.2.2. The hydrophobic nature of the membrane prevents liquid solutions from entering its pores due to the surface tension forces. As a result, liquid/vapor interfaces are formed at the entrances of the membrane pores. Under this circumstance, if a temperature gradient is imposed between both membrane surfaces, and due to the vapor pressure difference, vapor transfer can occur through the membrane pores. Such a non-isothermal transport of vapor can take place from the hot interface where evaporation occurs to the cold side where condensation takes place. Note that, although the phenomenology is similar, the transport mechanism is completely different from the case of TO, so that the new process was called Membrane Distillation (MD). Details on the previously used terms of this process can be found in the book [18].
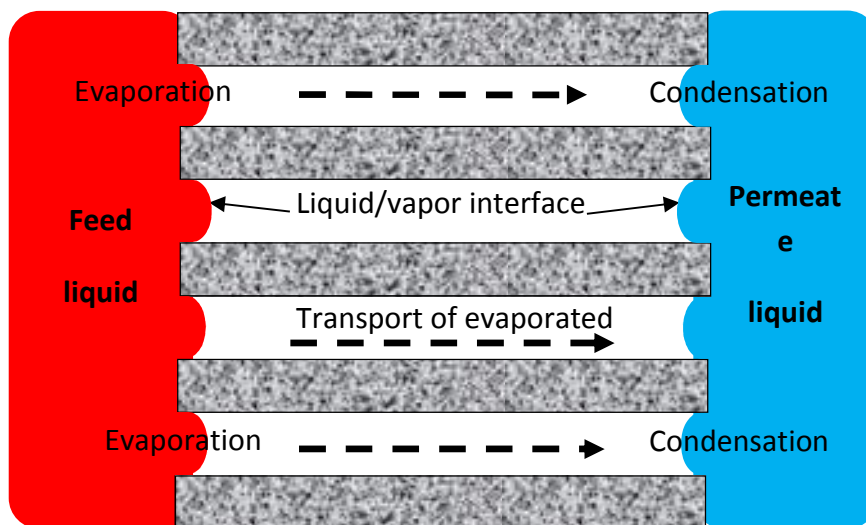
Fig. 1.2.2. Schema of liquid/vapor interface formation at both sides of the pores of single layer hydrophobic membrane supposed cylindrical.

In 1963, the first patent on MD was filled by Bodell [19], while the first scientific publication on this separation process was made by Findley four years later in the journal Industrial & Engineering Chemistry – Process Design & Development [20]. Since then, the interests on MD were faded quickly because of the unavailability of adequate membranes for this process. The real explosion of MD occurred since 1980s, when the first porous polytetrafluoroethylene (PTFE, Teflon) membrane type (Gore-Tex) started to be available in the market [18,21]. Figure 1.2.3 shows the significantly enhanced interest in MD field indicated by presenting the number of peer reviewed published studies in international Journals per year up to 31st December of last year. The total number of published papers is more than 7 times greater than that of TO (i.e. 757 papers for MD and 107 papers for TO). The MD permeate fluxes were two orders of magnitude higher than those of TO, which surprised the researchers of the time and generated some debates. Today, in contrast to the TO process, MD has made its way toward industrial implementation due to the continuous progress made in recent years developing membranes, modules and autonomous water treatment facilities that couple solar thermal collectors and photovoltaic panels [18]. In this chapter book, important key characteristics and fundamentals of MD process including some fields of applications are described.
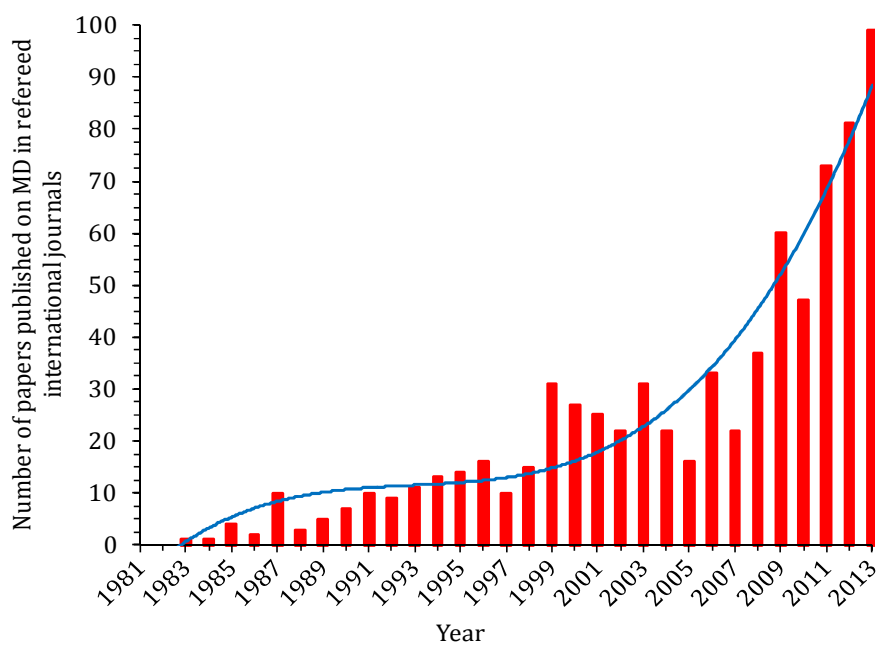
(a)
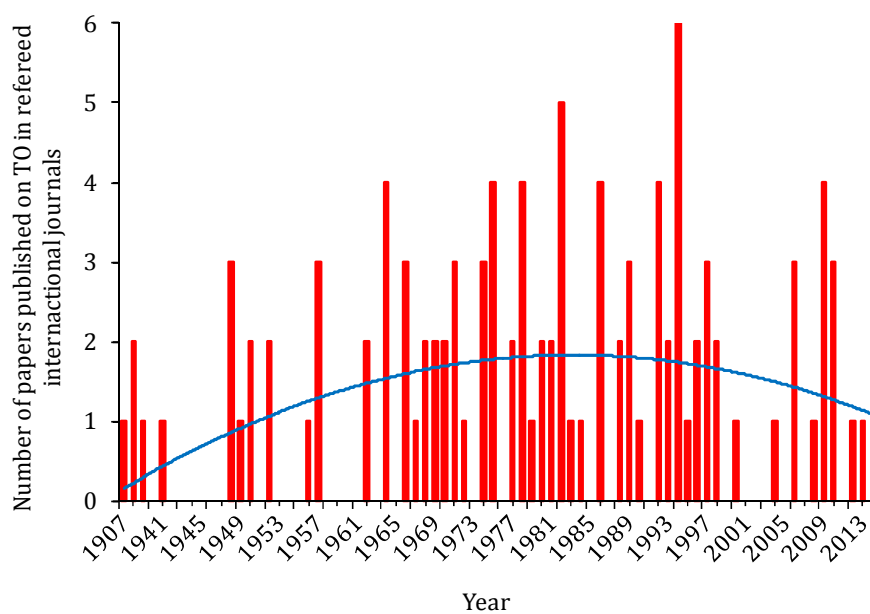
(b)

Fig. 1.2.3. Growth of research activity on MD (a) and TO (b) up to 31st December of 2013 represented as a plot of number of papers published in refereed international journals per year ((a) is an updated version of a figure adapted with permission from [21] Khayet (2011) ©2011 Elsevier B.V.).

1.2.2. Key characteristics of membrane distillation

As it is stated in the previous section, MD refers to a thermally driven transport of vapor through non-wetted porous hydrophobic membranes, the driving force is the vapor pressure difference between the two sides of the membrane pores, and the liquid feed to be treated by MD must be maintained in continuous direct contact with one side of the membrane without penetrating its dry pores. Therefore, the applied transmembrane hydrostatic pressure must be lower than the membrane liquid entry pressure (i.e. breakthrough pressure, *LEP*), which is one of the important key characteristic of MD technology.

LEP is defined as the minimum transmembrane pressure that is required for distilled water or the feed solution to enter into the pore (i.e. maximum pore size of the membrane), by overcoming the hydrophobic forces of the membrane material. This is a characteristic of each membrane and should be as high as possible. Otherwise pore wetting will occur leading to the deterioration of the produced water quality. *LEP* is related to the maximum pore size ($d_{p,max}$) of the membranes by means of Laplace equation [22]:

$$LEP = \left| \frac{4\ \alpha\ \sigma}{d_{p,max}} \cos\theta \right| \tag{1.2.1}$$

where σ is the surface tension of the liquid solution, α is the geometric factor of the maximum membrane pore, and θ is the contact angle of the liquid on the membrane surface.

A membrane with a high *LEP* value can be developed using materials of low surface energy or high hydrophobicity and small maximum pore size. However, when a membrane exhibits a small maximum pore size, this membrane also has a small mean pore size and, consequently, low membrane permeability is expected.

The pore size of the membrane and its distribution are critical parameters for MD membranes. The pore size may vary from several nanometers to few micrometers (e.g. 10 nm – 5 μm) and the pore size distribution should be as narrow as possible so that the maximum pore size is close to the mean pore size controlling better the risk of pores wetting. As it will be shown in section 1.2.4, membranes having different pore sizes exhibit different physical flow mechanisms.

The porosity of the membrane, which is the void volume fraction open to MD vapor flux, should be as high as possible without compromising its mechanical properties. A membrane with higher porosity provides a large space for evaporation and therefore high permeate flux as well as high thermal resistance, because the thermal conductivity of air entrapped in the void space of the membrane is smaller than that of the membrane matrix resulting in high thermal efficiency. As it will be reported later on, the MD membrane permeability is proportional to the porosity. Among all membranes used in MD, electrospun nanofibrous membranes (ENMs) exhibit the highest void volume fraction, up to 93% [23].

The tortuosity factor, which is the measure of the deviation of the pore structure from straight cylindrical pores normal to the surface, should be small close to unity. This is inversely proportional to the MD membrane permeability. For ENMs, the tortuosity can be predicted by means of fractal theory of random walks as the inverse of the void volume fraction [24]. In this case, the estimated tortuosity values of ENMs is as low as 1.07. For polymeric membranes prepared with ion bombardment, the tortuosity is unity [25]. Some authors considered a value of two to run their developed theoretical models or simply take the tortuosity as an adjusting parameter to fit the theoretical to the experimental MD permeate fluxes [18,21].

The thickness of the MD membrane should exhibit an optimized value because it is inversely proportional to the rate of both heat and mass transport through the membrane. Based on the theoretical established equations in MD (see section 1.2.4), a high mass transport is favored using a thin membrane; however a simultaneous high heat transport, which is considered to be a heat loss in MD, also takes place. Therefore, a compromise should be made between the mass and heat transfer, by properly adjusting the membrane thickness. The selection of the membrane thickness is strongly related to the type of the membrane, supported or unsupported, flat sheet or hollow fiber, type of membrane material, mechanical integrity, single-, double- or triple-layered membrane, etc.

The heat transfer by conduction through the whole membrane must be as low as possible in order to achieve high process thermal efficiency. This can be achieved optimizing the whole structure of the membrane including porosity, thickness and thermal conductivity of the used materials. When using a single layer hydrophobic porous membrane, the thermal conductivity of the used material should be as low as possible. Hydrophobic polymers have quite similar thermal conductivity coefficients

(e.g. 0.04 – 0.06 W/m.K for the commercial materials used in MD). However, when using double layer membrane, for example hydrophobic/hydrophilic composite membrane, the thermal conductivity of the hydrophobic layer must be as low as possible, whereas that of the hydrophilic layer in contact with the permeate side must be high in order to reduce the thermal polarization effect [26,27]. When using membranes with high porosity values, the membrane heat transfer by conduction is low since the conductive heat transfer coefficients of the gases entrapped in the pores are an order of magnitude smaller than most of the used membrane materials [18,21,24,26].

The membrane surface should be fabricated with a high fouling resistant material and the membrane as a whole should have good thermal stability as well as high chemical resistance to various types of solutes present in wastewaters. Furthermore, the membrane should not alter the vapor/liquid equilibrium established at the extreme of each pore (see Fig. 1.2.2) and should not let any condensation to occur inside its pores. It is worth noting that the commercial membranes used in MD are fabricated from the three hydrophobic polymers, polyvinylidene fluoride (PVDF), polypropylene (PP) and polytetrafluoroethylene (PTFE) and for other purposes rather than MD process [18,21]. During last 10 years, various types of membranes including surface modified membranes were proposed for MD. Interest on the design, fabrication and modification of membranes for MD is increasing as can be seen in Fig. 1.2.4. However, the number of studies published in refereed journal on MD membrane engineering is still only 16.8% of the total studies published in MD field up to 31st December of 2013. The ideal characteristics of the MD membrane are briefly summarized in Fig. 1.2.4.

High hydrophobicity	Optimized/ high pore size	Optimized thickness & mechanical properties	Low heat transfer
High porosity (void volume fraction)	Narrow pore size distribution	Low pore tortuosity	Low thermal conductivity for single layer
High *LEP*	Low maximum pore size	High chemical resistance & fouling resistance	High thermal stability
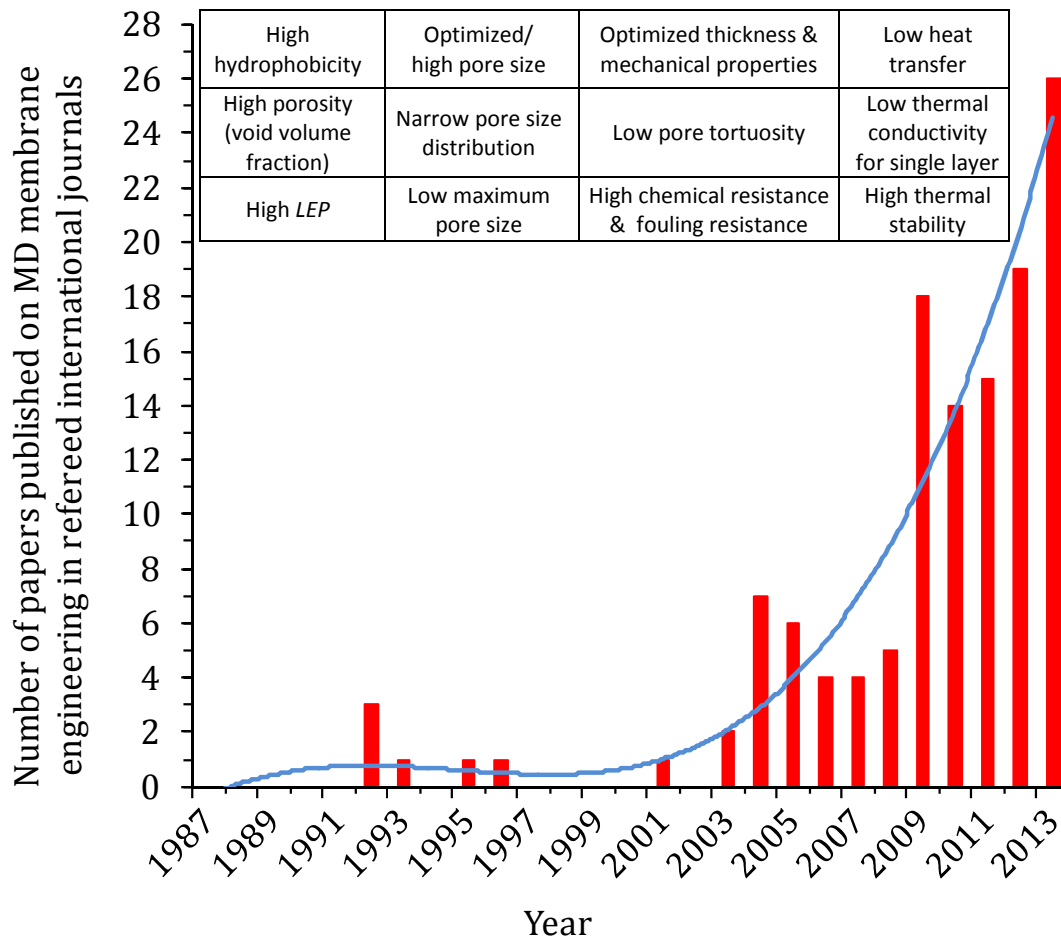
Fig. 1.2.4. Growth of research interests on MD membrane engineering up to 31st December of 2013 represented as a plot of number of papers published in refereed international journals per year and ideal characteristics of an MD membrane (This figure is an updated version of a figure adapted with permission from [21] Khayet (2011) ©2011 Elsevier B.V.).

Various key characteristics make MD attractive and promising separation process:

- Very close to 100% of non-volatile solute rejections (i.e. production of distilled, pure and ultrapure waters).

- Treatment of brines and very high concentrated saline solutions near saturation.

- Low operating hydrostatic pressures (near atmospheric pressure) and therefore less membrane mechanical properties are required.

- Low operating temperatures than conventional distillation processes (30ºC-95ºC).

- High potential to use waste heat as well as alternative energy sources (i.e. possibility to use solar energy systems and geothermal energy).

- Use of small and simple membrane modules working under tangential type of flow.
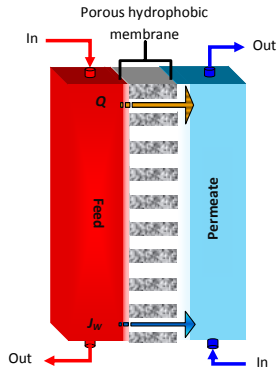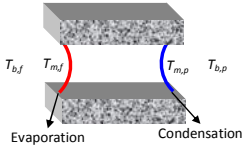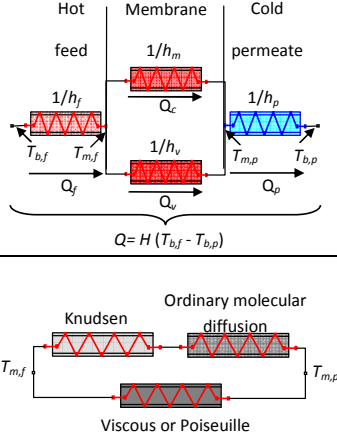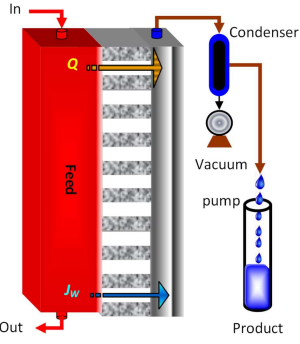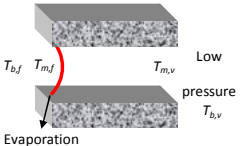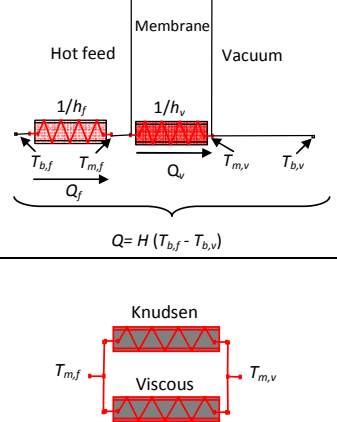
Although MD process exhibits the above cited key advantages, unfortunately from the commercial/industrial levels, still a lot of efforts must be made for full MD
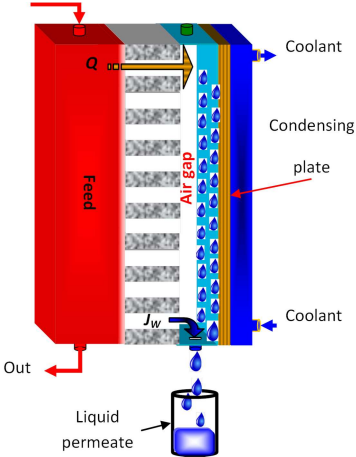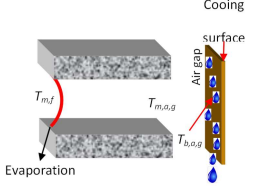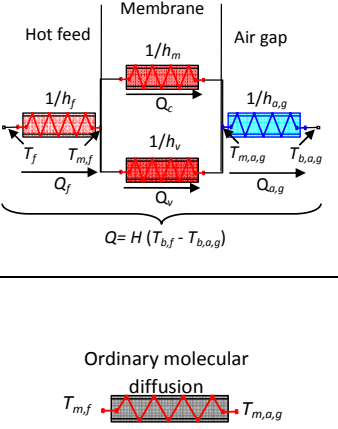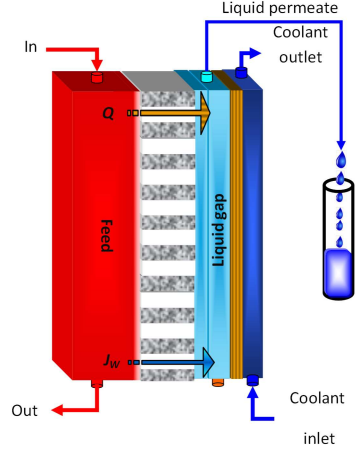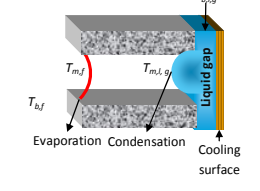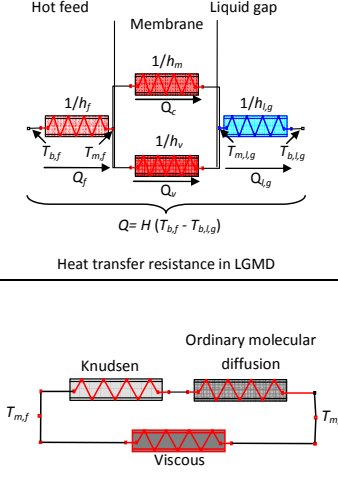
implementation in industry. Among the major barriers one can detect the lack of available membranes designed specifically for MD, the scarce and expensive membrane modules for MD, the high risk of membrane pore wetting, the low permeate flow rate and its decay with time as well as the uncertain energetic and economic costs of the process together with its long term operation [28].
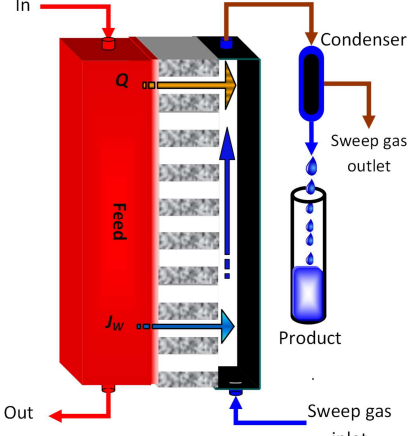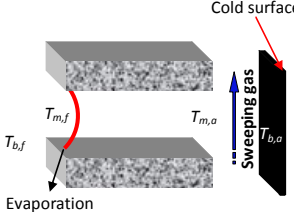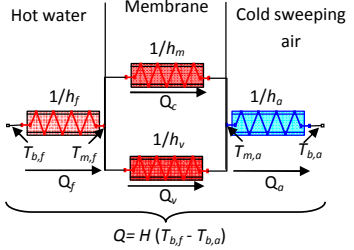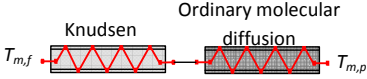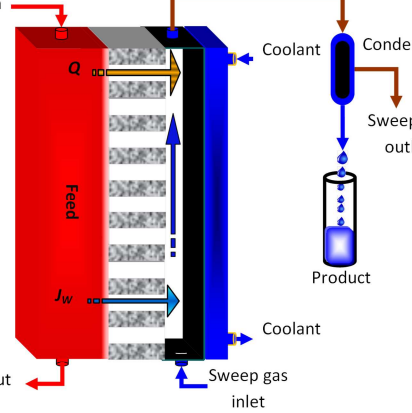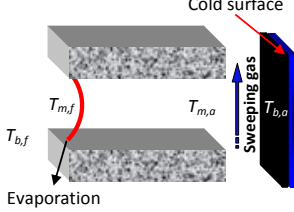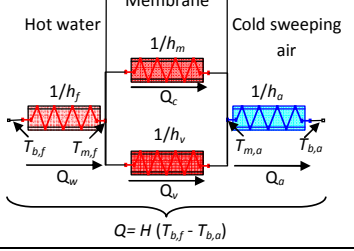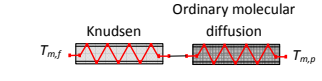
1.2.3. Types of membranes and membrane module configurations for membrane distillation

Depending on the used technology to establish the required driving force in MD, which is the transmembrane water vapor pressure, various configurations of MD were proposed as summarized in Table 1.2.1. In all MD variants, the feed solution to be treated is maintained in direct contact and circulated tangentially to the feed side of the membrane. The difference between all proposed configurations is localized only in the permeate side of the membrane.

Table 1.2.1. Different configurations of membrane distillation technology, heat and mass transfer resistances and considered variants for possible commercial/industrial applications.

MD Configuration	Schema of MD variant	Schema of membrane pore	Heat and mass Transfer resistances [a]	More details & remarks
Direct contact membrane distillation (DCMD)				- Most used in MD at laboratory scale - Simplest MD variant - Considered at commercial/industrial scale [b] - Knudsen or combined Knudsen/ordinary molecular diffusion type of flow - Viscous resistance neglected. - High heat loss by conduction through the membrane.
Vacuum membrane distillation (VMD)				- Considered at commercial/industrial scale with multi-effect AGMD [f] - High risk of membrane pore wetting.

63

MD Configuration	Schema of MD variant	Schema of membrane pore	Heat and mass transfer resistances [a]	More details & remarks
Air gap membrane distillation (AGMD)				- Most considered at commercial/industrial scale (Plate-and-Frame module, Spiral wound module, tubular module) [b,c,d,e] -Industrial multi-effect AGMD (plate-and-frame module) [f] - Low heat loss by conduction through the membrane - Stefan-Maxwell and Stefan Models - Membrane pore size should be considered in the theoretical models - Useful for VOCs from water.
Liquid gap membrane distillation (LGMD)				- Less used in MD at laboratory scale - Considered at commercial scale [b,c,d] - High heat loss by conduction through the membrane.

MD Configuration	Schema of MD variant	Schema of membrane pore	Heat and mass transfer resistances [a]	More details & remarks
Sweeping gas Membrane distillation (SGMD)	In, Q, Feed, J_W, Out, Condenser, Sweep gas outlet, Product, Sweep gas inlet	Cold surface, $T_{m,f}$, $T_{m,a}$, $T_{b,a}$, Sweeping gas, $T_{b,f}$, Evaporation	Hot water, Membrane, Cold sweeping air, $1/h_m$, Q_c, $1/h_f$, $1/h_a$, $1/h_v$, $T_{b,f}$, $T_{m,f}$, $T_{m,a}$, $T_{b,a}$, Q_f, Q_v, Q_a, $Q = H\,(T_{b,f} - T_{b,a})$ — Knudsen, Ordinary molecular diffusion, $T_{m,f}$, $T_{m,p}$	- Not considered yet at commercial/industrial scale - High temperature polarization effect - Combined Knudsen/ordinary molecular diffusion type of flow - Viscous resistance neglected - Useful for VOCs from water.
Thermostatic sweeping gas membrane distillation (TSGMD)	In, Q, Feed, J_W, Out, Coolant, Condenser, Sweep gas outlet, Product, Coolant, Sweep gas inlet	Cold surface, $T_{m,f}$, $T_{m,a}$, $T_{b,a}$, Sweeping gas, $T_{b,f}$, Evaporation	Hot water, Membrane, Cold sweeping air, $1/h_m$, Q_c, $1/h_f$, $1/h_a$, $1/h_v$, $T_{b,f}$, $T_{m,f}$, $T_{m,a}$, $T_{b,a}$, Q_w, Q_v, Q_a, $Q = H\,(T_{b,f} - T_{b,a})$ — Knudsen, Ordinary molecular diffusion, $T_{m,f}$, $T_{m,p}$	- Less used in MD at laboratory scale - Not considered yet at commercial/industrial scale - Combined Knudsen/ordinary molecular diffusion type of flow - Higher permeate flux than SGMD - Lower temperature polarization effect than SGMD - Useful for VOCs from water.

[a] The heat transfer coefficient of the membrane is $h_m=k_m/\delta$, the vapour heat transfer coefficient of the membrane is $h_v=(J_w\Delta H_v)/(T_{m,f}-T_{m,p})$; the heat transfer coefficient of the permeate for DCMD is changed to $h_{l,g}$ for LGMD, h_a for SGMD and TSGMD and $h_{a,g}$ for AGMD.
[b] Aqua/still (Aquastill, The Netherlands)
[c] Memstill, TNO (Netherlands Organisation for Applied Scientific Research) and Keppel Seghers (Belgium)
[d] Fraunhofer Institute for Solar Energy System and SolarSpring GmbH (Germany)
[e] Scarab Development AB and XZero AB (Sweden)
[f] Memsys (Germany, Singapoore) and Aquaver (The Netherlands).

When an aqueous solution colder than the feed solution is maintained in direct contact and circulated tangentially to the permeate side of the membrane, the configuration is known as Direct Contact Membrane Distillation (DCMD). The established transmembrane temperature difference induces the required vapor pressure difference. As a consequence, water and volatile molecules evaporate at the hot liquid/vapor interface, cross the membrane pores in vapor phase and condense in the cold liquid/vapor interface inside the membrane module (see Fig. 1.2.2).

If instead a cold liquid solution, a cold inert gas sweeps the permeate side of the membrane carrying the evaporated water and volatile molecules, the MD configuration is known as sweeping gas membrane distillation (SGMD). In this case condensation phenomenon takes place outside the membrane module.

When vacuum is applied in the permeate side of the membrane to reduce the pressure below the saturation pressure of water and volatile molecules present in the feed solution, the MD configuration is termed vacuum membrane distillation (VMD). In this case, condensation phenomenon also takes place outside of the membrane module.

When a cold surface is placed inside the permeate side of the membrane to carry out the condensation phenomenon, and the evaporated water together with the volatile molecules cross both the dry pores and the stagnant air gap to finally condense over this cold surface, the MD configuration is known as air gap membrane distillation (AGMD). In this case, the produced liquid permeate is collected from the lowest end of the membrane module and no liquid is brought into contact with the permeate surface of the membrane.

If in the previous configuration AGMD, a stagnant cold liquid fill all the permeate side of the membrane channel and kept in direct contact with the permeate membrane surface, this hybrid MD configuration is termed liquid gap membrane distillation (LGMD). It is actually a combination of DCMD and AGMD. In LGMD, the produced liquid permeate is collected from the highest end of the membrane module.

In the previous cited SGMD configuration, the sweeping gas temperature in the permeate side increases considerably along the membrane module length due to the heat transferred from the feed side through the membrane. In order to reduce this temperature and consequently enhance the driving force, a cold surface is placed in the permeate side similar to AGMD configuration. However, in this case condensation phenomenon is carried out outside the membrane module by means of external

condenser(s). This hybrid MD variants, which is termed thermostatic sweeping gas membrane distillation (TSGMD) is a combination of SGMD and AGMD.

Depending on the feed aqueous solution to be treated and the available resources in the place where the MD system is to be installed, an adequate configuration is selected from the above cited MD variants. As it is plotted in Fig. 1.2.5, compared to all MD configurations, DCMD is the most studied and applied one (i.e. more than half of the published studies in international journals up to 31st December of last year are reported on DCMD). This high interest on DCMD is attributed to its simplicity because condensation phenomenon is carried out at the permeate surface of the membrane. On the contrary, the hybrid configurations LGMD and TSGMD are less considered (i.e. contributions of only 0.5% and 0.3% for LGMD and TSGMD, respectively). This may be due to the lower permeate flux of LGMD compared to that of AGMD, attributed to the increased effect of temperature polarization for LGDM. On the other hand, TSGMD suffers the two technological complicated operational modes, that of SGMD, which needs external condenser(s) to collect the permeate plus a source of gas circulation, and that of AGMD, which needs a cold surface inside the membrane module, rendering fabrication of the membrane module together with the whole MD installation more complex (see Table 1.2.1).
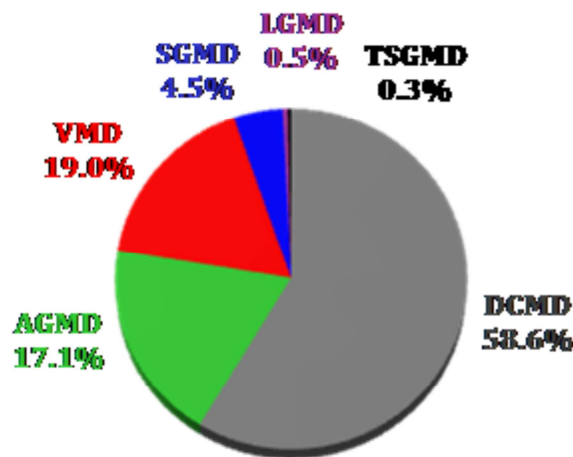
Fig. 1.2.5. Utilization rates of each MD configuration based on the papers published in refereed international journals up to 31st December of 2013.

Different types of membranes, flat sheets, capillaries and hollow fibers were used in MD applications and various types of modules were designed for each MD configuration [21]. Tables 1.2.2 and 1.2.3 summarize most of the commercial flat sheet, capillary and hollow fiber membranes commonly used in MD together with their principal characteristics as specified by the manufacturers. Three types of modules were considered in MD, plate-and-frame modules, shell-and-tube or tubular modules and spiral wound membrane modules. One of the important key characteristics of the MD membrane modules are:

- High membrane packing density.

- High heat and mass transfer coefficients with low temperature polarization effects and thermal efficiency.

- Low pressure drop.

- Easy inspection and defects reparation as well as easy membrane replacement in case of membrane wetting.

- High mass and heat transfer rates between the bulk solutions and the membrane surface.

- Low heat loss with good heat recovery, without erosion problems.

More details on membranes and modules for MD can be found in [18,21].

Table 1.2.2. Flat sheet commercial membranes used in MD (membrane thickness, δ, mean pore size, $d_{p,m}$; porosity, ε; liquid entry pressure of water, LEP_w). (Adapted with permission from [21] Khayet (2011) ©2011 Elsevier B.V.).

Membrane trade name	Manufacturer	Material	δ (µm)	$d_{p,m}$ (µm)	ε (%)	LEP_w (kPa)
TF200	Gelman	PTFE/PP [a]	178	0.20	80	282
TF450	Gelman	PTFE/PP [a]	178	0.45	80	138
TF1000	Gelman	PTFE/PP [a]	178	1.00	80	48
Taflen	Gelman	PTFE/PP [a]	60	0.8	50	--
TS22	Osmonics Crop.	PTFE/PP [a]	175	0.22	70	--
TS45	Osmonics Crop.	PTFE/PP [a]	175	0.45	70	--
TS1.0	Osmonics Crop.	PTFE/PP [a]	175	1.0	70	--
GVHP	Millipore	PVDF [b]	110	0.22	75	204
HVHP Durapore	Millipore	PVDF [b]	140	0.45	75	105 [c]
GVSP	Millipore	PVDF [b]	108	0.22	80	--
FGLP	Millipore	PTFE/PE [a]	130	0.20	70	280
FHLP	Millipore	PTFE/PE [a]	175	0.5	85	124
Gore		PTFE	64	0.2	90	368 [d]
Gore		PTFE	77	0.45	89	288 [d]
Gore		PTFE/PP [a]	184	0.2	44	463 [d]
Gore		PTFE/PP [a]	8.5 [f]	0.2 [f]	78 [f]	--
Sartorious		PTFE	70	0.2	70	--
Enka		PP	100	0.1	75	--
Enka		PP	140	0.2	75	--
Celgard 2500	Hoechst Celanese Co.	PP	28	0.05 [e]	45	--
Celgard 2400	Hoechst Celanese Co.	PP	25	0.02	38	--
Metricel [f]	Gelman	PP	90	0.1	55	--
PP22	Osmonics Corp.	PP	150	0.22	70	--
Membrana, Germany [g]		PP	91	0.2	--	--
Vladipore [h]		--	120	0.25	70	--
3MA	3M Corporation	PP	91	0.29 [i]	66	--
3MB	3M Corporation	PP	81	0.40 [i]	76	--
3MC	3M Corporation	PP	76	0.51 [i]	79	--
3MD	3M Corporation	PP	86	0.58 [i]	80	--
3ME	3M Corporation	PP	79	0.73 [i]	85	--
Teknokrama [j]		PTFE	--	0.2	80	--
Teknokrama [j]		PTFE	--	0.5	80	--
Teknokrama [j]		PTFE	--	1.0	80	--
G-4.0-6-7 [k]	GoreTex Sep GmbH	PTFE	100	0.20	80	463 [c]

[a] Flat sheet polytetrafluoroethylene, PTFE, membranes supported by polypropylene, PP, or polyethylene, PE. Active layer of PTFE/PP membranes purchased from Osmonics Corp. are between 5 and 10 µm.

[b] Flat sheet polyvinylidene fluoride, PVDF, membranes. [c] Measured value [29].

[d] Measured value [30]. [e] Maximum pore size (0.07 µm). [f] Reported in [31].

[g] Membrane used in [32]. [h] Membrane used in [33]. [i] Maximum pore size [34].

[j] Membrane used in [35].

[k] Spiral-wound module, SEP Gesellschaft für Technische Studien, Entwicklung, Planung mbH, filtration area: 4 m^2.

Table 1.2.3. Capillary and hollow fiber commercial membranes used in MD (membrane thickness, δ; internal diameter, d_i; mean pore size, $d_{p,m}$; porosity, ε). (Adapted with permission from [21] Khayet (2011) ©2011 Elsevier B.V.).

Membrane trade name	Manufacturer	Material	δ (μm)	d_i (mm)	$d_{p,m}$ (μm)	ε (%)
Accurel ® S6/2 MD020CP2N [a]	AkzoNobel Microdyn	PP	450	1.8	0.2	70
MD080CO2N	Enka Microdyn	PP	650	1.5	0.2	70
MD020TP2N		PP	1550	5.5	0.2	70
Accurel ® BFMF 06-30-33 [b]	Enka A.G. Euro-Sep	PP	200	0.33	0.2	70
Accurel ®	Enka A.G.	PP	150	--	0.43	70
Accurel ®	Enka A.G.	PP	150	0.33	0.5 [d]	66
Accurel ®	Enka A.G.	PP	400	1.8	0.6 [d]	74
Celgard X-20	Hoechst Celanese Co.	PP	25	--	0.03	35
Capillary membrane	Membrana GmbH, Germany	PP	510	1.79	0.2	75
EHF270FA-16 [c]	Mitsubishi	PE	55	0.135	0.1	70
UPE test fiber [c]	Millipore	PE	250	0.2	0.2	--
PTFE [e]	Sumitomo Electric	POREFLON	550	0.9	0.8	62
PTFE [f]	Gore-tex	TA001	400	1	2 [g]	50

[a] Shell-and-tube capillary membrane module: Filtration area: 0.1 m², length of capillaries: 470 mm, LEP_w = 140 kPa.
[b] Shell-and-tube capillary membrane module: Filtration area : 0.3 m², length of capillaries: 200 mm.
[c] PE hollow fiber [36].
[d] maximum pore size [37].
[e] PTFE hollow fiber [38].
[f] PTFE hollow fiber [39].
[g] maximum pore size.

1.2.4. Membrane distillation theory

In MD field of research, most of the published papers indicated in Fig. 1.2.3(a) are concerned with theoretical analysis and modeling of the different MD configurations. Figure 1.2.6 shows the number of published studies in refereed international journals on MD and involving theoretical model(s) for each MD variant. As it can be seen in Fig. 1.2.6, 39.8% of the MD publications dealt with theoretical models (i.e. 36.6% for DCMD, 36.7% for AGMD, 30.6% for VMD, 51.7% for SGMD, 50.0% for TSGMD and 33.3% for LGMD, being the contribution of the last two configurations negligible). In all MD configurations, heat and mass transfer through porous hydrophobic membranes are involved simultaneously in the direction from the feed to the permeate side of the membrane. Mass transport takes place through the membrane pores while heat transport occurs through both the membrane matrix and the pores. In addition, fluid boundary layers are built in both the feed and permeate channels of the MD membrane modules producing temperature, concentration and vapor pressure polarization phenomena.
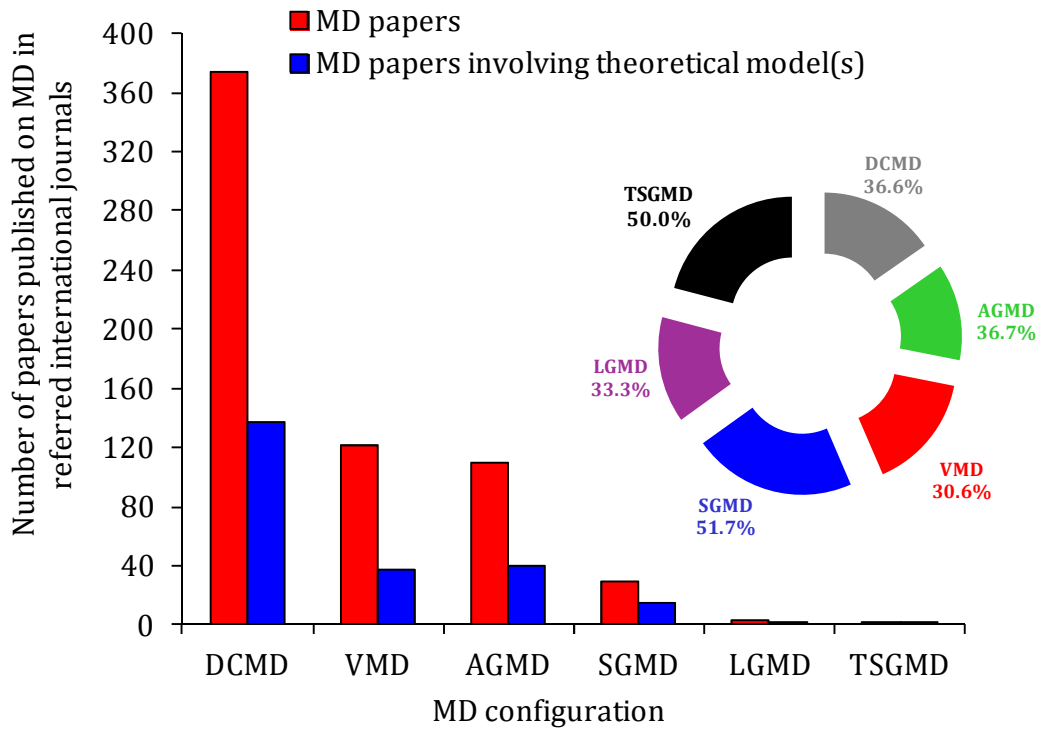
Fig. 1.2.6. Papers published on MD involving theoretical model(s) for each MD configuration up to 31st December of 2013 and corresponding percentages of MD publications dealing with theoretical model(s).

1.2.4.1. Models of mass transfer through the MD membrane

Various theoretical models have been developed based on the Kinetic Theory of Gases through porous media and for each MD configuration in order to predict the permeate flux of different types of membranes [18,21,22,40,41]. In general, as schematized in Fig. 1.2.7 based on an electrical analogy circuit, the different types of mass transport mechanisms proposed for the mass transport through MD membranes are Knudsen flow model, viscous flow model, ordinary molecular diffusion model and/or their combinations depending on the used MD variant and operating conditions.
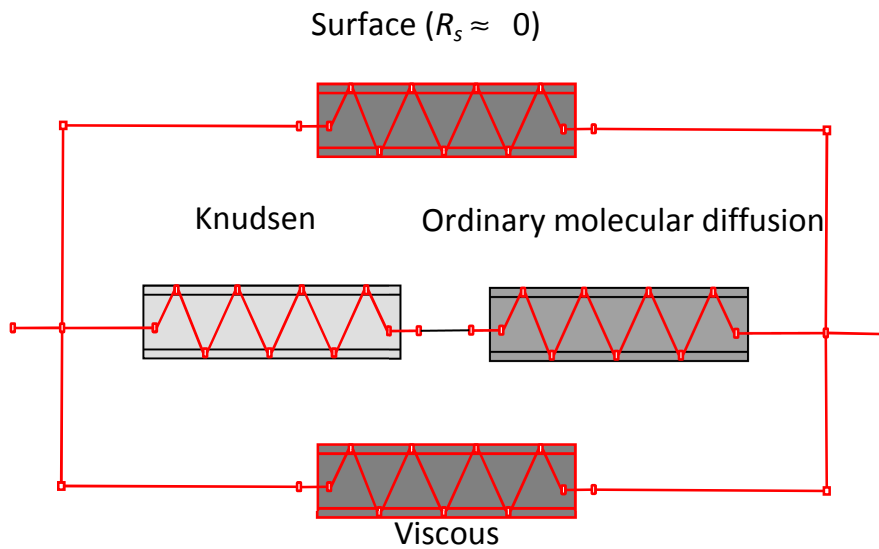
Surface ($R_s \approx 0$)

Fig. 1.2.7. Schematic representation of mass transport mechanisms through a single layer porous hydrophobic membrane based on an electrical analogy circuit with a surface resistance negligible in MD.

It must be pointed out that in MD surface diffusion is neglected. The transport of molecules through the membrane matrix is neglected because the diffusion area of the membrane matrix is small compared to the pore area [22]. As it is reported in the previous section, the porosity or void volume fraction of the MD membrane must be high. Moreover, for hydrophobic MD membranes, the affinity between water and the membrane material is very low and therefore the contribution of transport through the membrane matrix is negligible especially for porous membranes.

The key parameter used to determine the operating mass transport mechanism in a membrane pore maintained under given experimental conditions is Knudsen number (Kn) defined as:

$$kn = \frac{\lambda_i}{d_p} \qquad (1.2.2)$$

where λ_i is the mean free path of the transported vapor molecules through the membrane pore with a size d_p. For a single molecule type i, λ_i can be calculated using the following expression [21,22]:

$$\lambda_i = \frac{k_B T}{\sqrt{2}\pi\, P_m\, \sigma_i^2} \qquad (1.2.3)$$

where σ is the collision diameter, k_B is the Boltzmann constant, P_m is the mean pressure within the membrane pores and T is the absolute temperature.

For a binary mixture (i and j) in air, $\lambda_{i/j}$ is calculated using the following equation [42]:

$$\lambda_{i/j} = \frac{k_B\, T}{\pi\, P_m\, ((\sigma_i + \sigma_j)/2)^2} \frac{1}{\sqrt{1 + M_j/M_i}} \qquad (1.2.4)$$

where σ_i and σ_j are the collision diameters, and M_i and M_j are the molecular weight of the molecules i and j, respectively.

1.2.4.1.1. Knudsen model

When the membrane pore size is smaller than the mean free path (i.e. $Kn > 1$ or $d_p < \lambda_i$), the probability of molecule-pore wall collisions are dominant over that of molecule-molecule collisions as schematically shown in Fig. 1.2.8a and Knudsen type of flow occurs through the membrane pore. In this case the permeability through the membrane pore is expressed as [29]:

$$B^K = \frac{1}{6}\left(\frac{2\pi}{M\,R\,T}\right)^{1/2} \frac{d_p^3}{\tau\delta} \qquad (1.2.5)$$

where d_p is the pore size, M is the molecular weight of the transported specie through the pore, R is the gas constant and δ is the membrane thickness.

For the whole membrane, when an uniform pore size, $d_{p,m}$, is assumed the membrane permeability is expressed as [29,42]:

$$B_m^K = \frac{2}{3} \frac{\varepsilon}{\tau} \frac{d_{p,m}}{\delta} \left(\frac{2}{\pi M R T} \right)^{1/2}$$ (1.2.6)

1.2.4.1.2. Molecular diffusion model

When Knudsen number is lower than 0.01 (i.e. $Kn < 0.01$ or $d_p > 100\ \lambda_i$), the membrane is represented as a space full of stagnant air, which in the case of all MD configurations except VMD is trapped within the membrane pore due to the low solubility of air in water (Fig. 1.2.8b). In this case molecular diffusion model is used to describe the mass transport and the following equation is employed to determine the MD permeability through a membrane pore [29,42].

$$B^{MD} = \frac{\pi}{4RT} \frac{PD}{p_a} \frac{d_p^{\ 2}}{\tau\ \delta}$$ (1.2.7)

where D is the diffusion coefficient, P is the total pressure inside the pore and p_a is the air pressure in the membrane pore.

For water in air, the following expression can be used to calculate ($P\ D$ in Pa m^2/s) [29,43]:

$$PD = 1.895\ 10^{-5} T^{2.072}$$ (1.2.8)

For the whole membrane the permeability is written as follows [18]:

$$B_m^{MD} = \frac{1}{RT} \frac{\varepsilon}{\delta\ \tau} \frac{PD}{p_a} = \frac{1}{RT} \frac{\varepsilon}{\delta\ \tau} \frac{D}{Y_{lm}}$$ (1.2.9)

where Y_{lm} is the log-mean mole fraction of air defined as function of the mole fraction of air at the feed and permeate membrane surfaces $Y_{a,m,f}$ and $Y_{a,m,p}$, respectively:

$$Y_{lm} = \frac{Y_{a,m,f} - Y_{a,m,p}}{\ln\left(Y_{a,m,f} / Y_{a,m,p} \right)}$$ (1.2.10)

1.2.4.1.3. Viscous or poiseuille flow model

When a transmembrane hydrostatic pressure is applied and for membranes with larger pore size than the mean free path of the transported vapor molecules through the membrane pores (i.e. $d_p > 100\ \lambda_i$), the probability of molecule-molecule collisions are dominant compared to that of molecule-pore wall collisions (Fig. 1.2.8c). In this case mass transport takes place via Poiseuille type of flow also known as viscous flow, and the permeability through a single pore is expressed as [22,44,45]:

75

$$B^V = \frac{\pi}{2^7 RT} \frac{P_m}{\eta} \frac{d_p^{\ 4}}{\tau \ \delta} \qquad (1.2.11)$$

where η is the viscosity of the transported molecules and P_m is the average pressure in the pore.

For the whole membrane and assuming an uniform pore size $d_{p,m}$, the membrane permeability can be expressed as:

$$B_m^V = \frac{\varepsilon}{2^5 RT} \frac{P_m}{\eta} \frac{d_{p,m}^{\ 2}}{\tau \ \delta} \qquad (1.2.12)$$

(a)

(b)

(c)

● Evaporated molecule
◔ Stagnant air molecule
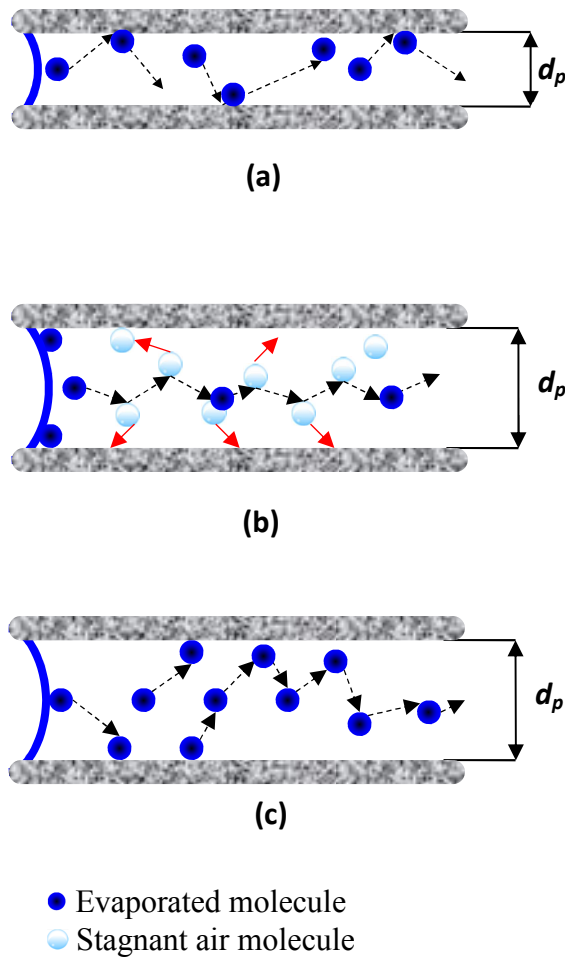
Fig. 1.2.8. Schematic representation of mass transport mechanisms through a pore of a membrane used in MD: (a) Knudsen type of flow, (b) molecular diffusion type of flow, (c) viscous or poisueille type of flow.

1.2.4.1.4. Combined flow models

When Knudsen number lies in the transition region, mass transport through membrane pores is caused by more than one mechanism and combined flow models are considered depending on the MD configuration, type of membrane and the MD operating conditions.

When air is present in the membrane pores, no transmembrane hydrostatic pressure is applied, for example in DCMD configuration, and Knudsen number is in the range, $0.01 < Kn < 1$ (i.e. $\lambda_i < d_p < 100\lambda_i$), both Knudsen model and ordinary diffusion model take place through the membrane pores and the mass transport can be described by a combined Knudsen/ordinary diffusion mechanism through a single pore as follows [29]:

$$B^{K\&MD} = \left(\frac{1}{B^K} + \frac{1}{B^{MD}} \right)^{-1} = \frac{\pi}{RT} \frac{1}{\tau \ \delta} \left[\left(\left(\frac{4 \ R \ T}{9\pi \ M} \right)^{\frac{1}{2}} d_p^3 \right)^{-1} + \left(\frac{1}{4} \frac{PD}{p_a} d_p^2 \right)^{-1} \right]^{-1} \quad (1.2.13)$$

Assuming an uniform pore size, $d_{p,m}$, for the whole membrane, the permeability is determined in this case by the following equation [18,21,29]:

$$B_m^{K\&MD} = \left(\frac{1}{B_m^K} + \frac{1}{B_m^{MD}} \right)^{-1} = \frac{1}{R \ T \ \delta} \left[\frac{\tau}{\varepsilon \ d_{p,m}} \left(\frac{9\pi \ M}{8 \ R \ T} \right)^{1/2} + \frac{p_a \tau}{\varepsilon \ PD} \right]^{-1} \quad (1.2.14)$$

In absence of air in the membrane pores, when a transmembrane hydrostatic pressure is applied, for example in VMD, and Knudsen number is in the transition range, 0.01-1, the ordinary molecular diffusion resistance is neglected and both molecule-molecule and molecule-pore wall interactions are considered. In this case, the pores contribute to the total mass transport by a mechanism operative in the Knudsen/viscous transition region and the permeability through a single pore is described by the following expression [44,45]:

$$B^{K\&V} = \left(\frac{1}{B^K} + \frac{1}{B^V} \right)^{-1} = \frac{\pi}{R \ T \ \tau \ \delta} \left[\left(\frac{4 \ R \ T}{9\pi \ M} \right)^{1/2} d_p^3 + \frac{d_p^4}{2^7 \eta} P_m \right] \quad (1.2.15)$$

The permeability of a membrane with an uniform pore size, $d_{p,m}$, is estimated as follows [21]:

$$B_m^{K\&V} = \left(\frac{1}{B_m^K} + \frac{1}{B_m^V} \right)^{-1} = \frac{\varepsilon \ d_{p,m}}{RT \ \tau\delta} \left(\left(\frac{8 \ RT}{9 \ \pi M} \right)^{1/2} + \frac{d_{p,m} P_m}{2^5 \ \eta} \right) \quad (1.2.16)$$

Once the mechanism of mass transport through a given membrane is established, the permeate flux can be calculated. For a given specie i, the permeate flux in MD, J_i, depends on both the membrane characteristics and the applied driving force as [18,21]:

$$J_i = B_m \Delta p_i = B_m(p^0_{i,f} a_{i,f} - p^0_{i,p} a_{i,p}) = B_m(p^0_{i,f} \gamma_{i,f} x_{i,f} - p^0_{i,p} \gamma_{i,p} x_{i,p}) \qquad (1.2.17)$$

where a_i, γ_i and x_i are the activity, the activity coefficient and the mole fraction of the specie i, respectively. p_i is the partial vapor pressure of the specie i expressed as:

$$p_i(x,T) = p^0_i(T) a_i(x) \qquad (1.2.18)$$

where p^0_i is the vapour pressure of the pure compound i determined with the Antoine Equation:

$$p^0_i(T) = \exp(A - \frac{B}{C+T}) \qquad (1.2.19)$$

where p^0_i is in Pa, T is the absolute temperature in K, and A, B, and C are available constants for each pure compound. For pure water, these constants are 23.1964, 3816.44 and -46.13, respectively.

It must be pointed out that the temperature of the feed solution is the most significant MD operating parameter controlling the MD permeate flux. As it can be expected from Eqs. ((1.2.17)-(1.2.19)), there is an exponential increase of the MD permeate flux with the feed temperature because the partial vapour pressure increases exponentially with temperature (Eq. 1.2.19). Moreover, a linear increase of the MD permeate flux with the vapour pressure difference between the feed and permeate was confirmed as indicated by Eq. (1.2.17) [46-48]. In addition, the MD permeate flux is lower for higher permeate temperature and higher non-volatile solute concentration of the feed solution [18,21,22,49].

Depending on the used MD configuration, Equation (1.2.17) can be simplified. For example, in the case of DCMD mode, distilled water is generally circulated through the permeate side of the membrane and the permeate flux is written as [24]:

$$J_w = B_m(p^0_{w,f} \gamma_{w,f} x_{w,f} - p^0_{w,p}) \qquad (1.2.20)$$

where the subscript w refers to water.

Providing that MD is applied most in desalination, for an aqueous solution of sodium chloride (NaCl), the used relationship between the activity coefficient of water, γ_w, and the mole fraction of sodium chloride x_{NaCl} is [18]:

$$\gamma_w = 1 - 0.5 \, x_{NaCl} - 10 \, x^2_{NaCl} \qquad (1.2.21)$$

When the salt concentration is increased in the feed aqueous solution, based on the last two equations, the MD water permeate flux is decreased since the water vapor

pressure at the feed membrane surface is reduced and therefore the driving force is also decreased.

1.2.4.1.5. Dusty gas model

The dusty gas model (DGM) is a complete model for all MD configurations [22,50]. It can be applied for multi-component mixtures of gases and vapors through porous media, where the pores are represented as stationary pseudo gas molecules with large size (i.e. dust). The model considers the effect of surface diffusion although it is generally considered negligible in MD process as it is stated previously. This model combines all transport mechanisms through the membranes: Knudsen diffusion, molecular diffusion, viscous flow and surface diffusion as follows (see Fig. 1.2.7) [18,21,22,33,50,51]:

$$\frac{J_i^D}{D_{ie}^K} + \sum_{j=1 \neq i}^{n} \frac{p_j J_i^D - p_i J_j^D}{D_{ije}^0} = -\frac{1}{RT} \nabla p_i \qquad (1.2.22)$$

$$J_i^V = -\frac{\varepsilon \, d_{p,m}^{\,2} \, p_i}{2^5 \, R \, T \, \tau \, \eta} \nabla P \qquad (1.2.23)$$

$$D_{ie}^K = \frac{\varepsilon \, d_{p,m}}{3 \, \tau} \left(\frac{8RT}{\pi M_i} \right)^{1/2} \qquad (1.2.24)$$

$$D_{ije}^0 = \frac{\varepsilon}{\tau} P D_{ij}^0 \qquad (1.2.25)$$

$$J_i = J_i^D + J_i^V \qquad (1.2.26)$$

where J^D is the diffusive flux, J^V is the viscous flux, D^K is Knudsen diffusion coefficient, D^0 is the ordinary diffusion coefficient, P is the total pressure, p is the partial pressure, η is the viscosity of the gas mixture, ε is the membrane porosity, M is the molecular weight, τ is the pore tortuosity and the subscripts e, i and j refer to the effective diffusion coefficients and the transported compounds i and j.

It can be observed that the effective Knudsen diffusion coefficient indicated by Eq. (1.2.24) can be related to the membrane permeability indicated by Eq. (1.2.6), and the membrane permeability that can be derived from the viscous flux indicated by Eq. (1.2.23) is the same as that presented in Eq. (1.2.12).

Although the dusty gas model was originally developed for isothermal systems, and MD is a non-isothermal process, it was successfully applied in MD assuming an

average temperature across the membrane [21,22]. It was stated that the dusty gas model reduced to the Knudsen/viscous transition flow (Eq. 1.2.16) for VMD configuration [34].

Another association of mass transfer resistances different from that shown in Fig. 1.2.7 is derived from Schofield model [52]. This considers first a resistance in parallel approach to Knudsen and viscous flows with molecular diffusion in parallel. A comparison between the dusty gas model and Schofield model was performed [53]. Based on the analysis of the obtained experimental data carried out using different types of gases (helium, air and argon) and DCMD experiments of distilled water used as feed, it was concluded that the dusty gas model is more recommendable because the transport mechanism combination is more correct from a physical point of view. However, recently the dusty gas model association has been questioned again arguing that it is not physically possible to have Knudsen and viscous flow occurring in the same pore and some modifications have been proposed to calculate the permeate flux in the Knudsen/molecular diffusion transition [54]. It will be interesting to investigate further this issue. It must be pointed out that for an MD membrane having a pore size distribution, Knudsen region and viscous region do exist and occur simultaneously.

In general, in most of the developed theoretical models in MD the membrane is assumed to have uniform and non-interconnected cylindrical pores. Nevertheless, practically all membranes used in MD, except those fabricated by heavy ion bombardment [25], exhibit pore size distribution and different mass transport mechanisms may occur simultaneously through the membrane. Some theoretical models were developed for different MD configurations considering the pore size distribution rather than the mean pore size (i.e. assumption of uniform membrane pore size equal to mean pore size) [29,43,55-57]; and in VMD configuration [44,45]. It was concluded that the influence of the effect of considering the pore size distribution in the model instead of the uniform pore size is relatively small, especially for commercial membranes having narrow pore size distributions. Furthermore, three-dimensional network models of interconnected cylindrical pores with size distributions were developed by means of Monte Carlo simulation [58-61]. The agreements between the predicted MD permeate fluxes and the experimental ones were found to be good.

One of the limitations of the combined flow models and dusty gas model is the consideration of equal contribution of each mass transport mechanism as presented in Fig. 1.2.7. Bosanquet equation developed in 1944 for self-diffusivity of different species

combining molecule-wall and molecule-molecule interactions, and reported four years later by Pollard and Present [62], is considered in various theoretical MD studies [18,21,22,41]. This equation suggested the collision frequency is simply additive and the effective diffusion is derived from a reciprocal additivity law considering equal contribution of each mass transfer resistance. Taking into account the variation of the contributions to mass transfer, the membrane permeability can be written by Eqs. ((1.2.27),(1.2.28)) instead of Eqs. ((1.2.14),(1.2.16)), respectively for the combined Knudsen/molecular diffusion model [24]:

$$B_m^{K\&MD} = \left(\frac{\alpha}{B_m^K} + \frac{1-\alpha}{B_m^{MD}} \right)^{-1} \tag{1.2.27}$$

and for the combined Knudsen/viscous transition model as:

$$B_m^{K\&V} = \left(\frac{\alpha}{B_m^K} + \frac{1-\alpha}{B_m^V} \right)^{-1} \tag{1.2.28}$$

where α is the contribution of Knudsen diffusion to mass transfer as schematized in Fig. 1.2.9.
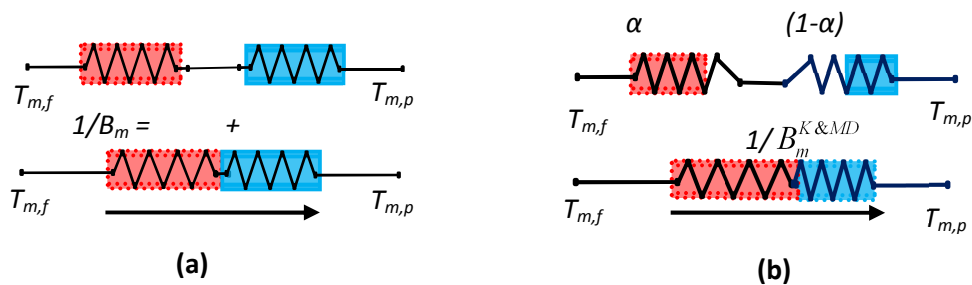
Fig. 1.2.9. Electrical analogy circuit presenting mass transport mechanism through a porous and hydrophobic membrane considering: (a) Bosanquet equation and (b) variable Knudsen contribution (α) schematized in this case as an example for molecular diffusion contribution to mass transport (1-α) (b). (Adapted with permission from [24] Essalhi and Khayet (2013) ©2013 Elsevier B.V.).

1.2.4.1.6. Recent models

Some empirical models based on artificial neural network (ANN) and response surface methodology (RSM) combined with a given statistical experimental design (e.g. factorial design) were developed for different MD configurations [63-68]. These models are completely data driven and do not include any mechanism of transport through the MD membrane. ANN is completely black box model. This is not the case for RSM, which together with a statistical design of experiments (DoE) allow to develop second order polynomial regression models relating the output response of the MD system and the input operating parameters. However, both ANN and RSM are considered for optimization of MD installations permitting to determine the input combination of operating parameters that maximize or minimize a given objective function (i.e. MD permeate flux, energy consumption, etc.). In addition, both models can be used to study the effects of the input operating parameters interactions on the MD performance.

Recently, the ballistic transport approach, which assumes a low frequency of molecule-molecule collisions and a diffuse reflection of particles from surface, was applied in VMD mode with membranes having different pore sizes and operating under Knudsen type of flow [69]. The hot feed liquid/vapor interface was assumed to behave as uniform source of molecules entering the pore with a Maxwell speed distribution, collide with the pore inner surfaces and reflect diffusely from them. The model predicts the permeate flux from high aspect ratio cylindrical pores up to 200 (i.e. pore length to diameter ratio). However, discrepancies of the water permeate fluxes of most membranes were observed between the predicted and experimental values. The model predictions did not take into consideration the temperature polarization effect while both the evaporation and condensation coefficients were considered as adjustment parameters. Although the model is complex, it is scientifically important simulating mechanistically Knudsen type of flow. Further developments and more reliable ballistic transport model(s) for MD with pore scale simulation are needed.

More details on developed theoretical studies on MD are reviewed in [18,21,22,41].

1.2.4.2. Models of heat transfer in MD process

In MD process, the heat transfer within the membrane is due to the latent heat accompanying the produced vapor flux (Q_v) and the heat transferred by conduction following fourier´s law (Q_c) across both the membrane matrix and the gas-filled membrane pores [18,21,22,40,41]:

$$Q_m = Q_v + Q_c \qquad (1.2.29)$$

In MD, Q_c is considered heat loss by thermal conduction through the membrane reducing both the energy efficiency and the water production rate of the process.

When only water vapor transport through an MD membrane, heat transfer at steady state is written as [18,21]:

$$Q_m = J_w \Delta H_v + \frac{k_m}{\delta}\left(T_{m,f} - T_{m,p}\right) \qquad (1.2.30)$$

where J_w is the water permeate flux, k_m is the thermal conductivity of the membrane, δ is the membrane thickness, ΔH_v is the heat of vaporization of water, $T_{m,f}$ is the temperature of the feed aqueous solution at the membrane surface and $T_{m,p}$ is the temperature of the permeate at the membrane surface.

Two models are used in MD literature to estimate the thermal conductivity of the membrane. The Isostrain model (i.e. resistances in parallel model, Eq. 1.2.31) and the Isostress model (i.e. resistances en series model, Eq. 1.2.32) [18,70]:

$$k_m = \varepsilon k_g + \left(1-\varepsilon\right)k_s \qquad (1.2.31)$$

$$k_m = \left(\frac{\varepsilon}{k_g} + \frac{1-\varepsilon}{k_s}\right)^{-1} \qquad (1.2.32)$$

where k_g is the thermal conductivity of the gas-filled void volume fraction of the membrane and k_s is the thermal conductivity of the solid matrix of the membrane.

As it is shown in Fig. 1.2.10, there is a presence of fluid boundary layers adjoining both the feed and permeate membrane sides. Heat transfer also occurs through the adjoining boundary fluid phases, both in the feed and permeate sides of the membrane. At steady state conditions, this heat flux must be the same as in Eq. (1.2.30):

$$Q_m = h_f\left(T_{b,f} - T_{m,f}\right) = h_p\left(T_{m,p} - T_{b,p}\right) \qquad (1.2.33)$$

83

where the subscript b refers to the bulk fluids, and h_f and h_p are the heat transfer coefficients in the feed and permeate boundary layers adjoining the membrane surfaces, respectively.

The coefficients h_f and h_p can be calculated from semi-empirical equations of the dimensionless numbers (Nusselt number, Nu, Reynolds number, Re and Prandtl number, Pr) [21,71,72]:

$$Nu = a \ Re^b \ Pr^c \qquad\qquad (1.2.34)$$

where a, b, c and d are characteristics constants of the liquid flow regime through the membrane module channel.
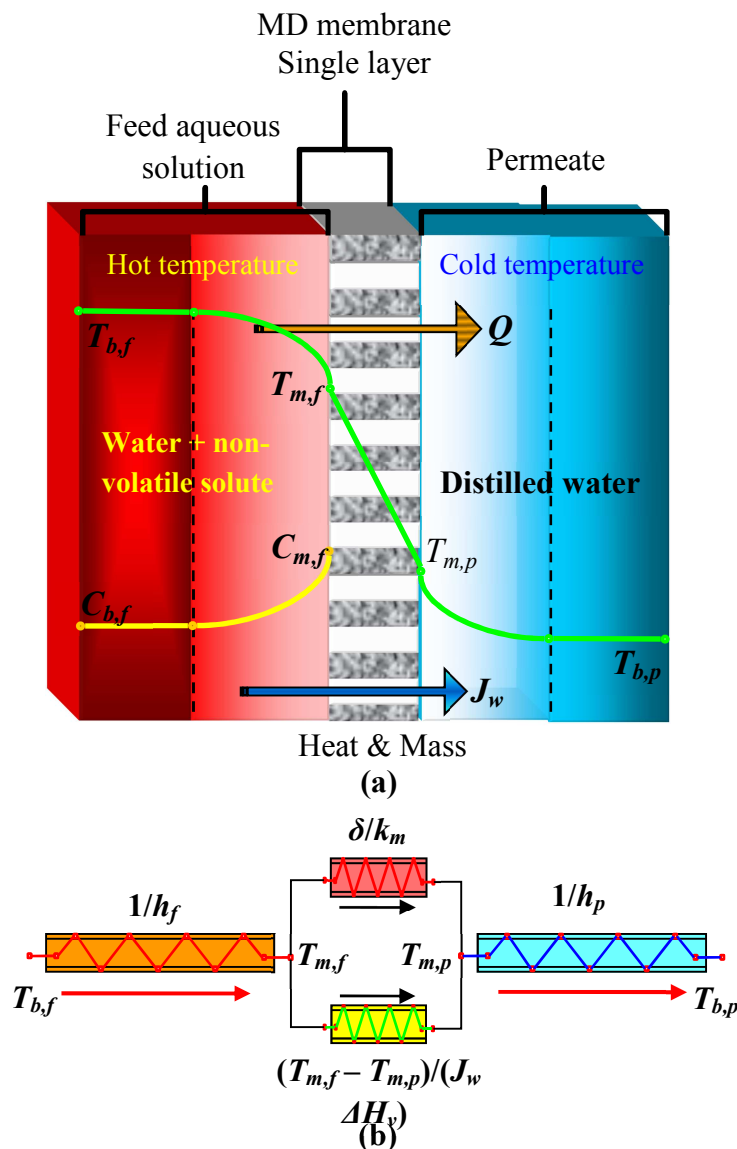
Fig. 1.2.10. Polarization phenomena (a) and electrical analogy circuit presenting heat transfer through a single layer porous and hydrophobic membrane used in DCMD mode.

Various semi-empirical equations were used in MD and most of them are reviewed in [21,22,71,72]. It must be pointed out that the selection of the adequate empirical heat transfer correlation of a given *MD* module is a complex task when developing theoretical models. The use of empirical heat transfer correlations in *MD* was questioned and even criticized as these correlations were developed originally for only heat exchangers and not for heat and mass transfer systems [73]. Special care must be taken when selecting the most suitable correlation.

From the above mentioned Eqs. ((1.2.30),(1.2.33)), the overall heat transfer coefficient (*H*) of the MD process can be determined [21,22,24]:

$$H = \frac{Q_m}{\left(T_{b,f} - T_{b,p}\right)} = \left[\frac{1}{h_f} + \frac{1}{\dfrac{k_m}{\delta} + \dfrac{J_w \Delta H_v}{T_{m,f} - T_{m,p}}} + \frac{1}{h_p} \right]^{-1}$$ (1.2.35)

In *VMD*, because of the applied vacuum in the permeate side of the membrane, the boundary layer resistance in the permeate side and the contribution of the heat transported by conduction through the membrane are frequently neglected [18,22,73].

The thermal efficiency (*EE*) of a given MD module is defined as the ratio of the vaporization heat associated to the mass transport through the membrane pores, Q_v, over the total heat flux transferred through the membrane, Q_m, [18,24]:

$$EE = \frac{Q_v}{Q_m} 100 = \frac{J_w \Delta H_v}{H(T_{b,f} - T_{b,p})} 100$$ (1.2.36)

In MD, the thermal efficiency should be as high as possible or which is the same Q_c should be as low as possible. In general, *EE* values in counter- current MD systems are in the range 60 – 70% [18]. However, when using electrospun nanofibrous membranes, higher *EE* values were obtained, 78.8 – 94.3 %, with Q_c values less than 20% [24].

1.2.4.3. Temperature, concentration and vapor pressure polarization phenomena: heat and mass transfer boundary layers

To predict the MD permeate flux, the use of Eq. (1.2.17) seems to be simple. However, Δp_i depends on both the temperatures and concentrations at the membrane surfaces, which are different from those at bulk solutions due to the simultaneous heat and mass transfers through the membrane (e.g. Fig. 1.2.10). These phenomena are

85

called temperature polarization and concentration polarization and are a major problem for MD reducing its efficiency. Fig. 1.2.10a shows as an example these phenomena for a single layer membrane used in DCMD desalination. For the other MD configurations, changes may be adopted in the permeate side. However, if instead of salts or non-volatile solutes, the feed solution contains volatile solutes, the concentration of these volatile solutes becomes lower at the feed membrane surface and higher at the permeate membrane surface than in the corresponding bulk phases.

1.2.4.3.1. Temperature polarization

Taking Fig. 1.2.10a as a reference, the temperature polarization coefficient is defined as the ratio of the temperature difference between the feed and permeate at the membrane surface over that at the bulk phases [18]:

$$\theta = \frac{T_{m,f} - T_{m,p}}{T_{b,f} - T_{b,p}} 100 \qquad (1.2.37)$$

Attempts have been made recently to measure the temperatures inside an MD membrane module and at the interface between the membrane and the liquid streams [74,75]. These were carried out by means of thermochromic liquid crystals recording color change [74] and by including small platinum thermocouples (Pt100) with sensitivity ±0.1ºC in the membrane cell assuming negligible local interruption of the flow dynamic caused by the sensors due to the very small diameter of the sensors compared to the dimensions of the cell [75]. More investigations should be performed in this MD research area in order to confirm the obtained temperatures at the membrane surface providing that the inclusion of any miniature object influence the thermal boundary layers and distorts the temperature measurement at the membrane surface. Instead, the temperature at the membrane surface was obtained using some calculations and in most cases some approximations were adopted. For example, from Eqs. (1.2.30) and (1.2.33) the temperatures $T_{m,f}$ and $T_{m,p}$ at the membrane surfaces can be estimated [24,29,72]:

$$T_{m,f} = \frac{k_m \left(T_{b,p} + \dfrac{h_f}{h_p} T_{b,f} \right) + \delta \left(h_f T_{b,f} - J_w \Delta H_v \right)}{k_m + h_f \left(\delta + \dfrac{k_m}{h_p} \right)} \qquad (1.2.38)$$

$$T_{m,p} = \frac{k_m \left(T_{b,f} + \dfrac{h_p}{h_f} T_{b,p} \right) + \delta \left(h_p T_{b,p} + J_w \Delta H_v \right)}{k_m + h_p \left(\delta + \dfrac{k_m}{h_f} \right)} \qquad (1.2.39)$$

The temperature polarization coefficient of an ideal MD module should be equal to 100%. However, due to the unavoidable presence of the feed and permeate boundary layers all MD modules have lower values and as consequence the MD process is heat transfer limited. Compared to the other MD configurations, in SGMD configuration, much lower temperature polarization coefficients (< 44%) were found [76,77]. This is attributed to the predominant effect of the permeate gas boundary layer indicating that the mass transport is predominantly controlled by heat transfer through the gas boundary layer, because the heat transfer coefficient through the liquid phase is very large compared with the heat transfer coefficient in the gas phase. In addition, when spacers and turbulent promoters are used in the feed and/or permeate channels of the membrane modules, the temperature polarization coefficients increased substantially approaching 100% [78,79].

1.2.4.3.2. Concentration polarization

As it is shown in Fig. 1.2.10a, because of the water vapor transfer, the salt concentration at the feed membrane surface ($C_{m,f}$) becomes greater than that of the bulk feed solution ($C_{b,f}$). Similarly to the temperature at the membrane surface, the concentration cannot be directly measured at the membrane surface and therefore it is obtained based on calculations and approximations. Nernst film model that neglects the eddy and thermal diffusions in relation to the ordinary diffusion is used to relate the two concentrations $C_{m,f}$ and $C_{b,f}$ [18,21,48,51,80]:

$$C_{m,f} = C_{b,f} \exp(J_w / k_{n,s}) \qquad (1.2.40)$$

where $k_{n,s}$ is the solute mass transfer coefficient for the diffusive mass transfer through the concentration boundary layer in the feed side of the membrane. This solute mass transfer coefficient can be estimated from Sherwood number (*Sh*) using the dimensionless empirical correlation for mass transfer derived from the analogy with that of heat transfer (Eq. 1.2.34):

$$Sh = a \ \text{Re}^b \ Sc^c \qquad\qquad (1.2.41)$$

where Sc is the dimensionless Schmidt number [21,22].

The concentration polarization coefficient (β) is defined as:

$$\beta = \frac{C_{m,f}}{C_{b,f}} \qquad\qquad (1.2.42)$$

Various theoretical approaches and a number of studies have been carried out on the analysis of the temperature and concentration polarization effects on the performance of the different MD variants [18,21,22,41,49,81]. When non-volatile solutes such as salts were considered, the concentration polarization effects was found to be insignificant (i.e. $\beta \approx$ 1.1) compared to temperature polarization effect [34,55,80,82].

1.2.4.3.3. Vapor pressure polarization

The temperature polarization together with the concentration polarization reduces the driving force of the MD process, which is the vapor pressure difference. Since the vapor pressure depends on both temperature and concentration, both polarization phenomena can be combined in one, the vapor pressure polarization, defined as the fraction of the externally applied driving force that contributes to the mass transfer [21,24,81]:

$$\psi = \frac{\Delta p_{w,m}}{\Delta p_{w,b}} 100 = \frac{p_{m,f} - p_{w,p}^0}{p_{b,f} - p_{w,p}^0} 100 \qquad\qquad (1.2.43)$$

where $\Delta P_{w,b}$ is the externally applied bulk driving force (i.e. bulk water vapor pressure difference) and $\Delta P_{w,m}$ is the water vapor pressure difference between the feed and permeate at the membrane surfaces.

When water was used as feed, the temperature and vapor pressure polarization coefficients were calculated and it was found a difference smaller than 0.6 % [81]. However, this difference was increased when salt aqueous solutions were considered [81].

In general, the polarization coefficients depend strongly on the fluid dynamics inside the membrane module, the membrane characteristics, the temperature and the type of feed aqueous solution. Smaller vapor pressure polarization coefficients were obtained for membranes having large pore size, when applying high temperatures and

low circulation flow rates [18,44]. The three polarization coefficients defined in Eqs. ((1.2.37),(1.2.42,(1.2.43)) can be reduced by including turbulence promoters in the module channels, increasing the flow rates of the fluids in order to operate the MD system under turbulent flow regime, by using spacers filled channels, etc. [18].

It must be mentioned that computational fluid dynamics (CFD) models were proposed to improve the hydrodynamic conditions in MD systems, to study heat or heat and transfer optimization inside the MD membrane module channels predicting the field temperature and concentration, to determine the temperature and/or concentration at the membrane surface and to simulate polarization effects [79,83-88].

1.2.5. Typical application of membrane distillation technology

MD technology is considered for different types of applications in which water is the predominantly component present in the feed solution. It is applied alone or integrated with other processes as a final stage in the following fields [89]:

- Desalination of brackish waters, seawaters, geothermal waters, brines derived from other separation processes such as reverse osmosis (RO) pilot plants and very high salinity aqueous solutions near their saturation as well as nuclear desalination of radioactive wastewaters.

- Crystallization producing high quality crystals by processing saturated saline aqueous solutions and looking at zero salty water discharge to the environment.

- Concentration of wastewaters for the simultaneous recovery of valuable components and production of water. Different types of wastewaters were treated by MD including textile, petrochemical, metallurgical, food, pharmaceutical, radioactive wastewaters.

- Production of distilled water, pure water and ultrapure water for semi-conductor, medical, pharmaceutical and food industries.

- Removal of volatile organic compounds (VOCs) from wastewaters such as alcohols, halogenated VOCs and benzene and recovery of aroma compounds, with interests in different fields: environmental, chemical, petrochemical, biotechnology, food, etc.

- Extraction of dissolved gases in water such as oxygen and ammonia.

It is worth quoting that the major MD application is desalination for processing high salinity waters looking at zero discharge of brines to the environment and for producing potable water, distilled water, pure water and ultra-pure water using membranes with narrow pore size distribution. It is indicated in section 1.2.2 that near

100% rejection can be achieved when processing aqueous solution containing non-volatile elyctrolytes solutes (i.e. sodium chloride, potassium chloride, lithium bromide, etc.) and no-elyctrolytes solutes (i.e. glucose, sucrose, fructose, etc.). The produced water by MD exhibits an electrical conductivity as low as 0.8 μS/cm with 0.6 ppm total dissolved solids (TDS) [90].

Most of the above cited MD applications are thoroughly described for each MD configuration in the recent published book [18] and reviewed in [21,22,40,41,49]. More other details are given in the following chapters of the present book.

1.2.6. Conclusions

During last decade, MD technology shows a continuous improvement because of the availability of novel and advanced materials as well as techniques necessary for membrane and module engineering. Care must be taken to choose the appropriate membrane and membrane module for a given water application in order to reduce energy consumption and enhance the produced water quality and quantity. However, although MD is known 50 years ago, still there is no company in the market offering MD membranes and therefore the technology is still not fully used commercially. The used membranes are fabricated for other purposes, microfiltration and ultrafiltration, rather than for MD process. The offered membrane modules and semi-pilot plants are expensive and most of the times are restricted to only some research groups for their further evaluations and experimental improvements at laboratory scale not for their industrial applications.

The lack of the significant industrial application of MD technology is due to the lack of proper membranes and modules. More must be done in the field of fabrication of membranes and modules engineering for MD to bring this technology to significant industrial applications.

1.2.7. Future trends, sources of further information and advises

A lot of efforts have been devoted to the understanding of both the experimental and theoretical fundamentals of MD. Various theoretical models have been developed to predict the permeate flux of the different MD configurations showing good agreements with the experimental data. Recent innovative MD models also appeared. For example, the ballistic transport model is scientifically interesting for MD but it should be improved and validated further. On the other hand, the well known dusty gas model, which was proved to be correct physically by different authors in MD, although it was performed for isothermal systems, has been questioned recently by proposing some modified equations. This issue merits more investigations.

The transport mechanism through the non-porous portion of the membrane is generally neglected in MD. However, this may have a significant contribution when predicting the MD performance. A couple of theoretical models were developed considering the contribution of solution-diffusion through the membrane matrix in MD, but more systematic studies are needed to clarify this point in different MD configurations especially when using low hydrophobic materials, and feed solutions containing organic compounds with high affinity to the membrane material, and membranes with low void volume fraction or porosity.

In AGMD configuration, it is assumed that the transport of vapors across the membrane is described by molecular diffusion theory admitting the air inside the pores of the membrane and in the gap space as a stagnant film. Stefan-Maxwell, Stefan diffusion and binary relations (i.e. Fick´s equation of molecular diffusion) were used to describe multicomponent mass transfer. In all these models, the diffusion coefficient was multiplied by the porosity and divided by the pore tortuosity and membrane thickness without considering the pore size of the membrane although the experimental AGMD permeate flux depends on the pore size. It would be interesting for MD to perform systematic theoretical and experimental studies on the effect of pore size and its distribution on the AGMD performance.

Semi-empirical heat and mass transfer correlations involving the dimensionless numbers (*Nu, Re, Pr, Sc, Sh,* etc.) are often used to estimate the temperature and/or the concentration at the membrane surface in MD. These semi-empirical correlations were obtained originally for non-porous heat exchangers, and selecting the adequate one for a given MD module is a complex task when developing a theoretical model. The use of

these correlations in *MD* was questioned and even criticized. Recent computational fluid dynamics (CFD) seems to be promising models enabling the determination of the field temperature and concentration inside membrane module channels, and therefore enable the estimation of the temperature and concentration polarization effects on the MD performance. Proper and improved CFD models, general not simplified models that take into account the mechanisms of heat and mass transfer through the membrane are needed for different MD configurations.

Air present in the membrane pores exerts a certain resistance to mass transfer reducing the MD permeate flux. Deaeration of DCMD modules were proposed especially when using membranes with large pore sizes. Enhancement of the DCMD performance was observed. More experimental studies including the corresponding energy consumption analysis should be carried out for different DCMD and LGMD configurations.

More experimental and theoretical studies are required on the hybrid MD configurations, TSGMD and LGMD including comparison to the other MD variants.

Identification of new applications of MD process including integrated MD systems to other separation processes and renewable energy sources (e.g. innovative and advanced solar energy systems) are necessary. Various propositions were indicated to improve the final product quantity and quality and reduce energy consumption of MD technology. Multi-staged MD configuration is one of the suggested propositions that may be beneficial for MD technology industrialization.

The principal challenges of MD are long term MD performance, scaling and fouling contamination of the membrane. Few studies are carried out in these fields. More researches are needed using different types of membranes and modules as well as different types of feed aqueous solutions and wastewaters.

Very few data are available on energy efficiency, economics, energy analysis and costs evaluations [28]. The reported scattered values on water production costs and energy consumption of MD systems lead to confusion resulting therefore in loss of confidence in this technology. Detailed energy and costs analysis must be included in the published energy and economic reports, even for the autonomous pilot plant based on renewable energy systems (solar energy, geothermal, etc.).

One of the key research areas roughly studied is membrane design and fabrication specifically for MD process. Innovative and advanced membranes for different MD

applications and different MD configurations as well as membrane modules are demanded.

The advised sources for further information and details may be found in [18,21,22,25,40,41,49].

References

[1] C.E. Reid, E.J. Breton, Water and ion flow across cellulosic membranes, J. Appl. Polymer Sci., 1 (1959) 133-143.

[2] S. Loeb, S. Sourirajan, Sea Water Deminaralization by Means of an Osmotic Membrane, Advan. Chem. Ser., 38 (1963) 117-132.

[3] W. Feddersen, Uber Thermodiffusion von Gasen, Pogg. Ann. Physik Chem, 148 (1873) 302-311.

[4] G. Lippman, Endosmose entre deux Liquides de Meme Composition Chimique et de Temperatures Differentes, Compt. Rend.Acad. Sci., 145 (1907) 104-105.

[5] M. Aubert, Thermo-Osmose. Ann. Chim. Phys., 26 (1912) 145.

[6] K.G. Denbigh, G. Raumann, The thermo-osmosis of gases through a membrane. II. Experimental, Proc. Roy. Soc. London A., 210 (1952) 518-533.

[7] R. Haase, C. Steinert, Thermoosmose in Flüssigkeiten. II. Messungen, Zeitschrift für Physikalische Chemie Neue Folge, Bd.21, S (1959) 270-297.

[8] R. Haase, H.J. DeGreiff, Thermoosmose in Füssigkeiten. III. Richtungsumkehr und Zeitverlanf, Zeitschrift für Physikalische Chemie Neue Folge, Bd.44, S (1965) 301-313.

[9] R. Haase, H.J. DeGreiff, Thermoosmose in Flüssigkeiten. V. Untersuchungen am System Cellophan + Methanol, Zeitschrift Naturforschung Teil A, 26a (1971) 1773-1974.

[10] H. Vink, S.A.A. Chisthi, Thermal osmosis in liquids, J. Membr. Sci., 1 (1976) 149-164.

[11] J.I. Mengual, J. Aguilar, Thermoosmosis of water through cellulose acetate membranes, J. Membr. Sci., 4 (1978) 209-219.

[12] R.P. Rastogi, K. Singh, Cross-phenomenological coefficients. Part 5. Thermoosmosis of liquids through cellophane membranes, Trans. Faraday Soc., 62 (1966) 1754-1761.

[13] M.S. Dariel, O. Kedem, Thermoosmosis in semipermeable membranes, J. Phys. Chem., 79 (1975) 336-342.

[14] F.S. Gaeta, D.G. Mita, Non-isothermal mass transport in porous media, J. Membr. Sci., 3 (1978) 191-214.

[15] F.S. Gaeta, D.G. Mita, Thermal diffusion across porous partitions: The process of thermodialysis, J. Phys. Chem., 83 (1979) 2276-2285.

[16] F. Belluci, E. Drioli, F.G. Summa, F.S. Gaeta, D.G. Mita, N. Paqliuca, Thermodialysis of non-ideal aqueous solutions: An experimental study, Trans. Faraday Soc., II. 75 (1979) 247-260.

[17] F. Belluci, E. Drioli, F.S. Gaeta, D.G. Mita, N. Pagliuca, D. Tomadacis, Temperature gradient affecting mass transport in synthetic membranes, J. Membr. Sci., 7 (1980) 169-183.

[18] M. Khayet, T. Matsuura, Membrane Distillation: Principles and Applications, Elsevier, The Netherlands 2011.

[19] B.R. Bodell, Silicone rubber vapor diffusion in saline water distillation, United States Patent Serial No. 285,032 (1963).

[20] M.E. Findley, Vaporization through porous membranes, Ind. & Eng. Chem. Process Des. Dev., 6 (1967) 226-237.

[21] M. Khayet, Membranes and theoretical modeling of membrane distillation: a review, Adv. Colloid Interface Sci., 164 (2011) 56-88.

[22] K.W. Lawson, D.R. Lloyd, Membrane distillation: Review, J. Membr. Sci., 124 (1997) 1-25.

[23] M. Essalhi, M. Khayet, Self-sustained webs of polyvinylidene fluoride electrospun nano-fibers: Effects of polymer concentration and desalination by direct contact membrane distillation, J. Membr. Sci., 454 (2014) 133-143.

[24] M. Essalhi, M. Khayet, Self-sustained webs of polyvinylidene fluoride electrospun nanofibers at different electrospinning times: 2. Theoretical analysis, polarization effects and thermal efficiency, J. Membr. Sci., 433 (2013) 180-191.

[25] M. Khayet, J.I. Mengual, G. Zakrzewska-Trznadel, Direct contact membrane distillation for nuclear desalination. Part I: Review of membranes used in membrane distillation and methods for their characterization, Int. J. Nuclear Desalination, 1 (2005) 435-449.

[26] M. Qtaishat, M. Khayet, T. Matsuura, Guidelines for preparation of higher flux hydrophobic/hydrophilic composite membranes for membranre distillation, J. Membr. Sci., 329 (2009) 193-200.

[27] M. Su, M.M. Teoh, K.Y. Wang, J. Su, T.S. Chung, Effect of inner-layer thermal conductivity on flux enhancement of dual-layer hollow fiber membranes in direct contact membrane distillation, J. Membr. Sci., 364 (2010) 278-289.

[28] M. Khayet, Solar desalination by membrane distillation: Dispersion in energy consumption analysis and water production costs (a review), Desalination, 308 (2013) 89-101.

[29] M. Khayet, A. Velázquez, J.I. Mengual, Modelling mass transport through a porous partition: Effect of pore size distribution, J. Non-Equilb. Thermodyn., 29 (2004) 279-299.

[31] M.A. Izquierdo-Gil, M.C. García-Payo, C. Fernández-Pineda, Air gap membrane distillation of sucrose aqueous solutions, J. Membr. Sci., 155 (1999) 291-307.

[31] M. Gryta, Osmotic MD and other membrane distillation variants, J. Membr. Sci., 246 (2005) 145-56.

[32] A. Criscuoli, M.C. Carnevale, E. Drioli, Evaluation of energy requirements in membrane distillation, Chem. Eng. Process., 47 (2008) 1098-105.

[33] P.P. Zolotarev, V.V. Ugrosov, I.B. Volkina, V.M. Nikulin, Treatment of waste water for removing heavy metals by membrane distillation, J. Hazard Mater., 37 (1994) 77-82.

[34] K.W. Lawson, D.R. Lloyd, Membrane distillation: II. Direct contact MD, J. Membr. Sci., 120 (1996) 123-33.

[35] M.I. Vázquez-González, L. Martínez, Non isothermal water transport through hydrophobic membranes in a stirred cell, Sep Sci Technol., 41 (1994) 1957-1966.

[36] C.M. Guijt, G.W. Meindersma, T. Reith, A.B. de Haan, Method for experimental determination of the gas transport properties of highly porous fibre membranes: a first step before predictive modeling of a membrane distillation process, Desalination, 147 (2002) 127-32.

[37] M. Tomaszewska, M. Gryta, Morawski AW. Study on the concentration of acids by membrane distillation, J. Membr. Sci., 102 (1995) 113-22.

[38] C.H. Lee, W. Hong, Effect of operating variables on the flux and selectivity in sweep gas membrane distillation for dilute aqueous isopropanol, J. Membr. Sci., 188 (2001) 79-86.

[39] R.L. Calibo, M. Matsumura, J. Takahashi, H. Kataoka, Ethanol stripping by pervaporation using porous PTFE membrane, J. Ferment. Technol., 65 (1987) 665-674.

[40] E. Curcio, E. Drioli, Membrane distillation and related Operations- A Review, Sep. & Purification Reviews, 34 (2005) 35-86.

[41] A. Alkhudhiri, N. Darwish, N. Hilal, Membrane distillation: A comprehensive review, Desalination, 287 (2012) 2-18.

[42] M. Khayet, Membrane Distillation, in Advanced Membrane Technology and Applications, Eds. N.N. Li, A.G. Fane, W.S.W. Ho, T. Matsuura, John Wiley & Sons, Inc, New York, NY, USA, Ch. 5 (2008) 297-370.

[43] J. Phattaranawik, R. Jiraratananon, A.G. Fane, Effect of pore size distribution and air flux on mass transport in direct contact membrane distillation, J. Membr. Sci., 215 (2003) 75-85.

[44] M. Khayet, T. Matsuura, Pervaporation and vacuum membrane distillation processes: Modeling and experiments, AIChE J., 50 (2004) 1697-1712.

[45] M. Khayet, K.C. Khulbe, T. Matsuura, Characterization of membranes for membrane distillation by atomic force microscopy and estimation of their water vapor transfer coefficients in vacuum membrane distillation process, J. Membr. Sci., 238 (2004) 199-211.

[46] H. Kurokawa, K. Ebara, O. Kuroda, S. Takahashi, vapor permeate characteristics of membrane distillation, Sep. Sci. Technol., 25 (1990) 1349-1359.

[47] F.A. Banat, J. Simandl, Theoretical and experimental study in membrane distillation, Desalination, 95 (1994) 39-52.

[48] F.A. Banat, J. Simandl, J. Desalination by membrane distillation: A parametric study, Sep. Sci. & Tech., 33 (1998) 201-226.

[49] M.S. El-Bourawi, Z. Ding, R. Ma, M. Khayet, A framework for better understanding membrane distillation separation process: Review, J. Membr. Sci., 285 (2006) 4-29.

[50] E.A. Mason, A.P. Malinauskas, Gas Transport in Porous Media: The Dusty Gas Model, Elsevier, Amsterdam 1983.

[51] K.W. Lawson, D.R. Lloyd, Membrane distillation. I. Module design and performance evaluation using vacuum membrane distillation, J. Membr. Sci., 120 (1996) 111-21.

[52] R.W. Schofield, A.G. Fane, C.J.D. Fell, Gas and vapour transport through microporous membranes. I. Knudsen-Poiseuille transition, J. Membr. Sci., 53 (1990) 159-171.

[53] C. Fernández-Pineda, M.A. Izquierdo-Gil, M.C. García-Payo, Gas permeation and direct contact membrane distillation experiments and their analysis using different models, J. Membr. Sci., 198 (2002) 33-49.

[54] R.W. Field, H.Y. Wu, J.J. Wu, Multiscale modeling of membrane distillation: Some theoretical considerations, Ind. Eng. Chem. Res., 52 (2013) 8822-8828.

[55] F. Laganà, G. Barbieri, E. Drioli, Direct contact membrane distillation: modelling and concentration experiments, J. Membr. Sci., 166 (2000) 1-11.

[56] L. Martínez, F.J Florido-Díaz, A. Hernández, P. Prádanos, Characterization of three hydrophobic porous membranes used in membrane distillation: Modelling and evaluation of their water vapor permeabilities, J. Membr. Sci., 203 (2002) 15-27.

[57] L. Martínez, F.J. Florido-Díaz, A. Hernández, P. Prádanos, Estimation of vapor transfer coefficient of hydrophobic porous membranes for applications in membrane distillation, Sep. & Pur. Tech., 33 (2003) 45-55.

[58] A.O. Imdakm, T. Matsuura, A Monte Carlo simulation model for membrane distillation processes: direct contact (MD), J. Membr. Sci., 237 (2004) 51-59.

[59] A.O. Imdakm, T. Matsuura, Simulation of heat and mass transfer in direct contact membrane distillation (MD): The effect of membrane physical properties, J. Membr. Sci., 262 (2005) 117-128.

[60] A.O. Imdakm, M. Khayet, T.Matsuura, A Monte Carlo simulation model for vacuum membrane distillation process, J. Membr. Sci., 306 (2007) 341-348.

[61] M. Khayet, A.O. Imdakm, T. Matsuura, Monte Carlo simulation and experimental heat and mass transfer in direct contact membrane distillation, Int. J. Heat & Mass Transfer, 53 (2010) 1249-1259.

[62] W.G. Pollard, R.D. Present, On gaseous self-diffusion in long capillary tubes, Phys. Rev., 73 (1948) 762-774.

[63] M. Khayet, C. Cojocaru, Artificial neural network modeling and optimization of desalination by air gap membrane distillation, Sep. Purif. Tech., 86 (2012) 171-182.

[64] M. Khayet, C. Cojocaru, Artificial neural network model for desalination by sweeping gas membrane distillation, Desalination, 308 (2013) 102-110.

[65] M. Khayet, C. Cojocaru, M.C. García-Payo, Application of response surface methodology and experimental design in direct contact membrane distillation, Ind. Eng. Chem. Res., 46 (2007) 5673-5685.

[66] P. Onsekizoglu, K.S. Bahceci, J. Acar, The use of factorial design for modeling membrane distillation, J. Membr. Sci., 349 (2010) 225-230.

[67] T. Mohammadi, M.A Safavi, Application of Taguchi method in optimization of desalination by vacuum membrane distillation, Desalination, 249 (2009) 83-89.

[68] M. Khayet, C. Cojocaru, A. Baroudi, Modeling and optimization of sweeping gas membrane distillation, Desalination, 287 (2012) 159-166.

[69] S. Soukane, S. Chelouche, M.W Naceur, A ballistic transport model for vacuum membrane distillation, J. Membr. Sci., 450 (2014) 397-406.

[70] J. Phattaranawik, R. Jiraratananon, A.G. Fane, Heat transport and membrane distillation coefficients in direct contact membrane distillation, J. Membr. Sci., 212 (2003), 177-193.

[71] M. Gryta, M. Tomaszewska, A.W. Morawski, Membrane distillation with laminar flow, Sep Purif Technol., 11 (1997) 93 -101.

[72] M. Gryta, M. Tomaszewska, Heat transport in the membrane distillation process, J. Membr. Sci., 144 (1998) 211-222.

[73] J.I. Mengual, M. Khayet, M.P. Godino, Heat and mass transfer in vacuum membrane distillation, Int. J. Heat & Mass Transfer, 47 (2004) 865-875.

[74] A. Tamburini, P. Pitò, A. Cipollina, G. Micale, M. Ciofalo, A thermochromic liquid crystals image analysis technique to investigate temperature polarization in spacer-filled channels for membrane distillation, J. Membr. Sci., 447 (2013) 260-273.

[75] A. Ali, F. Macedonio, E. Drioli, S. Aljlil, O.A. Alharbi, Experimental and theoretical evaluation of temperature polarization phenomenon in direct contact membrane distillation, Chem. Eng. Res. Des., 91 (2013) 1966-1977.

[76] M. Khayet, P. Godino, J.I. Mengual, Theory and experiments on sweeping gas membrane distillation, J. Membr. Sci., 165 (2000) 261-272.

[77] M. Khayet, M.P. Godino, J.I. Mengual, Thermal boundary layers in sweeping gas membrane distillation, AIChE J., 48 (2002) 1488-1497.

[78] J. Phattaranawik, R. Jiraratananon, A.G. Fane, C. Halim, C. Mass flux enhancement using spacer filled channels in direct contact membrane distillation, J. Membr. Sci., 187 (2001) 193-201.

[79] X. Yang, H. Yu, R. Wang, A.G. Fane, Analysis of the effect of turbulence promoters in hollow fiber membrane distillation modules by computational fluid dynamics (CFD) simulations, J. Membr. Sci., 415-416 (2012) 758-769.

[80] R.W. Schofield, A.G. Fane, C.J.D. Fell, R. Macoun, Factors affecting flux in membrane distillation, Desalination, 77 (1990) 279-294.

[81] L. Martínez-Díez, M.I. Vázquez-González, Temperature and concentration polarization in membrane distillation of aqueous salt solutions, J. Membr. Sci., 156 (1999) 265-273.

[82] M. Khayet, M.P. Godino, J.I. Mengual, Study of asymmetric polarization in direct contact membrane distillation, Sep. Sci. Technol., 39 (2004) 125-147.

[83] A. Cipollina, A.D. Miceli, J. Koschikowski, G. Micale, L. Rizzuti, CFD simulation of a membrane distillation module channel, Desalination and Water Treatment, 6 (2009) 177-183.

[84] K. Charfi, M. Khayet, M. Safi, Numerical simulation and experimental studies on heat and mass transfer using sweeping gas membrane distillation, Desalination, 259 (2010) 84-96.

[85] N. Tang, H. Zhang, W. Wang, Computational fluid dynamics numerical simulation of vacuum membrane distillation for aqueous NaCl solution, Desalination, 274 (2011) 120-129.

[86] H.J. Hwang, K. He, S. Gray, J. Zhang, I.S Moon, Direct contact membrane distillation (DCMD): Experimental study on the commercial PTFE membrane and modeling, J. Membr. Sci., 371 (2011) 90-98.

[87] H. Yu, X. Yang, R. Wang, A.G. Fane, Analysis of heat and mass transfer by CFD for performance enhancement in direct contact membrane distillation, J. Membr. Sci., 405-406 (2012) 38-47.

[88] S. Al-Sharif, M. Albeirutty, A. Cipollina, G. Micale, Modelling flow and heat transfer in spacer-filled membrane distillation channels using open source CFD code, Desalination, 311 (2013) 103-112.

[89] B. van der Bruggen, Integrated membrane separation processes for recycling of valuable wasteater streams: Nanofiltration, membrane distillation, and membrane crystallizers revisited, Ind. & Engi. Chem. Res., 52 (2013) 10335-10341.

[90] K. Karakulski, M. Gryta, A. Morawski, Membrane processes used for potable water quality improvement, Desalination, 145 (2002) 315-319.

CHAPTER 2

SURFACE MODIFIED FLAT SHEET MEMBRANES

FOR DESALINATION

BY MEMBRANE DISTILLATION (MD)

2.1. Surface Segregation of Fluorinated Modifying Macromolecule for Hydrophobic/Hydrophilic Membrane Preparation and Application in Air Gap and Direct Contact Membrane Distillation

Contents:

2.1.1. Introduction

2.1.2. Experimental

    2.1.2.1. Materials

    2.1.2.2. Synthesis and characterization of the fluorinated surface modifying macromolecule (SMM)

    2.1.2.3. Membrane preparation

    2.1.2.4. Membrane characterization

    2.1.2.5. Direct contact membrane distillation (DCMD)

    2.1.2.6. Air gap membrane distillation (AGMD)

2.1.3. Results and discussions

    2.1.3.1. Membrane parameters

    2.1.3.2. Membrane performance

2.1.4. Conclusions

References

Abstract:

A fluorinated surface modifying macromolecule (SMM) was synthesized and blended into the casting solution of polyetherimide used as host polymer. A composite porous hydrophobic/hydrophilic membrane was prepared by the phase inversion technique in a single casting step. The membrane was characterized by different techniques. During membrane formation, SMM migrates to the top membrane surface increasing its hydrophobicity and decreasing its pore size, nodule size and roughness parameters. The thickness of the porous hydrophobic top layer was found to be around 4 μm. The membrane was used for desalination by air gap membrane distillation and direct contact membrane distillation. The experiments were performed for different sodium chloride aqueous solutions and various operating conditions. The water production rate was found to be high for direct contact membrane distillation because of the low resistance to mass transport achieved by the diminution of the water vapour transport path length through the hydrophobic thin top-layer of the membrane.

2.1.1. Introduction

Membrane distillation (MD) is a thermally driven process, in which only vapor molecules are transported through porous hydrophobic membranes. The hydrophobic nature of the membrane prevents liquid solutions from entering its pores due to the surface tension forces. As a result, liquid/vapor interfaces are formed at the entrances of the membrane pores. Various MD modes differing in the technology applied to establish the driving force (i.e. transmembrane vapor pressure) can be used. Those are direct contact membrane distillation (DCMD), sweeping gas membrane distillation (SGMD), vacuum membrane distillation (VMD) and air gap membrane distillation (AGMD) [1-5].

The membranes to be used in MD must be porous and hydrophobic. It can be a single hydrophobic layer (i.e. conventional and most used membrane), a composite porous bilayered hydrophobic/hydrophilic membrane or hydrophilic/hydrophobic membrane, and a composite trilayered porous hydrophilic/hydrophobic/hydrophilic membrane or hydrophobic/hydrophilic/hydrophobic membrane [1]. Both supported and unsupported membranes were used in MD [6]. When employing porous supports for preparation of composite membranes, the supports must be chemically resistant against the solvent or solvent mixture from which the thin layer is formed and should have a high surface porosity as well as large pore sizes. In fact, the support should not provide any significant resistance to mass transport.

The pore size of the membranes frequently used in MD lies between 10 nm and 1 μm and the porosity should be as high as possible. It is generally admitted that the MD permeate flux increases with the increase of the pore size and/or porosity. The choice of a membrane for MD applications is a compromise between a low heat transfer flux by conduction achieved using thicker membranes and a high permeate flux achieved using thin membranes having large pore size, low pore tortuosity and high porosity. More characteristics required for an MD membrane were detailed elsewhere [1,2,7].

Developments in the MD process were made mainly in the early 1980s when hydrophobic polytetrafluoroethylene (PTFE) membranes became available. This polymer represents an ideal material for membrane manufacturing for MD since among other polymers it exhibits a high hydrophobic character, good chemical resistance and high thermal stability. The basic

disadvantage of PTFE lies in its difficult processability. At present, commercial PTFE membranes are usually produced through complicated extrusion, rolling and stretching or sintering procedures. Other polymers such as polypropylene (PP) and polyvinylidene fluoride (PVDF) were employed for the preparation of MD membranes [1]. For instance, PP membranes are prepared either by molten extrusion technique followed by stretching or by thermal phase separation process that needs polymer dissolution at high temperature in less common solvents [3]. PVDF dissolves at room temperature in a variety of solvents and therefore porous membranes can be easily produced by phase separation (i.e. phase inversion) method, simply immersing the cast solution film in a coagulant bath (i.e. non-solvent, frequently water). In this case, membrane porosity is controlled by the additives (i.e. pore forming agents) in the casting solution or by replacing water in the coagulation bath with a different non-solvent media [3]. Copolymers like polyvinylidenefluoride-*co*-hexafluoropropylene (PVDF-HFP) and polyvinylidene fluoride-tetrafluoroethylene (PVDF-TFE) were used to prepare MD membranes in flat sheet or hollow fiber using the phase inversion technique [8,9].

Membrane surface modification using different technologies such as grafting, coating or blending fluorinated surface modifying macromolecules (SMMs) with hydrophilic polymers were also tested for different MD systems and configurations [10-14]. Significant results were obtained recently in the preparation and modification of polymeric MD membranes [3]. As a consequence, the improvement of the *MD* permeate flux has increased the reliability of MD process.

In general, the membrane top skin layer governs the performance of a membrane separation process. Therefore, the goal of the preparation of composite membranes or surface modified membranes is to make the selective layer that governs the separation as thin as possible, while maintaining the membranes free of defects. Various methods were applied for membrane surface modification [3,15,16]. In MD field, surface modified membranes have been developed in a laboratory scale by radiation graft polymerization [17], plasma polymerization [5,17,18], grafting ceramic membranes [11], hydrophobic or hydrophilic surface coating [10] or casting hydrophobic polymer over flat sheet or porous fibers as supports [19], co-extrusion spinning [20,21] and use of surface modifying macromolecules (SMMs) [7,12-14].

One of the simplest surface modification methods is to introduce active additives that can migrate to the air/film interface and change its chemistry while leaving the bulk properties intact. This method was followed to prepare both porous and dense composite membranes using SMMs [7,12-14]. The SMM is an oligomeric fluoropolymer synthesized by polyurethane chemistry and tailored with fluorinated end groups. According to this method, membranes can be prepared by the phase inversion technique in only one casting step employing a polymer solution containing the host hydrophilic polymer and the SMM with/without another additive. Only a small quantity of SMM is required (i.e. less than 2.5 wt% in polymer solution). When the solution of a polymer blend is equilibrated with air, with which the solution is in contact, the SMM having the lowest surface energy will concentrate at the air/solution interface and reduce the system's interfacial tension as a consequence.

During the last ten years, hydrophobic/hydrophilic porous composite membranes were developed using different types of SMMs and tested in desalination by DCMD [12-14,22]. Different solvents, hydrophilic polymers and additives were used in order to optimize the DCMD performance of the composite hydrophobic/hydrophilic membranes. This type of membranes were found to be promising for desalination by DCMD as they combine the low resistance to mass flux, achieved by the diminution of the water vapor transport path through the hydrophobic thin top-layer, and a low conductive heat loss through the membrane, obtained by using a thicker hydrophilic sub-layer. In this study, an attempt is made to use the composite porous hydrophobic/hydrophilic membrane for desalination by AGMD configuration. The effects of different experimental parameters such as the feed temperature, the cooling temperature, the feed flow rate and the salt concentration on both the permeate flux and the salt rejection factor were studied. The AGMD performance of the composite porous hydrophobic/hydrophilic membrane is compared to its DCMD performance.

2.1.2. Experimental

2.1.2.1. Materials

The host polymer used is polyetherimide (Ultem®1010-1000) supplied by General Electric Company (GE Plastics Canada Ltd.). N,-methyl-2-pyrrolidione (NMP, Sigma-Aldrich) was employed as solvent to prepare the polymer casting solution and hydroxybutyric acid γ-lactone (GBL, Sigma-Aldrich) was used as the non-solvent additive.

The fluorinated surface modifying macromolecule (SMM) was synthesized using the diisocyanate 4,4´-methylene bis(phenyl isocyanate) (MDI, Sigma-Aldrich), the polyol 4,4´-sulfonyldiphenol (DPS, Sigma-Aldrich) and the monofunctional fluorinated alcohol (Zonyl fluorotelomer intermediate, 2-(perfluoroalkyl)ethanol, BA-L, Aldrich Chemical) with an average molecular weight of about 443 and a fluorine content of 70 wt%. N,N-dimethylacetamide (DMAC, Sigma-Aldrich) was employed as a solvent for the reaction of the MDI with the DPS.

2.1.2.2. Synthesis and characterization of the fluorinated surface modifying macromolecule (SMM)

The surface modifying macromolecule (SMM), MDI/DPS/BA-L, was synthesized by a two-step solution polymerization method using 3/2/2 stoichiometric ratio in a controlled atmosphere of a prepurified nitrogen (N_2) gas. The followed reaction is shown in Fig. 2.1.1. The initial step involved the reaction of the diisocyanate MDI with the polyol DPS in the solvent DMAC, which was previously distilled before use. MDI and DPS reacted at 50ºC for 3h to form the polyurethane prepolymer. The reaction was then terminated by the addition of the fluoroalcohol BA-L at 25ºC for 24 h to end-cap the prepolymer resulting in the formation of SMM with hydrophobic end groups. The SMM was precipitated from the solution with distilled water, washed three times with 30/70 v/v acetone/water mixture to leach out the unreacted monomer, and finally dried in oven at 50°C. The structure of the synthesized SMM is also shown in Fig. 2.1.1.

107

The fluorine content and the polystyrene molecular weights (i.e. the weight average molecular weight, M_w, and the number average molecular weight, M_n) were determined. The methodology and the instrumentation details were reported elsewhere [3,12,22]. The characteristics of the prepared SMM are a fluorine content of 19.8 wt% and a polydispersity (M_w/M_n) of 1.3 (i.e. $M_w = 0.65 \times 10^4$ and $M_n = 0.50 \times 10^4$). The polydispersity is less than two and therefore the SMM´s molecular weight distribution is very narrow. It is to point out that the most significant contribution to the SMM´s molecular weight comes from the size of the prepolymer chain generated in the first step of the polymerization reaction and not the size of the fluorine tail. This is because the addition of the fluoroalcohol is a chain-terminating step. Compared to other synthesized SMMs, the one prepared in this study exhibits low molecular weights and high fluorine content [12,14,22]. In fact, the fluorine content decreased with the increase of the SMM molecular weights [12].
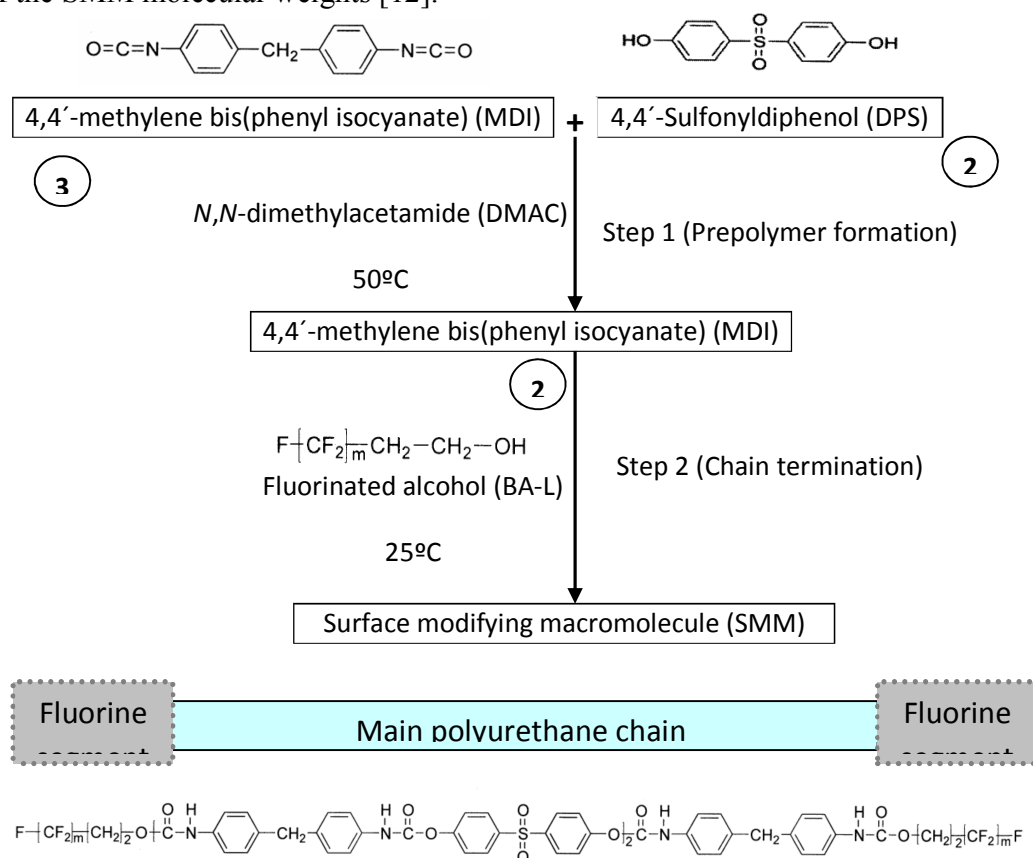

Figure 2.1.1. Reaction scheme for the synthesis of the fluorinated SMM (MDI/DPS/BA-L) with a 3/2/2 stoichiometric ratio and SMM chemical formula.

108

2.1.2.3. Membrane preparation

A flat-sheet composite porous membrane was prepared by the phase inversion technique from a casting solution containing 12 wt% of PEI polymer, 76 wt% NMP, 10 wt% GBL and 1.5 wt% SMM. First, PEI was heated under vacuum at 90ºC during 24 h and then dissolved in the NMP/GBL mixture kept under stirring at ambient temperature (22ºC) and 100 rpm. Subsequently, the SMM was dissolved in the prepared PEI solution by stirring in an orbital shaker (OVAN multipurpose rotation shaker 650-00001) for 48 h and 22ºC. The SMM/PEI blend solution was then degassed for 15 h at room temperature.

The prepared SMM/PEI solution was poured onto a glass plate (0.45 x 0.3 m^2) for casting at room temperature using the motorized film applicator with reservoir (Elcometer 4340). The casting speed was 7×10^{-3} m/s and the thickness of the applicator was 200 μm. The cast film was kept 30 s at ambient temperature to evaporate partially the solvent and to let SMM migrate to the polymer/air interface as shown in Fig. 2.1.2. Subsequently, the cast film and the glass plate were immersed in tap water kept at a temperature of about 17°C for 24 h. During coagulation, the membrane peeled off from the glass plate spontaneously. Finally, the membrane was further stored in distilled water at room temperature. Prior to characterization and application in desalination the membrane was dried in a desiccator under vacuum at 25ºC.
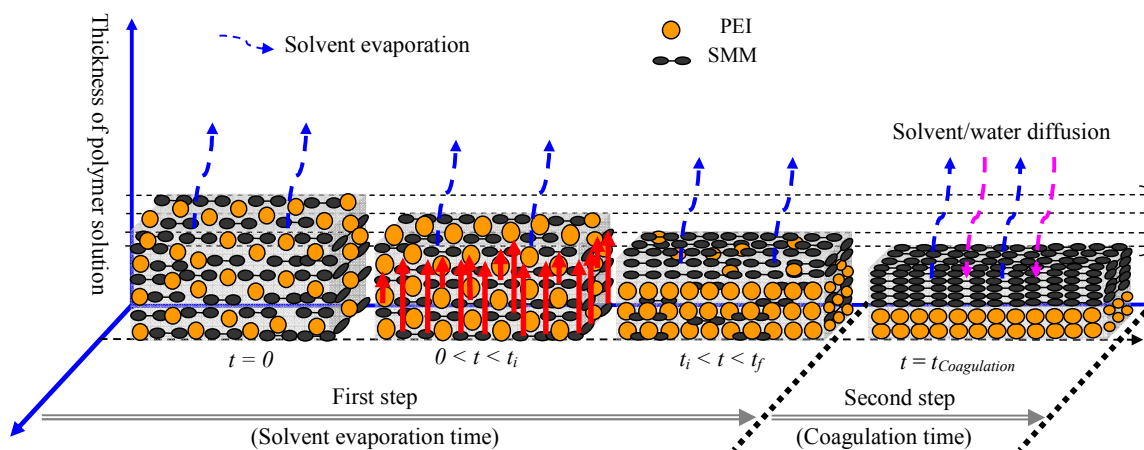

Figure 2.1.2. Schematic diagram illustrating SMM migration during membrane formation.

2.1.2.4. Membrane characterization

The thickness (δ) of the prepared membrane was measured by the micrometer Millitron Phywe (Mahr Feinprüf, type TYP1202IC), its cross-section was analyzed by the scanning electron microscope (SEM, JEOL Model JSM-6400) equipped with the energy-dispersive spectrometer (EDS, Oxford Instruments), the top and bottom membrane surfaces were studied by atomic force microscopy (AFM, Nanoscope III equipped with 1553D scanner, Digital Instruments Inc., Santa Barbara, CA), and the water contact angles (θ) of the top and bottom membrane surfaces were measured by a computerized optical system CAM100, equipped with a CCD camera, frame grabber and image analysis software. The liquid entry pressure of water (LEP_w) of the membrane and the gas permeation test were performed following the method reported in [22].

The cross-section of the SMM modified membrane was examined by SEM. First, the membrane sample was fractured in liquid nitrogen and then sputter-coated with a thin layer of gold using the evaporator Emitech (model K550X). The SEM images were taken at different cross-sectional regions of the membrane sample. The cross-section was then analyzed by X-ray energy dispersion spectroscopy (EDS) to determine the fluorine, carbon and oxygen content in the membrane wall using the software INCA (Oxford Instruments).

The AFM images of the top and bottom membrane surfaces were obtained over different areas of each surface using tapping mode. The procedure to take the AFM images has been described elsewhere [23,24]. The same tip was used to scan both membrane surfaces and all captured images were treated in the same way. The roughness parameters, the mean roughness (Ra), the root mean square of Z data (Rq) and the mean difference in height between the five highest peaks and the five lowest valleys (Rz) were determined using the same scan size (i.e. 1 μm×1 μm). The pore sizes (i.e. mean pore size, μ_p, geometric standard deviation, σ_p, and pore size distribution) and nodule sizes (i.e. minimum, average and maximum) were also evaluated based on the average of at least 50 measurements. The method followed to analyze the AFM images was detailed in [23]. In addition, the surface pore density of the top layer of the membrane, which is the number of pores per unit area (ρ_s) was obtained directly from the AFM analysis software program using two small scan sizes (250 nm x 250 nm and 500 nm x 500 nm).

From the pore size distribution the surface porosity (ε_s) was determined as reported elsewhere [23].

Contact angles of distilled water on the top and bottom surfaces of the prepared membrane were measured at room temperature [25]. A micro syringe Hamilton (0 - 100 μl) was used to produce a constant drop volume of about 2 μl on the membrane surface of 4 cm^2 area (2 x 2 cm). Side view images were captured at a rate of 10 frames/s. Water contact angles were performed at both left and right sides of each drop and were automatically calculated by fitting the captured drop shape to that calculated from the Young-Laplace equation. Fifteen readings were obtained and the average value together with the standard deviation were calculated and reported in this study.

Measurements of the LEP_w and the nitrogen gas permeation test were carried out using the same experimental system reported in [22]. The effective membrane area was 12.56 x 10^{-4} m^2. The gas permeation test was performed prior to the LEP_w measurements. When performing the gas permeation test a dry membrane was used and the pressurized container was filled with nitrogen gas at a pressure of 5 x 10^5 Pa; whereas for the LEP_w measurement the container was filled with 2 L distilled water and then the pressure was applied from the nitrogen cylinder on water. The gas permeation test permits to determine the product of average pore size and effective porosity per unit effective pore length ($r\varepsilon/L_p$). Details of the followed methods are described elsewhere [22]. These experiments were carried out three times using three different membrane samples made from different batches.

2.1.2.5. Direct contact membrane distillation (DCMD)

The set-up used to conduct the DCMD experiments is presented in Fig. 2.1.3. These experiments were carried out for pure water and a salt (NaCl) aqueous solution of concentration (C_f) 30 g/L at different bulk feed temperatures (T_f) varying from 35ºC to 80ºC, a stirring rate (w) of 500 rpm and a bulk permeate temperature (T_c) of 20ºC. The set-up is composted by two stainless steel cylindrical chambers. One of the chambers is connected to a heating system through its jacket to control the temperature of the liquid feed. The other chamber is connected to a cooling system to control the temperature of the permeate. The membrane was placed between the two chambers. The hot feed solution was brought into contact with the hydrophobic top layer of the membrane and the cold permeate solution is in contact with the hydrophilic part of the membrane. The effective membrane area of the DCMD system is 2.75 x 10^{-3} m^2. The bulk feed and permeate temperatures were measured, after steady state was reached, inside each chamber by a pair of sensors connected to a digital meter with an accuracy of $\pm 0.1\ ^oC$. Both the feed and permeate liquids were stirred inside the cell by graduated magnetic stirrers. The DCMD permeate flux was calculated in every case by measuring the condensate collected in the permeate chamber for a predetermined period. The NaCl concentration of both permeate and feed solutions was determined by a conductivimeter 712 ΩMetrohm and the salt rejection factor (α) was calculated.
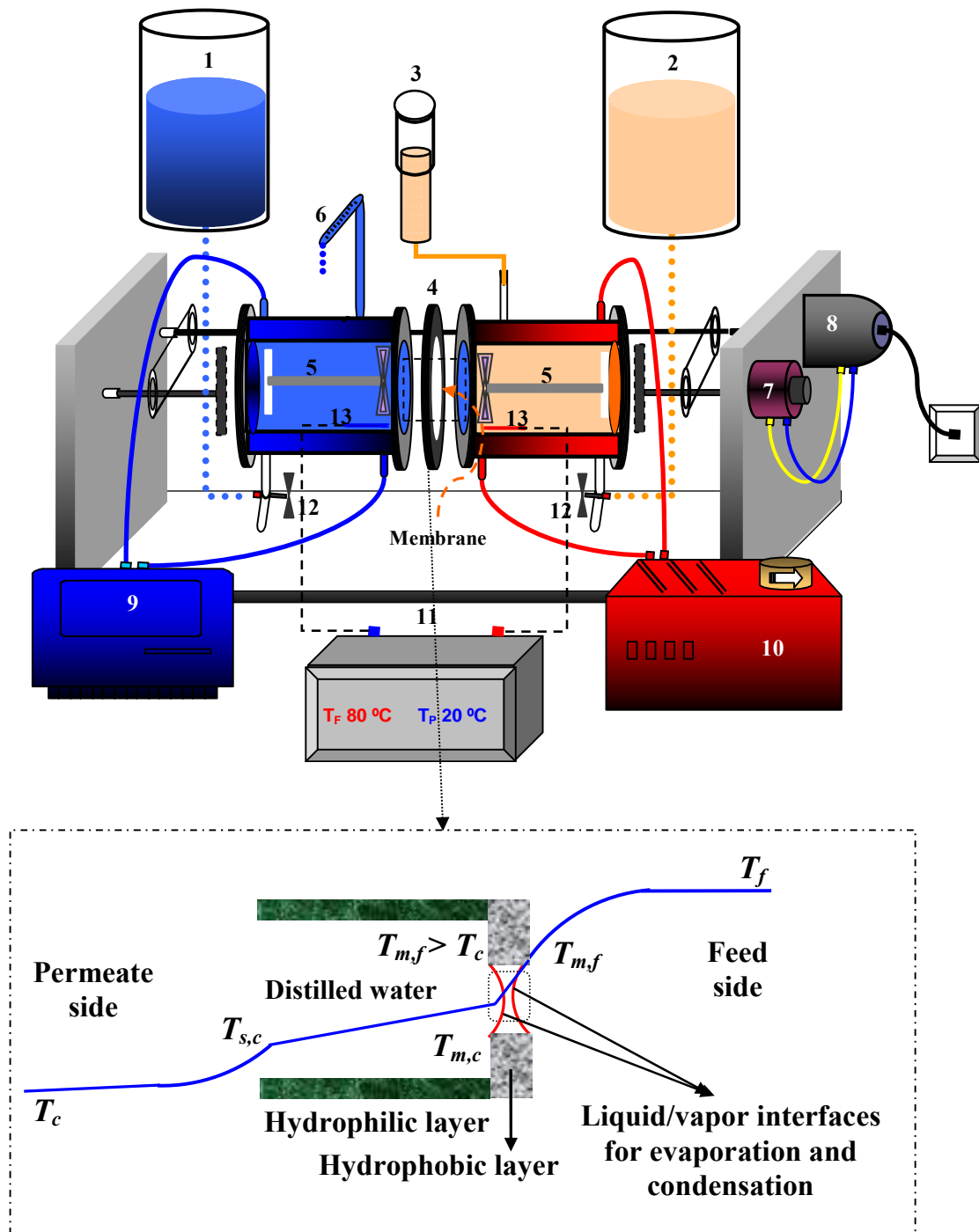
Figure 2.1.3. DCMD set-up: (1) permeate container, (2) feed container, (3) feed supplier during DCMD test, (4) membrane holder, (5) stirrers and magnets, (6) pipette for permeate flux measurement, (7) stirring rate regulator, (8) motor for stirring feed and permeate, (9) cryostat, (10) thermostat, (11) digital multimeter, (12) three way valves, (13) temperature sensors.

2.1.2.6. Air gap membrane distillation (AGMD)

The AGMD experiments were carried out using the experimental set-up presented schematically in Fig. 2.1.4. The membrane module is a modified plate and frame Filtron Minisette[TM] provided by Pall Corporation. The effective membrane area is 5.53 x 10^{-3} m^2. The feed solution was supplied from the feed tank to the feed chamber of the membrane module and the retentate was turned back to the feed tank by a circulation pump MasterFlex 7529-20. A cooling liquid (50 % ethylene glycol/water solution by volume) was recycled from the cooling tank of the cryostat (PolyScience Recirculator) to the cooling chamber of the membrane module. The evaporated water molecules at the liquid/membrane interface cross the membrane pores and the air gap chamber to finally condense over the cooling stainless steel metallic plate. The thickness of the air gap is 4.2 $\pm$ 0.4 mm. Pt-100 sensors connected to a digital multimeter Fluke Hydra were employed to measure the temperature at the inlets and outlets of the membrane module for both feed solution and cooling liquid. In order to avoid membrane pore wetting, the pressure at the feed inlet membrane module was measured by a manometer.

The AGMD tests were carried out first for distilled water used as feed and then salt (NaCl) aqueous solutions of different concentrations (12 g/L and 30 g/L). The permeate flux was determined gravimetrically by weighing the distillate collected in the permeate tank for a predetermined time. Each AGMD experimental test was carried out for 2 h. The salt concentration of feed and permeate as well as the salt rejection factor were determined as indicated previously for DCMD experiments.
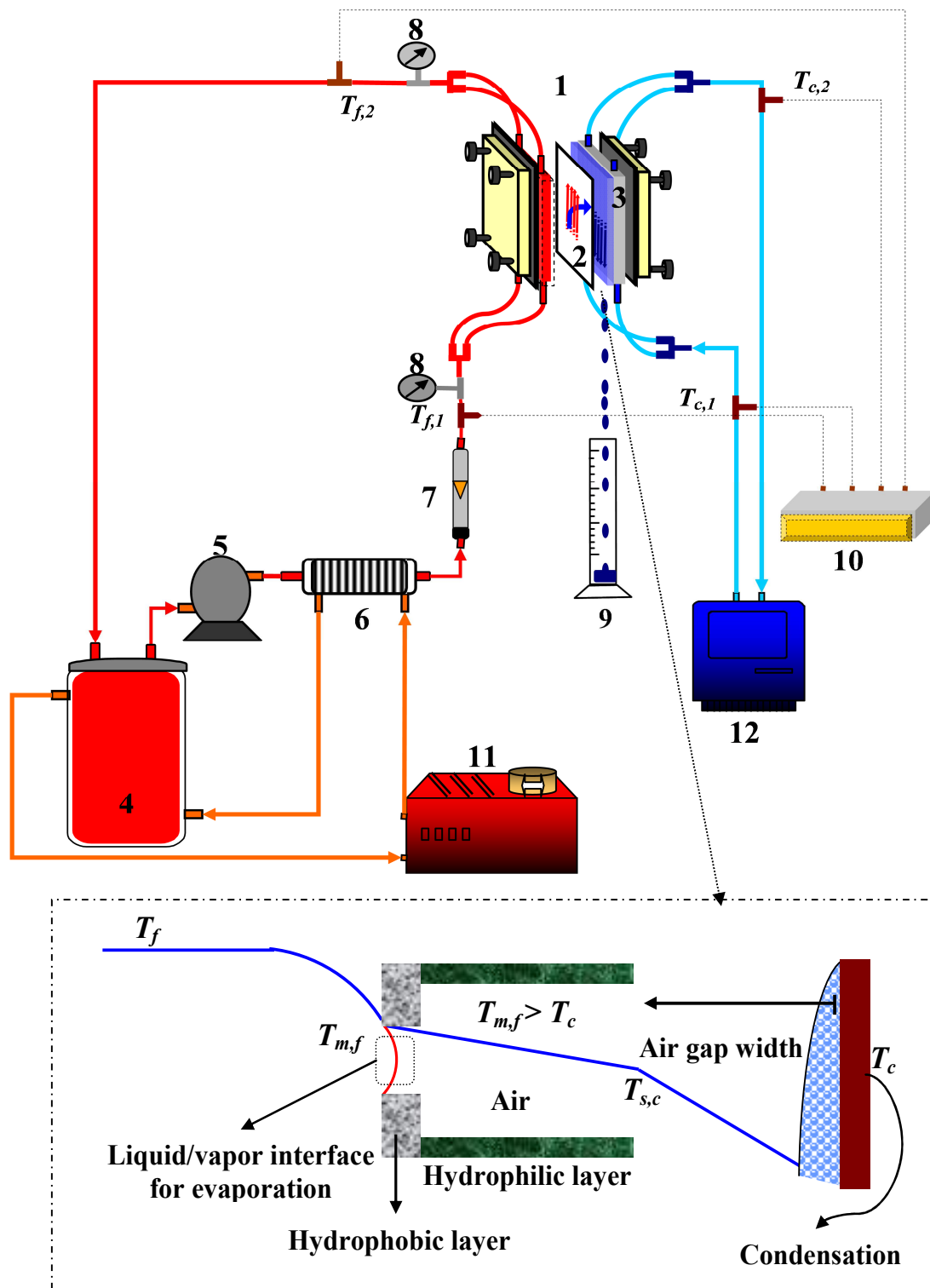
Figure 2.1.4. AGMD set-up: (1) membrane module, (2) flat-sheet membrane, (3) cooling chamber, (4) feed container, (5) circulation peristaltic pump, (6) heat exchanger, (7) flowmeter, (8) manometer, (9) permeate container, (10) digital multimeter, (11) thermostat, (12) cryostat.

115

2.1.3. Results and discussions

2.1.3.1. Membrane parameters

The membrane characteristics are shown in Tables 2.1.1 and 2.1.2. The water contact angle of the top membrane surface is higher than that of the bottom surface indicating the SMM migration to the top membrane surface rendering it more hydrophobic and decreasing its interfacial surface energy. This result was attributed to the hydrophobic nature of the SMM fluorine tails (see Fig. 2.1.1).

Table 2.1.1. Characteristics of the composite hydrophobic/hydrophilic membrane: Water contact angle (θ), total thickness (δ), liquid entry pressure of water (LEP_w), product of average pore size and effective porosity per unit effective pore length ($r\varepsilon/L_p$).

θ (°)	δ(μm)	LEP_w (10^5 Pa)	$r\varepsilon/L_p$ (10^{-5})
Top surface: 94.4 ±0.7 Bottom surface: 78.6 ±0.6	64.7 ±6.3	3.66 ±0.08	5.14 ±0.24

Table 2.1.2. Results of the AFM analysis of the composite hydrophobic/hydrophilic membrane: mean pore size (μ_p), geometric standard deviation (σ_p), pore density (ρ_s), surface porosity (ε_s), minimum nodule size (v_{min}), average nodule size (v_m), maximum nodule size (v_{max}) and roughness parameters (R_a, R_q, R_z).

Membrane surface	μ_p (nm)	σ_p	ρ_s (μm^{-2})	ε_s (%)	v_{min} (nm)	v_m (nm)	v_{max} (nm)	R_a (nm)	R_q (nm)	R_z (nm)
Top	26.95	1.175	477 ±8.4	29.2 ±0.6	14.6	32.7±12.0	62.5	5.1 ±1.9	6.6 ±2.4	35.6 ±13.3
Bottom	69.50	1.174	90 ±6	36.6 ±2.4	39.1	73.2 ±25.0	132.3	34.6±7.1	42.1 ±7.9	168.8 ±22.6

The SEM images of the membrane cross-section are shown in Fig. 2.1.5(a). The membrane exhibits an asymmetric structure with a sponge top-layer supported by a finger-like structure and macrovoids underneath. The formation of the top-layer sponge-like structure is due to the slow SMM/polymer coagulation during solvent evaporation time and SMM migration, whereas the finger-like structure is due to the fast phase separation in water. The finger-like structure became more irregular in the middle of the cross-section and ended with large macro-voids formed in horizontal direction. During the solvent evaporation step, partial solidification of the polymer film and SMM segregation towards the polymer/air interface take place forming a thin skin layer of solid SMM/polymer due to the loss of solvent. The porous thin layer that forms during solvent evaporation time becomes the top skin layer governing the MD performance of the membrane, while the porous structure having finger-like structure and macro-voids that forms during the solvent-water exchange becomes the porous sub-layer, providing the mechanical strength to the membrane. In this case, it can be seen in Fig. 2.1.5(a) that the wall of the fingers parallel to the membrane thickness is porous, which may favor mass transport through the membrane.

Figure 2.1.5(b) presents the SEM cross-section morphology together with the EDS spectra of fluorine, carbon and oxygen. It was observed that the concentration of fluorine associated to the SMM decreased from the top membrane surface to the inside of the membrane wall, whereas the concentration of carbon and oxygen increased. This corroborates the SMM migration to the membrane top surface as stated previously, rendering it hydrophobic and confirming the results of the water contact angle measurements. Similar observations were reported in other studies based on X-ray photoelectron spectroscopy (XPS) analysis, which indicated the gradient in fluorine concentration across the membrane cross-section as a result of the migration of fluorinated end-groups to the air side surface during membrane formation [27]. Based on the EDS spectra of different SEM cross-sectional images, the thickness of the hydrophobic layer was estimated to be 4.5 ± 1 μm. By using a theoretical model and DCMD experiments together with other membrane parameters and the heat and mass transfer equations Khayet et al. [13] estimated the thickness of the hydrophobic layer of this type of membranes to be less than 8.5 μm being the total membrane thickness in the range 51 to 54 μm.
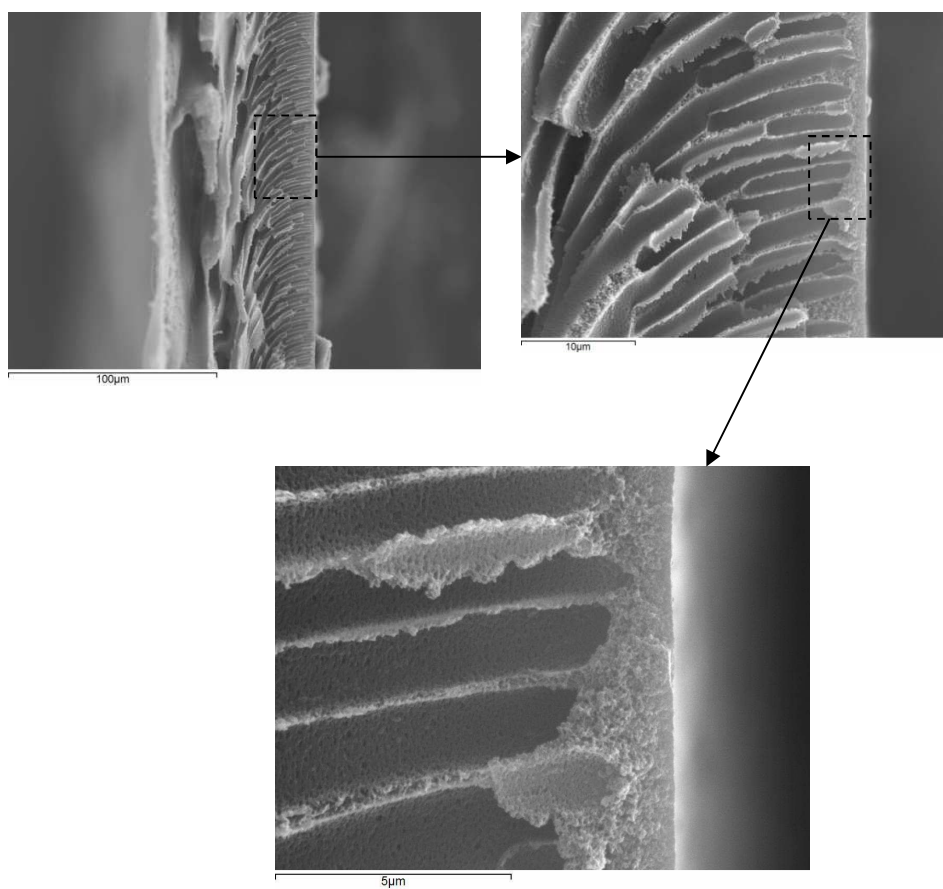
(a)

Figure 2.1.5. Cross-sectional SEM images of the composite porous hydrophobic/hydrophilic membrane at different magnifications (a) and EDS spectra of carbon, oxygen and fluorine throughout the membrane cross-section near the top surface (b). (To be continued)
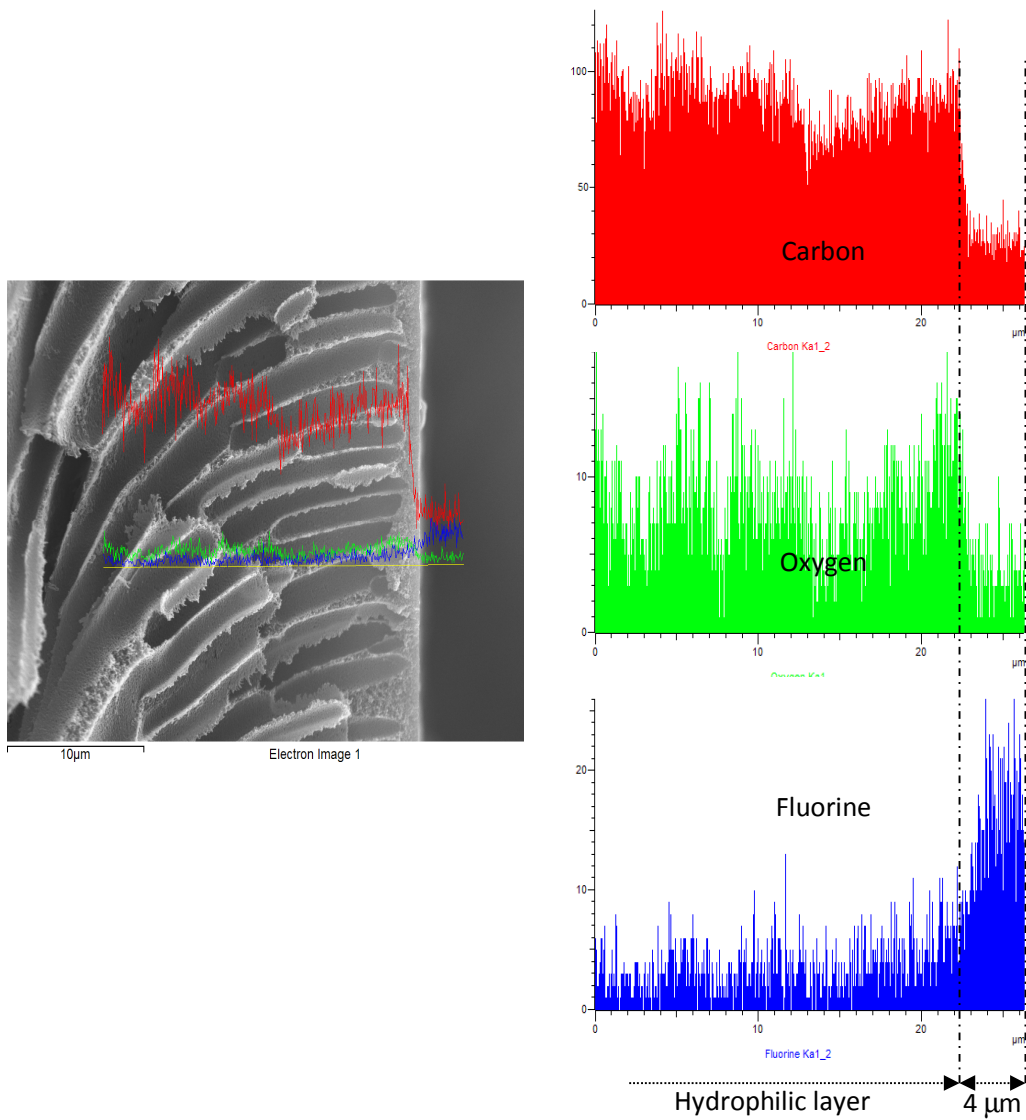
(b)

Figure 2.1.5. Cross-sectional SEM images of the composite porous hydrophobic/hydrophilic membrane at different magnifications (a) and EDS spectra of carbon, oxygen and fluorine throughout the membrane cross-section near the top surface (b). (Continuation)

The data for the LEP_w and ($r\varepsilon/L_p$) are also summarized in Table 2.1.1. In general, the LEP_w and ($r\varepsilon/L_p$) values were found to be quite similar to those of the porous composite membranes prepared by blending other types of SMMs and other hydrophilic polymers [14,22]. The porous composite membrane prepared in this study exhibits a LEP_w value higher than that of the commercial membranes commonly used in MD. For instance TF200 (Gelman) has a LEP_w of 2.82 x 10^5 Pa [1,3]. The obtained membrane parameters indicate that the prepared composite hydrophobic/hydrophilic membrane can be used in MD.

Figure 2.1.6 shows the three-dimensional AFM pictures of the top and bottom surfaces of the porous composite membrane. The images are presented in 1 μm × 1 μm scanning area with a Z range of 50 nm for the top-layer and 296 nm for the bottom membrane surface. As expected, the morphology of the membrane top hydrophobic layer is different from that of the bottom hydrophilic layer. The top-layer is smoother than the bottom surface (see roughness parameters in Table 2.1.2). This may be attributed to the presence of SMM in the top-layer and to its lower pore size and nodule size compared to the bottom surface. Since the roughness parameters depend on the Z values when the surface consists of deep depressions that characterize pores and high peaks that correspond to nodules, high roughness parameters are expected. For instance nodule-like structure and nodules aggregates are formed at both membrane surfaces being the nodule size greater at the bottom surface (Table 2.1.2). Different pore shapes were observed and the nodules are not necessarily circular. In this study, the pore sizes and the nodule sizes were recorded as the average of their lengths and widths. The pore size of the hydrophilic bottom layer is about 2.6 times larger than that of the top layer, whereas the nodule size is about 2.2 times greater for the bottom layer.
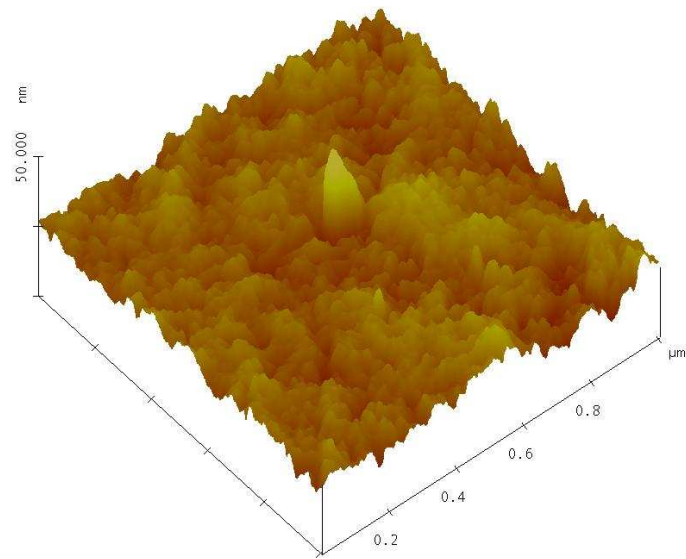
(a)
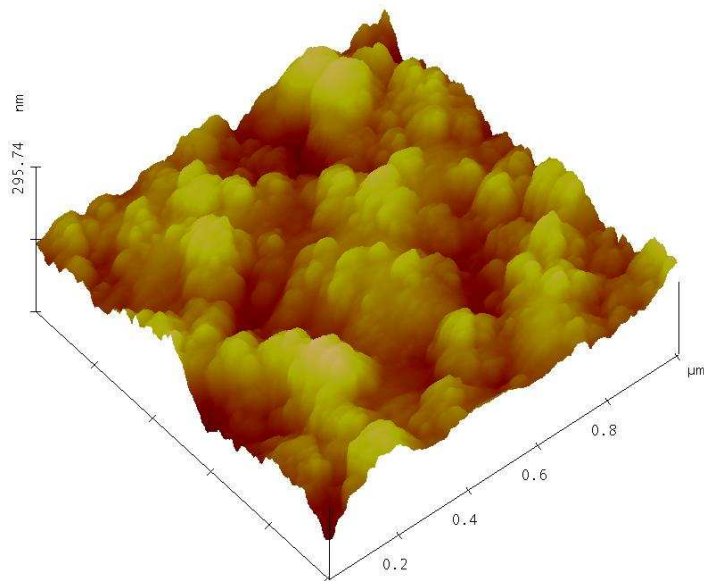
(b)

Figure 2.1.6. AFM images of the composite porous hydrophobic/hydrophilic membrane: (a) top surface and (b) bottom surface.

In Fig. 2.1.7, the pore sizes obtained from the AFM images are plotted against the median ranks, on a log-normal probability paper. Straight lines with reasonably high correlation coefficients (r^2) were obtained (i.e. 0.9815 for the top and 0.9686 for the bottom surface). The mean pore size and the geometric standard deviation were determined and the results are also given in Table 2.1.2. These values were used to generate the cumulative pore size distribution and the probability density function curves for the top and bottom membrane surfaces plotted in Fig. 2.1.8. The pore size distribution curve of the top membrane surface shifts totally to the left of that of the bottom surface indicating that some pores of the hydrophobic layer are smaller than the pores of the hydrophilic PEI layer.

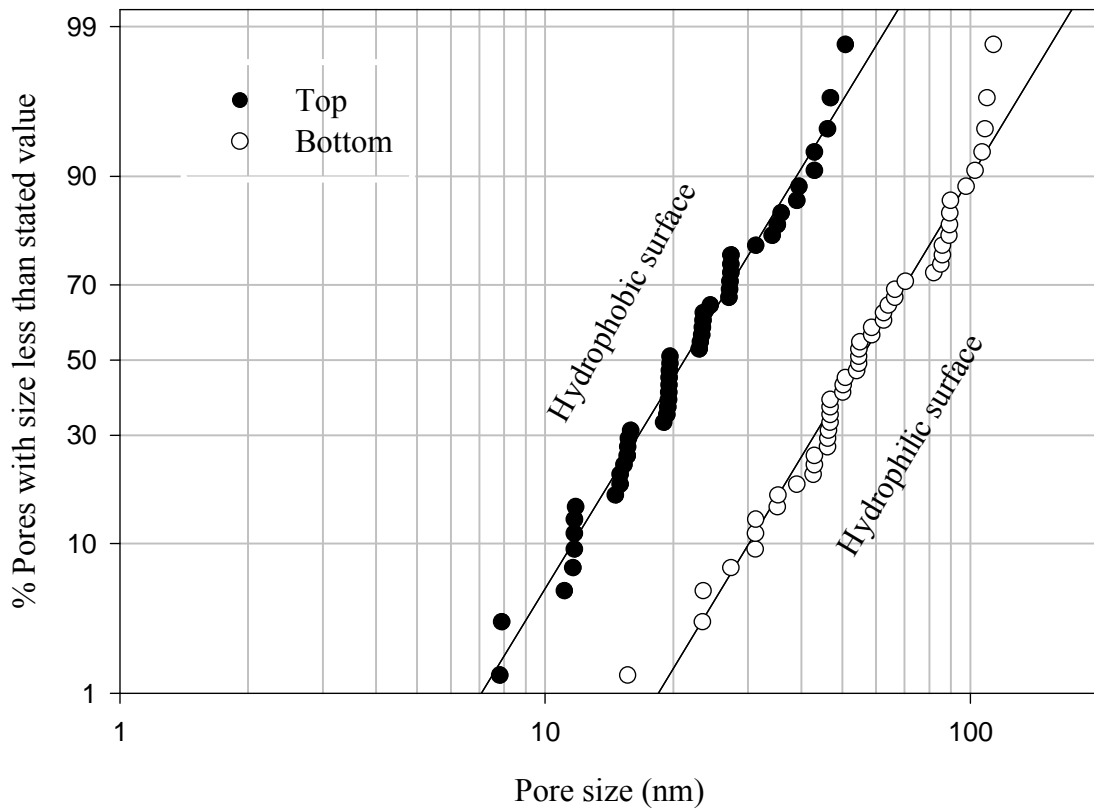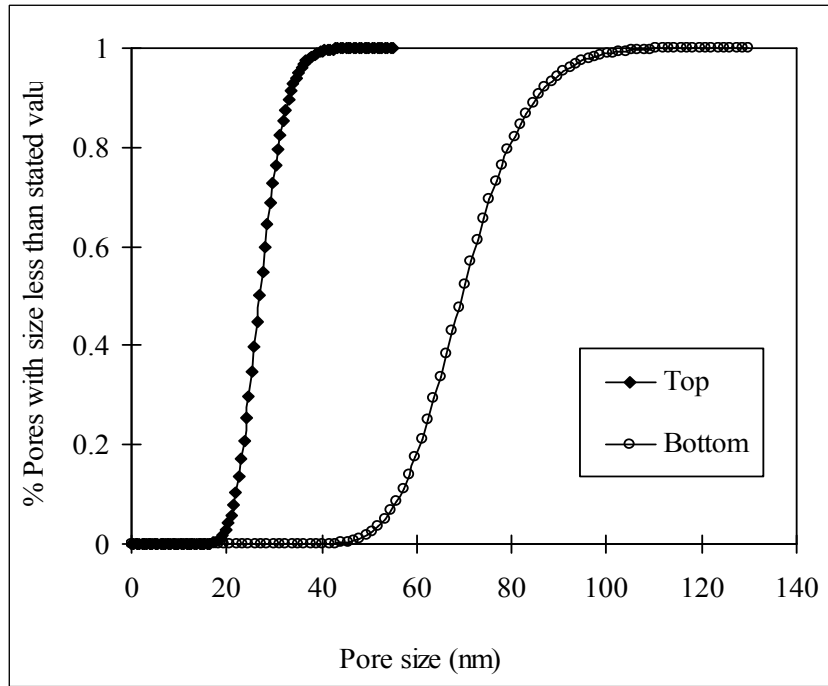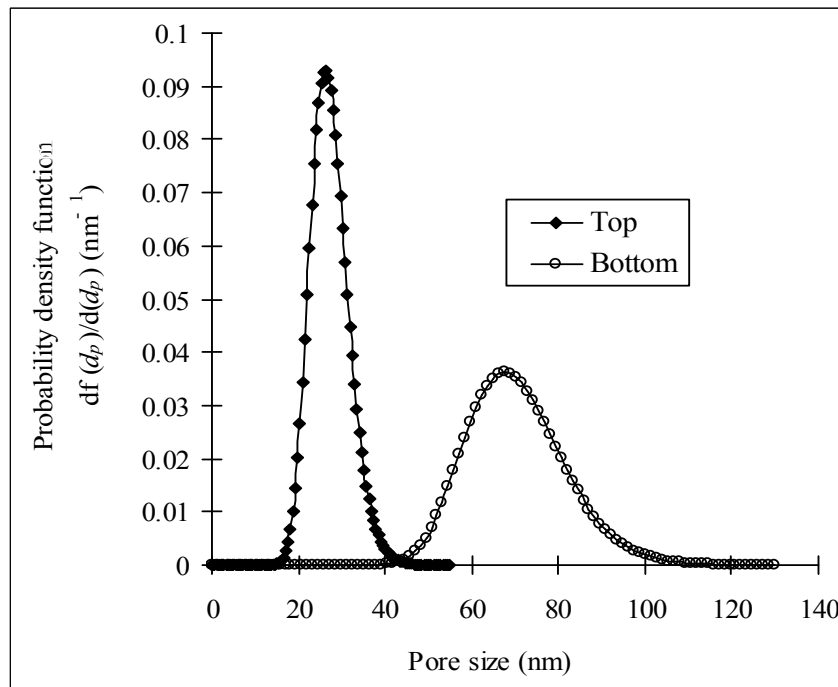**Figure 2.1.7**. Log-normal pore size distributions obtained from the AFM images at the top and bottom surfaces of the porous composite hydrophobic/hydrophilic membrane.

123

(a)

(b)

Figure 2.1.8. Cumulative pore size distribution (a) and probability density function (b) curves generated from the AFM images at the top and bottom surfaces of the porous composite hydrophobic/hydrophilic membrane.

The number of pores was counted for the top membrane surface of various AFM images covering scan areas of 250 nm×250 nm and 500 nm x 500 nm, and the surface porosity was calculated from the pore size distribution shown in Fig. 2.1.8. The obtained pore density and surface porosity data, summarized in Table 2.1.2, are an order of magnitude higher than those reported for other SMM modified membranes prepared with the solvent DMAC for ultrafiltration [27]. This is attributed to the solvent type effect on SMM migration kinetics and its evaporation step before coagulation. In this study, the membrane was prepared with a solvent evaporation step of 30 s at ambient temperature.

2.1.3.2. Membrane performance

The porous composite hydrophobic/hydrophilic membrane was used for desalination by AGMD. Figure 2.1.9 shows the effects of the inlet feed temperature on the AGMD permeate flux and on the salt rejection factor for different feed salt concentrations. Exponential trends between the *AGMD* permeate flux of the composite porous hydrophobic/hydrophilic membrane and the feed temperature were observed. The same behavior was observed in AGMD using membranes with a single hydrophobic layer [1,3,34,38,39].

Distilled water was obtained in the permeate indicating very high rejection factors (Fig. 2.1.9(b)). The salt rejection factor increases slightly between 99.4 and 99.9 % and it is smaller for 12 g/L. As it was expected, the increase of the salt concentration in the aqueous feed solution resulted in a reduction of the AGMD permeate flux due to the decrease of the water vapor pressure (i.e. driving force) [1,3].

Table 2.1.3 reviews the highest permeate fluxes observed in AGMD for some commercial and laboratory fabricated membranes. For example, a polyvinylidene fluoride (PVDF) nano-fibrous membrane was fabricated by the electro-spinning method for desalination by AGMD process [39]. Similar trends to those presented in this study were observed; however lower permeate fluxes of 11.1 kg/m2.h and 10.2 kg/m2.h were obtained with NaCl rejection factors higher than 99 % when using a cooling temperature of 22ºC, a feed temperature of 82ºC, a feed flow rate of 350 mL/min and NaCl feed concentrations of 35 g/L and 60 g/L, respectively.

Similarly, the obtained permeate fluxes of the fabricated superhydrophobic glass membranes with integrated and ordered arrays of nano-spiked micro-channels were as high as 11.3 kg/m2.h and the produced permeate water contained salt because of pore wetting [40]. These membranes have been modified by differential chemical etching for desalination by AGMD and exhibit pore sizes of about 3.4 μm, an inter-pore spacing of 2 μm, a porosity of 26 %, a thickness of 500 μm and water contact angles of about 165º [40]. In this study, the permeate flux of the composite porous hydrophobic/hydrophilic membrane increased nearly 8.5 times as the feed temperature varied from 35ºC to 80ºC, reaching a water production rate of 14.9 kg/m^2.h. The AGMD performance of the membrane used in this study is better than that of the fabricated membranes used so far in desalination by AGMD (Table 2.1.3) although the pore sizes of these membranes are an order of magnitude larger than those of the composite porous hydrophobic/hydrophilic membrane. This is due to the total membrane thickness and to the type of mass transport through the membrane pores.
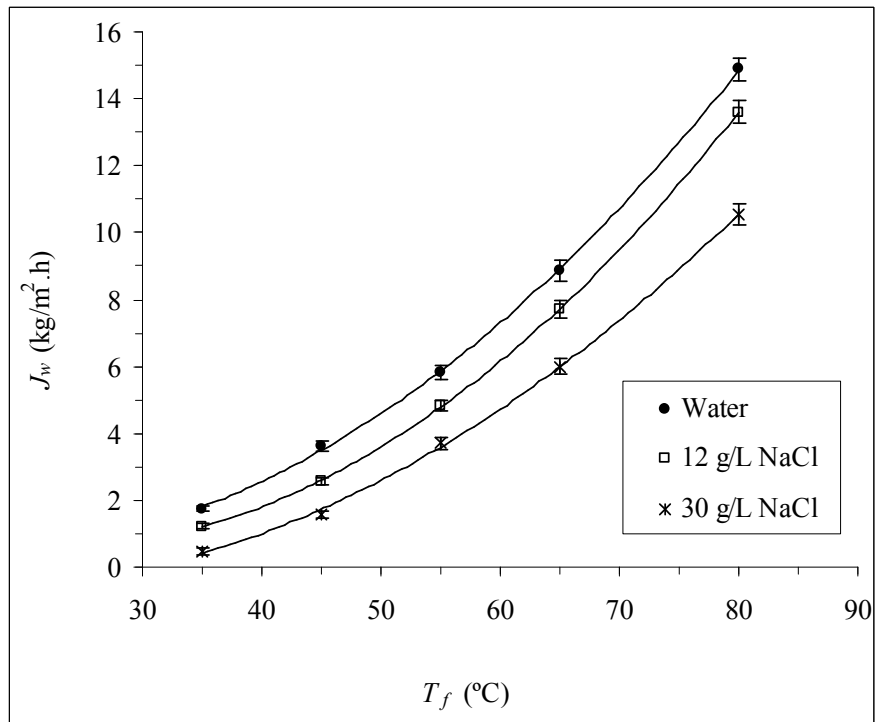
(a)
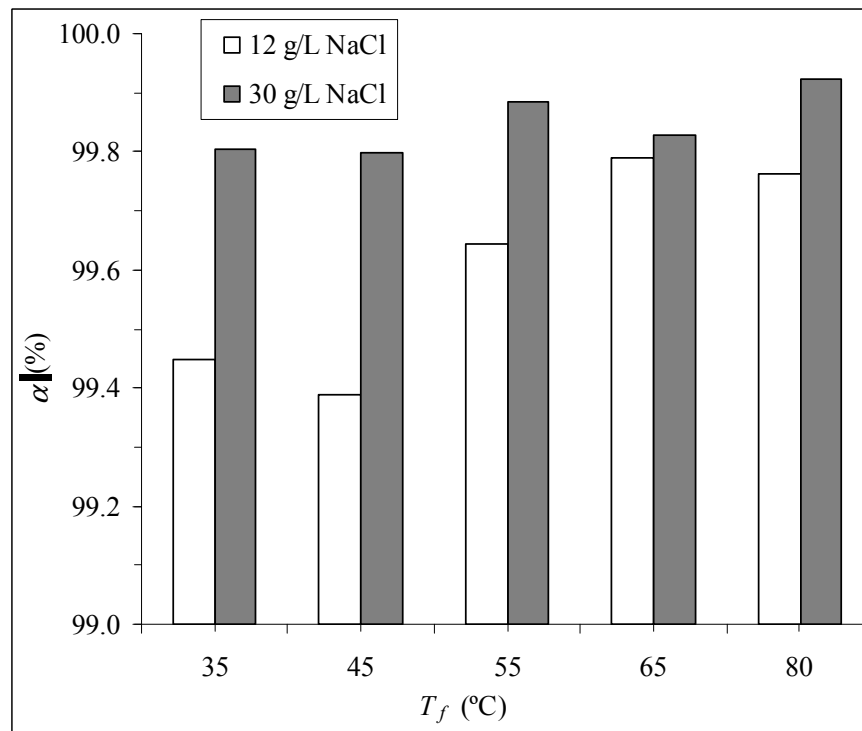
(b)

Figure 2.1.9. Effect of the feed temperature (T_f) and the NaCl concentration (C_f) on the AGMD permeate flux (J_w) (a) and on the salt rejection factor (α) (b), for $T_c = 20°C$ and $Q_f = 100$ L/h.

Table 3. Reported AGMD permeate flux (J_w) of different types of commercial, fabricated and modified membranes: feed temperature (T_f), cooling temperature (T_c), liquid flow rate (Q_f), liquid circulation velocity (v_f), air gap width (a), electrical conductivity of the permeate (ψ_p), electrical conductivity of the feed (ψ_f), salt rejection factor (α).

Membrane	J_w (kg/m².h)	Observation	Ref.
		Commercial membranes	
PTFE (≈ 0.2 μm pore size)	4.7	T_f=70ºC, T_c=30ºC, distilled water as feed. (Membrane: TF200, Gelman, μ_p = 0.2 μm, δ= 178 μm, ε = 80%, LEP_w = 282 kPa, PP support).	[28]
	6	T_f=45ºC, T_c=20ºC, 3 wt% NaCl, a=5 mm, Q_f=3.3 L/min. (Membrane: PTFE0.2, Fluoropore, Millipore, μ_p = 0.2 μm, δ= 175 μm, ε = 70 %).	[29]
	11	T_f=80ºC, T_c=15ºC, 3.5 wt% NaCl, a=1 mm, Q_f=0.25 L/min. (Membrane: Membrane Solutions, Shangai, China, μ_p = 0.22 μm, δ= 160±40 μm, PP support).	[30]
	22 21.8 21 12 11 10	T_f=60ºC, T_c=15ºC, a=1.2 mm, Q_f=50 L/h 2 g/L NaCl 4 g/L NaCl 6 g/L NaCl 25 g/L NaCl 30 g/L NaCl 35 g/L NaCl. (Membrane: Millipore, μ_p = 0.22 μm, δ= 175 μm, ε = 70 %).	[31]
PTFE (≈ 0.45 μm pore size)	11.5	T_f=80ºC, T_c=15ºC, 3.5 wt% NaCl, a=1 mm, Q_f=0.25 L/min. (Membrane: Membrane Solutions, Shangai, China, μ_p = 0.45 μm, δ= 160±40 μm, PP support).	[30]
	51.1	T_f=71ºC, T_c=13.9ºC, 30 g/L NaCl, a=3 mm, Q_f=205 L/h, α = 99.92%. (Membrane: TF450, Gelman, μ_p = 0.45 μm, δ= 178 μm, ε = 80%, LEP_w = 137.8 kPa, PP support).	[32]
	47.2	T_f=71ºC, T_c=13.9ºC, 30 g/L NaCl, a=5.6 mm, Q_f=183 L/h, α = 99.98%. (Membrane: TF450, Gelman, μ_p = 0.45 μm, δ= 178 μm, ε = 80%, LEP_w = 137.8 kPa, PP support).	[33]
	10.0	T_f=55ºC, T_c=7ºC, tape water (ψ_f=297μS/cm, ψ_p=7μS/cm). (Membrane: FHLP, Millipore, μ_p = 0.5 μm, δ= 175 μm, ε = 85 %, PE support).	[34]
	31.2	T_f=59ºC, T_c=13.9ºC, 30 g/L NaCl, a=5.6 mm, Q_f=205 L/h, α = 99.98%. (Membrane: TF450, Gelman, μ_p = 0.45 μm, δ= 178 μm, ε = 80%, LEP_w = 137.8 kPa, PP support).	[33]

Membrane	J_w (kg/m².h)	Observation	Ref.

PTFE (≈ 1 μm pore size)	12	T_f=80ºC, T_c=15ºC, 3.5 wt% NaCl, a=1 mm, Q_f=0.25 L/min. (Membrane: Membrane Solutions, Shangai, China, μ_p = 1 μm, δ = 160±40 μm, PP support).	[30]
	14.0 13.8	T_f=62ºC, T_c=27.5ºC, a=4 mm, v_f=0.063m/s, 1 wt% NaCl 5 wt% NaCl. (Membrane: Millipore, μ_p = 1 μm, δ= 150 μm, ε = 85 %, PE support).	[35]
	23 22.5 17	T_f=75ºC, T_c=20ºC, a=4 mm, Q_f=3.8 L/min, tap water 0.5 wt% NaCl 3 wt% NaCl. (Membrane: FALP, Millipore, μ_p = 1 μm, δ= 150 μm, ε = 85 %, PE support).	[36]
PVDF (≈ 0.22 μm pore size)	8.2	T_f=50ºC, T_c=20ºC, Q_f=70 L/h, a=1.8 mm, distilled water. (Membrane: GVHP, Millipore, μ_p = 0.22 μm, δ= 110 μm, ε = 75 %, LEP_w = 204 kPa).	[37]
PVDF (≈ 0.45 μm pore size)	10.0 7.5	T_f=70ºC, T_c=20ºC, seawater model solution (ψ_f=4±1μS/cm). a=0.19 cm, a=3.5 mm. (Membrane: Durapore, μ_p = 0.45 μm, δ= 110 μm, ε = 75 %).	[38]
	26.3 7.0 6.0	T_f=82ºC, T_c=7ºC, a=0.8 mm, tape water (ψ_f=297μS/cm). T_f=52ºC, T_c=7ºC, tape water (ψ_f=297μS/cm, 99% salt rejection). T_f=52ºC, T_c=7ºC, seawater model solution (ψ_f=37.6 mS/cm, ψ_p=1100 μS/cm). (Membrane: HVHP, Millipore, μ_p = 0.45 μm, δ= 140 μm, ε = 75 %, LEP_w = 105 kPa).	[34]

Membrane	J_w (kg/m^2.h)	Observation	Ref.
Fabricated and modified membranes			
PVDF nano-fiber	11.6 11.1 10.2	T_f=82ºC, T_c=22ºC, Q_f=21 L/h, a≈ 2mm, 1 wt % NaCl 3.5 wt % NaCl 6 wt % NaCl; (>98.7 % salt rejection).	[39]

129

Modified nanospiked glass [a]	11.3 9.7	T_f=95ºC; T_c=22ºC, 2.5 wt% NaCl 20 wt % NaCl.	[40]
Modified ZrO$_2$ (M1) [b]	6.8 6.0 4.0	T_f=95ºC, T_c=5ºC, Q_f=198-240 L/h, $a\approx$ 10mm, distilled water $\approx$ 2 M NaCl $\approx$ 4.6 M NaCl ($\approx$ 100 % salt rejection).	[11]
Modified ZrO$_2$ (M3) [b]	6.5 4.0	T_f=95ºC, T_c=5ºC, Q_f=198-240 L/h, $a\approx$ 10mm, (0.001-0.01) M NaCl $\approx$ 1 M NaCl ($\approx$ 100 % salt rejection).	[11]
Modified ZrO$_2$ (Zr50) [b]	5.2 4.6 4.0 4.0	T_f=95ºC, T_c=5ºC, Q_f=198-240 L/h, 0.5 M (Mediterranean seawater) 1 M NaCl 2 M NaCl 3M NaCl (95-100 % salt rejection).	[41]
Modified Al$_2$O$_3$ (Al200)[b]	4.2	T_f=95ºC, T_c=5ºC, Q_f=198-240 L/h, 2 M NaCl ($\approx$ 100 % salt retention).	[41]
Modified Al$_2$O$_3$ (Al800)[b]	2.5	T_f=95ºC, T_c=5ºC, Q_f=198-240 L/h, 2 M NaCl ($\approx$ 94 % salt rejection).	[41]
Modified aluminosilicate (AlSi400) [b]	2.5	T_f=95ºC, T_c=5ºC, Q_f=198-240 L/h, 2 M NaCl ($\approx$ 96 % salt rejection).	[41]
Modified TiO$_2$ (Ti5) [b]	0.8	T_f=95ºC, T_c=5ºC, 0.5 M NaCl (99.1 % salt rejection).	[42]
Modified ZrO$_2$ (Zr50) [b]	4.7	T_f=95ºC, T_c=5ºC, 0.5 M NaCl (99.8 % salt rejection).	[42]

PP: Polypropylene; PE: Polyethylene; PTFE: Polytetrafluoroethyelen; PVDF: Polyvinylidene fluoride.
[a] Fabricated superhydrophobic glass membrane with ordered arrays of nanospiked microchannels modified by differential chemical etching.
[b] grafted ceramic tubular membranes by 1H,1H,2H,2H-perfluorodecyltriethoxysilane (Zirconia, ZrO$_2$: d_p=50 nm); (Zirconia, ZrO$_2$: d_p=200 nm); (Titania, TiO$_2$: d_p=5 nm); (Alumina, Al$_2$O$_3$: d_p=200 nm); aluminosilicate (AlSi400) [11,41,42].

The same porous composite hydrophobic/hydrophilic membrane was used for desalination by DCMD. As can be seen in Fig. 2.1.10 for the same feed and permeate bulk temperatures applied previously in AGMD, the DCMD permeate flux is higher than the AGMD permeate flux. For example, for a feed temperature of 80ºC the DCMD permeate flux is 41.6 kg/m^2.h, which is about 2.8 times higher than the AGMD permeate flux when using distilled water as feed. This is because of the thin hydrophobic layer of the composite porous membrane that is the responsible of mass transport in DCMD (i.e. small path length between the hot and the cold liquid/vapour interfaces formed at both side of the hydrophobic thin top-layer of the membrane). On the other hand, there is also the contribution of the thick stagnant air layer interposed between the membrane and the condensation surface leading to an increase of the mass transfer resistance although there is a reduction of energy loss by heat conduction through membrane. In this case, the evaporated volatile molecules cross both the membrane pores and the air gap to finally condense over a cold surface inside the membrane module. Moreover, in AGMD configuration, the transport of vapors through the membrane is described by the theory of molecular diffusion admitting the presence of air inside the pores of the membrane and in the gap width as a stagnant film as well as the Knudsen type of flow (i.e. Knudsen/molecular diffusion type of flow). On the contrary, it was demonstrated that in DCMD the mass transport was described only by Knudsen flow for this type of porous composite hydrophobic/hydrophilic membrane having an order of magnitude smaller pore sizes than those of the membranes commonly used in MD [13,14]. Knudsen type of flow is predominant in pores with sizes lower than the mean free path of the transported water vapor molecules though the membrane pores.

Fig. 2.1.10(b) shows the effects of the feed temperature and the salt (NaCl) concentration on the rejection factor. It can be seen that this factor is maintained greater than 99.98% in all cases. For 12 g/L the salt rejection factor is lower than that corresponding to 30 g/L and enhances slightly with the increase of the feed temperature particularly for 12 g/L. This may be attributed to the exponential enhancement of the water vapor with the increase of the feed temperature.
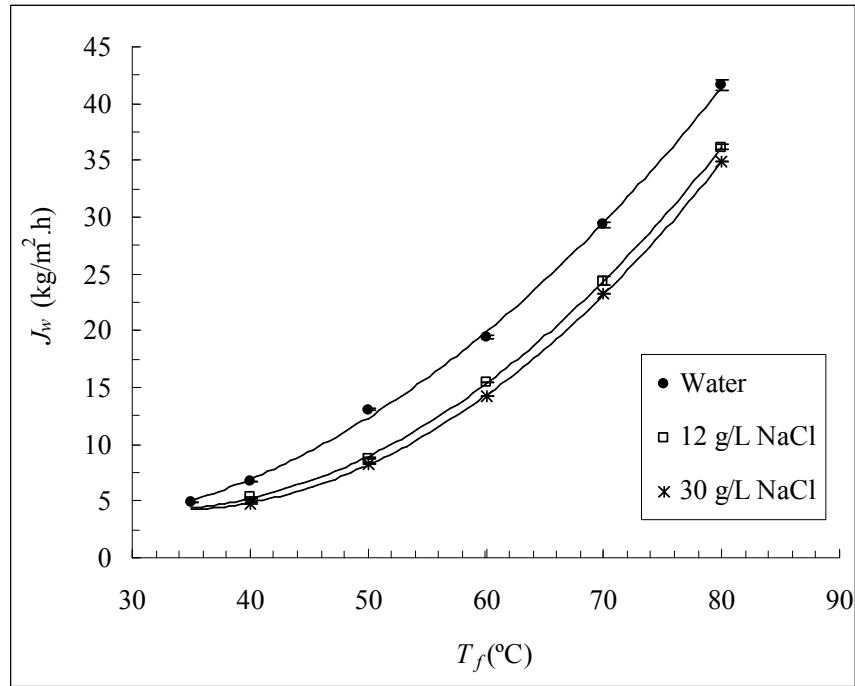
(a)
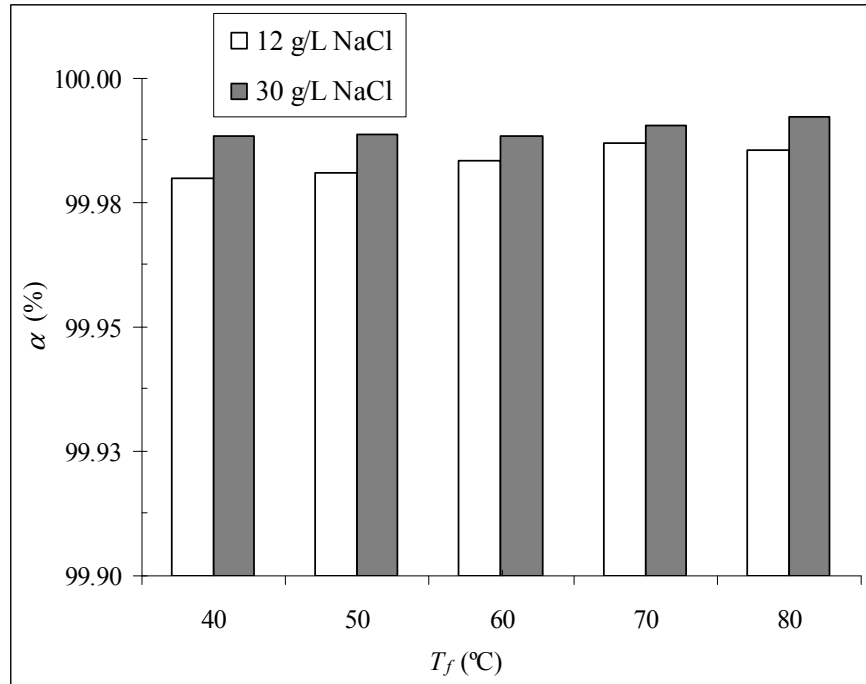
(b)

Figure 2.1.10. Effect of the feed temperature (T_f) and the NaCl concentration (C_f) on the DCMD permeate flux (J_w) (a) and on the salt rejection factor (α) (b), for $T_c = 20^{\circ}C$ and $w = 500$ rpm.

The AGMD water production rate can be enhanced further by decreasing the coolant temperature and by increasing the feed flow rate. A decrease of the permeate flux with the increase of the coolant temperature was observed for the composite hydrophobic/hydrophilic membrane as shown in Fig. 2.1.11 due to the decrease of the partial pressure gradient, which is the driving force. A linear relationship between the AGMD flux and the coolant temperature was plotted for both distilled water used as feed and salt aqueous solutions. This behavior was observed previously for different commercial membranes [3,38]. The salt ejection factor varies between 99.6 and 99.9 % with no clear trend with the cooling temperature. Again, the salt rejection factor of the feed salt solution 12 g/L is lower than that of 30 g/L. For both salt aqueous solutions distilled water was obtained with nearly similar quality (<116 µS/cm in all cases) and the observed difference of the salt rejection factor is only due to the definition of the salt rejection factor $(1-C_p/C_f)$.

One possible way to reduce the temperature and concentration polarization effects in *AGMD* process is to increase the feed flow rate in order to establish adequate hydrodynamic conditions and work under turbulent flow regime. The consequence is the enhancement of the heat transfer coefficient in the feed boundary layer and the approach of the temperature and the concentration at the membrane surface to the bulk ones. For feed aqueous solutions in laminar flow regime, the AGMD permeate flux is expected to increase by increasing the feed flow rate tangentially to the membrane surface. As can be seen in Fig. 2.1.12, this last case occurs indicating that the membrane module is operated under laminar flow regime. There is a considerable increase of the AGMD flux with the feed flow rate for different feed salt concentrations. Figure 2.1.12 shows also the effect of the feed flow rate on the salt rejection factor, which was varied between 99.7 and 99.9 % without any comprehensible trend due to the small variations of these data.

(a)

(b)

Figure 2.1.11. Effect of the coolant temperature (T_c) and the NaCl concentration (C_f) on the AGMD permeate flux (J_w) (a) and on the salt rejection factor (α) (b), for $T_f = 60ºC$ and $Q_f = 100$ L/h.
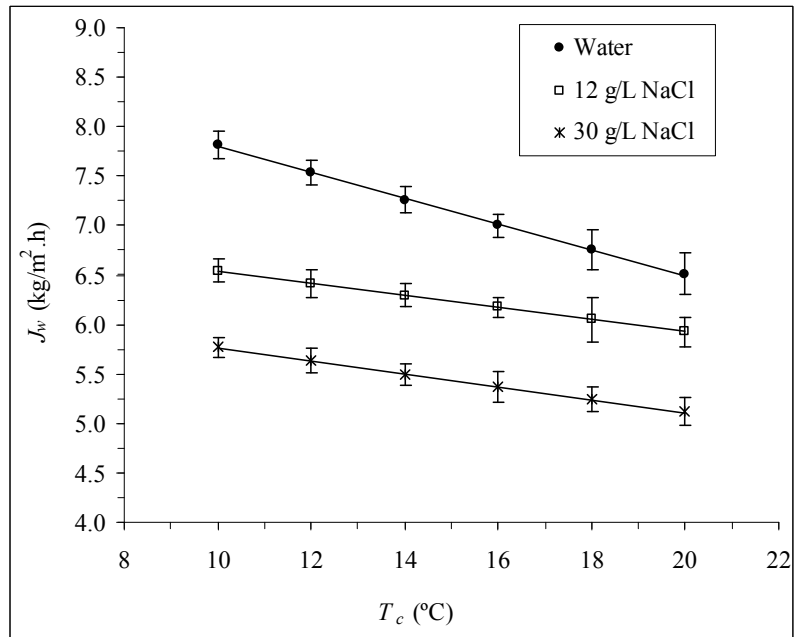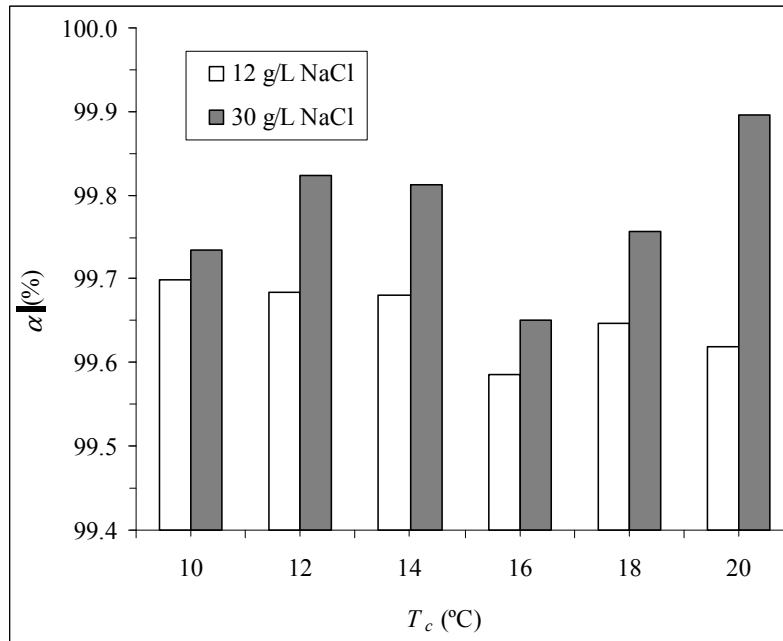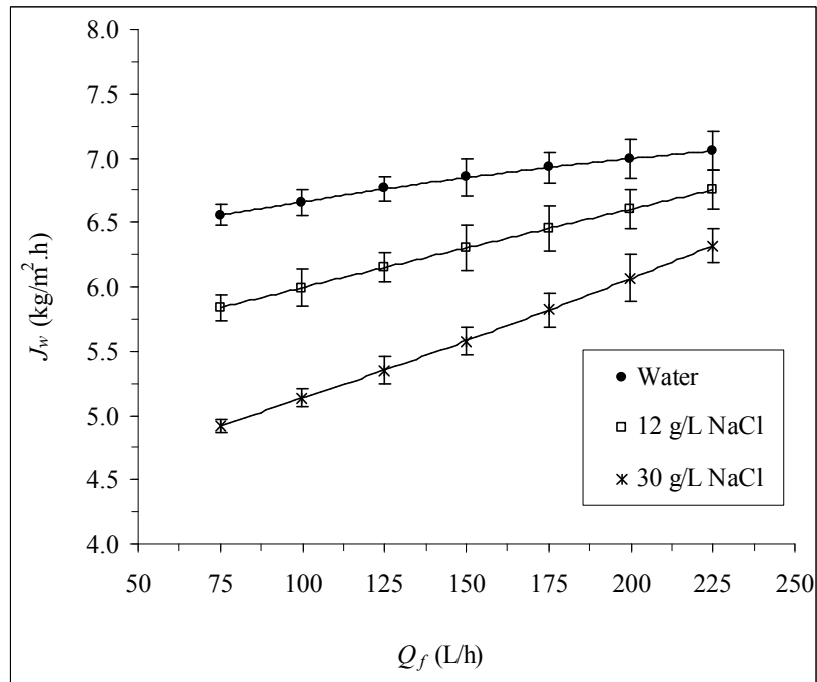
(a)
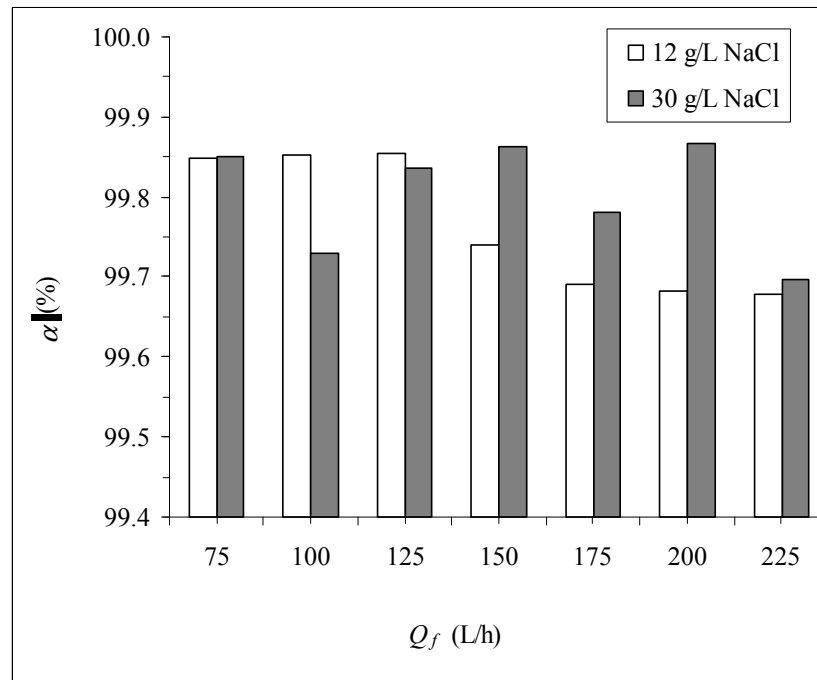
(b)

Figure 2.1.12. Effect of the feed flow rate (Q_f) and salt (NaCl) concentration (C_f) on the AGMD permeate flux (J_w) (a) and on the salt rejection factor (α) (b), for T_f = 60ºC and T_c = 20ºC.

2.1.4. Conclusions

135

A flat-sheet composite hydrophobic/hydrophilic membrane was fabricated using a fluorinated surface modifying macromolecule (SMM) and the hydrophilic host polymer polyetherimide (PEI). During the polymer solution casting procedure, SMM migrated to the membrane surface rendering it more hydrophobic with small pore size and nodule size and low roughness parameters compared to the bottom membrane surface.

It was observed that this type of membrane is more suitable for desalination by DCMD than for AGMD. The permeate flux of the composite hydrophobic/hydrophilic membrane in AGMD configuration reached a value of 14.9 kg/m^2.h and the salt rejection factor was higher than 99.4 %. In general, The DCMD permeate flux is 2.7 − 3.3 times higher than the AGMD permeate flux.

The high DCMD performance of the composite porous hydrophobic/hydrophilic membrane is due to various reasons: (i) the thin top hydrophobic layer that is the responsible of mass transport in DCMD, (ii) the contribution of the thick stagnant air layer interposed between the membrane and the condensation surface in AGMD leading to an increase of the mass transfer resistance although there is a reduction of energy loss by heat conduction through membrane, and (iii) the physical mass transport through the membrane, which is Knudsen type of flow in the case of DCMD and Knudsen/molecular diffusion for AGMD due to the presence of the air gap space between the membrane and the cooling surface.

References

[1] M. Khayet, Membranes and theoretical modeling of membrane distillation: a review, Adv. Colloid Interface Sci., 164(1-2) (2011) 56-88.

[2] E. Curcio, E. Drioli, Membrane distillation and related operations: a review, Sep. Purif. Rev., 34 (2005) 35–86.

[3] M. Khayet, T. Matsuura, Membrane Distillation: Principles and Applications, Elsevier, The Netherlands, 2011.

[4] P. Peng, A.G. Fane, X. Li, Desalination by membrane distillation adopting a hydrophilic membrane, Desalination, 173 (2005) 45-54.

[5] B. Li, K.K. Sirkar, Novel membrane and device for vacuum membrane distillation-based desalination process, J. Membr. Sci., 257 (2005) 60-75.

[6] M. Khayet, T. Matsuura, Preparation and characterization of polyvinylidene fluoride membranes for membrane distillation, Ind. Eng. Chem. Res., 40 (2001) 5710-5718.

[7] M. Khayet, T. Matsuura, J.I. Mengual, M. Qtaishat, Design of novel direct contact membrane distillation membranes, Desalination, 192 (2006) 105-111.

[8] M.C. García-Payo, M. Essalhi, M. Khayet, Preparation and characterization of PVDF-HFP copolymer hollow fiber membranes for membrane distillation, Desalination, 245 (2009) 469-473.

[9] C. Feng, B. Shi, G. Li, Y. Wu, Preparation and properties of microporous membrane from poly(vinylidene fluoride-co-tetrafluoroethylene) (F2.4) for membrane distillation, J. Membr. Sci., 237 (2004) 15-24.

[10] Z. Jin, D.L. Yang, S.H. Zhang, X.G. Jian, Hydrophobic modification of poly(phtalazinone ether sulfone ketone) hollow fiber membrane for vacuum membrane distillation, J. Membr. Sci., 310 (2008) 20-27.

[11] S.R. Krajewski, W. Kujawski, M. Bukowska, C. Picard, A. Larbot, Application of fluoroalkylsilanes (FAS) grafted ceramic membranes in membrane distillation process of NaCl solutions, J. Membr. Sci., 281 (2006) 253-259.

[12] M. Khayet, J.I. Mengual, T. Matsuura, Porous hydrophobic/hydrophilic composite membranes: Application in desalination using direct contact membrane distillation, J. Membr. Sci., 252 (2005) 101-113.

[13] M. Khayet, T. Matsuura, J.I. Mengual, Porous hydrophobic/hydrophilic composite membranes: Estimation of the hydrophobic-layer thickness, J. Membr. Sci., 266 (2005) 68-79.

[14] M. Qtaishat, M. Khayet, T. Matsuura, Novel porous composite hydrophobic/hydrophilic polysulfone membranes for desalination by direct contact membrane distillation, J. Membr. Sci., 341 (2009) 139-148.

[15] M. Bryjak, I. Gancarz, K. Smolinska, Plasma nanostructuring of porous membranes, Adv. Colloid Interface Sci., 161 (2010) 2-9.

[16] V. Kochkodan, N. Hilal, V. Melnik, O. Kochkodan, O. Vasilenko, Selective recognition of organic pollutants in aqueous solutions with composite imprinted membranes, Adv. Colloid Interface Sci., 159 (2010) 180-188.

[17] Y. Wu, Y. Kong, X. Lin, W. Liu, J. Xu, Surface-modified hydrophilic membranes in membrane distillation, J. Membr. Sci., 72 (1992) 189-196.

[18] Y. Kong, X. Lin, Y. Wu, J. Cheng, J. Xu, Plasma polymerization of octafluorocyclobutane and hydrophobic microporous composite membranes for membrane distillation, J. Appl. Polym. Sci., 46 (1992) 191-199.

[19] A. Bottino, G. Capannelli, A. Comite, Novel porous poly(vinylidene fluoride) membranes for membrane distillation, Desalination, 183 (2005) 375-382.

[20] S. Bonyadi, T.S. Chung, Flux enhancement in membrane distillation by fabrication of dual layer hydrophilic-hydrophobic hollow fiber membranes, J. Membr. Sci., 306 (2007) 134-146.

[21] M.M. Teoh, T.S. Chung, Y.S. Yeo, Dual-layer PVDF/PTFE composite hollow fibers with a thin macrovoid-free selective layer for water production via membrane distillation, Chem. Eng. J., 171 (2011) 684-691.

[22] M. Qtaishat, D. Rana, M. Khayet, T. Matsuura, Preparation and characterization of novel hydrophobic/hydrophilic polyetherimide composite membranes for desalination by direct contact membrane distillation, J. Membr. Sci., 327 (2009) 264-273.

[23] M. Khayet, K.C. Khulbe, T. Matsuura, Characterization of membranes for membrane distillation by atomic force microscopy and estimation of their water vapor transfer coefficients in vacuum membrane distillation process, J. Membr. Sci., 238 (2004) 199-211.

[24] D.J. Johnson, N.J. Miles, N. Hilal, Quantification of particle-bubble interactions using atomic force microscopy: a review, Adv. Colloid Interface Sci., 127 (2006) 67-81.

[25] C. Causserand, P. Aimar, Characterization of filtration membranes, in E. Drioli, L. Giorno, Comprehensive Membrane Science and Engineering, Elsevier, 2010.

[26] D.E. Suk, G. Chowdhury, T. Matsuura, Study on the kinetics of surface migration of surface modifying macromolecules in membrane preparation, Macromolecules, 35 (2002) 3017-3021.

[27] M. Khayet, C.Y. Feng, T. Matsuura, Morphological study of fluorinated asymmetric polyethermide ultrafiltration membranes by surface modifying macromolecules, J. Membr. Sci., 213 (2003) 159-180.

[28] C. Gostoli, G.C. Sarti, Separation of liquid mixtures by membrane distillation, J. Membr. Sci., 41 (1989) 211-224.

[29] S.T. Hsu, K.T. Cheng, J.S. Chiou, Seawater desalination by direct contact membrane distillation, Desalination, 143 (2002) 279–287.

[30] K. He, H.J. Hwang, Air gap membrane distillation on the different type membrane, Korean J. Chem. Eng., 28 (2011) 770 – 777.

[31] B.L. Pangarkar, M.G. Sane, Performance of Air Gap membrane distillation for desalination of ground water and seawater, Word Academy of Science, Engineering and Technology, 75 (2011) 973-977.

[32] M. Khayet, C. Cojocaru, Artificial neural network modelling and optimization of desalination by air gap membrane distillation, Sep. Pur. Tech., 86 (2012) 171-182.

[33] M. Khayet, C. Cojocaru, Air gap membrane distillation: Desalination, modelling and optimization, Desalination, 287 (2012) 138-145.

[34] F.A. Banat, J. Simandl, Theoretical and experimental study in membrane distillation, Desalination, 95 (1994) 39-52.

[35] C. Zhu, G.L. Liu, C.S. Cheung, C.W. Leung, Z.C. Zhu, Ultrasonic stimulation on enhancement of air gap membrane distillation, J. Membr. Sci., 161 (1999) 85-93.

[36] G. L. Liu, C. Zhu, C.S. Cheung, C.W. Leung, Theoretical and experimental studies on air gap membrane distillation, Heat and Mass Transfer, 34 (1998) 329 – 335.

[37] M.A. Izquierdo-Gil, M.C. García-Payo, C. Fernández-Pineda, Air gap membrane distillation of sucrose aqueous solutions, J. Membr. Sci., 155 (1999) 291-307.

[38] F.A. Banat, J. Simandl, Desalination by membrane distillation: A parametric study, Sep. Sci. Technol., 33 (1998) 201-226.

[39] C. Feng, K.C. Khulbe, T. Matsuura, R. Gopal, S. Kaur, S. Ramakrishna, M. Khayet, Production of drinking water from saline water by air-gap membrane distillation using polyvinylidene fluoride nanofiber membrane, J. Membr. Sci., 311 (2008) 1-6.

[40] Z. Ma, Y. Hong, L. Ma, M. Su, Superhydrophobic membranes with ordered arrays of nanospiked microchannels for water desalination, Langmuir Letter, 25 (2009) 5446-5450.

[41] L. Gazagnes, S. Cerneaux, M. Persin, E. Prouzet, A. Larbot, Desalination of sodium chloride solutions and seawater with hydrophobic ceramic membranes, Desalination, 217 (2007) 260-266.

[42] S. Cerneaux, I. Stuzynska, W.M. Kujawski, M. Persin, A. Larbot, Comparison of various membrane distillation methods for desalination using hydrophobic ceramic membranes, J. Membr. Sci., 337 (2009) 55-60.

2.2. Application of a Porous Composite Hydrophobic/Hydrophilic Membrane in Desalination by Air Gap and Liquid Gap Membrane Distillation: A Compartative Study

Contents:

2.2.1. Introduction

2.2.2. Experimental

    2.2.2.1. Materials

    2.2.2.2. Membrane characterization

    2.2.2.3. LGMD and AGMD experiments

2.2.3. Theoretical approach

2.2.4. Results and discussions

    2.2.4.1. Membrane characteristics

    2.2.4.2. Feed temperature effects on heat and mass transport in LGMD and AGMD

    2.2.4.3. Feed concentration effects on AGMD and LGMD performances

2.2.5. Conclusions

References

Abstract:

A first attempt was carried out comparing the two membrane distillation (MD) configurations, liquid gap (LGMD) and air gap (AGMD), using a porous composite hydrophobic/hydrophilic membrane, the same system and the same MD operating parameters. The surface modified membrane was prepared by the phase inversion technique in a single casting step using a fluorinated surface modifying macromolecule (SMM). Different membrane characterization techniques were applied. MD experiments were performed at different feed temperatures and sodium chloride aqueous solutions. The permeate fluxes were found to be slightly higher (2.2 – 6.5 %) for LGMD compared to that of AGMD although the resistance to mass transfer in LGMD is higher due to the presence of the liquid permeate layer between the membrane and the cooling solid surface. This observed enhancement is attributed partly to the small established distance between the liquid/vapor interfaces at both side of the hydrophobic thin top-layer of the membrane in LGMD configuration, and the higher thermal conductivity of water, which is an order of magnitude higher than that of air, resulting in higher heat transfer coefficient of the permeate in LGMD. The salt rejection factors were found to be almost similar for both MD variants and higher than 99.61%. Compared to AGMD, the thermal efficiency is higher for LGMD, whereas the specific internal heat loss is lower. A linear increase of the thermal efficiency with the feed inlet temperature was observed for both MD configurations. The global heat transfer coefficient and the heat transfer of the permeate membrane side were also found to be greater for LGMD. The temperature polarization effect was found to be slightly higher for AGMD, whereas the concentration polarization effect was slightly higher for LGMD due to its higher permeate flux. In general, the LGMD proved to be more attractive than AGMD for desalination when using bi-layered hydrophobic/hydrophilic membranes.

2.2.1. Introduction

To establish the necessary driving force in membrane distillation (MD) technology, which is the partial vapor pressure difference across the membrane, four principal configurations were first proposed in the 60´s, namely, direct contact membrane distillation (DMCD), sweeping gas membrane distillation (SGMD), vacuum membrane distillation (VMD) and air gap membrane distillation (AGMD) [1]. Then, during last decade some hybrid MD variants termed thermostatic sweeping gas membrane distillation (TSGMD) and liquid gap membrane distillation (LGMD) were considered in order to enhance the water production rate and the thermal efficiency of the MD technology [2-4]. For LGMD mode, which also termed permeate gap MD, the air gap space between the membrane and the condensing surface of the AGMD module is normally filled with the produced water. The permeate water exits from the top part of the membrane module whereas in AGMD the permeate water leaves the module from the bottom. The differences between all these MD configurations are made only in the permeate side.

TSGMD combines both SGMD and AGMD in order to minimize the temperature of the sweeping gas, which increases considerably along the membrane module length because of the heat transferred from the feed side through the membrane to the permeate side [3,4]. LGMD combines both DCMD and AGMD configurations. The gap between the membrane and the condensing surface in the permeate side of the AGMD system is filled by the produced distilled water acting as stagnant cold liquid solution inside the membrane module [2,5-7].

It is worth quoting that the most used MD variant is DCMD with 58.6 % (calculated taking into consideration the MD published studies in International Journals up to 31st December 2013) because its simplicity in operation as condensation phenomenon is carried out inside the membrane module. On the contrary, SGMD is the least studied MD variant with a contribution of only 4.5 % because it requires external condensers to collect the permeate and a gas source to generate the sweeping gas. On the other hand, a negligible number of studies were performed using the two MD hybrid variants TSGMD and LGMD (i.e. contribution of only 0.5% and 0.3% for LGMD and TSGMD, respectively).

It must be pointed out that very few comparative studies have been performed between the four principal MD configurations [6-11]. For an adequate comparison, the same membrane,

module if possible, feed side hydraulic installation and MD operating conditions must be maintained. Moreover, not only the MD performance (i.e. permeate flux and rejection factors) have to be compared but also the thermal efficiency of the membrane module, the heat lost and the specific energy consumption defined as the ratio between the total applied energy and the water production rate.

Khayet et al. [8] compared the permeate flux, the thermal efficiency, the heat loss the salt rejection factor of the DCMD, SGMD and VMD configurations using the same shell and tube capillary membrane module and the same feed MD operating conditions. It was found that the VMD permeate flux was 2.8 to 3.1 times higher than that of DCMD and the SGMD permeate flux was about 1.4 times greater than that of DCMD. These results were attributed to the internal heat lost by conduction through the membrane, which was very low in SGMD and VMD modes. When using chemically modified zirconia and titania ceramic membranes in desalination by DCMD, AGMD and VMD variants, Cerneaux et al. [9] observed higher AGMD permeate flux than DCMD while the greatest permeate flux was obtained with VMD configuration one with salt rejection factors of 99-100%.

In general, it is known that the air entrapped within the pores of a membrane used in DCMD results in a high mass transfer inefficiency, while the heat transferred by conduction through the membrane, which is considered heat loss in MD is high in DCMD configuration. On the other hand, SGMD configuration combines a relatively low conductive heat loss through the membrane with a reduced mass transfer resistance. In other words, in both AGMD and SGMD variants, there is a gas barrier that reduces the heat loss by conduction through the membrane. Nevertheless, compared to AGMD variant the gas in SGMD sweeps the membrane resulting in higher mass transfer coefficients and therefore higher permeate fluxes.

Recently, a couple of comparative attempts were made using the same AGMD system but different possibilities of the gap between the membrane and the cooling surface in the permeate side of the membrane module (solid porous material gap, free air gap, liquid gap, partial vacuum gap, etc.) [6,7]. Cipollina et al. [6], by considering AGMD, LGMD and partial vacuum gap (VGMD), observed the highest permeate flux for LGMD (12 kg/m^2.h at 80ºC feed inlet temperature, 17-20ºC condensing inlet temperature, 35 g/L feed inlet concentration, and 3 mm air gap) whereas the AGMD configuration exhibited the lower permeate flux. The obtained

values for the VGMD were between those of AGMD and LGMD. In terms of the specific thermal energy consumption, it was also found low values for LGMD followed by those of VGMD and the LGMD. It was argued that the benefit of using LGMD might be attributed to the faster and direct condensation step and the faster heat dissipation rate towards the membrane due to the higher thermal conductivity of the liquid compared to that of the air. Consequently, it was concluded that the best MD mode for their system was LGMD.

Francis et al. [7] observed a considerable enhancement of the water permeate flux when filling the gap between the membrane and the condensation solid surface of an AGMD module with sand, distilled water, sponge (polyurethane) and polypropylene mesh. The maximum increase, 820%, was observed for distilled water filling the gap (i.e. LGMD) as compared to AGMD under the same operating conditions (a feed temperature of 80ºC, a condensing temperature of 20ºC, a gap width of 13 mm, Red Sea as feed solution). The obtained AGMD permeate flux was 4.77 kg/m^2.h with 99.99% salt rejection; whereas a 428% increase in the permeate flux was observed (20.45 kg/m^2.h) when considering LGMD. The achieved salt rejection factors were 99.99% (i.e. the electrical conductivity was reduced from 61.4 mS/cm to less than 15 µS/cm in all desalination tests). Moreover, it was also reported that an increase in the water gap width from 9 mm to 13 mm enhanced the LGMD permeate flux. As it was expected, when increasing the porosity of the sand used in the gap, the water production rate was increased.

During the last years, various types of hydrophobic/hydrophilic porous composite membranes were prepared using different types of SMMs and host hydrophilic polymer for desalination by DCMD [12-15]. This type of membranes were found to be promising for desalination by DCMD as they combine the low resistance to mass flux, achieved by the diminution of the water vapor transport path through the hydrophobic thin top-layer, and a low conductive heat loss through the membrane, obtained by using a thicker hydrophilic sub-layer. Recently, a comparative desalination study between DCMD and AGMD was carried out using this type of membrane but different set-ups [10]. The effects of different experimental parameters such as the feed temperature, the cooling temperature, the feed flow rate and the salt concentration on both the permeate flux and the salt rejection factor were investigated. The AGMD performance of the composite porous hydrophobic/hydrophilic membrane is compared to its DCMD performance. It

146

was confirmed that this type of membrane are more adequate for DCMD than for AGMD configuration because of their significantly higher DCMD permeate flux attributed mainly to the low resistance to mass transport achieved by the reduction of the water vapour transport path length through the hydrophobic thin top-layer of the membrane.

In the present study an attempt is made using the same type of membrane, the same set-up and the same MD operating conditions to compare the LGMD and AGMD configurations in terms of their permeate fluxes, salt rejection factors, thermal efficiency, specific internal heat loss, heat transfer coefficients in the feed and permeate boundary layers, overall heat transfer coefficient, temperature and concentration polarization, etc.

2.2.2. Experimental

2.2.2.1. Materials

The flat sheet membrane used is a bi-layered porous composite hydrophobic/hydrophilic membrane prepared by the phase inversion technique employing a fluorinated surface modifying macromolecule (SMM) and polyetherimide (PEI) as reported elsewhere [10].

2.2.2.2. Membrane characterization

Different characterization techniques were applied to determine the membrane parameters as indicated in [10]. The total membrane thickness (δ) was measured by the micrometer Millitron Phywe (Mahr Feinprüf, type TYP1202IC). The membrane cross-section was analyzed by the scanning electron microscope (SEM, JEOL Model JSM-6400) equipped with the energy-dispersive spectrometer (EDS, Oxford Instruments). The water contact angles (θ_a) of the top and bottom membrane surfaces were measured by a computerized optical system CAM100, equipped with a CCD camera, frame grabber and image analysis software.

The liquid entry pressure of water (LEP_w) measurements were carried out using the experimental system schematized in [16]. The effective membrane area is 12.56 x 10^{-4} m^2. The

container was filled first with 2 L distilled water and then the pressure was applied gradually from the nitrogen cylinder on water at 23ºC. The minimum applied pressure before water penetrates into the pore of maximum size is the *LEP* value. These experiments were carried out three times using three different membrane samples made from different batches and the average values together with their standard deviations are reported.

To get the mean pore size (d_p) and the effective porosity (ε/L_p), which is defined as the ratio of the porosity and the effective pore length that takes into account the tortuosity of the membrane pores, the gas permeation method was applied by means of a Porometer (POROLUX™ 100, Porometer) using air and dry membrane samples. More details on the followed calculations may be found in [17]. These experiments were carried out three times using three different membrane samples made from different batches.

2.2.2.3. LGMD and AGMD experiments

The system used to conduct both the LGMD and AGMD experiments is presented in Fig. 2.2.1. A plate and frame membrane module with an effective membrane area of 5.53 x 10^{-3} m^2 was used. A circulation pump MasterFlex 7529-20 was used to circulate the feed solution from the hot feed tank to the feed chamber of the membrane module. The feed flow rate was 100 l/h. The hot feed solution was brought into contact with the hydrophobic top layer of the membrane. A cooling liquid (50 % ethylene glycol/water solution by volume) was circulated through the cooling chamber of the membrane module by the chiller (PolyScience Recirculator). In all cases, the temperature at the inlet of the cooling chamber was maintained at 20ºC. The thickness of the gap between the membrane and the cooling surface in the permeate side is 4.352 mm. Pt-100 sensors connected to a digital multimeter Fluke Hydra were employed to measure the temperature at the inlets and outlets of the membrane module for both feed solution and cooling liquid. In order to avoid membrane pore wetting, the pressure at the feed inlet membrane module was measured by a manometer. In all performed tests in this study the transmembrane pressure was in the range 0.4-0.8 10^5 Pa. In AGMD mode of operation (Fig. 2.2.1a), the evaporated water molecules at the liquid/membrane interface cross the membrane pores and the air gap chamber to finally condense over the cooling stainless steel metallic plate. The produced permeate is

collected from the bottom side of the membrane module. In LGMD mode of operation (Fig. 2.2.1b), the evaporated water molecules at the liquid/membrane interface cross the hydrophobic layer of the membrane in vapor phase and condense at the liquid/vapor interface formed in the interface between the hydrophobic and the hydrophilic layer. The produced permeate is collected from the top side of the membrane module leading the gap between the membrane and the cooling surface to be filled with the produced water.

All MD tests were carried out first for distilled water used as feed and then salt (NaCl) aqueous solutions of different concentrations (12 g/L and 30 g/L). The permeate flux was determined gravimetrically by weighing the distillate collected in the permeate container for a predetermined time after steady state was reached. *Each MD experimental test was carried out for 2 h.* The salt concentrations of feed and permeate were determined by a conductivimeter 712 ΩMetrohm.
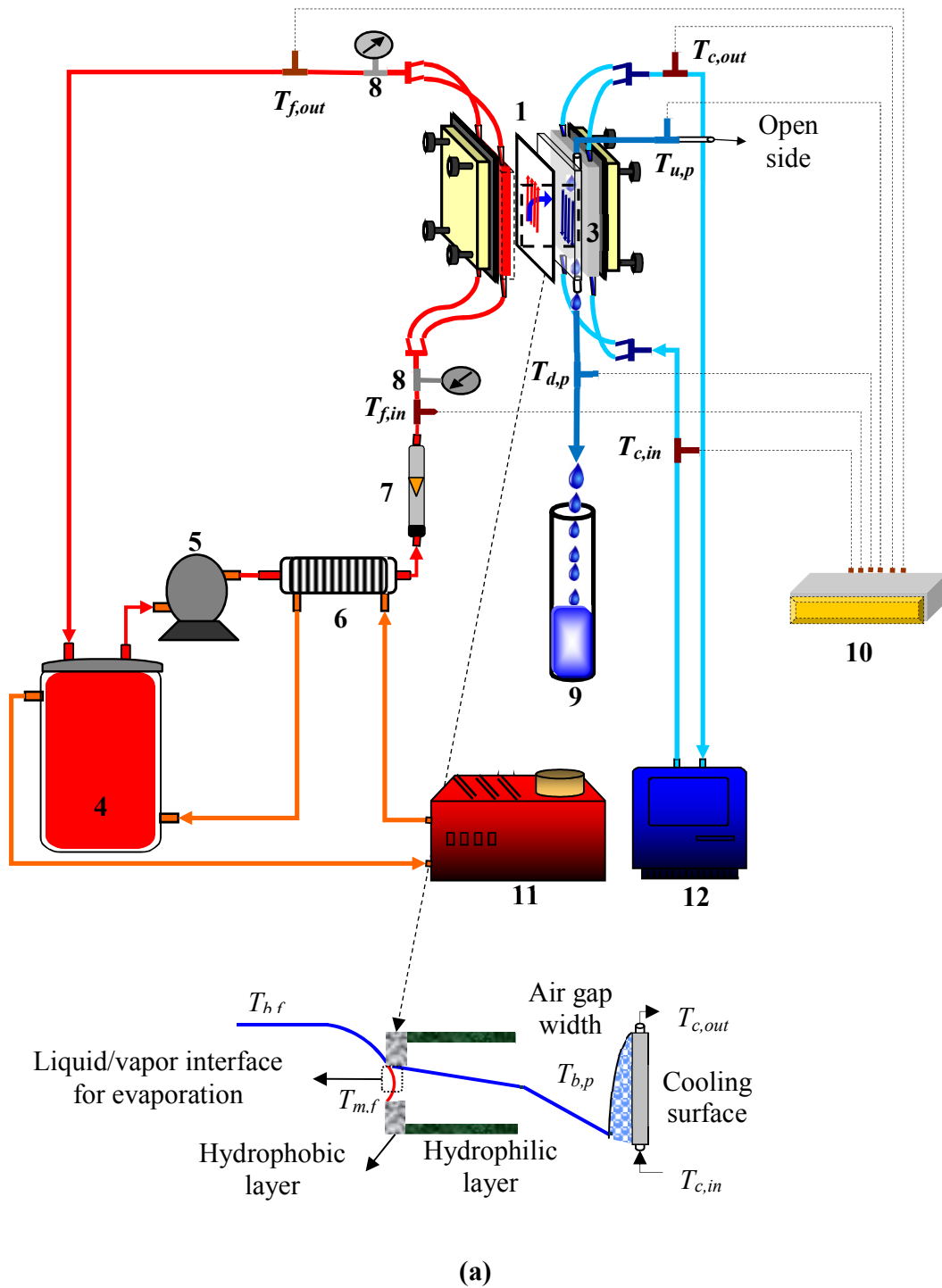
Figure 2.2.1. AGMD (a) and LGMD (b) set-up: (1) membrane module, (2) flat-sheet membrane, (3) cooling chamber, (4) feed container, (5) circulation peristaltic pump, (6) heat exchanger, (7) flowmeter, (8) manometer, (9) permeate container, (10) digital multimeter, (11) thermostat, (12) cryostat. (To be continued)
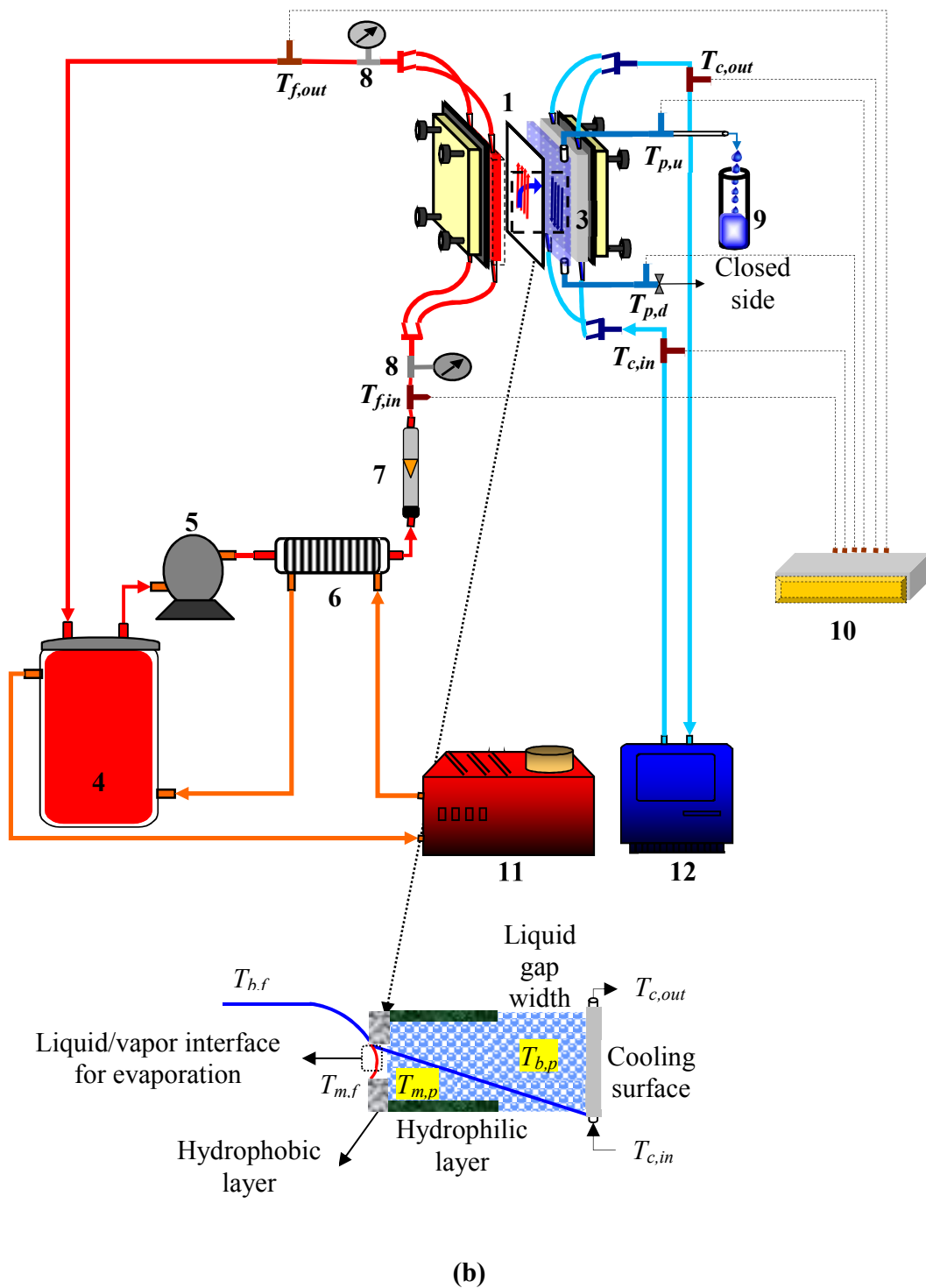
Figure 2.2.1. AGMD (a) and LGMD (b) set-up: (1) membrane module, (2) flat-sheet membrane, (3) cooling chamber, (4) feed container, (5) circulation peristaltic pump, (6) heat exchanger, (7) flowmeter, (8) manometer, (9) permeate container, (10) digital multimeter, (11) thermostat, (12) cryostat. (Continuation)

2.2.3. Theoretical approach

In all MD configurations, both heat and mass transfer take place simultaneously through the membrane. The total heat transfer through the membrane is due to the latent heat accompanying the produced vapor flux (Q_v) and the heat transferred by conduction following fourier´s law (Q_c) across both the membrane matrix and the gas-filled membrane pores [1,18]:

$$Q_m = Q_v + Q_c = J_w \Delta H_v + \frac{k_m}{\delta}\left(T_{m,f} - T_{m,p}\right) \tag{2.2.1}$$

where J_w is the water permeate flux, k_m is the thermal conductivity of the membrane, δ is the membrane thickness, ΔH_v is the heat of vaporization of water, $T_{m,f}$ is the temperature of the feed aqueous solution at the membrane surface and $T_{m,p}$ is the temperature of the permeate at the membrane surface.

In all MD configurations, Q_c is considered internal heat loss reducing both the thermal efficiency and the permeate flux of the process.

At steady state conditions, Q_m and the external heat lost Q_l (heat lost to the surrounding media) should be equal to the heat transfer in the feed channel of the membrane module Q_f:

$$Q_f = \frac{\dot{m}_f c_p}{A_m}(T_{f,in} - T_{f,out}) = Q_m + Q_l \tag{2.2.2}$$

where $\dot{m}_f$ is the feed flow rate, c_p is the specific heat of the feed solution, A_m is the effective membrane area and $T_{f,in}$ and $T_{f,out}$ are the temperatures of the feed solution at the inlet and outlet of the membrane module, respectively.

As it is well known in all heat transfer systems, there is a presence of fluid boundary layers adjoining both the feed and permeate membrane sides causing the temperature polarization phenomenon. At steady state conditions, the heat transfer through the adjoining fluid boundary layers must be the same as Q_m:

$$Q_m = h_f\left(T_{b,f} - T_{m,f}\right) = h_p\left(T_{m,p} - T_{b,p}\right) \tag{2.2.3}$$

where the subscript b refers to the bulk fluids, and h_f and h_p are the heat transfer coefficients in the feed and permeate boundary layers adjoining the membrane surfaces, respectively. In the present study, h_p represents the total heat transfer coefficient in the permeate side (i.e. for

LGMD: permeate liquid inside the hydrophilic membrane layer, liquid gap layer and coolant film liquid at the cooling solid surface; and for AGMD: condensate heat transfer coefficient and that of the air gap).

The overall heat transfer coefficient (H) of the MD process can be determined as [18-20]:

$$H = \frac{Q_m}{\left(T_{b,f} - T_{b,p}\right)} = \left[\frac{1}{h_f} + \frac{1}{\dfrac{k_m}{\delta} + \dfrac{J_w \Delta H_v}{T_{m,f} - T_{m,p}}} + \frac{1}{h_p}\right]^{-1}$$

(2.2.4)

Because of the change of the temperature along the membrane module length in both the feed and permeate sides, the use of the logarithmic mean temperature difference (ΔT_{ln}) is recommended and the total heat flux can be written as a function of H as follows:

$$Q_f = Q_m + Q_l = H \; \Delta T_{ln} + Q_l = H \; \frac{\Delta T_1 - \Delta T_2}{\ln\left(\dfrac{\Delta T_1}{\Delta T_2}\right)} + Q_l$$

(2.2.5)

where ΔT_1 and ΔT_2 are the temperature difference between the feed and the permeate at the inlet and outlet of the membrane module, respectively.

All the experimental tests carried out in this study were performed applying a feed flow rate of 100 l/h. The circulation velocity through the feed channel was calculated and the obtained Reynolds number (Re) was found to be between 887.6 and 2085.5 for distilled water as feed indicating the laminar feed flow regime. Therefore, the coefficient h_f can be calculated from the semi-empirical equation [18]:

$$Nu = \frac{h_f d_e}{k_f} = 1.86 \; (Re \, Pr \, d_e / L)^{1/3}$$

(2.2.6)

where Nu is the dimensionless Nusselt number, Pr is the Prandtl number, d_e is the equivalent diameter of the feed flow channel, L is the module length and k_f is the thermal conductivity of the feed solution.

By using Eqs. (2.2.3) and (2.2.4) the temperature polarization coefficient (θ) can be determined as [1]:

$$\theta = \frac{1}{1 + \dfrac{H}{h}}$$

(2.2.7)

where h is the heat transfer coefficient of both the feed and permeate boundary layers:

$$\frac{1}{h} = \frac{1}{h_f} + \frac{1}{h_p} \qquad (2.2.8)$$

The thermal efficiency (*EE*) of both LGMD and AGMD configurations can be calculated as [1,20]:

$$EE = \frac{Q_v}{Q_m}100 = \frac{J_w \Delta H_v}{H(T_{b,f} - T_{b,p})}100 \qquad (2.2.9)$$

The specific internal heat loss (*HL*) is also defined in MD as:

$$HL = \frac{Q_c}{J_w} \qquad (2.2.10)$$

The permeate flux (J_w) in MD process is written as [18]:

$$J_w = B_b \Delta p_{w,b} = B_m \Delta p_{w,m} \qquad (2.2.11)$$

where p is the vapor pressure of water, B the membrane permeability and the subscripts b, m, w refer to bulk, membrane and water, respectively.

The vapor pressure polarization coefficient (ψ) can be determined from Eq. (2.2.11) as:

$$\psi = \frac{\Delta p_{w,m}}{\Delta p_{w,b}} = \frac{B_b}{B_m} \qquad (2.2.12)$$

When distilled water is used as feed the coefficients ψ and θ are equal. Moreover, similar to the temperature, there is a change of the vapor pressure of water along the membrane module length in both the feed and permeate sides and therefore the logarithmic mean vapor pressure of water difference (Δp_{ln}) should be used to calculate the membrane permeability (B_b). On the other hand, for the SMM modified membrane, due to the small pore size (d_p) of the hydrophobic layer compared to the mean free path of the water evaporated molecules (λ_w), Khayet et al. [13] found that water vapor is transported following Knudsen type of flow. In other words, Knudsen type of flow is predominant in pores with sizes lower than the mean free path of the transported water vapor molecules. Therefore, the membrane permeability B_m can be calculated as [18]:

$$B_m = \frac{2}{3} \frac{\varepsilon}{L_p} d_p \left(\frac{2 M}{\pi R T} \right)^{1/2} \qquad (2.2.13)$$

154

where d_p is the pore size, M is the water molecular weight, R is the gas constant, L_p is the effective pore length and ε is the void volume fraction (i.e. porosity) of the membrane.

The salt concentration at the feed membrane surface ($C_{m,f}$) becomes greater than that of the bulk feed aqueous solution ($C_{b,f}$) because of the water vapor transport through the membrane. To calculate this concentration, Nernst film model was considered [1,18]:

$$C_{m,f} = C_{b,f} \exp\left(\frac{J_w}{k_s \rho_w}\right) \qquad (2.2.14)$$

where k_s is the solute mass transfer coefficient through the concentration boundary layer in the feed side of the membrane module and ρ_w is the water density. This can be estimated from Sherwood number (Sh) using the dimensionless empirical correlation for mass transfer derived from the analogy with Eq. (2.2.6), where Sc is the dimensionless Schmidt number [1,19].

$$Sh = \frac{k_s d_e}{D_{NaCl}} = 1.86 \ (\text{Re} \, Sc \ d_e / L)^{1/3} \qquad (2.2.15)$$

where D_{NaCl} is the diffusion coefficient of NaCl in water.

The concentration polarization coefficient (β) can then be calculated from the following expression:

$$\beta = \frac{C_{m,f}}{C_{b,f}} \qquad (2.2.16)$$

In this case, the permeate flux can be written as [18]:

$$J_w = B_m(p_{m,f} - p_{m,p}) = B_m(p_{w,f}^0 \gamma_{w,f} x_{w,f} - p_{w,p}^0) \qquad (2.2.17)$$

where $\gamma_{w,f}$, $x_{w,f}$ and $p_{w,f}^0$ are the activity coefficient, mole fraction and vapor pressure of water at the feed/membrane surface, respectively. $p_{w,p}^0$ is the vapor pressure of water in the permeate.

2.2.4. Results and discussions

2.2.4.1. *Membrane characteristics*

The obtained membrane characteristics are summarized in Table 2.2.1. The water contact angle of the top membrane surface is higher than that of the bottom surface. This confirms the

155

SMM migration to the top membrane surface increasing its hydrophobicity because of the fluorine groups associated to SMM [10,14,15,21]. Providing that the LEP_w is higher for high hydrophobicity membrane surface and low maximum pore size, a high LEP_w value up to $3.8 \ 10^5$ Pa was achieved for this hydrophobic/hydrophilic composite membrane and small pore size is expected.

From the reported SEM image (Fig. 2.2.2) it can be seen the asymmetric structure of the membrane having a sponge top-layer supported by a finger-like structure and macrovoids underneath. Pores can be seen at the bottom membrane surface whereas by means of SEM no pore can be detected at the top membrane surface indicating their very small size. The performed EDS analysis of fluorine, carbon and oxygen on the SEM cross-section images also proved SMM migration to the top membrane surface as the concentration of fluorine, which is associated to SMM decreased from the top surface of the membrane towards its inside, whereas the concentrations of carbon and oxygen were increased [10]. From the obtained EDS spectra of different SEM cross-sectional images, the thickness of the hydrophobic layer was estimated to be 4.5 ± 1 μm. For this type of membranes with a total thickness in the range of 51 to 54 μm, Khayet et al. [13] reported thickness values of the hydrophobic layer less than 8.5 μm.

Cross section		
x1500	x 3000	x10000
Top surface		
x5000		x30000
Bottom surface		
x5000		x30000
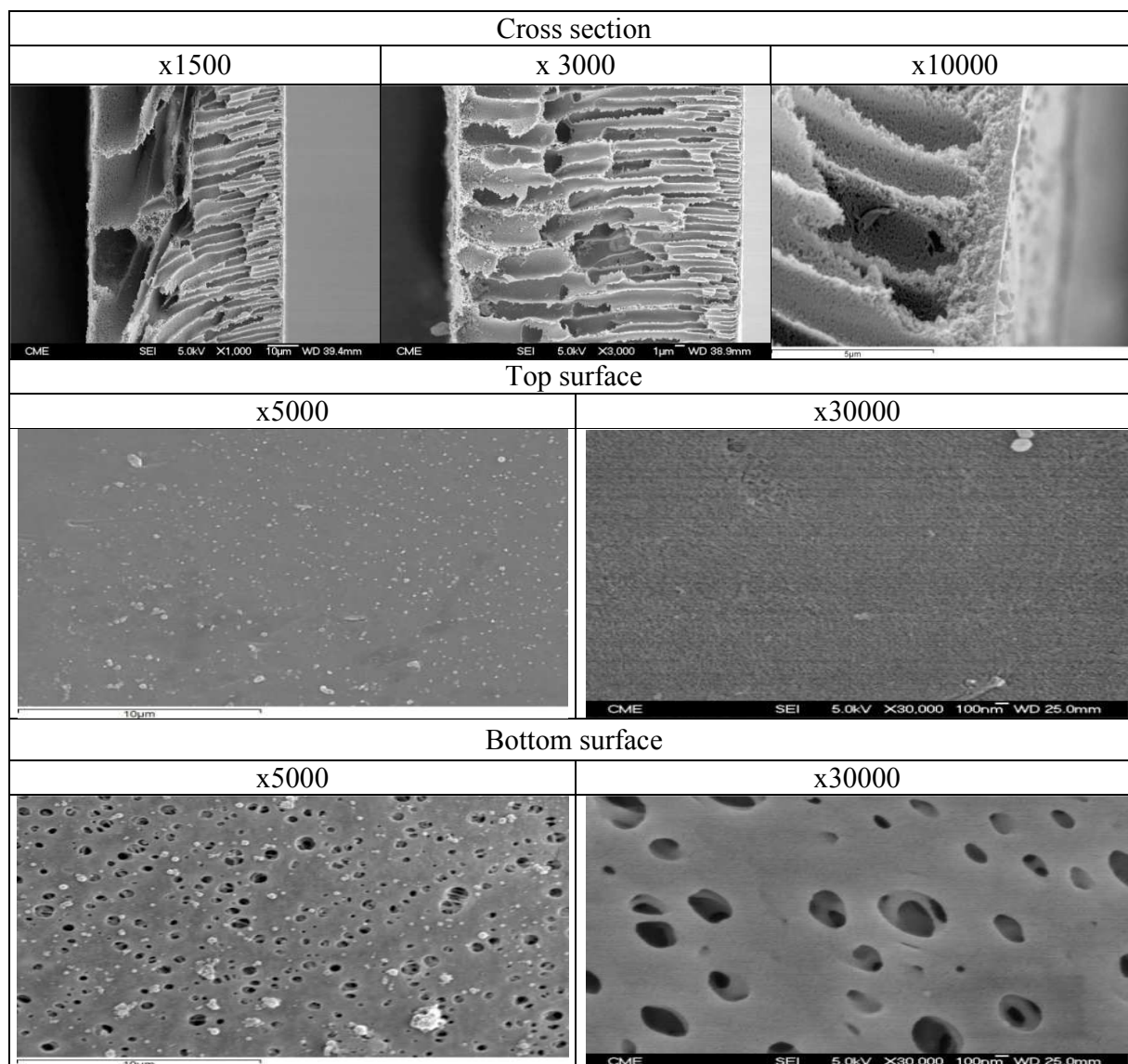
Figure 2.2.2. SEM images of the section, top and bottom surfaces of the porous composite hydrophobic/hydrophilic membrane at different magnifications.

Figure 2.2.3 shows the linear variation of the gas permeance (B_g) of the membrane as a function of the mean pressure (P_m) within the membrane. In general, B_g for a porous membrane contains both the diffusive term and the viscous term that depends on the pressure as reported in [1]:

$$B_g = \frac{4}{3}(\frac{2}{\pi M_g RT})^{0.5} r_P \frac{\varepsilon}{L_p} + \frac{P_m}{4\mu_g RT} r_p^2 \frac{\varepsilon}{L_p} = I + S\ P_m \qquad (2.2.18)$$

where r_p is the pore radius, R is the gas constant, T is the absolute temperature, M_g is the molecular weight of the gas and μ_g is the gas viscosity within the membrane. From the obtained intercept (I) and slope (S) of the linear plots of the membrane samples, r_p and the effective porosity (ε/L_p) can be determined using the following equations:

$$r_P = \frac{16}{3} \frac{S}{I} (\frac{8RT}{\pi M_g})^{0.5} \mu_g$$

(2.2.19)

$$\frac{\varepsilon}{L_p} = \frac{8\mu_g RT}{r_p^2} S \qquad (2.2.20)$$

The results are shown in Table 2.2.1. It must be pointed out that this method was originally developed for symmetric membranes. However, in the case of an asymmetric membrane with a skin layer, the measured pore size is characteristic of the skin layer. If only the diffusive term is considered in Eq. (2.2.16), the obtained factor ($r_p\varepsilon/L_p$) is found to be the same as that obtained considering both the diffusive and the viscous terms. This means that the contribution of the viscous (i.e. Poiseuille) term is negligible.
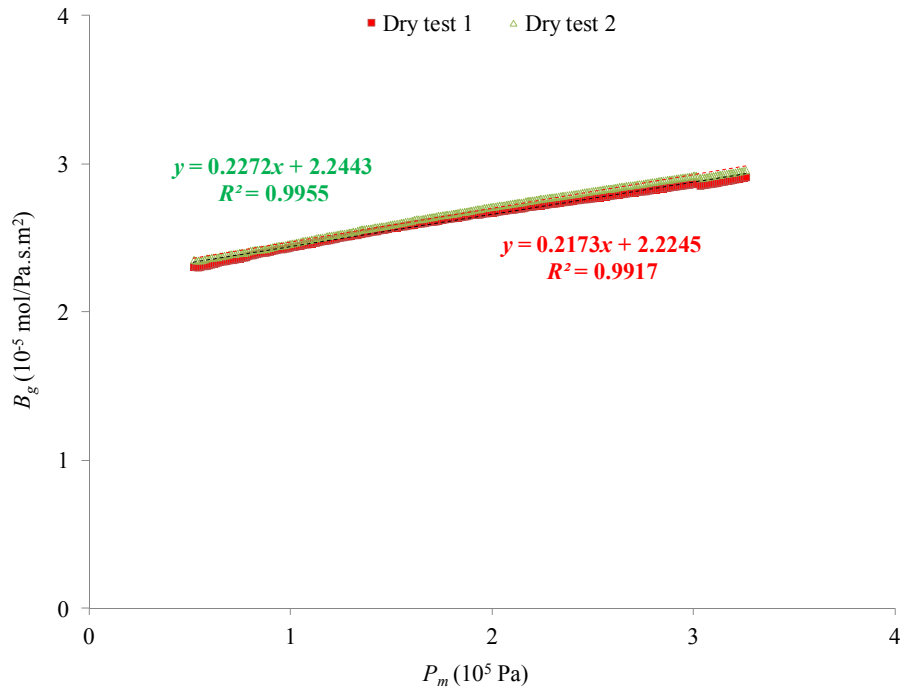
Figure 2.2.3. Gas permeance (B_g) of the porous composite hydrophobic/hydrophilic membrane as a function of the mean pressure (P_m) within the membrane obtained by means POROLUX™ 100, Porometer.

Table 2.2.1. Characteristics of the prepared composite hydrophobic/hydrophilic membrane.

Membrane parameter	Value
Total thickness, δ (μm)	64.7 ± 6.3
Hydrophobic layer thickness, δ_h (μm) [a]	4.5 ± 1
Advancing water contact angle, θ_a (º)	Top surface: 94.8 ± 0.5 Bottom surface: 74.3 ± 0.8
Liquid entry pressure of water, LEP_w (10^5 Pa)	3.82 ± 0.05
Pore radius, r_p (nm) [b]	46.10 ± 1.17
Effective porosity, ε/L_p ($10^3\ m^{-1}$) [b]	3.86 ± 0.08
$r_p\varepsilon/L_p (10^{-4})$ [b]	1.78 ± 0.01
$r_p\varepsilon/L_p (10^{-4})$ [c]	1.78 ± 0.01

[a] Determined by EDS associated to SEM.
[b] Determined by the gas permeation test considering both the diffusive and the viscous terms.
[c] Determined by the gas permeation test considering only the diffusive (Knudsen) term.

**2.2.4.2. Feed temperature effects on heat and mass transport in LGMD and AGMD**

Figure 2.2.4 shows the permeate flux (J_w) of the porous composite hydrophobic/hydrophilic membrane as a function of the inlet feed temperature in LGMD and AGMD configurations. An exponential increase of the permeate flux of both MD variants was observed when enhancing the feed temperature. This is due to the exponential increase of the water vapor pressure with temperature. In all studied feed temperature range, the permeate flux is slightly higher (2.2 – 6.5 %) for the LGMD configuration. The greater water production rate of LGMD may be due to different factors resulting in lower resistance to mass transfer in this configuration. For instance, the higher thermal conductivity of water compared to that of air (i.e. water has an order of magnitude higher thermal conductivity than air) results in a lower permeate temperature at the permeate side of the membrane and increases the transmembrane driving force. Moreover, the observed enhancement of the permeate flux for LGMD is attributed partly to the small established distance between the liquid/vapor interfaces at both side of the hydrophobic thin top-layer of the membrane as water penetrates inside the hydrophilic layer of the membrane. Cipollina et al. [6] also observed higher permeate fluxes with the LGMD configuration than with AGMD and VGMD configurations. The highest LGMD permeate flux obtained by Cipollina et al. [6] was 12 kg/m^2.h for 80ºC feed temperature, 17-20ºC cooling temperature and using the commercial (Gore^{TM} Microfiltration Media GMM-203) polytetrafluoroethylene (PTFE) membrane supported on polypropylene (PP) having 0.2 μm average pore size, 240 μm thickness and 80% porosity. This permeate flux is lower than that of the prepared porous composite hydrophobic/hydrophilic membrane in this study. When using another type of system, Lewis Cell, turbulent type of flow and a feed temperature of 80ºC, the obtained DCMD permeate flux of the porous composite hydrophobic/hydrophilic membrane was found to be 41.6 kg/m^2.h (i.e. about 2.8 times higher than the permeate fluxes obtained in this study when using distilled water as feed) [10]. This is also attributed to the high temperature polarization effects in LGMD and AGMD as it will be explained later on and to the contribution of the thick stagnant air layer (in AGMD) and water layer (in LGMD) interposed between the membrane and the cooling surface leading to an increase of the mass transfer resistance.
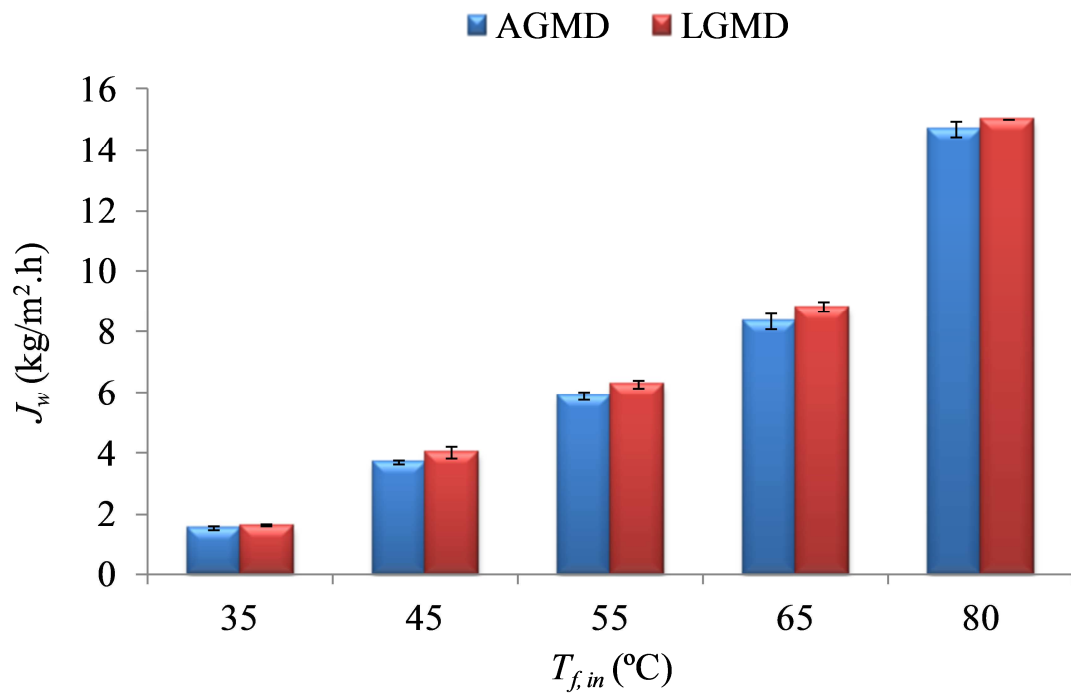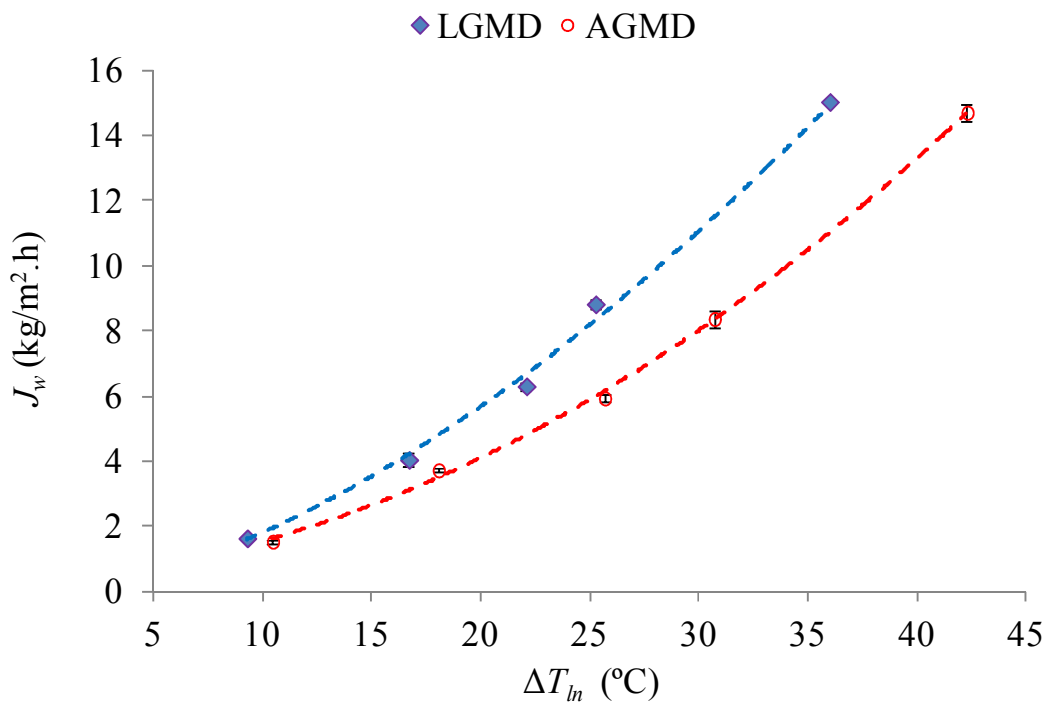
Figure 2.2.4. Permeate flux (J_w) of LGMD and AGMD configurations *versus* the feed inlet temperature ($T_{f,in}$) (a) and the logarithmic mean temperature difference (ΔT_{ln}) (b).

For LGMD configuration, the recorded time necessary to fill the permeate gap with the produced water is plotted in Fig. 2.2.5. There is a considerable reduction of the waiting time before water started to be collected from the permeate side of the membrane module. As it was mentioned before, this is related with the exponential increase of the water production rate with the feed temperature.
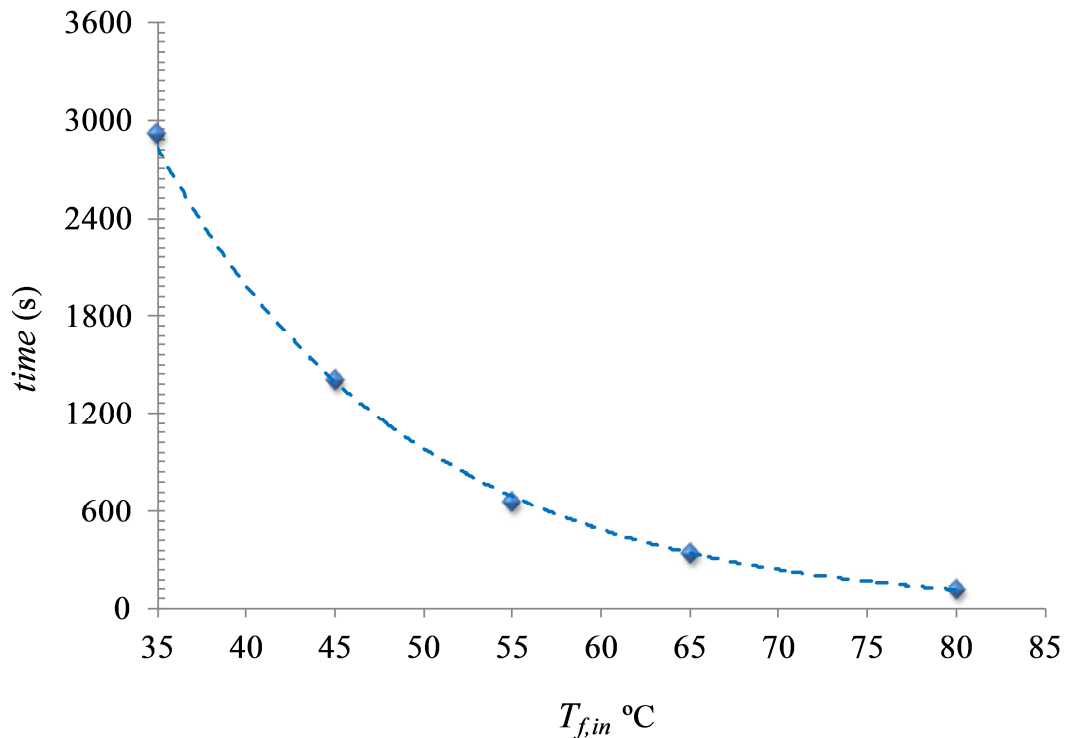
Figure 2.2.5. Necessary time required to fill the permeate gap with the produced water as a function of the applied feed inlet temperature ($T_{f,in}$).

In MD technology, the heat requirements represent a significant part of the process cost and the thermal energy consumption is very sensitive to the applied feed temperature. The heat flux in the feed channel of the membrane module (Q_f) was calculated for both LGMD and AGMD using Eq. (2.2.2). The results are presented in Fig. 2.2.6 for different logarithmic mean temperature difference (ΔT_{ln}). Straight lines with reasonably high correlation coefficients (> 0.9816) were plotted for both MD variants and both the overall heat transfer coefficient (H) and the external heat lost (Q_l) was determined as indicated previously by Eq. (2.2.5). These are 1153.5 W/m^2.K and 1370.9 W/m^2 for LGMD and 1027.1 W/m^2.K and 3966.6 W/m^2 for AGMD.

162

The global heat transfer coefficient was found to be greater for LGMD. In general Q_l depends on the used feed temperature. However, in this case the high obtained correlation coefficients in the studied temperature range indicate that Q_l is constant for both MD configurations.
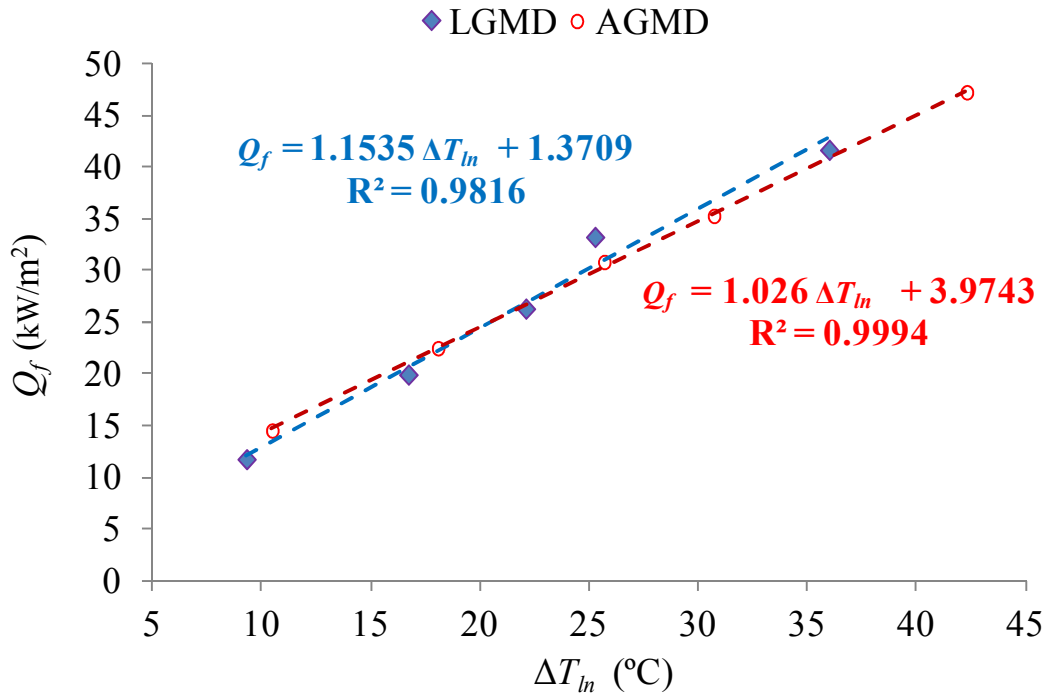
Figure 2.2.6. Heat flux in the feed membrane side (Q_f) of LGMD and AGMD configurations *versus* the logarithmic mean temperature difference (ΔT_{ln}).

In MD, the thermal efficiency (*EE*) should be as high as possible or which is the same Q_c should be as low as possible. The heat fluxes Q_v and Q_m were calculated at different feed inlet temperatures from Eqs. (2.2.1) and (2.2.2), respectively. Then, Q_c, *EE* and *HL* were determined for both LGMD and AGMD using Eqs. (2.2.1), (2.2.9) and (2.2.10), respectively. The results are shown in Fig. 2.2.7. Compared to AGMD, the thermal efficiency is higher for LGMD, whereas the specific internal heat loss is lower. A linear increase of the thermal efficiency with the feed inlet temperature was observed for both MD configurations indicating that it is better to run both AGMD and LGMD at higher temperatures, which is mainly due to the exponentially increased mass flux with temperature enhancement. Similar *EE* and *HL* trends were reported by Khayet et al. [8] for VMD, SGMD and DCMD. From the heat transfer point of view, it is better to operate at high feed temperature than to operate at low ones.

163

In general, *EE* values in counter current MD systems are in the range 60 − 70% [1]. However, for LGMD and AGMD these values were lower (see Fig. 2.2.7). This may be attributed to the high effects of the temperature polarization in both the feed and permeate side of the membrane. By combining Eqs. (2.2.11), (2.2.12) and (2.2.13), the temperature polarization coefficient (θ) can be estimated. Then the heat transfer coefficient of both the feed and permeate boundary layers (h) can be determined from Eq. (2.2.8). On the other hand, the heat transfer coefficient of the feed boundary layer (h_f) can be calculated from Eq. (2.2.6) and finally the heat transfer coefficient of the permeate boundary layer (h_p) can be determined. The *Re* number of the feed side ranges from 887.6 to 2085.5 indicating the laminar feed flow regime. The calculated θ values for both MD configurations are reported in Fig. 2.2.8 and the heat transfer coefficients are summarized in Table 2.2.2 for different feed inlet temperatures.

Similar to other MD configurations, θ decreases with the increase of the feed temperature for both LGMD and AGMD. However, the temperature polarization effect is greater for AGMD than for LGMD. This is attributed mainly to the contribution of the permeate boundary layer. A slight enhancement was observed for h_f because of the increase of the feed temperature. However, a significant decrease of h_p was detected in both LGMD and AGMD with the increase of the feed temperature. However, in all cases h_p is smaller for AGMD because of the lower thermal conductivity of the air compared to that of water. Francis et al. [7] also reported that the used distilled water and sand in the air gap enhanced the heat transfer.
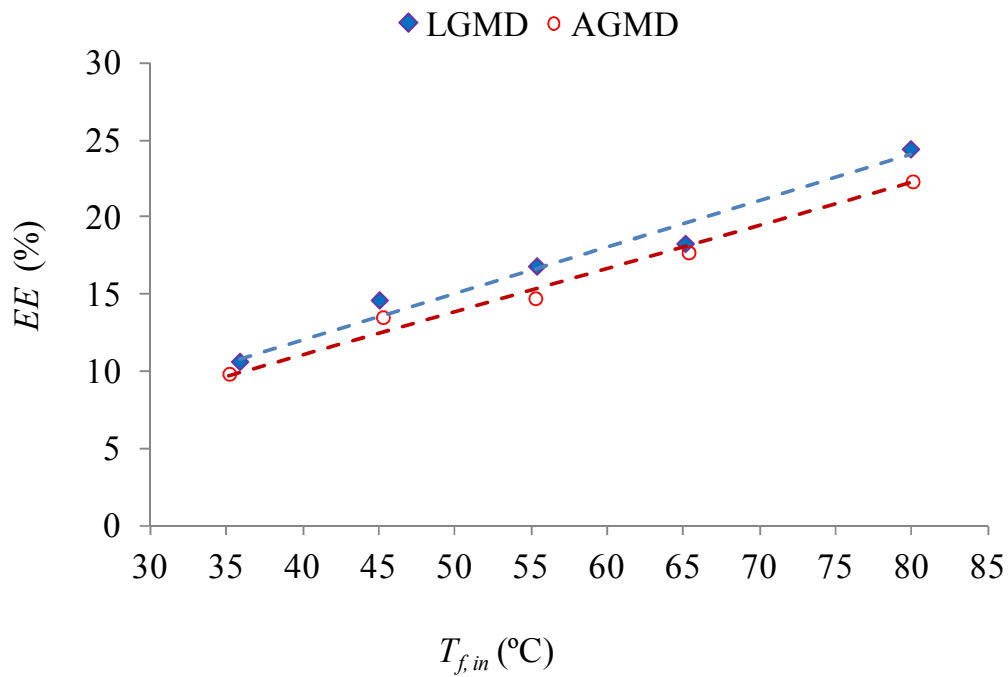
(a)
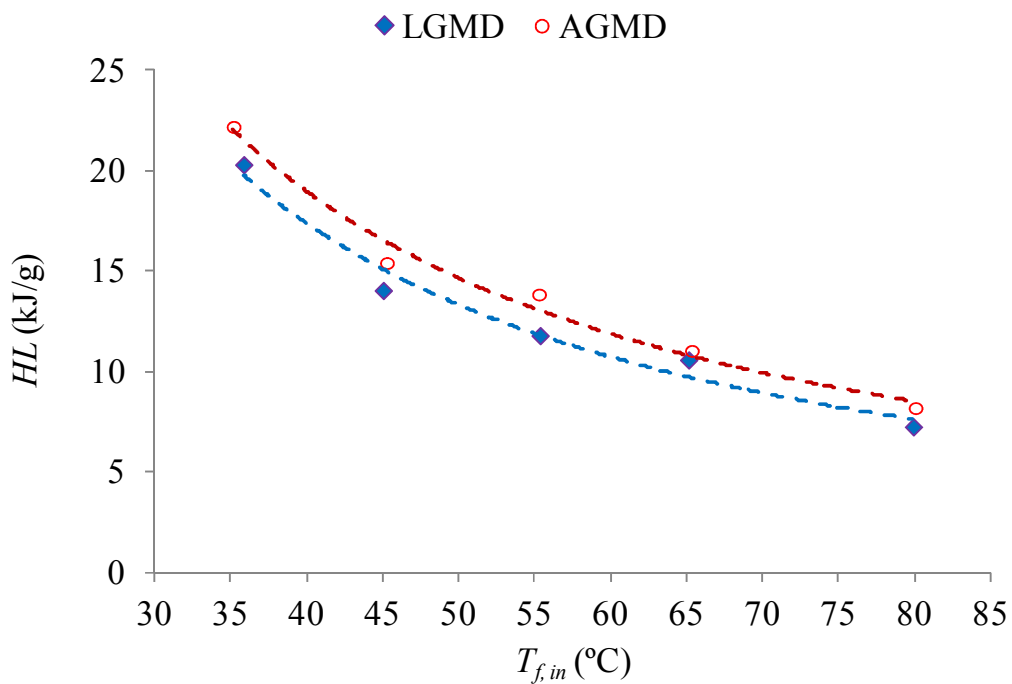
(b)

Figure 2.2.7. Thermal efficiency (*EE*) and specific internal heat loss (*HL*) through the composite hydrophobic/hydrophilic membrane using in LGMD and AGMD as a function of the feed inlet temperature ($T_{f,in}$).
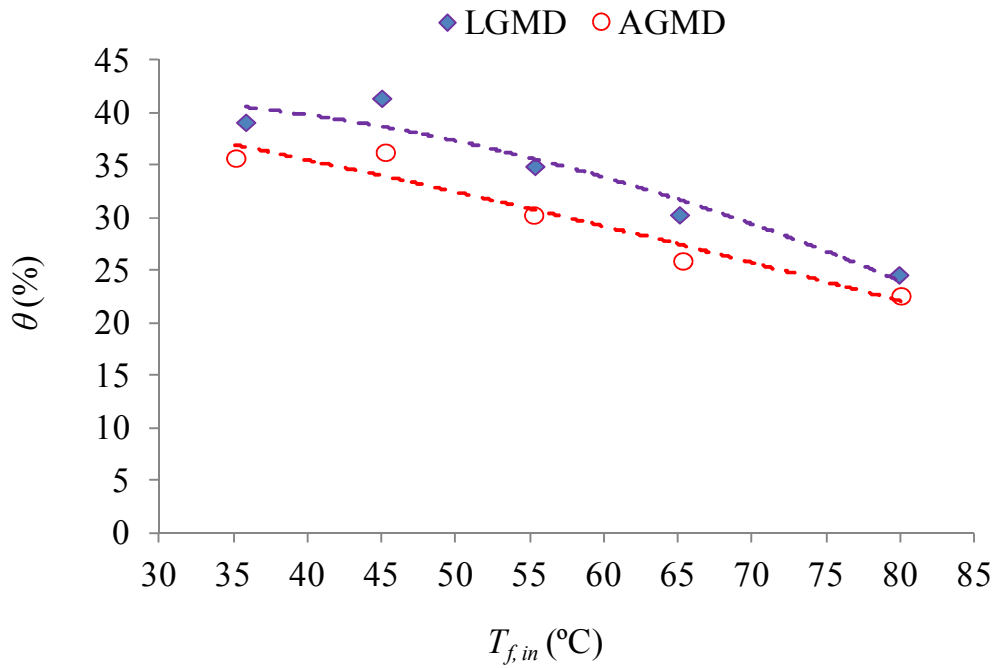
Figure 2.2.8. Temperature polarization coefficient (θ) as a function of the feed inlet temperature ($T_{f,in}$) for both LGMD and AGMD configurations.

Table 2.2.2. Heat transfer coefficients of the feed and permeate boundary layers of the LGMD and AGMD configurations for different feed inlet temperatures.

LGMD				AGMD			
$T_{f,in}$ (ºC)	h_f (W/m².K)	h (W/m².K)	h_P (W/m².K)	$T_{f,in}$ (ºC)	h_f (W/m².K)	h (W/m².K)	h_P (W/m².K)
35.8	1049.7	742.8	2540.4	35.2	1047.3	572.1	1260.7
45.0	1078.3	817.3	3376.3	45.3	1078.8	586.0	1282.7
55.3	1105.6	620.7	1415.3	55.3	1105.2	447.6	752.3
65.1	1121.1	503.1	912.6	65.3	1121.2	360.6	531.6
79.9	1116.2	377.5	570.3	80.0	1116.2	300.9	412.0

2.2.4.3. Feed concentration effects on AGMD and LGMD performances

Desalination by LGMD and AGMD was performed using the porous composite hydrophobic/hydrophilic membrane and two feed NaCl aqueous solutions (12 g/L and 30 g/L). The results are reported in Figs. 2.2.9 and 2.2.10 at different feed inlet temperatures for LGMD and AGMD, respectively.

Similar to distilled water used as feed, exponential trends between the permeate flux of the composite porous hydrophobic/hydrophilic membrane and the feed inlet temperature were observed for different saline solutions. As it was expected, the permeate flux of both MD configurations is decreased with the increase of the salt concentration in the aqueous feed solution. This is due to the decrease of the water vapor pressure and the contribution of the concentration polarization effect. Reasonably high rejection factors (i.e. 99.81 $>\alpha>$ 99.61%) were obtained for both MD configurations. The NaCl rejection factors were almost similar for both MD variants and for the two NaCl concentrations.

The concentration polarization coefficient (β) was evaluated using Eqs. (2.2.14), (2.2.15) and (2.2.16). The mean value of $C_{b,f}$ was considered because this increases through the module length. The results are presented in Fig. 2.2.11. For both AGMD and LGMD configurations, β increases with the feed inlet temperature and decreased slightly with the increase of the feed concentration. Lawson and Lloyd [22] and Essalhi and Khayet [20] also observed an enhancement of β with the feed temperature. Compared to the LGMD configuration, the AGMD exhibited slightly smaller β values due to its lower permeate fluxes. β values as high as 1.6 were reported for electrospun nanofibrous membranes (ENMs) with high permeate fluxes. In this study, the highest β value was 1.36 for LGMD. Taking into account that the feed flow regime in both LGMD and AGMD is laminar, high β values were calculated as can be seen in Fig. 2.2.11, especially at high feed inlet feed temperatures. This justifies the high decline of the permeate flux in both MD configurations.

One possible way to reduce the temperature and concentration polarization effects in both LGMD and AGMD is to increase the feed flow rate in order to establish adequate hydrodynamic conditions and work under turbulent flow regime instead of laminar one, and as consequence the

167

temperature and concentration at the feed membrane surface approach those of the bulk feed solution.
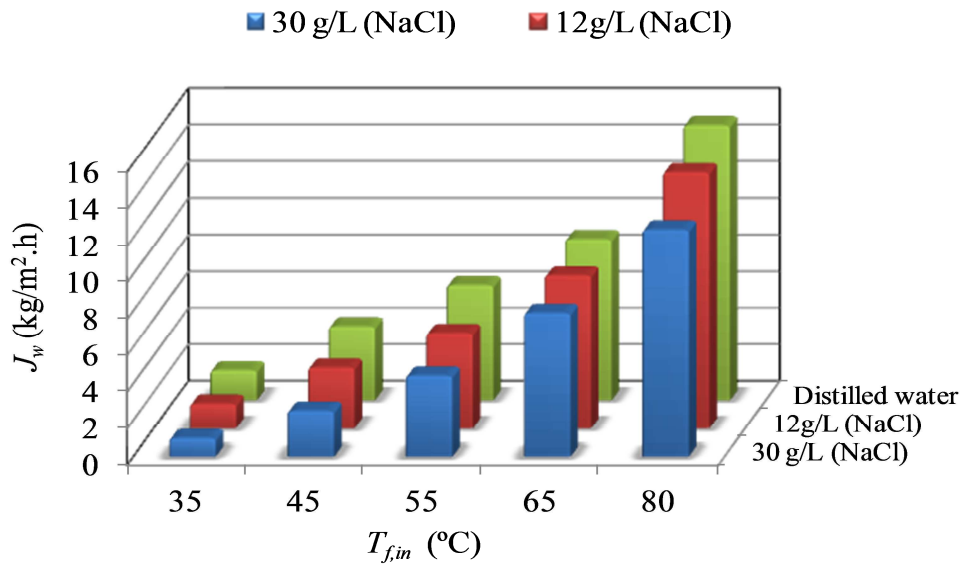
(a)
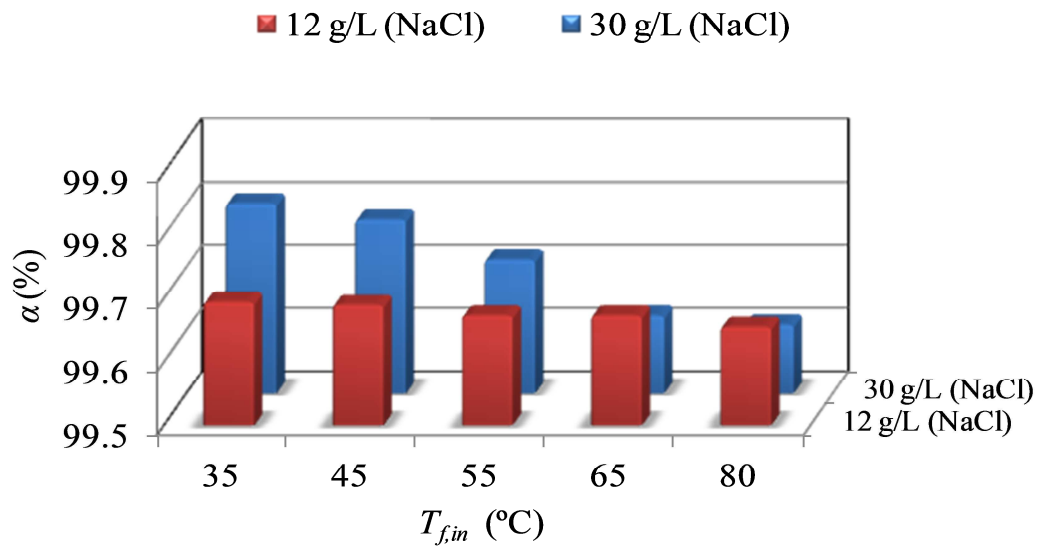
(b)

Figure 2.2.9. LGMD permeate flux (J_w) (a) and NaCl rejection factor ($\alpha=100\ (1-C_p/C_f)$) (b) of the porous composite hydrophobic/hydrophilic membrane used at different feed inlet temperatures ($T_{f,in}$) and feed concentrations ($C_{b,f}$).
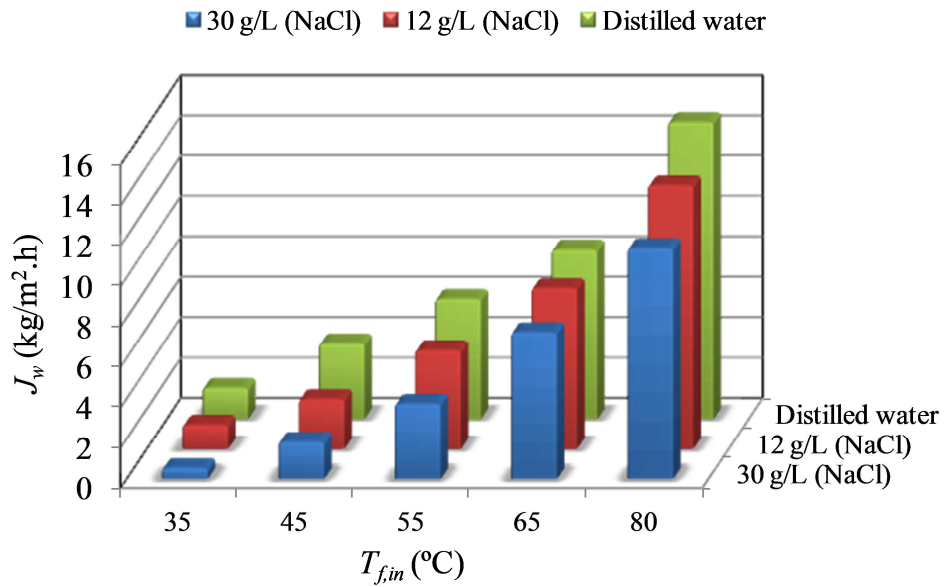
(a)
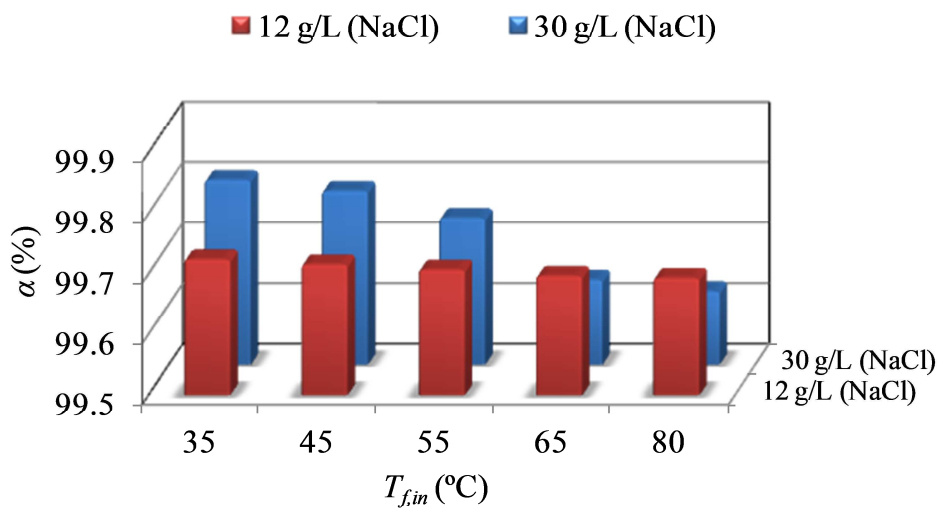
(b)

Figure 2.2.10. AGMD permeate flux (J_w) (a) and NaCl rejection factor ($\alpha=100\,(1-C_p/C_f)$) (b) of the porous composite hydrophobic/hydrophilic membrane used at different feed inlet temperatures ($T_{f,in}$) and feed NaCl concentrations ($C_{b,f}$).

170
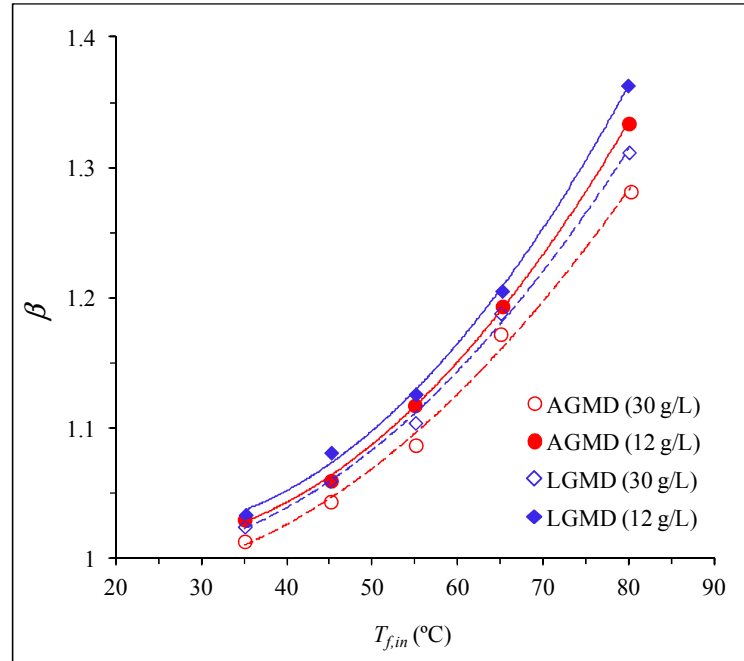
Figure 2.2.11. Concentration polarization coefficient (β) of the porous composite hydrophobic/hydrophilic membrane used in LAGMD and AGMD at different feed inlet temperatures ($T_{f,in}$) and feed NaCl concentrations ($C_{b,f}$).

2.2.5. Conclusions

A comparative MD study was carried out using a porous composite hydrophobic/hydrophilic membrane in LGMD and AGMD configurations under the same operation conditions. In LGMD, a stagnant water layer replaces the stagnant air gap established between the membrane and the condensing surface in AGMD set-up. This type of membrane is more suitable for desalination by LGMD than for AGMD.

Compared to AGMD, the permeate flux is slightly higher (2.2 – 6.5 %) for the LGMD configuration due to: i)- the higher thermal conductivity of water compared to that of air resulting in a lower permeate temperature at the permeate side of the membrane and a higher transmembrane driving force, and ii)- the small established distance between the liquid/vapor interfaces at both side of the hydrophobic thin top-layer of the membrane because water penetrates inside the hydrophilic layer of the membrane.

The overall heat transfer coefficient (H) was found to be higher for LGMD. However, in all cases the heat transfer coefficient of the permeate (h_p) was smaller for AGMD because of the lower thermal conductivity of air compared to that of water.

Compared to AGMD, the thermal efficiency (EE) is higher for LGMD, whereas the specific internal heat loss (HL) is lower.

Both MD configurations exhibited a linear increase of the thermal efficiency with the feed inlet temperature indicating that it is advisable to operate under higher feed temperatures.

The temperature polarization effect is greater for AGMD than for LGMD due mainly to the contribution of the thermal boundary layer of the permeate side. On the contrary, the concentration polarization effect is slightly higher for LGMD due mainly to its higher permeate flux.

The permeate flux of both MD configurations decreased with the increase of the salt concentration in the aqueous feed solution due to the decrease of the water vapor pressure and the contribution of the concentration polarization effect.

Reasonably high rejection factors (i.e. 99.81 $> \alpha >$ 99.61%) were obtained for both MD configurations. The salt rejection factors were almost similar for both MD variants.

For both AGMD and LGMD configurations, β increases with the feed inlet temperature and decreased slightly with the increase of the feed concentration.

Taking into account that the LGMD and AGMD studies were carried out under laminar feed flow regime ($887.6 < Re < 2085.5$), the effects of the temperature and concentration polarization can be reduced enhancing the feed flow rate.

The LGMD proved to be more attractive than AGMD for desalination when using bi-layered hydrophobic/hydrophilic membranes because of the obtained higher permeate flux and thermal efficiency of the LGMD and its lower specific internal heat loss.

Further studies should be carried out investigating the effects of the gap widths in LGMD configuration. Francis et al. [7] observed an increase of the water production rate with the increase of the water gap width from 9 mm to 13 mm. However, it is well known that in AGMD an opposite trend is generally observed (i.e. the water production rate increases with the decrease of the air gap width).

Nomenclature

Symbols

A_m	membrane area (m^2)
B	membrane permeability in Eq. (11) (kg/m^2.s.Pa)
B_g	gas permeance in Eq. (3.2.18) (mol/m^2.s.Pa)
C	salt concentration (g/L)
c_p	specific heat (kJ/kg.ºC)
d_p	mean pore size (nm)
D	diffusion coefficient (m/s)
d_e	equivalent diameter of the feed flow channel (m)
EE	thermal efficiency (%)
h	heat transfer coefficient (W/m^2.K)
H	overall heat transfer coefficient (W/m^2.K)
HL	specific internal heat loss (kJ/g)
I	intercept in Eq. (3.2.18)
J_w	permeate flux (kg/m^2.h)
k	thermal conductivity (W/m.K)
k_s	mass transfer coefficient (m/s)
L	module length (m)
L_p	effective pore length of the membrane (μm)
LEP	liquid entry pressure of water (Pa)
Nu	Nusselt number
$\dot{m}_f$	feed flow rate (kg/h)
M	molecular weight (g/mol)
p	partial pressure (Pa)
P_m	mean hydrostatic pressure within the membrane in Eq. (3.2.18) (Pa)
Pr	Prandtl number
Q	heat flux (W/m^2)
r_p	pore radius (nm)
R	gas constant (J/mol.K)
S	slope in Eq. (3.2.18)
T	temperature (ºC)
x	mole fraction
Sc	Schmidt number
Sh	Sherwood number
Re	Reynolds number

Greek letters

β	concentration polarization coefficient
δ	total membrane thickness (μm)
δ_h	hydrophobic layer thickness (μm)
ε/L_p	effective porosity (m^{-1})
ε	void volume fraction (%)
λ	mean free path (nm)
μ	dynamic viscosity (kg/m.s)
θ	temperature polarization coefficient (%)
θ_a	water contact angle (°)
ρ_w	water density (kg/m^3)
ΔH_v	latent heat of vaporization (kJ/kg)
ΔT_{ln}	logarithmic mean temperature difference (K)
ΔT_1	temperature difference between feed and permeate at the inlet of the membrane module
ΔT_2	temperature difference between feed and permeate at the outlet of the membrane module
Δp	vapor pressure difference (Pa)
Δp_{ln}	logarithmic mean vapor pressure of water difference (Pa)
γ	activity coefficient
ψ	vapor pressure polarization coefficient (%).

Subscripts

b	bulk
c	conduction
f	feed
g	gas
in	inlet of the membrane module
l	heat lost
m	membrane
NaCl	sodium chloride
out	outlet of the membrane module
p	permeate or pore
v	vapor
w	water

Superscripts

0	pure water

References

[1] M. Khayet, T. Matsuura, Membrane Distillation: Principles and Applications, Elsevier, The Netherlands, 2011.

[2] V.V. Ugrozov, I.B. Elkina, V.N. Nikulin, L.I. Kataeva, Theoretical and experimental research of liquid-gap membrane distillation process in membrane module, Desalination, 157 (2003) 325-331

[3] C.A. Rvier, M.C. García-Payo, I.W. Marison, U.V. Stockar, Separation of binary mixtures by thermostatic sweeping gas membrane distillation: I. Theory and simulations, J. Membr. Sci., 201 (2002) 1-16.

[4] M.C. García-Payo, C.A. Rvier, I.W. Marison, U.V. Stockar, Separation of binary mixtures by thermostatic sweeping gas membrane distillation: II. Experimental results with aqueous formic acid solutions, J. Membr. Sci., 198 (2002) 197-210.

[5] D. Winter, J. Koschikowski, M. Wieghaus, Desalination using membrane distillation: Experimetnal studies of full scale spiral wound modules, J. Membr. Sci., 375 (2011) 104-112.

[6] A. Cipollina, M.G. Di Sparti, A. Tamburini, G. Micale, Development of a membrane distillation module for solar energy seawater desalination, Chem. Eng. Res. & Design, 90 (2012) 2101-2121.

[7] L. Francis, N. Ghaffour, A.A. Alsaadi, G.L. Amy, Material gap membrane distillation: A new design for water, J. Membr. Sci., 448 (2013) 240-247.

[8] M. Khayet, M.P. Godino, J.I. Mengual, Possibility of nuclear desalination through various membrane distillation configurations: a comparative study, Int. J. Nuclear Desalination, 1 (2003) 30-46.

[9] S. Cerneaux, I. Struzynska, W.M. Kujawski, M. Persin, A. Larbot, Comparison of various membrane distillation methods for desalination using hydrophobic ceramic membranes, J. Membr. Sci., 337 (2009) 55-60.

[10] M. Essalhi, M. Khayet, Surface segregation of fluorinated modifying macromolecule for hydrophobic/hydrophilic membrane preparation and application in air gap and direct contact membrane distillation, J. Membr. Sci., 417-418 (2012) 163-173.

[11] M. Khayet, Solar desalination by membrane distillation: Dispersion in energy consumption analysis and water production costs (a review), Desalination, 308 (2013) 89-101.

[12] M. Khayet, J.I. Mengual, T. Matsuura, Porous hydrophobic/hydrophilic composite membranes: Application in desalination using direct contact membrane distillation, J. Membr. Sci., 252 (2005) 101–113.

[13] M. Khayet, T. Matsuura, J.I. Mengual, Porous hydrophobic/hydrophilic composite membranes: Estimation of the hydrophobic-layer thickness, J. Membr. Sci., 266 (2005) 68–79.

[14] M. Qtaishat, M. Khayet, T. Matsuura, Novel porous composite hydrophobic/hydrophilic polysulfone membranes for desalination by direct contact membrane distillation, J. Membr. Sci., 341 (2009) 139–148.

[15] M. Qtaishat, D. Rana, M. Khayet, T. Matsuura, Preparation and characterization of novel hydrophobic/hydrophilic polyetherimide composite membranes for desalination by direct contact membrane distillation, J. Membr. Sci., 327 (2009) 264–273.

[16] M. Essalhi, M. Khayet, Self-sustained webs of polyvinylidene fluoride electrospun nanofibers at different electrospinning times: 1. Desalination by direct contact membrane distillation, J. Membr. Sci., 433(2013) 167-179.

[17] M. Khayet, T. Matsuura, Preparation and characterization of polyvinylidene fluoride membranes for membrane distillation, Ind. Eng. Chem. Res., 40 (2001) 5710-5718.

[18] M. Khayet, Membranes and theoretical modeling of membrane distillation: a review, Adv. Colloid Interface Sci., 164(1-2) (2011) 56-88.

[19] K.W. Lawson, D.R. Lloyd, Review: membrane distillation, J. Membr. Sci. 124 (1997) 1 - 25.

[20] M. Khayet, M. Essalhi, Self-sustained webs of polyvinylidene fluoride electrospun nanofibers at different electrospinning times: 2. Theoretical analysis, J. Membr. Sci., 433 (2013) 180-191.

[21] M. Khayet, C.Y. Feng, T. Matsuura, Morphological study of fluorinated asymmetric polyethermide ultrafiltration membranes by surface modifying macromolecules, J. Membr. Sci., 213 (2003) 159-180.

[22] K.W. Lawson, D.R. Lloyd, Membrane distillation: II. Direct contact MD, J. Membr. Sci., 120 (1996) 123-133.

CHAPTER 3

HOLLOW FIBER MEMBRANES

FOR DESALINATION

BY MEMBRANE DISTILLATION (MD)

3.1. Preparation and characterization of PVDF-HFP copolymer hollow fiber membranes for membrane distillation

Contents:

3.1.1. Introduction

3.1.2. Experimental

      3.1.2.1. Materials

      3.1.2.2. Preparation of hollow fibers and characterization

3.1.3. Results and discussions

3.1.4. Conclusions

References

Abstract:

Poly(vinylidene fluoride-hexafluoropropylene) (PVDF-HFP) hollow fiber membranes were prepared by the dry/wet spinning technique at different copolymer concentrations from 17 wt% to 24 wt%. All the spinning parameters were kept constant except the copolymer concentration. The temperature of both the internal and external coagulants was maintained at 40ºC. The effects of the copolymer concentration on the morphological properties of the hollow fibers were studied in terms of external and internal diameter and scanning electron microscopy (SEM). It was found that the thickness of all tested hollow fibers did not change significantly. An evolution of the cross-section structure with the increase of the copolymer concentration was detected. The cross section of the hollow fiber prepared with the lowest copolymer concentration exhibited a *finger-like* structure in both the external and internal layers disappearing in the internal layer as the copolymer concentration increases. Finally, a *sponge-like* structure is formed through all cross section of the hollow fiber prepared with the highest concentration. This may be explained based on the decrease of the coagulation rate with the increase of the copolymer concentration in the dope solution.

3.1.1. Introduction

Poly(vinylidene fluoride-*co*-hexafluoropropylene) (PVDF-HFP) is a copolymer which has recently attracted attention as a potential membrane material. PVDF-HFP presents lower crystallinity and higher free volume compared to poly(vinylidene fluoride) (PVDF) homopolymer, due to the incorporation of an amorphous phase of HFP into the main constituent VDF blocks. The fluorine content also increases due to the addition of HFP group, which makes PVDF-HFP more hydrophobic than PVDF [1]. Therefore, PVDF-HFP is a potential candidate for some applications where the hydrophobicity of the membrane material is required like in membrane distillation [2,3].

Nowadays hollow fiber configuration is one of the most interesting membrane geometry in most separation applications because of its high surface area per unit volume, flexibility in operation, mechanically self-supporting, etc. [4]. Most of the PVDF-HFP membrane preparation studies reported in the literature were conducted for flat-sheet membranes. Recently, Shi et al. [5,6] studied the effects of the additives polyvinylpyrrolidone (PVP), lithium chloride (LiCl) and glycerol on the asymmetric structures of microporous hollow fiber PVDF-HFP hollow fiber membranes.

In the present study, PVDF-HFP hollow fibers have been prepared using the dry/wet spinning technique with different copolymer concentrations. The effects of the copolymer concentration on the cross section structure of the hollow fibers were studied using scanning electron microscopy (SEM).

3.1.2. Experimental

3.1.2.1. Materials

Poly(vinylidene fluoride-*co*-hexafluoropropylene) (PVDF-HFP) was purchased from Sigma-Aldrich Chemical Co. Reagent grade *N,N*-dimethyl acetamide (DMAC) was used as a solvent and poly(ethylene glycol) (PEG, M_w = 6000) was employed as a non-solvent additive (NSA). All chemicals were also obtained from Sigma-Aldrich Chemical Co. and used without further purification.

3.1.2.2. Preparation of hollow fibers and characterization

The solvent DMAC was first mixed with the non-solvent additive PEG at 3 wt.%. PVDF-HFP was added to the mixture and the polymer solution was agitated at 42 ºC for about 24 h until the copolymer was totally dissolved. Prior to spinning, the copolymer solution was degassed in an ultrasonic bath for 15 min. A series of PVDF-HFP/DMAC/PEG dope solutions with the copolymer concentration ranging from 17 to 24 wt.% (17, 19, 20, 22 and 24 wt.%) were prepared.

The dry/wet spinning technique was employed for preparation of the hollow fibers as described elsewhere [4]. The spinneret used has 0.7 mm inner diameter and 1 mm outer diameter. In this study, tap water was used as external coagulant while distilled water was used as internal coagulant (bore liquid). Both the bore liquid and the external coagulant were maintained at 40ºC by using a thermostat (Techne, TU-16D). A peristaltic pump was employed for the circulation of the bore liquid at a flow rate of 19 ml/min. The polymer solution was loaded into the spinning dope tank and forced to the

spinneret using pressurized nitrogen. The extrusion pressure of the copolymer solution was maintained at 50 kPa. The ratio of dope flow rate to bore fluid rate was constant for all spinning process. The gas gap distance was 27.5 cm and the take-up speed was 18 rpm (i.e. 9.18 m/min). After spinning, the fabricated hollow fibers were stored in a water bath at room temperature for at least 24 h to remove the residual solvent DMAC. Subsequently, the hollow fibers were dried in air at room temperature before characterization tests.

The inner and outer diameters of the fibers were measured by means of an optical microscope (OLYMPUS BX60M) with a precision of ± 1 μm. More than 6 hollow fiber samples and at least 20 measurements were conducted for each sample.

The cross-section of the PVDF-HFP hollow fibers was examined by a field emission scanning electron microscope (FESEM, JEOL Model JSM-6330F). PVDF-HFP hollow fiber samples were fractured in liquid nitrogen and then sputter-coated with a thin layer of gold. The SEM pictures were taken over different regions of the cross-section of each hollow fiber sample.

3.1.3. Results and discussions

The inner and outer diameters of all prepared PVDF-HFP hollow fibers were determined. An increase of about 30 % of both diameters was observed with increasing the copolymer concentration in the dope solution (i.e the external diameter for the hollow fiber prepared with 17 wt % copolymer concentration is 1635 ± 37 μm whereas that of the hollow fiber prepared with 24 wt % is 2099 ± 26 μm). It was found that the inner diameters range from 1525 μm to 1989 μm. It was also observed that the thickness

of all tested hollow fibers did not change significantly if the experimental errors are considered and the calculated mean thickness value was 80 ± 25 μm.

The void volume fraction or porosity of each hollow fiber was also determined. The void volume fraction is related to the ratio between the membrane density and the copolymer density as described previously in [7]. It is known that this parameter affects considerably the MD permeability of the hollow fibers. In fact, the transmembrane permeate flux is higher at higher porosity. The void volume fraction of the hollow fiber membranes prepared from a copolymer concentration of 17, 19, 20, 22 and 24 wt% was 0.76, 0.72, 0.71, 0.70 and 0.60 %, respectively. Therefore, it is expected that the MD performance will be better for the hollow fiber prepared with smaller copolymer concentration. In fact, only a slight decrease of the void volume fraction was detected with increasing the copolymer concentration and the pore size will also affect MD performance of these hollow fibers.

As stated earlier, a study of the cross-section structure was carried out by means of SEM analysis. The evolution of the cross-section structure with increasing the copolymer concentration is shown in Fig. 3.1.1. It can be seen that the cross-section of the hollow fiber prepared with the lowest copolymer concentration (17 wt%, Fig.3.1.1A) exhibits a *finger-like* structure in both the external and internal layers. As the copolymer concentration increases from 17 wt% to 19 wt%, the *finger-like* structure of the internal layer starts first to disappear as can be seen in Fig. 3.1.1B. This structure is absent in Fig. 3.1.1C corresponding to the hollow fiber prepared with 20 wt%. Furthermore, the *finger-like* structure of the external layer is not detected for the hollow fibers prepared with 20 wt% (Fig. 3.1.1D) and 24 wt% (Fig. 3.1.1E). Instead a *sponge-like* structure is formed through the whole cross-section of the hollow fibers prepared with higher copolymer concentration. This may be attributed to the decrease of the

coagulation rate of the copolymer PVDF-HFP with the increase of the copolymer concentration. Sponge-like structure is more favored for slow coagulation rate [8]. In hollow fiber spinning, coagulation starts from the internal surface of the nascent hollow fiber and solvent evaporation (i.e. DMAC) start from the outer surface of the nascent hollow fiber through the air gap distance until reaching the external coagulation bath. This explains that the internal layer starts first to disappear with increasing the copolymer concentration.

If one considers both membrane morphology and void volume fraction values, it is expected that the MD permeate flux will decrease with increasing the copolymer concentration.
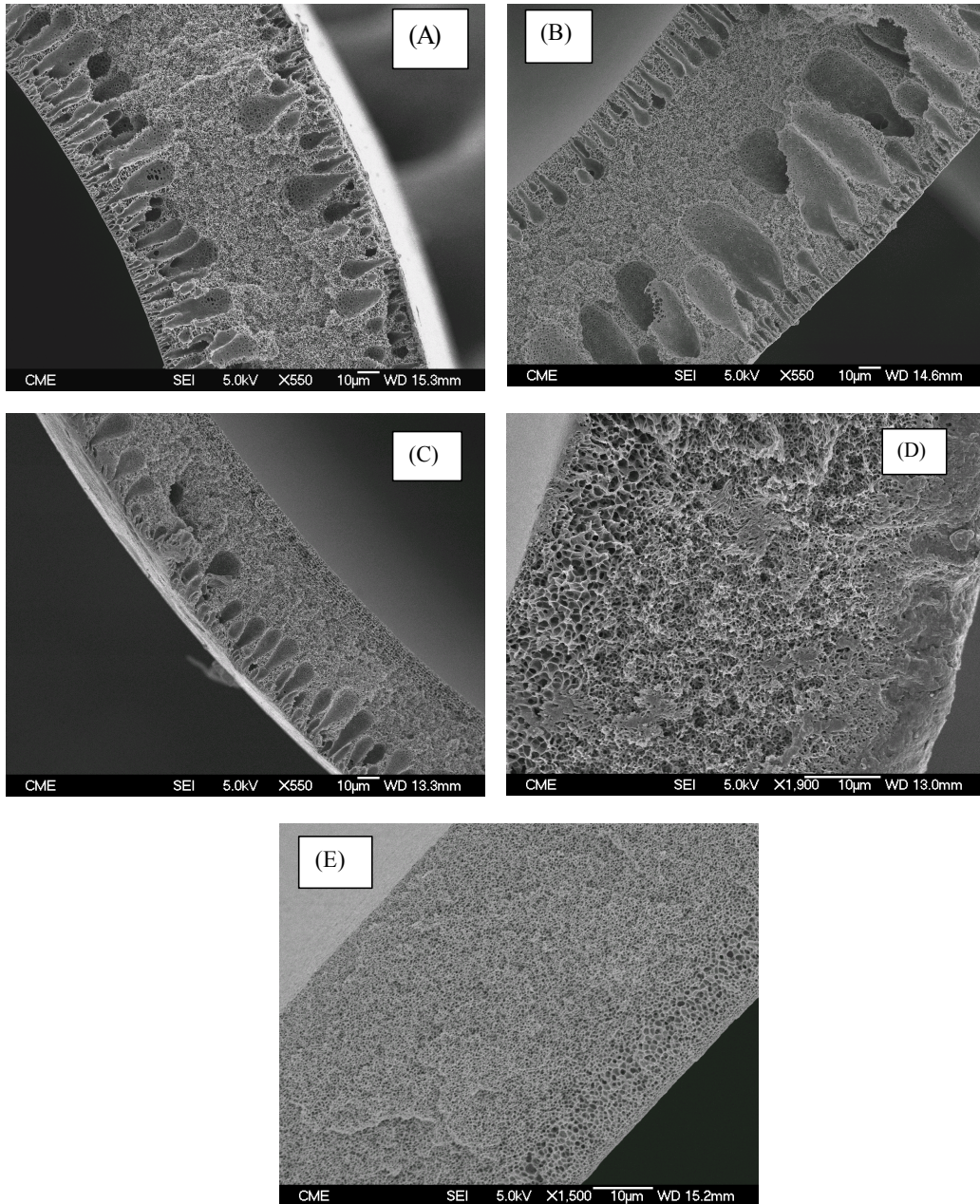
Figure 3.1.1. Cross-section morphology of hollow fibers prepared with different PVDF-HFP copolymer concentrations: (A) 17 wt%, (B) 19 wt%, (C) 20 wt%, (D) 22 wt% and (E) 24 wt%.

3.1.4. Conclusions

The change of the PVDF-HFP copolymer concentration of the dope solution does not affect the thickness of the prepared PVDF-HFP hollow fibers. On the contrary, a slight decrease of the void volume fraction was detected with increasing the PVDF-HFP concentration.

There is an evolution of the cross-section structure with the increase of the PVDF-HFP concentration from a *finger-like* structure in both the external and the internal layers for the lowest concentration (i.e. 17 wt%) to a *sponge-like* structure through the whole cross-section of the hollow fiber prepared with the highest concentration (24 wt%). This structural change may be due to the decrease of the coagulation rate of the PVDF-HFP copolymer at 40ºC with the increase of the copolymer concentration.

References

[1] C. Feng, R. Wang, B. Shi, G. Li, Y. Wu, Factors affecting pore structure and performance of poly(vinylidene fluoride-co-hexafluoropropylene) asymmetric porous membrane, J. Membr. Sci. 277 (2006) 55-64.

[2] M.S. El-Bourawi, Z. Ding, R. Ma, M. Khayet, A framework for better understanding membrane distillation separation process, J. Membr. Sci. 285 (2006) 4-29.

[3] M. Khayet, T. Matsuura, Application of surface modifying macromolecules for the preparation of membranes for membrane distillation, Desalination 158 (2003) 51-56.

[4] M. Khayet, The effects of air gap length on the internal and external morphology of hollow fiber membranes, Chem. Eng. Sc. 58 (2003) 3091-3104.

[5] L. Shi, R. Wang, Y. Cao, C. Feng, D.T. Liang, J.H. Tay, Fabrication of poly(vinylidene fluoride-co-hexafluoropropylene) (PVDF-HFP) asymmetric microporous hollow fiber membranes, J. Membr. Sci. 305 (2007) 215-225.

[6] L. Shi, R. Wang, Y. Cao, D.T. Liang, J.H. Tay, Effect of additives on the fabrication of poly(vinylidene fluoride-co-hexafluropropylene) (PVDF-HFP) asymmetric microporous hollow fiber membranes, J. Membr. Sci. 315 (2008) 195-204.

[7] M.A. Izquierdo-Gil, M.C. García-Payo, C. Fernández-Pineda, Direct contact membrane distillation of sugar aqueous solutions, Sep. Sci. Technol. 34 (1999) 1773-1801.

[8] K.C. Khulbe, C.Y. Feng, F. Hamad, T. Matsuura, M. Khayet, Structural and performance study of micro porous polyetherimide hollow fiber membranes prepared at different air gap, J. Membr. Sci. 245 (2004) 191-198.

3.2. Effects of PVDF-HFP Concentration on Membrane Distillation Performance and Structural Morphology of Hollow Fiber Membranes

Contents:

3.2.1. Introduction

3.2.2. Experimental

    3.2.2.1. Materials

    3.2.2.2. Preparation of hollow fiber membranes and characterization

3.2.3. Results and discussions

    3.2.3.1. Cross-sectional study by scanning electron microscopy

    3.2.3.2. Void volume fraction study

    3.2.3.3. Surface morphology study by atomic force microscopy

    3.2.3.4. Liquid entry pressure and DCMD experiments

3.2.4. Conclusions

References

Abstract:

Poly(vinylidene fluoride-hexafluoropropylene), PVDF-HFP, hollow fiber membranes were prepared by the dry/wet spinning technique using different copolymer concentrations in the dope solutions ranging from 17 wt.% to 24 wt.%. All the spinning parameters were maintained constant except the copolymer concentration. The morphological properties of the hollow fiber membranes were studied in terms of scanning electron microscopy (SEM), atomic force microscopy (AFM) and void volume fraction. The effects of PVDF-HFP content in the spinning solutions were also studied by measuring the water entry pressure and direct contact membrane distillation (DCMD) permeate flux of the hollow fiber membranes. An increase in the copolymer concentration of the spinning solution resulted in a decrease in the precipitation rate and a transition of the cross-section structure from a finger-type structure to a sponge-type structure. Pore size, nodule size and roughness parameters of both the internal and external hollow fiber surfaces were determined by AFM. It was observed that the pore size decreased in both the internal and external surfaces of the hollow fiber membranes with increasing the copolymer concentration and reached a minimum value at the outer surface for PVDF-HFP concentrations greater than 20 wt.%. Water entry pressure values were decreased whereas both the void volume fraction and the DCMD permeate flux increased with decreasing the copolymer concentration.

195

3.2.1. Introduction

Membrane distillation (MD) is one of the non-isothermal separation processes using porous hydrophobic membranes. The MD driving force is supplied by the vapour pressure difference resulting from either a temperature difference between both membrane sides or by applying vacuum in the permeate side [1,2]. Most of MD applications have been performed for the concentration of non-volatile solutes in aqueous solutions such as salts, sugar, fruit juices, macromolecules, colloids, etc. [1-6]. Furthermore, MD demonstrated also to have considerable potential for separation of volatile organic components such as alcohols, acids, etc. [7-10]. In addition, the lower operating temperatures required in MD permit this process to use waste heat or renewable energy sources such as solar energy.

In MD commercial hydrophobic microfiltration and ultrafiltration membranes have been generally used. These membranes do not necessarily fulfill all the characteristics needed for an adequate membrane to be used in MD. A MD membrane should exhibit a high bulk and surface porosities, optimum pore size and narrow pore size distribution, high pores interconnectivity, high hydrophobicity, high liquid entry pressure, low thermal conductivity, optimum thickness, high thermal stability, less susceptible to fouling and long term permeance stability [1,11-13].

Recently, various research studies have been focused on the fabrication of both flat-sheet and hollow fiber membranes specifically for MD process [14-16]. Among the various hydrophobic polymers used polyvinylidene fluoride (PVDF) is the most considered material, for preparation of non-solvent induced phase inversion (NIPS) membranes (i.e. immersion precipitation), because of its excellent chemical and thermal resistances and it can be dissolved in common organic solvents at low temperatures lower than 60 ºC [17,18].

The copolymer poly(vinylidene fluoride-*co*-hexafluoropropylene) (PVDF-HFP) appeared to be a highly promising material for membrane preparation by NIPS technique for various membrane processes [19-22]. Compared to PVDF, the copolymer PVDF-HFP is more hydrophobic, presents higher solubility, lower crystallinity, smaller glass transition temperature and greater free volume due to the incorporation of an amorphous phase of fluoropropylene (HFP) into the main constituent vinylidene fluoride (VDF) blocks [19-21].

196

The fluorine content also increases due to the addition of HFP group, which makes PVDF-HFP more hydrophobic than PVDF.

It is worthy to mention that most of the PVDF-HFP membrane preparation studies reported in the literature were conducted for flat-sheet membranes used in polymer battery technology [19-25]. Cao et al. [22] used dibutyl phthalate (DBP), polyvinylpyrrolidone (PVP) and polyethylene glycol (PEG) as additives for preparation of PVDF-HFP membranes and observed that the membranes prepared with DBP and PEG exhibited asymmetric structure and relatively small pore sizes; whereas nearly symmetric and microporous structure were observed when PVP was used as additive. The additive PEG was also used by Hwang et al. [23] and found that the morphology of the PVDF-HFP membranes changed considerably with the composition of the polymer and solvent. Feng et al. [26] reported on the preparation of PVDF-HFP flat-sheet asymmetric membranes for DCMD process and studied the effects on pore structure and permeate performance of different factors such as PEG molecular weight, type of additive (i.e. PEG or glycerol, trimethyl phosphate), temperature of the external coagulant and its nature. Higher permeate flux were obtained for PVDF-HFP membranes compared to PVDF membranes prepared under the same operating conditions.

Different structural and morphological types of polymeric hollow fiber membranes have been fabricated by the dry/wet spinning or wet spinning techniques using different dope solutions (polymer type and concentration, additive type and concentration, solvents) as well as different spinning parameters (geometry and dimensions of the spinneret, nature and temperature of the internal and external coagulants, flow rate of the bore fluid, dope extrusion pressure, length and type of the gas gap , wind-up speed, etc.) [27-33].

Several studies have been conducted to improve the properties of PVDF hollow fiber membranes and to investigate the effects of different spinning parameters [34-38]. Wang et al. [39] fabricated PVDF hollow fiber membranes for DCMD process and observed a large increase in permeate flux using ethylene glycol as a non-solvent additive in the dope solution compared to the hollow fibers fabricated without additive.

Shi et al. [40,41] studied the effects of the additives PVP, lithium chloride (LiCl) and glycerol on the asymmetric structures of PVDF-HFP hollow fiber membranes. The thermodynamic stability of the dope solution in reaction with water was reduced by adding each additive. The addition of LiCl or glycerol into the dope solution resulted in hollow fiber membranes with narrower pore size distributions compared to the hollow fiber membrane prepared using PVP additive. Moreover, the hydrophobicity of the hollow fiber membranes was changed following the sequence, PVP > LiCl > glycerol.

In this study, hollow fiber membranes have been prepared by the dry/wet spinning technique under a temperature of 40 ºC using different PVDF-HFP concentrations. The effects of the copolymer concentration on the morphological properties of the hollow fiber membranes have been studied in terms of scanning electron microscopy (SEM), atomic force microscopy (AFM) and void volume fraction. The water entry pressure has been measured and the PVDF-HFP hollow fiber membranes prepared with different copolymer concentrations were tested in DCMD.

3.2.2. Experimental

3.2.2.1. Materials

The spinning solutions were prepared from the copolymer poly(vinylidene fluoride-co-hexafluoropropylene), (PVDF-HFP; Mw = 455 kg/mol and Mn = 110 kg/mol), the solvent N,N-dimethyl acetamide (DMAC, reagent grade) and the non-solvent additive poly(ethylene glycol) (PEG; Mw = 6000). Isopropyl alcohol (IPA) was used as a wetting liquid for the measurements of the void volume fraction. All the above cited chemicals were purchased from Sigma-Aldrich Chemical Co.

3.2.2.2. Preparation of hollow fiber membranes and characterization

The solvent DMAC was mixed first with the non-solvent additive PEG forming a homogeneous solution containing 3 wt. % PEG. A predetermined amount of PVDF-HFP was then added to the mixture and the dope solution was stirred at 42 ºC for about 24 h until the copolymer was totally dissolved. Prior to spinning, the dope solution was degassed in an ultrasonic bath for 15 min. The concentration of PVDF-HFP in the spinning solution was varied from 17 to 24 wt. % (17, 19, 20, 22 and 24 wt. %).

The dry/wet spinning technique was employed for preparation of the hollow fibers as described elsewhere [29]. The spinneret used has 0.7 mm inner diameter and 1 mm outer diameter. All spinning conditions are indicated in Table 3.2.1. After spinning, the fabricated hollow fiber membranes were stored in a water bath at room temperature for at least 24 h to remove the residual solvent DMAC. Subsequently, the hollow fiber membranes were dried at room temperature before characterization tests.

Table 3.2.1. Spinning parameters of PVDF-HFP hollow fiber membranes.

Parameter	Operating conditions
Extrusion pressure (kPa)	50
Bore fluid	Distilled water
Bore fluid flow rate (m^3/s)	3.2 10^{-7}
External coagulant	Tap water
Bore fluid and external coagulation temperature (ºC)	40
Air gap distance (cm)	27.5
Take-up speed (m/s)	0.15

The inner and outer diameters of the prepared PVDF-HFP hollow fiber membranes were measured by means of an optical microscope (OLYMPUS BX60M) with a precision of ± 1 μm. More than 6 hollow fiber samples and at least 20 measurements were conducted for each sample.

The cross-section of the PVDF-HFP hollow fibers was examined by a field emission scanning electron microscope (FESEM, JEOL Model JSM-6330F). The sample was first fractured in liquid nitrogen and then sputter-coated with a thin layer of gold. The SEM images were taken at different cross-sectional regions of each hollow fiber sample.

The void volume fraction (i.e. porosity) of the PVDF-HFP hollow fiber membranes was determined following the method described in previous studies [4,15]. In this study the void volume fraction measurement was carried out using three different samples for each hollow fiber membrane. A fourth sample was measured when there was a dispersion of the results higher than 10%.

Both the internal and external surfaces of the PVDF-HFP hollow fibers were studied by atomic force microscopy (AFM). The images were obtained over different areas of each hollow fiber membrane using a tapping mode Nanoscope III equipped with 1553D scanner (Digital Instruments Inc., Santa Barbara, Ca). The procedure to take the AFM images has been described elsewhere [15,28,29]. The same tip was used to scan the surfaces of the hollow fiber membranes and all captured images were treated in the same way.

The hollow fiber membrane surfaces were characterized in terms of the mean roughness parameter, Ra (minimum, maximum and average values), pore sizes (i.e. mean pore size, geometric standard deviation and pore size distribution) and nodule sizes (i.e. minimum, average and maximum nodule size). The same scan size (i.e. 2x2 μm2) was considered to evaluate the roughness parameter, Ra, of both the internal and external surfaces of each hollow fiber membrane. The sizes of pores and nodules are based on the average of at least 25 measurements for each batch of PVDF-HFP hollow fiber membranes. The cumulative pore size distributions of both the internal and external

surfaces of the PVDF-HFP hollow fiber membranes together with the probability density function curves were obtained following the method described in previous studies [29,37].

The liquid entry pressure (*LEP*) is the highest applied transmembrane pressure on liquid feed before this liquid penetrates into the pores of the hydrophobic membranes. In this study distilled water was used to determine the *LEP* using the experimental set–up schematized in Fig. 3.2.1. Five hollow fibers having a length of about 10 cm were assembled in a stainless steel tube with epoxy resin and then connected to the outlet of a pressurized water tank. First, a slight pressure of about 0.3×10^5 Pa was applied for at least 10 min. Then the applied pressure was increased stepwise by means of a pressure valve. The pressure at which a flow was observed at the external surface of the hollow fiber membranes is the liquid entry pressure of water (LEP_w). This was measured on three different samples for each PVDF-HFP hollow fiber membrane. The measurement considering a fourth sample was carried out when a significant dispersion of the results was detected.
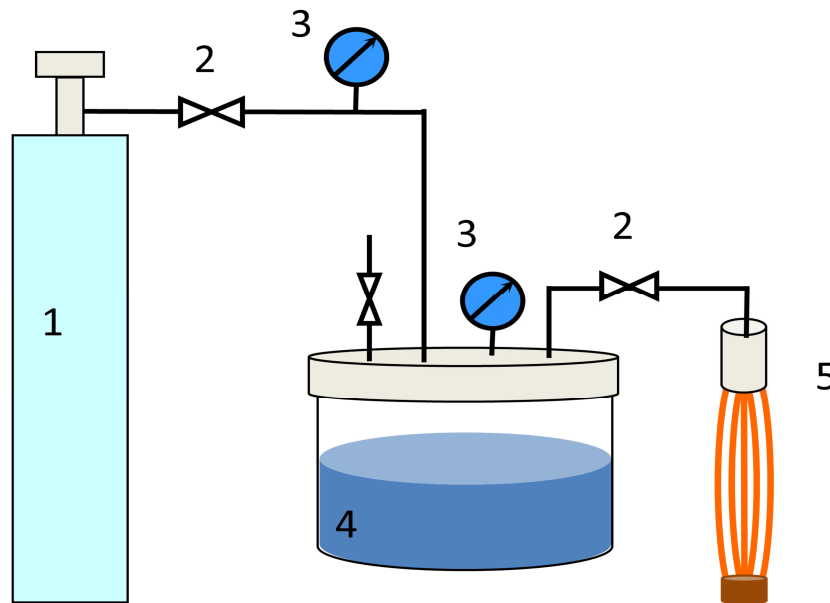
Figure 3.2.1. Experimental set-up for measurement of water entry pressure. (1) nitrogen tank; (2) regulating pressure valve; (3) pressure gauge; (4) water vessel; (5) hollow fiber sample.

DCMD experiments were carried out using the experimental set-up shown in Fig. 3.2.2. Tubular PVDF-HFP hollow fiber membrane modules were first prepared. Seven hollow fiber membranes were cut and packed in a stainless-steel shell-and-tube module using epoxy resin at both ends. The effective length of the hollow fiber membranes is 20 cm. Both the feed and permeate circulated through the membrane module by means of a double-head peristaltic pump (Watson Marlow, 323). The feed solution was circulated through the lumen side of the membrane module, whereas the permeate solution circulated through the shell side. The considered operating conditions to conduct the DCMD experiments are summarized in Table 3.2.2. The feed and permeate temperatures at the inlets of the membrane module were controlled by means of a heating thermostat (Techne, TU-16A) and a cooling thermostat (Polyscience, 6206), respectively. The feed and permeate containers were connected to the corresponding thermostats employing glass heat exchangers. Pt-100 probes were installed at both the inlets and outlets of the membrane modules and were connected to a digital meter (Fluke, Hydra data Logger with 2620 A module). The membrane module and all tubes were insulated. The permeate flux of each hollow fiber membrane module was determined by measuring the volume of distilled water transferred from the feed container to the permeate one.
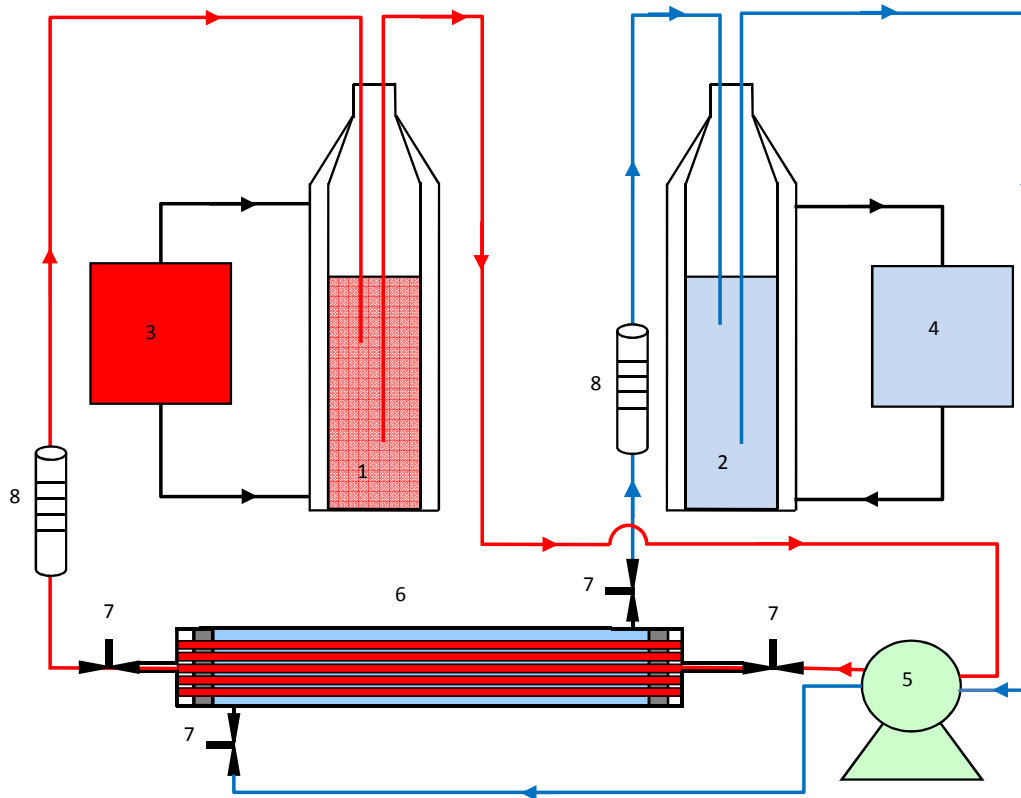
Figure 3.2.2. Experimental set-up for direct contact membrane distillation. (1) feed; (2) permeate; (3) hot thermostat; (4) cold thermostat; (5) double-head peristaltic pump; (6) hollow fiber membrane module; (7) Pt-100 probes; (8) flow meter.

Table 3.2.2. Operating conditions of DCMD experiments.

Feed flow rate (kg/h)	27.8 ± 0.6
Permeate flow rate (kg/h)	17.9 ± 0.9
Feed and permeate liquid	Distilled water
Feed temperature (ºC)	25, 30, 35, 40, 45
Permeate temperature (ºC)	20

3.2.3. Results and discussions

The internal and external diameters as well as the thickness of the prepared PVDF-HFP hollow fiber membranes are summarized in Table 3.2.3. It seems that there is an increase of the internal and external diameters with increasing the PVDF-HFP concentration in the dope solution. An enhancement of about 30% was observed between the hollow fiber membranes CO17 and CO24. It was also observed that the thickness of all tested hollow fiber membranes did not change significantly, if the experimental errors are considered, except the CO22 hollow fiber membrane, which was significantly thicker than the others. The increase of the diameters was attributed to the viscosity of the spinning solution, which increased with the copolymer concentration inducing an increase of the shear stress of the dope solution when extruded through the spinneret [40]. The release of the stress perpendicular to the axis resulted in the expansion of the fiber diameter, whereas the stress parallel to the fiber axis, which occurred through the air gap length due to the gravity, elongated the hollow fiber and the hollow fiber diameter diminished as consequence [41]. For the PVDF-HFP hollow fiber membranes, the molecular orientation induced by shear stress within the spinneret was found to be greater at higher polymer concentration and the elongation stress along the spinning line was not high enough to inhibit this effect.

Table 3.2.3. Dimensions of PVDF-HFP hollow fibers prepared with different copolymer concentrations.

Membrane name	Copolymer concentration (wt.%)	Inner diameter (μm)	Outer diameter (μm)	Thickness (μm)
CO17	17	1525 ± 22	1635 ± 27	55 ± 22
CO19	19	1591 ± 52	1716 ± 45	63 ± 34
CO20	20	1836 ± 15	1959 ± 22	62 ± 13
CO22	22	1712 ± 46	1900 ± 24	94 ± 26
CO24	24	1989 ± 27	2099 ± 22	55 ± 19

3.2.3.1. Cross-sectional study by scanning electron microscopy

As stated earlier, the cross-sectional structure of the PVDF-HFP hollow fiber membranes were studied by SEM. The evolution of the cross-section structure with increasing the copolymer concentration is shown in Fig. 3.2.3. It can be seen that the cross-section of the hollow fiber membrane CO17 (Fig. 3.2.3A) exhibits a *finger-like* structure at both the outer and inner layers. As the copolymer concentration increases from 17 wt.% to 19 wt.%, the *finger-like* structure of the internal layer starts first to disappear (Fig. 3.2.3B) changing to *sponge-like* structure. In Fig. 3.2.3C corresponding to the hollow fiber membrane prepared with 20 wt%, the *finger-like* structure is completely absent Furthermore, no *finger-like* structure is detected at the outer layer of the hollow fiber membranes CO22 (Fig. 3.2.3D) and CO24 (Fig. 3.2.3E) and their cross-sections exhibit a *sponge-type* structure. Therefore, it can be stated that a low copolymer concentration in the spinning solution tends to precipitate in a finger structure, while high copolymer concentrations tend to form sponge-structured membranes. Higher copolymer concentration in the spinning solution produces a higher polymer concentration at the point of precipitation, which will thus tend to

increase the strength of the surface layer of copolymer first precipitated, and tend to prevent initiation fingers.
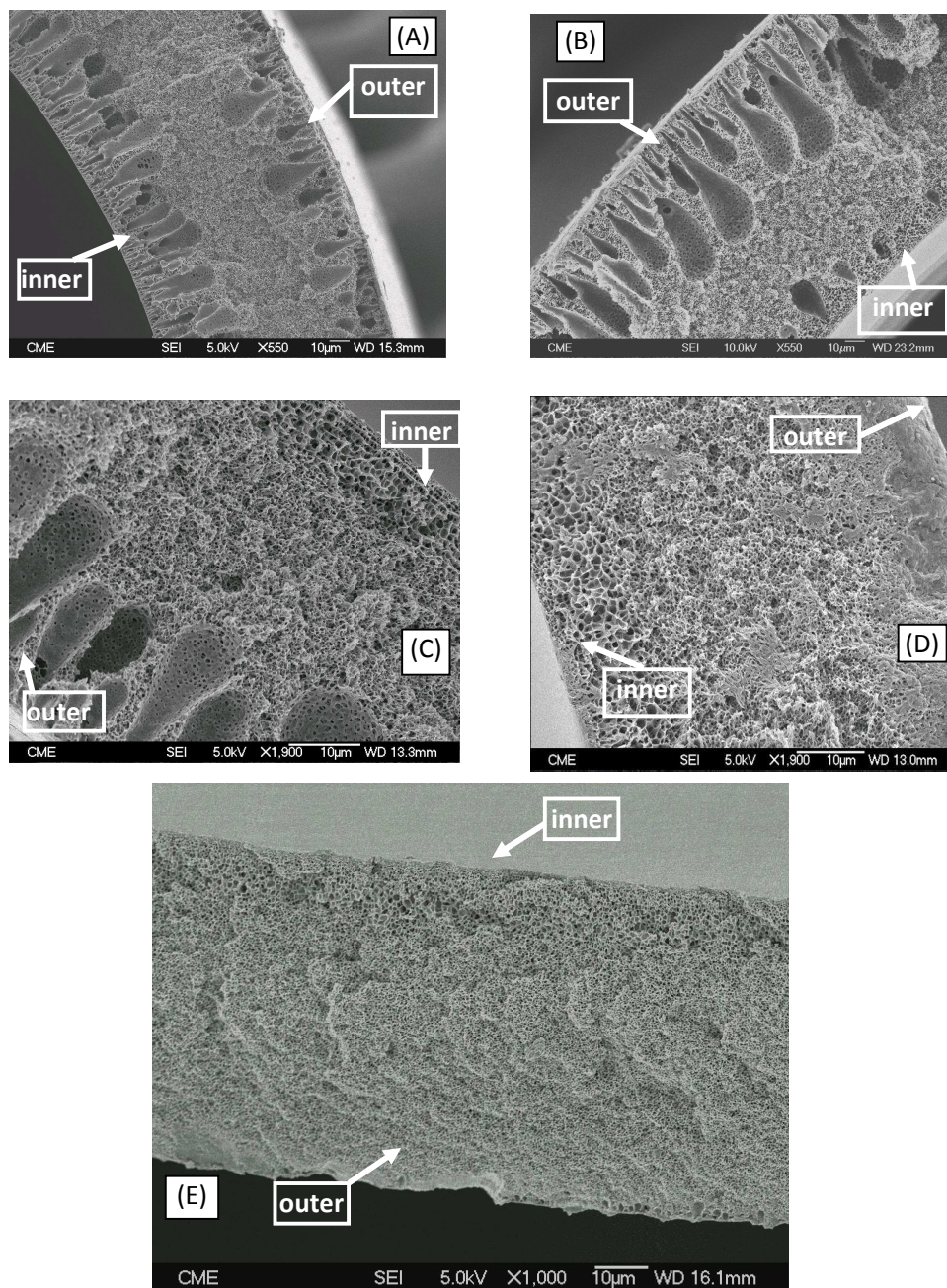

Figure 3.2.3. Cross-section morphology of hollow fiber membranes prepared with different PVDF-HFP copolymer concentrations: (A) CO17, (B) CO19, (C) CO20, (D) CO22 and (E) CO24.

It is known that increasing the polymer concentration of the dope solution generally results in a decrease in the precipitation rate and a transition from a finger-type structure to a sponge-type structure [42]. Therefore, the obtained structures presented above may be attributed to the coagulation rate of the PVDF-HFP, which decreases with increasing its concentration in the spinning solution. In fact, the coagulation starts from the internal surface of the nascent hollow fiber membrane and solvent evaporation (i.e. DMAC) took place from the outer surface through the air gap distance until reaching the coagulation bath. This explains the asymmetric structure observed between the inner and outer layers of the hollow fiber membranes prepared with different PVDF-HFP concentrations and to the fact that the finger-like structure disappeared first from the internal layer.

Changes of membrane structure are believed to be associated to the change of both thermodynamic and kinetic properties of the system. During hollow fiber membrane formation, due to the presence of non-solvent (water), the copolymer solution becomes thermodynamically unstable and liquid-liquid phase separation occurs, which is followed by precipitation. It must be mentioned that the additive PEG used in this study has good affinity with water and increased the thermodynamic instability of the copolymer solution in reaction with water, which facilitated a rapid phase demixing and resulted in macrovoid formation as observed in Fig. 3.2.3A. In fact, the increase of the copolymer concentration is related to the decrease of the additive in the dope solution. Therefore, as the copolymer concentration increases in the dope solution, the size and number of dispersed droplets formed after phase separation decrease resulting in smaller pore size and porosity (Table 3.2.5 and Figs. (3.2.5),(3.2.8),(3.2.9)). The formed sponge-like structure observed in Figs. 3.2.3D and 3.2.3E may be due to the delayed liquid-liquid phase separation with the increase of the copolymer concentration. The diffusions among solvent and non-solvent in the phase inversion may be hindered by the rapid demixing that results in a thinner selective layer due to the increase of the copolymer concentration (kinetic effect). As a result, a delayed precipitation in the sub-layer takes place inducing more sponge-like structure.

More detailed SEM images of the inner and outer layers of the PVDF-HFP hollow fiber membrane CO17 and the inner layer of the hollow fiber membrane CO22 are shown as examples in Fig. 3.2.4. As can be seen in Figs. 3.2.4A and 3.2.4B, the walls of the fingers are porous. It is worth noting that still some differences can be detected through the sponge-structured hollow fiber membranes CO22 and CO24, between the inner, outer and middle sections. In Fig. 3.2.4C, the sponge-like structure of the inner layer exhibits bigger pores than those of the middle layer. Similar differences were observed between the inner and the middle sections in Figs. 3.2.3C and 3.2.3E corresponding to the hollow fiber membranes CO20, CO22 and CO24.
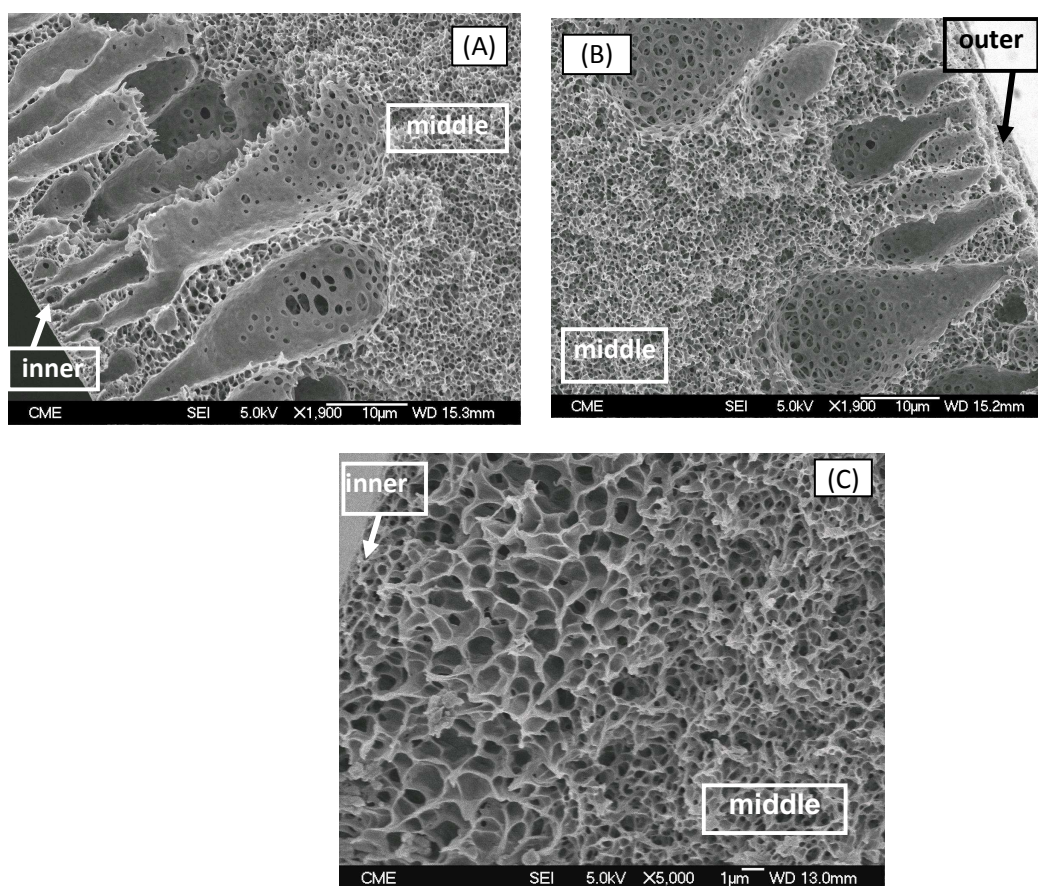
Figure 3.2.4. SEM details: (A) inner section of CO17 hollow fiber membrane; (B) outer section of CO17 hollow fiber membrane and (C) inner section of the CO22 hollow fiber membrane.

3.2.3.2. Void volume fraction study

The effect of PVDF-HFP concentration on the void volume fraction of the hollow fiber membranes is shown in Fig. 3.2.5. It was found that the void volume fraction diminished gradually with the increase of the PVDF-HFP content in the spinning solution. This may be related with the structure of the hollow fiber membrane, which changed from the *finger-like* structure to a complete *sponge-like* structure. It should be pointed out that the void volume fraction affects considerably the MD flux [1,2]. The transmembrane permeate flux is higher at higher porosity. Therefore, it is expected that the MD flux will be greater for the hollow fiber membrane prepared with smaller PVDF-HFP concentration.
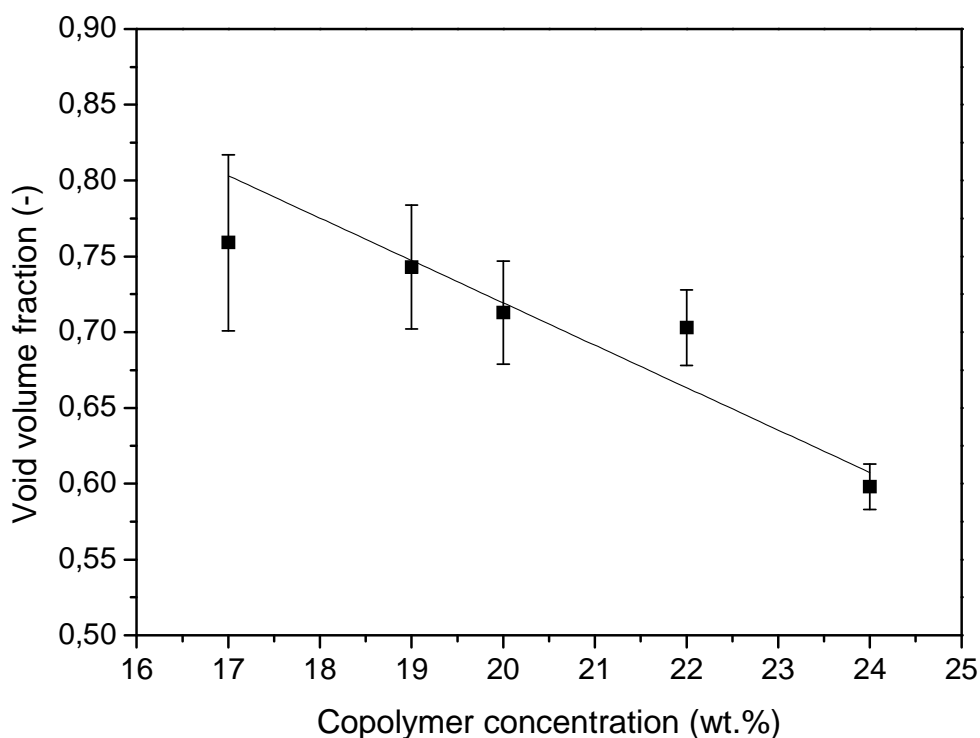
Figure 3.2.5. Effect of copolymer concentration on void volume fraction of PVDF-HFP hollow fiber membranes.

3.2.3.3. Surface morphology study by atomic force microscopy

Figs. (3.2.6) and (3.2.7) show the 3D AFM images of the inner and outer surfaces of the PVDF-HFP hollow fiber membranes, respectively. From Fig. 3.2.6 it can be seen that the nodules aggregates at the inner surfaces and are aligned parallel to the shear direction (i.e. perpendicular to the spinning direction). Furthermore, the nodule alignment is more pronounced as the copolymer concentration increases. However, this nodules alignment is not observed clearly at the outer surfaces of the hollow fiber membranes. This may be due to the relaxation of the copolymer macromolecules that takes place at the outer surface of the hollow fiber membranes due to gravity. It was reported that molecular orientation induced by shear stress within the spinneret might relax in the air gap region affecting the structure of the outer surfaces of the hollow fiber membranes [30-32]. Therefore, molecular orientation induced by shear stress affects significantly the inner surface of the nascent fiber and becomes more pronounced with increasing the copolymer concentration since the viscosity increases.

The mean roughness parameter was determined as stated earlier and the minimum, maximum and average values of both the external and internal surfaces of the hollow fiber membranes are summarized in Table 3.2.4. From the obtained data no clear trend can be plotted between the mean surface roughness and the PVDF-HFP concentration. The external surface of the hollow fiber membranes CO17, CO19 and CO20 are rougher than their internal surfaces, whereas for higher PVDF-HFP concentrations than 20 wt. % the mean roughness parameters, R_a, of the internal surfaces are higher. In general, the mean roughness of the outer surface decreased as the PVDF-HFP concentration was increased in the spinning solution. This result may be attributed to the viscosity of the dope solution, which increases with increasing the PVDF-HFP content in the spinning solution causing a slower coagulation rate of the inner surface and increasing the corresponding surface roughness. On the contrary, elongation stress caused by gravity becomes more pronounced at the external surface of the nascent hollow fibers with increasing viscosity of the dope solution and this diminishes the outer surface roughness due to the change of nodule size and pore size as will be shown later on.
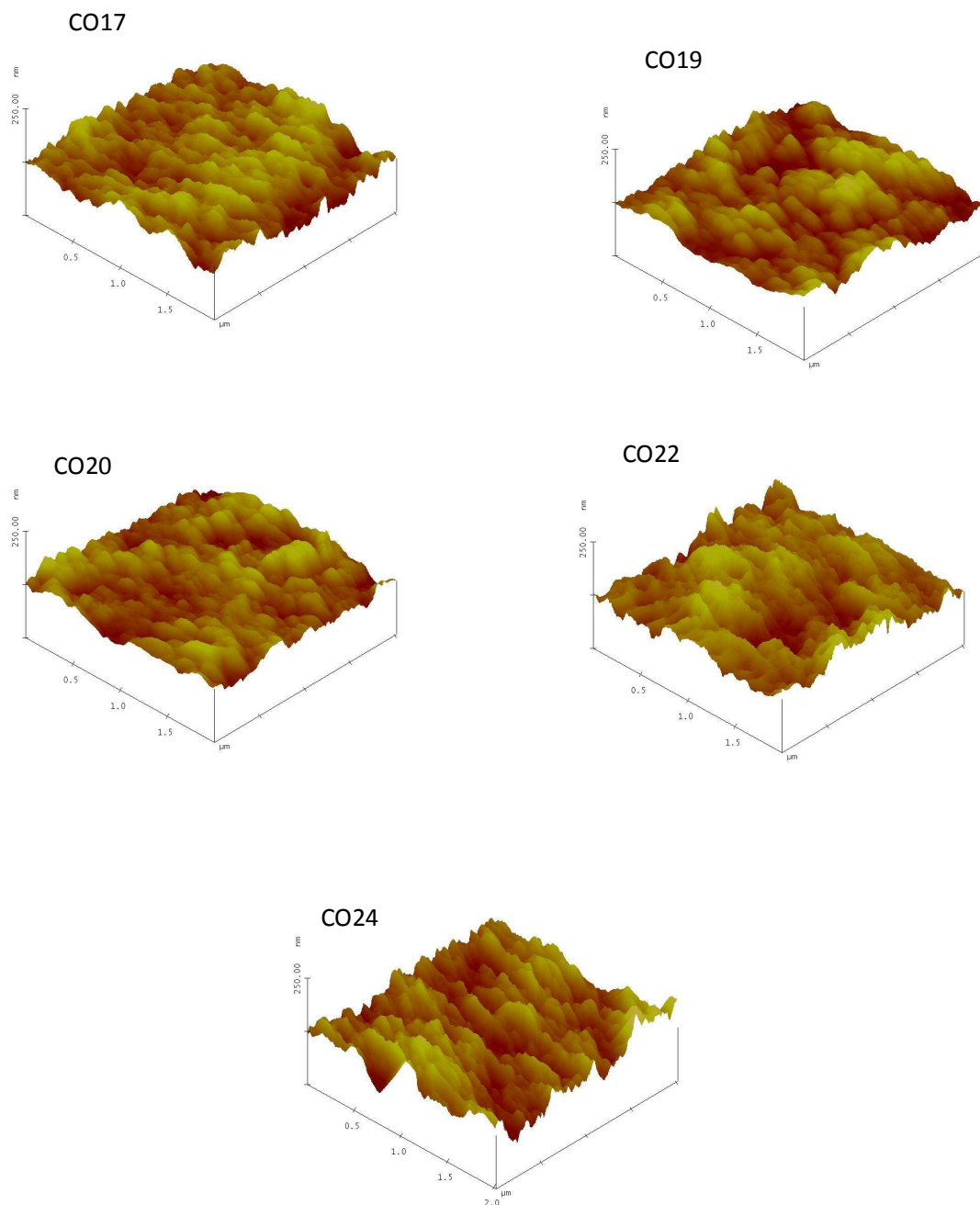
Figure 3.2.6. *3D* AFM images of the inner surfaces of the PVDF-HFP hollow fibers prepared with different copolymer concentrations.
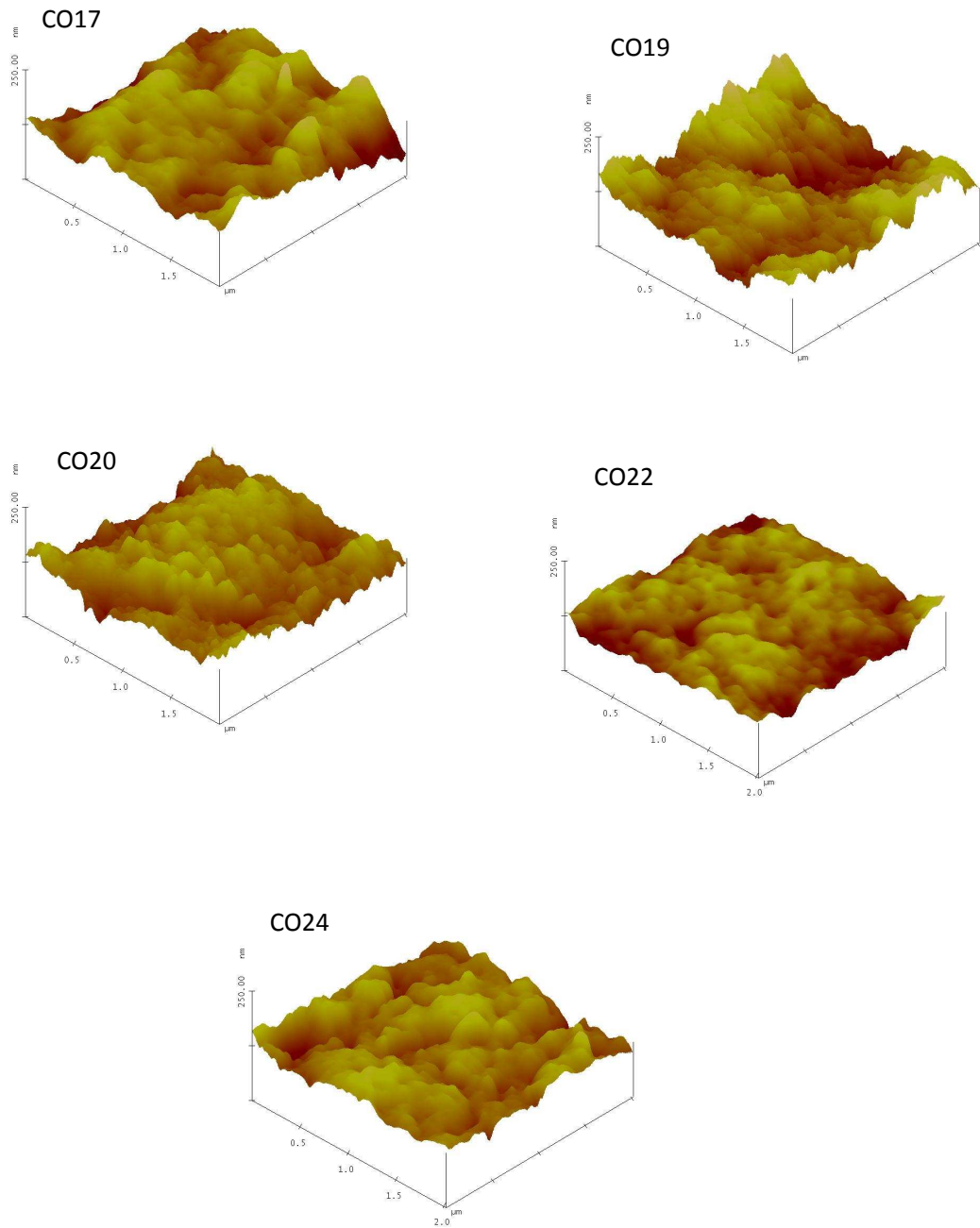
Figure 3.2.7. *3D* AFM images of the outer surfaces of the PVDF-HFP hollow fiber membranes prepared with different copolymer concentrations.

Table 3.2.4. Minimum, maximum and average mean roughness parameter, R_a, together with the corresponding standard deviation values of the internal and external surfaces of the PVDF-HFP hollow fibers prepared with different copolymer concentrations (scan range considered 2 x 2 μm^2).

Membrane	R_a (nm) Inside			R_a (nm) Outside		
	Minimum	Maximum	Average	Minimum	Maximum	Average
CO17	10.6	17.2	14.1 ± 2.0	15.0	25.0	20.0 ± 2.7
CO19	9.6	13.3	11.7 ± 1.2	15.2	33.5	22.9 ± 5.4
CO20	8.3	15.9	11.9 ± 2.1	15.3	24.7	20.9 ± 3.3
CO22	13.5	19.1	16.1 ± 1.4	7.1	15.2	11.5 ± 2.2
CO24	14.9	18.1	16.8 ± 1.0	11.7	18.8	14.6 ± 2.1

The pore sizes of both the internal and external surfaces of the PVDF-HFP hollow fiber membranes were evaluated and the mean pore sizes together with the corresponding geometric standard deviations were calculated as stated in previous studies [29,37]. Table 3.2.5 summarizes these values for both the inner and outer surfaces. The cumulative pore size distributions and the probability density function curves are presented in Figs. 3.2.8 and 3.2.9. From the reported values of the mean pore size in Table 3.2.5 and the curves plotted in Figs. (3.2.8) and (3.2.9), it can be seen that the copolymer concentration is affecting both the internal and external surfaces of the PVDF-HFP hollow fiber membranes as it is discussed in the following paragraphs.

Different pore sizes were obtained in both the inner and outer surfaces depending on the PVDF-HFP concentration in the spinning solution. All hollow fiber membranes have smaller inner pore sizes and narrower pore size distributions at the internal surfaces than at the corresponding external surfaces. Moreover, both the external and internal pore sizes were found to be larger for the hollow fiber membranes prepared with lower PVDF-HFP

concentrations. Besides, the mean pore size of the inner surfaces decreased gradually with the increase of the copolymer concentration. In contrast, the mean pore size of the outer surfaces decreased with increasing the copolymer concentration up to 20 wt. % and then leveled off for higher copolymer concentrations (see Fig. 3.2.9 and Table 3.2.5).

Table 3.2.5. AFM mean pore size, μ_p, and geometric standard deviation, σ_p, of the internal and external surfaces of the PVDF-HFP hollow fibers prepared with different copolymer concentrations.

Membrane	Inner surface		Outer surface	
	μ_p (nm)	σ_p	μ_p (nm)	σ_p
CO17	77.83	1.09	114.17	1.09
CO19	73.96	1.08	85.72	1.10
CO20	62.97	1.09	71.09	1.08
CO22	56.53	1.08	68.86	1.08
CO24	46.33	1.08	68.21	1.07

The nodule sizes (minimum, maximum, average and standard deviation) are presented in Table 3.2.6 for both the internal and external surfaces of the hollow fiber membranes. The corresponding cumulative distribution curves and probability density function curves generated from the measured nodule sizes are plotted in Figs. 3.2.10 and 3.2.11. Larger nodule sizes were observed for the hollow fiber membranes prepared with lower PVDF-HFP concentrations and for the same hollow fiber membrane smaller nodule sizes formed at the inner surface. It was reported that larger pore sizes and higher nodule sizes lead to rougher surfaces [28,29,42]. This statement can be only applied for the outer surfaces of the PVDF-HFP hollow fiber membranes.

**Figure 3.2.8.** Cumulative distribution of pore sizes (a) and probability density function (b) curves generated from the pore sizes measured from AFM images of the inner surfaces of the PVDF-HFP hollow fiber membranes prepared with different copolymer concentrations.
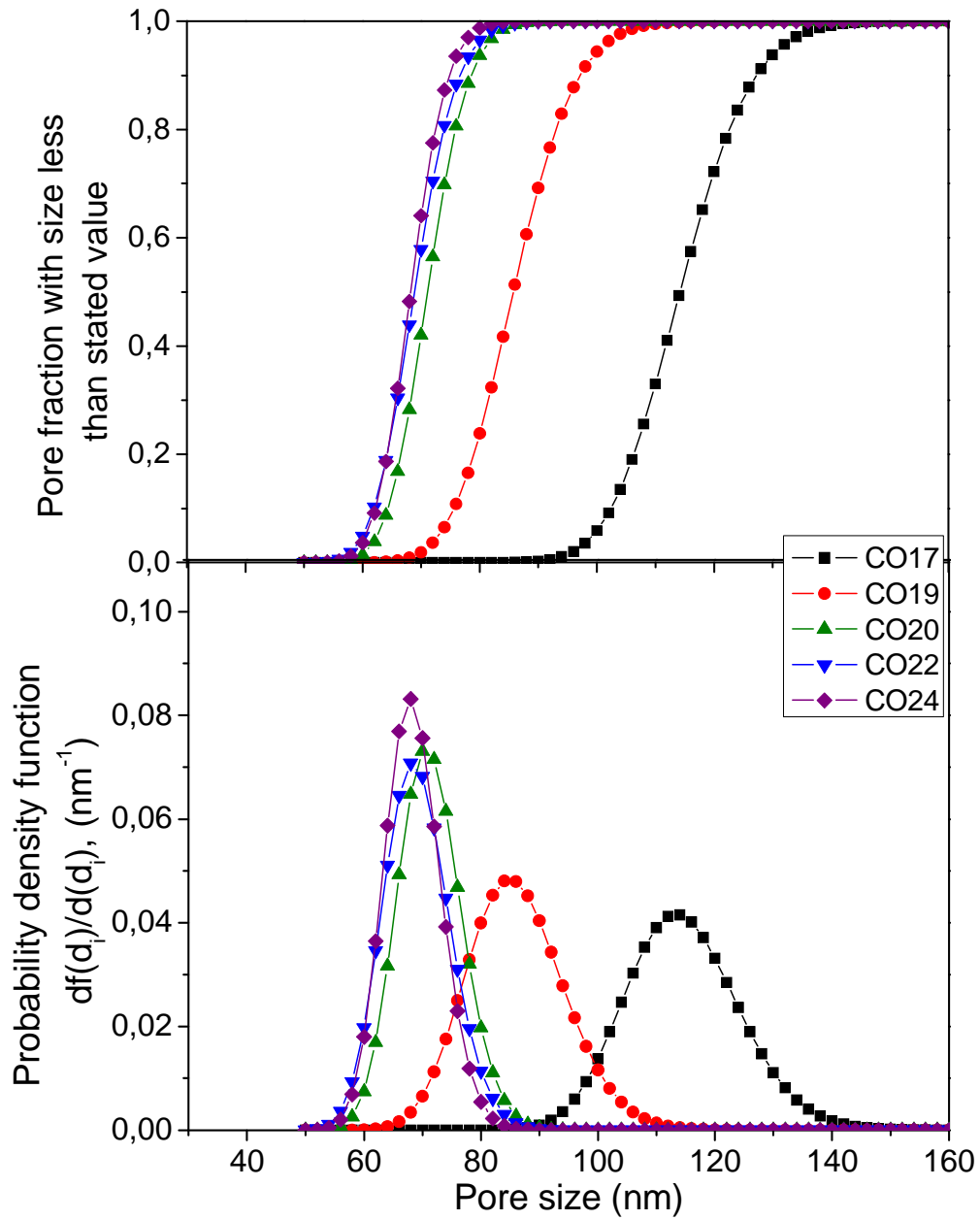
Figure 3.2.9. Cumulative distribution of pore sizes (a) and probability density function (b) curves generated from the pore sizes measured from AFM images of the outer surfaces of the PVDF-HFP hollow fiber membranes prepared with different copolymer concentrations.

Table 3.2.6. Nodule size (minimum, maximum, average and standard deviation values) of the internal and external surfaces of PVDF-HFP hollow fiber prepared with different copolymer concentrations.

Membrane	Inner nodule size (nm)			Outer nodule size (nm)		
	Minimum	Maximum	Average	Minimum	Maximum	Average
CO17	55	125	79 ± 13	62	203	126 ± 27
CO19	55	125	93 ± 17	55	161	104 ± 22
CO20	55	117	80 ± 16	55	120	85 ± 17
CO22	47	109	71 ± 15	55	112	84 ± 14
CO24	35	94	60 ± 13	55	118	88 ± 15
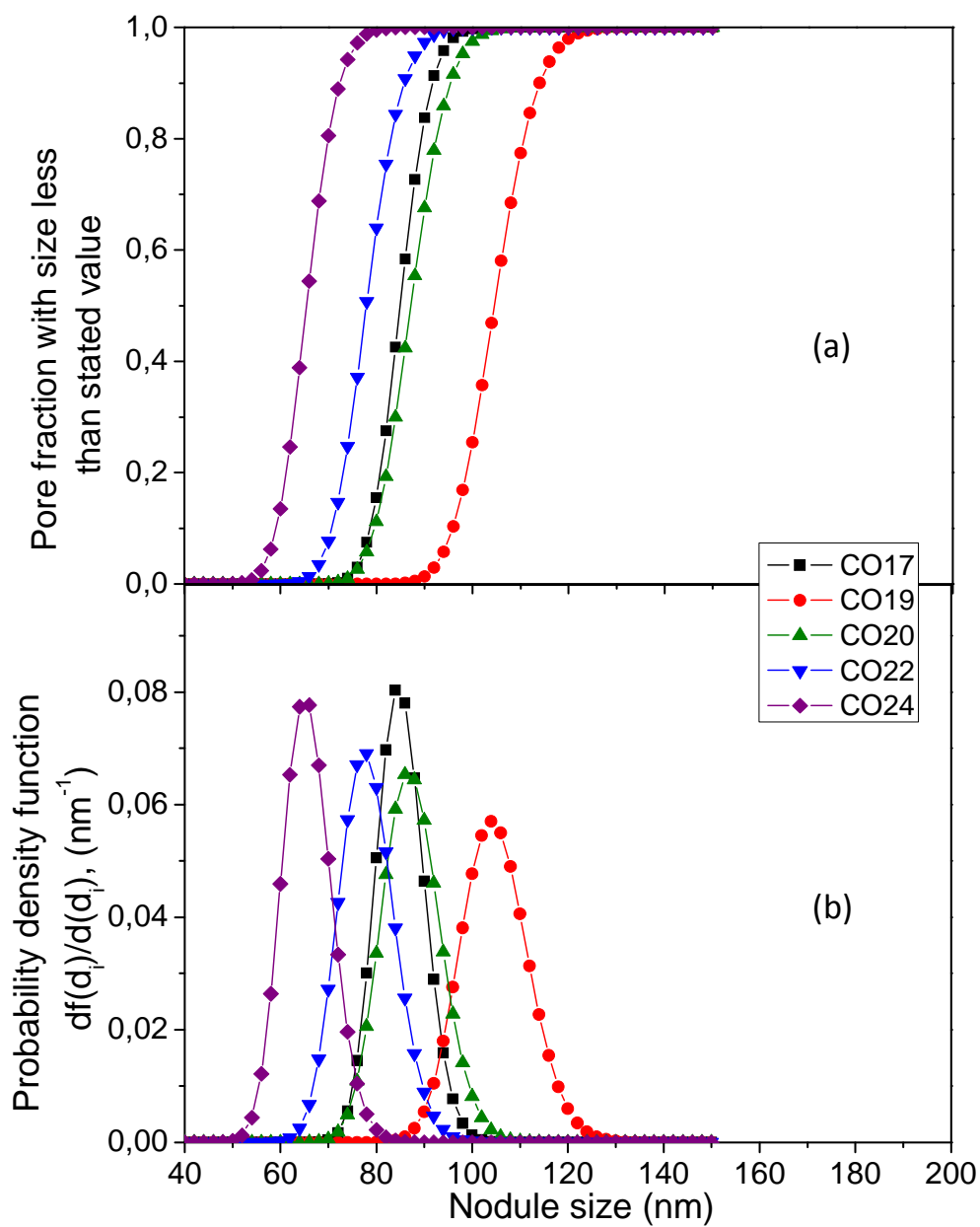
Figure 3.2.10. Cumulative distribution of nodule sizes (a) and probability density function (b) curves generated from the nodule sizes measured from AFM images of the inner surfaces of the PVDF-HFP hollow fiber membranes prepared with different copolymer concentrations.
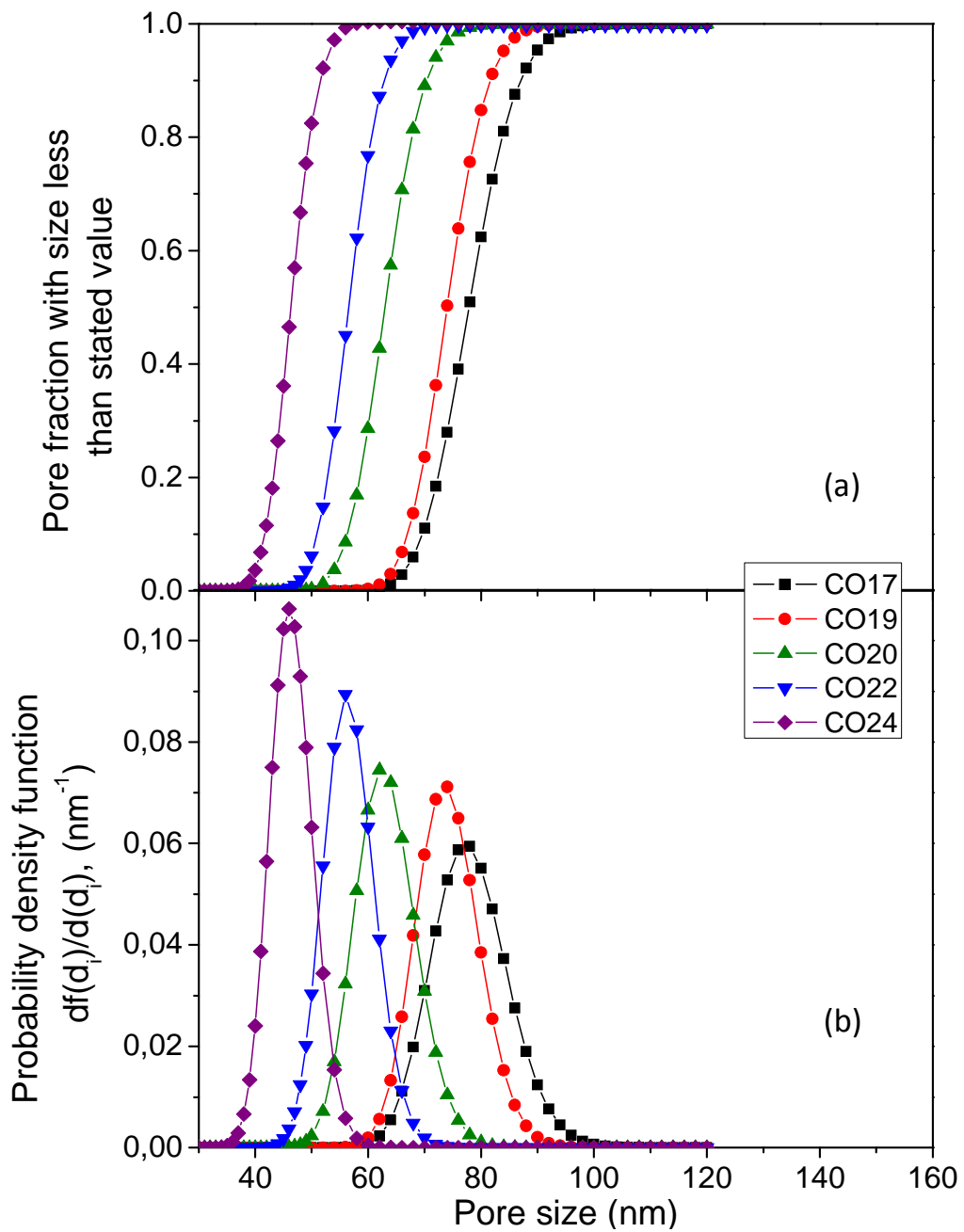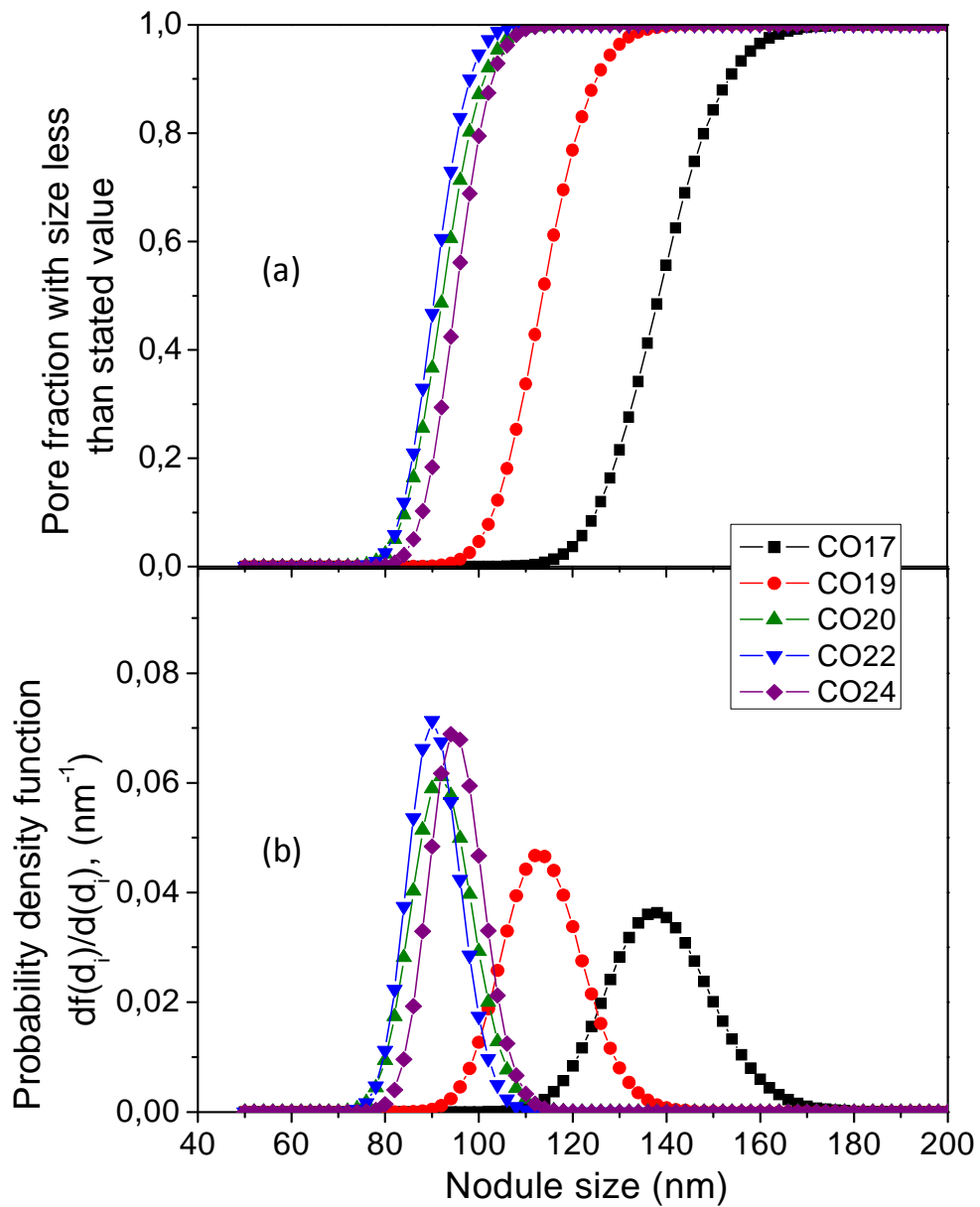
Figure 3.2.11. Cumulative distribution of nodule sizes (a) and probability density function (b) curves generated from the nodule sizes measured from AFM images of the outer surfaces of the PVDF-HFP hollow fiber membranes prepared with different copolymer concentrations.

3.2.3.4. Liquid entry pressure and DCMD experiments

The liquid entry pressure of water (LEP_w) is related to the hydrophobicity of the used material as well as to the maximum pore size [43]. The measured LEP_w values of the hollow fiber membranes are shown in Fig. 3.2.12 as a function of the PVDF-HFP concentration in the spinning solution. The LEP_w values of the PVDF-HFP hollow fiber membranes are similar to those of the commercial PVDF membranes [43]. There is an increase of the LEP_w with the increase of the copolymer concentration. This result may be due to the decrease of the maximum pore size because the same copolymer material was used for preparation of all hollow fiber membranes. It is worth quoting that Feng et al. [26] investigated the effect of PEG (of different molecular weights: 400 - 6000 kg/mol) on the hydrophobicity of PVDF-HFP flat-sheet membranes and stated that PEG traces could not be washed out completely from the membrane matrix decreasing the membrane hydrophobicity. The experimental results obtained for the LEP_w of the PVDF-HFP hollow fiber membranes indicates that the change of the hydrophobicity due to PEG traces is not the cause of LEP_w variation.
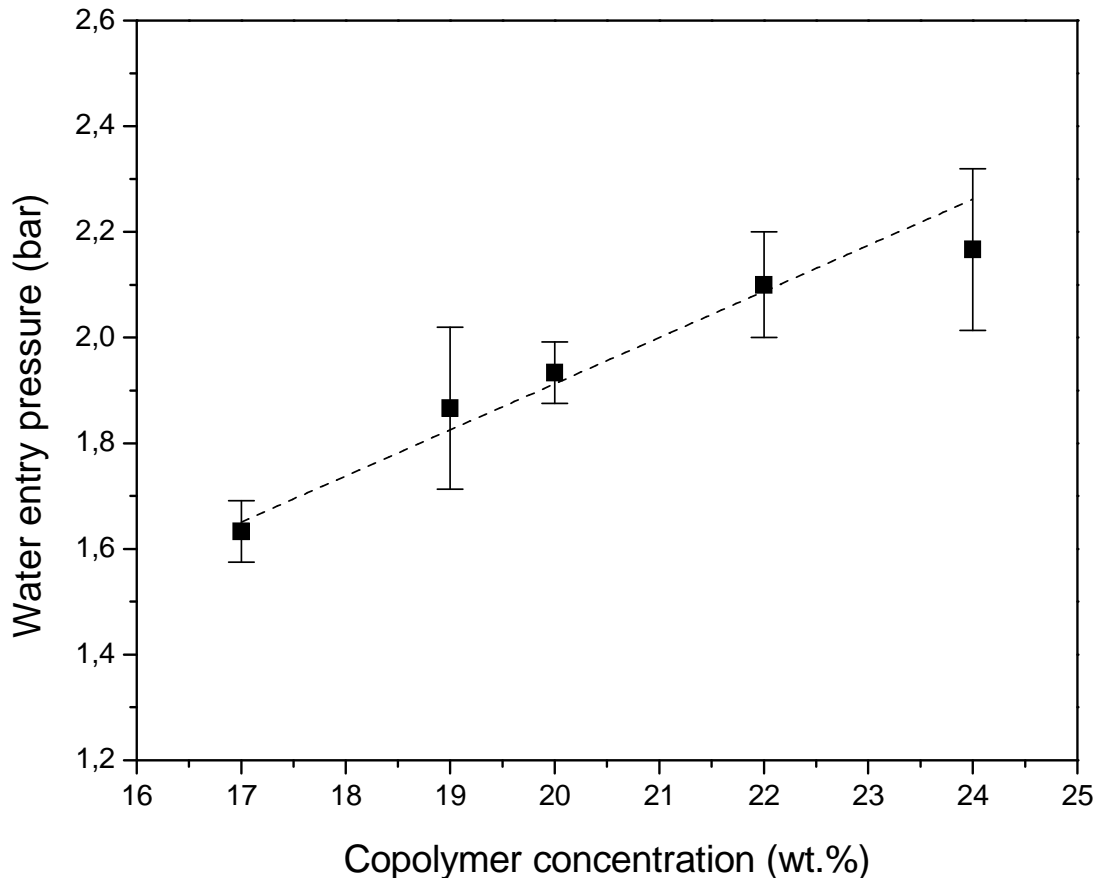
Figure 3.2.12. Effect of copolymer concentration on water entry pressure of the PVDF-HFP hollow fiber membranes prepared with different copolymer concentrations.

Based on the obtained LEP_w values, all prepared PVDF-HFP hollow fiber membranes can be used in DCMD. Fig. 3.2.13 shows the permeate DCMD flux of all prepared PVDF-HFP hollow fiber membranes as a function of different feed temperatures maintaining the permeate temperature at 20ºC. As it was expected, the permeate flux strongly depends on the PVDF-HFP concentration in the dope solution. The permeate flux increases as the PVDF-HFP concentration decreases. This is due to the higher porosities and pore sizes of the hollow fiber membranes prepared with lower PVDF-HFP concentrations. As it is well known in MD, the feed temperature is one of the operating variables that affect considerably the MD flux due to the exponential increase of the vapor pressure with temperature [1,44]. In Fig. 3.2.13, the exponential

221

variation of the permeate flux with the feed temperature is more pronounced for the hollow fiber membranes prepared with lower PVDF-HFP concentrations.
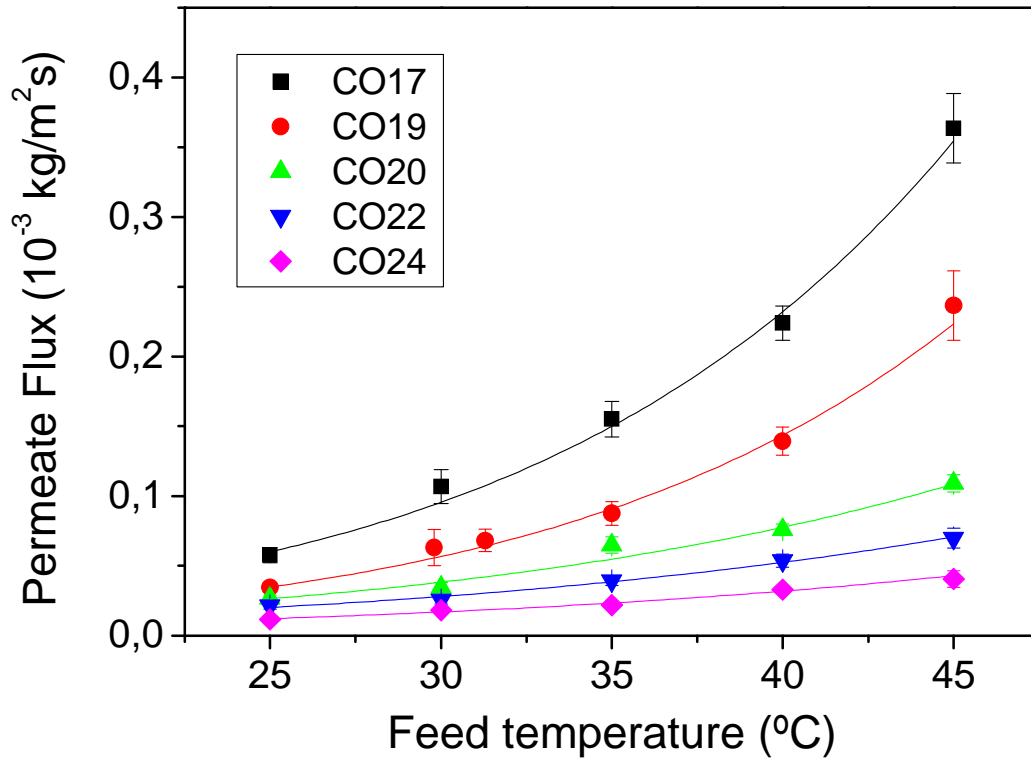
Figure 3.2.13. Effects of copolymer concentration and feed temperature on the DCMD permeate flux. Solid lines represent the best exponential fit of the experimental data.

3.2.4. Conclusions

PVDF-HFP hollow fiber membranes were prepared with different copolymer concentrations. An increase of both the internal and external diameters of the hollow fiber membranes was observed with increasing the copolymer concentration in the dope solution. However, a gradual decrease of the void volume fraction was detected with increasing the PVDF-HFP concentration.

The cross-section structure varied from a *finger-type* structure at both the external and the internal layers of the hollow fiber membrane prepared with the lowest copolymer concentration (CO17) to a *sponge-type* structure through the whole cross-section of the hollow fiber membrane prepared with the highest copolymer concentration (CO24). This structural change was attributed to the decrease of the coagulation rate of the PVDF-HFP copolymer at 40ºC with the increase of the copolymer concentration.

In general, the pore sizes of both the internal and external surfaces of the PVDF-HFP hollow fiber membranes decreased with increasing the copolymer concentration and it seems that the pore size distribution of the external surface reached a minimum value for higher copolymer concentrations than 20 wt.%. Similarly, the mean nodule size of both the internal and external surfaces decreased as the copolymer concentration was increased.

The liquid entry pressure of water was found to be higher for the hollow fiber membranes prepared with higher copolymer concentrations and the DCMD fluxes were greater for the hollow fiber membranes prepared with the lowest copolymer concentration.

References

[1] M. Khayet, Membrane distillation, in: N.N. Li, A.G. Fane, W.S.W. Ho, T. Matsuura (Eds.), Advanced Membrane Technology and Applications, John Wiley & Sons, New Jersey, 2008, pp. 297-370.

[2] M.S. El-Bourawi, Z. Ding, R. Ma, M. Khayet, A framework for better understanding membrane distillation separation process, J. Membr. Sci. 285 (2006) 4-29.

[3] M. Qtaishat, D. Rana, M. Khayet, T. Matsuura, Preparation and characterization of novel hydrophobic/hydrophilic polyetherimide composite membranes for desalination by direct contact membrane distillation, J. Membr. Sci. 327 (2009) 264-273.

[4] M.A. Izquierdo-Gil, M.C. García-Payo, C. Fernández-Pineda, Direct contact membrane distillation of sugar aqueous solutions, Sep. Sci. Technol. 34 (1999) 1773-1801.

[5] Z.P. Zhao, F.W. Ma, W.F, Liu, D.Z. Liu, Concentration of ginseng extracts aqueous solution by vacuum membrane distillation. 1. Effects of operating conditions Desalination 234 (2008) 152-157.

[6] M. Gryta, M. Tomaszewska, K. Karakulski, Wastewater treatment by membrane distillation, Desalination 198 (2006) 67-73.

[7] M.C. García-Payo, M.A. Izquierdo-Gil, C. Fernández-Pineda, Air gap membrane distillation of aqueous alcohol solutions, J. Membr. Sci. 169 (2000) 61-80.

[8] M.C. García-Payo, C.A. Rivier, I.W. Marison, U. von Stockar, Separation of binary mixtures by thermostatic sweeping gas membrane distillation: II. Experimental results with aqueous formic acid solutions, J. Membr. Sci. 198 (2002) 197-210.

[9] M. Khayet, A. Velázquez, J.I. Mengual, Direct contact membrane distillation of humic acid solutions, J. Membr. Sci. 240 (2004) 123-128.

[10] M.S. EL-Bourawi, M. Khayet, R. Ma, Z. Ding, Z. Li, X. Zhang, Application of vacuum membrane distillation for ammonia removal, J. Membr. Sci. 301 (2007) 200-209.

[11] M. Gryta, Fouling in direct contact membrane distillation process, J. Membr. Sci. 325 (2008) 383-394.

[12] S. Al-Obaidani, E. Curcio, F. Macedonio, G. Di Profio, H. Al-Hinai, E. Drioli, Potential of membrane distillation in seawater desalination: Thermal efficiency, sensitivity study and cost estimation, J. Membr. Sci. 323 (2008) 85-98.

[13] L. Martínez, J.M. Rodríguez-Maroto, Membrane thickness reduction effects on direct contact membrane distillation performance, J. Membr. Sci. 312 (2008) 143-156.

[14] M. Tomaszewska, Preparation and properties of flat-sheet membranes from poly(vinylidene) fluoride for membrane distillation, Desalination 104 (1996) 1-11.

[15] M. Khayet, T. Matsuura, Preparation and characterization of polyvinylidene fluoride membranes for membrane distillation, Ind. Eng. Chem. Res., 40 (2001) 5710.

[16] H.H. Park, B.R. Deshwal, I.W. Kim, H.K. Lee, Absorption of SO2 from flue gas using PVDF hollow fiber membranes in a gas–liquid contactor, J. Membr. Sci. 319 (2008) 29-37.

[17] W.H. Seol, Y.M. Lee, J.K. Park, Enhancement of the mechanical properties of PVdF membranes by non-solvent aided morphology control, J. Power Sources 170 (2007) 191-195.

[18] M. Zhang, A.Q. Zhang, B.K. Zhu, C.H. Du, Y.Y. Xu, Polymorphism in porous poly(vinylidene fluoride) membranes formed via immersion precipitation process, J. Membr. Sci. 319 (2008) 169-175.

[19] A.M. Stephan, D. Teeters, Characterization of PVDF-HFP polymer membranes prepared by phase inversion techniques I. Morphology and charge-discharge studies, Electrochim. Acta 48 (2003) 2143-2148.

[20] N.T. K. Sundaram, A. Subramania, Microstructure of PVDF-co-HFP based electrolyte prepared by preferential polymer dissolution process, J. Membr. Sci. 289 (2007) 1-6.

[21] A.M. Stephan, N.G. Renganathan, S. Gopukumar, D. Teeters, Cycling behavior of poly(vinylidene fluoride-co-hexafluoro propylene) (PVDF-HFP) membranes prepared by phase inversion method, Mater. Chem. Phys. 85 (2004) 6-11.

[22] J.H. Cao, B.K. Zhu, Y.Y. Xu, Structure and ionic conductivity of porous polymer electrolytes based on PVDF-HFP copolymer membranes, J. Membr. Sci. 281 (2006) 446-453.

[23] Y.J. Hwang, S.K. Jeong, K.S. Nahm, A.M. Stephan, Electrochemical studies on poly(vinylidene fluoride-hexafluoropropylene) membranes prepared by phase inversion method, Eur. Polym. J. 43 (2007) 65-71.

[24] G.C. Li, P. Zhang, H.P. Zhang, L.C. Yang, Y.P. Wu, A porous polymer electrolyte based on P(VDF-HFP) prepared by simple phase separation process, Electrochem. Commum.10 (2008) 1883-1885.

[25] X. Tian, X. Jiang, Poly(vinylidene fluoride-co-hexafluoropropylene) (PVDF-HFP) membranes for ethyl acetate removal from water, J. Hazard. Mater. 153 (2008) 128-135.

[26] C. Feng, R. Wang, B. Shi, G. Li, Y. Wu, Factors affecting pore structure and performance of poly(vinylidene fluoride-co-hexafluoropropylene) asymmetric porous membrane, J. Membr. Sci. 277 (2006) 55-64.

[27] T.S.N. Chung, Fabrication of hollow-fiber membranes by phase inversion, in: N.N. Li, A.G. Fane, W.S.W. Ho, T. Matsuura (Eds.), Advanced Membrane Technology and Applications, John Wiley & Sons, New Jersey, 2008, pp. 821-840.

[28] M. Khayet, M.C. García-Payo, F.A. Qusay, K.C. Khulbe, C.Y. Feng, T. Matsuura, Effects of gas gap type on structural morphology and performance of hollow fibers, J. Membr. Sci. 311 (2008) 259–269.

[29] M. Khayet, The effects of air gap length on the internal and external morphology of hollow fiber membranes, Chem. Eng. Sci. 58 (2003) 3091-3104.

[30] J. Qin, T.S. Chung, Effect of dope flow rate on the morphology, separation performance, thermal and mechanical properties of ultrafiltration hollow fiber membranes, J. Membr. Sci., 157 (1999) 35-51.

[31] A.F. Ismail, M.I. Mustaffar, R.M. Illias, M.S. Abdullah, Effect of dope extrusion rate on morphology and performance of hollow fibers membrane for ultrafiltation, Sep. Purf. Tech., 49 (2006) 10-19.

[32] S. Mok, D.J. Worsfold, A.E. Fouda, T. Matsuura, S. Wang, K. Chan, Study on the effect of spinning conditions and surface treatment on the geometry and performance of polymeric hollow-fibre membranes, J. Membr. Sci., 100 (1995) 183-192.

[33] S. Elmore, G.G. Lipscomb, Analytical approximations of the effect of a fiber size distribution on the performance of hollow fiber membrane separation devices, J. Membr. Sci. 98 (1995) 49-56.

[34] M. Khayet, C.Y. Feng, K.C. Khulbe, T. Matsuura, Study on the effect of a non-solvent additive on the morphology and performance of ultrafiltration hollow-fiber membranes, Desalination 148 (2002) 31-37.

[35] D. Wang, K. Li, W.K. Teo, Preparation and characterization of polyvinylidene fluoride (PVDF) hollow fiber membranes, J. Membr. Sci. 163 (1999) 211-220.

[36] M.L. Yeow, Y.T. Liu, K. Li, Morphological studies of poly(vinylidene fluoride) asymmetric membranes: effect of the solvent, additive and dope temperature, J. Appl. Polym. Sci. 92 (2004) 1782-1789.

[37] M. Khayet, C. Feng, K.C. Khulbe, T. Matsuura, Preparation and characterization of polyvinylidene fluoride hollow fiber membranes for ultrafiltration, Polymer 43 (2002) 3879-3890.

[38] S. Bonyadi, T.S. Chung, Highly porous and macrovoid-free PVDF hollow fiber membranes for membrane distillation by a solvent-dope solution co-extrusion approach, J. Membr. Sci. 331 (2009) 66-74.

[39] K. Y. Wang, T. S. Chung, M. Gryta, Hydrophobic PVDF hollow fiber membranes with narrow pore size distribution and ultra-thin skin for the freshwater production through membrane distillation, Chem. Eng. Sci. 63 (2008) 2587-2596.

[40] L. Shi, R. Wang, Y. Cao, C. Feng, D.T. Liang, J.H. Tay, Fabrication of poly(vinylidene fluoride-co-hexafluoropropylene)(PVDF-HFP) asymmetric microporous hollow fiber membranes, J. Membr. Sci. 305 (2007) 215-225.

[41] L. Shi, R. Wang, Y. Cao, D.T. Liang, J.H. Tay, Effect of additives on the fabrication of poly(vinylidene fluoride-co-hexafluropropylene) (PVDF-HFP) asymmetric microporous hollow fiber membranes, J. Membr. Sci. 315 (2008) 195-204.

[42] K.C. Khulbe, C.Y. Feng, F. Hamad, T. Matsuura, M. Khayet, Structural and performance study of micro porous polyetherimide hollow fiber membranes prepared at different air gap, J. Membr. Sci. 245 (2004) 191-198.

[43] M.C. García-Payo, M.A. Izquierdo-Gil, C. Fernández-Pineda, Wetting study of hydrophobic membranes via liquid entry pressure measurements with aqueous alcohol solutions, J. Colloid Interf. Sci. 230 (2002) 420-431.

[44] M. Qtaishat, T. Matsuura, B. Kruczek, M. Khayet, Heat and mass transfer analysis in direct contact membrane distillation, Desalination 219 (2008) 272-292.

3.3. Hollow Fiber Spinning Experimental Design and Analysis of Defects for Fabrication of Optimized Membranes for Membrane Distillation

Contents:

3.3.1. Introduction

3.3.2. Experimental

    3.3.2.1. Materials

    3.3.2.2. Spinning experiments

    3.3.2.3. Hollow fiber membrane characterization and DCMD

3.3.3. Results and discussions

    3.3.3.1. Hollow fiber spinning factorial design

    3.3.3.2. Hollow fibers characteristics

    3.3.3.3. Hollow fibers DCMD performance

3.3.4. Conclusions

References

Abstract:

A fractional factorial design and a steepest ascent method were applied for possible fabrication of hollow fibers by the dry/wet spinning technique. Seven spinning factors were taken into account. Different concentrations of the copolymer poly(vinylidene fluoride-*co*-hexafluoropropylene), PVDF-HFP with 400,000 g/mol molecular weight and the additive polyethylene glycol, PEG with 10,000 g/mol molecular weight were dissolved in *N,N*-dimethyl acetamide, DMAC. The developed approach permits localization of the region of experimentation, defect-free spinning conditions, to produce hollow fibers. The obtained hollow fiber membranes were characterized by scanning electron microscopy and atomic force microscopy. Penetration liquid in membrane pores and porosity were also determined. Finally the membranes were tested for desalination by direct contact membrane distillation. An optimal hollow fiber membrane was finally fabricated using the determined optimum spinning conditions: a copolymer concentration of 20% w/w, a PEG concentration of 6% w/w, an air gap length of 25 cm, an internal/external coagulation temperature of 37.5 $^{\circ}$C, an internal coagulant flow rate of 19 ml/min, a pressure of 0.3 bar and free falling. This membrane exhibits the highest performance index and the greatest global desirability (i.e. high permeate flux and salt rejection factor).

3.3.1. Introduction

Hollow fiber membrane modules normally exhibit large surface area per unit volume. The packing capacity of a hollow fiber membrane module may reach up to 500 - 9000 m^2/m^3 resulting in a high productivity per unit volume. Furthermore, hollow fiber membranes are mechanically self-supporting, have good flexibility and are easy to assemble in modules for different membrane applications. These characteristics make hollow fiber membranes attractive from industrial point of view.

Various hollow fiber membranes have been prepared using different polymers such as polyvinylidene fluoride (PVDF), solvents and additives [1-10]. These hollow fiber membranes were tested in membrane distillation (MD) and some of them exhibited high MD performance (i.e. high permeate flux and high salt rejection factor) [1-10]. Dry/wet or wet spinning and melt-extruded/cold-stretching are the most applied techniques. It should be pointed out that PVDF has been frequently used as the base material for preparation of hydrophobic hollow fiber membranes [1-6]. This can be explained by its high chemical resistance to most of corrosive chemicals and organic compounds, thermal stability and hydrophobicity. For example, recently Wang et al. [5] prepared a PVDF hollow fiber membrane for direct contact membrane distillation (DCMD) using the solvent N-methyl-1-pyrrolidone (NMP) and ethylene glycol as a non-solvent additive. The dry/jet wet spinning method was employed for hollow fiber fabrication. The PVDF concentration was 12 wt % and that of ethylene glycol was 8 wt %. The fabricated PVDF hollow fiber exhibited 0.16 μm mean pore size, a very narrow pore size distribution and an external ultra-skin layer over a porous support layer. It was mentioned that the fully porous membrane structure had the advantage of decreasing the vapor transport resistance, leading to an enhancement of the permeation flux. When using an aqueous salt solution of 3.5 wt % as a feed, a feed temperature of 79.3 ºC and a permeate temperature of 17.5 ºC, the PVDF hollow fiber membrane produced 41.5 kg/m^2.h with a rejection factor as high as 99.99 %. The authors claimed developing a membrane with a DCMD performance comparable or superior to most of commercially available PVDF hollow fiber membranes.

Melt-extruded/cold-stretching method was used by Li et al. [7] to prepare polyethylene (PE) and polypropylene (PP) hollow fiber membranes for desalination by DCMD and vacuum

membrane distillation (VMD). Compared to PP hollow fiber membranes, higher water fluxes have been obtained for the PE membranes in both DCMD and VMD. This was attributed to the larger pore size of the PE membranes. The highest permeate flux reported was 0.8 L/m^2.h in DCMD and about 4 L/m^2.h in VMD.

Recently, the copolymer poly(vinylidene fluoride-*co*-hexafluropropylene), PVDF-HFP, has been used for fabrication of hollow fiber membranes for MD [8,9]. This copolymer is more hydrophobic than PVDF. However, it was noticed that the obtained MD permeate fluxes of the PVDF-HFP hollow fiber membranes are lower than those of PVDF membranes [5,6,8,9].

Until now, the preparation of hollow fiber membranes is still a complex process. Various spinning parameters are involved (air gap distance, internal coagulant flow rate, pressure applied on the dope solution, temperature, nature of internal and external coagulants, structure and dimensions of the spinneret, fiber take-up speed, dope extrusion rate, dope solution characteristics, etc.). Therefore, it is not an easy task to identify the adequate spinning conditions for a given polymer. Moreover, the interaction effects between the spinning parameters (i.e. variables) also play an important role to obtain an optimum hollow fiber membrane. Frequently, spinning adequate hollow fibers is based on trial and error tests. Moreover, different types of defects often appeared on the surface of the spun hollow fibers, discontinuous spinning also happens and in most of the cases hollow fiber fabrication can not be carried out successfully due to the inadequate selection of the spinning conditions. It should be pointed out that generally, researchers are looking for the proper conditions of spinning in a small experimental domain where spinning is possible by maintaining all parameters fixed except one that is varied in a small range (i.e. univariate study where the variables are studied one by one). By using adequate design of spinning experiment (DoE) many process variables can be studied at the same time and the number of tests will be reduced compared to the conventional spinning approach based on trial and error. This multivariate study permits complete exploration in the experimental range and was applied in various field of research [11-15].

Attempts are made in this study to apply a fractional factorial design and the steepest ascent method, taking in the initial step a large domain of experimental factors. In such a large experimental domain spinning hollow fibers can be successful or not possible. In case of failure, the resultant product that may not have a fiber shape, may not be hollow or simply

may have defects, is analyzed statistically trying to avoid the inadequate spinning condition for the next step and to figure out, in a systematic manner, the proper experimental domain for spinning (i.e. region of interest). To the best of our knowledge no research group has analyzed rigorously the defects in spinning as a way for improving spinning process.

3.3.2. Experimental

3.3.2.1. Materials

Poly(vinylidene fluoride-*co*-hexafluoropropylene), PVDF-HFP, with an average weight of 400,000 g/mol was supplied by Sigma-Aldrich. The solvent *N,N*-dimethyl acetamide, DMAC, with analytical purity 99.8% was purchased from Fluka. The non-solvent additive polyethylene glycol, PEG, with molecular weight of 10,000 g/mol was supplied by Sigma-Aldrich. The copolymer, solvent and additive were used to prepare the spinning dope.

Sodium chloride NaCl supplied by Sigma-Aldrich was used to prepare the feed salt aqueous solutions for DCMD tests.

3.3.2.2. Spinning experiments

First, a PEG/DMAC mixture was prepared using a predetermined amount of PEG. Then, PVDF-HFP was dissolved in the PEG/DMAC mixture at a temperature of 55ºC under stirring for about 24 h to ensure the complete dissolution of the polymer. According to the fractional factorial experimental design, the concentration of PVDF-HFP, PEG and DMAC are determined and summarized in Table 3.3.1. All prepared dopes were homogeneous at room temperature. Before spinning, the prepared dope was degassed to remove the trapped gas bubbles.

The dope was spun employing the dry/wet spinning technique following in a first step the conditions given by the fractional factorial experimental design (Table 3.3.1). The experimental set-up used for spinning is reported elsewhere [16]. Tap water was used as internal and external coagulants. The spun product was stored in a water bath at room temperature for at least 48 h to remove the residual solvent and finally dried in air at room

temperature before analysis. The good hollow fiber membranes were characterized by different techniques and tested for desalination by DCMD.

Table 3.3.1. Fractional factorial experimental spinning design in coded and actual variables.

Product	PVDF-HFP concentration (% w/w)		PEG concentration (% w/w)		Air gap length (cm)		Temperature (°C)		Internal coagulant flow rate (ml/min)		Take-up speed (rpm)		Pressure (bar)	
	x_1	z_1	x_2	z_2	x_3	z_3	x_4	z_4	x_5	z_5	x_6	z_6	x_7	z_7
SD-1	1	20	1	6	1	40	1	50	1	36.4	1	50	1	0.5
SD-2	-1	15	1	6	1	40	-1	25	-1	9.5	1	50	-1	0.1
SD-3	1	20	-1	2	1	40	-1	25	1	36.4	-1	25	-1	0.1
SD-4	-1	15	-1	2	1	40	1	50	-1	9.5	-1	25	1	0.5
SD-5	1	20	1	6	-1	1	1	50	-1	9.5	-1	25	-1	0.1
SD-6	-1	15	1	6	-1	1	-1	25	1	36.4	-1	25	1	0.5
SD-7	1	20	-1	2	-1	1	-1	25	-1	9.5	1	50	1	0.5
SD-8	-1	15	-1	2	-1	1	1	50	1	36.4	1	50	-1	0.1

3.3.2.3. Hollow fiber membrane characterization and DCMD

The obtained hollow fiber membranes were characterized by means of microscopy techniques. Field emission scanning electron microscope (FESEM, JEOL Model JSM-6330F) was used to examine the cross-section of the fibers, whereas atomic force microscopy (AFM) was used to study the internal and external surfaces of the hollow fibers.

Spinning products were recorded by a digital camera (Canon, PowerShot A570IS).

The liquid entry pressure of water (LEP_w) is the minimum required pressure for water to go into dry membrane pores. The LEP_w and the porosity of the hollow fibers were measured as reported elsewhere [17,18].

The experimental set-up used for DCMD experiments is reported elsewhere [9]. Tubular PVDF-HFP hollow fiber membrane modules were first prepared. Five hollow fiber membranes were cut and packed in a stainless-steel shell-and-tube module using epoxy resin at both ends. The effective length of the hollow fiber membranes was 20 cm. Both the feed and permeate circulated through the membrane module by means of a double-head peristaltic pump (Watson Marlow, 323). The feed solution was circulated through the lumen side of the membrane module, whereas the permeate solution circulated through the shell side. More detailed descriptions of the experimental set-up used to conduct the DCMD experiments may be found in [9].

A concentration of 0.5 M NaCl aqueous solution was used as feed solution and the permeate flux as well as the salt rejection factor were determined. The feed was circulated through the lumen side, whereas the permeate distilled water was circulated through the shell side of the membrane modules.

3.3.3. Results and discussions

3.3.3.1. Hollow fiber spinning factorial design

In factorial design the levels of the factors (spinning variables in this study) are coded as +1 for the higher level and −1 for the lower level. Two level fractional designs are expressed using 2^{k-m}, where k is the number of factors and m describes the size of the fraction of the full factorial. In this study, the experimental conditions for hollow fiber spinning were planned according to a fractional factorial design having 7 factors described as 2^{7-4} (i.e. a total number of 8 experiments must be accomplished according to fractional factorial design). The factors involved in the experimental design are: 1) the PVDF-HFP copolymer concentration in the dope (z_1), 2) the PEG additive concentration in the dope (z_2), 3) the air gap length of the spinning system (z_3), 4) the internal/external coagulation temperature (z_4), 5) the internal coagulant flow rate (z_5), 6) the take-up speed (z_6) and 7) the operating pressure (z_7).

The fractional factorial design adopted in this study consisted of 2^{7-4} experimental tests shown in Table 3.3.1 with both the actual and coded variables. As can be seen, a large domain of variation was selected for each variable. Therefore, the probability that spinning hollow fibers cannot be possible in some of the designed spinning conditions is high. However, in the followed approach both positive result (i.e. possible hollow fiber spinning with cylindrical shape and spinning continuity without defects) and negative result (i.e. impossible spinning and defective fibers) are taken into account. The spinning product was coded as SD-i where i refers to the number of spinning test in Table 3.3.1. As indicated earlier, the visual morphology of the spinning products were recorded by a digital camera and some results are shown in Fig. 3.3.1. As can be seen good and bad spinning products were obtained. SD-1 and SD-5 could be spun and are free of visible defects, whereas SD-2, SD-3 and SD-7 have defects such as loops and coiled segments. For example, SD-2 could be spun only partially (i.e. discontinuous hollow fiber spinning) appearing some loops during spinning, twisted fibers appeared when spinning SD-3 and SD-7. SD-4 could not be spun, while flat shapes were spun for SD-6 and SD-8.
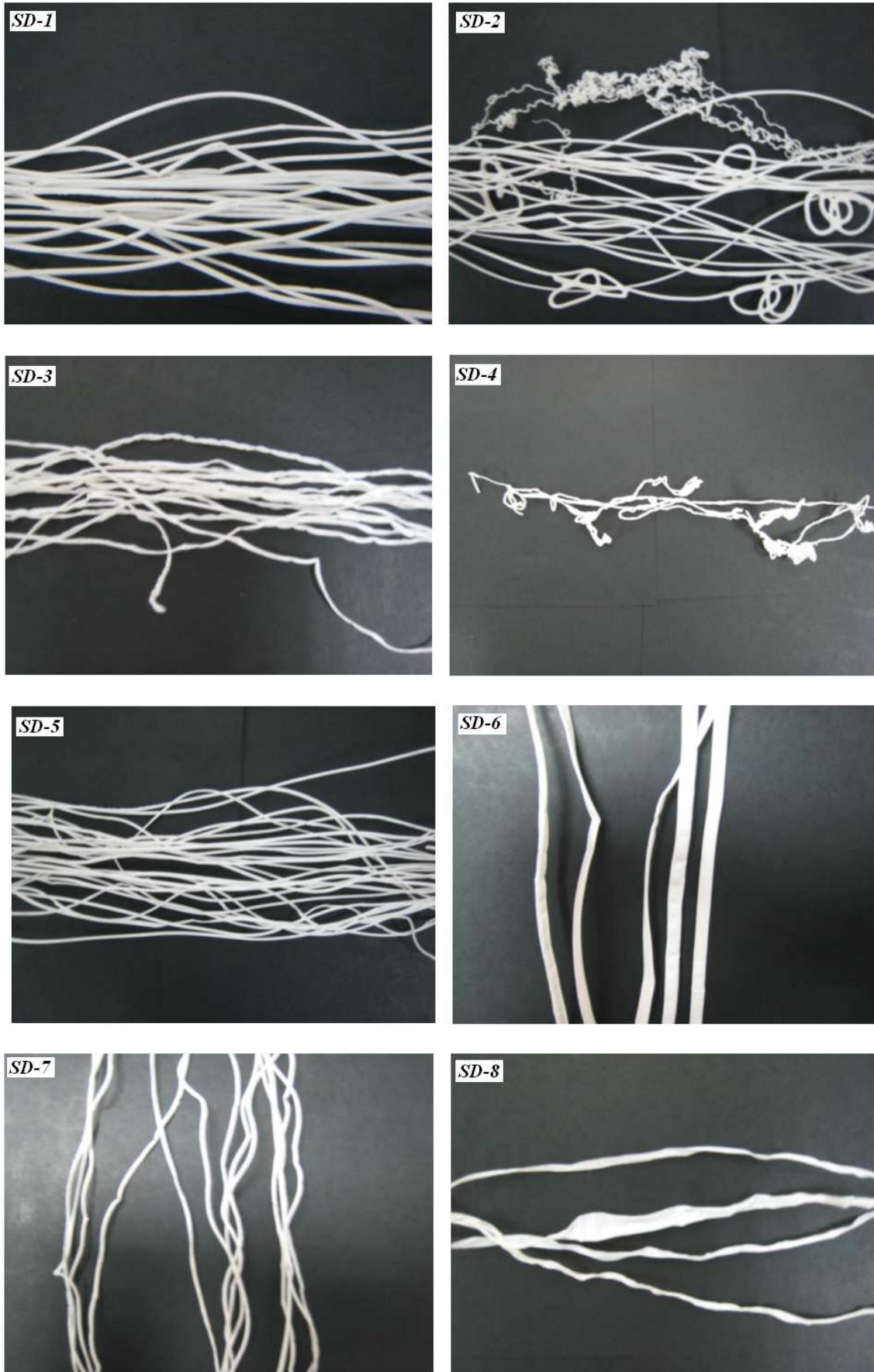
Figure 3.3.1. Pictures of PVDF-HFP spun products.

239

All the spinning products shown in Fig. 3.3.1 have been analyzed by a simple visual inspection taking into consideration the spinning continuity (i.e. fiber length), cylindrical and hollow shapes, and visible defects in spinning. Table 3.3.2 shows the results of this analysis. Among the 8 experimental tests, only the 3 products SD-1, SD-2 and SD-5 demonstrated their proximity to be possible candidates for PVDF-HFP hollow fiber spinning. This is due to the wide operating range selected for the 7 variables.

Table 3.3.2. Analysis and visual inspection of the spun products.

Spinning product	Continuity and length	Cylindrical shape	Hollow shape	Defects in spinning (loops, coiled segments, twisted spots, etc.)	Possible Spinning of hollow fiber
SD-1	Y	Y	Y	N	Y
SD-2	Y	Y	Y	Y	Y
SD-3	Y	N	N	Y	N
SD-4	N	N	N	Y	N
SD-5	Y	Y	Y	N	Y
SD-6	Y	N	Y / N	Y	N
SD-7	Y	Y / N	Y / N	Y	N
SD-8	Y	N	N	Y	N

Based on the results given in Table 3.3.2 and the recorded pictures presented in Fig. 3.3.1, the obtained spinning products were ranked (1 for the most unsuitable hollow fiber candidate and 8 for the most appropriate hollow fiber candidate). The results are summarized in Table 3.3.3 together with the average rank of each spinning product. Taking into consideration the average rank of the spinning products (Table 3.3.3), the main effects of factors were estimated in order to assess the contribution of each factor to the average rank (response). The main effects were computed as follows [19,20]:

$$b_j = \frac{1}{N}\sum_{i=1}^{N} x_{ji}Y_i \qquad (3.3.1)$$

240

where b_j means the main effect of the factor j, x_j is the coded level of the factor, Y denotes the average rank and N is the total number of experiments (8 in our case).

Table 3.3.3. Ranks of the obtained spinning products by dry/wet spinning technique.

Product	Rank$_1$	Rank$_2$	Rank$_3$	Average rank
SD-1	7.5	7	8	7.5
SD-2	6	8	6	6.7
SD-3	4	4	4	4.0
SD-4	1	1	1	1.0
SD-5	7.5	6	7	6.8
SD-6	3	2	2	2.3
SD-7	5	5	5	5.0
SD-8	2	3	3	2.7

The mathematical relationship between the average rank and the experimental factors can be described by the following linear equation:

$$Y = 4.5 + 1.33x_1 + 1.33x_2 + 0.29x_3 - 0.375x_5 + 0.96x_6 - 0.54x_7 \qquad (3.3.2)$$

It should be noted that, from Eq. (3.3.2), the most important main effects are attributed to the dope composition indicating that for a good spinning condition the PVDF-HFP and the PEG concentrations must be high. The other spinning factors also exert significant influence on the response except the temperature that does not affect the response (i.e. the corresponding coefficient in Eq. (3.3.2) is zero). Based on the main effects of factors we tried to identify the optimal region for spinning (i.e. region of interest) using the steepest ascent method proposed by Box and Wilson (named hereafter, Box-Wilson steepest ascent method) [20,21]. In this case the direction of the steepest ascent is given by the gradient, which is a vector and the components of this vector are the coefficients estimating the main spinning effects shown in Eq. (3.3.2). According to Box-Wilson steepest ascent method, the displacement from a start point is made in order to find a new value for each factor. The

displacement is proportional to the product ($b_j \, \Delta z_j$) where Δz_j is the step of searching. For a variable j the displacement from a start point is given by the following relationship [20]:

$$\Delta_j = \frac{\Delta_0}{b_0 \Delta z_0} \times b_j \Delta z_j \qquad\qquad (3.3.3)$$

where Δ_0 is the displacement for the factor of reference (subindex 0). Table 3.3.4 shows the developed steepest ascent parameters for each factor.

To move along the gradient according to Box-Wilson steepest ascent method we have selected as a start point the centre level of each variable except the take-up speed, which was selected to be the lowest value, i.e. 1 rpm. This exception was made because the operating values of this variable were too high affecting considerably spinning continuity. In other words, if the take-up speed is high the spun fibers are stretched without looping step and the risk of breaking a fiber is high.

The movement along the gradient was calculated for about 10 displacements from the start point and the results of the calculations are shown in Table 3.3.5. The final computed point (i.e. 10th point) is given by the following spinning conditions: 20 % w/w PVDF-HFP, 6 % w/w PEG, 24.8 cm air gap distance, 37.5 ºC temperature, 19.2 ml/min flow rate of the internal coagulant, 10 rpm take-up speed and 0.2 bar pressure. Compared with the previous operating conditions reported in Table 3.3.1, the determined spinning conditions are found to be localized inside the initial region of experimentation for most of the variables except the take-up speed that resulted to be much lower.

The hollow fiber membrane spun using the determined spinning conditions is denoted as RI-1. Additionally, we have performed other spinning experiments very close to the conditions of RI-1 in order to explore more deeply the region of interest. The prepared hollow fiber membranes are named hereafter, RI-2, RI-3, RI-4, RI-5 and RI-6. The experimental spinning conditions used for the fabrication of these hollow fibers are shown in Table 3.3.6. Figure 3.3.2 shows pictures of the obtained hollow fibers. Note that, the hollow fiber membranes RI-4, RI-5 and RI-6 were performed without take-up speed (i.e. free falling) and with different internal coagulant flow rates. As can be seen in Fig. 3.3.2, all the prepared hollow fibers (RI-1, RI-2, RI-3, RI-4, RI-5 and RI-6) are straight and hollow without visual defects. If we compare the initial spinning products shown in Fig. 3.3.1 (SD_i , $1 \leq i \leq 8$) with

the last hollow fibers shown in Fig. 3.3.2 (RI-j, $1 \leq j \leq 6$), it may be concluded that the statistical method proposed in this study effectively improves the spinning conditions.

In the following sections, the characteristics and DCMD performance of the hollow fiber membranes RI-1, RI-2, RI-3, RI-4, RI-5 and RI-6 are presented and discussed. Finally, the optimum hollow fiber membrane is identified.

Table 3.3.4. Box-Wilson steepest ascent parameters for the spinning parameters.

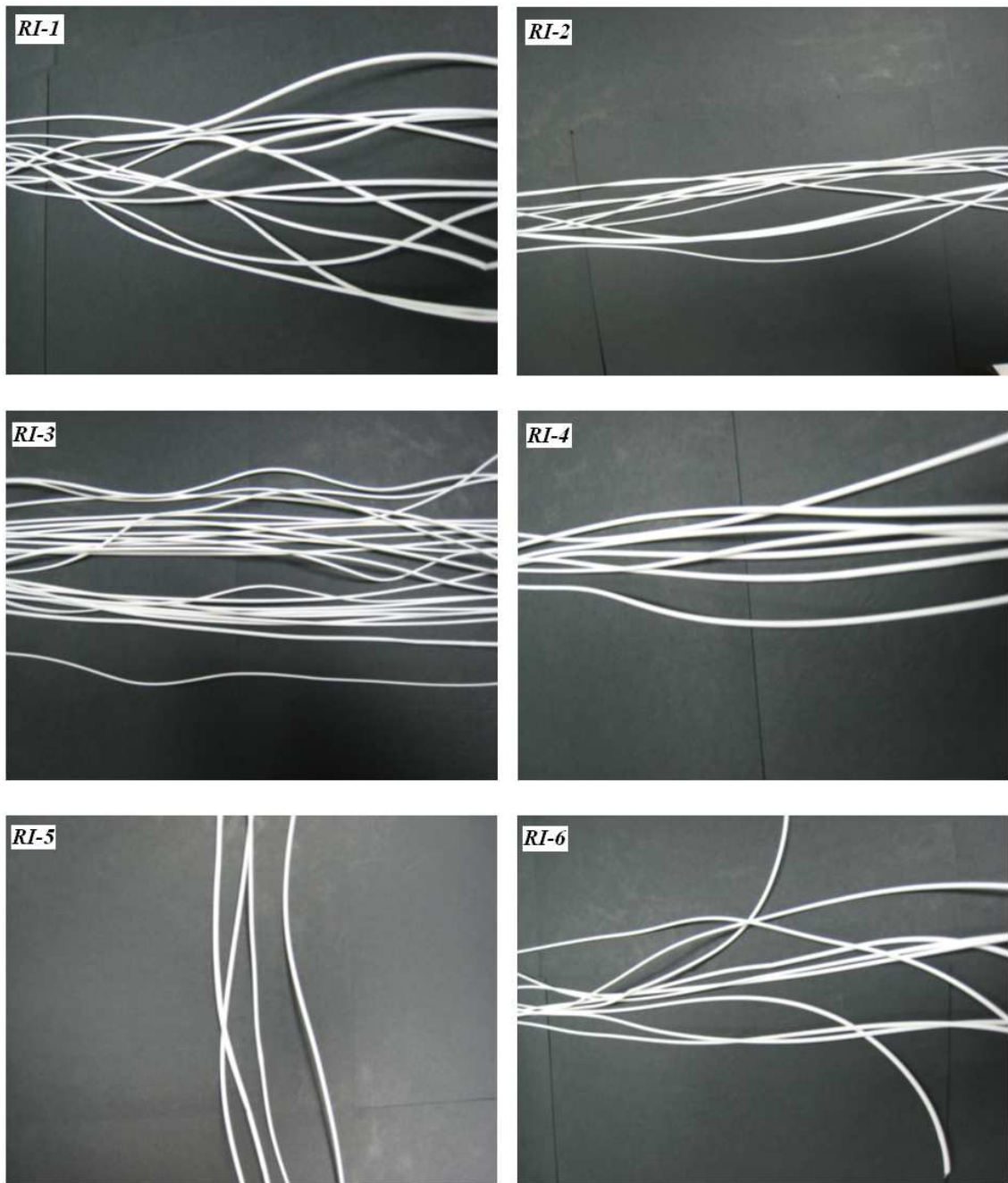|	PVDF-HFP concentration (% w/w)	PEG concentration (% w/w)	Air gap length (cm)	Temperature (^oC)	Internal coagulant flow rate (ml/min)	Take-up speed (rpm)	Pressure (bar)
	z_1	z_2	z_3	z_4	z_5	z_6	z_7
b (main effect)	1.33	1.33	0.29	0	-0.375	0.96	-0.54
z_0 (centre level)	17.5	4	20.5	37.5	22.95	37.5	0.3
Δz (step)	2.5	2	19.5	12.5	13.45	12.5	0.2
$b \cdot \Delta z$	3.325	2.66	5.655	0	-5.04375	12	-0.108
Δ (displacement)	0.25	0.200	0.425	0.000	-0.379	0.902	-0.008

Figure 3.3.2. Pictures of PVDF-HFP hollow fiber membranes fabricated by applying Box-Wilson steepest ascent method.

Table 3.3.5. Steepest ascent displacements to identify the spinning region of interest.

	PVDF-HFP concentration (% w/w)	PEG concentration (% w/w)	Air gap length (cm)	Temperature (°C)	Internal coagulant flow rate (ml/min)	Take-up speed (rpm)	Pressure (bar)
	z_1	z_2	z_3	z_4	z_5	z_6	z_7
Start point	17.50	4.00	20.50	37.50	22.95	1.00	0.30
1	17.75	4.20	20.93	37.50	22.57	1.90	0.29
2	18.00	4.40	21.35	37.50	22.19	2.80	0.28
3	18.25	4.60	21.78	37.50	21.81	3.71	0.28
4	18.50	4.80	22.20	37.50	21.43	4.61	0.27
5	18.75	5.00	22.63	37.50	21.05	5.51	0.26
6	19.00	5.20	23.05	37.50	20.67	6.41	0.25
7	19.25	5.40	23.48	37.50	20.30	7.32	0.24
8	19.50	5.60	23.90	37.50	19.92	8.22	0.24
9	19.75	5.80	24.33	37.50	19.54	9.12	0.23
10	20.00	6.00	24.75	37.50	19.16	10.02	0.22

Table 3.3.6. Experimental conditions for fabrication of hollow fibers in the region of interest.

	PVDF-HFP concentration (% w/w)	PEG concentration (% w/w)	Air gap length (cm)	Temperature ($^{\circ}$C)	Internal coagulant flow rate (ml/min)	Take-up speed (rpm)	Pressure (bar)
	z_1	z_2	z_3	z_4	z_5	z_6	z_7
RI-1	20	6	25	37.5	19	10	0.2
RI-2	20	6	25	37.5	19	10	0.3
RI-3	20	6	25	37.5	19	20	0.3
RI-4	20	6	25	37.5	19	0	0.3
RI-5	20	6	25	37.5	15.8	0	0.3
RI-6	20	6	25	37.5	28.5	0	0.3

3.3.3.2. Hollow fibers characteristics

The cross-sectional structure of the hollow fiber membranes RI-1, RI-2, RI-3, RI-4, RI-5 and RI-6 was examined by SEM. The SEM images are shown in Fig. 3.3.3. Four layers were detected: (1) inner-edge layer, (2) inner-middle layer, (3) outer-middle layer and (4) outer-edge layer.

As can be seen in Fig. 3.3.3 all membranes exhibit a finger-like structure in all outer and inner layers. Moreover, both the inner-middle and the outer-middle layers contain macro-voids. The thickness of each layer was estimated and the results are presented in Fig. 3.3.4. The highest thickness corresponds to the inner-middle layer (2) and the inner-edge and outer-edge layers are very thin. In addition, based on SEM images the percentage of area covered by macrovoids was estimated for each hollow fiber membrane. The results are summarized in Fig. 3.3.5. The hollow fiber membrane RI-4 exhibits the highest percentage of macrovoids (75.75%).
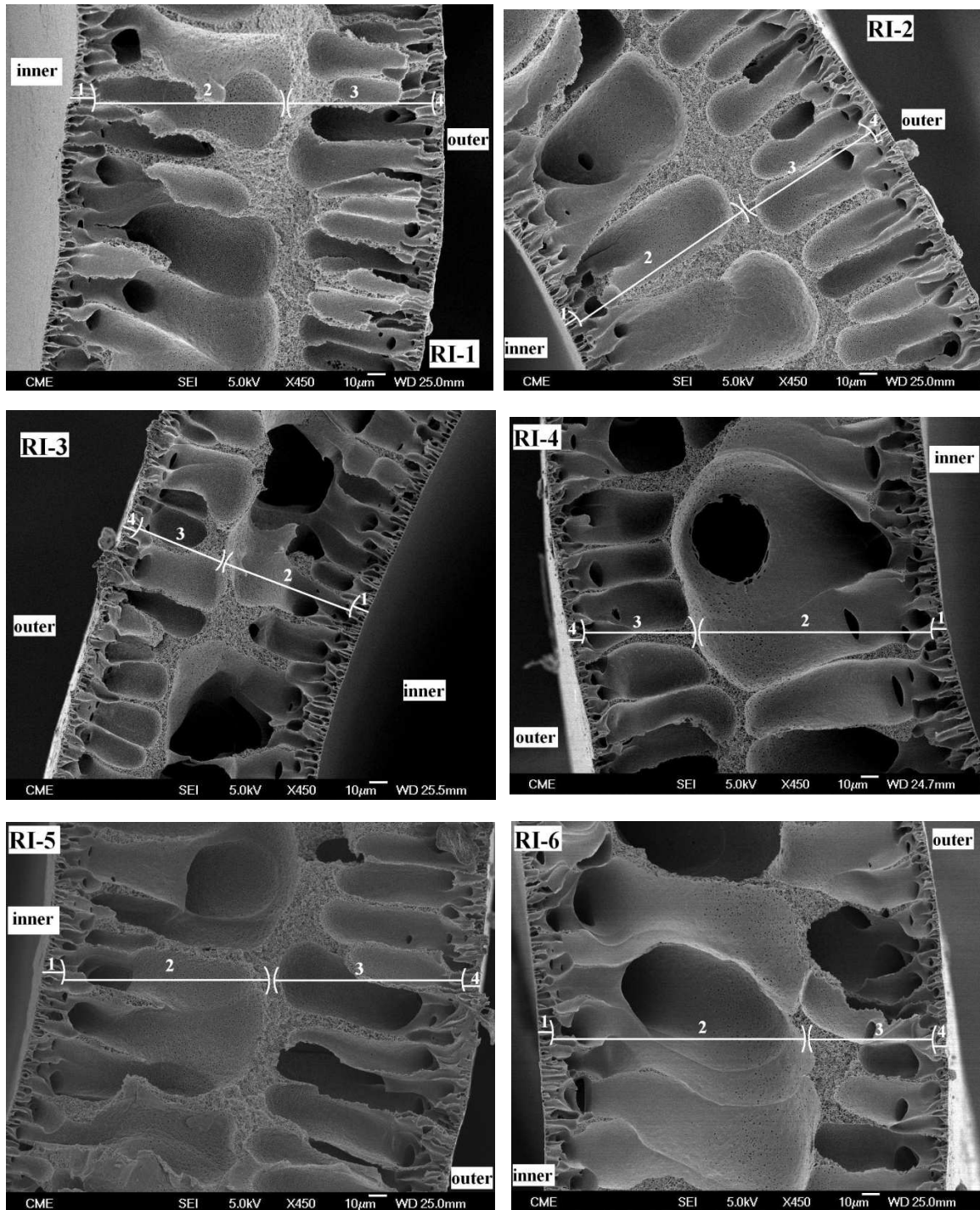
Figure 3.3.3. SEM cross-sectional structure of PVDF-HFP hollow fiber membranes.
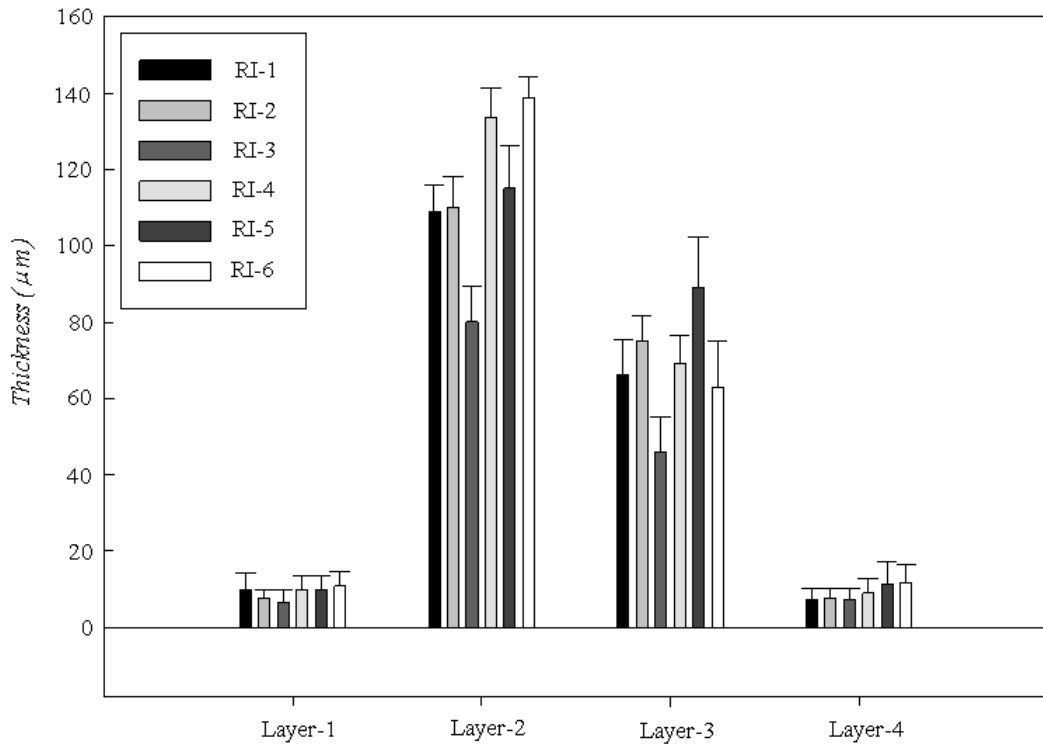
Figure 3.3.4. Estimated thickness of the inner-edge layer (1), inner-middle layer (2), outer-middle layer (3) and outer-edge layer (4) of the SEM images of PVDF-HFP hollow fiber membranes presented in Fig. 3.3.3.
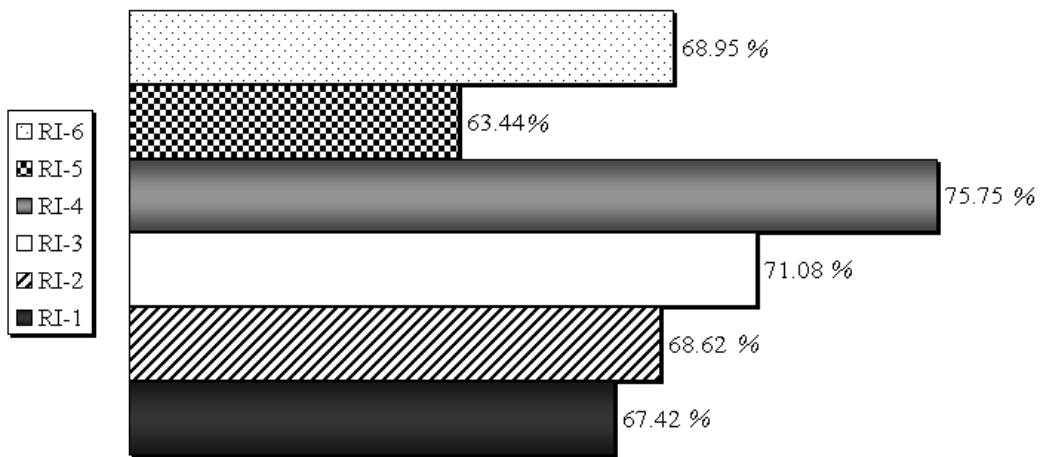
Figure 3.3.5. Estimated area covered by macrovoids in SEM cross-sectional images of the PVDF-HFP hollow fiber membranes presented in Fig. 3.3.3.

The inner and outer surfaces of the hollow fiber membranes (RI-1, RI-2, RI-3, RI-4, RI-5 and RI-6) were characterized by AFM. Figures 3.3.6 and 3.3.7 illustrate the 3D AFM images of the inner and outer surfaces, respectively. AFM images revealed that the surfaces of all membranes are not smooth and possess nodule-like and valley-like structures. The nodules are seen as bright peaks, whereas the pores are seen as dark depressions (i.e. valleys).

Figure 3.3.6. AFM images of the inner surface of PVDF-HFP hollow fibers.

Figure 3.3.7. AFM images of the outer surface of PVDF-HFP hollow fibers.

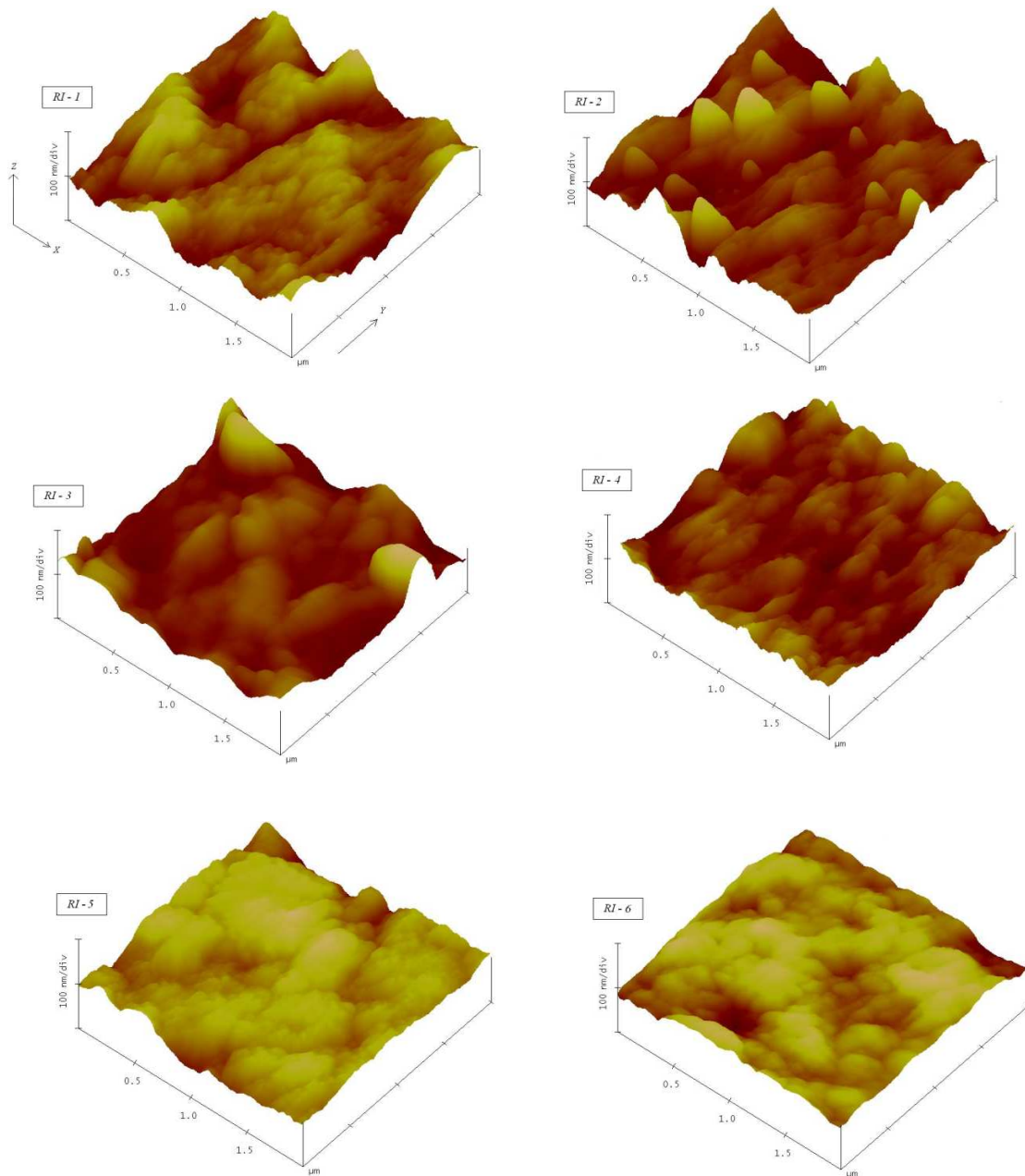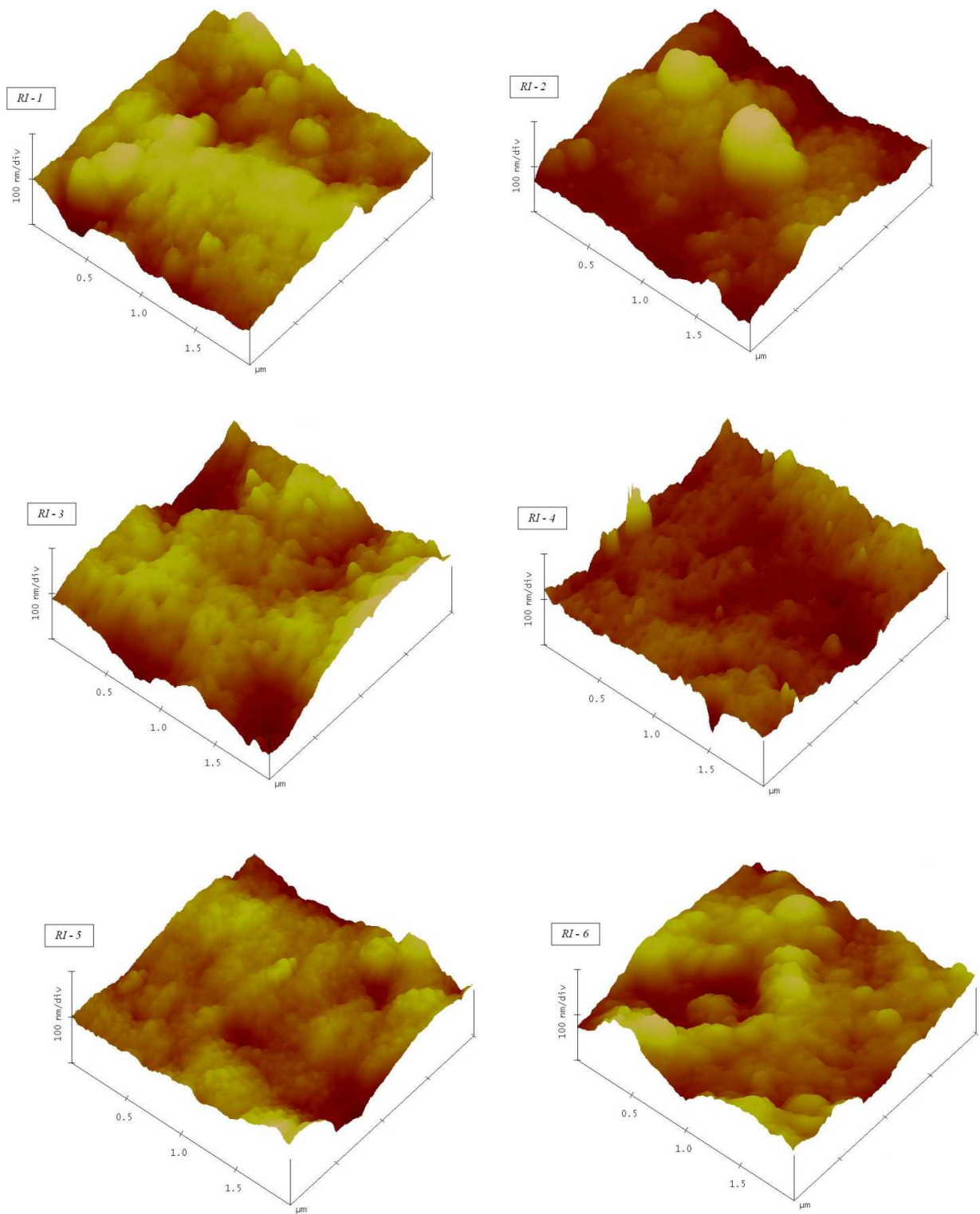The pore sizes, pore size distribution, nodule sizes and the mean roughness of both the inner and outer surfaces were determined from the AFM images as stated elsewhere [22,23]. The mean pore size and its geometric standard deviation as well as the minimum, maximum and mean nodule size of each hollow fiber membrane are summarized in Table 3.3.7. The mean roughness of the outer surface is higher than that of the inner surface, whereas no clear tendency can be detected from Table 3.3.7 for the mean pore size and the mean nodule size.

Table 3.3.7. AFM mean pore size, nodule size and mean roughness of the spun hollow fiber membranes.

Membrane / Thickness (µm)	Surface	Mean pore size (µm)	Nodule size (µm)	Mean roughness (nm)
RI-1 (176 ± 29) µm	Inner	104.6±1.144	Min: 46.875; Max: 242.19 Mean: 150.24±1.161	12.641
	Outer	95.09±1.130	Min: 54.680; Max: 218.75 Mean: 119.99±1.128	14.989
RI-2 (159 ± 8) µm	Inner	111.22±1.139	Min: 54.68; Max: 195.31 Mean:136.84±1.114	15.219
	Outer	90.68±1.146	Min: 70.313; Max: 468.00 Mean:166.45±1.160	22.878
RI-3 (203 ± 24) µm	Inner	117.81±1.114	Min: 78.125; Max: 250.00 Mean:158.57±1.122	12.498
	Outer	77.85±1.118	Min: 46.875; Max: 156.25 Mean:100.63±1.106	13.384
RI-4 (235 ± 13) µm	Inner	101.33±1.139	Min: 46.875; Max: 187.50 Mean: 119.28±1.125	10.806
	Outer	83.09±1.137	Min: 39.063; Max: 156.25 Mean:103.54±1.125	12.570
RI-5 (203 ± 54) µm	Inner	98.15±1.111	Min: 62.50; Max: 203.13 Mean:133.14±1.100	8.878
	Outer	126.49±1.122	Min: 78.125; Max: 226.56 Mean: 146.14±1.098	9.230
RI-6 (154 ± 9) µm	Inner	117.93±1.140	Min: 70.313; Max: 210.94 Mean: 150.34±1.101	10.434
	Outer	121.26±1.123	Min: 62.50; Max: 218.75 Mean:143.16±1.104	14.035

The cumulative pore size distribution and the probability density function curves are plotted in Figs. 3.3.8 and 3.3.9 for the inner and outer surfaces, respectively. A narrow pore size distribution is observed for the inner surfaces.
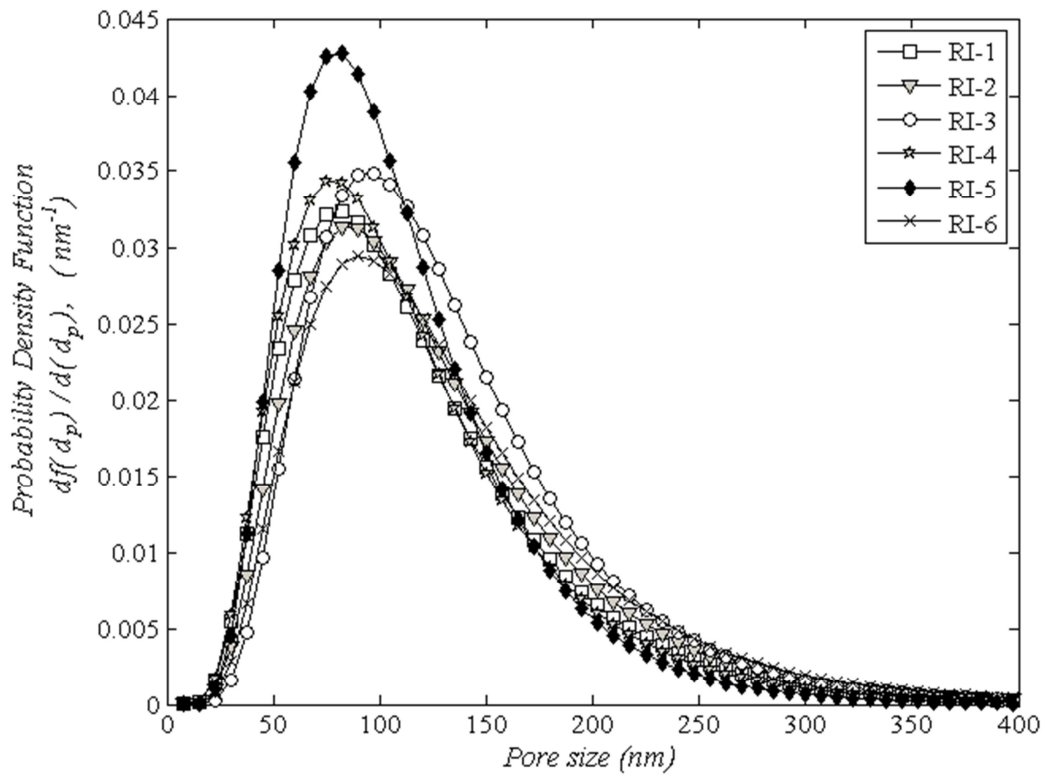

Figure 3.3.8. Probability density function of pores sizes determined from AFM images of the inner surfaces of the PVDF-HFP hollow fiber membranes
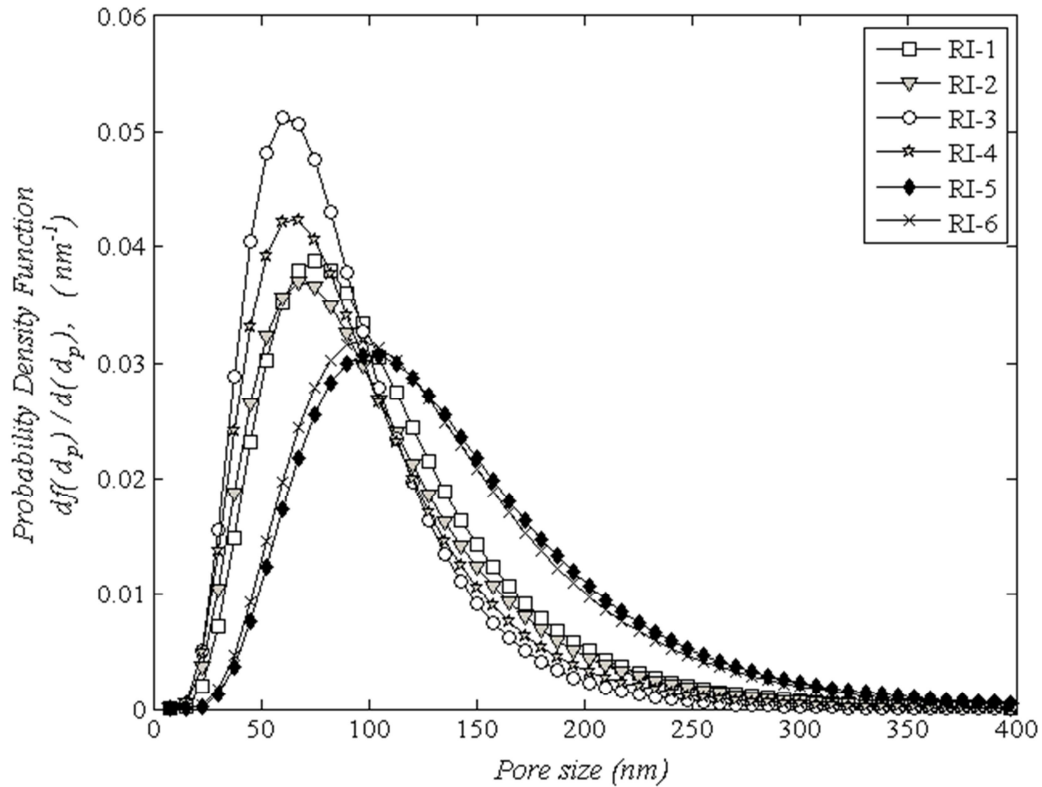
Figure 3.3.9. Probability density function of pores sizes determined from AFM images of the outer surfaces of the PVDF-HFP hollow fiber membranes.

It is known that the liquid entry pressure of water (LEP_w) is related to the hydrophobicity of the hollow fiber and to the maximum pore sizes [17,18]. The LEP_w decreases with the increase of the maximum pore size and/or the decrease of the water contact angle at the membrane surface (i.e. less hydrophobicity).

The measured LEP_w values of the hollow fiber membranes are shown in Fig. 3.3.10 (a). The highest LEP_w corresponds to the membrane RI-3 followed by RI-5 and RI-4. The hollow fiber membranes RI-2 and RI-6 have quite similar LEP_w value, while RI-1 membrane shows the smallest LEP_w value. Therefore, due to the fact that the same hydrophobic material (PVDF-HFP) is used for fabrication of all hollow fiber membranes, it may be expected a decrease of the maximum pore size of the hollow fiber membranes following the order: RI-1 > RI-6 > RI-2 > RI-4 > RI-5 > RI-3. However, this order can not be obtained from the AFM pore sizes (Figs. 3.3.8

255

and 3.3.9) because the pore sizes of both the inner and outer surfaces of the hollow fibers should be taken into consideration.
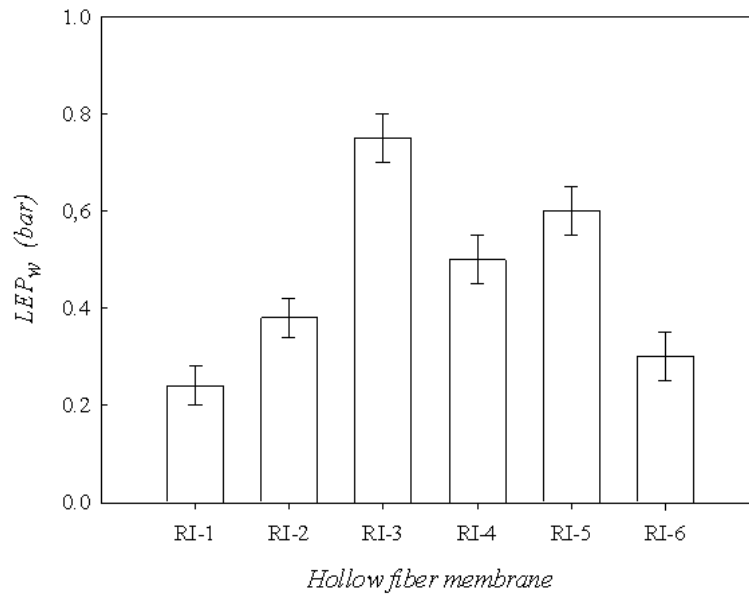
(a)
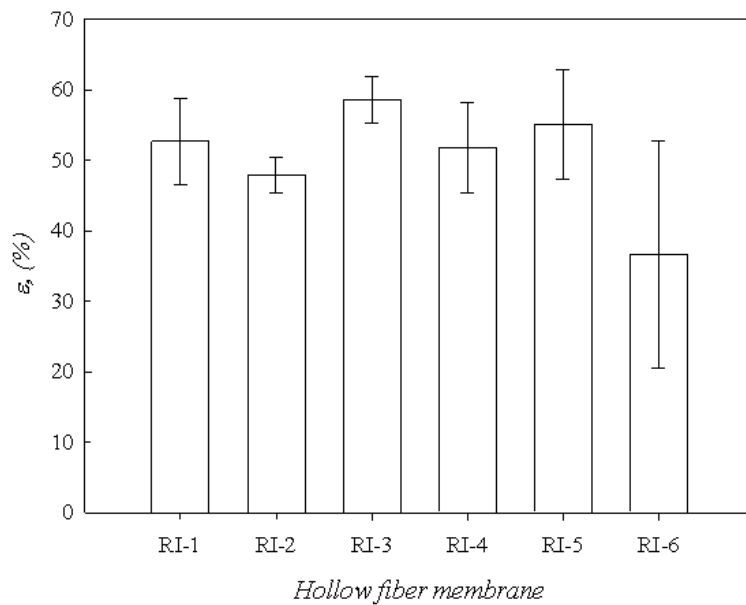
(b)

Figure 3.3.10. Liquid entry pressure of water, LEP_w (a) and porosity, ε (b) of the PVDF-HFP hollow fiber membranes.

The porosity was determined for each hollow fiber membrane and the results are shown in Fig. 3.3.10 (b). As can be seen, the porosity varies in the range 37 - 55 %. The highest porosity was found for the membrane RI-3, while the lowest porosity was obtained for the hollow fiber membrane RI-6. By comparing the porosity with the void volume presented in Fig. 3.3.5, no clear relationship can be built. This may be attributed to the porosity values that are close to each other, to the high standard deviation of the measured porosity value and also partly to the possible presence of dead-ended void volume.

3.3.3.3. Hollow fibers DCMD performance

Taking into consideration the characteristics of the prepared hollow fiber membranes RI-1, RI-2, RI-3, RI-4, RI-5 and RI-6, those were tested in desalination by DCMD. The permeate fluxes of feed distilled water and salt aqueous solution (0.5M NaCl) were measured as stated earlier at a feed inlet temperature of 75 ºC, a permeate inlet temperature of 20 ºC, a feed flow rate of 0.2 L/min and a permeate flow rate of 0.3 L/min. Note that 5 fibers with the length of 20 cm were packed in each module. The salt rejection factor (R) was determined and all membranes show rejection factors varying from 91.9% to 97.5%.

The DCMD permeate flux are reported in Fig. 3.3.11. The highest permeate flux was obtained for the membrane RI-4. This result can be correlated with the high content of macrovoids of this hollow fiber membrane (Fig. 3.3.5). The inner and outer pore sizes of the membrane RI-4 is smaller than some of the other membranes, while the porosity is similar to the other membranes taking into account the standard deviation. Similarly high permeate fluxes were obtained for the membranes RI-3 and RI-6. Again, these membranes exhibited high content of macrovoids through their cross-section. No clear trends could be plotted between the permeate flux and the pore sizes neither with the porosity. It should be noted that the thickness of the hollow fiber membranes also affect the DCMD permeate flux.
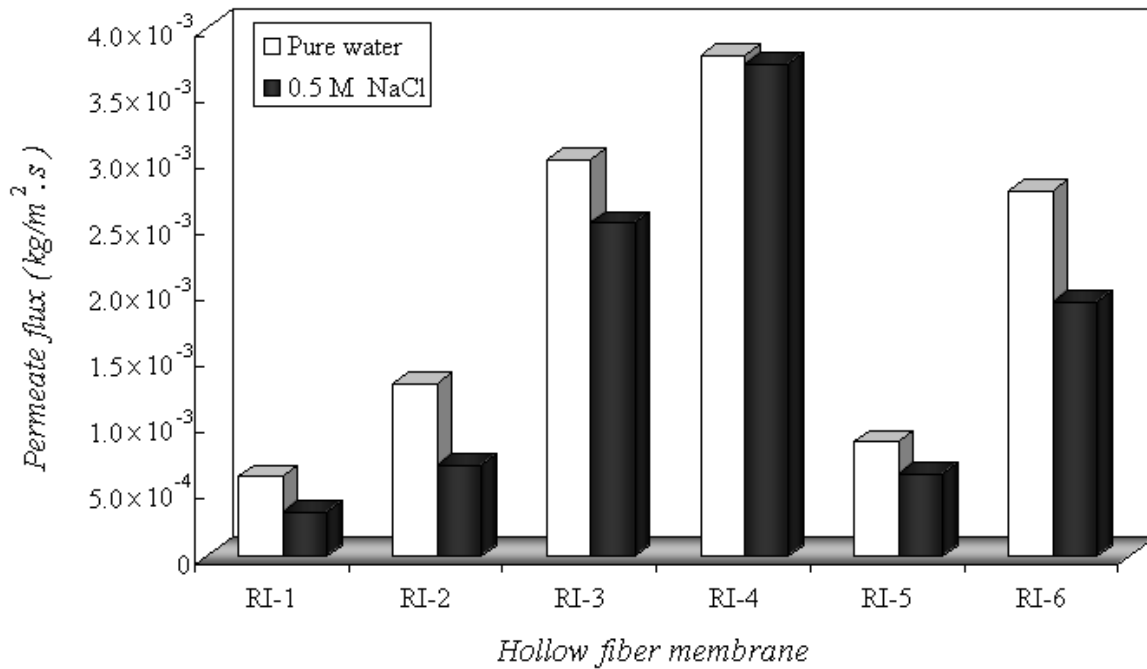
Figure 3.3.11. DCMD permeate flux of feed distilled water and salt aqueous solution of the PVDF-HFP hollow fiber membranes.

The optimal membrane was selected based on the high DCMD performance (i.e. permeate flux and salt rejection factor). In this case, although the contribution of the salt rejection factor to the DCMD performance is not significant compared to the contribution of the permeate flux, the salt rejection factor was also taken into consideration. To choose the optimal hollow fiber membrane, the permeate flux and the salt rejection factor can be joined in a single response, the performance index (PI), which is calculated as follows:

$$PI = J \cdot R \tag{3.3.4}$$

The desirability function was also employed. In this case, each individual response (i.e. permeate flux and salt rejection factor) was converted into a dimensionless value called individual desirability (d_J for the permeate flux and d_R for the salt rejection factor) that varies in the range $0 \leq d_i \leq 1$. Then the global desirability (D) was computed as a geometric mean of the two individual desirability values. In our case, for the two responses, the permeate flux (J) and the salt rejection factor (R), the overall desirability was written as:

258

$$D = \sqrt{d_J \times d_R}$$

(3.3.5)

where d_J and d_R are the individual desirability values for the permeate flux and salt rejection factor, respectively. Since we are looking for the maximal values of both the permeate flux and the salt rejection coefficient, the corresponding individual desirability values were computed based on the individual desirability functions of LTB-type (the-larger-the-best) [24,25].

Figure 3.3.12 shows the performance index and the overall desirability for each hollow fiber membrane. The result indicates that the optimal hollow fiber membrane is the membrane RI-4 exhibiting the highest DCMD flux (3.74×10^{-3} kg/m^2.s), the highest performance index and the greatest desirability. Remember that the optimal PVDF-HFP membrane RI-4 was prepared using the following spinning conditions: 20% w/w PVDF-HFP, 6% w/w PEG, 25 cm air gap distance, 37.5 °C an internal/external coagulation temperature, 19 ml/min flow rate of the internal coagulant, 0.3 bar pressure and free falling.

Figure 3.3.12. DCMD performance index and global desirability of PVDF-HFP hollow fiber membranes.

It is worth quoting that Wang et al [26] prepared hydrophobic PVDF hollow fiber membranes for fresh water production using DCMD and observed a permeate flux as high as 11.53×10^{-3} kg/m^2.s for a feed inlet temperature of 79.3 ^{o}C, a permeate inlet temperature of 17.5 ^{o}C and 3.5 wt% NaCl feed aqueous solution. Dual layer hydrophobic/hydrophilic PVDF hollow fiber membranes were fabricated by Bonyadi and Chung for desalination by DCMD [27]. A permeate flux as high as 15.3×10^{-3} kg/m^2.s was obtained for a feed inlet temperature of 90 ^{o}C a feed temperature of 16.5 ^{o}C and 3.5 wt% NaCl feed aqueous solution. These permeate fluxes are greater than the permeate flux obtained in this study for the optimum PVDF-HFP hollow fiber membrane. This is attributed in part to the higher DCMD driving force (i.e. high feed temperature and low permeate temperature) applied in [26,27] and also to the type of the polymer used. Compared to other PVDF-HFP hollow fiber membranes fabricated with the same copolymer [8,9], the permeate flux of the optimum membrane prepared in this study is higher.

4. Conclusion

A fractional factorial experimental design was applied for hollow fiber spinning using a large domain of variation of 7 factors namely, polymer concentration, additive concentration, air gap length, temperature of both internal and external coagulants as well as the temperature of the polymer solution, flow rate of the internal coagulant, take-up speed and pressure applied on the polymer solution. Due to the wide range of operation, different spun products were obtained (hollow fiber with cylindrical shape and spinning continuity without defects, impossible spinning, fibers with visible defects such as loops and coiled segments, discontinuous spun hollow fiber, twisted fibers, flat shapes, etc.). These spun products were analyzed from a qualitative point of view in terms of spinning continuity, cylindrical and hollow shapes and magnitude of visible defects. Box-Wilson steepest ascent method was applied to localize the spinning experimental region of interest. Once the experimental region was defined, 6 hollow fiber membranes with different spinning parameters were prepared. These membranes were characterized by SEM, AFM, *LEPw* measurement and porosity measurements. were determined for each hollow fiber membrane. Finally the hollow fiber membranes were tested for desalination by DCMD. The optimal hollow fiber membrane was identified based on the highest DCMD performance index and desirability (i.e. the highest product between the permeate flux and the salt rejection factor). More research studies are needed to increase the DCMD performance of PVDF-HFP hollow fiber membranes. The approach presented in this work is useful to avoid the inadequate spinning conditions and to figure out a proper experimental domain for spinning (i.e. region of interest).

References:

[1] Y. Fujii, S. Kigoshi, H. Iwatani, M. Aoyama, Selectivity and characteristics of direct contact membrane distillation type experiment: I. Permeability and selectivity through dried hydrophobic fine porous membranes, J. Membrane Sci., 72 (1992) 53-72.

[2] Y. Fujii, S. Kigoshi, H. Iwatani, M. Aoyama, Y. Fusaoka, Selectivity and characteristics of direct contact membrane distillation type experiment: II. Membrane treatment and selectivity increase, J. Membrane Sci., 72 (1992) 73-89.

[3] B. Wu, K. Li, W.K. Teo, Preparation and characterization of poly(vinylidene fluoride) hollow fiber membranes for vacuum membrane distillation, J. Appl. Polymer Sci., 106 (2007) 1482-1495.

[4] B. Wu, X. Tan, K. Li, W.K. Teo, Removal of 1,1,1-trichloroethane from water using a poly(vinylidene fluoride) hollow fiber membrane module: Vacuum membrane distillation operation, Sep. & Purf. Tech., 52 (2006) 301-309.

[5] K.Y. Wang, T.S. Chung, M. Gryta, Hydrophobic PVDF hollow fiber membranes with narrow pore size distribution and ultra-skin for the fresh water production through membrane distillation, Chem. Eng. Sci., 63 (2008) 2587-2594.

[6] S. Bonyadi, T.S. Chung, Highly porous and macrovoid-free PVDF hollow fiber membranes for membrane distillation by a solvent-dope solution co-extrusion approach, J. Membrane Sci., 331 (2009) 66-74.

[7] J. Li, Z. Xu, Z. Liu, W. Yuan, H. Xiang, S. Wang, Y. Xu, Microporous polypropylene and polyethylene hollow fiber membranes: Part 3. Experimental studies on membrane distillation for desalination, Desalination, 155 (2003) 153-156.

[8] M.C. García-Payo, M. Essalhi, M. Khayet, Preparation and characterization of PVDF–HFP copolymer hollow fiber membranes for membrane distillation, Desalination, 245 (2009) 469-473.

[9] M.C. García-Payo, M. Essalhi, M. Khayet, Effects of PVDF-HFP concentration on membrane distillation performance and structural morphology of hollow fiber membranes, J. Membrane Sci., 347 (2010) 209-219.

[10] X. Yang, R. Wang, L. Shi, A.G. Fane, M. Debowski, Performance improvement of PVDF hollow fiber-based membrane distillation process, J. Membrane Sci., 369 (2011) 437-447.

[11] R.E. Raj, B.S.S. Daniel, Customization of closed-cell aluminium foam properties usind design of experiments, Mater. Sci. Eng. A, 528 (2011) 2067-2075.

[12] K. Dehghani, A. Nekahi, M.A.M. Mirzaie, Using response surface methodology to optimize the strain aging response of AA5052, Mater. Sci. Eng., A 527 (2010) 7442-7451.

[13] M. Khayet, C. Cojocaru, G. Zakrzewska-Trznadel, Response surface modeling and optimization in pervaporation, J. Membrane Sci. 321 (2008) 272-283.

[14] M. Khayet, C. Cojocaru, C. García-Payo, Application of response surface methodology and experimental design in direct contact membrane distillation, Ind. Eng. Chem. Res., 46 (2007) 5673-5685.

[15] M. Khayet, C. Cojocaru, M.C. García-Payo, Experimental design and optimization of asymmetric flat-sheet membranes prepared for direct contact membrane distillation, J. Membrane Sci., 351 (2010) 234-245.

[16] M. Khayet, M.C. García-Payo, F.A. Qusay, M.A. Zubaidy, Structural and performance studies of poly(vinyl chloride) hollow fiber membranes prepared at different air gap lengths, J. Membrane Sci., 330 (2009) 30-39.

[17] M. Khayet, C. Y. Feng, K. C. Khulbe, T. Matsuura, Preparation and characterization of polyvinylidene fluoride hollow fiber membranes for ultrafiltration, Polymer, 43 (2002) 3879-3890.

[18] M. Khayet, A. Velázquez, J.I. Mengual, Direct contact membrane distillation of humic acid solutions, J. Membrane Sci., 240 (2004) 123-128.

[19] T. Lundstedt, E. Seifert, L. Abramo, B. Thelin, Å. Nyström, J. Pettersen, R. Bergman, Experimental design and optimization, Chemometrics & Intelligent Laboratory Systems, 2 (1998) 3-40.

[20] S. Akhnazarova and V. Kafarov, Experiment Optimization in Chemistry and Chemical Engineering, Mir Publishers, Moscow, 1982.

[21] G.E.P. Box, K.B. Wilson, On the Experimental Attainment of Optimum Conditions. J. Royal Statistical Society Series B, 13 (1951) 1 – 45.

[22] M. Khayet, Membrane surface modification and characterization by X-ray photoelectron spectroscopy, atomic force microscopy and contact angle measurements, Applied Surface Sci., 238 (2004) 269-272.

[23] M. Khayet, T. Matsuura, Determination of surface and bulk pore sizes of flat-sheet and hollow-fiber membranes by atomic force microscopy, gas permeation and solute transport methods Desalination 158(1-3) (2003) 57-64.

[24] G. Derringer and R. Suich, Simultaneous optimization of several response variables, J. Qual. Technol. 12 (1980) 214–221.

[25] I.J. Jeong and K.J. Kim, D-STEM: a modified step method with desirability function concept, Comput. Oper. Res. 32 (2005) 3175–3190.

[26] K.Y. Wang, T.S. Chung, M. Gryta, Hydrophobic PVDF hollow fiber membranes with narrow pore size distribution and ultra-thin skin for the fresh water production through membrane distillation, Chem. Eng. Sci., 63 (2008) 2587-2594.

[27] S. Bonyadi, T.S. Chung, Flux enhancement in membrane distillation by fabrication of dual layer hydrophilic–hydrophobic hollow fiber membranes, J. Membrane Sci., 306 (2007) 134-146.

CHAPTER 4

NANO-FIBROUS AND MICRO-FIBROUS MEMBRANES

FOR DESALINATION

BY MEMBRANE DISTILLATION (MD)

4.1. Response Surface Modeling and Optimization of Electrospun Nanofiber Membranes

Contents:

4.1.1. Introduction

4.1.2. Materials and Methodology

    4.1.2.1. Materials

    4.1.2.2. Preparation of electro-spun PVDF fibers

    4.1.2.3. Characterization

4.1.3. Results and Discussions

4.1.4. Conclusions

References

Abstract:

The experimental design and response surface methodology (RSM) have been used to develop predictive models for simulation and optimization of electrospun polyvinylidene fluoride non-woven membranes. The objective is to prepare electrospun fibers with small diameters and narrow diameter distribution. The factors considered for experimental design were the polymer dope solution flow rate, the applied electric voltage and the distance between the needle tip and the collector. A full factorial design was considered. The obtained electrospun fibers were characterized by scanning electron microscopy. The response for the model was the quality loss function that takes into account the quadratic effects of both the weighted arithmetic mean of the fibers diameter and the standard deviation. Minimal output response has been predicted and confirmed experimentally. The optimum operating conditions guarantying a small polyvinylidene fluoride nanofiber diameter with a narrow distribution were a voltage of 24.1 kV, an air gap of 27.7 cm and a polymer flow rate of 1.23 mL/h. The fabricated optimum membrane was characterized by different techniques and applied for desalination by membrane distillation. The obtained permeate fluxes in this study are higher than those reported so far for electrospun nanofibrous membranes.

4.1.1. Introduction

Electrospinning has been recognized as an efficient technique for the fabrication of polymer nanofibers. These have attracted increasing attentions in the last ten years because of their very large surface area to volume ratio, flexibility in surface functionalities and superior mechanical performance compared with any other known form of materials. These outstanding properties make the polymer nanofibers optimal candidates for many advanced applications in fields such as biomedical engineering and biotechnology, environmental engineering, energy storage, tissue engineering, drug delivery, affinity membranes, enzyme immobilization, etc [1-6].

Electrospinning can also organize nanofibers of various types such as porous, hollow and core/sheath into well-defined arrays or hierarchical architectures in three-dimensional networks. Numerous studies have been carried out to gain deep understanding of the process for a better control of fiber formation [7-14].

Nowadays, systematic investigations of the effects of electrospinning variables on diameter and morphology of the electrospun fibers are of great interest. Obviously, there is an important need to produce fibers with small and uniform size so that the electrospinning process can be reproduced in large industrial applications [2,5,15]. Many parameters can affect the morphological structure and dimensions of electrospun fibers. These are system parameters such as polymer type and its molecular weight, polymer concentration, solvent type and polymer solution properties (viscosity, conductivity and surface tension); process parameters such as electric potential or voltage, flow rate of polymer solution, distance between the capillary and collector and ambient parameters (temperature, humidity and air velocity) [7-10,16-21]. Moreover, for preparation of nanofibrous membranes, the conventional or classical method of experimentation, which involves changing one of the independent parameters while maintaining the others fixed at given values, has been considered [16-21]. As it is well known, this conventional method of experimentation involves many tests, which are time-consuming, ignores interaction effects between the operating parameters and induces a low efficiency in optimization. These limitations can be avoided by applying the Response Surface Methodology (RSM) that involves statistical design of experiments (DoE) in which all factors are varied together over a set of experimental runs [22,23]. In fact, the statistical method of experimental design offers several advantages over the frequently used conventional method being rapid and reliable, helps

in understanding the interaction effects between factors and reduces the total number of experiments tremendously resulting in saving time and costs of experimentation. Moreover, RSM can be used to evaluate the relative significance of several affecting factors even in the presence of complex interactions [22-29].

In recent years various statistical experimental designs and RSM have been applied progressively to different processes [22-29]. However, among them few reports were dedicated to electrospinning [20,30]. Yördem et al. [20] studied the effects of electrospinning parameters on polyacrylonitrile (PAN) nanofiber diameter using RSM. Their investigations were carried out using only two variables (applied voltage, solution concentration) but several collector distances. The effect of the applied voltage on fiber diameter was insignificant when the solution concentration and collector distance were high. Similarly, Gu et al. [30] applied RSM for PAN nano-fibers and also reported no significant effect of the voltage on the PAN nanofibers. Both studies have been conducted considering two variables while the third parameter was maintained fixed, and therefore possible interactions between the three parameters were not studied [20,30].

Polyvinylidene fluoride (PVDF) is an attractive material used in many applications due to its outstanding properties such as high mechanical strength, thermal stability, chemical resistance and good electrochemical stability compared to other commercialized polymeric materials. Electrospinning technique has also been applied to the fabrication of PVDF nanofibers and fibrous thin films for various applications [11-14].

In the present study a full factorial experimental design for fabrication of electrospun PVDF fibers has been considered. The polymer solution parameters (polymer type, molecular weight, solvents) and the environmental conditions (temperature and humidity) are maintained the same to prepare all ENMs. The main objective of this paper is to investigate the individual and mutual effects of the electrospinning variables (applied voltage, polymer solution flow rate and distance between the needle tip and the collector) on the diameter of the electrospun PVDF fibers as well as on fiber distribution. Furthermore, the optimum electrospinning conditions to ensure minimum fiber diameter with a narrow size distribution has been determined. An interesting application for ENMs is the non-isothermal distillation, which can be carried out for advanced water treatments without applying any transmembrane hydrostatic pressure and therefore self-sustained webs can be used [31-35]. Therefore, the fabricated

271

optimum membrane was characterized by different techniques and applied for desalination by direct contact membrane distillation (DCMD) using different salt (NaCl) aqueous concentrations. The DCMD performance is compared to other electrospun nanofibrous membranes [34,35].

4.1.2. Materials and Methodology

4.1.2.1. Materials

The spinning solutions were prepared from the polymer PVDF (M_w = 275 kg/mol and M_n = 107 kg/mol) and the mixed solvents *N,N*-dimethyl acetamide (DMAC) and acetone purchased from Sigma–Aldrich Chemical Co. Isopropyl alcohol (IPA) was used to determine the void volume fraction and the size of the inter-fiber space, and the sodium chloride (NaCl) used in DCMD experiments was also purchased from Sigma-Aldrich Chemical Co.

4.1.2.2. Preparation of electro-spun PVDF fibers

The polymer solution was prepared using 25 wt% PVDF in the mixture 20 wt% acetone in DMAC. The electrospinning set-up is shown in Fig. 4.1.1 and consists of a syringe (50 ml, Nikepal) to hold the polymer solution, a pump (KDS Scientific, model 200), two electrodes (a metallic needle of 0.60 mm internal diameter and a grounded copper collector covered with aluminum foil) and a DC voltage supply in the kV range (Iseg, TCIP300 304p). The formed fibers were then dried in an oven at 80ºC for 5 min (i.e. post-treatment).
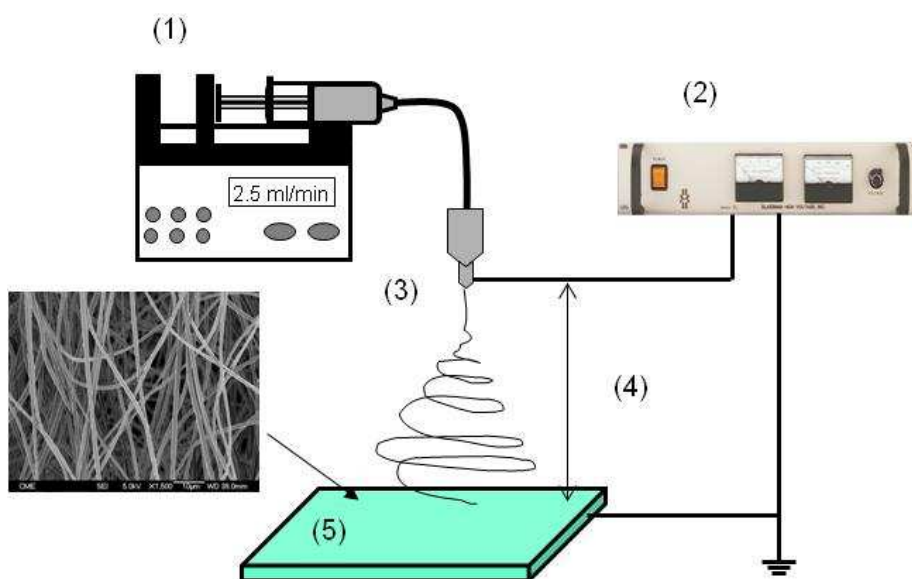
Figure 4.1.1. Schematic diagram of electrospinning set-up. (1) Syringe with polymer solution, (2) high voltage supply, (3) spinneret, (4) distance between the needle tip and the collector, (5) collector.

PVDF electrospun fibers have been prepared following the experimental design conditions summarized in Table 4.1.1. The electrospinning parameters are the dope solution flow rate F (mL/h), the voltage U (kV) and the distance A (cm) between the needle tip and the collector, named hereafter as collector distance.

Table 4.1.1. Full factorial design for electrospinning experiments.

Run	Voltage		Collector distance		Polymer flow rate	
	x_1	$U\ (kV)$	x_2	$A\ (cm)$	x_3	$F\ (mL/h)$
B1	+1	24.5	+1	28.23	+1	3.28
B2	-1	10.5	+1	28.23	+1	3.28
B3	+1	24.5	-1	11.77	+1	3.28
B4	-1	10.5	-1	11.77	+1	3.28
B5	+1	24.5	+1	28.23	-1	1.22
B6	-1	10.5	+1	28.23	-1	1.22
B7	+1	24.5	-1	11.77	-1	1.22
B8	-1	10.5	-1	11.77	-1	1.22
B9	0	17.5	0	20	0	2.25
B10	0	17.5	0	20	0	2.25

4.1.2.3. Characterization

The surface of the non-woven electrospun PVDF membranes was examined by a field emission scanning electron microscope (FESEM, JEOL Model JSM-6330F). Micrographs from the SEM analysis were analyzed by UTHSCSA ImageTool 3.0 to determine the fiber diameter. For each sample more than 5 SEM images have been considered and the diameters of a total number of 100 fibers have been measured. Statistical analysis have been applied in order to determine the fiber size distribution and to estimate the arithmetic weighted mean of the fiber diameters and their dispersion (i.e. weighted standard deviation).

The electrospun nanofibrous PVDF membrane, prepared using the obtained optimum electrospinning conditions over a period of 3h30min, was characterized by different techniques to determine the liquid entry pressure (*LEP*) of distilled water and saline aqueous solutions of different concentrations (12 g/L, 30 g/L and 60 g/L), the

mean size of the inter-fiber space (d_i) by the wet/dry flow method, the advancing water contact angle (θ_a) by a computerized optical system CAM100 (7.1 μL water drop), the void volume fraction (ε) from density measurements and the thickness (δ) by the micrometer Millitron Phywe (Mahr Feinprüf, type TYP1202IC). Details of the characterization techniques used are explained elsewhere [32].

Direct contact membrane distillation (DCMD) was carried out using the fabricated optimum electrospun PVDF membrane under different salt (NaCl) concentrations (0 g/L, 12 g/L, 30 g/L and 60 g/L), a feed temperature of 80ºC and permeate temperature of 20ºC and a stirring rate of both the feed and permeate of 500 rpm. The experimental system used is detailed in [36].

4.1.3. Results and Discussions

The SEM images, together with their corresponding histograms showing the sizes of the electrospun fibers, are presented in Fig. 4.1.2. Differences exist between the SEM images of the samples depending on the electrospinning conditions. The best electrospun fibers have been obtained for the experimental run 5 (B5 in Fig. 4.1.2). The corresponding electrospinning values facilitate stretching of polymer solution along the distance between the needle and the collector and enhance the solvent evaporation leading to the formation of electrospun fibers with small diameters. The worst spinning conditions correspond to the experimental run 4 (B4 in Fig. 4.1.2), which involves the setting of factors at the opposite levels to those in experimental run 5. Such conditions seem to hinder solvent evaporation leading to fusion of fibers. As a result, more fiber-to-fiber contacts are formed.
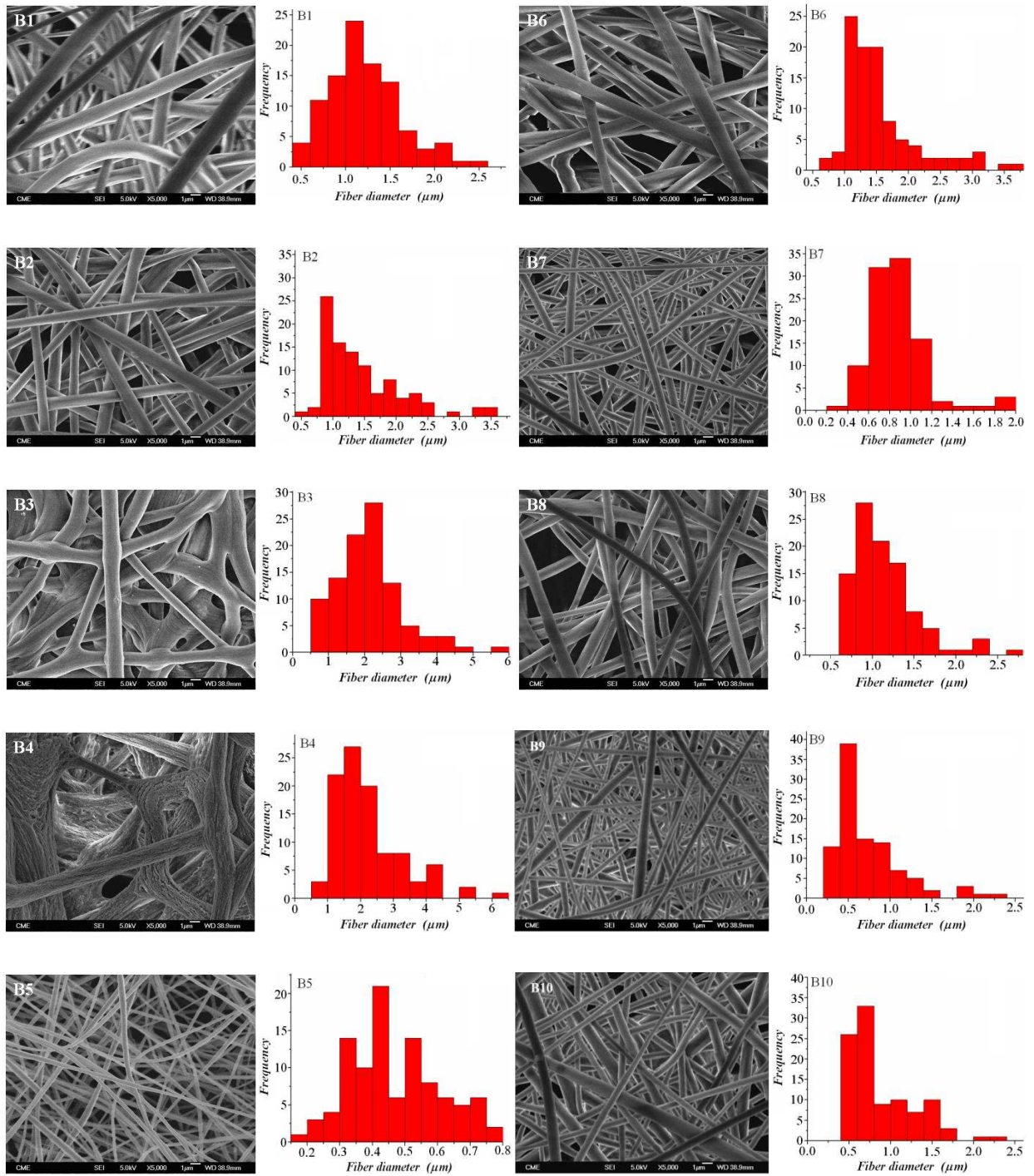
Figure 4.1.2. SEM images of electrospun PVDF fibers (B1,B2,B3,…B10) prepared applying the electrospinning experimental runs summarized in Table 4.1.1.

Based on the statistical analysis of the histograms shown in Fig. 4.1.2, the weighted arithmetic mean (λ_w) of the fiber diameters and the corresponding weighted standard deviation (s_w) have been determined as follows [37]:

$$\lambda_w = \lambda_0 + \frac{h}{N} \sum_{j=1}^{m} u_j \cdot FC_j \tag{4.1.1}$$

$$s_w = \sqrt{\left(\frac{1}{N} \cdot \sum_{j=1}^{m} \left(u_j^2 \cdot FC_j \right) - \left(\frac{1}{N} \cdot \sum_{j=1}^{m} \left(u_j \cdot FC_j \right) \right)^2 \right) \cdot h^2} \tag{4.1.2}$$

where m denotes the number of bins (disjoint categories), h is the bin width, $h = (\lambda_{max} - \lambda_{min})/m$, FC is the frequency count, N is the number of samples in the statistical set (in our case $N=100$), λ_0 is the dominant characteristic of the statistical set that corresponds to the highest peak, u is a variable defined as $u = (\lambda_c - \lambda_0)/h$ and λ_c is the bin characteristic (or bin center).

Finally, the quality loss function (Y) that summarizes the quadratic effect of both weighted arithmetic mean and standard deviation as response for factorial modeling and optimization has been considered. This response is defined as follows [37,38]:

$$Y = \lambda_w^2 + s_w^2 \tag{4.1.3}$$

In this case low Y value means good electrospinning process performance (i.e. low values of λ_w and s_w). Table 4.1.2 summarizes the obtained values of λ_w, s_w and Y determined according to the experimental design. In general, it was found that an increase of s_w is associated to λ_w. The electrospun fiber sample B5 exhibits the lowest values of λ_w, s_w and Y. In contrast, the electro-spun fiber sample B4 has the highest values of λ_w, s_w and Y.

Table 4.1.2. Responses resulted from statistical analysis of electrospun fiber diameter distributions.

Membrane	λ_w (µm)	s_w (µm)	$Y = \lambda_w^2 + s_w^2$ (µm^2)
B1	1.218	0.410	1.652
B2	1.452	0.633	2.509
B3	2.130	0.928	5.398
B4	2.235	1.050	6.098
B5	0.470	0.138	0.240
B6	1.564	0.599	2.805
B7	0.874	0.285	0.845
B8	1.150	0.394	1.478
B9	0.738	0.413	0.715
B10	0.828	0.399	0.844

Based on the regression techniques and the results presented in Tables (4.1.1) and (4.1.2), a factorial model with interactions has been developed. Eq. (4.1.4) shows the obtained factorial model in terms of coded variables:

$$\hat{Y} = 2.628 - 0.594x_1 - 0.827x_2 + 1.286x_3 - 0.261x_1x_2 + 0.205x_1x_3 - 1.007x_2x_3 + 0.222x_1x_2x_3$$

subjected to: $-1 \leq x_i \leq +1$; $\quad \forall i = \overline{1, \ 3}$ \hfill (4.1.4)

where $\hat{Y}$ is the predictor of the response (quality loss function, Y). The significance of each individual regression coefficient has been tested by means of Student's t-test [39].

The analysis of variance (ANOVA) has been used to check the statistical significance of the factorial model. F-value has been determined based on the ratio of the mean square of group variance due to the error [40]. The larger is the difference of F-value from unity, the more certain it is that the designed variables (factors) adequately explain the variation in the mean of the data. In this case, the F-value is higher than 1 (2.159) and the coefficient of multiple determination R^2 indicated that 81.2% of the data variation can be explained by the factorial model. Therefore, the developed interaction factorial model can be accepted for the prediction of the response in the considered range of experimentation (valid region). It must be pointed out that the obtained regression coefficients in Eq. (4.1.4) cannot be considered for electrospun modelling of other polymer solutions and other environmental conditions (i.e. temperature and humidity). The same DoE and RSM can be applied and other regression coefficients may be obtained.

Figure 4.1.3 reports a comparison of the predicted and experimentally measured response. The predicted data are almost identical to the experimental ones for the orthogonal points (i.e runs 1–8). However, for the center point (i.e. runs 9 and 10) the discrepancy between the predicted and experimental data is higher compared to the other experimental runs. This means that the regression equation does not describe very accurately the response in the center point. This behaviour can be attributed to the orthogonal property of the factorial design. However, based on the ANOVA statistical test the overall prediction may be considered satisfactory.
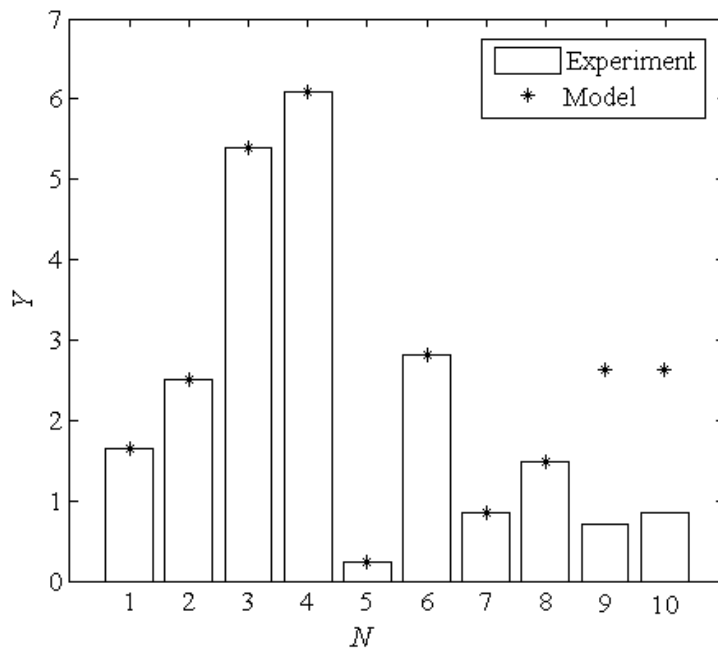

Figure 4.1.3. Comparison between experimental and predicted data by the developed factorial model.

For graphical representation and analysis of response surface, the factorial model in terms of coded variables has been converted to an empirical model in terms of actual variables. The obtained factorial model in terms of actual variables is as follows:

$$\hat{Y} = -5.445 + 0.11U + 0.393A + 4.436F - 0.013U\,A - 0.046U\,F - 0.184A\,F + 3.741 \times 10^{-3}U\,A\,F$$
$$(4.1.5)$$

This model equation is valid for the following region of experimentation:

$10.5 \leq U \leq 24.5$ (kV); $11.77 \leq A \leq 28.23$ (cm); $1.22 \leq F \leq 3.28$ (mL/h);

Figures (4.1.4), (4.1.5) and (4.1.6) present the response surface plots and contour lines maps of Y as a function of the design variables.

279
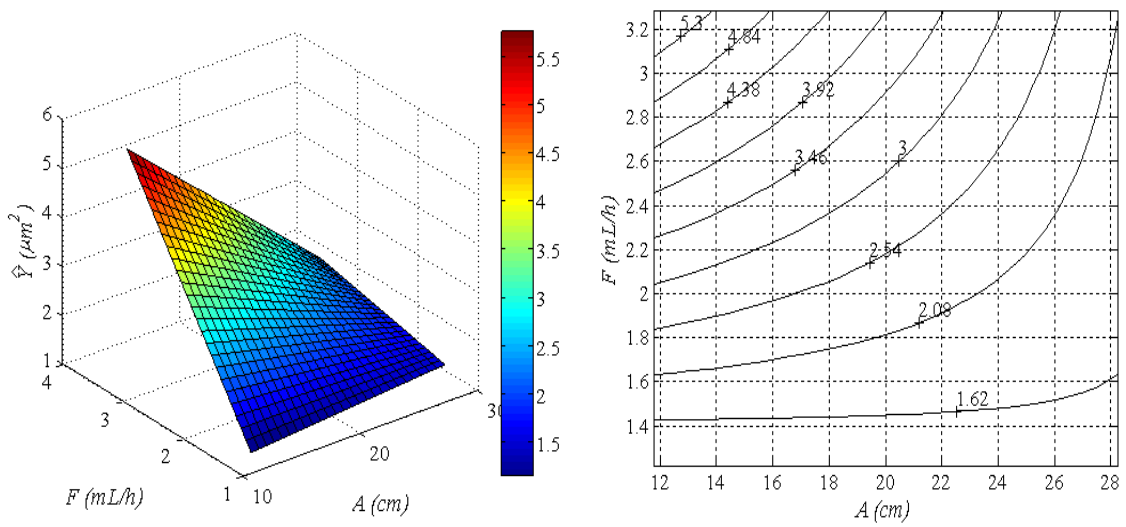
Figure 4.1.4. Quality loss function (*Y*) *versus* the variables *F* (mL/h) and *A* (cm) maintaining *U* at 17.5 kV.
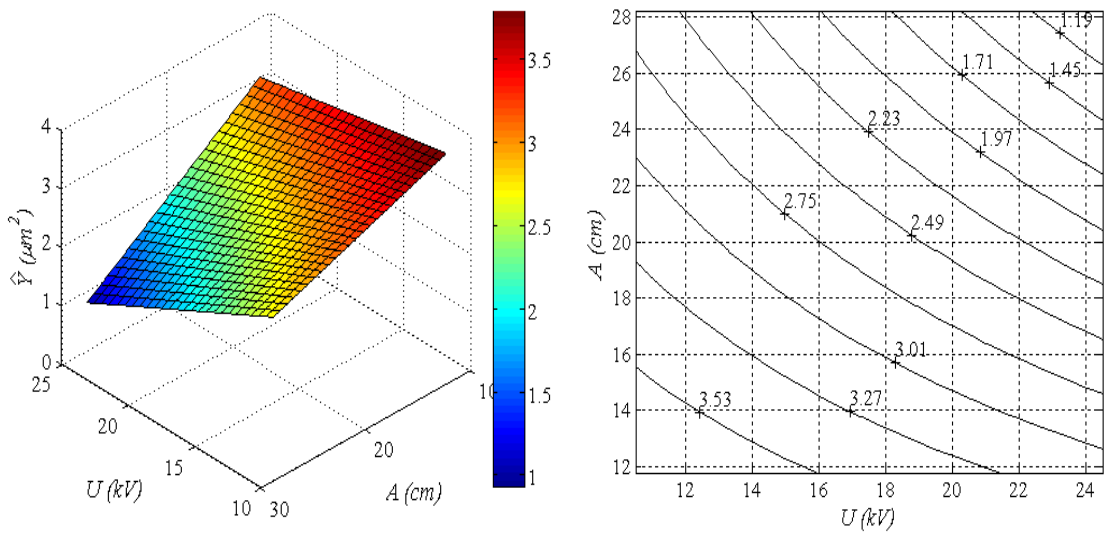

Figure 4.1.5. Quality loss function (*Y*) *versus* the variables *U* (kV) and *A* (cm) maintaining *F* at 2.25 mL/h.
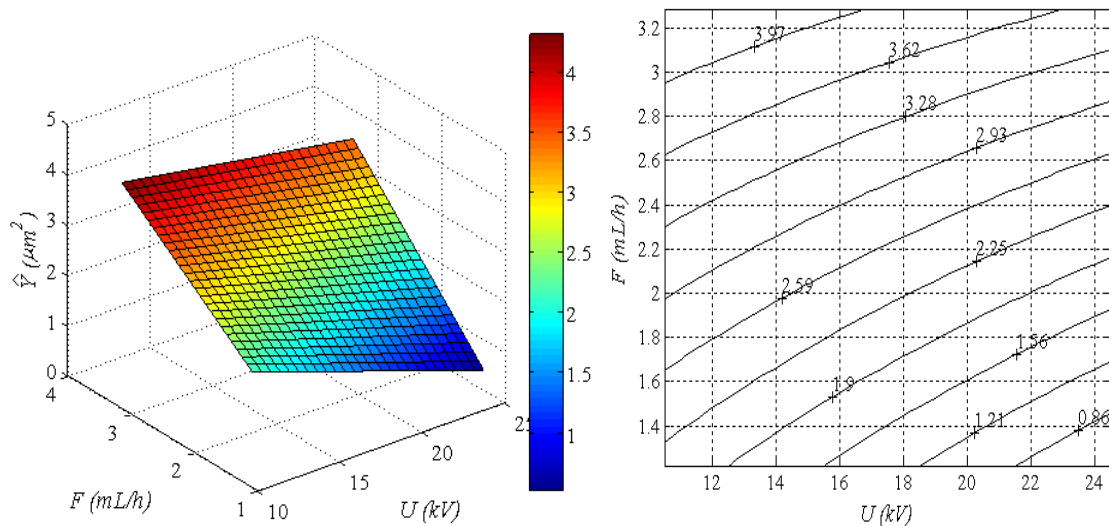
Figure 4.1.6. Quality loss function (*Y*) *versus* the variables *U* (kV) and *F* (mL/h) maintaining *A* at 20 cm.

It is known that polymer flow rate determines the quantity of the solution available for electrospinning. When the polymer flow rate is increased, the diameter of the electrospun fiber is also increased [18,21]. If the polymer flow rate is too high, greater volume of polymer solution will be drawn from the needle tip and the electrospinning jet will take more time to dry. As a result, the solvents in the deposited fibers over the collector may not have enough time to evaporate. Therefore, the residual solvent may cause the fibers to fuse together forming denser fibrous membrane. This will affect the volume charge density and the electrical current of the polymer solution, which increase or decrease depending on the polymer solution. Nasir et al. [18] observed that the PVDF fiber diameter decreased with increasing polymer flow rate up to 5 µL/min and then remained constant for higher flow rates.

The flight time of the electrospinning jet along the gap distance may affect considerably the fiber's characteristics. Decreasing the gas distance has the same effect as increasing the electrical voltage inducing higher electric field strength. When the gap distance is too short, the instability of the jet increases and the spinning solution cannot be fully stretched, resulting in greater fiber diameter. When the gap distance is too large, the strength of the electric field becomes weak resulting in an increase of fiber diameter and sometimes electrospinning is hard to accomplish. Depending on the polymer solution parameters, varying the distance may or may not have a significant effect on the fiber morphology. Nasir et al. [18] reported that the gap distance had no significant effect on the PVDF fiber diameter and explained that the increase of the gap distance

281

induced a decrease of the electrical field strength when a constant electrical voltage was applied, whereas the solvent evaporation time of the polymer jet increased. Megelski et al. [21] also observed no significant change of the electrospun polystyrene fiber size with the change of the gap distance. However, inhomogeneous distribution of elongated beads took place when the gap distance was reduced. Park et al. [41] observed a decrease of the diameter of electrospun polyvinylacetate (PVAc) fiber with increasing the gap distance down to a minimum value followed by a gradual increase of the fiber diameter. This is due to the decrease in the electrostatic field strength resulting in less stretching of the fibers and indicates that there is an optimal electrostatic field strength below which the stretching of the solution will decrease resulting in increased fiber diameter. Therefore, the study of interaction effect in electrospinning is of great interest.

Figure 4.1.4 shows the influence of the polymer flow rate F (mL/h) and the collector distance A (cm) on Y. As can be observed a strong interaction effect exists between these two parameters F and A. The decrease of the flow rate reduces Y, and due to the mutual interaction between F and A the overall effect of F is more apparent at lower level of A. On the contrary, the decrease of the collector distance leads to an enhancement of the quality loss function. Owing to the interaction effect, the influence of A is tiny at lower F and very strong at higher values of F. A high collector distance and low flow rate minimize the quality loss function and improve the performance of the electrospinning process. This can be attributed to the fact that such setting of factors ensures a sufficient time for solvent evaporation.

It is worth quoting that the high voltage will produce the necessary charges on the polymer solution initiating electrospinning process when the electrostatic force in the solution overcomes the surface tension of the solution. When the applied voltage is higher, the greater amount of the induced charges will cause faster acceleration of the electrospinning jet and then a higher quantity of polymer solution will be drawn from the needle tip. These will result in a larger fiber diameter. Depending on the polymer flow rate of the dope and the polymer concentration, a high voltage may be required so that the Taylor cone is stable. The columbic repulsive force in the jet will then stretch the viscoelastic solution. In various cases, a higher electric voltage causes greater stretching of the polymer solution reducing in this way the diameter of electrospun fibers.

Figure 4.1.5 illustrates the effects of U and the collector distance on Y. As can be seen, the increment of both variables diminishes the response and improves the

electrospinning process performance. The effect of U is stronger at higher levels of A, and the effect of A is more evident at high values of U. Therefore, according to the predictions, the best result must be obtained for high values of both the applied voltage and the collector distance.

The effects of U and F on Y are plotted in Fig. 4.1.6. The graphical analysis reveals that increasing U and decreasing F reduce Y. The interaction effects between the applied voltage and the polymer flow rate is minor compared to the previous ones (Figs. (4.1.4) and (4.1.5)). However, the influence of U is stronger at lower levels of F. In contrast, the overall effect of F is stronger for higher levels of U. According to the response surface plot shown in Fig. 4.1.6 the smallest fiber diameters are obtained applying high values of the U and low values of F.

To determine the optimum electrospinning conditions, the factorial model (Eq. 4.1.4) has been used. Monte Carlo method was employed for stochastic simulations and optimization in order to minimize the objective function. Table 4.1.3 reports the obtained optimal solution in terms of both coded and actual variables. Experimental confirmation run was performed using the optimum electrospinning conditions in order to confirm or disapprove the optimal point from experimental standpoint. SEM image and histogram of the electrospun PVDF fiber prepared applying the determined optimum experimental conditions are shown in Fig. 4.1.7. It was found 4.3 % deviation between the predicted quality loss function and the experimental one confirming the optimal point.

Table 4.1.3. Electrospinning optimal point determined by Monte Carlo method.

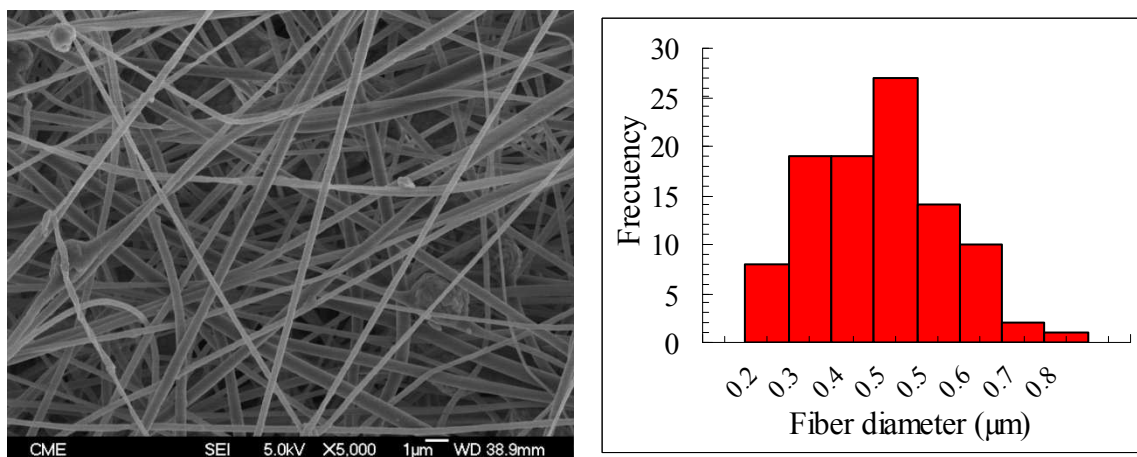| Voltage		Collector distance		Polymer flow rate		$Y_{predicted}$	$Y_{experimental}$
x_1	U (kV)	x_2	A (cm)	x_3	F (mL/h)	(μm^2)	(μm^2)
0.952	24.1	0.937	27.7	-0.989	1.23	0.328	0.314±0.099

Figure 4.1.7. SEM image and fiber diameter distribution of the electrospun PVDF fiber prepared applying the optimum experimental conditions.

By applying the obtained optimum electrospinning conditions, a PVDF electrospun membrane was prepared during 3h30min electrospinning time and characterized by different techniques as indicated previously. The results are summarized in Table 4.1.4. The water contact angle of the prepared optimum PVDF nanofibrous membrane is greater than that of the PVDF nanofibrous membranes reported by Feng et al. [34] and Prince et al. [35] (128º). The obtained high water contact angle in this study is attributed to the distinct PVDF polymer used and to the small fiber diameter achieved of the PVDF electrospun membrane fabricated by optimum electrospinning conditions. Feng et al. [34] and Prince et al. [35] reported a higher *LEP* values for PVDF electrospun membranes than the *LEP* values obtained in this study, 121.4 kPa and 90 kPa, respectively. These results are due to the distinct PVDF polymer solution used, to the different electrospinning parameters applied and to the different maximum inter-fiber space. For instance, the optimum PVDF electrospun membrane prepared in this study exhibits a higher inter-fiber space (d_i) than those of the PVDF nanofibrous membranes prepared by Feng et al. [34] (0.32 µm) and Prince et al. [35] (0.58-0.64 µm). Moreover, the void volume fraction (ε) of the optimum PVDF electrospun membrane is found to be slightly higher than that of the PVDF electrospun membranes prepared by Feng et al. [34] (76%) and Prince et al. [35] (81%).

Table 4.1.4. Characteristics of the PVDF nanofibrous membrane prepared applying the optimum electrospinning conditions: void volume fraction (ε), advancing water contact

angle (θ_a), mean size of the inter-fiber space (d_i), liquid entry pressure (*LEP*) of distilled water and NaCl aqueous solutions (12 g/L, 30 g/L and 60 g/L).

ε (%)	θ_a (°)	δ(μm)	d_i (μm)	*LEP* (kPa)			
				Distilled water	12 g/L	30 g/L	60 g/L
81.6 ±4.2	150.1 ±1.1	567.2 ±25.4	0.82 ±0.09	33.5 ±0.7	37.0 ±1.4	40.5 ±3.5	42.5 ±4.9

As stated previously, the prepared PVDF membrane was applied for desalination by direct contact membrane distillation (DCMD) using different feed salt (NaCl) concentrations (distilled water, 12 g/L, 30 g/L and 60 g/L), 80ºC feed temperature and 20ºC permeate temperature. The obtained permeate fluxes were 58.8±0.2 kg/m^2.h, 57.3±0.4 kg/m^2.h, 53.5±0.4 kg/m^2.h and 51.3±0.3 kg/m^2.h, for distilled water, 12 g/L, 30 g/L and 60 g/L, respectively. The salt rejection factors were greater than 99.94%. The observed decrease of the permeate flux with the increase of the feed salt concentration is due to the reduction of the water vapour pressure at the feed/membrane interface, which decrease the driving force (i.e. transmembrane water vapour pressure), and to the concentration polarization effect [32]. Although the thickness of the optimum electrospun membrane prepared in this study is higher than that of the PVDF nanofibrous membranes prepared by Feng et al. [34] and Prince et al. [35], the obtained permeate fluxes are more than 4.4 times greater. The highest permeate flux obtained by Feng et al. [34] for a PVDF electrospun membrane was 11.5 kg/m^2.h whereas that reported by Prince et al. [35] was even lower 5.8 kg/m^2.h. The obtained high permeation flux in the present study may be attributed to the higher size of the inter-fiber space and to the smaller fiber diameter affecting to some extent the mechanism of mass transport through the inter-fiber space of the electrospun nanofibrous membranes [32,33].

4.1.4. Conclusions

In this work a full factorial design 2^3 was employed for fabrication of electro-spun PVDF fibers. Three independent variables were considered for the first time in experimental design related to electro-spinning. These variables are the applied voltage, the polymer solution flow rate and the distance between the needle tip and the collector. As response of interest the quality loss function was used. This takes into account both the weighted arithmetic mean of fibers diameter and its dispersion. The main and interaction effects of the electro-spinning variables on experimental response were revealed. Thus, a strong interaction effect was detected between polymer flow rate and the collector distance by means of three dimensional surface plot and contour-line map. A high collector distance and a low flow rate both minimize the quality loss function and improve the performance of the electro-spinning process because both ensure a sufficient time for solvent evaporation through the air gap of the polymer jet. Finally, the optimal point was determined using the factorial model and Monte Carlo optimization method. Under the obtained optimum operating conditions, 1.23 mL/h polymer flow rate, 24.1 kV voltage and 27.7 cm air gap a small PVDF nano-fiber diameter and narrow dispersion were obtained experimentally.

The fabricated membrane applying the determined optimum electrospinning parameters was characterized by different techniques and applied for desalination by direct contact membrane distillation (DCMD). The obtained permeate fluxes were 58.8±0.2 kg/m^2.h, 57.3±0.4 kg/m^2.h, 53.5±0.4 kg/m^2.h and 51.3±0.3 kg/m^2.h, for distilled water, 12 g/L, 30 g/L and 60 g/L salt (NaCl) aqueous solutions, respectively; with salt rejection factors greater than 99.94%. These permeate fluxes are more than 4.4 times greater than those reported so far for electrospun nanofibrous membranes used in membrane distillation (MD).

The statistical experimental design and response surface methodology can be applied for other polymer solutions and other electrospinning environmental conditions (Temperature and humidity). Different regression coefficients (Eq. 4.1.4) and different optimum electrospinning conditions may be obtained.

References

[1] D. Li, Y. Xia, Electrospinning of nanofibers: reinventing the wheel?, Adv. Mater. 16 (2004) 1151-1170.

[2] S. Ramakrishna, K. Fujihara, W.E. Teo, T. Yong, Z. Ma, R. Ramaseshan, Electrospun nanofibers: solving global issues, Mater Today. 9 (2006) 40-50.

[3] N. Bhardwaj, S.C. Kundu. Electrospinning: A fascinating fiber fabrication technique, Biotechnol. Adv. 28 (2010) 325-347.

[4] Z.M. Huang, Y.Z. Zhang, M. Kotaki, S. Ramakrishna, A review on polymer nanofibers by electrospinning and their applications in nanocomposites, Composit. Sci. Technol. 63 (2003) 2223-2253.

[5] D. Liang, B.S. Hsiao, B. Chu, Functional electrospun nanofibrous scaffolds for biomedical applications, Adv. Drug. Deliv. Rev. 59 (2007) 1392-1412.

[6] J.H. Jang, O. Castano, H.W. Kim, Electrospun materials as potential platforms for bone tissue engineering, Adv. Drug. Deliv. Rev. 61 (2009) 1065-1083.

[7] A. Baji, Y.W. Mai, S.C. Wong, M. Abtahi, P. Chen, Electrospinning of polymer nanofibers: Effects on oriented morphology, structures and tensile properties, Composites Sci. Technol. 70 (2010) 703-718.

[8] C.L. Casper, J.S. Stephens, N.G. Tassi, D.B. Chase, J.F. Rabolt, Controlling surface morphology of electrospun polystyrene fibers: effect of humidity and molecular weight in the electrospinning process, Macromolecules. 37 (2004) 573-578.

[9] D. Zhang, J. Chang, Electrospinning of three-dimensional nanofibrous tubes with controllable architectures, Nano Letter. 8 (2008) 3283-3287.

[10] H. Jiang, D. Fang, B.S. Hsiao, B. Chu, W. Chen, Optimization and characterization of dextran membranes prepared by electrospinning, Biomacromolecules. 5 (2004) 326-333.

[11] W.A. Yee, M. Kotaki, Y. Liu, X. Lu, Morphology, polymorphism behavior and molecular orientation of electrospun poly(vinylidene fluoride) fibers, Polymer. 48 (2007) 512-521.

[12] I.B. Rietveld, K. Kobayashi, H. Yamada, K. Matsushige, Morphology control of poly(vinylidene fluoride) thin film made with electrospray, J. Colloid Interface Sci. 298 (2006) 639-651.

[13] S.W. Choi, S.M. Jo, S.W. Lee, Y.R. Kim, An electrospun poly (vinylidene fluoride) nanofibrous membrane and its battery applications, Adv. Materials. 15 (2003) 2027-2031.

[14] Z.Z. Zhao, J.Q. Li, Z.Y. Yuan, X. Li, Y.Y. Zhang, J. Sheng, Preparation and properties of electrospun poly (vinylidene fluoride) membranes, J. Appl. Polym. Sci. 97 (2005) 466-474.

[15] A.K. Haghi, M. Akbari, Trends in electrospinning of natural nano-fibers, Phys. Status Solidi. 204 (2007) 1830-1834.

[16] J.M. Deitzel, J. Kleinmeyer, D. Harris, N.C.B. Tan, The effect of processing variables on the morphology of electrospun nanofibers and textiles, Polymer. 42 (2001) 261-272.

[17] C.S. Ki, D.H. Baek, K.D. Gang, K.H. Lee, I.C Um, Y.H. Park, Characterization of gelatin nanofiber prepared from gelatin-formic acid solution, Polymer. 46 (2005) 5094-5102.

[18] M. Nasir, H. Matsumoto, T. Danno, M. Minagawa, T. Irisawa, M. Shioya, A. Tanioka, Control of diameter, morphology, and structure of PVDF nanofiber fabricated by electrospray deposition, J. Polym. Sci. Part B: Polym. Phys. 44 (2006) 779-786.

[19] D.H. Reneker, A.L. Yarin, Electrospinning jets and polymer nano-fibers, Polymer. 49 (2008) 2387-2425.

[20] O.S. Yördem, M. Papila, Y.Z. Menceloğlu, Effects of electrospinning parameters on polyacrylonitrile nanofiber diameter: an investigation by response surface methodology, Materials & Design. 29 (2008) 34-44.

[21] S. Megelski, J.S. Stephens, D.B. Chase, J.F. Rabolt, Micro-and nanostructured surface morphology on electrospun polymer fibers, Macromolecules. 35 (2002) 8456-7466.

[22] W. Donglai, C. Zhenshan, C. Jun, Optimization and tolerance prediction of sheet metal forming process using response surface model, Computational Materials Sci. 42 (2008) 228-233.

[23] M. Khayet, C. Cojocaru, G. Zakrzewska-Trznadel, Response surface modelling and optimization in pervaporation, J. Membr. Sci. 321 (2008) 272-283.

[24] A. Idris, F. Kormin, M.Y. Noordin, Application of response surface methodology in describing the performance of thin film composite membrane, Sep. Purif. Technol. 49 (2006) 271-280.

[25] M. Khayet, C. Cojocaru, M.C. García-Payo, Application of response surface methodology and experimental design in direct contact membrane distillation, Ind. Eng. Chem. Res. 46 (2007) 46, 5673-5685.

[26] A.F. Ismail, P.Y. Lai, Development of defect-free asymmetric polysulfone membranes for gas separation using response surface methodology, Sep. Purif. Technol. 40 (2004) 191-207.

[27] M. Khayet, C. Cojocaru, M.C. García-Payo, Experimental design and optimization of asymmetric flat-sheet membranes prepared for direct contact membrane distillation, J. Membr. Sci. 351 (2010) 234-245.

[28] M. Khayet, M.N. Abu Seman, N. Hilal, Response surface modeling and optimization of composite nanofiltration modified membranes, J. Membr. Sci. 349 (2010) 113-122.

[29] W. Cui, X. Li, S. Zhou, J. Weng, Investigation on process parameters of electrospinning system through orthogonal experimental design, J. Appl. Polym. Sci. 103 (2007) 3105-3112.

[30] S.Y. Gu, J. Ren, G.J. Vansco, Process optimization and empirical modeling for electrospun polyecrylonitrile (PAN) nanofiber precursor of carbon nano-fibers, Eur. Polym. J. 41 (2005) 2559-2568.

[31] M. Khayet, M.C. García-Payo, Nanostructured flat membranes for direct contact membrane distillation, PCT/ES2011/000091, WO/2011/117443, 2011.

[32] M. Khayet, T. Matsuura Membrane distillation: Principles and applications, Elsevier, The Netherlands 2011.

[33] M. Khayet, Membranes and theoretical modeling of membrane distillation: a review, Adv. Colloid Interface Sci. 164 (2011) 56-88.

[34] C. Feng, K.C Khulbe, T. Matsuura, R. Gopal, S. Kaur, S. Ramakrishna, M. Khayet, Production of drinking water from saline water by air-gap membrane distillation using polyvinylidene fluoride nanofiber membrane, J. Membr. Sci. 311 (2008) 1-6.

[35] J.A. Prince, G. Singh, D. Rana, T. Matsuura, V. Anbharasi, T.S. Shanmugasundaram, Preparation and characterization of highly hydrophobic poly(vinylidene fluoride)-clay nanocomposite nanofiber membranes (PVDF-clay NNMs) for desalination using direct contact membrane distillation, J. Membr. Sci. 397-398 (2012) 80-86.

[36] M. Essalhi, M. Khayet, Surface segregation of fluorinated modifying macromolecule for hydrophobic/hydrophilic membrane preparation and application in air gap and direct contact membrane distillation, J. Membr. Sci. 417-418 (2012) 163-173.

[37] D. Taloi, C. Bratu, E. Florian, E. Berceanu, Optimization of the metallurgical processes, (in Romanian), Didactical & Pedagogical Publishing House, Bucharest 1983.

[38] J. Alexis, Taguchi method applied for industrial practice: Experimental designs, (in Romanian), Tehnical Publishing House, Bucharest 1999.

[39] S. Akhnazarova, V. Kafarov, Experiment optimization in chemistry and chemical engineering, MIR Publishers, Moscow 1982.

[40] D.C. Montgomery, Design and Analysis of Experiments, 5th Edition, Wiley & Sons, New York 2001.

[41] J.Y. Park, I.H. Lee, G.N. Bea, Optimization of the electrospinning conditions for preparation of nanofibers from polyvinylacetate (PVAc) in ethanol solvent, J. Ind. Eng. Chem. 14 (2008) 707-713.

4.2. Self-Sustained Webs of Polyvinylidene Fluoride Electrospun Nano-fibers: Effects of Polymer Concentration and Desalination by Direct Contact Membrane Distillation

Contents:

Abstract:

The effects of the polymer polyvinylidene fluoride (PVDF) concentration on the characteristics and direct contact membrane distillation (DCMD) desalination performance of self-sustained electrospun nano-fibrous membranes (ENMs) have been studied. Different polymer concentrations ranging from 15 to 30wt% were considered in the solvent mixture *N,N*-dimethyl acetamide and acetone, while all other electrospinning parameters were maintained the same. Viscosity, electrical conductivity and surface tension of the polymer solutions were measured and the effects of the PVDF concentration on fiber diameter, thickness, water contact angle, inter-fiber space, void volume fraction, liquid entry pressure, mechanical and thermal properties of the ENMs were investigated. The minimum polymer concentration, critical chain entanglement concentration, required for electrospinning beaded fibers and the concentration needed for the formation of bead-free fibers were localized. Two groups of ENMs were identified based on the surface structure of the ENMs, their void volume fraction and inter-fiber space. Bead-free ENMs, prepared with PVDF concentration higher than 22.5wt%, exhibit higher DCMD permeate flux than the beaded ENMs. Beaded ENMs can be used in desalination by DCMD. Among the prepared ENMs, the optimized membrane exhibiting the highest DCMD performance was prepared with 25wt% PVDF concentration.

4.2.1. Introduction

Electrospinning technique has attracted a lot of attention to produce nano-fibers during last 10 years [1-4]. Recently, some electrospun nano-fibrous membranes (ENMs) have been proposed for membrane distillation (MD) [5-16]. These types of membranes exhibit various outstanding characteristics attractive for MD applications such as their high hydrophobicity, high void volume fraction (i.e. very large surface area to volume ratio), high surface roughness, low thermal conductivity (i.e. low heat transfer by conduction through the ENMs and therefore high thermal efficiency of the MD process), interconnected open structure, sufficient mechanical strength, etc [15]. Despite the observed encouraging results, still a lot of research studies are needed to be performed in the field of ENMs applications in MD process. By understanding both the system and process electrospinning parameters, it will be possible to prepare ENMs for MD with various forms and arrangements.

It was observed that the following parameters and processing variables affect the physical properties of the electrospun fibers including their fiber shape, diameter and surface morphology [17-25]: i)- System parameters such as type and molecular weight of the polymer, polymer concentration, solvent type and polymer solution properties (viscosity, electrical conductivity and surface tension); ii)- Process parameters such as the applied electric potential or voltage, flow rate of polymer solution and hydrostatic pressure in the capillary tube, distance between the needle tip and collector, the size of the needle (nozzle) and motion of the collector; and iii)- Ambient parameters (temperature, humidity and air flow in the electrospinning chamber).

The systematic effects of the above cited parameters on the MD performance are not studied yet although the influence of these parameters on the nano-fibers characteristics has been previously reported in various studies [5,6].

An important dimensionless parameter controlling beads and fibers formation was considered to explain qualitatively the morphologies of the product obtained by electrospinning technique. This parameter ($Vq/\mu_p R^2$) is defined as the ratio of the electric energy (Vq, where q is the charge of the polymer solution) to the surface free energy ($\mu_p R^2$, where μ_p is the surface tension and R the radius of the formed Taylor cone droplet) [26]. In order to originate a jet from the Taylor cone, the electric energy, which is the driving force for the ejection of the jet, must overcome the surface free energy

that is the force opposing the jet ejection (i.e. $Vq/\gamma R^2 > 1$). As the electric energy is increased, the morphology of polymer solution jet changes from beads to beaded fibers and then to fibers [17]. If the surface tension of the polymer solution is reduced, changes from beads to fibers can also be observed [27]. In addition, the polymer concentration is one of the most important parameters in the electrospinning process affecting beads and fibers formation because it is strongly related to the viscosity of the solution [28]. When very low polymer concentrations are used, the process is known as electrospraying [28-30]. When low polymer concentrations are used, beads, droplets or microspheres appeared in the electrospun products [28-30]. By increasing the polymer concentration, the numbers and sizes of beads may be decreased, and then eliminate beads completely.

Taking into consideration that the properties of the polymer dope have the most significant effect on the resultant nano-fiber morphology, the main objective of the current investigation is to determine the solution concentration at which the transition between beaded-fibers and continuous fibers of PVDF occurs and to investigate the individual effects of the polymer concentration on both the characteristics and DCMD desalination performance of ENMs. All other electrospinning parameters were maintained the same.

4.2.2. Experimental

4.2.2.1. Materials

The electrospinning solutions were prepared from the polymer PVDF and the mixed solvents *N,N*-dimethyl acetamide (DMAC) and acetone purchased from Sigma–Aldrich Chemical Co. Isopropyl alcohol (IPA) was used to determine the void volume fraction (ε) of the ENMs and sodium chloride (NaCl) used in DCMD experiments were also purchased from Sigma-Aldrich Chemical Co. POREFIL125, a Fluorinated Hydrocarbon (chemical nature: pefluoroether, with a surface tension of 16 mN/m, a vapour pressure of 3.33 Pa, a viscosity of 4.4 mPa.s, Porometer) was used as a wetting liquid to perform the inter-fiber space measurements.

4.2.2.2. Preparation and characterization of the polymer solutions

The polymer solution was prepared using different concentrations of PVDF ranging from 15 to 30 wt% in the mixture 20 wt% acetone in DMAC. The polymer was added to the solvent mixture and kept at 45ºC under agitation for about 24 h until it was totally dissolved. Prior to electrospinning, the polymer solution was degassed overnight at room temperature.

The viscosities of the PVDF polymer solutions (μ_p) were measured at 23 ± 0.5ºC using a digital Viscosimeter (Brookfield, DV-I+) connected to a thermostat (Model HETO 21-DT-1, Rego S.A). The rotating speeds of the used spindles *LV1, LV2, LV3 Y LV4* ranged between 0.5 and 100 rpm.

The surface tension (σ_p) was measured at room temperature by the pendant drop shape analysis using an Optical Contact Angle Meter (CAM 200). The needle used has an outer diameter of 1.827 mm and the drop volume was kept constant for all polymer solutions at 12.76±0.83 µL. The surface tension can be related to the drop shape through the following equation:

$$\sigma_p = \frac{\Delta\rho \ g \ R^2}{\beta} \tag{4.2.1}$$

where $\Delta\rho$ is the difference in density between fluids at the interface, g is the gravitational constant, R is the radius of the drop curvature at apex and β is the shape factor defined through the Young-Laplace equation [31]. The Cam200 fits the Young-Laplace equation to the drop image. For each polymer solution, average values from at least fifteen measurements are reported.

The electrical conductivity (χ_p) of the prepared polymer solutions was measured at room temperature using the conductivity meter (CyberScan con11 Conductivity/TDS/ºC, Eutech Instruments).

4.2.2.3. Preparation of electro-spun PVDF fibers

The electrospinning set-up used was described in a previous study [15]. The used polymer solutions and the prepared ENMs are given in Table 4.2.1. The electrospinning system consists of a glass syringe (50 ml, Nikepal) to hold the polymer solution, a

circulation pump (kd Scientific, Panlab S.I.; model KD.S-200-CE), two electrodes (a metallic needle of 0.6/0.9 mm inner/outer diameters and a grounded cupper horizontal collector covered with aluminum foil) and a DC voltage supply in the kV range (Iseg; model T1CP 300 304P; 1x30 kV/0.3 mA) with an electric intensity in the range of μA. A slight increase of the electric intensity from 0.25 to 0.95 μA was detected with the increase of the PVDF concentration in the electrospinning polymer solution. This is due to the slight increase of the electrical conductivity of the polymer solution with the PVDF concentration (Table 4.2.1). The previously obtained optimum electrospinning parameter conditions by means of statistical factorial model and Monte Carlo optimization method are applied in this study, a voltage of 24.1 kV, an air gap of 27.7 cm and a polymer flow rate of 1.23 mL/h [32]. The electrospinning time was 2h. The electrospinning temperature was 23ºC and the humidity was 37.5 %. The formed fibers were dried in an oven at 80ºC for 30 min (i.e. post-treatment).

Table 4.2.1. Membrane name, PVDF concentration (C_p) in the electrospinning polymer solution, electrical current of the DC voltage supply of the electrospinning system (I), surface tension (σ_p), electrical conductivity (χ_p) and viscosity (μ_p) of the PVDF polymer solutions at 23ºC.

Membrane	C_p (wt%)	I (µA)	σ_p (mN/m)	χ_p (µS/cm)	μ_p (Pa.s)
ENM15	15	0.25 ±0.10	32.49 ±0.38	8.67 ±0.01	0.364 ±0.003
ENM17-5	17.5	0.45 ±0.07	32.42 ±0.25	8.87 ±0.03	0.469 ±0.003
ENM20	20	0.55 ±0.07	32.12 ±0.36	9.04 ±0.03	0.983 ±0.004
ENM22-5	22.5	0.65 ±0.07	32.02 ±0.38	9.48 ±0.04	2.347 ±0.004
ENM25	25	0.77 ±0.25	32.41 ±1.12	9.57 ±0.03	3.108 ±0.005
ENM27-5	27.5	0.80 ±0.10	32.27 ±0.74	9.68 ±0.01	5.724 ±0.005
ENM30	30	0.95 ±0.10	32.50 ±0.78	9.83 ±0.03	9.380 ±0.006

4.2.2.4. ENMs Characterization

The surface and the cross-section of the self-sustained ENMs membranes were examined by a field emission scanning electron microscope (FESEM, JEOL Model JSM-6330F). The ENMs samples were first fractured in liquid nitrogen. Then samples were placed over a support and coated with gold under vacuum conditions. The SEM images of the top surface of the ENMs were analyzed by UTHSCSA ImageTool 3.0 to determine the fiber diameter. For each sample more than 3 SEM images have been considered and the diameters of a total number of 100 fibers have been measured. Statistical analysis have been applied in order to determine the fiber size distribution and to estimate the arithmetic weighted mean of the fiber diameters and their dispersion (i.e. weighted standard deviation).

Differential scanning calorimetry (DSC) (Mettler Toledo, DSC1 Star^e System, Spain) was used to study the thermal properties of the ENMs. The ENM sample, about 10.8 mg, was heated from 75ºC to 300ºC at 15ºC/min and then cooled down to room temperature. For each ENM at least two different samples were considered and the first heating and cooling cycle of each ENM sample was used in this study to determine the thermal parameters of the ENM. The melting temperature (T_m), the enthalpy of melting (ΔH_m), the crystallization temperature (T_c) and the heat of crystallization (ΔH_c) of both the PVDF polymer and ENMs were determined by Star^e software (Version 10.00d Build 3690).

The mechanical properties of the PVDF ENMs were investigated according to ASTM D 3379-75 specifications using an Instron dynamometer (model 3366) at room temperature, and at a cross-head speed of 22 mm/min with an initial length of the ENM sample of 50 mm and 4.15 mm width. At least five specimens of each ENM sample were tested.

The liquid entry pressure of water (*LEP*) measurements of distilled water and 30 g/L NaCl aqueous solution were carried out using the experimental system detailed elsewhere [15]. The used effective membrane area is 12.56 x 10^{-4} m^2. The container was filled first with 2 L liquid sample and a pressure of about 5 kPa is applied from the nitrogen cylinder on the liquid sample at room temperature for 5 min. Subsequently, the applied pressure was increased gradually by 2 kPa every 2 min. The minimum applied pressure before liquid penetrates into the inter-fiber space is the *LEP* value. These experiments were carried out three times using three different membrane samples made

from different batches and the average values together with their standard deviations are reported.

The inter-fiber space was measured applying a capillary flow porometer (POROLUX™ 100) that uses the pressure scan method within a pressure range of 0-0.7 MPa at a room temperature. The inter-fiber space was calculated from the obtained wet and dry flow curves. POREFIL125 (Porometer) was used as a wetting liquid agent. The gas used was compressed air and the effective membrane area is 2.688 x 10^{-4} m^2. First, air permeation flow is measured through the dry ENM sample at different pressures to obtain the dry curve. Subsequently, the ENM is wetted by POREFIL125 and again the gas permeation flow is measured at increasing transmembrane pressures to obtain the S shaped wet curve. At least 3 tests were performed for each ENM sample and the size of the inter-fiber space was calculated using Washburn equation. The mean size of the inter-fiber space was determined from the intersection between the half-dry curve corresponding to 50 % gas flow through the dry ENM sample and the wet curve (i.e. the half-dry curve is the mathematical half of the dry curve). The distribution of the inter-fiber space was also determined using the software POROLUX100 (Porometer).

The water contact angle of the surface of each ENM was measured at room temperature by a computerized optical system CAM100, equipped with a CCD camera, frame grabber and image analysis software. Distilled water drops of about 2 μl were deposited on the membrane surface employing a tight syringe. The contact angles were performed at both left and right sides of each drop and were automatically calculated by fitting the captured drop shape to that calculated from the Young-Laplace equation. More than 25 readings were obtained for each ENM sample and an average value was calculated and reported together with the standard deviation.

The void volume fraction of the ENMs was determined by measuring the density of each ENM using isopropyl alcohol (IPA), which penetrates inside the inter-fiber space of the ENM sample and distilled water, which does not enter in the inter-fiber space. The applied method was reported elsewhere [6].

The thickness (δ) of the ENMs was measured by the micrometer Millitron Phywe (Mahr Feinprüf, type TYP1202IC) in different points of the sample, at least 100, of three different membrane samples made from different batches and the average values together with their standard deviations are reported.

The experimental system used to carry out the DCMD experiments through ENMs was detailed in a previous study [33]. The top side of the ENM is brought into contact

with the feed solution, while the permeate liquid is maintained in contact with its bottom side. In this study, the experiments were conducted first with distilled water as feed, then with 30 g/L NaCl aqueous solution and finally with distilled water again to check if there is any change of the permeate flux with time of the ENMs. The applied feed temperature was 80°C, the permeate temperature was 20°C and both the feed and permeate circulation rates were 500 rpm, which corresponds to turbulent flow regime in both feed and permeate chambers. The total DCMD operation time of each membrane was at least 10 h. The DCMD system is composed of two cylindrical stainless steel chambers. One of the chambers is connected to a heating system through its jacket to control the temperature of the liquid feed, while the other chamber is connected to a cooling system to control the temperature of the permeate (distilled water). The ENM having an effective area of $2.75 \ 10^{-3} \ m^2$ was placed between the two chambers. The permeate flux was calculated in every case by measuring the condensate collected in the permeate chamber for a predetermined period (at least for 3 h). The NaCl concentration of both the permeate and feed solutions was determined by a conductivimeter 712 ΩMetrohm. A calibration curve was made using different NaCl aqueous solutions in order to relate the electrical conductivity to the NaCl concentration of the feed and permeate aqueous solutions.

4.2.3. Results and discussions

4.2.3.1. SEM images of the ENMs and effects of the PVDF polymer concentration

Figure 4.2.1 shows the SEM images of the surface and cross-section of the PVDF ENMs prepared with different polymer concentrations. Differences exist between the SEM images of the samples depending on the concentration of the PVDF in the polymer solution. There is formation of films consisting of droplets (i.e. spherical beads or microspheres), characteristic of the electrospray process, when using low PVDF polymer concentrations (e.g. ENM15, ENM17-5). The morphology of the beads changed from spherical to elongated or elliptical with increasing the PVDF concentration (e.g. ENM20 and ENM22-5). A combination of fibers and beads is observed. The density of beads decreases considerably with increasing the concentration of PVDF in the polymer solution from 15 to 22.5 wt%, while the amount of fiber formation was increased. The estimated density of beads was 238.4, 63.8, 18.7 and 3.7 x10^{-3} µm^{-2} for ENM15, ENM17-5, ENM20 and ENM22-5, respectively. Among the total number of beads, the quantity of elongated beads was 0, 17.9, 25.8 and 89.5% for ENM15, ENM17-5, ENM20 and ENM22-5, respectively.
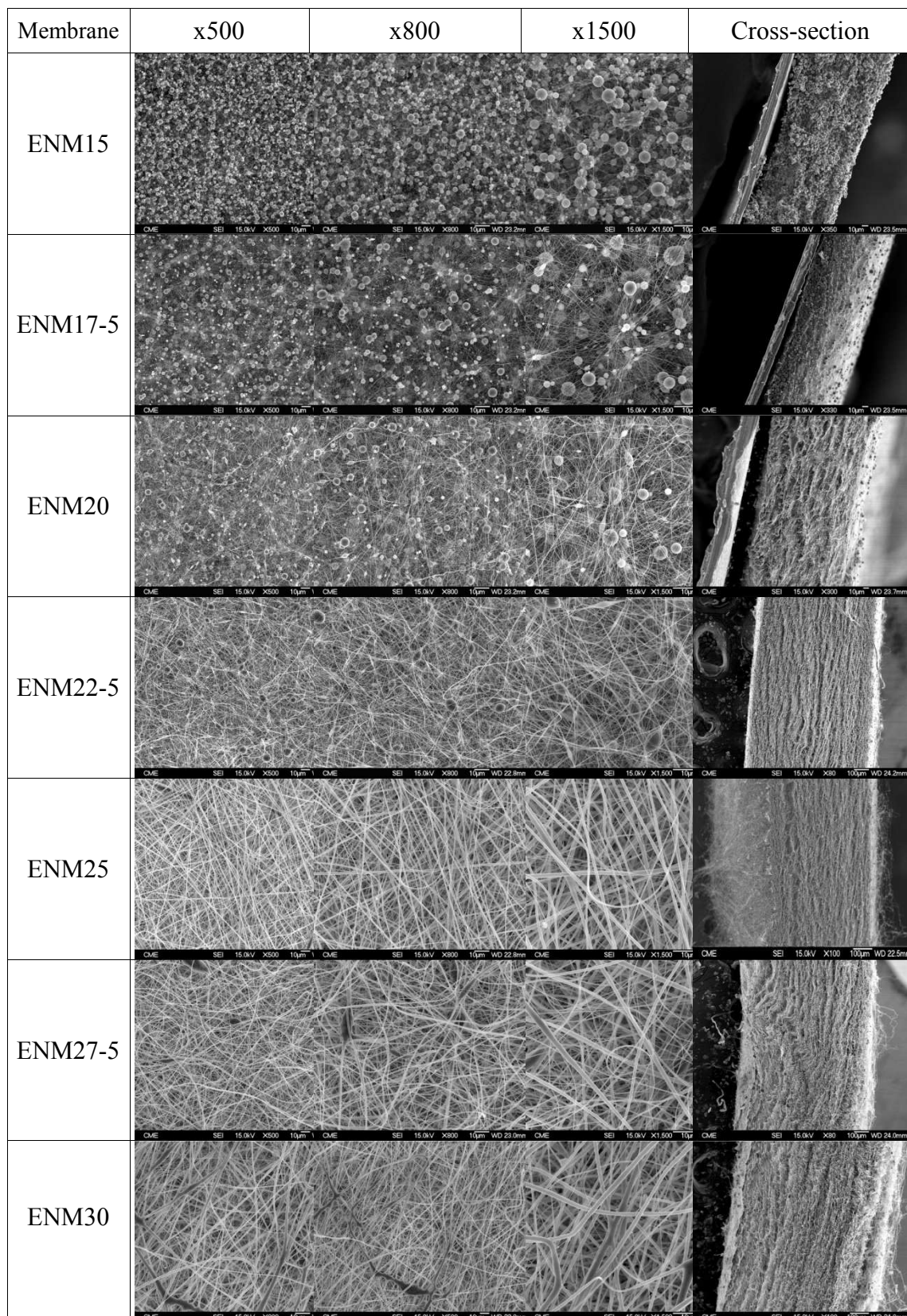
Membrane	x500	x800	x1500	Cross-section
ENM15				
ENM17-5				
ENM20				
ENM22-5				
ENM25				
ENM27-5				
ENM30				

Figure 4.2.1. SEM images of the surface (at different magnifications: x500, x800 and x1500) and cross-section of the PVDF ENMs prepared with different PVDF concentrations in the electrospinning polymer solution.

The aspect ratio (L/W) of the bead, defined as the ratio of the bead length (L) along the fiber (major axis) to the bead length perpendicular to the fiber (W, minor axis), was calculated for the ENMs prepared with PVDF concentrations lower than 22.5 wt%. As can be seen in Fig. 4.2.2 the aspect ratio increases with increasing the PVDF concentration in the electrospinning polymer solution. This result is due to the gradual increase of the number of elongated beads on the ENMs surface with increasing the PVDF concentration.
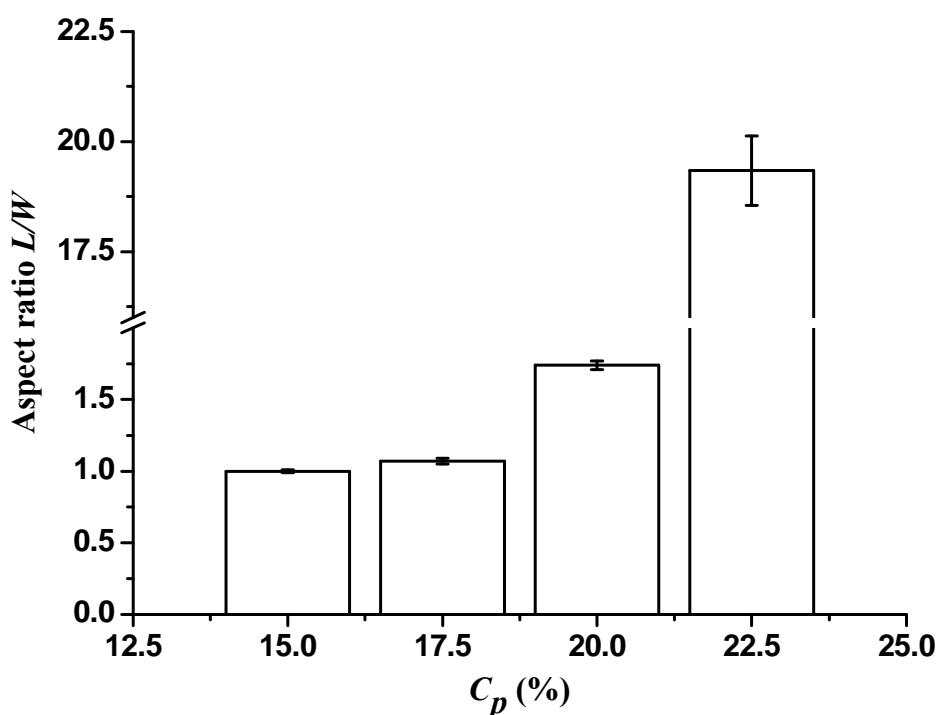

Figure 4.2.2. Change of the aspect ratio (L/W) with PVDF polymer concentration (C_p) in the electrospinning solution.

With increasing PVDF concentration in the polymer solution, the morphology of ENMs changed from spherical beads to a mixture of spherical beads and fibers, then to elongated beaded fibers and finally to bead-free continuous fibers for higher PVDF concentrations than 22.5 wt%. The SEM images of the ENM25, ENM27.5 and ENM30 show fibers arranged in a three dimensional network structure with improved homogeneity and no droplets, indicating that these concentrations are the optimum for obtaining ENMs.

Beads formation is affected by several factors such as surface tension, polymer concentration, solution viscosity, net charge density or electrical conductivity of the polymer solution [6,34]. It is known that beads and polymer droplets are caused by the surface tension of the polymer solution, which has the effect of decreasing the surface area per unit mass of a liquid. Low surface tension tends to form more beads in the electrospun film as the jet would be broken down easily into drops. However, the surface tension is more likely a function of solvent compositions and is less dependent on polymer concentration. As can be seen in Table 4.2.1, a slight change was observed for the surface tension (σ_p) of the used PVDF polymer solutions in this study. In addition, to form a polymer jet by electrospinning, the electrostatic forces in the electric field must overcome the surface tension of the polymer solution. A better electric conductivity of the jet results in a higher charge density on the surface of the ejected jet when it flew from the metallic needle to the collector and thus, in a higher electrostatic force leading to small sizes of beads and their morphology become spindle-like [30]. As it is reported previously, the electric energy (Vq) and surface free energy ($\sigma_p R^2$) of the polymer solution are important parameters controlling Taylor cone and fiber/bead formations. In this study, an increase of only 13.4% from 8.67 to 9.83 μS/cm was detected for the electrical conductivity (χ_p) of the polymer solution with increasing PVDF concentration from 15 to 30 wt% (Table 4.2.1).

Taking into consideration the slight change of both the surface tension and the electrical conductivity of the PVDF polymer solution with the increase of the PVDF concentration, the results can be explained based on the viscoelastic behaviour of polymer solutions. The reason for the observed different morphological structures of the electrospinning films might be mainly caused by the increase of the viscosity with the increase of the PVDF concentration in the polymer solution. Polymer solutions having low viscosity results in more instability of the electrified jet and the risk of breaking into droplets is high. This is related with the number of polymer entanglements that is controlled by the polymer molecular weight, molecular weight distribution, polymer concentration and therefore polymer solution viscosity [26]. In a dilute polymer solution, chain overlapping is absent and as the polymer concentration increases, the molecular chains start to overlap and entangle with each other. Sufficient polymeric chain entanglements are needed to enhance the stability of the ejected solution jet and help the formation of nano-fibers.

Table 4.2.1 summarizes the measured viscosity (μ_p) of the PVDF solutions and Figure 4.2.3 shows the logarithmic plot of the PVDF solution viscosity as a function of the PVDF concentration in the polymer solution. An inflexion concentration corresponding to the critical chain entanglement concentration, C_e = 18.28 wt%, of PVDF solution is observed in Fig. 4.2.3 with two different slopes. Below this polymer concentration, the application of voltage to the solution results in electrospraying or bead formation due to Rayleigh instability [26]. The change of the slope from 2.675 to 6.980 marked C_e the boundary between the semidilute un-entangled and semi-dilute entangled regions.
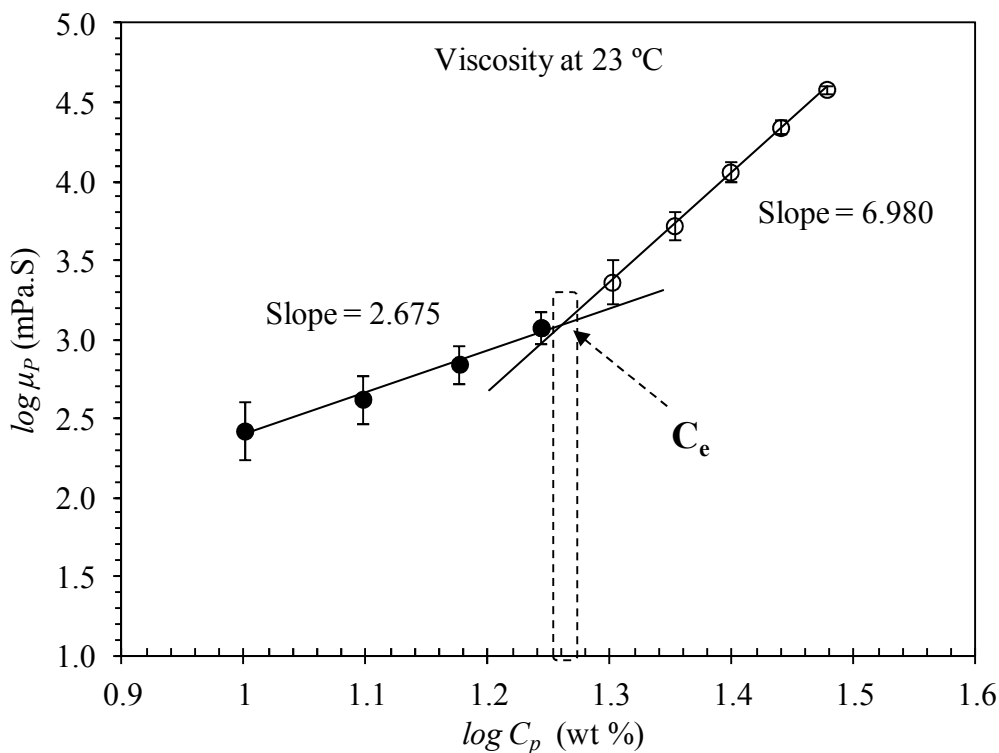

Figure 4.2.3. Viscosity of polymer solution (μ_p) *versus* PVDF concentration (C_p) in the polymer solution. C_e is the critical chain entanglement concentration.

Research studies [35-37] indicated that the two power law ($\mu_p \alpha C_p^n$, where C_p is the polymer concentration and n the exponent) exists for good polymer solutions within the semidilute regime (i.e. semidilute un-entangled, $C^* < C < C_e$, where C^* is the overlap concentration) and semidilute entangled ($C > C_e$). The theoretical predictions suggest n = 1.0 when $C < C^*$, n = 1.25 when $C^* < C < C_e$, and n = 4.8 when $C_e < C$ for neutral good polymer solutions [38]. In the semidilute un-entanglement regime ($C^* < C < C_e$), the obtained n =2.675 indicates a stronger concentration dependence than the theoretical

306

prediction $n = 1.25$. In the semidilute entanglement regime (C > C_e), the obtained $n = 6.980$ is again stronger concentration dependence than the theoretical prediction $n = 4.8$. It was observed that some experimental n exponents are consistent with the theoretical prediction while others deviate from them. However, all the plotted logarithmic curves of the polymer viscosity as a function of the polymer concentration showed an inflection concentration corresponding to C_e with two different slopes above and below this inflection concentration. For example, for the polymer poly (methyl methacrylate) (PMMA) in dimethyl formamide (DMF) solutions with molecular weights ranging from 1.24×10^4 to 3.66×10^5 g/mol, Gupta et al. [39] found a concentration exponent $n = 0.65$ when ($C^* < C < C_e$) and $n = 5.3$ when (C > C_e); whereas McKee et al. [40] reported n values ranging from 3.2 to 6.1 when C > C_e for PMMA and poly(methyl methacrylate- co-methacrylic acid) (PMMA-co-PMAA) in a mixture of solvents DMF and chloroform (CHCl$_3$).

The minimum PVDF concentration required for electrospinning beaded fibers is $C_e = 18.28$ wt%, while the minimum concentration required for electrospinning uniform bead-free fibers is slightly higher than 1.23 times C_e (ENM22-5) as can be seen in Fig. 4.2.1. The low solution viscosities of the PVDF concentrations 17.5 and 20 wt%, which are slightly higher than C_e, indicate low polymers entanglements in these polymer solutions. Beaded fibers are obtained at these concentrations and as the PVDF concentration turns to be greater than 20 wt%, the polymer/polymer entanglements become significant and the solution viscosity increases dramatically with increasing the PVDF concentration. Therefore, these experimental observations in electrospinning confirm that a minimum level of PVDF polymer concentration is required for the fiber formation to occur.

4.2.3.2. Characteristics of the ENMs

The mean fiber diameter (d_f) and its distribution were determined. The results are presented in Table 4.2.2 and in Fig. 4.2.4. The fiber diameter increases and its distribution become broader with increasing PVDF concentration. This is attributed to the viscoelastic force that changes to be stronger than the Coulombic force with the increase of the polymer concentration resulting in a greater resistance of the solution to bending and stretching of the jet along the distance between the needle tip and the collector, and therefore lead to an increase of the fiber diameter [41]. Since nano-fibers

are resulted from evaporation and solidification of polymer fluid jets, the fiber diameters depend primarily on the jet sizes as well as on the polymer contents in the jets. In general, higher polymer concentration dissolved in a solvent results in a higher viscosity of the solution, and a higher viscosity results in a larger fiber diameter.

Table 4.2.2. Mean fiber diameter (d_f), thickness (δ), melting temperature (T_m), heat of melting (ΔH_m), degree of crystallinity of melting (X_m), crystallization temperature (T_c), heat of crystallization (ΔH_c) and degree of crystallinity of melting (X_c) of the PVDF ENMs prepared with different PVDF concentrations in the electrospinning polymer solution.

| Membrane	d_f (nm)	δ (μm)	T_m (ºC)	ΔH_m (kJ/kg)	X_m (%)	T_c (ºC)	ΔH_c (kJ/kg)	X_c (%)
ENM15	62.6 ± 16.4	69.3 ± 5.8	---	---	---	---	---	---
ENM17-5	94.5 ± 35.1	95.2 ± 5.9	158.1 ± 0.6	48.9 ± 0.3	46.6 ± 0.3	140.6 ± 0.8	67.7 ± 0.5	64.6 ± 0.5
ENM20	136.6 ± 53.4	167.4 ± 16.4	158.5 ± 0.1	51.5 ± 0.2	49.1 ± 0.2	137.8 ± 0.5	69.2 ± 0.4	66.0 ± 0.4
ENM22-5	248.3 ± 126.4	191.9 ± 19.9	159.1 ± 0.2	53.5 ± 0.2	51.0 ± 1.6	136.8 ± 0.1	72.3 ± 0.6	69.0 ± 0.6
ENM25	335.6 ± 208.4	320.4 ± 28.6	159.5 ± 0.6	54.9 ± 0.1	52.3 ± 0.1	136.1 ± 0.3	73.0 ± 0.4	69.6 ± 0.4
ENM27-5	386.1 ± 224.7	410.4 ± 27.2	160.1 ± 0.5	55.7 ± 0.8	53.1 ± 0.8	135.7 ± 0.7	73.8 ± 0.5	70.3 ± 0.5
ENM30	506.3 ± 271.7	439.7 ± 32.0	160.4 ± 0.6	56.9 ± 0.2	54.2 ± 0.2	134.2 ± 0.8	74.5 ± 0.3	71.0 ± 0.3
PVDF polymer			159.6 ± 0.1	42.0 ± 0.2	40.1 ± 0.2	141.2 ± 0.03	40.6 ± 0.5	38.7 ± 0.4
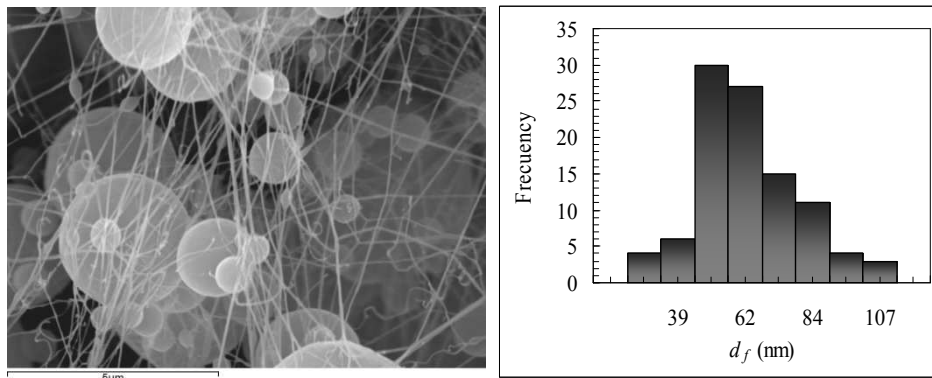
ENM15
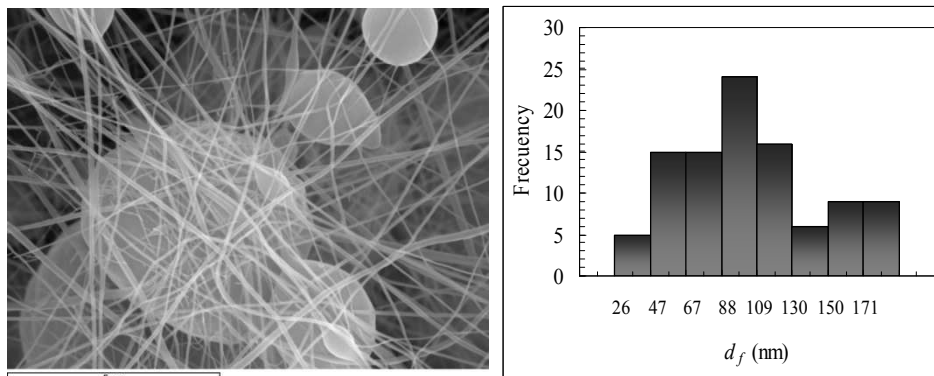
ENM17-5
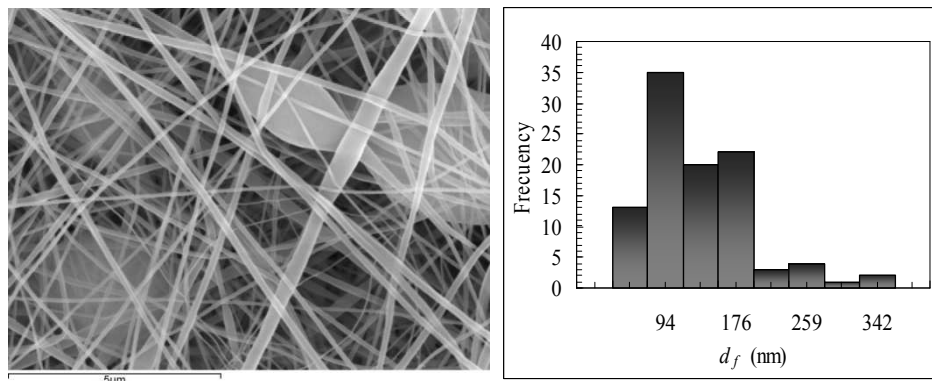
ENM20
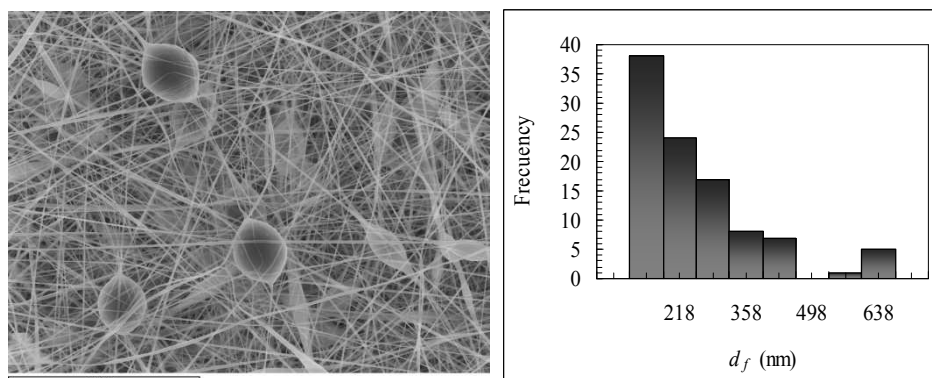
ENM22-5

Figure 4.2.4. Distribution of the fiber diameter (d_f) obtained from SEM images of the surface of the ENMs prepared with different PVDF concentrations in the electrospinning solution. (To be continued)

309

ENM25

ENM27-5

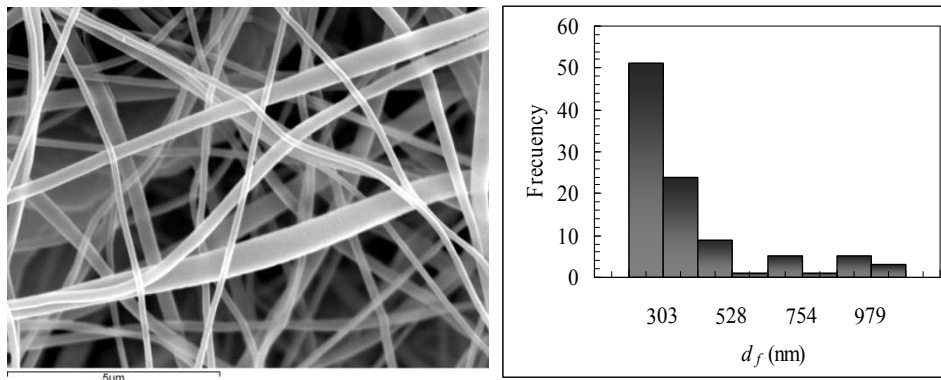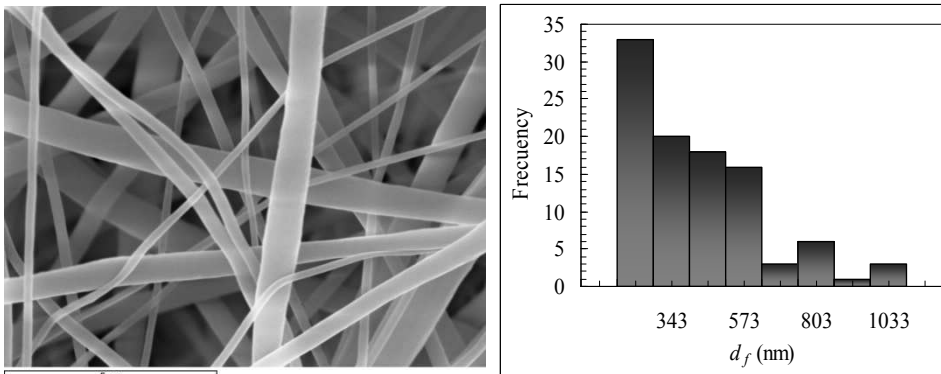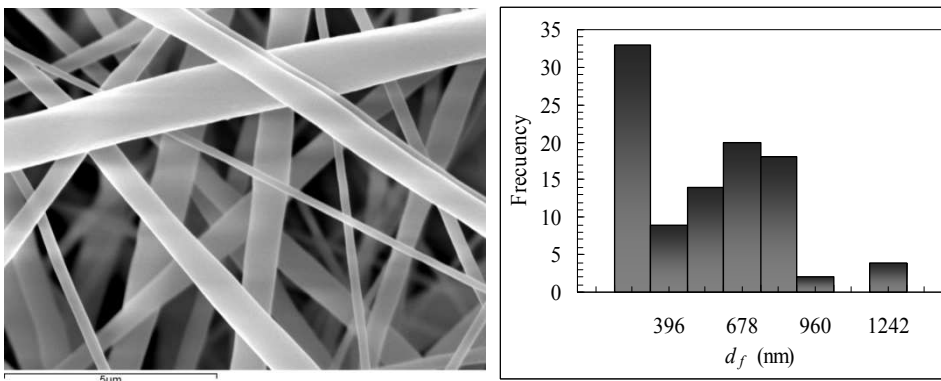ENM30

Figure 4.2.4. Distribution of the fiber diameter (d_f) obtained from SEM images of the surface of the ENMs prepared with different PVDF concentrations in the electrospinning solution. (Continuation)

Deitzel et al. [42] pointed out that the fiber diameter increased with increasing polymer concentration according to a power law relationship. The average size of the nano-fibers was correlated with the normalized PVDF polymer concentration (C/C_e) as plotted in Fig. 4.2.5. A power law relationship between the fiber diameter and C/C_e was fitted reasonably well as follows:

$$d_f = 113.9 \left(C_p / C_e \right)^{3.14}$$
(4.2.2)

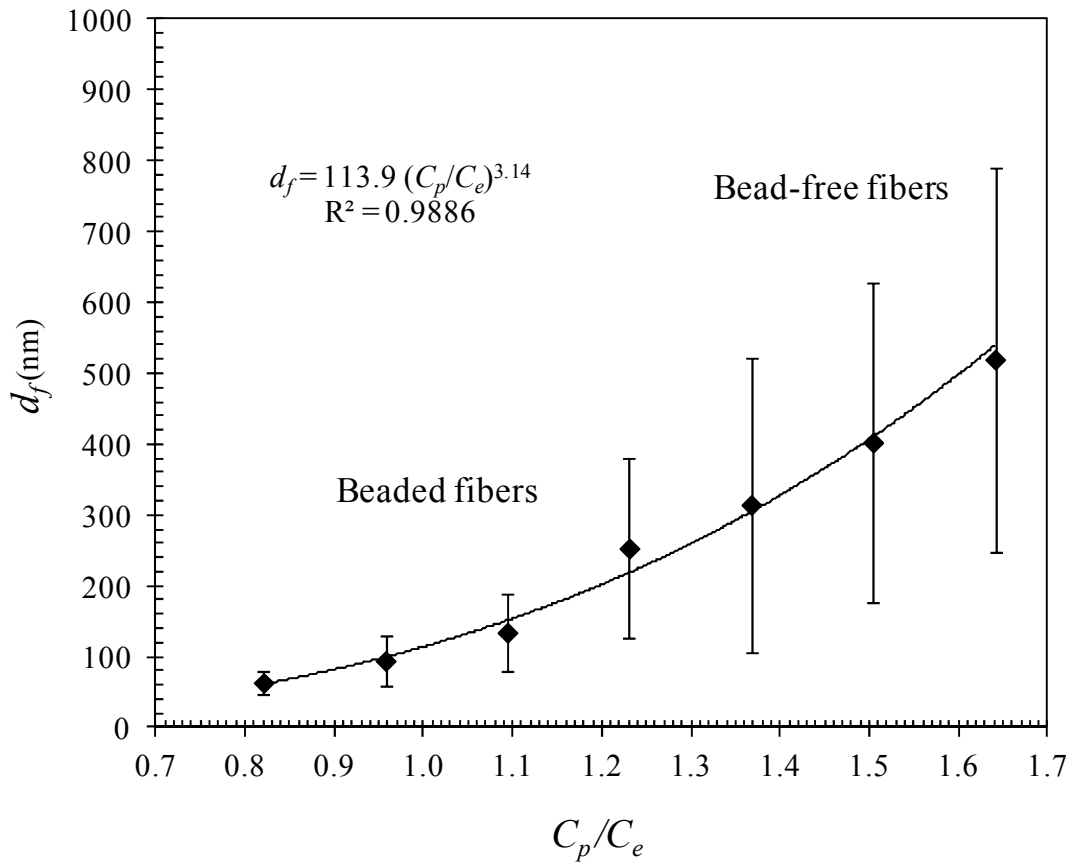Similar correlations were observed in previous studies [39,40,43].

Figure 4.2.5. Variation of the mean fiber diameter (d_f) with the normalized concentration (C/C_e) of ENMs prepared with different PVDF concentrations in the electrospinning solution.

The thickness (δ) of the ENMs is presented in Table 4.2.2. It can be observed that δ of the PVDF ENMs enhances with the increase of the PVDF concentration in the polymer solution. This is attributed to the increase of the fiber diameter with the increase of the PVDF concentration in the polymer solution (Fig. 4.2.5). When the fiber diameter is small, it is more prone to dissipate the electric charges to the metallic collector and the repulsion among fibers will be reduced favouring a tightly packed ENM structure with a thin thickness. However, for a larger fiber diameter, the presence of electrostatic charges causes fibers to repel each other, giving a more loosely packed and thicker ENM structure.

It must be pointed out that the ENM15 prepared with the lowest PVDF concentration in the electrospinning solution (15 wt%) can not be separated from the metallic collector because of its poor mechanical properties. This membrane is easily broken when trying to separate it from the collector. This is why it is not considered for further analysis. On the other hand, ENMs with higher PVDF concentrations than 30 wt% could not be electrospun because the metallic needle tip often became blocked due to the very high viscosity of the polymer solutions.

The effects of the PVDF concentration on the melting temperature (T_m), the heat of melting (ΔH_m), degree of crystallinity of melting (X_m), crystallization temperature (T_c), heat of crystallization (ΔH_c) and degree of crystallinity of melting (X_c) of the PVDF ENMs were determined from their DSC heating and cooling curves shown in Fig. 4.2.6. More details may be found in a previous published paper [15]. The obtained values of these parameters for both the ENMs and the PVDF polymer are shown in Table 4.2.2. As the PVDF concentration in the polymer solution was increased from 17.5 to 30 wt% a very slight increase (1.5%) was detected for the melting temperature and the crystallization temperature was decreased slightly (4.6%). In addition, all the other experimental parameters ΔH_m, X_m, ΔH_c and X_c were higher for the PVDF ENMs prepared with greater PVDF concentrations in the polymer solution and all ENMs exhibited higher values than those of the PVDF polymer. These results indicate that both the PVDF polymer concentration that results in higher fiber diameters and thicker ENMs as well as the electrospinning process conditions with a rapid rearrangement of the highly stretched chains and large elongational strains affect the thermal properties of the ENMs.
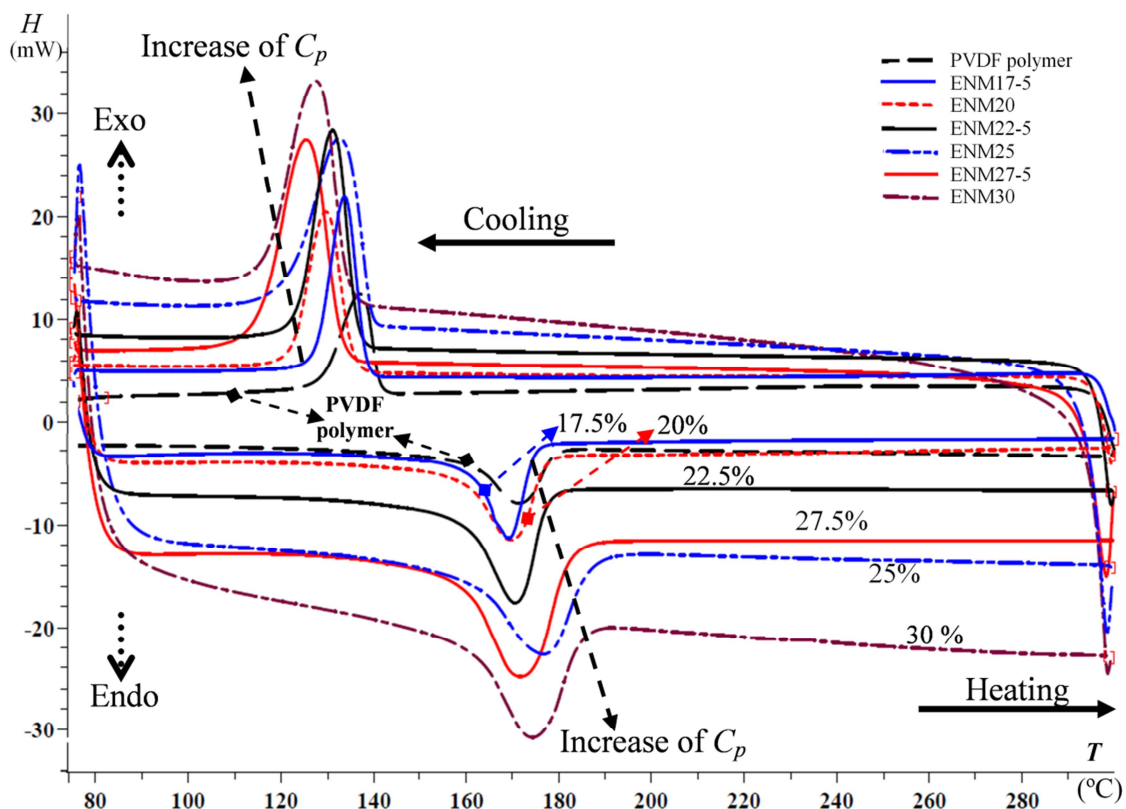
Figure 4.2.6. DSC exotherms and endotherms of the PVDF polymer and ENMs prepared with different concentrations of PVDF in the electrospinning polymer solution.

Although MD process is commonly operated under atmospheric pressure, a membrane to be used in MD should exhibit adequate mechanical properties to guarantee a successful packing in modules. The tensile behaviour of the prepared PVDF ENMs is presented in Fig. 4.2.7 and the corresponding mechanical data are summarized in Table 4.2.3. A gradual increase of the Young´s modulus and tensile strength of the ENMs was detected with the increase of the PVDF concentration in the polymer solution. However, no clear trend can be detected for the elongation at break with the PVDF concentration because of the high obtained values due to the web structure of the PVDF ENMs. It is important to note that the elongation at break of the prepared PVDF ENMs are an order of magnitude greater than the measured value of the Millipore commercial membrane HVHP (140 μm thickness, 0.45 μm mean pore size and 75 % porosity), which is 31.3 ± 5.0 % [15].
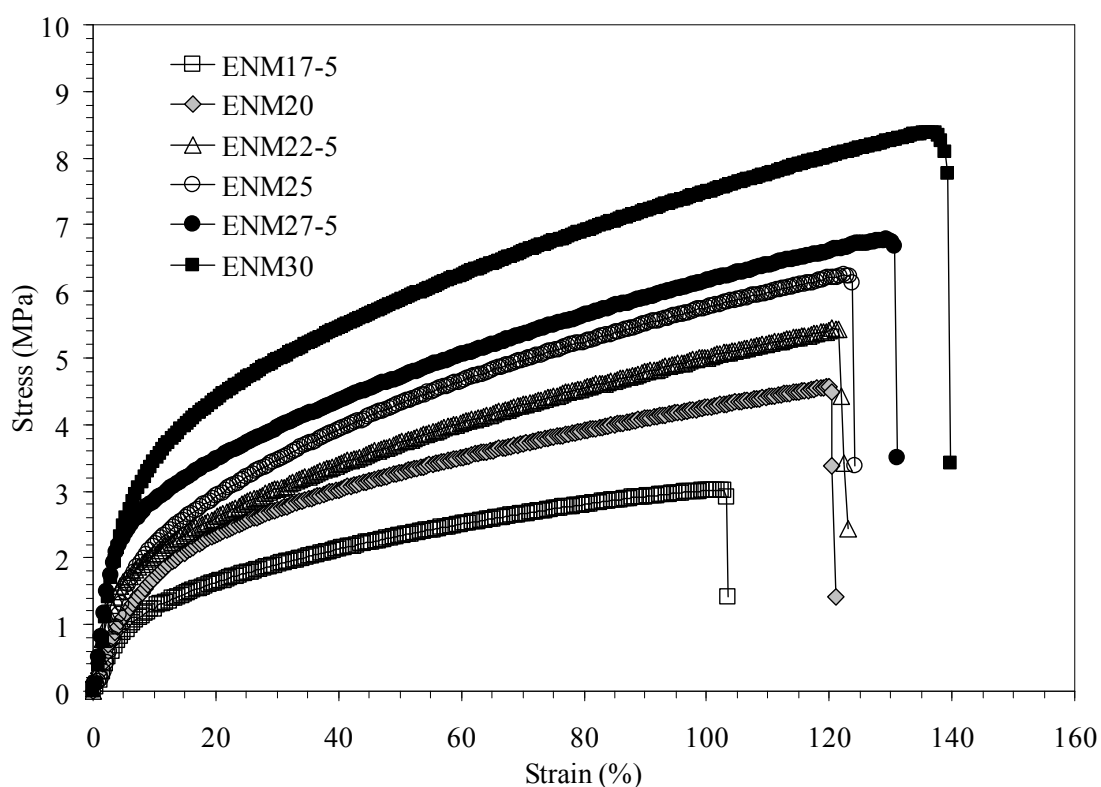
Figure 4.2.7. Stress–strain curves of the ENMs prepared with different PVDF concentrations in the electrospinning polymer solution.

The measured water contact angle (θ_a), liquid entry pressure (*LEP*), void volume fraction (ε) and size of inter-fiber space (d_i) of the PVDF ENMs are also summarized in Table 4.2.3. It was observed a slightly higher θ_a values of the PVDF ENMs with structures containing beads and droplets than the bead-free ENMs. In general, the water contact angle seems to decrease with the increase of the PVDF polymer concentration due to the decrease of the total beads density, the change from predominantly spherical to elongated beads and then to free-bead fibrous ENMs surface.

Table 4.2.3. Mechanical properties (Young's modulus, Y_M; tensile strength, T_S; elongation at break, E_b), water contact angle (θ_a), liquid entry pressure (*LEP*) of distilled water and 30 g/L NaCl aqueous solution, void volume fraction (ε), and mean size of inter-fiber space (d_i) of the PVDF ENMs prepared with different PVDF concentrations in the electrospinning polymer solution.

Membrane	Y_M (MPa)	T_S (MPa)	E_b (%)	(θ_a) (°)	LEP H_2O (10^3 Pa)	LEP 30 g/L (10^3 Pa)	ε (%)	d_i (µm)
ENM15	---	---	---	148.4 ± 2.4	---	---	---	--
ENM17-5	9.8 ± 0.7	2.6 ± 0.6	102.8 ± 1.5	148.0 ± 1.7	51.0 ± 2.8	53.5 ± 2.1	58.8 ± 1.8	1.64 ± 0.04
ENM20	13.9 ± 0.3	4.7 ± 0.2	128.9 ± 12.6	146.3 ± 2.6	62.5 ± 2.1	68.0 ± 1.4	65.8 ± 1.4	1.18 ± 0.01
ENM22-5	15.7 ± 1.2	5.3 ± 0.1	130.4 ± 14.0	145.7 ± 2.7	74.0 ± 1.4	67.0 ± 1.4	73.0 ± 1.5	1.00 ± 0.02
ENM25	17.9 ± 0.4	6.1 ± 0.2	120.5 ± 2.5	145.3 ± 0.6	46.5 ± 0.7	50.0 ± 1.4	93.3 ± 0.6	2.26 ± 0.25
ENM27-5	19.9 ± 0.3	6.6 ± 0.3	140.7 ± 16.3	143.9 ± 4.0	52.0 ± 1.4	58.0 ± 1.4	87.2 ± 1.1	1.45 ± 0.05
ENM30	26.7 ± 1.4	8.3 ± 0.1	128.4 ± 11.1	143.1 ± 3.4	65.5 ± 2.1	68.0 ± 1.4	79.0 ± 1.3	1.39 ± 0.15

The *LEP* of both distilled water and 30 g/L NaCl solution and the void volume fraction (ε) of the PVDF ENMs are plotted in Fig. 4.2.8 as a function of the PVDF concentration in the polymer solution. For all ENMs the obtained *LEP* of 30 g/L NaCl aqueous solution is slightly higher than that of distilled water. This is attributed to the higher surface tension of the salt aqueous solution compared to that of distilled water. The measured surface tension of 30 g/L NaCl in water is 75.7 ± 0.1 mN/m and that of water is 72.7 ± 0.1 mN/m. It is worth noting that based on the obtained *LEP* values and the SEM images of the ENMs (Fig. 4.2.1), the prepared ENMs can be divided into two groups, one containing the ENMs fabricated with low PVDF concentrations with

beaded structures (ENM17-5, ENM20 and ENM22-5) and the other group formed by bead-free ENMs electrospun with higher PVDF concentrations (ENM25, ENM27-5 and ENM30). In each group, the *LEP* values of both distilled water and 30 g/L NaCl aqueous solution increased with the increase of the PVDF concentration in the polymer solution. These results may be attributed partly to the decrease of the size of the inter-fiber space since the obtained water contact angles were varied slightly with the PVDF concentration. Therefore, it is expected a decrease of the maximum size of the inter-fiber space in each group of ENMs with increasing the PVDF concentration in the polymer solution. The *LEP* values of the prepared PVDF ENMs in this study are similar to that of the commercial membrane TF1000 (polytetrafluoroethylene supported on polypropylene net, Gelman) having a mean pore size of 844.3 nm [6].
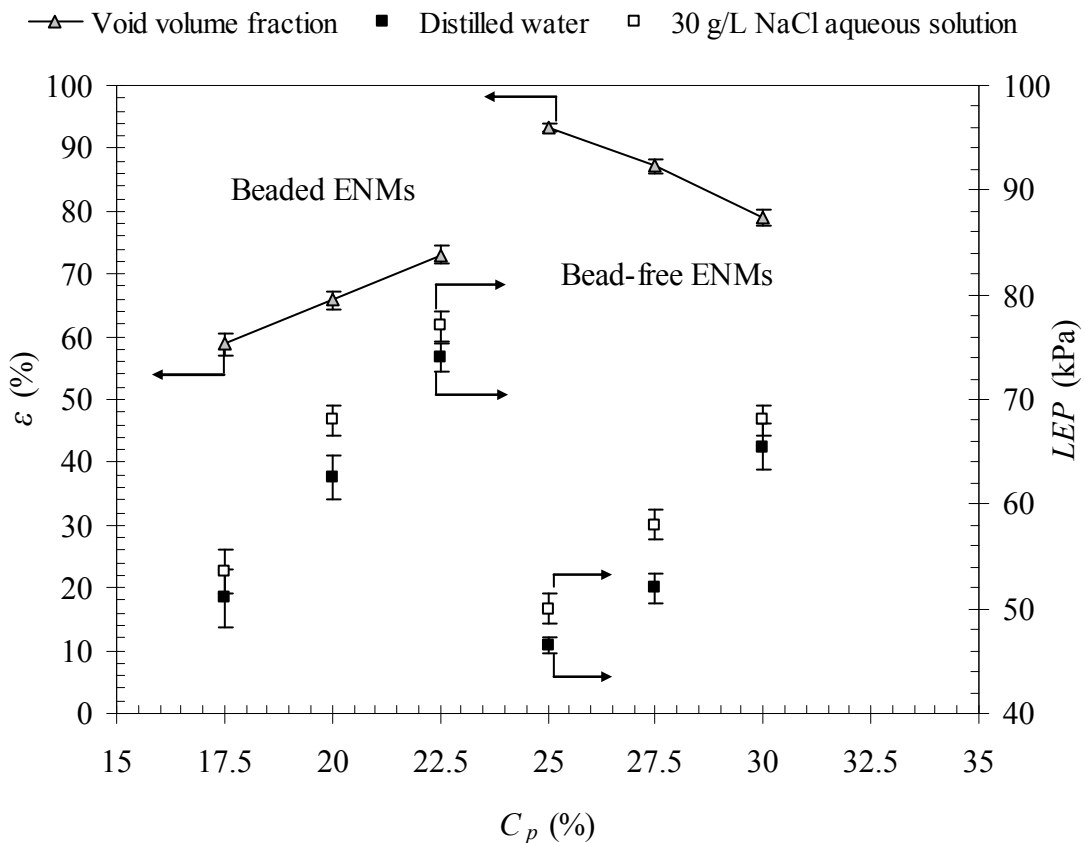

Figure 4.2.8. Effects of the PVDF concentration in the polymer solution on the void volume fraction (ε) and liquid entry pressure (*LEP*), of water and 30 g/L NaCl in aqueous solution, of the ENMs.

For the first group of PVDF ENMs (ENM17-5, ENM20 and ENM22-5), the void volume fraction (ε) increases from 58.8 to 73.0 % with the increase of the PVDF

concentration; whereas it decreases from 93.3 to 79.0 % for the second group of ENMs (ENM25, ENM27-5 and ENM30). Again, these results are attributed to the presence of beads. The observed increase of ε for the first group of ENMs may be attributed to the decrease of the bead density and the increase of the fibrous network. The decrease of ε for the bead-free ENMs is attributed partly to the increase of the fiber diameter. The highest ε value is obtained for the membrane ENM25.

The sizes of the inter-fiber space (d_i) of each PVDF ENM were evaluated. Both the cumulative inter-fiber space and its distribution are plotted in Fig. 4.2.9. The mean, minimum and maximum sizes are given in Table 4.2.3. Again, based on the obtained inter-fiber space, the prepared ENMs can be divided into the same two groups indicated previously. In each group, the inter-fiber space is reduced with increasing the PVDF concentration in the polymer solution. This is attributed to the increase of the nano-fiber size. This result was expected from the *LEP* values of each group of ENMs. Based on the void volume fraction and the inter-fiber space, it may be expected a higher DCMD permeate flux of the second group of ENMs (ENM25, ENM27-5 and ENM30) compared to the other group of ENMs.
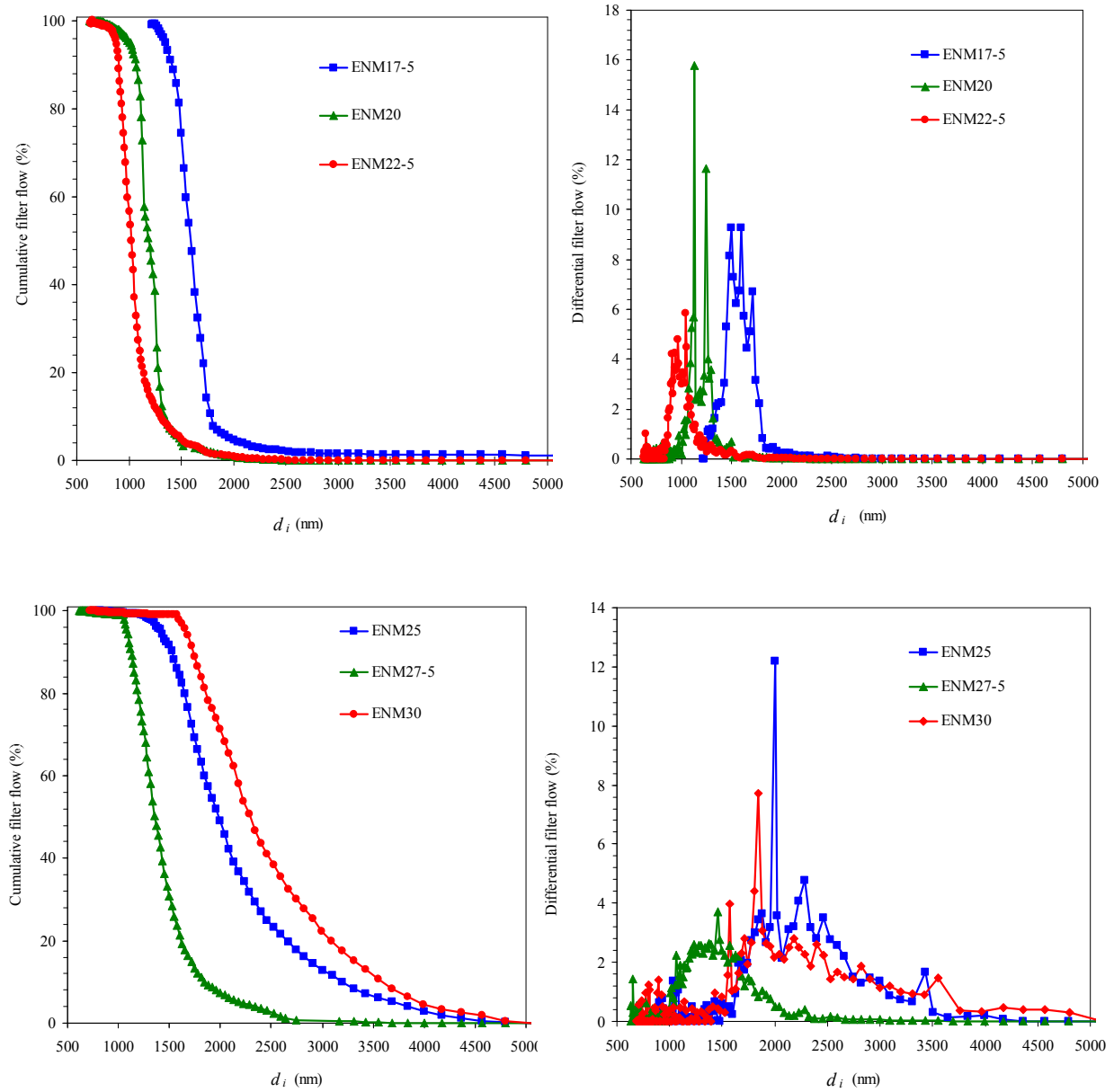
Figure 4.2.9. Cumulative and distribution of the inter-fiber space of ENMs prepared with different PVDF concentrations in the electrospinning polymer solution.

4.2.3.3. DCMD performance of the PVDF ENMs

Desalination by DCMD using the PVDF ENMs was performed as stated previously. Figure 4.2.10(a) shows the measured DCMD permeate fluxes of the PVDF ENMs of 30 g/L NaCl aqueous feed solution and distilled water before and after each desalination test. The permeate flux of all tested ENMs decreases with the addition of salt to the feed aqueous solution because of the reduction of the water vapour pressure at the feed/ENM interface and to the concentration polarization effect. No clear changes were observed between the initial permeate flux of distilled water and that measured after desalination experiment indicating that the stable permeability of the prepared ENMs. As it was expected, the DCMD permeate flux is much higher for bead-free ENMs (ENM25, ENM27-5 and ENM30) although these ENMs are thicker than the membranes belonging to the first group of ENMs. This is mainly attributed to the greater void volume fraction of these ENMs and to some extent to their lower heat transfer by conduction and mechanism of vapour transport through the inter-fiber space of the ENMs as reported in a previous study [16].

Furthermore, among the bead-free ENMs (second group), the permeate flux is higher for the ENM exhibiting higher void volume fraction, higher inter-fiber space and thinner ENM. However, among the beaded ENMs (first group) the permeate flux is lower for the ENM exhibiting higher void volume fraction, lower inter-fiber space and thicker ENM. It is known that the thinnest is the ENM the highest is the water production rate because the membrane permeability is inversely proportional to the membrane thickness. The distance between evaporation and condensation phenomena that occur at the liquid/vapour interfaces formed at both sides of the ENM is smaller for thinner ENMs and hence the water production rate is enhanced. However, as the thickness is increased the heat loss by conduction through the ENM is decreased favouring the energy efficiency of the DCMD process. The choice of a membrane for MD applications is a compromise between a low heat transfer flux by conduction achieved using thicker membranes and a high permeate flux achieved using thin membranes having large pore size, low pore tortuosity and high porosity. The thickness normalized permeate flux of the ENMs was calculated and it was found that it is an order of magnitude higher for the bead-free ENMs.
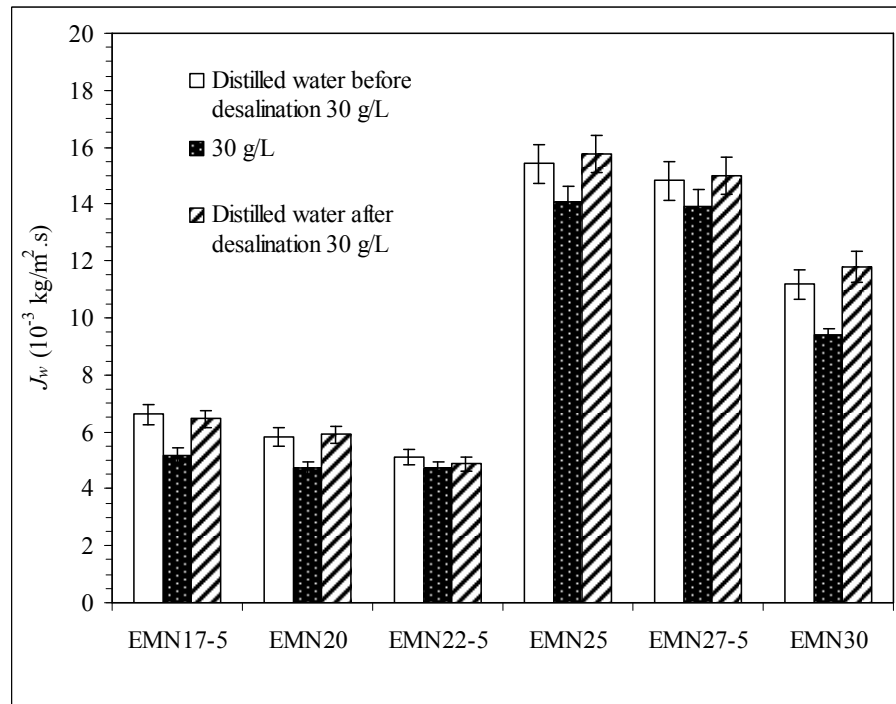
(a)
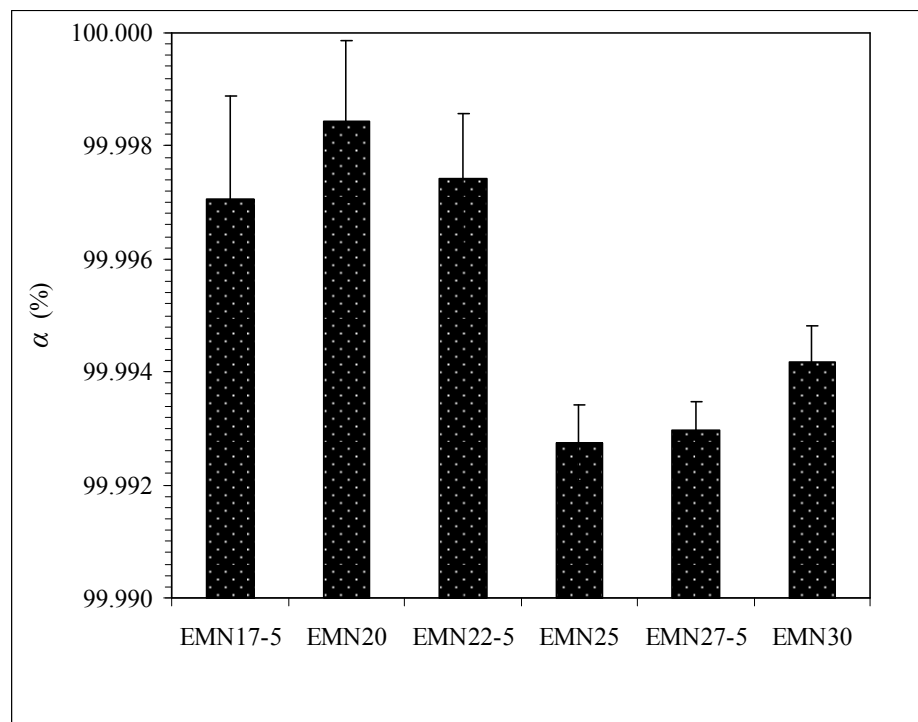
(b)

Figure 4.2.10. DCMD permeate flux (J_w) (a) and salt rejection factor (α) of the ENMs prepared with different PVDF concentrations in the electrospinning solution.

Figure 4.2.10(b) shows the salt rejection factor ($\alpha = \left(1 - C_{b,p} / C_{b,f}\right) \, 100$, where $C_{b,p}$ and $C_{b,f}$ are the salt concentration of the bulk permeate and feed solutions, respectively) of the PVDF ENMs. In general, the obtained α values for all tested PVDF ENMs are greater than 99.99 % indicating that all tested ENMs produced distilled water.

The bead-free PVDF ENMs prepared in this study exhibit similar MD performance to those obtained in our previous studies [15,16] and, as can be seen in Table 4.2.4, exhibit higher MD performance than the PVDF ENMs reported by other authors [8,10-14]. The highest MD permeate fluxes were reported by Maab et al. [11] using fluorinated polyxadiaxoles and polytriazoles and were patented by Khayet and García-Payo [7] using the copolymer Polyvinylidene fluoride-co-hexafluoropropylene (PVDF-HFP).

Table 4.2.4. Reported MD permeate flux (J_w) of different electrospun nano-fibrous membranes used for desalination.

Membrane type	J_w (10^{-3} kg/m^2.s)	Observation	Ref.
Polyvinylidene fluoride-co-hexafluoropropylene (PVDF-HFP)	> 22.8	DCMD; α> 99.5%	[7]
PVDF	3.2	AGMD; α> 98.5%	[8]
PVDF-clay nanocomposite	~1.6 [a]	DCMD; α> 99%	[10]
Fluorinated polyxadiaxoles & polytriazoles	23.6	DCMD; α< 99.95%	[11]
PVDF	5.7	DCMD; χ< 5 µS/cm	[12]
Superhydrophobic Integrally modified PVDF (I-PVDF)	8.8	DCMD; χ < 5 µS/cm	[13]
Polyvinylidene fluoride-co-hexafluoropropylene (PVDF-HFP)	~6.1	DCMD; α> 98%	[14]
PVDF	15.2	DCMD; α> 99.39%	[15,16]
PVDF	10.8	DCMD; α> 99.99%	This study

[a] ~5.7 kg/m^2.h (we believe that this is the right unit although in Ref. [10] the permeate flux was reported in kg/m/hr).
[b] Electrical conductivity of the MD permeate (χ in µS/cm).

4.2.4. Conclusions

Both beaded and bead-free ENMs have been prepared for desalination by DCMD using different PVDF concentrations in the solvent mixture 80/20 wt% of *N,N*-dimethyl acetamide and acetone. The previously optimum electrospinning parameters obtained by means of statistical factorial model and Monte Carlo optimization method are applied in this study, a voltage of 24.1 kV, an air gap of 27.7 cm and a polymer flow rate of 1.23 mL/h [32].

Taking into consideration the surface tension, electrical conductivity and viscosity of the used PVDF polymer solutions, the reason for the observed different morphological structures of the electrospinning films might be due the increase of the viscosity and polymeric chain entanglements with the increase of the PVDF concentration in the polymer solution. The critical chain entanglement concentration (C_e), which is the minimum PVDF concentration required for electrospinning beaded fibers, was found to be 18.28 wt%. The morphology of the beads changed from spherical to elongated or elliptical and their density decreases with increasing the PVDF concentration of PVDF in the polymer solution from 15 to 22.5 wt%, while the amount of fiber formation was increased. The minimum concentration required for electrospinning uniform bead-free fibers was found to be slightly higher than 22.5 wt%.

The mean fiber diameter (d_f) and the thickness (δ) of the ENMs increased with increasing PVDF concentration. Two groups of ENMs were identified.

Based on the SEM images, *LEP* and void volume fraction (ε) values of the PVDF ENMs, two groups were identified. Bead-free ENMs fabricated with higher PVDF concentrations than 22.5 wt% and the other group of ENMs having different types of beads prepared with lower PVDF concentrations.

In each group of ENMs, the inter-fiber space is reduced with increasing the PVDF concentration in the polymer solution. However, due to the bead-free cohesive web of fibrous structure the group of ENMs prepared with higher PVDF concentration than 22.5 wt% exhibits higher void volume fractions and DCMD desalination performance than the other group of ENMs containing beads.

The optimum PVDF concentration for electrospun nano-fiber formation was found to be 25 wt%. This ENM exhibits a DCMD permeate flux of 12.15 x 10^{-3} kg/m^2.s and 10.8 x 10^{-3} kg/m^2.s for distilled water and 30 g/L NaCl feed aqueous solution operating at a feed temperature of 80 ºC and a permeate temperature of 20 ºC. The NaCl rejection factor was higher than 99.99 %.

References

[1] Z.M. Huang, Y.Z. Zhang, M. Kotaki, S. Ramakrishna, A review on polymer nanofibers by electrospinning and their applications in nanocomposites, Composites Sci. Technol. 63 (2003) 2223–2253.

[2] R.S. Barhate, S. Ramakrishna, Nanofibrous filtering media: Filtration problems and solutions from tiny materials: Review, J. Membr. Sci., 296 (2007) 1-8.

[3] I.S. Chronakis, Novel nanocomposites and nanoceramics based on polymer nanofibers using electrospinning process: A review, Mat. Proc. Tech., 167 (2005) 283-293.

[4] C. Feng, K.C. Khulbe, T. Matsuura, S. Tabe, A.F. Ismail, Review: Preparation and characterization of electro-spun nanofiber membranes and their possible applications in water treatment, Sep. Purf. Tech., 102 (2013) 118-135.

[5] M. Khayet, Membranes and theoretical modeling of membrane distillation: a review, Adv. Colloid Interface Sci., 164(1-2) (2011) 56-88.

[6] M. Khayet, T. Matsuura, Membrane Distillation: Principles and Applications, Elsevier, The Netherlands, 2011.

[7] M. Khayet, M.C. García-Payo, Nanostructured Flat membranes for Direct Contact Membrane Distillation. PCT/ES2011/000091, WO/2011/117443 (2011).

[8] C. Feng, K.C. Khulbe, T. Matsuura, R. Gopal, S. Kaur, S. Ramakrishna, M. Khayet, Production of drinking water from saline water by air-gap membrane distillation using polyvinylidene fluoride nanofiber membrane, J. Membr. Sci., 311 (2008) 1-6.

[9] C. Feng, K.C. Khulbe, S. Tabe, Volatile organic compound removal by membrane gas stripping using electro-spun nanofiber membrane, Desalination, 287 (2012) 98-102.

[10] J.A. Prince, G. Singh, D. Rana, T. Matsuura, V. Anbharasi, T.S. Shanmugasundaram, Preparation and characterization of highly hydrophobic poly(vinylidene fluoride)-clay nanocomposite nanofiber membranes (PVDF-clay NNMs) for desalination using direct contact membrane distillation, J. Membr. Sci., 397-398 (2012) 80-86.

[11] H. Maab, L. Francis, A. Al-Saadi, C. Aubry, N. Ghaffour, G. Amy, S.P. Nunes, Synthesis and fabrication of nanostructured hydrophobic polyazole membranes for low-energy water recovery, J. Membrane Sci., 423-424 (2012) 11-19.

[12] Y. Liao, R. Wang, M. Tian, C. Qiu, A.G. Fane, Fabrication of polyvinylidene fluoride (PVDF) nanofiber membranes by electro-spinning for direct contact membrane distillation, J. Membrane Sci., 425-426 (2013) 30-39.

[13] Y. Liao, R. Wang, A.G. Fane, Engineering superhydrophobic surface on poly(vinylidene fluoride) nanofiber membranes for direct contact membrane distillation, J. Membrane Sci., 440 (2013) 77-87.

[14] B.S. Lalia, E.G. Burrieza, H.A. Arafat, R. Hashaikeh, Fabrication and characterization of polyvinylidenefluoride-*co*-hexafluoropropylene (PVDF-HFP) electrospun membranes for direct contact membrane distillation, J. Membrane Sci., 428 (2013) 104-115.

[15] M. Essalhi, M. Khayet, Self-sustained webs of polyvinylidene fluoride electrospun nano-fibers at different electrospinning times: 1. Desalination by direct contact membrane distillation, J. Membrane Sci., 433 (2013) 167-179.

[16] M. Essalhi, M. Khayet, Self-sustained webs of polyvinylidene fluoride electrospun nano-fibers at different electrospinning times: 2. Theoretical analysis, polarization effects and thermal efficiency, J. Membrane Sci., 433 (2013) 180-191.

[17] J.M. Deitzel, J. Kleinmeyer, D. Harris, N.C.B. Tan, The effect of processing variables on the morphology of electrospun nanofibers and textiles, Polymer 42 (2001) 261–272.

[18] S. Megelski, J.S. Stephens, D.B. Chase, J.F. Rabolt, Micro-and nanostructured surface morphology on electrospun polymer fibers, Macromolecules 35 (2002) 8456–8466.

[19] D. Li, Y. Xia, Electrospinning of nanofibers: Reinventing the Wheel?, Advanced Materials, 16 (2004) 1151-1170.

[20] C. Casper, J. Stephens, N. Tassi, D. Chase, J. Rabolt, Controlling surface morphology of electrospun polystyrene fibers: effect of humidity and molecular weight in the electrospinning process, Macromolecules, 37 (2004) 573–578.

[21] M. Nasir, H. Matsumoto, T. Danno, M. Minagawa, T. Irisawa, M. Shioya, A. Tanioka, Control of diameter, morphology, and structure of PVDF nanofiber fabricated by electrospray deposition, J. Polym. Sci. Part B: Polym. Phys. 44 (2006) 779–786.

[22] S.W. Choi, J.R. Kim, Y.R. Ahn, S.M. Jo, E.J. Cairns, Characterization of electrospun PVdF fiber-based polymer electrolytes, Chem. Materi., 19 (2007) 104-115.

[23] O.S. Yördem, M. Papila, Y.Z. Menceloğlu, Effects of electrospinning parameters on polyacrylonitrile nanofiber diameter: an investigation by response surface methodology, Mater. Des. 29 (2008) 34–44.

[24] D. Zhang, J. Chang, Electrospinning of three-dimensional nanofibrous tubes with controllable architectures, Nano Lett. 8 (2008) 3283–3287.

[25] A. Baji, Y.W. Mai, S.C. Wong, M. Abtahi, P. Chen, Electrospinning of polymer nanofibers: Effects on oriented morphology, structures and tensile properties, Comp. Sci. Technol. 70 (2010) 703–718.

[26] S.L. Shenoy, W.D. Bates, H.L. Frisch, G.E. Wnek, Role of chain entanglements on fiber formation during electrospinning of polymer solutions: good solvent, non-specific polymer-polymer interaction, Polymer, 46 (2005) 3372-3384.

[27] L. Yao, T.W. Haas, A. Guiseppi-Elie, G.L. Bowlin, D.G. Simpson, G.E. Wnek, Electrospinning and stabilization of fully hydrolyzed poly(vinyl alcohol) fibers, Chem. Mater., 15 (2003) 1860-1864.

[28] K.H. Lee, H.Y. Kim, H.J. Bang, Y.H. Jung, S.G. Lee, The change of bead morphology formed on electrospun polystyrene fibers, Polymer, 44 (2003) 4029-4034.

[29] C.M. Hsu, S. Shivkumar, Nano-sized beads and porous fiber constructs of poly(ε-caprolactone) produced by electrospinning, J. Materials Sci., 39 (2004) 3003-3013.

[30] Y. Liu, J.H. He, J.Y. Yu, H.M. Zeng, Controlling numbers and sizes of beads in electrospun nano-fibers, Polym. Int., 57 (2008) 632-636.

[31] A.W. Adamson, Physical Chemistry of Surfaces, John Wiley & Sons, New York, 1990.

[32] M. Essalhi, M. Khayet, C. Cojocaru, M.C. García-Payo, P. Arribas, Response surface modeling and optimization of electrospun nanofiber membranes, The Open Nanoscience Journal, 7 (2013) 8-17.

[33] M. Essalhi, M. Khayet, Surface segregation of fluorinated modifying macromolecule for hydrophobic/hydrophilic membrane preparation and application in air gap and direct contact membrane distillation, J. Membr. Sci., 417- 418 (2012) 163-173.

[34] H. Fong, I. Chun, D.H. Reneker, Beaded nanofibers formed during electrospinning, Polymer, 40 (1999) 4585-4592.

[35] A.V. Dobrynin, R.H. Colby, M. Rubinstein, Scaling theory of polyelectrolyte solutions, Macromolecules, 28 (1995) 1859-1871.

[36] W.E. Krause, J.S. Tan, R.H. Colby, Semidilute solution rheology of polyelectrolytes with no added salt, J. Polym. Sci. Part B Polym Phys, 37 (1999) 3429-3437.

[37] K.H. Chang, H.L. Lin, Electrospin of polysulfone in N,N´-dimethyl acetamide solutions, J. Polym. Res. 16 (2009) 611-622.

[38] M.G. McKee, G.L. Wilkes, R.H. Colby, T.E. Long, Correlations of solution rheology with electrospun fiber formation of linear and branched polyesters, Macromolecules, 37 (2004) 1760-1767.

[39] P. Gupta, C. Elkins, T.E. Long, G. L. Wilkes, Electrospinning of linear homopolymers of poly(methyl methacrylate): exploring relationships between fiber formation, viscosity, molecular weight and concentration in a good solvent, Polymer, 46 (2005) 4799-4810.

[40] M.G. McKee, C.L. Elkins, T.E. Long, Influence of self-complementary hydrogen bonding on solution rheology/electrospinning relationships, Polymer, 45 (2004) 8705-7815.

[41] C. Mit-uppatham, M. Nithitanakul, P. Supaphol, Ultrafine electrospun polyamide-6 fibers: Effect of solution conditions on morphology and average fiber diameter, Macromol. Chem. Physic., 205 (2004) 2327-2338.

[42] J.M. Deitzel, J. Kleinmeyer, J.K. Hirvonen, T.N.C. Beck, Controlled deposition of electrospun poly(ethylene oxide) fibers, Polymer, 42 (2001) 8163-8170.

[43] M.M. Demir, I. Yilgor, E. Yilgor, B. Erman, Electrospinning of polyurethane fibers, Polymer, 43 (2002) 3303-3309.

4.3. Self-Sustained Webs of Polyvinylidene Fluoride Electrospun Nanofibers at Different Electrospinning Times: 1. Desalination by Direct Contact Membrane Distillation

Contents:

4.3.1. Introduction

4.3.2. Experimental

      4.3.2.1. Materials

      4.3.2.2. ENMs fabrication

      4.3.2.3. ENMs characterization

      4.3.2.4. Direct contact membrane distillation (DCMD)

4.3.3. Results and discussions

      4.2.3.1. SEM images of the ENMs and effects of the PVDF polymer concentration

      4.2.3.2. Characteristics of the ENMs

      4.2.3.3. DCMD performance of the PVDF ENMs

4.3.4. Conclusions

References

Abstract:

Self-sustained electrospun nanofibrous membranes (ENMs) were prepared using the polymer polyvinylidene fluoride (PVDF) and applied for desalination by direct contact membrane distillation (DCMD). Different electrospinning times were considered to prepare the PVDF ENMs of different thicknesses ranging from 144.4 to 1529.3 µm. A systematic experimental study on the effects of membrane thickness on the DCMD performance is carried out for the first time. The surface and cross-section of the ENMs were studied by scanning electron microscopy and the mean size of the fibers together with its distribution were determined. The water contact angle, the inter-fiber space, the void volume fraction and the liquid entry pressure of water inside the inter-fiber space were determined by different characterization techniques. It was observed an enhancement of the thickness and the liquid entry pressure of water with the increase of electrospinning time, a decrease of the mean size of the inter-fiber space, whereas no significant changes were observed for the diameter of the electrospun fibers (1.0 – 1.3 µm), the void volume fraction (0.85 – 0.93) and the water contact angle (137.4 - 141.1º). The size of the inter-fiber space is not uniform throughout the thickness of the ENMs. The effects of the ENMs thickness on the DCMD performance was studied for different feed temperatures and sodium chloride feed aqueous solutions with concentrations up to 60 g/L, which is about two times greater than a typical seawater concentration. The permeate flux of the ENMs is lower for longer electrospinning time and the obtained permeate fluxes in this study are higher than those reported so far for PVDF ENMs.

4.3.1. Introduction

Electrospinning or electrostatic spinning has emerged as a very attractive approach for the fabrication of nanometer- and submicrometer-sized fibers under the application of a strong electric field to a polymer or biopolymer liquid solution [1,2]. Although the first patent for the electrospinning technique dates in 1934 [3], during last years a great attention has been paid to this technology using both synthetic and natural polymers for a wide range of applications such as in tissue engineering, drug delivery, sensors, semi-conductive materials, photovoltaic cells, reinforced nanocomposites, membrane filtration, and many more [4-12].

Electrospun nanofibrous membranes (ENMs) exhibit several attractive attributes for separation technology such as high void volume fraction, interconnected open structure, high surface-to-mass (or volume) ratio, good resistance to the penetration of chemical and biological agents, highly ordered polymer chains, more controllable structure than the phase inversion hollow fiber and flat sheet membranes, etc. Despite the observed encouraging results, still a lot of research studies should be performed in the field of ENMs and especially in pressure-driven separation processes such as microfiltration (MF), ultrafiltration (UF) and nanofiltration (NF) applied for water treatment [12-17]. ENMs for these separation processes require the use of adequate supports to provide them with the necessary strength and to make them strong enough to prevent their deflection and rupture without increasing the mass transfer resistance [12,14,15]. Surface or bulk modifications of ENMs were also considered [16,17].

An interesting application for ENMs is the non-isothermal distillation, which can be carried out for advanced water treatments without applying any transmembrane hydrostatic pressure and therefore self-sustained webs can be used [18-21]. Additionally, ENMs offer some attractive characteristics for membrane distillation (MD) such as a high hydrophobicity and therefore ENMs are less susceptible to wetting by the feed water solutions if the inter-fiber space is adequately designed (i.e. liquid entry pressure, *LEP*, in the inter-fiber space should be high to let only vapor to transport through the ENM); a high void volume fraction providing large spaces for evaporation, a low thermal conductivity to reduce heat loss by conduction through ENMs (i.e. the conductive heat transfer through ENMs is slightly associated to vapor transfer through their void volume as the thermal conductivity of gas-filled inter-fiber space is an order of

magnitude smaller than the thermal conductivity of the polymer fiber); and a high surface roughness, which reduces both the temperature and concentration polarization effects enhancing therefore the water production rate [22].

Last year a patent was filed by Khayet and García-Payo on the development of ENMs for MD [18]. Different polymers and copolymers were proposed. Feng et al. [19,20] and Prince et al. [21] reported also on the use of poly(vinylidene fluoride) (PVDF) ENMs membranes in MD. Feng et al. [19,20] electro-span a PVDF membrane of a thickness 0.15 mm with a polymer solution containing 18 wt% PVDF (Kynar 761, Elf-Chem USA) in the solvent dimethylformamide (DMF) using 18 kV voltage, 2 ml/h flow rate of the polymer solution and 18 cm air gap between the needle and the flat metallic collector. After electrospinning, the ENM was dried in a fume hood for 24 h at room temperature. As specified by the authors, the prepared ENM exhibited a contact angle of 128°, a fiber diameter of about 500 nm, a mean "pore" size (i.e. size of the inter-fiber space) of 0.32 μm, a "porosity" (i.e. void volume fraction) of 76% and a liquid entry pressure of water (*LEP*) of 121.35 kPa [20]. This ENM was applied first for desalination by air gap membrane distillation (AGMD) using different sodium chloride (NaCl) feed concentrations (0, 35, 60 g/L) and feed temperatures (37 – 82ºC), and then used for the removal of volatile organic compounds (1000 ppm chloroform in water) from water by membrane gas striping at 23ºC and 60ºC feed temperatures [19]. Similar AGMD trends as those observed for other types of membranes were obtained for desalination by the PVDF ENM and the values of the permeate flux was as high as 11.5 kg/m^2.h with NaCl rejection factors higher than 98.5%. It was claimed that the AGMD permeate flux is comparable to the permeate fluxes of the commercial microfiltration (MF) membranes (5 – 28 kg/m^2.h) at transmembrane temperatures ranging from 25ºC to 83ºC. The same ENM membrane was also applied for chloroform removal from water by nitrogen gas striping at two different feed temperatures 23ºC and 60ºC using an initial chloroform concentration of 1000 ppm in water. It was observed a reduction of chloroform concentration in the feed container with time and this was attributed to the chloroform transport through the PVDF ENM, which was higher at 60ºC than at 23ºC (i.e. higher mass transfer coefficient at 60ºC, 11.32 10^{-5} m/s, than at 23ºC, 2.40 10^{-5} m/s). Feng et al. [20] concluded that chloroform could be removed by the PVDF ENM due to its high surface hydrophobicity and appropriate size of the inter-fiber space. The obtained overall mass transfer

coefficients of chloroform for PVDF ENM was higher than the highest value obtained for hollow fiber membranes applied so far in gas stripping.

Prince et al. [21] used the same PVDF polymer (Kynar 761, supplied by Arkema Pte. LTD., Singapore) to prepare four PVDF-clay (Cloisite® 20A, Southern Clay products Inc. TX USA) nanocomposite ENMs for desalination by direct contact membrane distillation (DCMD). A lower polymer concentration was considered, 12 wt% in the solvent mixture *N,N´*-dimethyl acetamide (DMAC) and acetone (ratio 2:3 by weight), and electrospinning was carried out applying a lower voltage (16 kV) and a lower polymer flow rate (1 ml/h) than those applied by Feng et al. [19,20]. The air gap between the needle and the collector was not provided and a rotating metal drum was employed to collect the ENMs with a thickness of 300 ± 25 µm. After electrospinning the ENMs were dried at room temperature for one day. The concentration of the clay was varied in the range $0 - 8$ wt%. With the addition of clay nanocomposite it was observed an increase of the surface hydrophobicity of the PVDF ENM from 128.0º to 154.2º, the fibers diameter from 417 to 625 nm, the mean size of the inter-fiber space from 0.58 to 0.64 µm and the *LEP* from 90 to 200 kPa, whereas the void volume fraction was maintained practically the same at 81-82%. It was reported that the DCMD performance was improved with the addition of clay nanocomposite. When using a feed salt NaCl concentration of 35 g/L, feed temperatures ranging from 50ºC to 80ºC and a permeate temperature of 17ºC, the salt rejection factor was increased from 98.27% for the PVDF ENM to 99.97% for the PVDF-clay nanocomposite ENM prepared with 8 wt% clay concentration in the polymer solution. The permeate flux increased also with the increase of the feed temperature up to ~5.7 kg/m^2.h (we believe that this is the right unit although in Ref. [21] the permeate flux was reported in kg/m/hr). For the PVDF ENM prepared without clay or with 2 wt% clay concentration, the permeate flux and the salt rejection factor declined after 3 h DCMD tests. This was attributed to the inter-fiber space wetting of these ENMs. It is worth quoting that the DCMD permeate fluxes of these PVDF-clay nanocomposite ENMs are smaller than the AGMD permeate flux of the PVDF ENM reported by Feng et al. [19]. This is attributed mainly to the thickness of the ENMs, which were 2 times greater for the PVDF ENMs prepared by Prince et al. [21] compared to the PVDF ENM prepared by Feng et al. [19].

It is generally admitted that the MD permeate flux increases with the increase of the pore size and/or porosity and decreases with the increase of the membrane thickness [22-29]. The

334

choice of a membrane for MD applications is a compromise between a low heat transfer flux by conduction achieved using thicker membranes and a high permeate flux achieved using thin membranes having large pore size, low pore tortuosity and high porosity. More characteristics required for an MD membrane were detailed elsewhere [22-29].

In this study, PVDF ENMs of different thicknesses are prepared by electrospinning and applied for desalination by DCMD using different feed temperatures and salt (NaCl) concentrations. A systematic experimental study on the effects of the membrane thickness on the DCMD performance is carried out for the first time. The DCMD performance is compared to the above cited ENM membranes proposed by Feng et al. [19] and Prince et al. [21] and to other types of membranes used in DCMD.

4.3.2. Experimental

4.3.2.1. Materials

The polymer PVDF purchased from Sigma-Aldrich Chemical Co., was used for the fabrication of ENMs. The dope solution was prepared by a mixture of acetone (Sigma-Aldrich Chemical Co.) and *N,N*-dimethyl acetamide (DMAC, Sigma-Aldrich Chemical Co.). Isopropyl alcohol (IPA) was used to determine the void volume fraction and the size of the inter-fiber space, and the sodium chloride (NaCl) used in DCMD experiments was also purchased from Sigma-Aldrich Chemical Co.

4.3.2.2. ENMs fabrication

The polymer solution was first prepared by dissolving 25 wt% PVDF in the solvent mixture acetone/DMAC (20/80 wt%). The polymer PVDF was added to the solvent mixture and kept at 45ºC under agitation for about 24 h until it was totally dissolved. The PVDF electrospun solution has 34.7 ± 0.4 mN/m surface tension, 17.28 Pa.s viscosity and 12.92 ± 0.04 μS/cm electrical conductivity at 20ºC. Prior to electrospinning, the polymer solution was degassed overnight at room temperature.

Electrospinning permits the formation of micro- and nano-fibers through an electrically charged jet of the polymer PVDF solution. A high voltage 24 kV is applied to the PVDF solution such that charges are induced within it. A jet erupts from the droplet at the tip of the needle resulting in the formation of a Taylor cone. The electrospinning jet travels towards the region of lower potential, which in this case is a grounded metallic collector. In this study, the electrospinning set-up used to fabricate the self-sustained PVDF webs is shown in Fig. 4.3.1. It consists of a glass syringe (Nikepal, 50 mL) to hold the polymer solution connected to a circulation pump (kd Scientific, Panlab S.I.; model KD.S-200-CE), two electrodes (a metallic needle and a grounded metallic collector kept in horizontal position) and a DC voltage supply in the kV range (Iseg; model T1CP 300 304P; 1x30 kV/0.3 mA) with an electric intensity in the range of μA. The polymer drop from the tip of the needle (0.6/0.9 mm inner/outer diameters) connected to the syringe by a Teflon tube is drawn into a fiber due to the high voltage. The jet is electrically charged and the charge causes the fibers to bend. Every time the polymer fiber loops in the air gap between the needle and the horizontal collector, its diameter is reduced. As the electrified jet travels through the air gap (23ºC temperature and 36% humidity), the solvent evaporates while the polymer fiber is stretched, elongated, whipped and finally deposited on the form of a non-woven mat on the grounded metallic collector during a predetermined time (1 − 4 h). The needle and the metallic collector are placed inside an open glass box (30 cm x 30 cm x 55 cm length x width x height). The polymer flow rate is 1.23 mL/h and the air gap distance between the needle and the collector is 27.7 cm. After electrospinning the ENMs were dried in oven at 80ºC for 30 min (i.e. post-treatment).
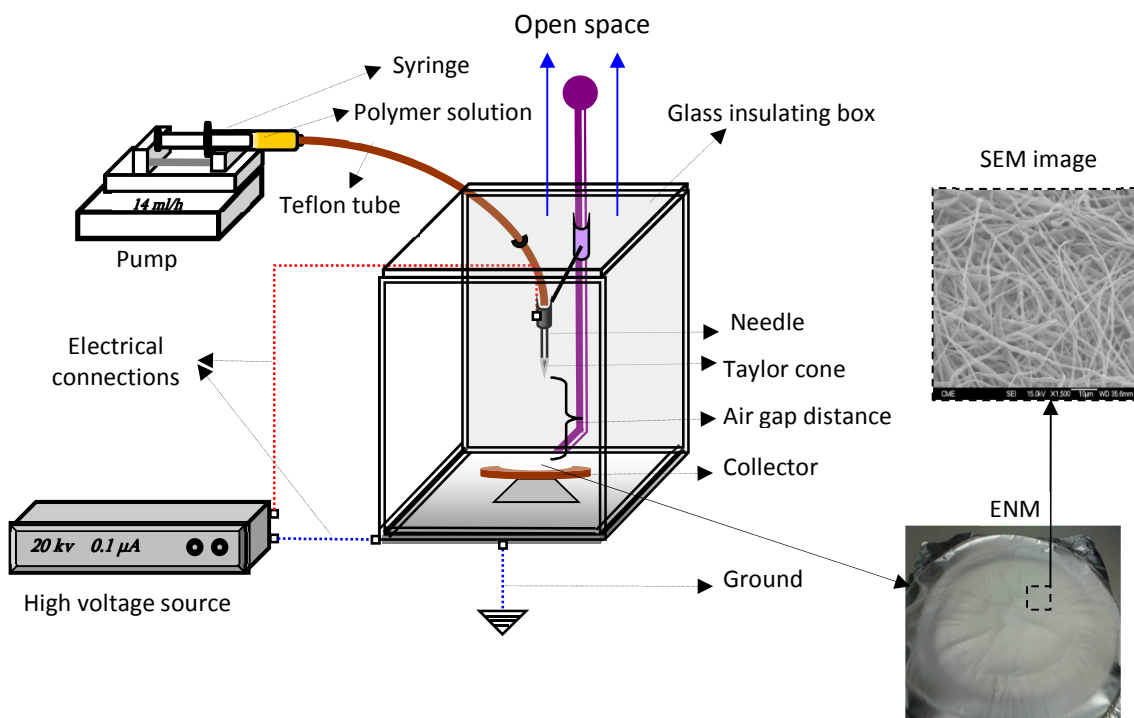
Figure 4.3.1. Schematic diagram of electrospinning set-up.

4.3.2.3. ENMs characterization

Differential scanning calorimetry (DSC) (Mettler Toledo, DSC1 Star^e System, Spain) was used to study the thermal properties of the ENMs and the polymer PVDF. The ENM sample, about 9 mg, was heated from 30ºC to 300ºC at 15ºC/min and then cooled down to room temperature. The heating and cooling cycle was repeated at least 7 times for each sample. For each ENM three different samples were considered. The melting temperature (T_m), the enthalpy of melting (ΔH_m), the crystallization temperature (T_m) and the heat of crystallization (ΔH_c) of both the PVDF polymer and ENMs were determined by Star^e software (Version 10.00d Build 3690).

The surface and the cross-section of the self-sustained PVDF webs were examined by a field emission scanning electron microscope (SEM, JEOL Model JSM-6330F). First, the ENMs samples were fractured in liquid nitrogen, then they were placed over a support and coated with

gold under vacuum conditions. Micrographs from the SEM analysis were analyzed by UTHSCSA ImageTool 3.0 to determine the size of the fibers. For each sample more than 5 SEM images have been considered and the diameters of a total number of 100 fibers have been measured. Statistical analysis have been applied in order to determine the fiber size distribution and to estimate the arithmetic weighted mean of the fiber diameters and their dispersions.

The mechanical properties of the PVDF ENMs were investigated according to ASTM D 3379-75 specifications on an Instron dynamometer (model 3366) at 23ºC, and at a cross-head speed of 22 mm/min with an initial length of the ENM sample of 50 mm and 4.15 mm width. At least five specimens taken from the center of ENM samples were tested. For comparison, the tensile test of the commercial PVDF membrane (HVHP, Millipore) was carried out.

The liquid entry pressure of water (*LEP*) measurements were carried out using the experimental system schematized in Fig. 4.3.2. The effective membrane area is 12.56 x 10^{-4} m^2. The container was filled first with 2 L distilled water and then the pressure was applied gradually from the nitrogen cylinder on water at 23ºC. The minimum applied pressure before water penetrates into the inter-fiber space is the *LEP* value. These experiments were carried out three times using three different membrane samples made from different batches and the average values together with their standard deviations are reported.
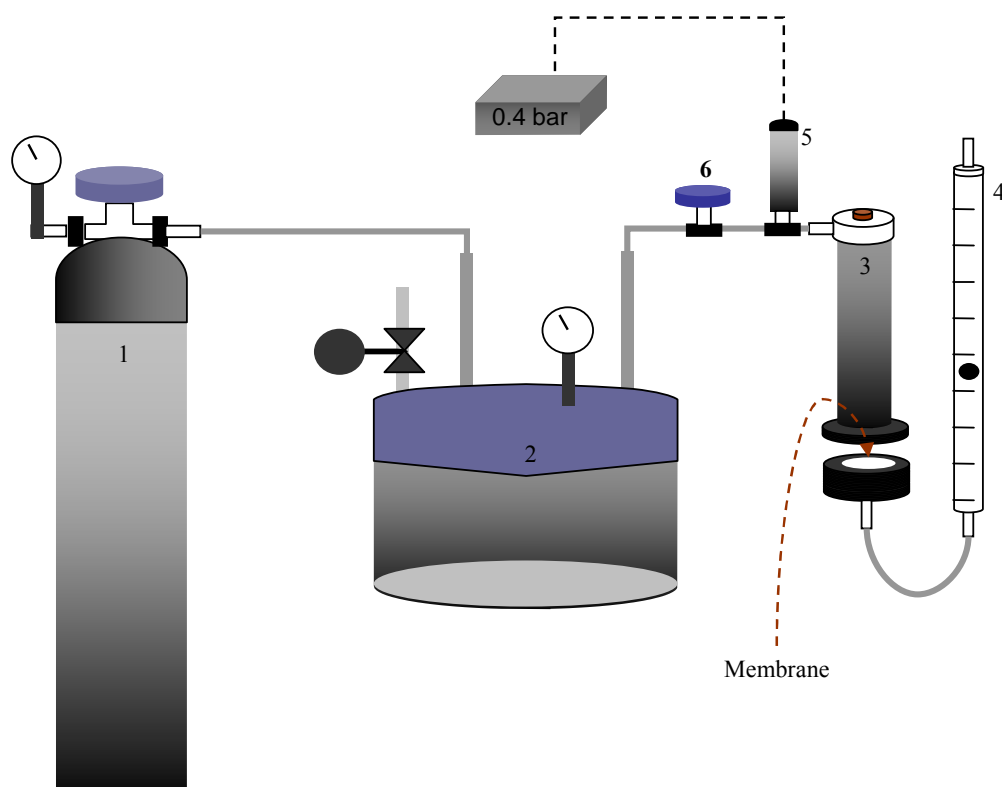
Figure 4.3.2. Set-up used for *LEP* measurements: (1) air cylinder, (2) pressurized container (Millipore), (3) membrane cell filled with water, (4) flowmeter, (5) digital manometer, (6) pressure regulator.

Figure 4.3.3 shows the experimental system used to determine the size of the inter-fiber space of the PVDF ENMs at room temperature 23ºC following the wet/dry flow method. The effective membrane area is 12.56 x 10^{-4} m^2. First, the nitrogen gas permeation flow is measured through a dry ENM at different pressures (dry curve). Subsequently, the ENM is wetted by isopropyl alcohol (IPA) that fills the inter-fiber space of the ENM and again the gas permeation flow is measured at increasing transmembrane pressures (wet curve). In this case, the dependence of the gas flow rate on the applied pressure is not linear. As the pressure increases, it reaches a point where it overcome the surface tension of the wetting IPA in the largest size of the inter-fiber space and drives the IPA out of it (i.e. bubble point). At transmembrane pressures lower than the bubble point, the inter-fiber space remains filled with IPA and the gas flow rate is practically zero. Above the bubble point, the gas flow keeps increasing with the increase of the pressure because smaller sizes of the inter-fiber space are opened progressively with the

enhancement of the pressure until all inter-fiber space becomes empty at the pressure that corresponds to the minimum size of the inter-fiber space. With the application of further higher pressures the gas flow rate varies linearly with the applied transmembrane pressure. The dry curve is needed for the calculation of the mean flow size of the ENMs. At least 3 tests were performed for each ENM sample and the size of the inter-fiber space was calculated using Washburn equation. The mean size of the inter-fiber space was determined from the intersection between the half-dry curve corresponding to 50% gas flow through dry ENM and the wet curve (i.e. the half-dry curve is the mathematical half of the dry curve). Details of the followed method are described elsewhere [22,30].
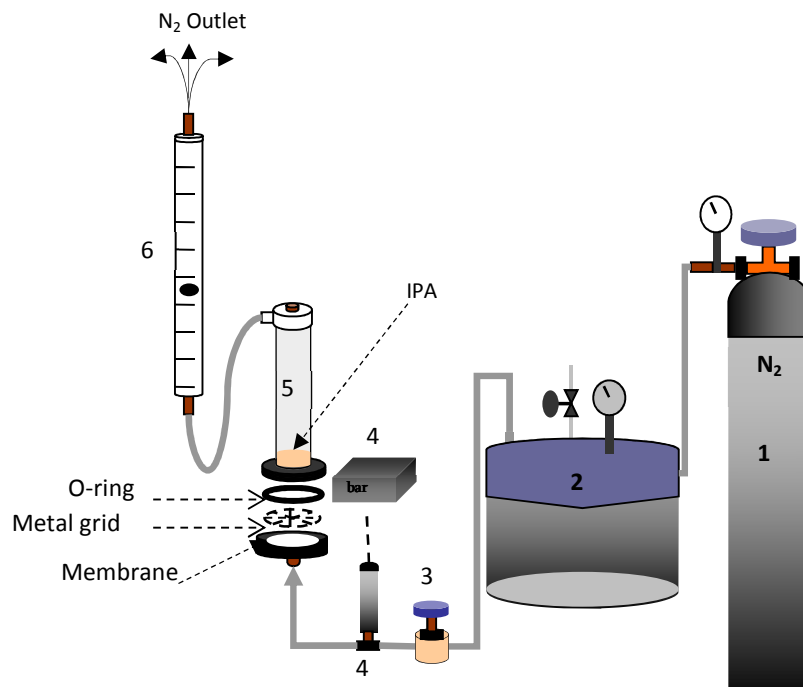

Figure 4.3.3. Wet/dry gas permeation set-up: (1) nitrogen gas cylinder, (2) pressurized container (Millipore), (3) gas regulator, (4) digital manometer, (5) membrane cell, (6) flowmeter.

The water contact angle of the surface of each ENM was measured at room temperature (23ºC) by a computerized optical system CAM100, equipped with a CCD camera, frame grabber and image analysis software. Distilled water drops of about 2 µl were deposited on the membrane surface employing a tight syringe. The contact angles were performed at both left and right sides of each drop and were automatically calculated by fitting the captured drop shape to that calculated from the Young-Laplace equation. More than 15 readings were obtained for each

ENM sample and an average value was calculated and reported together with their standard deviations.

The void volume fraction of the ENMs was determined by measuring the density of each ENM using isopropyl alcohol (IPA), which penetrates inside the inter-fiber space of the ENMs and distilled water, which does not enter in the inter-fiber space. The applied method was reported elsewhere [22].

The thickness (δ) of the ENMs was measured by the micrometer Millitron Phywe (Mahr Feinprüf, type TYP1202IC) in different points, at least 50, of three different membrane samples made from different batches and the average values together with their standard deviations are reported. All characterized samples were cut from about $3\ 10^{-3}$ m^2 circular area taken from the center of the prepared ENMs.

4.3.2.4. Direct contact membrane distillation (DCMD)

The experimental system used to carry out the DCMD experiments through ENMs is detailed in [31]. The temperature in MD is the operating variable that most significantly affects the permeate flux. In this study, the experiments were conducted first with distilled water and then with salt NaCl aqueous solutions of different concentrations as feed (0, 12, 30 and 60 g/L). Different feed temperatures were considered ranging from 40ºC to 80ºC, the permeate temperature was 20ºC and both the feed and permeate circulation rates were 500 rpm.

The DCMD system is composed of two cylindrical stainless steel chambers. One of the chambers is connected to a heating system through its jacket to control the temperature of the liquid feed. The other chamber is connected to a cooling system to control the temperature of the permeate (distilled water). The ENM was placed between the two chambers. The effective ENM area in the distillation system is $2.75\ 10^{-3}$ m^2. The tested sample was taken from the center of each prepared ENM. The permeate flux was calculated in every case by measuring the condensate collected in the permeate chamber for a predetermined period (at least for 3 h) of each feed solution. First distilled water was used as feed and then different NaCl feed aqueous solutions (12 g/L, 30 g/L and 60 g/L) were tested. Finally, the permeate flux of distilled water

used as feed was measured again to check if there is any change of the ENM due to fouling or wetting. Therefore, a total of at least 25 h of DCMD operation tests were carried out for each ENM. The NaCl concentration of both the permeate and feed solutions was determined by a conductivimeter 712 ΩMetrohm [31].

4.3.3. Results and discussions

Figure 4.3.4 shows the SEM images of the surface of the PVDF ENMs prepared at different electrospinning times (1 – 4 h) together with the distribution of the electrospun fiber diameters and their cross-sections. From Fig. 4.3.4(a) it can be detected the random motion of the electrospinning jet indicating its chaotic nature. The use of the two solvents with different affinities towards the polymer favors coagulation of the electrospun nanofiber through the air gap established between the needle and the collector (in Fig. 4.3.1) preventing beads formation. The used solvents facilitate bonding of intersecting fibers, creating a strong cohesive porous structure with a high void volume as will be shown later on. From higher magnification SEM images, it can be seen that the nanofibers are fused together indicating the adequate post-treatment followed for the preparation of the PVDF ENMs. For instance, the melting temperature (T_m) is higher than the temperature applied for the post-treatment. Both T_m and ΔH_m of the PVDF and the ENMs are similar as can be seen in Fig. 4.3.5 that shows the DSC heating and cooling curves. The experimental crystallization temperature (T_c) and the heat of crystallization (ΔH_c) of all PVDF ENMs are also similar indicating that electrospinning time does not affect the thermal properties of the PVDF ENMs.
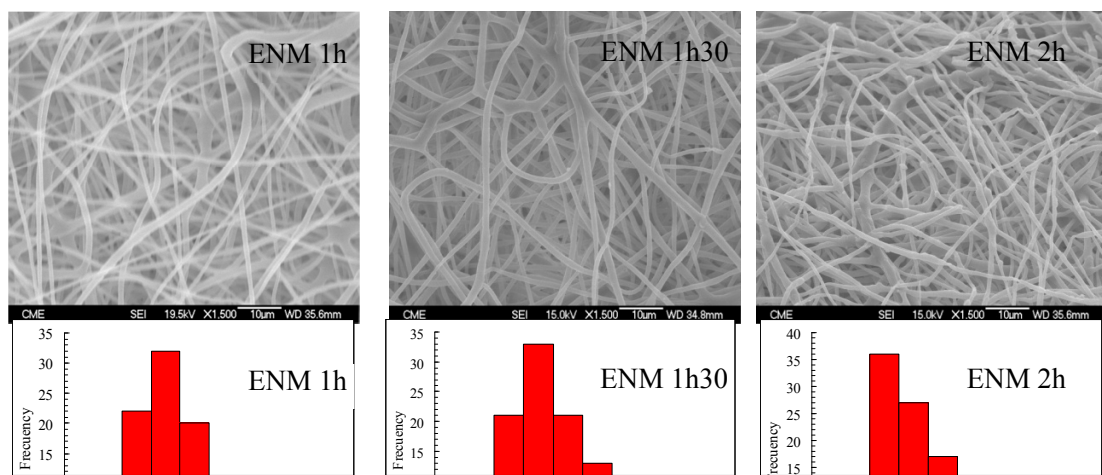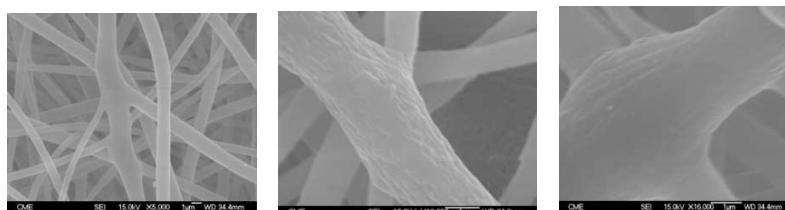
Figure 4.3.4. SEM images of the PVDF ENMs prepared at different electrospinning times (*t*). (To be continued)
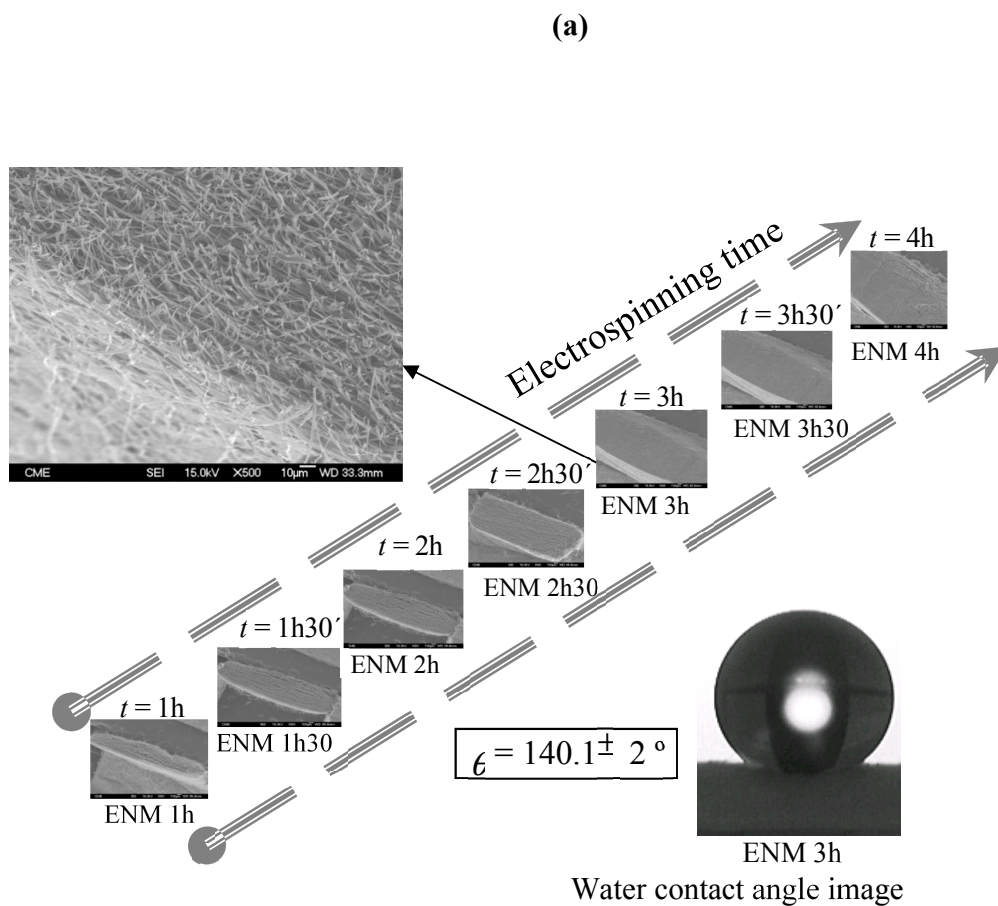
(a)

(b)

Figure 4.3.4. SEM images of the PVDF ENMs prepared at different electrospinning times (*t*). (a) SEM images of the top surface at different magnifications and the corresponding distributions of the fiber diameters; (b) SEM cross-sectional images showing the effect of the electrospinning time (*t*) on the ENMs thickness (δ), and a water contact angle image (θ_a) on the surface of the ENM 3h shown as an example. (Continuation)
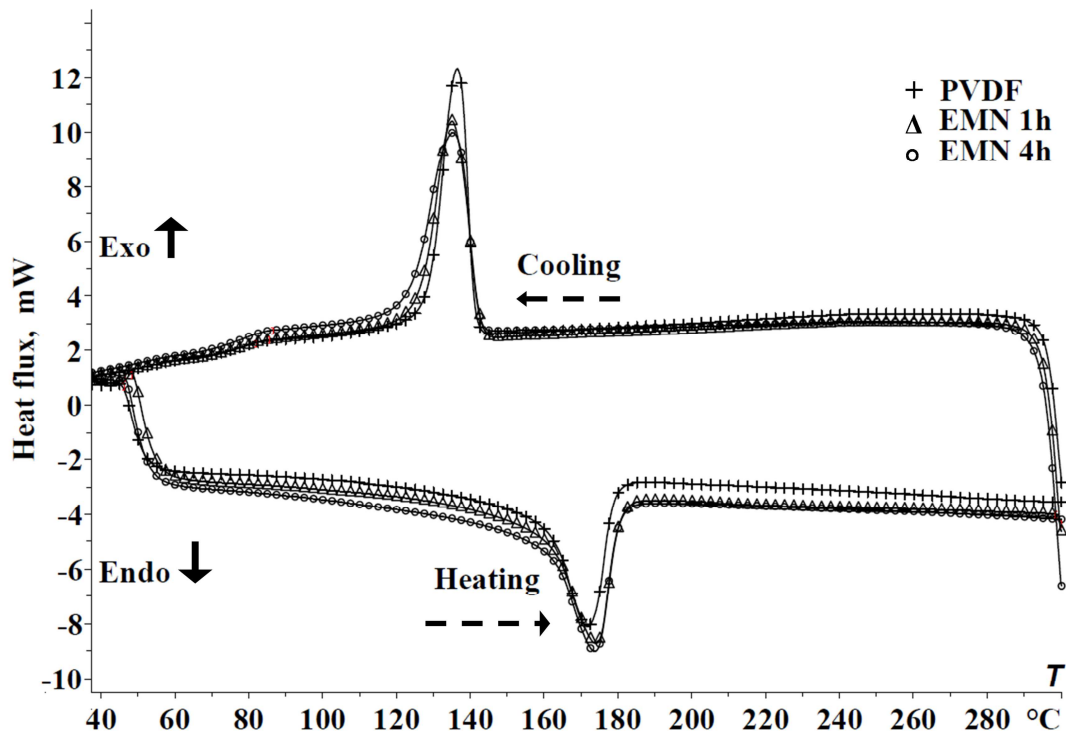
344

Figure 4.3.5. DSC exotherms and endotherms of the PVDF polymer and PVDF ENMs (ENM 1h and ENM 4h, shown as an example) prepared at different electrospinning times.

All PVDF ENMs show an endothermic melting peak around 159°C and an exothermic crystallization peak around 140.6°C in Fig. 4.3.5, indicating that the electrospinning time has no effect on the thermal properties of PVDF ENMs. Prince et al. [21] reported a slightly higher T_m value (164.21°C) for a PVDF ENM of 300 μm thickness than that obtained in this study (159.3± 0.2°C). On the contrary, Feng et al. [19] reported a smaller T_m value (153°C). These variations may be attributed to the type of PVDF polymer, solvent or the electrospinning conditions applied.

The degree of crystallinity of the PVDF ENMs can be determined from the melting or crystallization DSC scans, X_m and X_c, respectively [32]:

$$X_m = \frac{\Delta H_m}{\Delta H^*} 100 \qquad (4.3.1)$$

$$X_c = \frac{\Delta H_m}{\Delta H^*} 100 \qquad (4.3.2)$$

where ΔH^* is the heat of fusion of pure crystalline PVDF (104.6 kJ/kg [33]). As shown in Table 4.3.1 the degree of crystallinity of the PVDF ENMs are similar because the same solvents and electrospinning conditions were considered.

It can be observed from Fig. 4.3.4(b) that the thickness (δ) of the PVDF ENMs enhances considerably with the increase of the electrospinning time. The thickness (δ), the mean fiber diameter (d_f) and water contact angle (θ_a) of the ENMs are presented in Table 4.3.1. No significant changes were detected for the diameter of the electrospun fibers, which were maintained in the range 1.03 – 1.30 µm. Similarly, the water contact angle values of the PVDF ENMs were quite similar, 137.4 - 141.1º. These results are expected since the electrospinning operation conditions were maintained the same as stated previously. It is worth quoting that the water contact angle values of the PVDF ENMs prepared in this study are greater than those of the PVDF ENMs reported by Feng et al. [19,20] and Prince et al. [21] (128º). An enhancement of the water contact angle to 154.2º was observed with the addition of clay nanocomposite to PVDF electrospinning solution.

Although MD process is commonly operated under atmospheric pressure, for its industrial applications the MD membranes should exhibit adequate mechanical properties to guarantee successful packing in modules preventing any possible rupture due to hydraulic impact and flow disturbance. The tensile behavior of the PVDF ENMs is presented in Fig. 4.3.6 and the relevant mechanical data are summarized in Table 4.3.2. The increase of the ENM thickness leads to a gradual enhancement of the Young´s modulus and tensile strength, but no clear trend can be detected for the elongation at break because of the high obtained values attributed to the web structure of the PVDF ENMs. The elongation at break of the PVDF ENMs are an order of magnitude greater than the measured value of the commercial membrane HVHP (140 µm thickness, 0.45 µm mean pore size and 75% porosity as specified by the manufacturer Millipore), which is 31.3 ±5.0%.

Table 4.3.1. Thickness (δ), mean fiber diameter (d_f), water contact angle (θ_a), melting temperature (T_m), crystallization temperature (T_m), enthalpy of melting (ΔH_m), heat of crystallization (ΔH_c), degree of crystallinity of melting (X_m) and degree of crystallinity of crystallization of the PVDF ENMs prepared at different electrospinning times.

Membrane	δ (µm)	d_f (µm)	θ_a (°)	T_m (°C) [a]	ΔH_m (kJ/kg) [a]	X_m (%)	T_c (°C) [a]	ΔH_c (kJ/kg) [a]	X_c (%)
EMN 1h	144.5 ± 7.3	1.2 ± 0.4	139.7 ± 0.4	158.8 ± 0.4	40.3 ± 0.2	38.5 ± 0.2	141.4 ± 0.3	39.6 ± 0.5	37.8 ± 0.5
EMN 1h30	219.8 ± 20.0	1.2 ± 0.3	137.4 ± 0.3	160.6 ± 0.2	39.7 ± 0.5	37.9 ± 0.4	140.4 ± 0.1	39.9 ± 0.3	38.1 ± 0.3
EMN 2h	464.1 ± 27.2	1.3 ± 0.3	139.1 ± 0.3	159.2 ± 0.1	39.1 ± 0.3	37.4 ± 0.3	140.0 ± 0.6	38.9 ± 0.1	37.1 ± 0.1
EMN 2h30	625.9 ± 59.1	1.1 ± 0.3	140.1 ± 0.4	159.3 ± 0.1	40.1 ± 1.0	38.3 ± 0.9	140.0 ± 0.2	40.8 ± 0.7	38.9 ± 0.7
EMN 3h	833.4 ± 66.5	1.1 ± 0.3	140.1 ± 0.2	158.7 ± 0.1	40.6 ± 0.4	38.7 ± 0.4	140.9 ± 0.4	41.1 ± 0.7	39.3 ± 0.7
EMN 3h30	1206.3 ± 114.2	1.0 ± 0.3	141.1 ± 0.1	158.5 ± 0.3	40.0 ± 0.6	38.2 ± 0.5	139.4 ± 0.6	39.9 ± 0.6	38.1 ± 0.6
EMN 4h	1529.3 ± 121.5	1.1 ± 0.3	139.4 ± 0.4	159.3 ± 0.7	39.9 ± 0.5	38.2 ± 0.5	141.3 ± 1.0	40.4 ± 0.4	38.6 ± 0.4

[a] PVDF: T_m = 159.7 ± 0.2°C, ΔH_m = 40.1 ± 0.9 kJ/kg, T_c = 141.5 ± 0.1°C, ΔH_c = 39.3 ± 0.5 kJ/kg.
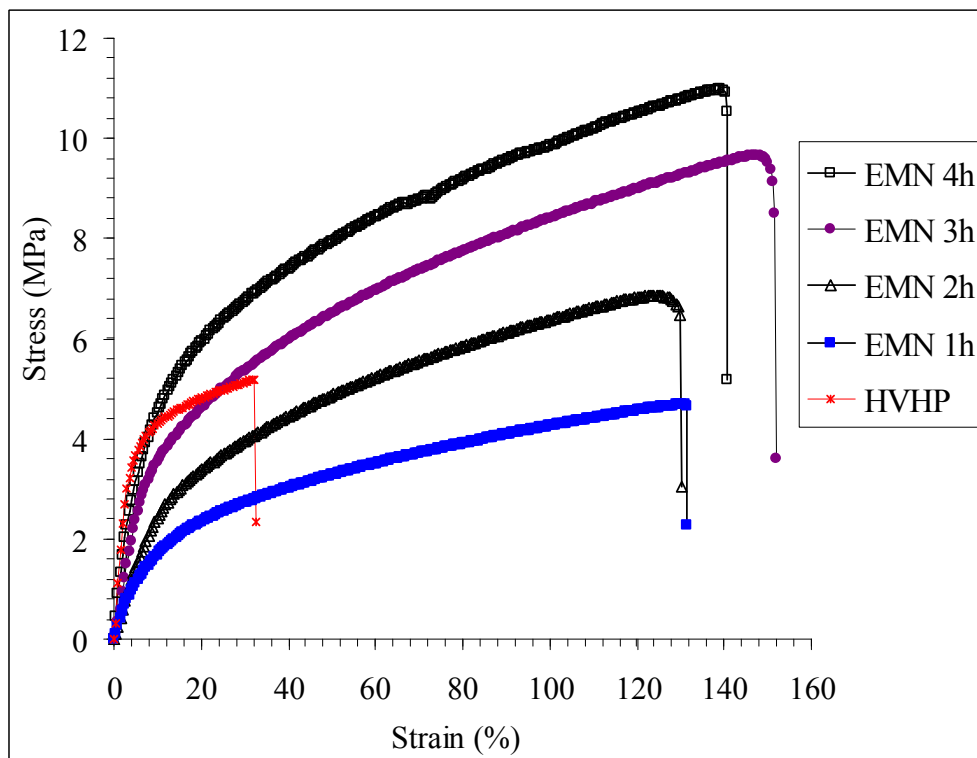
Figure 4.3.6. Stress-strain curves of the PVDF ENMs prepared at different electrospinning times (1 – 4 h) and the commercial membrane HVHP (Millipore).

Table 4.3.2. Mechanical properties of the PVDF ENMs prepared at different electrospinning times.

Membrane	Young´s Modulus (MPa)	Tensile strength (MPa)	Elongation at break (%)
EMN 1h	23.9 ± 6.0	4.5 ± 1.2	138.1 ± 16.8
EMN 1h30	34.3 ± 14.4	5.9 ± 0.9	120.5 ± 18.2
EMN 2h	34.6 ± 14.4	6.4 ± 1.7	134.2 ± 11.2
EMN 2h30	36.5 ± 14.6	6.8 ± 1.8	127.6 ± 2.6
EMN 3h	43.5 ± 14.5	7.2 ± 0.8	133.9 ± 33.8
EMN 3h30	52.3 ± 7.6	7.4 ± 2.3	131.9 ± 11.6
EMN 4h	74.7 ± 12.6	10.2 ± 2.0	130.2 ± 20.5

The void volume fraction, the thickness, the *LEP* and the mean size of the inter-fiber space of the PVDF ENMs are plotted in Figs. 4.3.7(a) and (b) as a function of the electrospinning time. The *LEP* value increased with the increase of the thickness of the ENMs. This is attributed to the variation of the size of the inter-fiber space since the water contact angles were practically similar for all PVDF ENMs. Therefore, it is expected a decrease of the maximum size of the inter-fiber space with increasing the thickness of the ENMs (i.e. increase of electrospinning time). Feng et al. [19,20] reported a higher *LEP* value, 121.35 kPa, than those presented in Fig. 4.3.7. However, Prince et al. [21] found a lower *LEP* value, 90 kPa, which is close to those given in Fig. 4.3.7. This is attributed to the distinct PVDF polymer solution used and to the different electrospinning parameters applied.

Because of the observed high hydrophobic nature of the prepared PVDF ENMs, one expects high *LEP* values than those reported for the membranes commonly used in MD [22]. For example, these are 276, 149, 58, 204, and 105 kPa for the membranes TF200 (Gelman), TF450 (Gelman), TF100 (Gelman), GVHP (Millipore) and HVHP (Millipore), respectively. The mean pore sizes of these membranes determined by the gas permeation test are 199.0, 418.8, 844.3, 283.2 and 463.9 nm, respectively. Therefore, the maximum size of the inter-fiber space of the PVDF ENMs is expected to be greater than these values.
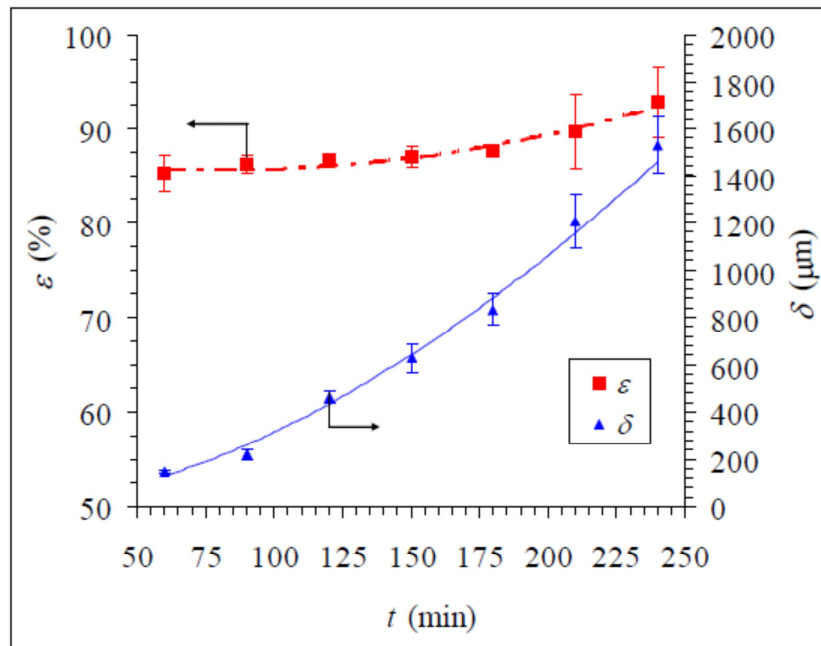
(a)
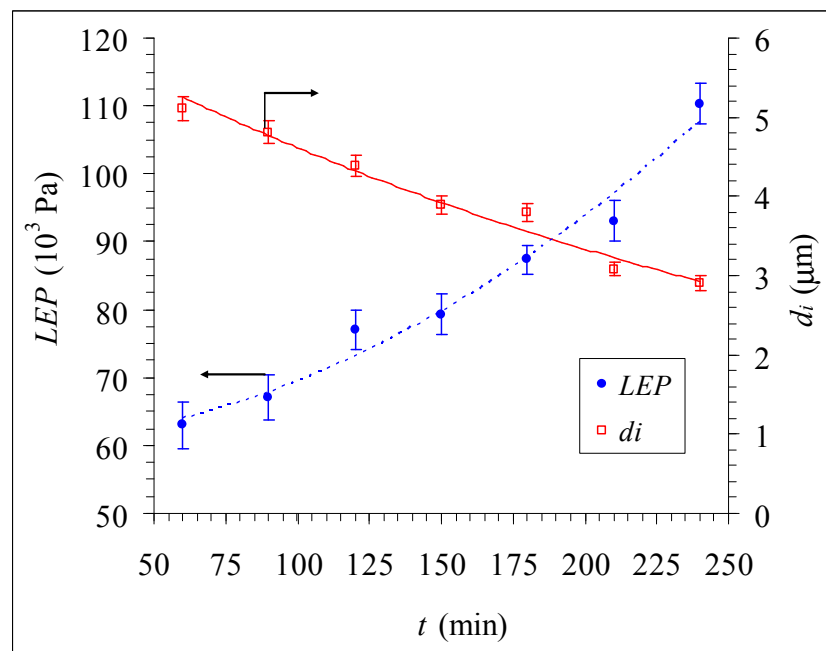
(b)

Figure 4.3.7. Effects of electrospinning time on (a) the ENMs thickness (δ) and the void volume fraction (ε) and (b) the liquid entry pressure of water (*LEP*) and the mean size of the inter-fiber space (d_i) of the ENMs.

The results of the wet/dry flow tests of some PVDF ENMs are shown as examples in Fig. 4.3.8. The wet curves of all PVDF ENMs exhibit an S shape and meet their corresponding dry curves at the smallest size of the inter-fiber space. The mean size of the inter-fiber space (d_i) of each PVDF ENM was evaluated and the results are plotted in Fig. 4.3.7. As it was expected from the LEP values, d_i was reduced with the increase of the thickness of the ENMs. Therefore, both the LEP and d_i are not uniform throughout the thickness of the ENMs. Feng et al. [19,20] and Prince et al. [21] reported smaller sizes of inter-fiber space than those obtained in this study. This may be attributed partly to the characterization technique used, to the electrospinning conditions and to the PVDF polymer solution. Moreover, an enhancement of the void volume fraction (ε) from 0.85 to 0.93 was detected with the increase of the electrospinning time (Fig. 4.3.7). This is also attributed to the increase of the ENMs thickness. Although the same electric voltage is applied to electrospun all PVDF ENMs, as the thickness of the ENM is enhanced the distance between the needle and the metallic collector is reduced slightly and the formed layer of the ENM acts as an insulator affecting therefore the dissipation of the electric charge to the collector and resulting in a less packed fiber web. When the self-sustained web is thin, it will dissipate the electric charges to the metallic collector and will reduce the repulsion among fibers, favoring a tightly packed ENM structure. However, when the self-sustained web is thick, the presence of electrostatic charges causes fibers to repel each other, giving a more loosely packed fibrous network and a higher void volume fraction.

It is worth quoting that the obtained void volume fraction (ε) values of the PVDF ENMs are higher than those reported by Feng et al. [19,20] and Prince et al. [21], 76% and 81-82%, respectively. Furthermore, the PVDF ENMs exhibit greater ε values than those of the phase inversion flat sheet PVDF membranes (26.8 - 79.6%) [34], and the commercial flat sheet membranes commonly used in MD (TF200, TF450, TF1000 from Gelman) made of polytetrafluoroethylene supported by a polypropylene net (64.3 – 68.7%) and (GVHP, HVHP from Millipore) made of PVDF (70.1 – 71.3%) [22].

Based on the obtained characteristics of the ENMs (the higher LEP and the smaller size of the inter-fiber space observed for the thicker membranes, Fig. 4.3.7(b)), in DCMD tests the top side of the ENM is brought into contact with the feed solution, while the permeate liquid is

maintained in contact with its bottom side. Desalination by DCMD using the PVDF ENMs was performed as stated previously.
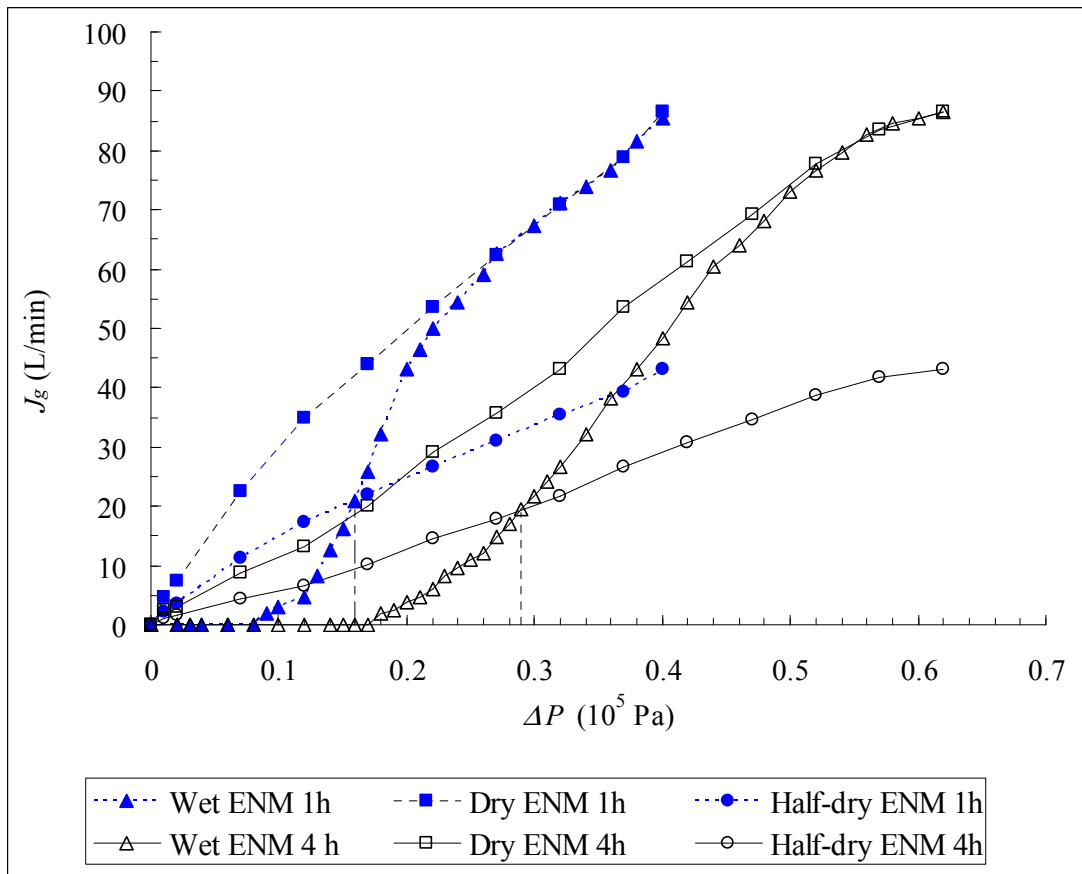

Figure 4.3.8. Wet/dry curves presenting the measured gas flow rate (J_g) of the wet and dry PVDF ENMs *versus* the applied pressure (ΔP).

Figure 4.3.9 shows the DCMD permeate fluxes of the PVDF ENMs having different thicknesses at different feed temperatures (40 – 80ºC) and different NaCl salt concentrations (0, 12, 35, 60 g/L). The permeate flux is higher for a thinner ENM, a higher feed temperature and a lower salt concentration. The permeate flux increases with the feed temperature following an Arrhenius type of dependence due to the increase of the vapor pressure at the feed/ENM interface and to the temperature polarization effect. In addition, the permeate flux decreases with the increase of the salt concentration in the feed aqueous solution because of the reduction of the water vapor pressure at the feed/ENM interface and the concentration polarization effect.

Figure 4.3.9. Permeate flux (J_w) of PVDF ENMs at different feed temperatures ($T_{b,f}$) and different concentrations of salt NaCl in water (0, 12, 30 and 60 g/L). The plotted solid lines of J_w against $T_{b,f}$ are the fitting to an Arrhenius type of dependence. The stirring rate of the feed and permeate liquid solutions is 500 rpm and the permeate temperature ($T_{b,p}$) is 20ºC. (To be continued)
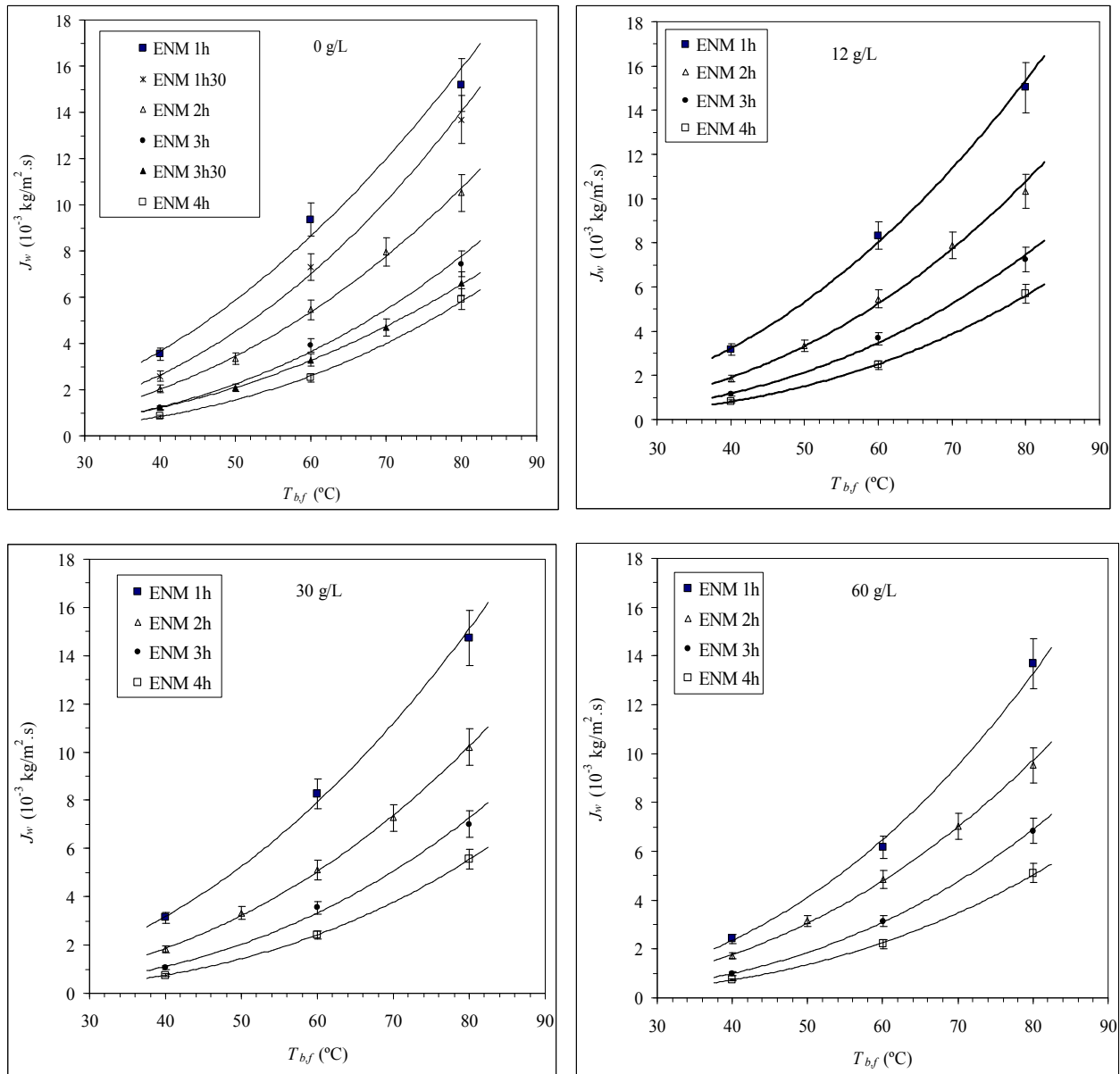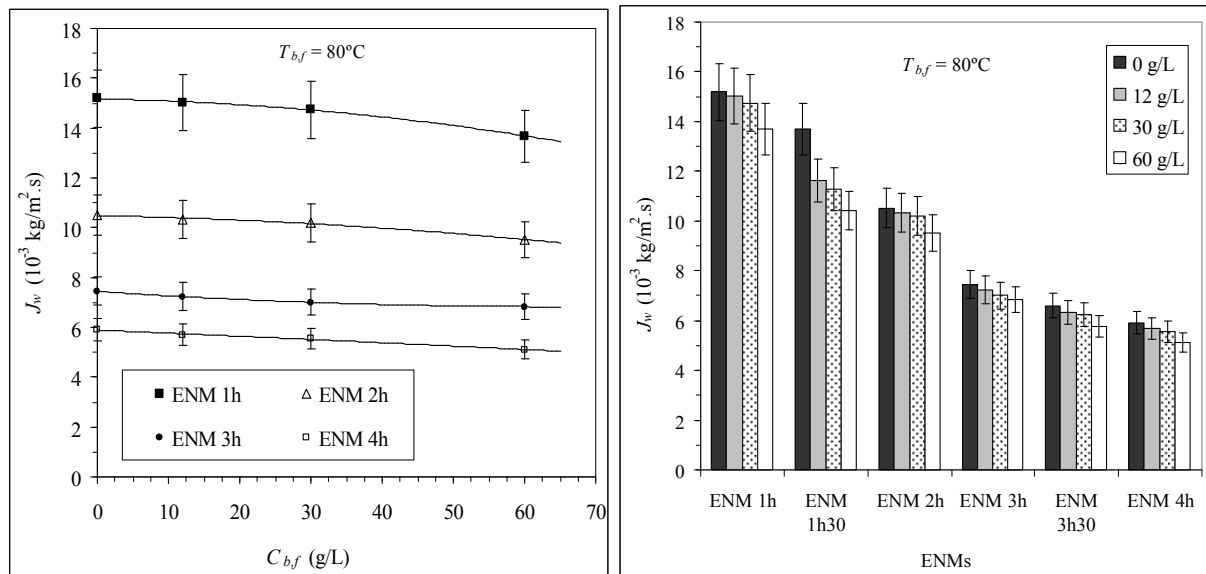
Figure 4.3.9. Permeate flux (J_w) of PVDF ENMs at different feed temperatures ($T_{b,f}$) and different concentrations of salt NaCl in water (0, 12, 30 and 60 g/L). The plotted solid lines of J_w against $T_{b,f}$ are the fitting to an Arrhenius type of dependence. The stirring rate of the feed and permeate liquid solutions is 500 rpm and the permeate temperature ($T_{b,p}$) is 20°C. (Continuation)

Like other pressure-driven membrane processes (MF, UF, NF), in this case the thinnest is the ENM the highest is the water production rate because the membrane permeability is inversely proportional to the membrane thickness. In other words, the distance between evaporation and condensation phenomena that occur at the liquid/vapor interfaces formed at both sides of the ENM is smaller for thinner ENMs and hence the water production rate is enhanced (Fig. 4.3.10). However, as the thickness is increased the heat loss by conduction through the ENM is decreased favoring the energy efficiency of the DCMD process. This justifies the non-linearity of the permeate flux variation with the inverse of the thickness of the ENMs. For the same variation of the ENMs thickness, the permeate flux decline is more significant in the zone of thinner ENMs ($\delta \leq 400$ μm) than in the zone of thicker ENMs ($\delta \geq 400$ μm), and the permeate flux variation is greater for higher feed temperatures. The obtained trends in this study agree well with those reported by Al-Obaidani et al. [35] and Martínez and Rodríguez-Maroto [36] for other types of membranes.
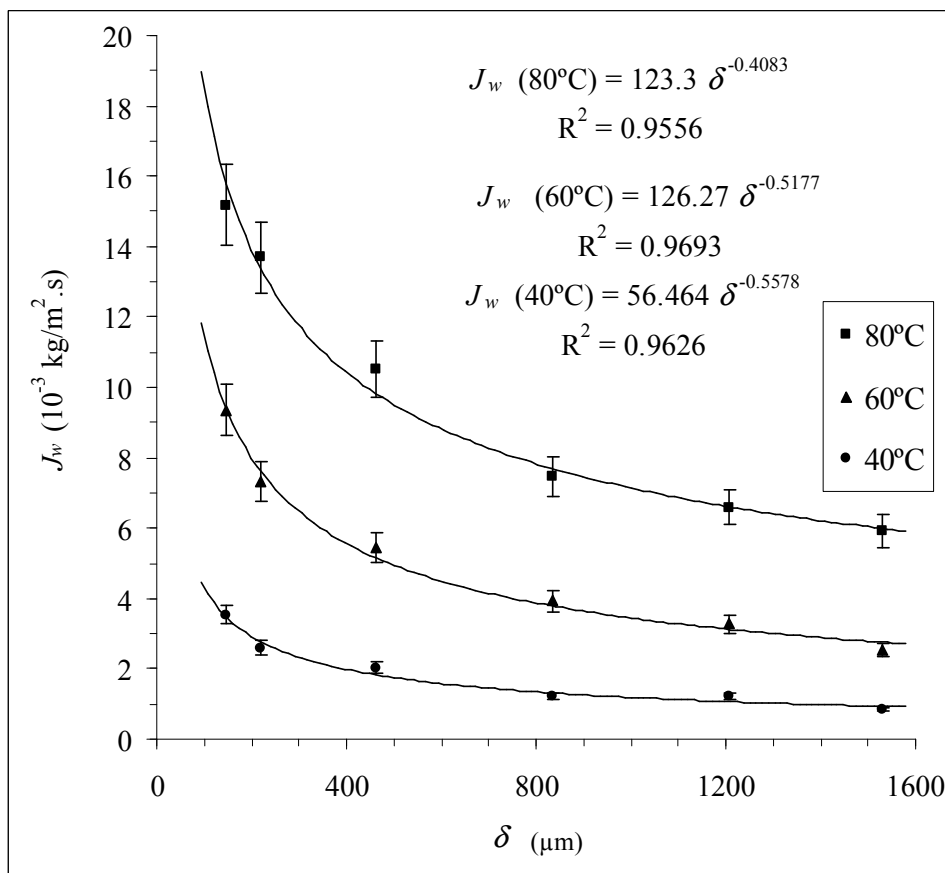
Figure 4.3.10. Effect of the PVDF ENMs thickness (δ) on the water permeate flux (J_w) at different feed temperatures ($T_{b,f}$). The stirring rate of the feed and permeate liquid solutions is 500 rpm and the permeate temperature ($T_{b,p}$) is 20°C.

Figure 4.3.11 shows the effects of the feed temperature and the NaCl concentration on the salt rejection factor ($\eta = \left(1 - C_{b,p} / C_{b,f}\right) 100$, where $C_{b,p}$ and $C_{b,f}$ are the salt concentration of the bulk permeate and feed solutions, respectively). In general, the obtained η values are greater than 99.39%. It was observed that η was slightly smaller for thinner ENMs prepared with less than 1h30min electrospinning time (ENM 1h). This is attributed to the lower *LEP* value of the ENM 1h (Fig. 4.3.7(b)). The high salt rejection factor is attributed to the high *LEP* values. In general, there is a small variation of the salt rejection factor with the feed temperature and NaCl concentration. It seems that the salt rejection factor of the membranes electrospun for more than

355

1h30min enhances slightly with the increase of the feed temperature. This may be attributed to the exponential increase of the water vapor transport through ENMs with temperature.
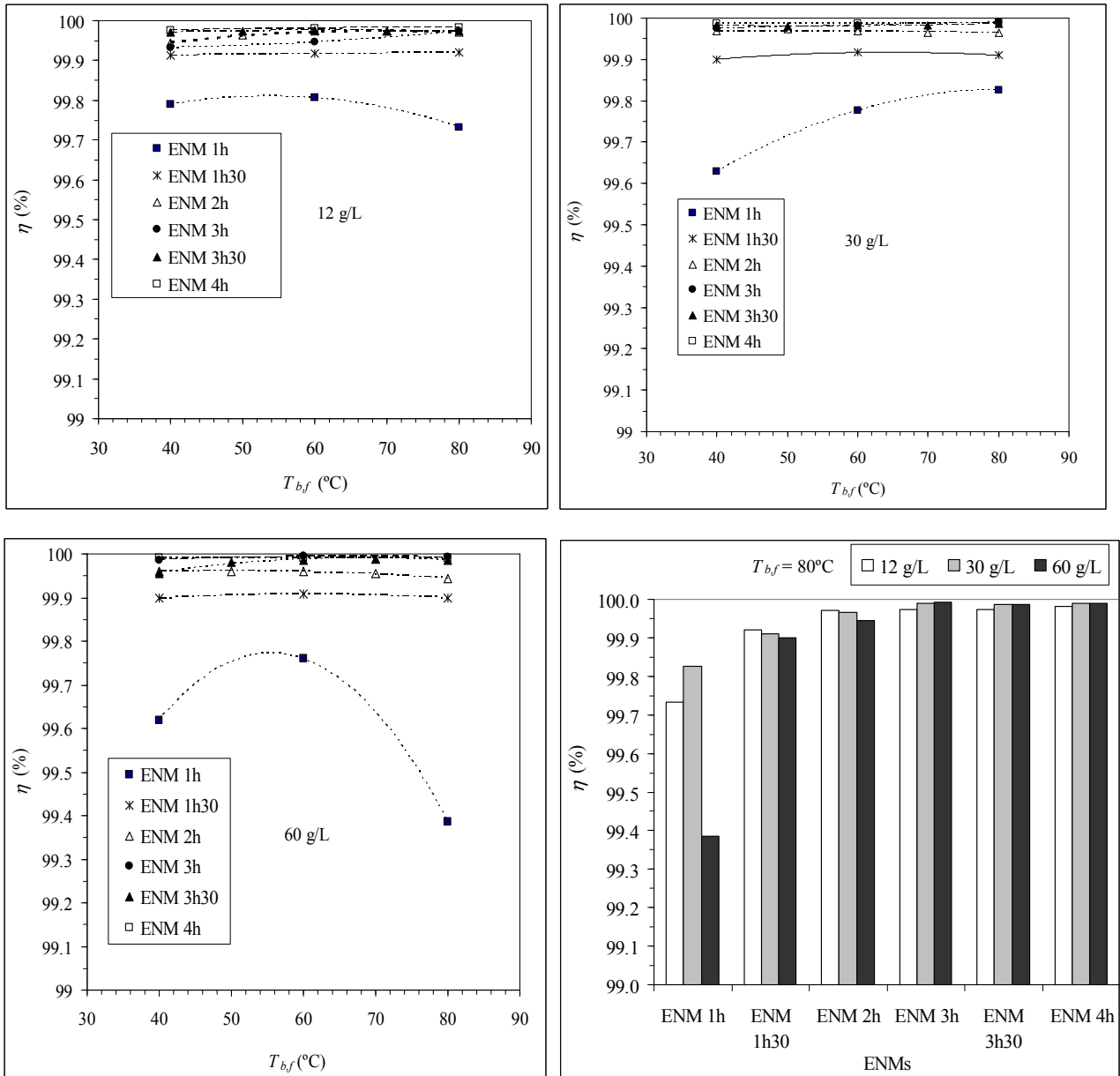

Figure 4.3.11. Effect of the feed temperature ($T_{b,f}$) and the feed salt concentration ($C_{b,f}$, 12, 30 and 60 g/L) on the salt rejection factor (η) of PVDF ENMs. The plotted discontinuous lines are only guide for the eye showing the effect of $T_{b,f}$. The stirring rate of the feed and permeate liquid solutions is 500 rpm and the permeate temperature ($T_{b,p}$) is 20ºC.

As stated previously, the permeate flux of each ENM using distilled water as feed was measured before and after desalination tests (12 g/L, 30 g/L and 60 g/L). For each membrane sample a total of at least 25 h of DCMD operation tests were performed following the same protocol (distilled water, 12 g/L, 30 g/L, 60 g/L and distilled water as feed solutions). No significant changes were observed for the permeate flux measured for feed distilled water before and after desalination with NaCl aqueous solutions (i.e. below 5% deviation) and for the permeate concentration with time during desalination tests (i.e. no wetting was detected during the 25 h DCMD operating period).

The PVDF ENMs prepared in this study exhibit much higher MD performance than those reported by Feng et al. [19] for desalination by AGMD (i.e. highest permeate flux 3.2 10^{-3} kg/m^2.s) and Prince et al. [21] for desalination by DCMD (i.e. 1.6 10^{-3} kg/m^2.s). The obtained high permeation flux in the present study may be attributed to the greater void volume fraction together with the size of the inter-fiber space and to some extent to the mechanism of mass transport through the inter-fiber space of the ENMs. The kinetic theory of gases through porous media can be applied also to water vapor transport through ENMs. The size of the fibers, the interconnection of the inter-fiber space of the ENM and the applied MD operating conditions play an important role in determining the mechanism(s) of vapor transport through ENMs. Because of the web configuration of ENMs, collisions occur between water vapor molecules and nanofibers together with collisions between water vapor molecules and each others and between water vapor molecules and air present inside the void volume space of the ENMs. A detailed theoretical analysis taking into consideration the parameters of the PVDF ENMs prepared in this study is reported in [37]. The developed theoretical model permits the prediction of the DCMD permeate flux through ENMs.

In general, similar DCMD trends as those obtained for other types of membranes were observed in this study for PVDF ENMs. However, the DCMD permeate flux is found to be higher for the PVDF ENMs compared to other laboratory fabricated and modified flat sheet membranes. Table 4.3.3 reviews the highest permeate fluxes observed in DCMD for some laboratory fabricated or modified flat sheet membranes and commercial flat sheet membranes. Only the commercial membranes (TS22, TS45 from Osmonics Corp. [51]) and (3MA, 3MB, 3MC, 3MD and 3ME from 3M Corporation [52]) exhibit higher permeate fluxes than those of

the PVDF ENMs obtained in this study. In fact, the highest permeate flux obtained so far in DCMD is 40.5 10^{-3} kg/m^2.s and 32.4 10^{-3} kg/m^2.s using distilled water as feed at 80ºC and 42.2 g/L (1.3 mol%) NaCl feed aqueous solution at 74ºC, a permeate temperature of 20ºC and the commercial membrane 3ME [52]. This membrane is made of polypropylene (PP) with 79 µm thickness, 0.73 maximum pore size 0.73 µm and 85% porosity.

Table 4.3.3. Reported DCMD permeate flux (J_w) of different types of fabricated, modified and commercial flat sheet membranes.

Membrane type	J_w (10^{-3} kg/m^2.s)	Observation	Ref.
Fabricated or modified flat sheet membranes			
PVDF unsupported	2.70	10 – 20 g/L NaCl; $T_{b,f}$=60ºC; $T_{b,p}$=20ºC.	[38]
	1.86	17.5 g/L NaCl; $T_{b,f}$=55ºC; $T_{b,p}$=25ºC.	[39]
Copolymer F2.4 [a]	2.03	17.5 g/L NaCl; $T_{b,f}$=55ºC; $T_{b,p}$=25ºC.	[39]
Modified CN [b]	8.33	29.5 g/L NaCl; $T_{b,f}$=60ºC; $T_{b,p}$=25ºC (η=99%).	[40]
Modified CA [c]	0.38	29.5 g/L NaCl; $T_{b,f}$=50ºC; $T_{b,p}$=20ºC (η=99.1%).	
SMM/PEI (M12) [d]	4.1 3.5	$T_{b,f}$=50ºC; $T_{b,p}$=40ºC Distilled water as feed 29.5 g/L NaCl (η=99.9%).	[41]
SMM/PEI (M1) [d]	7.5 5.8	$T_{b,f}$=55ºC; $T_{b,p}$=15ºC Distilled water as feed 29.5 g/L NaCl (η=99%).	[42]
SMM/PEI [d]	11.6 10.0 9.7	$T_{b,f}$=80ºC; $T_{b,p}$=20ºC Distilled water as feed 12 g/L NaCl (η=99.99%) 30 g/L NaCl (η=99.99%).	[31]
SMM/PS (M1) [e]	2.65 2.30	$T_{b,f}$=50ºC; $T_{b,p}$=40ºC Distilled water as feed 29.5 g/L NaCl (η=99.9%).	[43]
SMM/PES (M1) [f]	3.0 2.6	$T_{b,f}$=50ºC; $T_{b,p}$=40ºC Distilled water as feed 29.5 g/L NaCl (η=99.9%).	[44]
PFS/anodisc [g]	4.78	5.9 g/L NaCl; $T_{b,f}$=53ºC; $T_{b,p}$=18ºC (93%<η<99%).	[45]
PVA/PEG/PVDF [h]	6.72 6.53	$T_{b,f}$=70ºC; $T_{b,p}$=22ºC Distilled water as feed 35 g/L NaCl (η=99%).	[46]
PVDF ENM [i]	1.6	$T_{b,f}$=80ºC; $T_{b,p}$=17ºC (δ=300 ±25 μm) 35 g/L NaCl (η=98.3%)	[21]
PVDF ENM 1h	15.2 15.0 14.7 13.7	$T_{b,f}$=80ºC; $T_{b,p}$=20ºC (δ=144.5±7.3 μm) Distilled water as feed 12 g/L NaCl (η=99.7%) 30 g/L NaCl (η=99.8%) 60 g/L NaCl (η=99.4%).	This study
Membrane type	J_w (10^{-3} kg/m^2.s)	Observation	Ref.
Commercial flat sheet membranes			

GVHP [j]	13.52	Distilled water as feed; $T_{b,f}$=90.7ºC; $T_{b,p}$=19.7ºC.	[47]
	9.00	Distilled water as feed; $T_{b,f}$=70ºC; $T_{b,p}$=20ºC.	[48]
	0.89	3 g/L NaCl; ΔT_b=10ºC; $T_{b,f}$=51.9ºC.	[49]
	0.83	64.5 g/L NaCl; ΔT_b=10ºC; $T_{b,f}$=52.7ºC.	[49]
HVHP [k]	18.61 16.39 11.11	Deareation *DCMD*; $T_{b,f}$=80ºC; $T_{b,p}$=21ºC Distilled water NaCl (14 g/L) NaCl (25 g/L).	[50]
	10.80	Distilled water as feed; $T_{b,f}$=70ºC; $T_{b,p}$=20ºC.	[48]
TF200 [l]	18.69	Distilled water as feed; $T_{b,f}$=80.1ºC; $T_{b,p}$=20.1ºC.	[47]
	2.90	1.9 g/L NaCl; ΔT_b=10ºC; $T_{b,f}$=52.2ºC.	[49]
	2.23	64.5 g/L NaCl; ΔT_b=10ºC; $T_{b,f}$=52.7ºC.	[49]
PTFE Sartorious [m]	14.00	Distilled water as feed; $T_{b,f}$=70ºC; $T_{b,p}$=20ºC.	[48]
TS22 [n]	21.67	0.6 g/L NaCl; $T_{b,f}$=60ºC; $T_{b,p}$=20ºC.	[51]
TS45 [o]	22.22	0.6 g/L NaCl; $T_{b,f}$=60ºC; $T_{b,p}$=20ºC.	[51]
PP22 [p]	7.78	0.6 g/L NaCl; $T_{b,f}$=60ºC; $T_{b,p}$=20ºC.	[51]
3MA [q]	25.2 22.5 19.8	$T_{b,f}$=74ºC; $T_{b,p}$=20ºC; distilled water as feed 19.5 g/L 42.2 g/L.	[52]
3MB [r]	21.6	Distilled water as feed; $T_{b,f}$=70ºC; $T_{b,p}$=20ºC.	[52]
3MC [s]	37.8	Distilled water as feed; $T_{b,f}$=80ºC; $T_{b,p}$=20ºC.	[52]
3MD [t]	27	Distilled water as feed; $T_{b,f}$=70ºC; $T_{b,p}$=20ºC.	[52]
3ME [u]	40.5 32.4	Distilled water; $T_{b,f}$=80ºC; $T_{b,p}$=20ºC 42.2 g/L NaCl; $T_{b,f}$=74ºC; $T_{b,p}$=20ºC.	[52]

PP: Polypropylene; PTFE: Polytetrafluoroethyelen; PVDF: Polyvinylidene fluoride.

[a] F2.4: Poly(vinylidene fluoride-co-tetrafluoroethylene).

[b] Modified cellulose nitrate by plasma polymerization using vinyltrimethylsilicon (VTMS)/carbon tetrafluoride (CF_4).

[c] Modified cellulose acetate by radiation polystyrene grafting using styrene (St)- pyridine (Pyd)-carbon tetrachloride (CCl_4).

[d] polyetherimidie (PEI) fabricated using surface modifying macromolecules (SMMs).

[e] polysulfone (PS) fabricated using surface modifying macromolecules (SMMs).

[f] polyethersulfone (PES) fabricated using surface modifying macromolecules (SMMs).

[g] Modified alumina anodisc[TM] membrane of pore size 200 nm by surface treatment using 1H,1H,2H,2H-perfluorodecyltriethoxysilane (PFS).

[h] Hydrophilic modified PVDF (GVSP, Millipore) membranes using polyvinyl alcohol (PVA) blended with polyethylene glycol (PEG) and crosslinked by aldehydes and sodium acetate.

[i] The unit of J_w reported in [21] is kg/m/hr. we believe that the right unit is kg/m^2.h.

[j] Millipore PVDF membrane: 0.22 μm mean pore size (δ= 110 μm, ε = 75 %, *LEP* = 204 kPa).

[k] Millipore PVDF membrane: 0.45 μm mean pore size (δ= 140 μm, ε = 75 %, *LEP* = 105 kPa).

[l] Gelman PTFE membrane with PP net support: 0.2 μm mean pore size (δ=178 μm, ε = 80%, *LEP* = 282 kPa).

[m] Sartorious PTFE membrane: 0.2 μm mean pore size (δ= 70 μm, ε = 70 %).

[n] Osmonics Corporation PTFE membrane with PP support: 0.22 μm mean pore size (δ= 175 μm, ε = 70%).

[o] Osmonics Corporation PTFE membrane with PP support: 0.45 μm mean pore size (δ= 175 μm, ε = 70%).

[p] Osmonics Corporation PP membrane: 0.22 μm mean pore size (δ= 150 μm, ε = 70%).

[q] 3M Corporation PP membrane: 0.29 μm maximum pore size (δ= 91 μm, ε = 66%).

[r] 3M Corporation PP membrane: 0.40 μm maximum pore size (δ=81 μm, ε = 76%).

[s] 3M Corporation PP membrane: 0.51 μm maximum pore size (δ=76 μm, ε = 79%).

[t] 3M Corporation PP membrane: 0.58 μm maximum pore size (δ= 86 μm, ε = 80%).

[u] 3M Corporation PP membrane: 0.73 μm maximum pore size (δ=79 μm, ε = 85%).

4.3.4. Conclusions

In this paper we demonstrate the feasibility of ENMs for desalination by DCMD. Analysis of the PVDF ENMs thickness effect on the DCMD performance was carried out.

A considerable increase of both the thickness and the liquid entry pressure of water with the electrospinning time were observed, while only a slight enhancement was detected for the void volume fraction. In contrast, a considerable reduction of the size of inter-fiber space was detected and no significant changes were observed for the diameter of the electrospun fibers and the water contact angle.

When the self-sustained web is thick, the presence of electrostatic charges causes fibers to repel each other, giving a more loosely packed fibrous network and a higher void volume fraction. In contrast, when the self-sustained web is thin, it dissipates the electric charges to the metallic collector and reduces the repulsion among fibers, favoring a tightly packed ENM structure.

The size of the inter-fiber space and the liquid entry pressure of water are not uniform throughout the thickness of the ENMs.

The effects of the DCMD operating conditions, feed temperature and salt concentration, on the permeate flux follow similar trends to those of other types of membranes used in DCMD.

The permeate flux did not decline linearly with the thickness of the ENMs. This is attributed to the decrease of the energy lost by heat conduction through the ENMs with the increase of the thickness.

The permeate flux of the PVDF ENMs in DCMD configuration reached a value of $15.2 \ 10^{-3}$ kg/m^2.s with a feed temperature of 80ºC and a permeate temperature of 20ºC, and the salt (NaCl) rejection factor was higher than 99.39%. No wetting was detected for 25 h DCMD operating time and the change of the permeate flux of distilled water used as feed before and after desalination tests was below 5%.

The DCMD performance of the PVDF ENMs reported in this study is better than that of the fabricated flat sheet membranes used so far in desalination by DCMD (Table 4.3.3) and the PVDF ENMs reported by Feng et al. [19] and Prince et al. [21]. This is due to the greater void volume fraction, greater sizes of inter-fiber space, and possibly to the mechanism of mass

transport through ENMs. A theoretical model that takes into consideration the parameters of the PVDF ENMs prepared in this study is reported in [37] in order to predict the DCMD permeate flux of ENMs.

References

[1] Y. Dzenis, Spinning continuous fibers for nanotechnology, Science, 304 (2004) 1917-1919.

[2] X. Wang, B. Ding, J. Yu, M. Wang, Engineering biomimetic superhydrophobic surfaces of electrospun nanomateriales, Nano Today, 6 (2011) 510-530.

[3] A. Formhals, Process and apparatus for preparing artificial threads, U.S. Patent Nº 1,975,504 (1934).

[4] X.R. Li, J.W. Xie, J. Lipner, X.Y. Yuan, S. Thomopoulos, Y.N. Xia, Nanofiber scaffolds with gradations in mineral content for mimicking the tendom-to-bone insertion site, Nano Lett. 9 (2009) 2763-2768.

[5] E.R. Kenawy, G.L. Bowlin, K. Mansfield, J. Layman, D.G. Simpson, E.H. Sanders, G.E. Wnek, Release of tetracycline hydrochloride from electrospun poly(ethylene-co-vinylacetate), poly(lactic acid), and a blend, J. Controlled Release 81 (2002), 57-64.

[6] A. Yang, X.M. Tao, R.X. Wang, S.C. Lee, C. Surya, Room temperature gas sensing properties of SnO2/multiwall-carbon-nanotube composite nano-fibers, Appl. Phys. Lett. 91 (2007) 133110-1,133110-3.

[7] S.W. Choi, S.M. Jo, W.S. Lee, Y.R. Kim, An electrospun poly(vinylidene fluoride) nanofibrous membrane and its battery applications, Adv. Mater. 15 (2003) 2027-2032.

[8] C. Drew, X. Wang, K. Senecal, H. Schreuder-Gibson, J. He, J. Kumar, L.A. Samuelson, Electrospun photovoltaic cells, J. Macromol. Sci. Pure Appl. Chem. 39 (2002) 1085-1094.

[9] X. Yan, G. Liu, F. Liu, B.Z. Tang, H. Peng, A.B. Pakhomov, C.Y. Wong, Superparamagnetic triblock copolymer/Fe$_2$O$_3$ hybrid nano-fibers, Angew. Chem. Int. Ed. 40 (2001) 3593-3596.

[10] R. Gopal, S. Kaur, Z. Ma, C. Chan, S. Ramakrishna, T. Matsuura, Electrospun nanofibrous filtration membrane, J. Membrane Sci., 281 (2006) 581-586.

[11] M.G. Hajra, K. Mehta, G.G. Chase, Effects of humidity, temperature, and nano-fibers on drop coalescence in glass fiber, Sep. Purif. Technol. 30 (2003) 79-88.

[12] R.S. Barhate, S. Ramakrishna, Nanofibrous filtering media: Filtration problems and solutions from tiny materials: Review, J. Membr. Sci., 296 (2007) 1-8.

[13] R. Wang, Y. Liu, B. Li, B.S. Hsiao, B. Chu, Electrospun nanofibrous membranes for high flux microfiltration, J. Membr. Sci. 392-393 (2012) 167-174.

[14] N.N. Bui, M.L. Lind, E.M.V. Hoek, J.R. McCutcheon, Electrospun nanofiber supported thin film composite membranes for engineered osmosis, J. Membr. Sci. 385-386 (2011) 10-19.

[15] K. Yoon, K. Kim, X. Wang, D. Fang, B.S. Hsiao, B. Chu, High flux ultrafiltration membranes based on electrospun nanofibrous PAN scaffolds and chitosan coating, Polymer, 47 (2006) 2434-2441.

[16] Z. Zhao, J. Zheng, M. Wang, H. Zhang, C.C. Han, High performance ultrafiltration membrane based on modified chitosan coating and electrospun nanofibrous PVDF scaffolds, J. Membr. Sci. 394-395 (2012) 209-217.

[17] W. Ritcharoen, P. Supaphol, P. Pavasant, Development of polyelectrolyte multilayer-coated electrospun cellulose acetate fiber mat as composite membranes, Eur. Pol. J. 44 (2008) 3963-3968.

[18] M. Khayet, M.C. García-Payo, Nanostructured Flat membranes for Direct Contact Membrane Distillation. PCT/ES2011/000091, WO/2011/117443 (2011).

[19] C. Feng, K.C. Khulbe, T. Matsuura, R. Gopal, S. Kaur, S. Ramakrishna, M. Khayet, Production of drinking water from saline water by air-gap membrane distillation using polyvinylidene fluoride nanofiber membrane, J. Membr. Sci., 311 (2008) 1-6.

[20] C. Feng, K.C. Khulbe, S. Tabe, Volatile organic compound removal by membrane gas stripping using electro-spun nanofiber membrane, Desalination, 287 (2012) 98-102.

[21] J.A. Prince, G. Singh, D. Rana, T. Matsuura, V. Anbharasi, T.S. Shanmugasundaram, Preparation and characterization of highly hydrophobic poly(vinylidene fluoride)-clay nanocomposite nanofiber membranes (PVDF-clay NNMs) for desalination using direct contact membrane distillation, J. Membr. Sci., 397-398 (2012) 80-86.

[22] M. Khayet, T. Matsuura, Membrane Distillation: Principles and Applications, Elsevier, The Netherlands, 2011.

[23] M. Khayet, Membranes and theoretical modeling of membrane distillation: a review, Adv. Colloid Interface Sci., 164(1-2) (2011) 56-88.

[24] A. Alkhudhiri, N. Darwish, N. Hilal, Membrane distillation: A comprehensive review, Desalination, 287 (2012) 2-18.

[25] E. Drioli, E. Curcio, G. Di Profio, State of the art and recent progresses in membrane contactors, Chem. Eng. Res. Des., 83(A3) (2005) 223-233.

[26] M. Khayet, T. Matsuura, J.I. Mengual, M. Qtaishat, Design of novel direct contact membrane distillation membranes, Desalination, 192 (2006) 105-111.

[27] B. Li, K.K. Sirkar, Novel membrane and device for direct contact membrane distillation-based desalination process, Ind. Eng. Chem. Res., 43 (2004) 5300-5309.

[28] B. Li, K.K. Sirkar, Novel membrane and device for vacuum membrane distillation-based desalination process, J. Membr. Sci., 257 (2005) 60-75.

[29] K.Y. Wang, T.S. Chung, M. Gryta, Hydrophobic PVDF hollow fiber membranes with narrow pore size distribution and ultra-thin skin for the fresh water production through membrane distillation, Chem. Eng. Sci., 63 (2008) 2587-2594.

[30] R. Gopal, S. Kaur, C.Y. Feng, C. Chan, S. Ramakrishna, S. Tabe, T. Matsuura, Electrospun nanofibrous polysulfone membranes as pre-filters: Particulate removal, J. Membr. Sci., 289 (2007) 210-219.

[31] M. Essalhi, M. Khayet, Surface segregation of fluorinated modifying macromolecule for hydrophobic/hydrophilic membrane preparation and application in air gap and direct contact membrane distillation, J. Membr. Sci., 417-418 (20129 163-173.

[32] G. Mago, D.M. Kalyon, F.T. FISHER, Membranes of polyvinylidene fluoride and PVDF nanocomposites with carbon nanotubes via immersion precipitation, J. Nanomaterials, 2008, doi:10.1155/2008/759825.

[33] Y.J. Park, Y.S. Kang, C. Park, Micropatterning of semicrystalline poly(vinylidene fluoride) (PVDF) solutions, Eur. Polymer J., 41 (2005) 1002-1012.

[34] M. Khayet, T. Matsuura, Preparation and characterization of polyvinylidene fluoride membranes for membrane distillation, Ind. Eng. Chem. Res., 40 (2001) 5710.

[35] S. Al-Obaidani, E. Curcio, F. Macedonio, G.D. Profio, H. Al-Hinai, E. Drioli, Potential of membrane distillation in seawater desalination: Thermal efficiency, sensitivity study and cost estimation, J. Membr. Sci., 323 (2008) 85-98.

[36] L. Martínez, J.M. Rodríguez-Maroto, Membrane thickness reduction effects on direct contact membrane distillation performance, J. Membr. Sci., 312 (2008) 143-156.

[37] M. Khayet, M. Essalhi, Self-sustained webs of polyvinylidene fluoride electrospun nanofibers at different electrospinning times: 2. Theoretical analysis, J. Membr. Sci., 433 (2013) 180-191.

[38] M. Tomaszewska, Preparation and properties of flat-sheet membranes from polyvinylidene fluoride for membrane distillation, Desalination, 104 (1996) 1-11.

[39] C. Feng, B. Shi, G. Li, Y. Wu, Preparation and properties of microporous membrane from poly(vinylidene fluoride-co-tetrafluoroethylene) (F2.4) for membrane distillation, J. Membrane Sci., 237 (2004) 15-24.

[40] Y. Wu, Y. Kong, X. Lin, W. Liu, J. Xu, Surface-modified hydrophilic membranes in membrane distillation, J. Membrane Sci., 72 (1992) 189-196.

[41] M. Khayet, J.I. Mengual, T. Matsuura, Porous hydrophobic/hydrophilic composite membranes: Application in desalination using direct contact membrane distillation, J. Membrane Sci., 252 (2005) 101-113.

[42] M. Qtaishat, D. Rana, M. Khayet, T. Matsuura, Preparation and characterization of novel hydrophobic/hydrophilic polyetherimide composite membranes for desalination by direct contact membrane distillation, J. Membrane Sci., 327 (2009) 264-273.

[43] M. Qtaishat, M. Khayet, T. Matsuura, Novel porous composite hydrophobic/hydrophilic polysulfone membranes for desalination by direct contact membrane distillation, J. Membrane Sci., 341 (2009) 139-148.

[44] M. Qtaishat, T. Matsuura, M. Khayet, K.C. Khulbe, Comparing the desalination performance of SMM blended polyethersulfone to SMM blended polyetherimide membranes by direct contact membrane distillation, Desalination and Water Treatment, 5 (2009) 91-98.

[45] Z.D. Hendren, J. Brant, M.R. Wiesner, Surface modification of nanostructured ceramic membranes for direct contact membrane distillation, J. Membrane Sci., 331 (2009) 1-10.

[46] P. Peng, A.G. Fane, X. Li, Desalination by membrane distillation adopting a hydrophilic membrane, Desalination, 173 (2005) 45-54.

[47] M. Khayet, A.O. Imdakm, T. Matsuura, Monte Carlo simulation and experimental heat and mass transfer in direct contact membrane distillation, Int. J. Heat & Mass Transfer, 53 (2010) 1249-1259.

[48] J. Phattaranawik, R. Jiraratananon, A.G. Fane, Effect of pore size distribution and air flux on mass transport in direct contact membrane distillation, J. Membrane Sci., 215 (2003) 75-85.

[49] M. Khayet, C. Cojocaru, M.C. García-Payo, Application of response surface methodology and experimental design in direct contact membrane distillation, Ind. Eng. Chem. Res., 46 (2007) 5673-5685.

[50] R.W. Schofield, A.G. Fane, C.J.D. Fell, R. Macoun, Factors affecting flux in membrane distillation, Desalination, 77 (1990) 279-294.

[51] T. Cath, V.D. Adams, A.E. Childress, Experimental study of desalination using direct contact membrane distillation: a new approach to flux enhancement, J. Membrane Sci., 228 (2004) 5-16.

[52] K.W. Lawson, D.R. Lloyd, Membrane distillation: II. Direct contact MD, J. Membrane Sci., 120 (1996) 123-133.

4.4. Self-Sustained Webs of Polyvinylidene Fluoride Electrospun Nanofibers at Different Electrospinning Times: 2. Theoretical Analysis, Polarization Effects and Thermal efficiency

Contents:

Abstract:

A novel theoretical model that considers the gas transport mechanisms through the inter-fiber space of self-sustained electrospun nanofibrous membranes (ENMs) is developed for direct contact membrane distillation (DCMD). The theoretical model involves the structural characteristics of the ENMs, the heat transfer mechanisms and the nature of mass transport through the self-sustained web. The permeate fluxes of different ENMs prepared with different electrospinning times and therefore different thicknesses were predicted for different feed temperatures and sodium chloride salt concentrations up to 60 g/L. The used ENMs exhibit different parameters such as liquid entry pressure of water, inter-fiber space, void volume fraction, thickness, etc.. In contrast to what reported in other theoretical MD studies considering Bosanquet equation with equal mass transport contributions for Knudsen diffusion and ordinary molecular diffusion, in this study the contribution of each mass transport mechanism was determined. It was found that the Knudsen contribution increases with the increase of the ratio of the mean electrospun fiber diameter to the inter-fiber space. The predicted permeate fluxes were compared with the experimental ones and reasonably good agreements between them were found. The temperature polarization coefficient (θ) and the vapor pressure polarization coefficient (ψ) both increase with the thickness of the ENMs, whereas the concentration polarization coefficient (β) decreases indicating the dominant effect of the temperature polarization effect. β was found to be higher for the ENMs having higher permeate fluxes and for greater feed temperatures, whereas it decreases slightly with the increase of the feed salt concentration. The thermal efficiency (EE) is enhanced with the increase of the feed temperature being in all cases for all studied ENMs greater than 78.8% and the heat transfer by conduction less than 20% of the total heat transferred through the ENMs.

369

4.4.1. Introduction

Various worldwide research laboratories have started to produce their own membranes for membrane distillation (MD) in order to improve the MD water production rates as well as its quality [1]. An increase of the number of published papers on MD membrane engineering (i.e. design, fabrication, modification and testing in MD is seen since only 7 years ago) [1,2]. Fortunately, the trend of the yearly published papers on MD membrane engineering continues increasing. Improved MD membranes with different pore sizes, porosities, thicknesses, materials, micro-and nano-structures are required in order to carry out systematic MD studies for better understanding mass transport in different MD configurations and thereby improving the MD permeate flux.

Recently, nanofibrous membranes are proposed for MD applications [3-7]. Based on experimental analysis only, it is observed that this type of membranes is promising for MD. In general, polymer nanofibers have attracted increasing attentions in the last ten years because of their high surface-to-mass (or volume) ratio and special characteristics attractive for advanced applications [8-18]. Several techniques were used for their fabrication such as electrospinning or electrostatic spinning [8-17], vacuum filtration of carbon nanotubes (CNs) dispersion [18], melt-blown [19,20], phase separation [21], molecular self assembly [22-24] and template synthesis [25,26]. Among all used techniques, electrospinning is the most preferred one to use for preparation of polymeric nanofibers. It is simple, cost effective and able to produce continuous nanofibers of various materials.

It is worth quoting that the nanofibers assembled into a membrane-like structure exhibit among others good tensile strength, high surface area per unit mass, highly ordered polymer chains, micro scaled interstitial space, high void volume and interconnectivity, and more controllable parameters (void volume fraction, size of inter-fiber space, thickness) compared to other types of membranes. These characteristics make electrospun nanofibrous membranes (ENMs) interesting candidates for a wide variety of applications and ideal substrate for separation processes including desalination by MD [3,4,6,7].

In MD literature, various theoretical models have been developed based on the kinetic theory of gases to predict the MD permeate flux depending on the membrane characteristics, the MD

370

configuration and the MD operating conditions [1,2,27]. The first theoretical calculations on MD process have been reported by Findley et al. [28] for direct contact membrane distillation (DCMD). The study considered for the first time heat and mass transfer as well as the thermal conductivity of the membrane together with the heat transfer coefficients in the hot and cold boundary layers adjoining the membrane surfaces. Their experimental studies indicated that the major factor affecting the rates of heat and mass transfer was the diffusion through the stagnant gas (i.e. air) in the membrane pores [28]. Since then different types of mechanisms have been proposed for the transport of gases or vapors through microporous hydrophobic membranes, namely, Knudsen flow model, viscous flow model, ordinary molecular diffusion model and/or the combination between them [1,2,27]. The most general model, Dusty Gas model (DG) proposed by Mason et al. [29], also neglects surface diffusion but combines these different mass transport mechanisms, has been considered in MD [27,30-32].

In DCMD mode, air is trapped within the membrane pores with pressure values close to the atmospheric pressure and the permeate flux was successfully predicted by various authors via the combined Knudsen/molecular diffusion mechanism [33-38].

Most of the theoretical studies in MD assumed a uniform pore size of the entire membrane [1,2,26,28,29,32-37]. However, the MD membranes possess collection of pores with size distribution and more than one mechanism of mass transport can occur simultaneously through the entire membrane. The pore size distribution of MD membranes has been considered in DCMD, vacuum membrane distillation (VMD) and air gap membrane distillation (AGMD) theoretical models rather than the mean pore size (i.e. assumption of uniform membrane pore size equal to mean pore size) [33,34,39-42].

Laganà et al. [39] reported that the DCMD permeate flux of commercial porous membranes, calculated assuming all pores having the same size and the one calculated with a Gaussian (symmetric) function are similar and the predicted fluxes were lower than the experimental ones. Phattaranawik et al. [33] by using commercial membranes also concluded that the influence of the pore size distribution on the predicted DCMD flux was insignificant. Martínez et al. [40,41] also considered the pore size distribution to predict the permeability of commercial membranes used in DCMD under different operating conditions. When air was present in the pores, both molecular and Knudsen diffusion resistances were found to be important, but it was observed a

high contribution of Knudsen diffusion resistance for membranes with pore sizes less than 0.6 μm. Without stagnant air within the pores both viscous and Knudsen contributions were important in general, but it was observed a negligible viscous contribution for the membranes with small pores at low water vapor pressures (i.e. low temperatures). However, for membranes with large pores (> 0.45 μm) the viscous contribution reached up to 25% of the Knudsen contribution.

From a theoretical perspective, Woods et al. [42] investigated how pore size distribution could affect the predicted DCMD and AGMD permeate fluxes. It was found that the committed error in vapor flux by neglecting pore size distribution was strongly dependent on the width of the pore size distribution. By considering a membrane with a mean pore size of 0.1 μm and a geometric standard deviation of the pore size of 1.2, the calculated error was 3.5% for DCMD and less than 1% for AGMD. For membranes with greater pore sizes than 0.5 μm, the committed error was smaller.

Khayet et al. [34] found slightly higher DCMD permeability of commercial membranes when including pore size distribution than that predicted from mean pore sizes. This result was attributed to the low values of the geometric standard deviations of the pore size distributions. It was concluded that larger discrepancies may be detected if laboratory made membranes with broad pore size distributions were used [34].

In general, the theoretical models published in MD literature describe vapor flux through membrane pores ignoring pore space interconnectivity. Monte Carlo (MC) simulation models have been developed to study both heat and mass transfer in DCMD and VMD configurations considering inter-connected pores [43-46]. These MC models were designed so that the membrane pore space was described by a three-dimensional network of inter-connected cylindrical pores (bonds) with size distribution and nodes (sites). The MC models consider all possible transport mechanisms, membrane physical characteristics and MD operating parameters. The comparisons between the simulated DCMD results and the experimental data were found to be in excellent qualitative and quantitative agreement [43].

In this study, a theoretical model that considers the gas transport mechanisms through the inter-fiber space of ENMs together with the contribution of each mechanism of mass transport is proposed for the first time to predict the permeate flux of ENMs used at different feed

temperatures and salt (NaCl) concentrations. The considered ENMs were prepared with different electrospinning times. The model is based on the temperature and concentration polarization effects as well as on the mechanism of heat and mass transfer. The predicted permeate fluxes were compared with the corresponding experimental ones.

4.4.2. Experimental

4.4.2.1. Materials and methods

The polyvinylidene fluoride (PVDF) ENMs used in this study were synthesized by electrospinning technique. The used polymer solution was prepared by dissolving 25 wt% PVDF in the solvent mixture acetone/*N,N*-dimethyl acetamide (DMAC) (20/80 wt%) [7]. The electrospinning conditions were 24 kV electric voltage, 1.23 mL/h polymer flow rate, 27.7 cm air gap and different electrospinning times (1 – 4 h). After electrospinning the ENMs were dried in oven at 80ºC for 30 min.

The PVDF ENMs were characterized by different techniques as reported elsewhere [2,7]. The field emission scanning electron microscope (SEM, JEOL Model JSM-6330F) was used to analyze the surface of the ENMs. The SEM images were analyzed by UTHSCSA ImageTool 3.0 to determine the size of the fibers (d_f). Statistical analysis have been applied in order to determine the fiber size distribution and to estimate the arithmetic weighted mean of the fiber diameters and their dispersions. The Instron dynamometer (model 3366) was used to study the mechanical properties of the ENMs. At least five specimens taken from the center of ENM samples were tested. The tensile strength, Young´s modulus and elongation at break of the ENMs were determined for each sample. The liquid entry pressure of water (*LEP*) and the size of the inter-fiber space of the ENMs were determined following the procedures reported in [7]. The *LEP* is the minimum applied pressure before water penetrates into the inter-fiber space. The water contact angle of the surface of each ENM was measured at room temperature (23ºC) by a computerized optical system CAM100, equipped with a CCD camera, frame grabber and image analysis software. More than 15 readings were obtained for each ENM sample and an average

value was calculated and reported together with their standard deviations. The void volume fraction of the ENMs was determined by measuring the density of each ENM using isopropyl alcohol (IPA), which penetrates inside the inter-fiber space of the ENMs and distilled water, which does not enter in the inter-fiber space. The applied method was reported elsewhere [2]. The thickness (δ) of the ENMs was measured by the micrometer Millitron Phywe (Mahr Feinprüf, type TYP1202IC) in different points, at least 50, of three different membrane samples made from different batches and the average values together with their standard deviations are reported. All characterized samples were cut from about $3 \ 10^{-3} \ m^2$ circular area taken from the center of the prepared ENMs.

4.4.2.2. Direct contact membrane distillation (DCMD)

DCMD experiments were carried out for distilled water as feed, different feed salt (NaCl) aqueous solutions (12, 30 and 60 g/L) and feed temperatures using the DCMD system presented elsewhere [47]. The tested sample was taken from the center of each prepared ENM. The concentration of NaCl was increased up to 60 g/L, while the temperature was varied in the range 40ºC - 80ºC maintaining the permeate temperature at 20ºC and the stirring rate at 500 rpm. The DCMD experiments were made in similar sets for all PVDF ENMs. The permeate flux was calculated in every case by measuring the condensate collected in the permeate chamber for a predetermined period (at least for 3 h) of each feed solution. First distilled water was used as feed and then different NaCl feed aqueous solutions (12 g/L, 30 g/L and 60 g/L) were tested. Finally, the permeate flux of distilled water used as feed was measured again to check if there is any change of the ENM due to fouling or wetting. Therefore, a total of at least 25 h of DCMD operation tests were carried out for each ENM.

4.4.3. Theoretical approach

As shown in Fig. 4.4.1, the ENM is placed between the feed saline aqueous solution to be treated and the permeate liquid kept at a lower temperature than the feed temperature (20ºC in this study). The high hydrophobic nature of the ENM prevents the feed and permeate liquids from entering its inter-fiber space due to the high surface tension forces of the ENM. As a result, liquid/vapor interfaces are formed at the ENM surfaces. The transmembrane temperature difference induces the necessary vapor pressure difference, which is the driving force for mass transfer through the void volume fraction of the ENM. Water molecules evaporate at the hot feed liquid/vapor interface of the ENM, cross its void volume in vapor phase, and finally condense at the cold permeate liquid/vapor interface. Heat and mass transports are simultaneously involved to generate steady mass flux of water vapor. The mechanism of mass transport through the ENM is based on the kinetic theory of gases. The size of the fibers, the interconnection of the inter-fiber space of the ENM and the applied temperature will play an important role in determining the mechanism(s) of vapor transport through the void space of the ENM as it is analyzed later on.

Air is present inside the ENM and therefore vapor migration through ENM is governed by two major transport mechanisms Knudsen and molecular diffusion [2]. Under the proposed configuration in Fig. 4.4.1, viscous (Poiseuille) type of flow is negligible because the hydrostatic pressures of the feed and permeate are maintained at atmospheric pressure. Therefore, the resistance to mass transfer associated to viscous type of transport can not be considered [43].

The governing quantity that provides a guideline in determining the operative mechanism in a given membrane pore under a given experimental condition is Knudsen number (K_n) defined as the ratio of the mean free path (λ) of the transported molecules to the pore size of the membrane. In DCMD mass transport through the membrane pores occurs in three regions depending on the pore size and λ [33]: Knudsen region, continuum region (or ordinary-diffusion region) and transition region (or combined Knudsen/ordinary-diffusion region). When λ is large in relation with the membrane pore size (i.e. $K_n > 1$), the molecule-pore wall collisions are dominant over the molecule-molecule collisions and Knudsen type of flow is the responsible for mass transport. In DCMD mode, air is always trapped within the membrane pores with pressure values close to the atmospheric pressure. Therefore, when $K_n < 0.01$, molecular-diffusion is always used to

describe the mass transport in continuum region caused by the virtually stagnant air trapped within each membrane pore due to the low solubility of air in water, which is about 10 ppm. This indicates that the transmembrane flux of air through a membrane applied in DCMD is many orders of magnitude lower than that of water vapor. In the transition region ($0.01 < K_n < 1$), the molecules of water vapor collide with each other and diffuse among the air molecules. In this case, the mass transport takes place via the combined Knudsen/ordinary-diffusion mechanism [33,34].
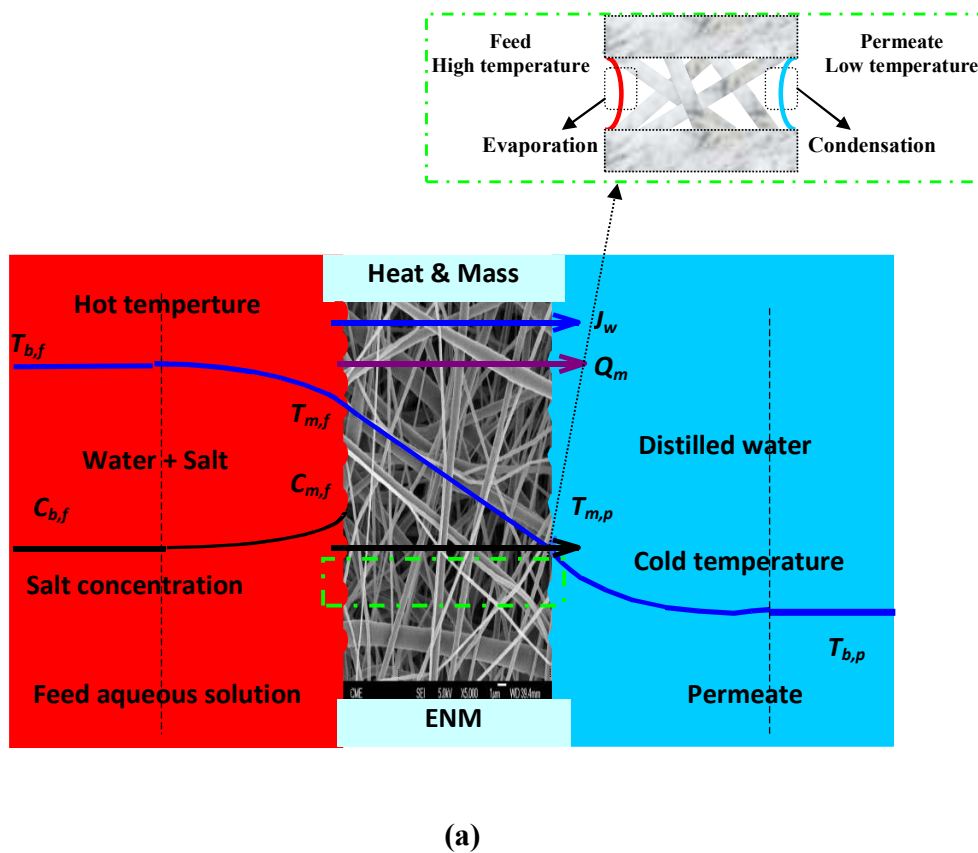

(a)

Figure 4.4.1. DCMD through an ENM placed between a feed saline aqueous solution and a permeate liquid kept at a lower temperature with presentation of the temperature polarization and concentration polarization phenomena (a), electrical analogy circuit presenting heat transfer through an ENM (b), and mass transport mechanism through an ENM considering Bosanquet equation (c) and variable Knudsen contribution (α) and molecular diffusion contribution to mass transport (1-α) (d). (Knudsen diffusion, D_K; molecular diffusion, D_M; effective diffusion coefficient, D_e). (To be continued)
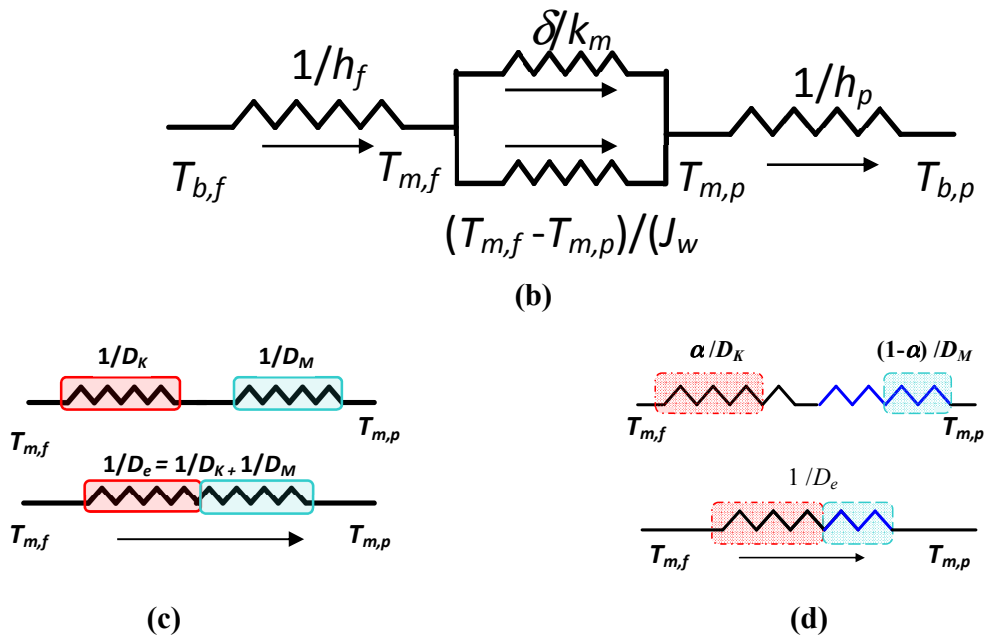
Figure 4.4.1. DCMD through an ENM placed between a feed saline aqueous solution and a permeate liquid kept at a lower temperature with presentation of the temperature polarization and concentration polarization phenomena (a), electrical analogy circuit presenting heat transfer through an ENM (b), and mass transport mechanism through an ENM considering Bosanquet equation (c) and variable Knudsen contribution (α) and molecular diffusion contribution to mass transport (1-α) (d). (Knudsen diffusion, D_K; molecular diffusion, D_M; effective diffusion coefficient, D_e). (Continuation)

For a temperature range 40 - 80ºC and atmospheric pressure, λ varies only between $1.02 \ 10^{-7}$ and $1.09 \ 10^{-7}$ m, which is two orders of magnitude smaller than the mean size of the inter-fiber space of the ENMs. K_n increases slightly with the feed temperature in the range ($0.02 \leq K_n \leq 0.04$) (Fig. 4.4.2). These indicate the presence of collisions between water vapor molecules with each others and between water vapor molecules and air inside the void volume space of the ENM. In addition, due to the web configuration of ENM, there are also collisions between water vapor molecules and fibers and their contribution is high for small size of inter-fiber spaces and large diameters of fibers. Therefore, a combination of Knudsen diffusion and molecular diffusion should be applied for water vapor transport through ENMs (Fig. 4.4.1(c) and Fig. 4.4.1(d)) [2,33].

The Bosanquet equation developed in 1944 for self-diffusivity of different species combining molecule-wall and molecule-molecule interactions, and reported four years later by Pollard and Present [48], was considered in a mayor number of theoretical MD studies [1,2]. Bosanquet equation suggested the collision frequency is simply additive and thus the effective diffusion (D_e) is also derived from a reciprocal additivity law of Knudsen diffusion (D_K) and molecular diffusion (D_M) (i.e. $1/D_e = 1/D_K + 1/D_M$) (Fig. 4.4.1(c)). This equation can be also derived as a limiting case of DG model for binary mixture diffusion by taking the species in the mixture to be identical to each other [49].
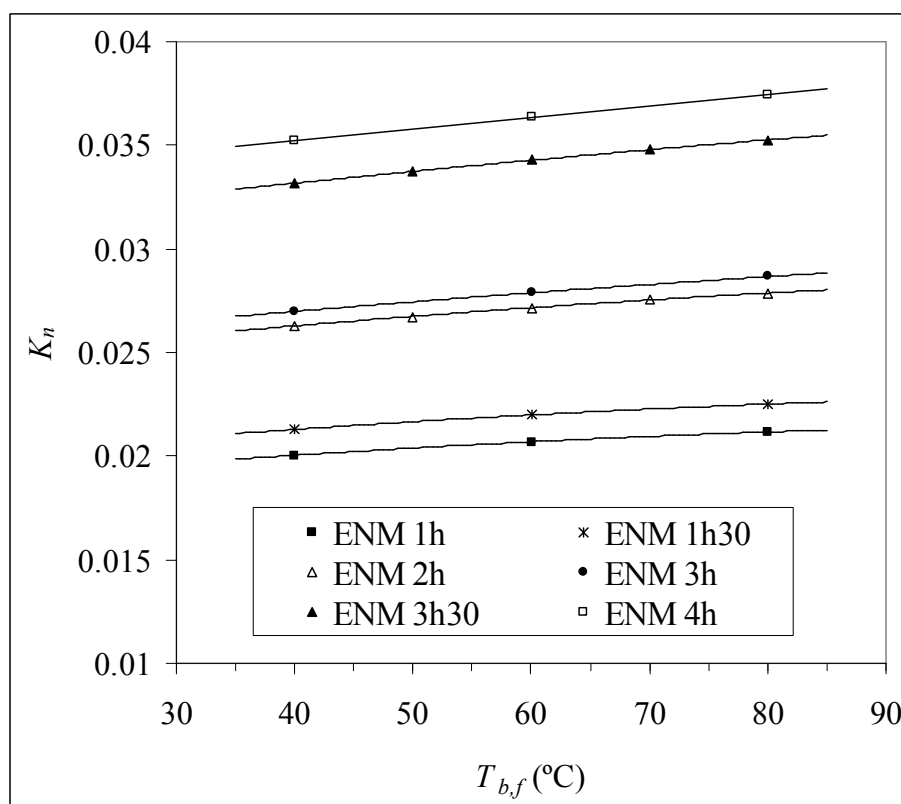

Figure 4.4.2. Calculated Knudsen number (K_n) of PVDF ENMs at different feed distilled water temperatures ($T_{b,f}$).

Taking into account the variation of Knudsen and molecular diffusion contributions to mass transfer through the inter-fiber space of the ENM (Fig. 4.4.1(d)), in contrast to what have been considered in various theoretical MD studies (Fig. 4.4.1(c)) [1,2], the effective diffusion coefficient (D_e) can be written as:

378

$$D_e = \left(\alpha \frac{3\delta\tau}{2\varepsilon\ d_i} \left(\frac{\pi RT}{8M_w} \right)^{1/2} + (1-\alpha) \frac{RT}{M_w} \frac{\delta\tau}{\varepsilon} \frac{p_a}{PD_{w/a}} \right)^{-1} = \left(\frac{\alpha}{D_K} + \frac{1-\alpha}{D_M} \right)^{-1}$$ (4.4.1)

where D_k is Knudsen diffusion coefficient, D_M is molecular diffusion coefficient, α is the contribution of Knudsen diffusion to mass transfer, M_w is the molecular weight of water, R is the gas constant, δ is the thickness of the ENM, d_i is the mean size of the inter-fiber space, ε is the void volume fraction, τ is the tortuosity of the path length through the thickness of the ENM, p_a is the air pressure inside the ENM, P is the total pressure (atmospheric pressure in this case) and $D_{w/a}$ is the ordinary diffusion of water vapor in air. The tortuosity (τ) defines the effective length of the path of the water vapor flow through the ENM and can be used to approximate the geometry and interconnectivity of the inter-fiber space of the ENM. Based on fractal theory of random walks, which is a mathematical formalization of a trajectory that consists of taking successive random steps, τ can be predicted from ε as ($\tau = 1/\varepsilon$) [50,51]. This expression was considered for ENMs by Barhate et al. [50] for the fibers randomly arranged in the network, and confirmed by Singh and Sirkar [51] for flat sheet polytetrafluoroethylene (PTFE) membrane (0.03 μm pore size, W.L. Gore and Associates) used in DCMD.

As schematized in Fig. 4.4.1(b) both heat and mass transfer occur simultaneously through the ENM and the temperatures and concentration at the vapor/liquid interfaces differ from those at the bulk phases leading to a decrease of the driving force (i.e. transmembrane water vapor pressure) and the decline of the DCMD permeate flux. The temperature polarization and concentration polarization effects will be discussed later on.

The heat transfer within the ENM (Q_m) involves the latent heat required for water evaporation at the hot feed liquid/vapor interface (Q_v) and the heat transferred by conduction across the fibers of the ENM and the gas-filled void space (Q_c):

$$Q_m = Q_v + Q_c = J_w \Delta H_v + \frac{k_m}{\delta} \left(T_{m,f} - T_{m,p} \right) = J_w \Delta H_v + \left(\frac{\varepsilon}{k_g} + \frac{1-\varepsilon}{k_p} \right)^{-1} \frac{T_{m,f} - T_{m,p}}{\delta}$$ (4.4.2)

where J_w is the permeate flux of the ENM, ΔH_v is the heat of vaporization of water, k_m is the thermal conductivity of the ENM determined following the isostress model [52], k_g is the thermal conductivity of the gas-filled void volume fraction of the ENM, k_p is the thermal conductivity of

the PVDF electrospun fiber (0.18 W/m.K), $T_{m,f}$ is the temperature at the feed liquid/vapor interface and $T_{m,p}$ is the temperature at the permeate liquid/vapor interface.

In addition, as shown in Fig. 4.4.1, heat transfer occurs through the adjoining liquid phases, both in the feed and permeate sides of the ENM. At steady state conditions, the heat flux must be the same as in Eq. (4.4.2):

$$Q_m = h_f \left(T_{b,f} - T_{m,f} \right) = h_p \left(T_{m,p} - T_{b,p} \right) \tag{4.4.3}$$

where h_f and h_p are the heat transfer coefficients in the feed and permeate boundary layers adjoining the ENM surfaces, respectively. These can be calculated from the semi-empirical equation of the dimensionless numbers [1,53].

$$Nu = a \ \text{Re}^b \ \text{Pr}^c \left(\frac{\mu_b}{\mu_m} \right)^d \tag{4.4.4}$$

where Nu, Re, and Pr are Nusselt, Reynolds and Prandtl numbers, respectively; a, b, c and d are characteristics constants of the liquid flow regime (in this case, turbulent flow regime, $a = 0.027$, $b = 4/5$, $c = 0.4$ for feed and 0.3 for permeate, and $d = 0.14$). μ_b and μ_m are the dynamic viscosity of the aqueous solution at the bulk and at the corresponding side of the ENM, respectively [34].

From Eqs. (4.4.2) and (4.4.3) the temperatures $T_{m,f}$ and $T_{m,p}$ can be written as [53]:

$$T_{m,f} = \frac{k_m \left(T_{b,p} + \dfrac{h_f}{h_p} T_{b,f} \right) + \delta \left(h_f T_{b,f} - J_w \Delta H_v \right)}{k_m + h_f \left(\delta + \dfrac{k_m}{h_p} \right)} \tag{4.4.5}$$

$$T_{m,p} = \frac{k_m \left(T_{b,f} + \dfrac{h_p}{h_f} T_{b,p} \right) + \delta \left(h_p T_{b,p} + J_w \Delta H_v \right)}{k_m + h_p \left(\delta + \dfrac{k_m}{h_f} \right)} \tag{4.4.6}$$

In DCMD, the temperature polarization coefficient is defined as [2]:

$$\theta = \frac{T_{m,f} - T_{m,p}}{T_{b,f} - T_{b,p}} 100 \tag{4.4.7}$$

When the salt concentration is increased in the feed aqueous solution, the water production rate of the MD system is reduced since the chemical potential of water between both sides of the

membrane is decreased, taking into account that the chemical potential depends on both temperature and concentration of solutes in water. In other words, the water vapor pressure decreases with the increase of the salt in the feed solution and hence the driving force of the distillation process ($\Delta p_{w,m}$) is reduced. In this case the water production rate can be calculated using the following equation [1]:

$$J_w = D_e \, \Delta p_{w,m} = D_e(p_{m,f} - p_{m,p}) = D_e(p^0_{w,f} a_{w,f} - p^0_{w,p}) = D_e(p^0_{w,f} \gamma_{w,f} x_{w,f} - p^0_{w,p}) \quad (4.4.8)$$

where $a_{w,f}$, $\gamma_{w,f}$, $x_{w,f}$ and $p^0_{w,f}$ are the activity, activity coefficient, mole fraction and vapor pressure of water at the feed/ENM surface, respectively. $p^0_{w,p}$ is the vapor pressure of water in the permeate.

Due to water vapor transfer, the salt concentration at the feed/ENM interface ($C_{m,f}$) becomes greater than that of the bulk feed aqueous solution ($C_{b,f}$) (Fig. 4.4.1(a)). This concentration gradient leads to a diffusive flow of salt from the ENM surface to the bulk phase. Steady state concentration profile is established when the convective transport of salt to the ENM surface is counterbalanced by a diffusive flux of the retained salt back to the bulk solution. Nernst film model that neglects the eddy and thermal diffusions in relation to the ordinary diffusion can be used in this case to relate $C_{m,f}$ to $C_{b,f}$ [1,2]:

$$C_{m,f} = C_{b,f} \exp(J_w / k_s) \tag{4.4.9}$$

where k_s is the solute mass transfer coefficient for the diffusive mass transfer through the concentration boundary layer in the feed side of the ENM. This is not the case for the permeate side since distilled water is produced. k_s can be estimated from Sherwood number (Sh) using the dimensionless empirical correlation for mass transfer (Sh = f(Re,Sc)) derived from the analogy with the empirical correlation for heat transfer (Eq. (4.4.4)), where Sc is the dimensionless Schmidt number [2,27]. The concentration polarization coefficient (β) is defined in this case as:

$$\beta = \frac{C_{m,f}}{C_{b,f}} \tag{4.4.10}$$

Both the temperature polarization and concentration polarization produce a decrease of the driving force (i.e. vapor pressure difference). Therefore, both polarization effects were combined in one termed vapor pressure polarization effect defined by means of the following coefficient:

$$\psi = \frac{\Delta p_{w,m}}{\Delta p_{w,b}} = \frac{p_{m,f} - p_{w,p}^0}{p_{b,f} - p_{w,p}^0} 100 \qquad (4.4.11)$$

where $\Delta P_{w,b}$ is the externally applied bulk driving force (i.e. bulk water vapor pressure difference) and $\Delta P_{w,m}$ is the water vapor pressure difference between the feed and permeate ENM/liquid interfaces.

The overall heat transfer coefficient for the DCMD process can be determined as follows [1,2]:

$$H = \left[\frac{1}{h_f} + \frac{1}{\dfrac{k_m}{\delta} + \dfrac{J_w \Delta H_v}{T_{m,f} - T_{m,p}}} + \frac{1}{h_p} \right]^{-1} \qquad (4.4.12)$$

The thermal efficiency (*EE*) of the DCMD process is the ratio of the vaporization heat associated to the mass transport through the void volume space of the ENMs over the total heat flux. It is also the fraction of the latent heat required for water evaporation at the hot feed liquid/vapor interface (Q_v) to the total heat (Q_m) transferred through the ENM:

$$EE = \frac{Q_v}{Q_m} 100 = \frac{J_w \Delta H_v}{H(T_{b,f} - T_{b,p})} 100 \qquad (4.4.13)$$

To determine the DCMD permeate flux of the ENM, an iterative program was built as shown in Fig. 4.4.3 using the above cited equations. In the first step, the structural parameters of the ENM and the DCMD operating parameters are established as independent variables. Since the procedure is iterative, the temperatures and concentration at the ENM surfaces were considered initially the same as those of the bulk phases (i.e. without considering the effects of the temperature polarization and concentration polarization).
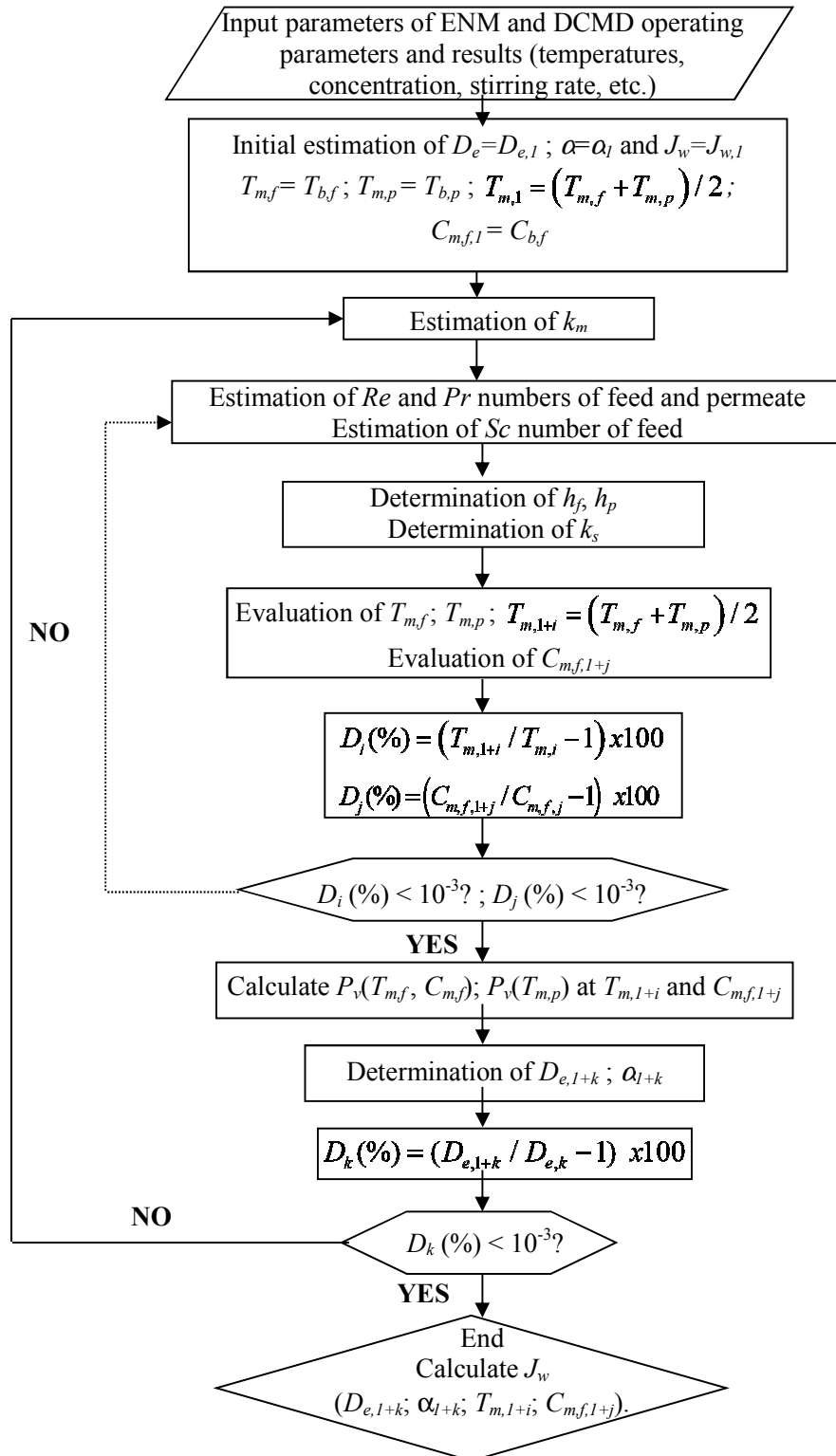
Figure 4.4.3. Flow diagram of the followed algorithm for the prediction of the DCMD permeate flux (J_w) of the ENMs.

4.4.4. Results and discussions

Figure 4.4.4 shows as an example the SEM images together with the fiber size distribution of the PVDF ENMs prepared at 1 h and 4 h electrospinning time. The used PVDF ENMs exhibit different thicknesses, void volume fractions, sizes of inter-fiber spaces, liquid entry pressure of water values, etc. Table 4.4.1 summarizes the characteristics of the used ENMs obtained by means of different characterization techniques as reported in [7]. The thickness and the liquid entry pressure of water (*LEP*) of the PVDF ENMs prepared with larger electrospinning time are higher than those prepared with shorter electrospinning time, whereas the mean size of the inter-fiber space (d_i) was smaller for larger electrospinning time. As the maximum size of the inter-fiber space is reduced the water *LEP* is enhanced. This is corroborated by Young-Laplace equation. No significant changes were observed for the diameter of the electrospun fibers (d_f), which varies from 1.0 μm to 1.3 μm, the void volume fraction (ε) increases slightly from 0.85 to 0.93 with increasing electrospinning time and the water contact angle (θ_a) is varied in the range 137.4° - 141.1°. A gradual increase of the Young´s modulus and tensile strength were observed with the increase of the thickness of the ENMs. Because of the web structure of the ENMs and the high obtained values of the elongation at break compared to other types of membranes used in MD [2,7], no clear trend was detected between the elongation at break and the thickness of the ENMs.

The DCMD permeate flux (J_w) of the ENMs was predicted as explained in the previous section considering different feed temperatures up to 80ºC and NaCl concentrations of the feed aqueous solutions up to 60 g/L. It was observed that Knudsen diffusion (D_k) is 17.9 to 37.4 times greater than molecular diffusion (D_M) and for each ENM D_k decreases slightly with the increase of the feed temperature, whereas a small enhancement was detected for D_M as shown in Fig. 4.4.5 for the ENM 2h and ENM 3h30. The contribution of Knudsen diffusion to mass transfer, factor α in Eq. (4.4.1), varies between 0.29 and 0.4 and increases with the ratio of the mean fiber diameter to the size of the inter-fiber space (d_f/d_i) as can be seen in Fig. 4.4.6. This indicates that Knudsen contribution in ENMs is high for small size of inter-fiber spaces and large diameters of fibers because of the high probability of collisions between water vapor molecules and fibers. When Knudsen diffusion alone was considered ($\alpha = 1$ in Eq. (4.4.1)), the predicted permeate

384

fluxes were extremely high compared to the experimental ones (i.e. the calculated permeate fluxes were 10.1-28.2 higher than the experimental ones), whereas when molecular diffusion alone was considered ($\alpha = 0$ in Eq. (4.4.1)), the predicted permeate fluxes were very low compared to the experimental ones (i.e. the predicted permeate fluxes were 0.45 – 0.82 times lower than the experimental ones).
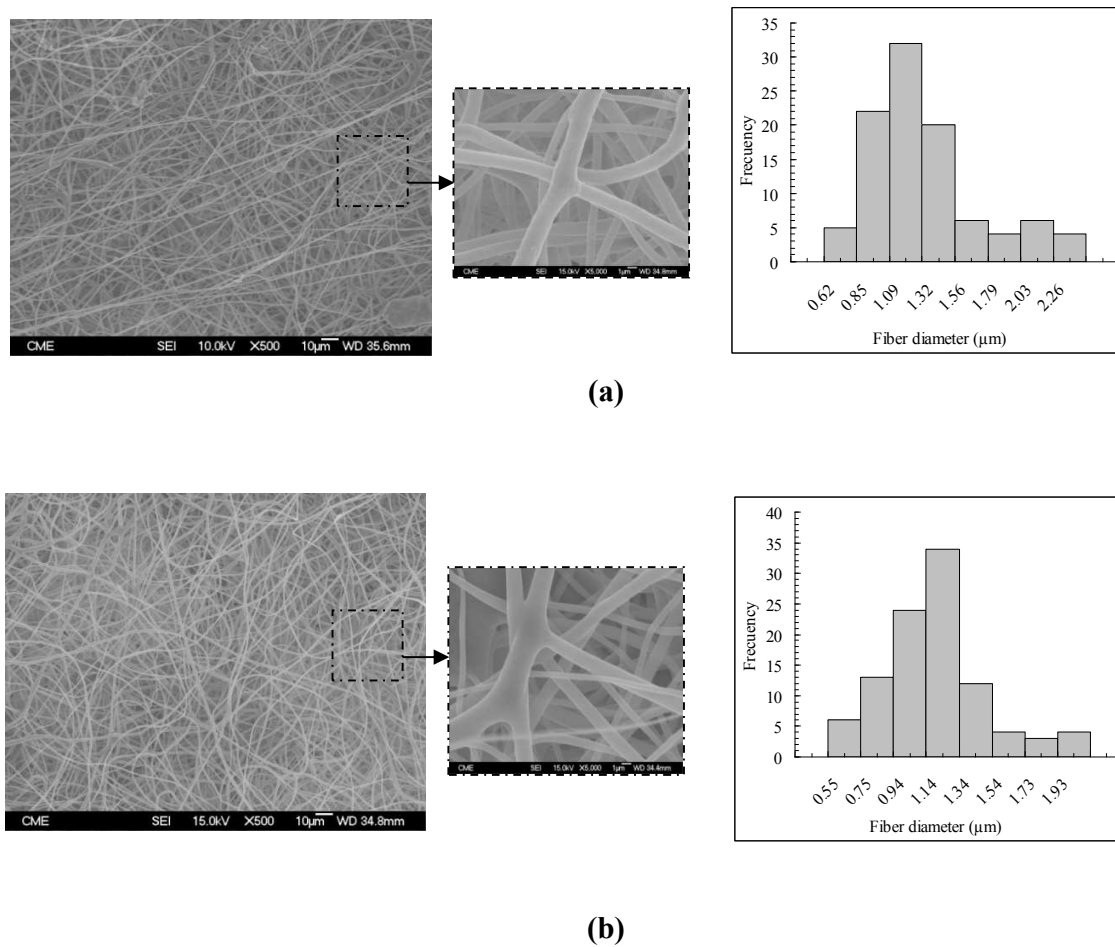

(a)

(b)

Figure 4. SEM images of the top surface of PVDF ENMs and the corresponding distributions of the fiber diameters: (a) ENM 1h, (b) ENM 4h.

Table 4.4.1. Mean fiber diameter (d_f), inter-fiber space (d_i), water contact angle (θ_a), liquid entry pressure of water (*LEP*), void volume fraction (ε), thickness (δ) and mechanical characteristics of the PVDF ENMs prepared at different electrospinning times.

| ENMs	d_f (µm)	d_i (10^{-7} m)	θ_a (°)	*LEP* (10^4 Pa)	ε (%)	δ (µm)	Mechanical characteristics		
							Young´s Modulus (MPa)	Tensile strength (MPa)	Elongation at break (%)
ENM 1h	1.2 ± 0.4	51.1 ± 1.5	139.7 ± 0.4	6.3 ± 0.4	85.3 ± 1.9	144.5 ± 7.3	23.9 ± 6.0	4.5 ± 1.2	138.1 ± 16.8
ENM 1h30	1.2 ± 0.3	48.1 ± 1.6	137.4 ± 0.3	6.7 ± 0.3	86.2 ± 0.9	219.8 ± 20.0	34.3 ± 14.4	5.9 ± 0.9	120.5 ± 18.2
ENM 2h	1.3 ± 0.3	43.9 ± 1.3	139.1 ± 0.3	7.7 ± 0.3	86.6 ± 0.5	464.1 ± 27.2	34.6 ± 14.4	6.4 ± 1.7	134.2 ± 11.2
ENM 3h	1.1 ± 0.3	37.9 ± 1.0	140.1 ± 0.2	8.7 ± 0.2	87.5 ± 0.3	833.4 ± 66.5	43.5 ± 14.5	7.2 ± 0.8	133.9 ± 33.8
ENM 3h30	1.0 ± 0.3	30.8 ± 0.9	141.1 ± 0.1	9.3 ± 0.3	89.6 ± 4.0	1206.3 ± 114.2	52.3 ± 7.6	7.4 ± 2.3	131.9 ± 11.6
ENM 4h	1.1 ± 0.3	29.1 ± 1.0	139.4 ± 0.4	11.0 ± 0.3	92.9 ± 3.9	1529.3 ± 121.5	74.7 ± 12.6	10.2 ± 2.0	130.2 ± 20.5
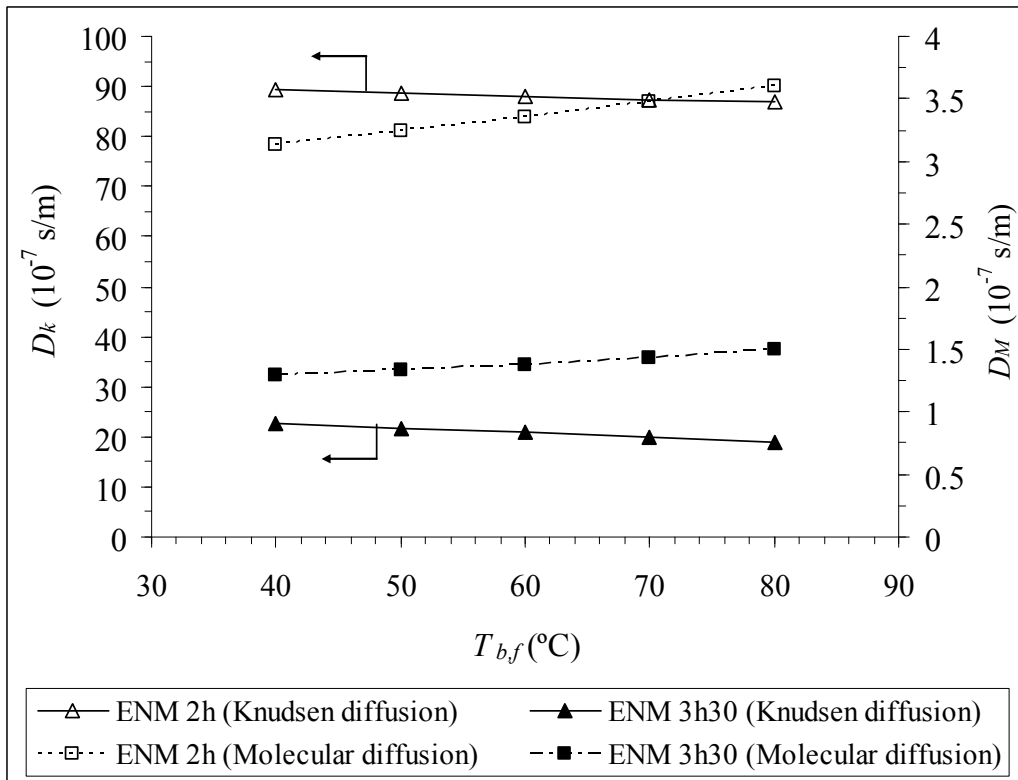
Figure 4.4.5. Effect of distilled water feed temperature ($T_{b,f}$) on Knudsen diffusion (D_k) and molecular diffusion (D_M) of the ENM 2h and ENM 3h30 shown as examples.
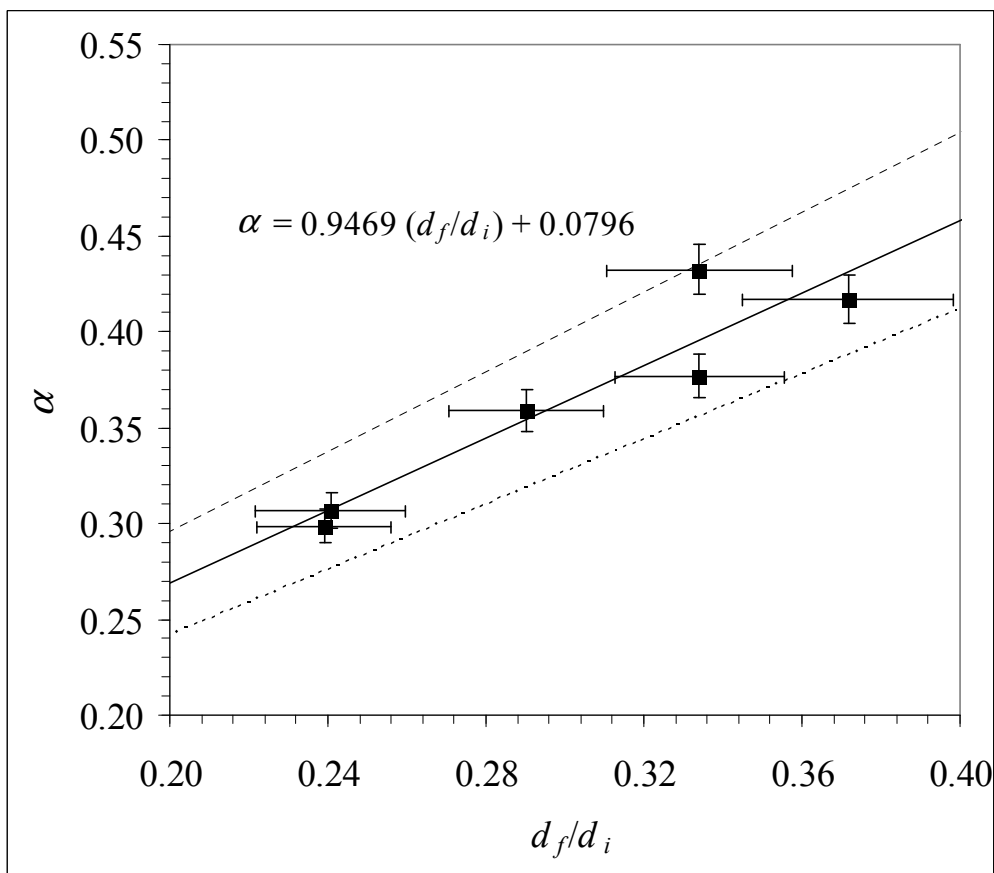
Figure 4.4.6. Knudsen contribution to mass transfer (α) as a function of the ratio of the mean fiber diameter to the size of inter-fiber space (d_f/d_i). The dotted lines represent $\pm 10\%$ deviation of the solid fitting line. (Distilled water was used as feed).

Figure 4.4.7 shows both the experimental and the predicted DCMD water permeate fluxes of the ENMs at different feed temperatures. As occurred experimentally, the predicted permeate flux increases exponentially with the feed temperature due to the increase of the vapor pressure at the feed/ENM interface and it is higher for thinner ENMs (i.e. ENMs prepared with short electrospinning time). Reasonably good agreements were found between the predicted permeate fluxes of all studied ENMs and the corresponding experimental ones over the entire range of feed temperature investigated in this study (Fig. 4.4.7(b), $R^2 = 0.988$).

(a)

$$J_{w,predicted} = 1.0339\,J_{w,experimental}$$
$$R^2 = 0.9881$$

(b)
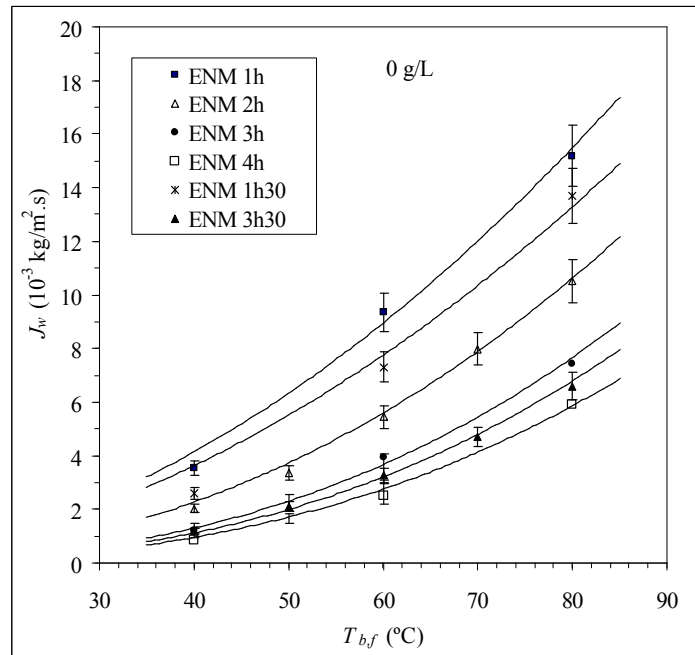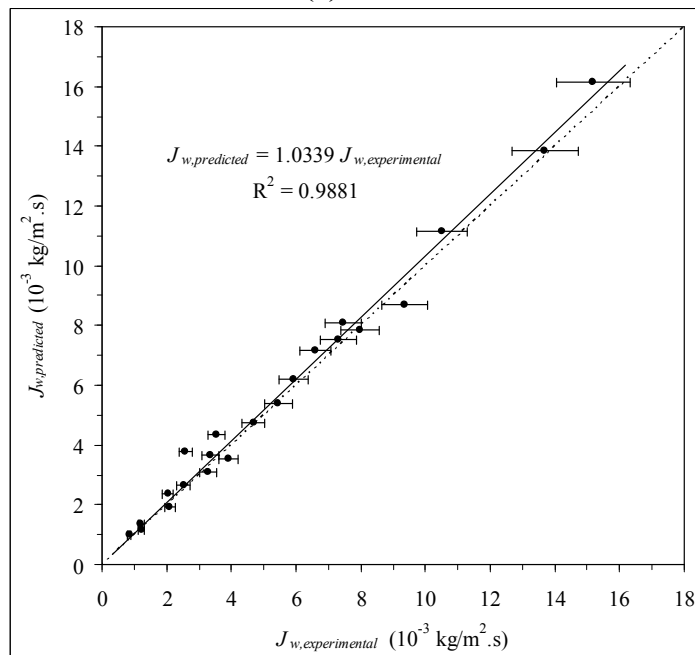
Figue 4.4.7. Predicted and experimental DCMD permeate flux (J_w) of different ENMs: (a) Effect of feed temperature ($T_{b,f}$) on J_w; (b) Predicted permeate flux *vs.* Experimental permeate flux. Distilled water used as feed, 500 rpm stirring rate of feed and permeate and 20ºC permeate temperature.

The DCMD permeate flux increases with the feed temperature following an Arrhenius type of dependence due to the increase of the vapor pressure at the feed/ENM interface and to the temperature polarization effect. As stated previously, the temperature polarization coefficient (θ) and the thermal efficiency (*EE*) were calculated using Eqs. (4.4.7) and (4.4.13), respectively. The results for distilled water as feed are reported in Fig. 4.4.8. For all ENMs the temperature polarization effect is less significant at low feed temperatures (Fig. 4.4.8(a)) and for thicker ENMs (i.e. θ increases with δ and tends to an asymptotic θ value for high δ depending on the feed temperature. The temperature polarization effect is more significant at high feed temperatures reducing the permeate flux considerably. However, the thermal efficiency (*EE*) is enhanced with the increase of the feed temperatures being in all cases greater than 78.8% (Fig. 4.4.8(b,c)). This is because the heat transfer by conduction through the ENMs (Q_c), considered heat lost in MD, becomes less significant at high operating feed temperatures compared to the latent heat required for water evaporation (Q_v). Therefore, it is advisable to work under high feed temperatures although the effect of the temperature polarization effect is more significant.
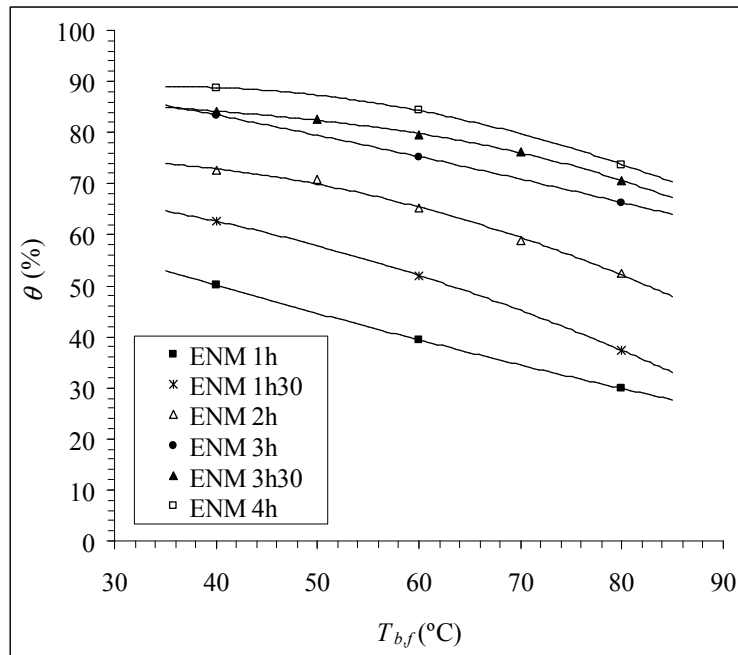
(a)
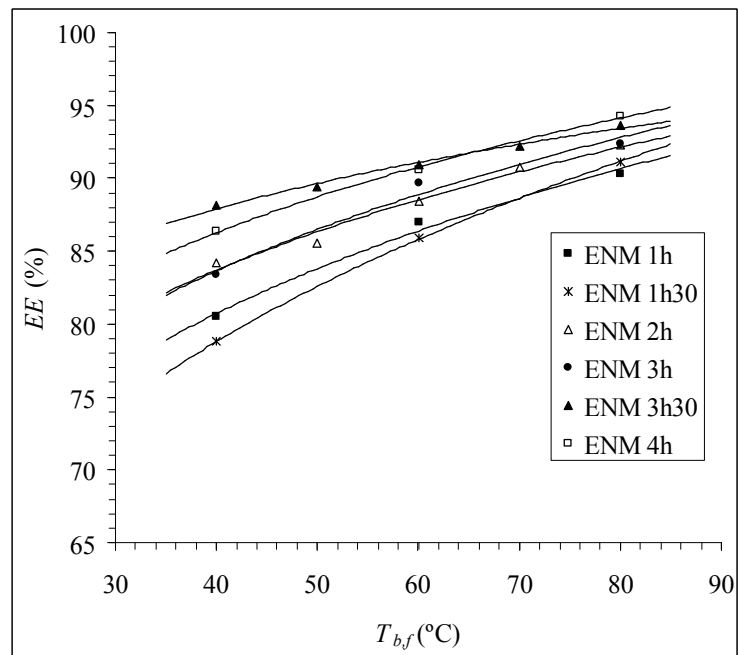
(b)

Figure 4.4.8. Temperature polarization coefficient (θ) (a) and thermal efficiency (*EE*) (b,c), of the PVDF ENMs at different feed temperatures ($T_{b,f}$) and thickness of the ENMs (δ). The plotted solid lines are only a guide to the eye. Distilled water used as feed, 500 rpm stirring rate of feed and permeate and 20ºC permeate temperature. (To be continued)
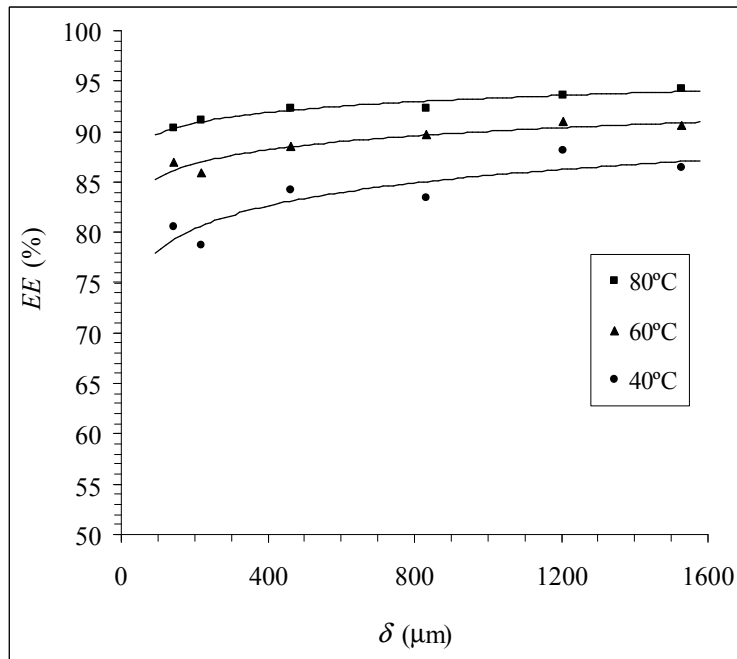
(c)

Figure 4.4.8. Temperature polarization coefficient (θ) (a) and thermal efficiency (*EE*) (b,c), of the PVDF ENMs at different feed temperatures ($T_{b,f}$) and thickness of the ENMs (δ). The plotted solid lines are only a guide to the eye. Distilled water used as feed, 500 rpm stirring rate of feed and permeate and 20ºC permeate temperature. (Continuation)

In this study, *EE* reaches a high value of 94.3% (ENM 4h at 80ºC feed temperature and 20ºC permeate temperature). This value is greater than that the highest value indicated by Lee et al. [54] (88%) when multiple cross-flow hollow fiber modules are employed in an overall countercurrent flow configuration for both the hot feed and the cold distillate. In general, *EE* in countercurrent DCMD is around 60-70% [2].

In this study, the ENM 4h reaches a θ value of 90%. The highest θ value in DCMD (85%) was reported by Lawson and Lloyd [31] for pure water as feed at 30ºC using 3MA membrane (3M Corporation: PP membrane having 0.29 μm maximum pore size, 66% porosity and 91 μm thickness). In general, θ value ranges between 40% for high permeate flux and 70% for low permeate flux [31].

It is to point out that the *EE* values of the ENMs are higher than those observed for other membranes used in MD [2,35,36,52]. In this study, Q_c of the PVDF ENMs is less than 20% of

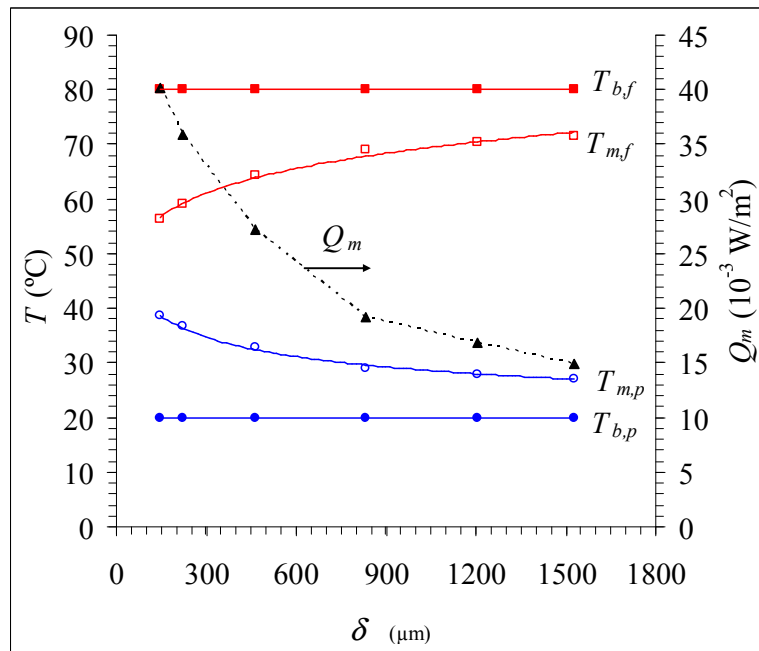the total heat transferred through each ENM (Q_m in Eq. (4.4.2)). For example, Q_c varies in the range 9.7 - 19.5% for ENM 1h and 5.7 – 13.6% for ENM 4h. This means that between 80.5 and 94.3% of energy is consumed as latent heat for water production (Q_v). The obtained high thermal efficiency of the distillation process demonstrates that ENMs are adequate for water production with high energy efficiency.

Fig. 4.4.9(a) shows the calculated overall heat transfer coefficient (H) by means of Eq. (4.4.12) as a function of δ of the ENMs at different feed temperatures. The decrease of H is due to the decrease of the feed temperature (i.e. decrease of J_w) and the increase of δ following Eq. (4.4.12). For instance, a gradual increase of the feed temperature at the ENM surface was observed with the increase of δ, whereas the permeate temperature at the ENM surface decreased (Fig. 4.4.9(b)). Although the transmembrane temperature is high for thick ENMs, the heat transfer through the ENM Q_m is low because both J_w and Q_c decrease with the increase of δ as shown in Fig. 4.4.7(a) and Fig. 4.4.9(c), respectively. Based on Eq. (4.4.2), when δ increases both Q_c and Q_m decrease in accordance with Fig. 4.4.9(b) and 9(c), respectively. The improvement of EE with the increase of δ is attributed to the reduction of Q_c, which is more significant than the decrease of Q_v due to the permeate flux decline at high δ values. A similar result was observed previously by Al-Obaidani et al. for commercial shell-and-tube capillary PP membrane module (MD020CP2N, Mycrodyn) [36].

In Fig. 4.4.9(c) it can be seen the reduction of Q_c with the increase of δ (see Eq. (4.4.2)) favoring the energy efficiency of the DCMD process as plotted in Fig. 4.4.8(c), which shows the increase of EE with δ up to asymptotic values that depend on the feed temperature. This justifies the non-linearity of the permeate flux variation with the inverse of the thickness of the ENMs as reported in [7].

(a)

(b)

Figure 4.4.9. Effect of the thickness of the ENMs (δ) on (a) the overall heat transfer coefficient (H), (b) temperatures ($T_{m,f}$, $T_{m,p}$) and heat transfer through the ENMs (Q_m) and (c) heat transfer by conduction through the ENMs (Q_c). Distilled water used as feed, 500 rpm stirring rate of feed and permeate and 20ºC permeate temperature. (To be continued)
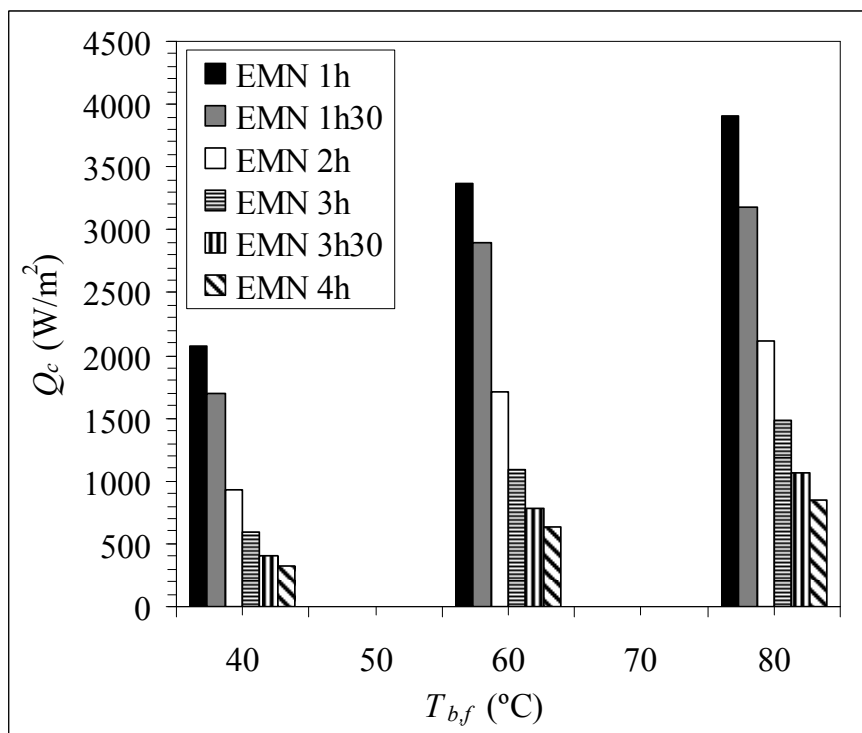
Figure 4.4.9. Effect of the thickness of the ENMs (δ) on (a) the overall heat transfer coefficient (H), (b) temperatures ($T_{m,f}$, $T_{m,p}$) and heat transfer through the ENMs (Q_m) and (c) heat transfer by conduction through the ENMs (Q_c). Distilled water used as feed, 500 rpm stirring rate of feed and permeate and 20ºC permeate temperature. (Continuation)

In Fig. 4.4.10, it can be seen that a slight increase of D_e was observed with the increase of the feed temperature (Fig. 4.4.10). However, a significant drop on water vapor permeability of the ENMs with the increase of their thickness was detected. It is to point out that the water vapor permeability of the PVDF ENMs prepared in this study with an electrospinning time lower than 2h is greater than that of the PVDF Millipore membranes (GVHP, HVHP) and Sartorious (PTFE) membrane reported by Phattaranawik et al. [33,52]. However, the water vapor permeability of the ENMs is similar to that of Gelman membranes (PTFE supported on polypropylene PP net: TF200, TF450 and TF1000 having 0.2, 0.45 and 1 μm mean pore size, respectively; 80% porosity, 178 μm total thickness and 110 μm thickness of the PP support [34,40,55]) found by Martínez et al. [41] and Khayet et al. [34], and the permeability of the

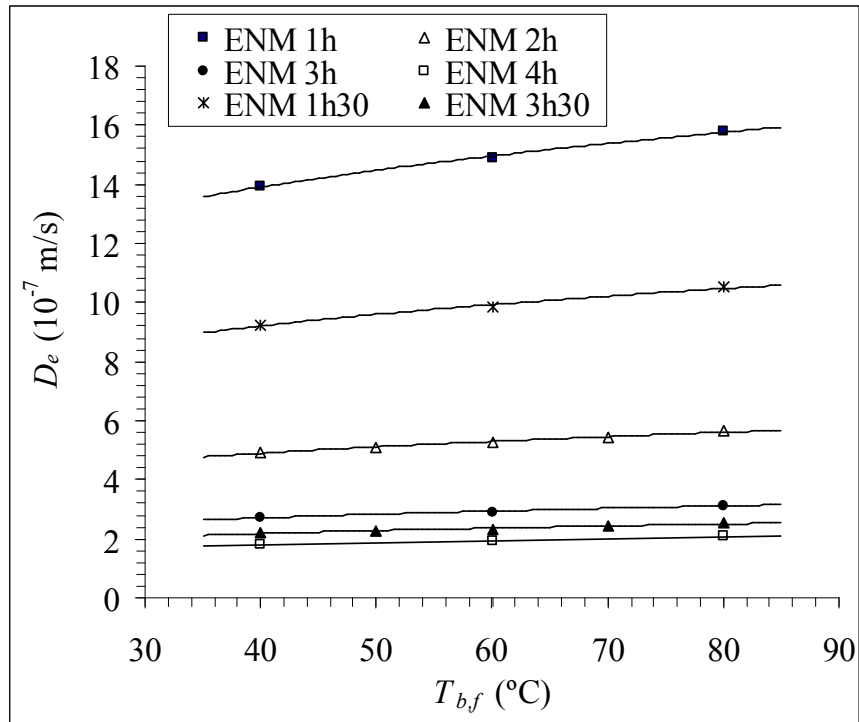fabricated porous hydrophobic/hydrophilic composite membranes by surface modifying macromolecules (SMMs) [55].

Figure 4.4.10. Effective diffusion coefficient (D_e) of the PVDF ENMs as a function of distilled water feed temperature ($T_{b,f}$).

When salt concentration is increased in the feed aqueous solution, the water production rate through ENMs was reduced [7]. This is expected since the chemical potential of water between both sides of the ENM is decreased, taking into account that the chemical potential depends on both temperature and concentration of solutes in water. Figure 4.4.11 shows the predicted and experimental DCMD permeate flux of different ENMs for different feed temperatures and salt concentrations as well as the effect of the feed concentration on the thermal efficiency. The corresponding salt rejection factors of the ENMs were found to be greater than 99.39% and in general very small variations of the salt rejection factor were detected with the feed temperature and NaCl concentration [7]. As can be seen in Fig. 4.4.11, the agreement between the predicted

and the experimental permeate fluxes is reasonably good and it is better for thicker ENMs (i.e. lower permeate fluxes). This may be attributed to the experimental error due to the high water production rate of thin ENMs.
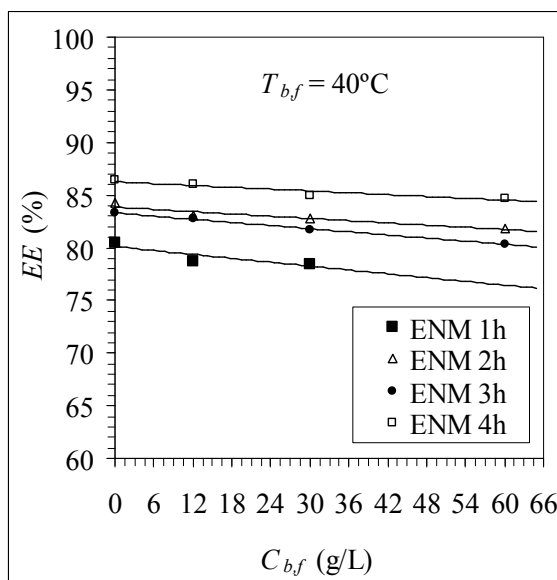
For all PVDF ENMs, the thermal efficiency decreases with the increase of the salt concentration in the feed aqueous solution up to 60 g/L (Fig. 4.4.11(c)). This is due to the reduction of the vaporization heat associated with the permeate flux of the ENMs (Q_v) as shown in Fig. 4.4.11(d). Similar results were reported for commercial membranes but with low *EE* values (< 58%) [35,36].

The concentration polarization coefficient (β) and the vapor pressure polarization coefficient (ψ) were evaluated using Eq. (4.4.10) and Eq. (4.4.11), respectively. Some results are shown in Fig. 4.4.12. For all ENMs, when the feed temperature is increased, both ψ and θ decrease whereas β increases and its enhancement is stronger at high feed temperatures and low δ values. This is because the temperature polarization effect is more dominant compared to the concentration polarization effect. The contribution of the concentration polarization to the vapor pressure polarization effect is less than 2%, and this contribution is small for low NaCl feed concentrations. When using a commercial shell-and-tube capillary PP membrane (MD020CP2N, Mycrodyn), Khayet et al. [56] also observed that the global temperature polarization coefficient in DCMD was slightly lower than the global vapor pressure polarization coefficient confirming the small contribution of the concentration polarization effect. Lawson and Lloyd [31] also observed an increase of β with the increase of the feed temperature and only a slight variation of θ was detected as the feed concentration was increased.
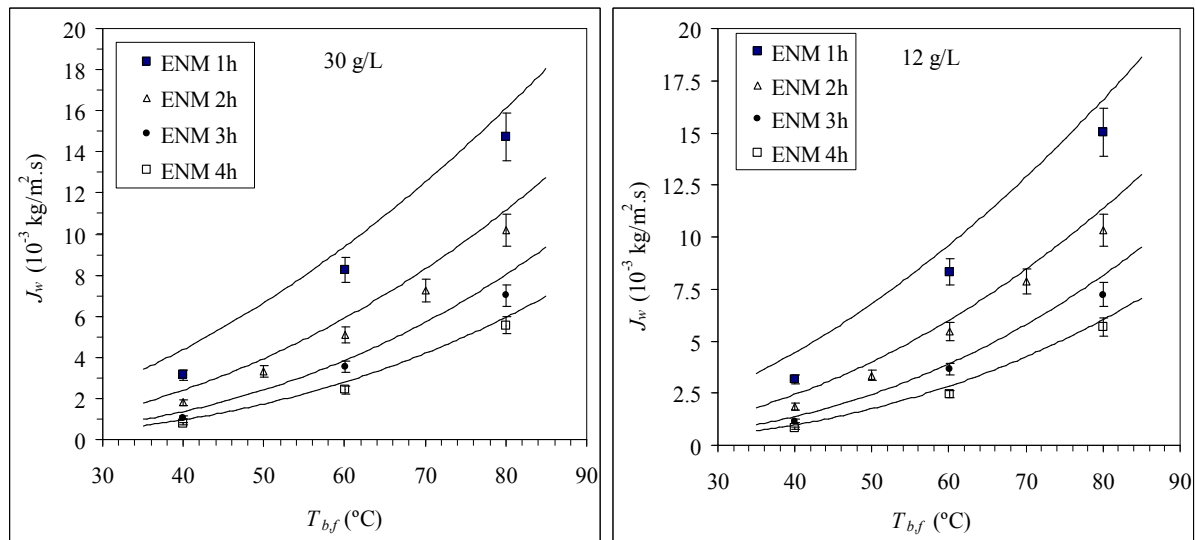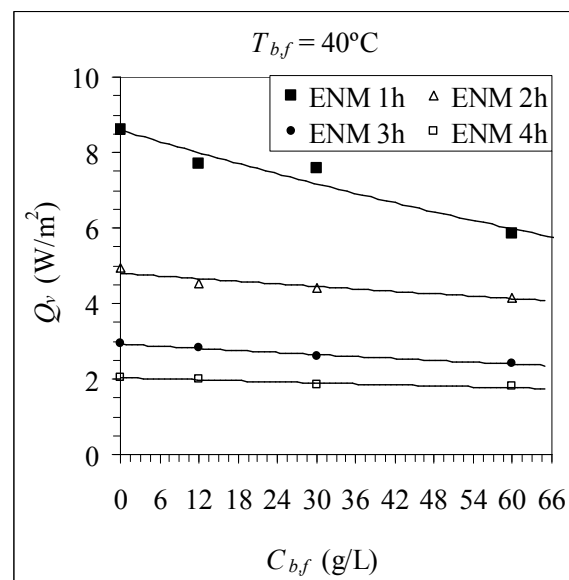
Figure 4.4.11. Predicted and experimental DCMD permeate flux (J_w) of different ENMs at different feed temperatures ($T_{b,f}$) and NaCl concentrations ($C_{b,f}$): 12 g/L (a) and 30 g/L (b); and effects of $C_{b,f}$ on the thermal efficiency (*EE*) and on the heat transfer due to mass transfer (Q_v) at a feed temperature ($T_{b,f}$ = 40ºC). The stirring rate of the feed and permeate liquids is 500 rpm and the permeate temperature is 20ºC.

The coefficient ψ represents the reduction in the driving force due to the heat and mass boundary layers resistances in both the feed and permeate sides of the ENMs. As it was observed for the coefficient θ (Fig. 4.4.8(a)) ψ also increases with the increase of δ of the ENMs (Fig. 4.4.12(c)). The coefficients ψ and θ are low for the ENMs exhibiting high permeate fluxes. On the contrary, β decreases with the increase of δ tending to asymptotic values, which are small for low feed temperatures (Fig. 4.4.12(c)). Furthermore, it was observed that the feed salt concentration practically did not affect ψ (Fig. 4.4.12(d)). It is found for all tested feed temperature range (40ºC – 80ºC) that ψ values range between 20.9 and 88.7% (i.e. 22.0-88.7% for 12 g/L, 21.6-88.6% for 30 g/L and 20.9-88.4% for 60 g/L). ψ is high for ENMs exhibiting low water production rates (Fig. 4.4.12(b) and Fig. 4.4.12(c)), while for each ENM it decreases with the increase of the feed temperature. As it was indicated previously, it is better to operate under high feed temperatures in order to increase the thermal efficiency.
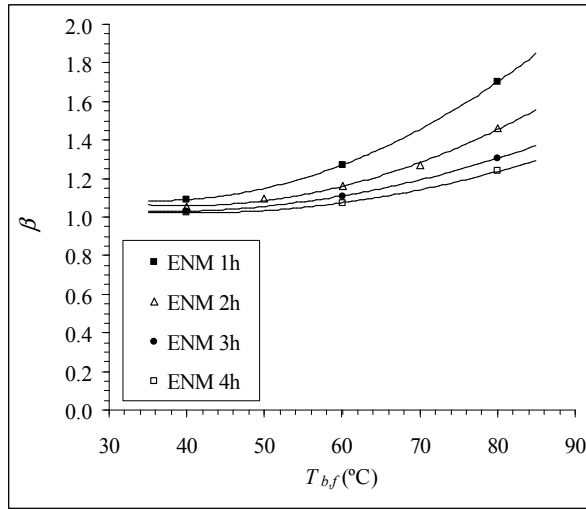
(a)
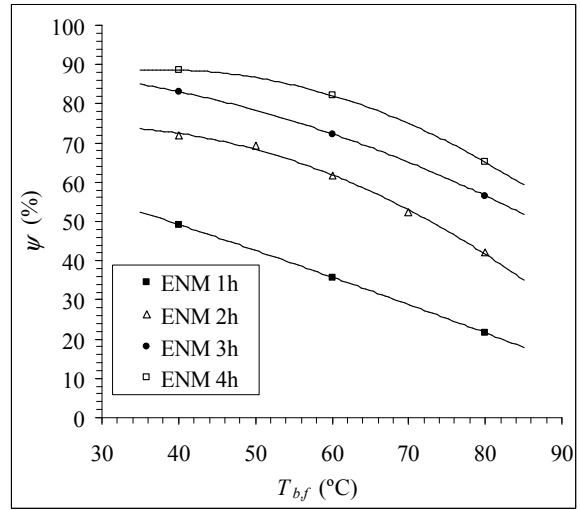
(b)
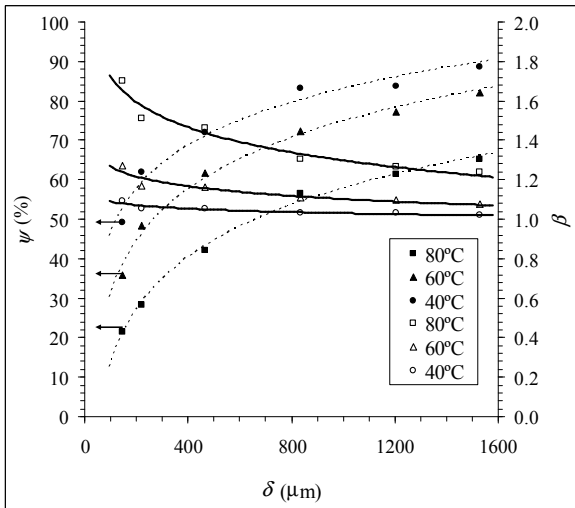
(c)
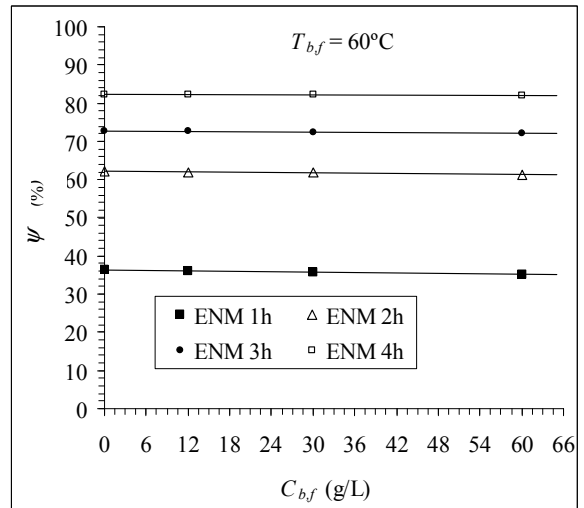
(d)

Figure 12. Concentration polarization coefficient (β) and vapor pressure polarization coefficient (ψ) of PVDF ENMs at different feed temperatures ($T_{b,f}$) and 30 g/L NaCl feed concentration (a,b,c) and different feed NaCl concentrations at $T_{b,f}$ = 60ºC (d). The plotted solid lines are only a guide to the eye. The stirring rate of the feed and permeate liquids is 500 rpm and the permeate temperature is 20ºC.

400

4.4.5. Conclusions

The kinetic theory of gases through porous media can be applied also to water vapor transport through ENMs. The size of the fibers, the inter-fiber space of the ENM and the applied MD operating conditions play important roles in determining the mechanism(s) of vapor transport through ENMs. Because of the web configuration of ENMs, collisions occur between water vapor molecules and nanofibers together with collisions between water vapor molecules and each others and between water vapor molecules and air present inside the void volume space of the ENMs. Knudsen diffusion (D_k) was found to be 17.9 to 37.4 times greater than molecular diffusion (D_M) and for each ENM D_k decreases slightly with the increase of the feed temperature, whereas a small enhancement was observed for D_M. The contribution of Knudsen diffusion to mass transfer was found to vary between 0.29 and 0.4 and increases with the ratio of the mean fiber diameter to the size of the inter-fiber space (d_f/d_i).

The theoretical model showed reasonably good correlation between the predicted and the experimental permeate DCMD fluxes of the PVDF ENMs over a wide range of feed temperature and salt concentration. The model can be applied to predict the DCMD permeate flux of other ENMs prepared with other polymers and electrospinning conditions.

A temperature polarization coefficient (θ) of up to 90% was achieved in this study for the ENM 4h. This value is higher than those reported so far in the DCMD literature. Moreover, the thermal efficiency (EE) was found to be greater than 78.8% for all PVDF ENMs and it is greater for higher feed temperatures. Again, the obtained EE values of the ENMs are higher than those reported in the DCMD literature. In addition, the heat transfer by conduction through the PVDF ENMs (Q_c) was found to be less than 20% of the total heat transferred through each ENM (Q_m).

For all ENMs, when the feed temperature was increased, both the vapor pressure polarization coefficient (ψ) and the temperature polarization coefficient (θ) decrease whereas the concentration polarization coefficient (β) increases and its enhancement is stronger at high feed temperature and low thickness of the ENMs. These indicate that the temperature polarization effect is more dominant compared to the concentration polarization effect. The contribution of the concentration polarization to the vapor pressure polarization effect was found to be less than

401

2%, and this contribution is low for low NaCl feed concentrations. Furthermore, it was observed that the feed salt concentration practically did not affect ψ.

Nomenclature

Symbols

a	activity or characteristic constant in Eq. (4.4.6)
c	salt concentration (g/L)
d_i	mean size of inter-fiber space (µm)
d_f	mean size of fiber diameter (µm)
D	diffusion coefficient (m/s)
EE	thermal efficiency (%)
h	heat transfer coefficient (W/m^2.K)
H	overall heat transfer coefficient (W/m^2.K)
J_w	DCMD permeate flux (g/m^2.s)
k	thermal conductivity (W/m.K)
k_s	mass transfer coefficient (m/s)
K_n	Knudsen number
LEP	liquid entry pressure of water (Pa)
Nu	Nusselt number
M_w	molecular weight of water (g/mol)
P	total pressure (Pa)
P_a	air pressure (Pa)
Pr	Prandtl number
Q	heat flux (W/m^2)
R	gas constant (J/mol.K)
T	temperature (ºC)
x	mole fraction
Sc	Schmidt number
Sh	Sherwood number
Re	Reynolds number

Greek letters

α	contribution of Knudsen diffusion to mass transfer
β	concentration polarization coefficient
δ	thickness (µm)
ε	void volume fraction (%)
λ	mean free path (nm)
μ	dynamic viscosity (kg/m.s)
θ	temperature polarization coefficient (%)
θ_a	water contact angle (°)
τ	pore tortuosity
ΔH_v	latent heat of vaporization (kJ/mol)
Δp	vapor pressure difference (Pa)
γ	activity coefficient
ψ	vapor pressure polarization coefficient (%).

Subscript

b	bulk
c	conduction
f	feed
g	gas
m	membrane
p	permeate or pore
s	solute
v	vapor
w/a	water vapor in air
K	Knudsen
M	molecular
w	water

Superscripts

b	characteristic constant in Eq. (4.4.6)
c	characteristic constant in Eq. (4.4.6)
d	characteristic constant in Eq. (4.4.6)
0	pure water

References

[1] M. Khayet, Membranes and theoretical modeling of membrane distillation: a review, Adv. Colloid Interface Sci., 164(1-2) (2011) 56-88.

[2] M. Khayet, T. Matsuura, Membrane Distillation: Principles and Applications, Elsevier, The Netherlands, 2011.

[3] M. Khayet, M.C. García-Payo, Nanostructured Flat membranes for Direct Contact Membrane Distillation. PCT/ES2011/000091, WO/2011/117443 (2011).

[4] C. Feng, K.C. Khulbe, T. Matsuura, R. Gopal, S. Kaur, S. Ramakrishna, M. Khayet, Production of drinking water from saline water by air-gap membrane distillation using polyvinylidene fluoride nanofiber membrane, J. Membr. Sci., 311 (2008) 1-6.

[5] C. Feng, K.C. Khulbe, S. Tabe, Volatile organic compound removal by membrane gas stripping using electro-spun nanofiber membrane, Desalination, 287 (2012) 98-102.

[6] J.A. Prince, G. Singh, D. Rana, T. Matsuura, V. Anbharasi, T.S. Shanmugasundaram, Preparation and characterization of highly hydrophobic poly(vinylidene fluoride)-clay nanocomposite nanofiber membranes (PVDF-clay NNMs) for desalination using direct contact membrane distillation, J. Membr. Sci., 397-398 (2012) 80-86.

[7] M. Essalhi, M. Khayet, Self-sustained webs of polyvinylidene fluoride electrospun nanofibers at different electrospinning times: 1. Desalination by direct contact membrane distillation, J. Membr. Sci., 433(2013) 167-179.

[8] Z.M. Huang, Y.Z. Zhang, M. Kotaki, S. Ramakrishna, A review on polymer nanofibers by electrospinning and their applications in nanocomposites, Composites Sci. & Tech., 63 (2003) 2223-2253.

[9] D. Li, Y. Xia, Electrospinning of nanofibers: Reinventing the Wheel?, Adv. Materials, 16 (2004) 1151-1170.

[10] I.S. Chronakis, Novel nanocomposites and nanoceramics based on polymer nanofibers using electrospinning process: A review, Mat. Proc. Tech., 167 (2005) 283-293.

[11] M. Bognitzki, W. Czado, T. Frese, A. Schaper, M. Hellwig, M. Steinhart, A. Greiner, J.H. Wendorff, J.H. Wendorf, Nanostructured fibers via electrospinning, Adv. Materials, 13 (2001) 70-72.

[12] S. Megelski, J.S. Stephens, D.B. Chase, J.F. Rabolt, Micro- and nanostructured surface morphology on electrospun polymer fibers, Macromolecules, 35 (2002) 8456-8466.

[13] X. Wang, C. Drew, S.H. Lee, K.J. Senecal, J. Kumar, L.A. Samuelson, Electrospun nanofibrous membranes for highly sensitive optical sensors, Nano Lett., 2 (2002) 1273-1275.

[14] S.S. Choi, Y.S. Lee, C.W. Joo, S.G. Lee, J.K. Park, K.S. Han, Electrospun PVDF nanofiber web as polymer electrolyte or separator, Electrochimica Acta, 50 (2004) 339-343.

[15] Z. Ma, M. Kotaki, S. Ramakrishna, Electrospun cellulose nanofiber as affinity membrane, J. Membr. Sci., 265 (2005) 115-123.

[16] R. Gopal, S. Kaur, Z. Ma, C. Chan, S. Ramakrishna, T. Matsuura, Electrospun nanofibrous filtration membrane, J. Membr. Sci., 281 (2006) 581-586.

[17] R.S. Barhate, S. Ramakrishna, Nanofibrous filtering media: Filtration problems and solutions from tiny materials: Review, J. Membr. Sci., 296 (2007) 1-8.

[18] L.F. Dumée, K. Sears, J. Schütz, N. Finn, C. Huynh, S. Hawkins, M. Duke, S. Gray, Characterization and evaluation of carbon nanotube Bucky-Paper membranes for direct contact membrane distillation, J. Membrane Sci., 351 (2010) 36-43.

[19] X. Yan, G. Liu, F. Liu, B.Z. Tang, H. Peng, A.B. Pakhomov, C.Y. Wong, Superparamagnetic tribloc copolymer/Fe_2O_3 hybrid nanofibers, Angew. Chem. Int. Ed., 40 (2001) 3593-3596.

[20] S. Borkar, B. Gu, M. Dirmyer, R. Delicado, A. Sen, B.R. Jackson, J.V. Badding, Polytetrafluoroethylene nano-microfibers by jet blowing, Polymer, 47 (2006) 8337-8343.

[21] R.G. Flemming, C.J. Murphy, G.A. Abrams, S.L. Goodman, P.F. Nealey, Effects of synthetic micro-and nano-structured surfaces on cell behavior, Biomaterials, 20 (1999) 573-588.

[22] T.A. Desai, Micro-and nanoscale structures for tissue engineering constructs, Med. Eng. & Physics, 22 (2000) 595-606.

[23] A. Curtis, C. Wilkinson, Nanotechniques and approaches in biotechnology, Trends Biotechn., 19 (2001) 97-101.

[24] H.G. Graighead, C.D. James, A.M.P. Turner, Chemical and topographical patterning for directed cell attachment, Curr. Opin. Solid State & Mater. Sci., 5 (2001) 177-184.

[25] C.T. Laurencin, A.M. Ambrosio, M.D. Borden, J.A. Cooper Jr., Tissue engineering: Orthopedic applications, Ann. Rev. Biomed. Eng. 1 (1999) 19-46.

[26] H. Li, Y. Ke, Y. Hu, Polymer nanofibers prepared by template melt extrusion, J. Appl. Polym. Sci., 99 (2006) 1018-1023.

[27] K.W. Lawson, D.R. Lloyd, Review: membrane distillation, J. Membr. Sci. 124 (1997) 1 - 25.

[28] M.E. Findley, V.V. Tanna, Y.B. Rao, C.L. Yeh, Mass and heat transfer relations in evaporation through porous membranes, AIChE J., 15 (1969) 483 - 489.

[29] R.B. Evans, G.M. Watson, E.A. Mason, Gaseous diffusion in porous media at uniform pressure, J. Chem. Phys, 35(6) (1961) 2076-2083.

[30] R.W. Schofield, A.G. Fane, C.J.D. Fell, Gas and vapour transport through microporous membranes. I. Knudsen-Poiseuille transition, J. Membrane Sci., 53 (1990) 159-171.

[31] K.W. Lawson, D.R. Lloyd, Membrane distillation: II. Direct contact MD, J Membr. Sci., 120 (1996) 123 - 133.

[32] K.W. Lawson, D.R. Lloyd, Membrane distillation: I. Module design and performance evaluation using vacuum membrane distillation, J. Membr. Sci., 120 (1996) 111 - 121.

[33] J. Phattaranawik, R. Jiraratananon, A.G. Fane, Effect of pore size distribution and air flux on mass transport in direct contact membrane distillation, J. Membr. Sci., 215 (2003) 75 - 85.

[34] M. Khayet, A. Velázquez, J.I. Mengual, Modelling mass transport through a porous partition: effect of pore size distribution, J. Non Equilibr. Thermodyn., 29 (2004) 279 - 299.

[35] L. Martínez, J.M. Rodríguez-Maroto, On transport resistances in direct contact membrane distillation, J. Membr. Sci., 295 (2007) 28-39.

[36] S. Al-Obaidani, E. Curcio, F. Macedonio, G.D. Profio, H. Al-Hinai, E. Drioli, Potential of membrane distillation in seawater desalination: Thermal efficiency, sensitivity study and cost estimation, J. Membr. Sci., 323 (2008) 85-98.

[37] M. Khayet, M.P. Godino, J.I. Mengual, Modelling transport mechanism through a porous partition, J. Non-Equilb. Thermodyn., 26 (2001) 1 - 14.

[38] M. Su, M.M. Teoh, K.Y. Wang, J. Su, T.S. Chung, Effect of inner-layer thermal conductivity on flux enhancement of dual-layer hollow fiber membranes in direct contact membrane distillation, J. Membr. Sci., 364 (2010) 278-289.

[39] F. Laganà, G. Barbieri, E. Drioli, Direct contact membrane distillation: modelling and concentration experiments, J. Membr. Sci., 166 (2000) 1–11.

[40] L. Martínez, F.J. Florido-Díaz, A. Hernández, P. Prádanos, Characterization of three hydrophobic porous membranes used in membrane distillation: modelling and evaluation of their water vapor permeabilities, J. Membr. Sci., 203 (2002) 15 - 27.

[41] L. Martínez, F.J. Florido-Díaz, A. Hernández, P. Prádanos, Estimation of vapor transfer coefficient of hydrophobic porous membranes for applications in membrane distillation, Sep. Purif. Technol., 33 (2003) 45–55.

[42] J. Woods, J. Pellegrino, J. Burch, Generalized guidance for considering pore-size distribution in membrane distillation, J. Membr. Sci., 368 (2011) 124-133.

[43] M. Khayet, A.O. Imdakm, T. Matsuura, Monte Carlo simulation and experimental heat and mass transfer in direct contact membrane distillation, Int. J. Heat Mass Transfer, 53 (2010) 1249 - 1259.

[44] A.O. Imdakm, T. Matsuura, A Monte Carlo simulation model for membrane distillation processes: direct contact (MD), J. Membr. Sci., 237 (2004) 51 - 59.

[45] A.O. Imdakm, T. Matsuura, Simulation of heat and mass transfer in direct contact membrane distillation (MD): the effect of membrane physical properties, J. Membr. Sci., 262 (2005) 117 - 128.

[46] A.O. Imdakm, M. Khayet, T. Matsuura, A Monte Carlo simulation model for vacuum membrane distillation process, J. Membr. Sci., 306 (2007) 341 - 348.

[47] M. Essalhi, M. Khayet, Surface segregation of fluorinated modifying macromolecule for hydrophobic/hydrophilic membrane preparation and application in air gap and direct contact membrane distillation, J. Membr. Sci., 417-418 (2012) 163-173.

[48] W.G. Pollard, R.D. Present, On gaseous self-diffusion in long capillary tubes, Phys. Rev., 73 (1948) 762-774.

[49] E.A. Mason, A.P. Malinauskas, Gas Transport in Porous Media: The Dusty Gas Model, Elsevier, Amsterdam, 1983.

[50] R.S. Barhate, C.K. Loong, S. Ramakrishna, Preparation and characterization of nanofibrous filtering media, J. Membr. Sci., 283 (2006) 209-218.

407

[51] D. Singh, K.K. Sirkar, Desalination of brine and produced water by direct contact membrane distillation at high temperatures and pressures, J. Membr. Sci., 389 (2012) 380-388.

[52] J. Phattaranawik, R. Jiraratananon, A.G. Fane, Heat transport and membrane distillation coefficients in direct contact membrane distillation, J. Membr. Sci., 212 (2003) 177-193.

[53] M. Gryta, M. Tomaszewska, Heat transport in the membrane distillation process, J. Membr. Sci., 144 (1998) 211-222.

[54] H. Lee, F. He, L. Song, J. Gilron, K.K. Sirkar, Desalination with a cascade of crossflow hollow fiber membrane distillation devices integrated with a hollow fiber heat exchanger, AIChE J. 57(7) (2011) 1780-1795.

[55] M. Khayet, J.I. Mengual, T. Matsuura, Porous hydrophobic/hydrophilic composite membranes: Application in desalination using direct contact membrane distillation, J. Membrane Sci., 252 (2005) 101-113.

[56] M. Khayet, M.P. Godino, J.I. Mengual, Study of asymmetric polarization in direct contact membrane distillation, Sep. Sci. & Tech., 39 (2004) 125-147.

CHAPTER 5

GENERAL CONCLUSIONS AND FUTURE DIRECTIONS

IN MEMBRANE DISTILLATION (MD)

General Conclusions and Future Directions in Membrane Distillation (MD)

Contents:

5.1. General Conclusions

5.2. Future Directions in Membrane Distillation

5.3. General Conclusions in Spanish: (Conclusiones Generales)

5.4. Future Directions in Membrane Distillation in Spanish: (Futuras direcciones en la destilación en membrana)

5.1. General Conclusions

After more than forty five years of hard and continuous researches, recently membrane distillation (MD) technology begins to acquire industrial interests boosted by some companies such as Memsys, Memstill, Scarab Development AB, Keppel Seghers and Fraunhofer ISE.

Although MD is known 50 years ago, still there is no company in the market offering MD membranes and therefore the technology is still not fully used commercially. The used membranes are fabricated for other purposes, microfiltration and ultrafiltration, rather than for MD process. The offered membrane modules and pilot plants are expensive and most of the times are restricted to only some research groups for their further evaluations and experimental improvements at laboratory scale not for their industrial applications. The lack of the significant industrial application of MD technology is due to the lack of proper membranes and modules. Among the MD areas that are less studied are membrane engineering for preparation of improved and novel membranes. Therefore, the main objective of the present PhD. Thesis is to develop novel and advanced membranes for desalination by MD.

The main conclusions drawn from this PhD. Thesis are the followings:

* A novel flat-sheet composite hydrophobic/hydrophilic membrane was fabricated using a fluorinated surface modifying macromolecule (SMM) and the hydrophilic host polymer polyetherimide (PEI). During the polymer solution casting procedure, SMM migrated to the membrane surface rendering it more hydrophobic with small pore size and nodule size and low roughness parameters compared to the bottom membrane surface. It was observed that this type of membrane is more suitable for desalination by direct contact membrane distillation (DCMD) than for air gap membrane distillation (AGMD) and liquid gap membrane distillation (LGMD). The permeate flux of the composite hydrophobic/hydrophilic membrane in AGMD configuration reached a value of 14.9 $kg/m^2.h$ and the salt rejection factor was higher than 99.4 %. In general, The DCMD permeate flux is 2.7 – 3.3 times higher than the AGMD permeate flux.

* The high DCMD performance of the composite porous hydrophobic/hydrophilic membrane is due to various reasons: (i) the thin top hydrophobic layer that is the responsible of mass transport in DCMD, (ii) the contribution of the thick stagnant air

413

layer interposed between the membrane and the condensation surface in AGMD leading to an increase of the mass transfer resistance although there is a reduction of energy loss by heat conduction through membrane, and (iii) the physical mass transport through the membrane, which is Knudsen type of flow in the case of DCMD and Knudsen/molecular diffusion for AGMD due to the presence of the air gap space between the membrane and the cooling surface.

* A comparative MD study was carried out using the porous composite hydrophobic/hydrophilic membrane in LGMD and AGMD configurations under the same operation conditions. It was observed that this type of membrane is more suitable for desalination by LGMD. Compared to AGMD, the permeate flux is slightly higher (2.2 – 6.5 %) for the LGMD configuration due to: i)- the higher thermal conductivity of water compared to that of air resulting in a lower permeate temperature at the permeate side of the membrane and a higher transmembrane driving force, and ii)- the small established distance between the liquid/vapor interfaces at both side of the hydrophobic thin top-layer of the membrane because water penetrates inside the hydrophilic layer of the membrane. Reasonably high rejection factors (i.e. $99.81 > \alpha > 99.61\%$) were obtained for both MD configurations and the salt rejection factors were almost similar for both MD variants. The LGMD proved to be more attractive than AGMD for desalination when using bi-layered hydrophobic/hydrophilic membranes because of the obtained higher permeate flux and thermal efficiency of the LGMD and its lower specific internal heat loss.

* Because of the various spinning parameters involved in the dry/wet spinning method, a fractional factorial experimental design together with Box-Wilson steepest ascent method were applied for the first time to localize the adequate region of experimentation for the fabrication of defect-free hollow fibers and finally prepare an optimum hollow fiber membrane for desalination by DCMD (i.e. the highest product between the permeate flux and the salt rejection factor).

* Novel hollow fiber membranes were prepared with different concentrations of the copolymer poly(vinylidene fluoride-hexafluoropropylene), PVDF-HFP, and the additive polyethylene glycol (PEG) for desalination by MD. Changes of the hollow

fiber morphology and internal structure were detected with the variation of the PEG and the PVDF-HFP concentration in the spinning solution. When increasing the PVDF-HFP concentration it was observed an increase of both the internal and external diameters of the hollow fiber membranes and the liquid entry pressure of water in the pores, and a gradual decrease of the void volume fraction and the pore size of the internal and external surfaces of the hollow fibers. It was also observed an increase of the hollow fiber membrane thickness and the void volume fraction with increasing the PEG concentration in the spinning PVDF-HFP solution. The structural changes of the hollow fiber membrane were attributed to the variation of the coagulation rate of the PVDF-HFP solution with the variation of the PEG and PVDF-HFP concentrations. The DCMD permeate fluxes were greater for the hollow fiber membranes prepared with higher PEG concentration.

* The full factorial design and response surface methodology (RSM) were employed to fabricate electro-spun PVDF fibers with small diameters and narrow dispersions. The interaction effects of the electrospinning parameters were studied and Monte Carlo optimization method was applied to determine the optimum electrospinning operating conditions. These were 1.23 mL/h polymer flow rate, 24.1 kV electrical voltage and 27.7 cm air gap. The fabricated membrane applying the determined optimum electrospinning parameters was characterized by different techniques and applied for desalination by DCMD. The obtained permeate fluxes were more than 4.4 times greater than those reported so far for electrospun nanofibrous membranes used in MD and the salt rejection factors greater than 99.94%.

* Both beaded and bead-free electrospun micro- and nano-fibrous membranes (ENMs) were prepared for desalination by DCMD using different PVDF concentrations and the previously optimum electrospinning parameters. The observed different morphological structures of the ENMs were related to the viscosity and polymeric chain entanglements. The minimum concentration required for electrospinning uniform bead-free fibers was found to be slightly higher than 22.5 wt%. The optimum PVDF concentration was found to be 25 wt%. This ENM exhibits a DCMD permeate flux of 43.7 kg/m^2.h and 38.9 kg/m^2.h for distilled water and 30 g/L NaCl feed aqueous solution operating at a feed temperature of 80 ºC and a permeate temperature of 20 ºC. The NaCl rejection factor was higher than 99.99 %.

* Analysis of the PVDF ENMs thickness effect on the DCMD performance was also carried out. A considerable increase of both the thickness and the liquid entry pressure of water with the electrospinning time were observed, while only a slight enhancement was detected for the void volume fraction. In contrast, a considerable reduction of the size of inter-fiber space was detected and no significant changes were observed for the diameter of the electrospun fibers and the water contact angle. The size of the inter-fiber space and the liquid entry pressure of water are not uniform throughout the thickness of the ENMs. The permeate flux of the PVDF ENMs in DCMD configuration reached a value of 54.7 kg/m^2.h with a feed temperature of 80ºC and a permeate temperature of 20ºC, and the salt (NaCl) rejection factor was higher than 99.39%. The DCMD performance of the prepared PVDF ENMs is better than that of the fabricated flat sheet membranes used so far in desalination by DCMD.

* A new theoretical model that takes into consideration the parameters of the PVDF ENMs and the kinetic theory of gases through porous media was developed in order to predict the DCMD permeate flux of ENMs. Because of the web configuration of ENMs, collisions occur between water vapor molecules and nanofibers together with collisions between water vapor molecules and each other and between water vapor molecules and air present inside the void volume space of the ENMs. A variable contribution of Knudsen diffusion was considered and evaluated. This was found to vary between 0.29 and 0.4 and increases with the ratio of the mean fiber diameter to the size of the inter-fiber space. The theoretical model showed reasonably good correlation between the predicted and the experimental DCMD permeate flux of the PVDF ENMs over a wide range of feed temperature and salt concentration.

* The thermal efficiency of the ENMs was found to be greater than 78.8%. This value is higher than those reported in the DCMD literature. In addition, the heat transfer by conduction through the PVDF ENMs was found to be less than 20% of the total heat transferred through each ENM.

* The high DCMD performance and thermal efficiency of the PVDF ENMs together with their long-term DCMD stability indicate that the ENMs are attractive membranes for desalination.

5.2. Future Directions in Membrane Distillation

Innovative and advanced membranes for different MD applications and different MD configurations as well as membrane modules are demanded. More must be done in the field of fabrication of membranes and modules engineering for MD to bring this technology to significant industrial applications.

Further studies in the area of bi-layered or multi-layered porous composite hydrophobic/hydrophilic membranes using surface modifying macromolecules (SMMs) should be carried out not only for fabrication of novel flat sheet membranes both also hollow fiber membranes and electro-spun micro- and nano-fibrous membranes.

The effects of the gap widths on the performance of flat-sheet porous composite hydrophobic/hydrophilic membrane in liquid gap membrane distillation (LGMD) configuration should be investigated. It is well known that in air gap membrane distillation (AGMD) the water production rate increases with the decrease of the air gap width. However, an opposite trend was claimed for LGMD.

In order to increase further the permeate flux of PVDF-HFP hollow fiber membranes, experiments should be performed using other type of solvents and coagulants.

In order to reduce the thickness of the electro-spun membranes (ENMs) maintaining their mechanical properties, mixed matrix ENMs can be prepared using nano-aditives such as carbon nanotubes. In this case electrospinning time can be reduced leading to thinner ENMs with similar mechanical properties and higher MD permeate fluxes than those obtained in this PhD. Thesis.

Innovative and advanced bi-layered or tri-layered ENMs for desalination by DCMD and LGMD using different hydrophobic and hydrophilic polymers can be prepared by electrospinning or co-electrospinning.

In general, still MD researchers are looking for identification of new applications of MD process including integrated MD systems to other separation processes and renewable energy sources (e.g. new generation solar energy systems). Various propositions were indicated to improve the final product quantity and quality and reduce energy consumption of MD technology. Multi-staged MD configuration is one of the suggested propositions that may be beneficial for MD technology industrialization.

The principal challenges of MD are long term MD performance, scaling and fouling contamination of the membrane. Few studies are carried out in these fields. More researches are needed using different types of membranes and modules as well as different types of feed aqueous solutions and wastewaters.

Very few reference data are available on energy efficiency, economics, energy analysis and costs evaluations. The reported scattered values on water production costs and energy consumption of MD systems lead to confusion resulting therefore in a possible loss of confidence in this technology. Detailed energy and costs analysis must be included in the published energy and economic reports, even for the autonomous pilot plant based on renewable energy systems (solar energy, geothermal, etc.).

5.3. Conclusiones Generales

Después de más de cuarenta y cinco años de investigaciones continúas y a veces complicadas, recientemente la tecnología de la destilación en membrana (DM) comienza a adquirir intereses industriales impulsados por algunas empresas como Memsys, Memstill, Scarab Development AB, Keppel Seghers and Fraunhofer ISE.

Aunque la DM se conoce hace 50 años, todavía no hay ninguna empresa en el mercado que ofrece membranas DM, por lo que la tecnología no está implementada totalmente a nivel comercial. Las membranas empleadas son fabricadas para otros fines, para la microfiltración o la ultrafiltración y no para el proceso DM. Los módulos de membrana y las plantas piloto que se ofrecen son caros y en la mayoría de las veces sus usos se limitan sólo a algunos grupos de investigación para sus nuevas evaluaciones y mejoras experimentales a escala de laboratorio, no para sus aplicaciones industriales inmediatas. La falta de la aplicación industrial de la tecnología DM es atribuida a la falta de membranas y módulos adecuados. Entre las áreas de la DM que son menos estudiadas se encuentra la ingeniería de membranas cuyo objetivo es preparar membranas novedosas para las diferentes configuraciones DM. Por consiguiente, el objetivo principal de la presente Tesis Doctoral es el desarrollo de nuevas membranas para la desalación por DM.

Las principales conclusiones de esta Tesis Doctoral son las siguientes:

* Un nuevo tipo de membrana plana compuesta hidrófoba/hidrofílica fue fabricado por el simple método de inversión de fase, en una sola etapa, empleando una macromolécula modificadora de superficie fluorada (SMM) y un polímero hidrofílico polieterimida (PEI). Durante la formación de la membrana, la SMM migra a su superficie superior haciéndola más hidrófoba y reduciendo su tamaño de poro, nódulo y rugosidad en comparación con su superficie inferior. Se observó que este tipo de membrana es más adecuado para la desalación por destilación en membrana con contacto directo (DMCD) que para la destilación en membrana con cámara de aire (DMCA) o cámara de líquido (DMCL). El flujo de permeado de esta membrana compuesta hidrófoba/hidrofílica en la configuración DMCA alcanzó un valor de 14.9 kg/m^2.h y el factor de rechazo de sal fue mayor que 99.4%. En general, el flujo de

permeado de esta membrana en la configuración DMCD es 2.7 – 3.3 veces mayor que el flujo de permeado en la configuración DMCA.

* El alto rendimiento de la membrana hidrófoba/hidrófilica porosa compuesta utilizada en la configuración DMCD es debido a varias razones: (i) la delgada capa hidrófoba superior que es la responsable del transporte de masa en la DMCD, (ii) la contribución de la capa de aire estancado entre la membrana y la superficie de condensación en la configuración DMCA que aumenta la resistencia a la transferencia de masa, aunque existe una reducción de las pérdidas de energía por conducción de calor a través de la membrana, y (iii) el transporte de masa a través de la membrana, que es tipo Knudsen en el caso de la DMCD, y combinado Knudsen/Difusión molecular para la DMCA debido a la presencia de aire entre la membrana y la superficie de condensación.

* Se realizó un estudio comparativo utilizando la membrana compuesta porosa hidrófoba/hidrofílica en las configuraciones DMCL y DMCA bajo las mismas condiciones de operación. Se observó que esta membrana es más adecuada para la desalación por DMCL. En comparación con la DMCA, el flujo de permeado es ligeramente superior (2.2 – 6,5%) para la configuración DMCL debido a: i)- la alta conductividad térmica del agua en comparación con la del aire dando lugar a una temperatura en el permeado más baja y por consiguiente una mayor fuerza motriz, y ii) - la pequeña distancia establecida entre ambos lados de las interfaces líquido/vapor de la delgada capa superior hidrófoba de la membrana, ya que el agua producida en el permeado penetra dentro de la capa hidrófílica de la membrana. Los factores de rechazo de sales obtenidos fueron razonablemente altos para ambas configuraciones de DM (es decir, 99.81 > α > 99.61%) y fueron prácticamente similares para ambas modalidades de DM. La DMCL demostró ser más atractiva que la DMCA para la desalación cuando se usan membranas de doble capa hidrófoba/hidrofílicas debido a su alta tasa de producción de agua y su alta eficiencia térmica así como su baja pérdida específica de calor interno "*specific internal heat loss*".

* Debido a que diferentes parámetros intervienen simultáneamente en el método de hilatura por inversión de fase seco/mojado "dry/wet spinning", un diseño experimental factorial fraccionado Box-Wilson junto con el método de ascenso más rápido se

aplicaron por primera vez para localizar la región experimentación adecuada para la fabricación de fibras huecas sin defectos y finalmente preparar una membrana de fibra hueca óptima para la desalación por DMCD (es decir Valores más altos del producto, flujo de permeado y factor de rechazo de sal).

* Nuevas membranas de fibra hueca fueron preparadas con diferentes concentraciones del copolímero poli(fluoruro de vinilideno-hexafluoropropileno), PVDF-HFP y del aditivo polietilenglicol (PEG) para la desalación por DM. Se detectaron cambios de la morfología de la fibra hueca y de su estructura interna con la variación de la concentración de PEG y de PVDF-HFP en la disolución copolimérica. Cuando se incrementa la concentración de PVDF-HFP, se observó un aumento de los diámetros internos y externos de las fibras huecas, un incremento de la presión de entrada de agua en sus poros y una disminución gradual de la fracción de volumen vacío y tamaño de poro de las superficies internas y externas. También se observaron aumentos del espesor de las membranas de fibra hueca y de su fracción de volumen vacío con el aumento de la concentración de PEG en la disolución copolimérica de PVDF-HFP. Los cambios estructurales de la membrana de fibra hueca fueron atribuidos a la variación del ritmo de coagulación de la disolución de PVDF-HFP con la variación de las concentraciones de PEG y PVDF-HFP. Los flujos de permeado de DMCD fueron mayores para las membranas de fibra hueca preparadas con mayor concentración de PEG.

* El diseño factorial completo "*full factorial design*" y la metodología de superficie de respuesta "*response surface methodology*, RSM" fueron empleados para fabricar fibras electro-hiladas de PVDF con diámetros pequeños y estrechas dispersiones. Se estudiaron los efectos de interacción de los parámetros de electro-hilatura "*electro-spinning*" y se aplicó el método de optimización Monte Carlo para determinar las condiciones óptimas de electro-hilatura. Éstos fueron un caudal de la disolución polimérica de 1,23 mL/h, un voltaje eléctrico de 24,1 kV y un hueco de aire entre la aguja y el colector de 27,7 cm. La membrana fabricada aplicando estos parámetros óptimos fue caracterizada por medio de diferentes técnicas y finalmente aplicada en la desalación por DMCD. Los flujos de permeado obtenidos fueron más de 4.4 veces mayor que los flujos de permeado reportados hasta la fecha en la literatura para las membranas nano-fibrosas electro-hiladas y utilizadas en la DM. Los factores de rechazo

de sal de la membrana nano-fibrosa fabricada aplicando los parámetros óptimos fueron superiores a 99,94%.

* Se prepararon membranas nano- y micro-fibrosas (ENMs) con o sin defectos "*beads*" para la desalación por DMCD utilizando diferentes concentraciones de PVDF y aplicando los parámetros óptimos de electro-hilatura previamente determindado. Las diferentes estructuras morfológicas de las ENMs observadas fueron relacionadas con la viscosidad y el entrelazamiento de las cadenas poliméricas. La concentración de PVDF mínima para la fabricación de fibras libres de defectos "*beads*" y uniformes resultó ser ligeramente superior a 22,5% en peso. La concentración óptima de PVDF en la disolución polimérica fue de 25% en peso y la correspondiente membrana ENM exhibe unos flujos de permeado de 43,7 kg/m^2.h y 38,9 kg/m^2.h para agua destilada y una solución acuosa de 30 g/L de NaCl como alimento operando a una temperatura de 80 ºC y una temperatura de permeado de 20 ºC. Su factor de rechazo NaCl fue superior a 99,99%.

* Se llevó a cabo un estudio sistemático del efecto del espesor de las membranas ENMs de PVDF sobre el rendimiento de la DMCD. Se observó un aumento considerable tanto del espesor de las membranas ENMs como de su presión de entrada de agua con el incremento del tiempo de electro-hilatura; mientras que la fracción de volumen vacío vio solamente un leve aumento. En cambio, se detectó una considerable reducción del tamaño del espacio entre fibras y no se observaron cambios significativos del diámetro de las fibras y de los ángulos de contacto para el agua. El tamaño del espacio entre fibras y la presión de entrada de agua no son uniformes a lo largo de todo el espesor de las membranas ENMs. El flujo de permeado de las membranas ENMs de PVDF en la configuración DMCD alcanzó un valor de 54,7 kg/m^2.h para una temperatura de alimentación de 80 ºC y una temperatura de permeado de 20 ºC, y el factor de rechazo de sal (NaCl) fue superior a 99.39%. El rendimiento de las membranas ENMs de PVDF preparadas en este trabajo para la DMCD es mejor que el rendimiento de las membranas planas fabricadas hasta el momento para la desalación por DMCD.

* Se desarrollo un nuevo modelo teórico que tiene en consideración los parámetros de las membranas ENMs de PVDF y la teoría cinética de gases a través de medios porosos para predecir los flujos de permeado de la DMCD. Debido a la red de nano-fibras de las

membranas ENMs, las colisiones ocurren por un lado entre moléculas de vapor de agua y las nano-fibras y por otro entre moléculas de vapor de agua y las demás y entre las moléculas de vapor de agua y el aire atrapado en el espacio de volumen vacío de las membranas ENMs. Una contribución variable de la difusión tipo Knudsen fue considerada en el modelo y evaluada. Esta contribución varía entre 0,29 y 0,4 y aumenta con la razón que existe entre el diámetro medio de las fibras y el tamaño del espacio entre fibras. El modelo teórico desarrollado mostró un acuerdo razonable entre el flujo de permeado calculado y el flujo experimental en un amplio intervalo de temperaturas de alimentación y concentraciones.

* La eficiencia térmica de las membranas ENMs fue mayor que 78,8%. Este valor es superior a los publicados en la literatura para la DMCD. Además, la transferencia de calor por conducción a través de estas membranas ENMs fue inferior al 20% del calor total transferido a través de cada membrana ENM.

* El alto rendimiento y eficiencia térmica de las membranas ENMs de PVDF junto con su estabilidad a largo tiempo en la DMCD indican que estas membranas son atractivas para la desalación.

5.6. Futuras direcciones en la destilación en membrana

Membranas innovadoras y avanzadas para las diferentes aplicaciones y configuraciones de la DM, así como los módulos de membrana son muy demandados. Más investigación se debe realizar en el campo de la fabricación de membranas y la ingeniería de módulos para la DM con el objetivo de llevar esta tecnología a aplicaciones industriales importantes.

Más estudios deben llevarse a cabo en el área de membranas bi-capa porosas compuestas hidrófoba/hidrofílicas o de múltiples capas utilizando las macromoléculas modificadoras de superficie (SMMs), no solamente para la fabricación de nuevas membranas planas pero también de fibras huecas y membranas micro- y nano-fibrosas por electro-hilatura (ENMs).

El efecto del espesor de la cámara de agua en el rendimiento de la membrana plana porosa compuesta hidrófoba/hidrofílica utilizada en la configuración (DMCL) debe ser investigada. Es bien sabido que en la configuración (DMCA) la tasa de producción de agua aumenta con la disminución de la anchura del espacio de aire estancado entre la membrana y la superficie condensadora. Sin embargo, una tendencia opuesta fue reclamada para la variante DMCL.

Para aumentar aún más el flujo de permeado de las membranas de fibra hueca de PVDF-HFP, se deben realizarse experimentos utilizando otro(s) tipo(s) de disolvente(s) y coagulante(s).

Con el fin de reducir el espesor de las membranas electro-hiladas (ENMs) manteniendo sus propiedades mecánicas, membranas ENMs de matriz mixta pueden ser preparadas usando nano-aditivos tales como los nanotubos de carbono. En este caso, el tiempo de electro-hilado puede reducirse dando lugar a membranas ENMs más delgadas con propiedades mecánicas parecidas y por consiguiente mayores flujos de permeado en la DM que los obtenidos en esta Tesis Doctoral.

Se pueden fabricar membranas ENMs innovadoras y avanzadas de doble o triple capas para la desalación por DMCD y DMCL utilizando diferentes polímeros hidrofóbicos e hidrofílicos por electro-hilatura o co-electro-hilatura.

En general, los investigadores todavía están buscando la identificación de nuevas aplicaciones de la tecnología DM, incluyendo sistemas integrados de DM a otros procesos de separación y fuentes de energías renovables (por ejemplo, sistemas de energía solar de última generación). Varias propuestas fueron indicadas para mejorar la calidad y la cantidad del producto final y reducir el consumo energético de la tecnología DM. La configuración DM de múlti-etapa es una de las proposiciones sugeridas que puede ser beneficiosa para la industrialización de la tecnología DM.

Los principales retos de la DM son el largo tiempo de funcionamiento, el incrustamiento y ensuciamiento de la membrana. Pocos son los estudios llevados a cabo en estos campos. Se necesitan más investigaciones empleando diferentes tipos de membranas y módulos así como diferentes tipos de disoluciones acuosas de alimentación y aguas residuales.

Se dispone de muy pocos datos bibliográficos sobre la eficiencia energética, la evaluación y análisis de costes económicos y energéticos. Los valores publicados sobre los costes de producción de agua y del consumo energético de sistemas DM son confusos llevando a una posible pérdida de confianza en esta tecnología. Un análisis detallado de costes energéticos y económicos deben incluirse en los artículos e informes publicados sobre costes y energía de la DM, incluso para las plantas piloto autónomas basadas en sistemas de energías renovables (energía solar, geotérmica, etc.).